Anil Pandey

Practical **Microstrip** and **Printed** Antenna Design

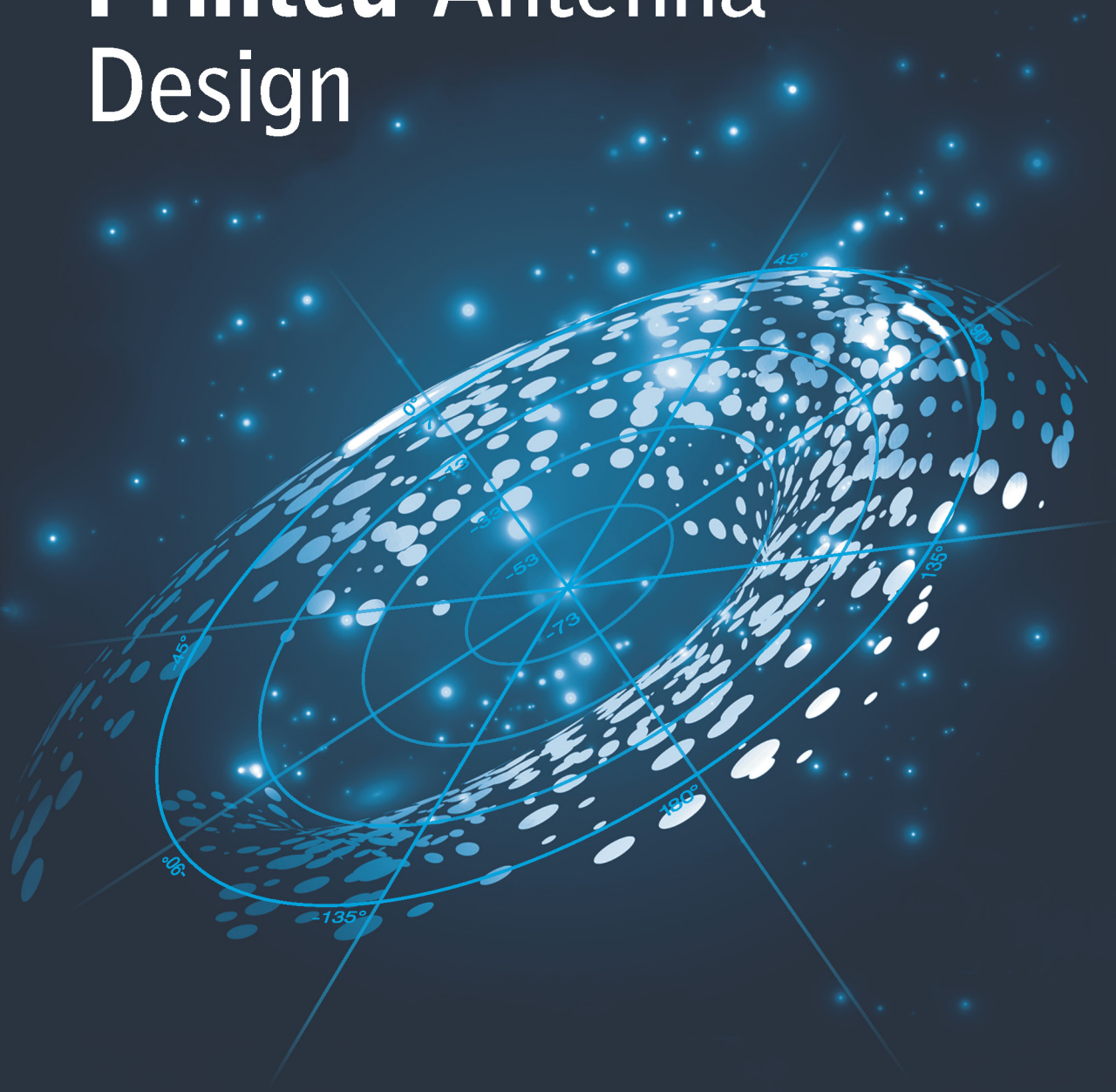

Practical Microstrip and Printed Antenna Design

For a listing of recent titles in the
Artech House Antennas and Electromagnetics Analysis Library,
turn to the back of this book.

Practical Microstrip and Printed Antenna Design

Anil Pandey

ARTECH HOUSE
BOSTON | LONDON
artechhouse.com

Library of Congress Cataloging-in-Publication Data
A catalog record for this book is available from the U.S. Library of Congress.

British Library Cataloguing in Publication Data
A catalog record for this book is available from the British Library.

ISBN-13: 978-1-63081-668-1

Cover design by John Gomes

© 2019 Artech House
685 Canton Street
Norwood, MA 02062

All rights reserved. Printed and bound in the United States of America. No part of this book may be reproduced or utilized in any form or by any means, electronic or mechanical, including photocopying, recording, or by any information storage and retrieval system, without permission in writing from the publisher.

All terms mentioned in this book that are known to be trademarks or service marks have been appropriately capitalized. Artech House cannot attest to the accuracy of this information. Use of a term in this book should not be regarded as affecting the validity of any trademark or service mark.

10 9 8 7 6 5 4 3 2 1

To my father and mother, B. P. Pandey and B .D. Pandey
and to my family, my wife Shraddha Pandey, my daughter Anushka Pandey,
and my son Atharva Pandey

Contents

Preface xvii

Acknowledgments xxi

CHAPTER 1

Printed Antennas 1

1.1 Introduction 1
1.2 Types of Printed Antennas 2
1.2.1 Microstrip Antenna 2
1.2.2 Slot Antenna 2
1.2.3 Inverted-F Antenna 3
1.2.4 Planar Inverted-F Antenna 3
1.2.5 Printed Dipole Antenna 4
1.2.6 Monopole Antenna 4
1.2.7 Printed Inductor Antenna 4
1.2.8 Printed Quasi-Yagi Antenna 5
1.2.9 Log-Periodic and Fractal Antenna 5
1.2.10 Customized Printed Antenna 6
1.2.11 Comparison of Planar Antennas 6
1.3 Important Specifications of Antenna Design 8
1.3.1 Operating Frequency 8
1.3.2 Impedance 8
1.3.3 Return Loss and VSWR 8
1.3.4 Radiation Pattern 9
1.3.5 Directivity and Gain 10
1.3.6 Antenna Efficiency 11
1.3.7 Bandwidth 11
1.3.8 Half-Power Beamwidth 11
1.3.9 Sidelobes 11
1.3.10 Polarization 11
1.4 Analysis and Simulation Software for Antenna Design 12
1.4.1 Transmission-Line Circuit Model 12
1.4.2 Cavity Model 12
1.4.3 Full-Wave Analysis Technique 13
1.4.4 Comparison between MOM, FEM, and FDTD 16
1.5 RF and Microwave Frequency Band and Applications 17

1.6 Overview of the Book 19
References 22
Selected Bibliography 24

CHAPTER 2
Microstrip Antenna Design 27
2.1 Introduction 27
2.2 Microstrip Antenna 27
2.2.1 Microstrip Antenna Working Principle 28
2.2.2 Microstrip Antenna Design Process 30
2.2.3 Radiating Element Design of Microstrip Antenna 31
2.2.4 Criteria for the Substrate Selection 32
2.2.5 Losses in Microstrip Antennas 33
2.3 Feed Techniques for Single-Element 34
2.3.1 Microstrip Line Feed 34
2.3.2 Coaxial Feed 35
2.3.3 Aperture-Coupled Feed 35
2.3.4 Proximity- or Electromagnetically Coupled Feed 36
2.4 Design and EM Simulation of Microstrip Antennas 37
2.4.1 Design Process 37
2.4.2 Feed-Point Location of a Single Patch Antenna 37
2.4.3 Microstrip Patch Antenna Design Parameters 38
2.4.4 Patch Antenna Design and Analysis Result at 2.4 GHz 39
2.4.5 Coaxial-Fed Patch Antenna for Coal Mines 40
2.5 Circularly Polarized Microstrip Patch Antennas 42
2.5.1 Single-Fed Circularly Polarized Patch Antenna 42
2.5.2 Dual-Orthogonal Fed Circularly Polarized Patch 44
2.6 Antenna Measurements 45
2.6.1 S-Parameter and Input Impedance 46
2.6.2 Radiation Pattern Measurements 47
2.7 Summary 47
References 48
Selected Bibliography 49

CHAPTER 3
Antenna Design for Wireless Communication and Mobile Phones 51
3.1 Introduction 51
3.2 Mobile Communication Standards 52
3.3 Mobile Phone Antennas 53
3.4 Multiband Antenna Design for Mobile Phones 54
3.4.1 Feeding Structures 54
3.5 Dual-Band Monopole Antenna Design for WLAN 55
3.5.1 Antenna Design 55
3.5.2 Mathematical Modeling 58
3.5.3 Antenna Design Parametric Study 59

3.5.4 Simulated Result of the Optimized Design 61
3.6 Inverted-F Bluetooth Antenna 63
3.7 LTE Band PIFA 65
3.8 MIMO Antenna Design for LTE Mobile Terminals 67
3.9 Mobile Antenna Performance with Components and Standard Anthropomorphic Model Head 70
3.9.1 Cross-Talk of Bluetooth Antenna with MIMO Antenna 71
References 73

CHAPTER 4

Smartphone Antenna Design Compliances and Measurement 77
4.1 Introduction 77
4.2 Design Challenges in Smartphone Systems 78
4.3 Smartphone Antenna Simulation Workflow 79
4.4 Smart Antenna System Using the MIMO and Diversity Technique 79
4.4.1 MIMO Antenna Configuration 80
4.4.2 Antenna Diversity 81
4.4.3 MIMO Antenna Design Challenges 82
4.4.4 Antenna Diversity Simulation and Measurement 83
4.4.5 Antenna Diversity Modeling 83
4.5 Mobile Phone Compliances and Measurement 86
4.5.1 EMC and EMI Compliance 86
4.5.2 HAC Compliance 86
4.5.3 SAR Compliance 87
4.6 HAC 87
4.6.1 M and T Ratings 88
4.6.2 HAC Measurement 88
4.7 SAR 89
4.7.1 SAR Testing 90
4.7.2 SAR Measurement 92
4.8 EMI and EMC in Mobile Phones 93
4.8.1 EMC Simulation Model 95
4.8.2 EMI Simulation Model 97
4.9 Summary 99
References 99
Selected Bibliography 101

CHAPTER 5

Reconfigurable Frequency and Polarization Diversity Antennas 103
5.1 Introduction 103
5.2 Reconfigurable Antennas 104
5.2.1 Electrically Reconfigurable Antenna 105
5.2.2 Frequency-Reconfigurable Antenna 105
5.2.3 Polarization Reconfigurable Antenna 105
5.2.4 Pattern Reconfigurable Antenna 106

5.2.5 Hybrid Reconfigurable Antenna 106
5.2.6 Antenna Switching Techniques 106
5.3 Reconfigurable Frequency and Polarization Antenna Design 107
5.3.1 Antenna Mathematical Modeling 110
5.3.2 Antenna Operating Principle and Results 113
5.4 Summary 116
References 117
Selected Bibliography 118

CHAPTER 6

Printed Antenna Arrays 121
6.1 Introduction 121
6.2 Microstrip Antenna Arrays 122
6.3 Array Antenna Radiating Elements 122
6.3.1 Linear Microstrip Arrays 123
6.3.2 Planar Microstrip Antenna Arrays 124
6.4 Feed Techniques for Array Antenna 124
6.4.1 Corporate Feed Network 125
6.4.2 Inline Series Feed Network 126
6.4.3 Multilayer Feed Network 127
6.4.4 Feed Network for Shaped Beam Pattern Arrays 129
6.4.5 Feed Network for Active Antenna Arrays 129
6.5 Printed Antenna Array Design for Rainfall Radar 129
6.5.1 Antenna Design Specifications 131
6.5.2 Design and Optimization of a Single Element 131
6.5.3 Design of the Corporate Feed Network 132
6.5.4 Planar Antenna Design 134
6.5.5 Complete Antenna Design and Simulation 136
6.5.6 Antenna Fabrication 137
6.5.7 Circular Aperture Array Antenna 138
6.6 Bandwidth Enhancement Technique of Microstrip Array Antenna 139
6.6.1 Edge-Coupled Patches 140
6.6.2 Multilayer Structure 140
6.7 Multilayer Antenna Design with Wideband Performance 141
6.8 Millimeter-Wave Antenna Array for Automotive Radar 142
6.8.1 Equivalent Model of a Series-Fed Antenna Array 143
6.8.2 Series-Fed Antenna Array Design 144
6.9 Conformal Printed Antennas 144
6.9.1 Patch Antenna Printed on Circular Cylindrical Structure 146
6.9.2 Antenna on Missile Surface 151
6.9.3 Conformal Microstrip Antenna Array Fed with Waveguide 152
6.10 Summary 154
References 154
Selected Bibliography 157

CHAPTER 7

Antenna Arrays for Microwave Sensing and Imaging 159

7.1 Introduction 159
7.2 Microwave Remote Sensing and Imaging 160
7.2.1 Microwave Remote-Sensing Frequency Bands 161
7.2.2 Antenna Polarization in Remote-Sensing Applications 162
7.3 SAR 162
7.3.1 Antenna Types Used in SAR Systems 164
7.4 Dual-Polarized SAR Antennas Design 164
7.4.1 Design of Microstrip Patch Radiator 166
7.4.2 Antenna Performance with Different Types of Slots 168
7.5 Array Antenna Design for X-Band SAR 169
7.5.1 The Design of the Feed Network 171
7.5.2 Antenna Performance Results 172
7.5.3 Coupling in Feed Lines 173
7.6 Summary 173
References 173
Selected Bibliography 174

CHAPTER 8

Airborne SAR Antenna Arrays 177

8.1 Introduction 177
8.2 SAR Antenna Pattern Synthesis 178
8.2.1 Cosecant Square Shaped Pattern 179
8.2.2 Woodward-Lawson Pattern Synthesis Technique 179
8.2.3 Theoretical Predicted Patterns 182
8.3 Design of Airborne SAR Antenna 183
8.3.1 SAR Antenna Design Flow and Methodology 183
8.3.2 SAR Antenna Design 184
8.3.3 Shaped Pattern BFN 185
8.3.4 Antenna Array Design Realization and Simulation 186
8.4 High-Power Feed Network Design 189
8.4.1 Rectangular Coaxial Line 189
8.4.2 Corona and Multipaction Breakdown in the High-Power Feed Network 190
8.4.3 Design of the Feed Network 191
8.4.4 High-Power Calculation of the SCL 196
8.5 Integrated Array Antenna Design 197
8.6 Summary 197
References 198
Selected Bibliography 199

CHAPTER 9

Multifrequency Shared-Aperture Microstrip Antenna Arrays 201

9.1 Introduction 201

9.1.1 SAR Imaging 202
9.2 Dual-Frequency Shared Aperture Antenna Array 204
9.3 Design of C-Band and X-Band Radiating Element 204
9.3.1 Design of Patch Antenna at C-Band 205
9.3.2 Design of the Slot Antenna at X-Band 205
9.4 Array Design 206
9.4.1 Design of the C-Band Linear Array 206
9.4.2 Design of the X-Band Linear Array 207
9.4.3 Integrated Array 208
9.5 Summary 209
References 210
Selected Bibliography 211

CHAPTER 10
Phased Array Antennas 213
10.1 Introduction 213
10.2 Phased Array Types 214
10.2.1 Passive Phased Arrays 214
10.2.2 Active Phased Arrays 216
10.2.3 Hybrid Phased Arrays 217
10.3 Phased Array Theory 218
10.3.1 Grating Lobes 221
10.4 Active Phased Array Antenna Design 222
10.4.1 Antenna Configuration 222
10.4.2 Dual-Polarized Feed Network 226
10.5 Planar Array Antenna Design 229
10.6 Measurement of Phased Array Antenna 230
10.6.1 Microwave Holography 231
10.7 Summary 232
References 232
Selected Bibliography 233

CHAPTER 11
Broadband Antennas 235
11.1 Introduction 235
11.2 Metamaterials 236
11.3 Antenna Designs Based on EBG 236
11.3.1 Microstrip Patch Antenna on Mushroom-Like-EBG Structure 239
11.3.2 Uniplanar EBG Cells with a Rectangular Microstrip Antenna 243
11.3.3 Bowtie Antenna with EBG Cells 244
11.3.4 Array Antenna Design Using EBG 245
11.4 FSS 247
11.5 Antennas on PBG 249
11.6 Fractal Antennas 253
11.6.1 Fractal Antenna Geometries 254
11.6.2 Sierpinski Gasket Fractal Antenna 254

11.6.3 Square Shape Fractal Antenna Design 256
11.6.4 Koch Snowflake Fractal Antenna 258
11.6.5 UHF Hilbert Antenna Array for Partial Discharge (PD) Detection 260
11.7 UWB Antenna 262
11.7.1 UWB Hexagonal Printed Monopole Antenna for GPR Systems 263
11.7.2 Broadband Rectangular Patch 264
11.7.3 Slot-Loaded Patch 265
11.7.4 Wideband Spiral Antenna for Software-Defined Ratio-Based Radar 267
11.7.5 UWB Vivaldi Antennas 267
11.8 Substrate-Integrated Waveguide Microstrip Patch Antenna for Radar Applications 269
11.9 Summary 272
References 272
Selected Bibliography 274

CHAPTER 12

Modern Printed Antennas Design Trends and Applications 277

12.1 Introduction 277
12.2 RFID Antennas 278
12.2.1 RFID System Working Principle 278
12.2.2 RFID Frequency Band Allocation 279
12.2.3 RFID Antennas 279
12.2.4 RFID Tag Antenna Design 280
12.2.5 Fat-Tag or Dog-Bone RFID Antenna 282
12.2.6 RFID Printed Tag Antenna on Hydrophobic Paper 282
12.2.7 Reader Antenna 283
12.2.8 RFID Read Range Calculation 286
12.3 Radio Navigation Satellite System Antennas 287
12.3.1 RNSS Frequency Bands 288
12.3.2 Antennas for RNSS 288
12.3.3 GPS Spiral Antenna Design 290
12.3.4 Sine-Wave Meander Archimedean Spiral Antenna 293
12.4 Printed Antennas for Medical Applications 294
12.4.1 Antenna Design for Wireless Body Area Network (WBAN) 296
12.5 IoT Antennas 298
12.5.1 Low-Power Wide Area Network (LPWAN) IoT Antenna Design 299
12.5.2 Quasi-Yagi IoT Antenna Design 300
12.6 Summary 302
References 302
Selected Bibliography 304

CHAPTER 13

Automotive Antennas 305

13.1 Introduction 305
13.2 Frequency-Modulated Continuous-Wave Automotive Radar System 306
13.3 Automotive Antenna Design Requirements 308

13.4 Antennas for Automotive Radars 310
13.4.1 Low-Frequency Automobile Antennas 311
13.4.2 High-Frequency Automobile Antennas 311
13.5 Automotive Glass-Mounted FM/DAB Antennas 312
13.6 Shark-Fin Antenna 313
13.6.1 LTE/GSM Antenna Design 315
13.6.2 GPS Antenna 316
13.6.3 WLAN Antenna 317
13.7 Grid Array Antenna for 24-GHz Automotive SRR 318
13.7.1 Microstrip Comb-Line Antenna Arrays for LRR 320
13.7.2 Amplitude Tapered Antenna Array 322
13.7.3 Amplitude Tapered 45° Antenna Array 324
13.8 Planar Array for Millimeter-Wave Automotive Radar 325
13.8.1 ACC Radar System Requirements 326
13.8.2 ACC Radar Antenna Design 327
13.8.3 Rotman Lens Design for Electronic Scanning of the Antenna Beam 328
13.9 Automotive System-Level Simulation 331
13.10 Antenna Array for the ETC System 332
13.10.1 Phased Array Antenna for ETC Application at 5.8 GHz 333
13.11 Summary 336
References 336
Selected Bibliography 338

CHAPTER 14

Transceiver for Phased Array Radar 341

14.1 Introduction 341
14.2 TRM Architecture 342
14.3 TRM Design and Simulation 344
14.3.1 MMIC LNA Design 346
14.3.2 PA Design 349
14.3.3 MMIC SPDT Switch Design 351
14.3.4 LTCC LPF 355
14.3.5 A 6-Bit MMIC Phase Shifter 357
14.3.6 Antenna with TRM 359
14.4 Design of Phased Array Radar Using the Transceiver Module 360
14.5 Summary 361
References 362
Selected Bibliography 363

CHAPTER 15

Phased Array and BFN for 5G Communication Systems 365

15.1 Introduction 365
15.2 5G Communication System 366
15.2.1 Massive MIMO and Antenna Technologies 367
15.2.2 MIMO Antennas for Picocells 368
15.2.3 Spectrum for 5G Communication 369

15.2.4 Path Loss Model in a Cellular Cell 369
15.2.5 The 60-GHz Spectrum for 5G Application 370
15.3 Millimeter-Wave 5G BFN 371
15.3.1 A 3-dB Hybrid Coupler Design 373
15.3.2 The 0-dB Crossover Design 373
15.3.3 The 22.5°, 45°, and 67.5° Phase Shifter Designs 374
15.3.4 The 8 × 8 BFN Design 374
15.4 A 60-GHz Microstrip Antenna Array Design 375
15.5 Phase Array System 377
15.6 FD-MIMO 378
15.7 FD-MIMO Phased Array System 379
15.8 5G Communication System Design 379
15.9 The 5G Phased Array System Design 383
15.9.1 System-Level Design and Simulation 383
15.9.2 Antenna Design and Simulation 385
15.9.3 RF Circuit Design and Simulation 386
15.10 System Validation and Test 388
15.11 Massive MIMO Based on Digital Beamforming 390
15.12 Summary 392
References 393
Selected Bibliography 394

Appendix A
Important Antenna and Electromagnetics Formulas 397
A.1 Maxwell's Equations 397
A.2 Microstrip Antenna Radiation Pattern and Directivity 397
A.3 Antenna Bandwidth Calculation 399
A.4 Constants 400

Appendix B
Designed Antenna Project List 401

Acronyms and Abbreviations 403

About the Author 407

Index 409

Preface

The purpose of this book is to provide a practical antenna design guide to cover various real-world applications for those attempting to plunge into this area. There are many excellent textbooks on antenna theory, mathematical formulations, and design. This book focuses more on practical antenna design than theoretical analysis. It tries to make a good balance between the antenna fundamentals and the design of printed antennas. This book is all about practical-world antenna design beyond too many formulations and theories. The book chapters include the most useful recent work available from research in the printed antenna and microstrip antenna fields.

This book is the result of several years of my research work in antenna design and development for various applications, research investigations, and experience with practical antennas. The book is for new antenna engineers as well as for experienced designers, particularly those focusing on real-world practical antenna designs, as well as academics and researchers looking to keep up with this dynamically changing field. In industry, research labs, and academia, one may find it hard to get a general understanding of the field before engaging in any specialized techniques. Designers of planar microstrip antennas and printed antennas who develop antennas for wireless applications, the aerospace, automobile, and healthcare industries, fifth generation (5G), radars, phased array systems, and many other areas will find this book useful. Many of the antenna projects and topics chosen for discussion are those that I have found to be useful during my career.

Senior antenna designers and engineering managers can use this book as a guide to train and teach new hires. New hires and students can learn antenna designs by using the book and design projects discussed in this book and will be able to quickly gain expert-level proficiencies. Telecom network equipment engineers, who desire a stronger sense of antenna principles, as well as electronic engineering students studying electromagnetics, will find this book to be a good learning resource. I believe that this concise and readable book, with scope and depth, theoretical background, design projects, and recent progress, will be a welcome addition to the collection of books on this subject.

Several books have been published about printed and microstrip antenna design, which has many theoretical aspects. This book narrows the focus to those designs that have extensive utility and simplicity. Results from full-wave electromagnetic numerical methods such as finite difference time domain (FDTD), finite element method (FEM), or method of moments (MoM) are presented with input

dimensions and parameters that were used to generate antenna designs. These designs are straightforward for the reader to reproduce and alter designs to aid their understanding.

Each chapter covers sufficient details to enable antenna designers, researchers, students, and scientists from all areas to follow and understand. The book begins with the elementary printed and microstrip antenna topics needed by engineers and students with no background in antenna theory to study and understand the basic design principles and features of antennas. Several antenna design topics and antenna projects are presented in this book for the first time. These include new designs in the areas of 5G, wearable antennas, automobile antennas, system-level antenna simulation, phased array beamforming designs, metamaterial antennas, and fractal antennas.

Applications of antennas are also changing with an increasing emphasis on the commercial use of antenna technology for wireless communication systems, automotive radar, remote sensing, 5G, Internet of Things (IoT), radars, medical devices, radio frequency identification (RFID), direct broadcast satellite televisions, and many other systems related to information infrastructures. These developments suggest that there will be no shortage of challenging problems in antenna engineering and that there is a clear need for engineers with creativity and understanding of practical design aspects of antenna engineering. I have tried to present the design approach and the logic behind these designs so that the reader can see and understand the process of applying fundamental concepts to arrive at useful results. In Chapters 1 and 2, the fundamentals of printed and microstrip antenna are stressed.

I have tried to organize the contents in a flow starting from single-element printed antennas and finishing with system-level designs to lead the readers in a logical way. The book covers the topic of antennas from three vantage points: printed antenna fundamentals, antenna design technique, and design of real-world application-based antennas. Moreover, this book contains some recent developments including my own research results. Electronics Design Automation (EDA) software based on electromagnetic numerical techniques are the essential tools of today's microwave engineer. Most of the antenna projects described in this book are designed using full-wave electromagnetic simulation techniques.

Chapter 1 discusses the various types of printed antennas and important antenna specifications that are needed to start an antenna design. Chapter 2 examines the most widely used printed antenna, microstrip antennas, to solidify concepts developed in this chapter and provides specific antenna design concepts for complex and array antenna designs in later chapters. Printed antennas are heavily used in wireless communication and mobile phone antennas. Chapter 3 gives an overview of antenna designs used in smartphones. Mobile phone designers are struggling every day with various compliance-related problems that see critical products fail to pass compliance certification and cause a big loss of profit. Chapter 4 introduces the concept of various compliances in mobile phone antenna design and methodology to measure these compliances. The frequency and polarization reconfiguration antenna design that is used in modern wireless communication systems is discussed in Chapter 5.

Printed antennas are not only used as a single element but are also very popular in arrays. Chapter 6 outlines the design of the printed array antenna for several applications. Microwave remote sensing antennas, synthetic aperture radar (SAR)

antennas, and antenna pattern synthesis are described comprehensively using various antenna design methods in Chapter 7, while a high-power SAR antenna system is discussed in Chapter 8. For airborne applications, multifrequency antennas are required to collect data at different frequency bands without landing the aircraft for mounting of a different antenna at different frequency bands. In Chapter 9, the design and analysis of a multifrequency antenna using a shared aperture is presented.

Phased array antennas are common in modern communication systems and radar because of the benefit of far-field beam-shaping and -steering for specific, agile operational conditions. All design aspects of a phase array antenna with a real-world spaceborne application are discussed in Chapter 10. The arrival of the broadband system in the wireless communication area has required the design of antennas that must operate effectively over a wide range of frequencies. The design of broadband antennas is discussed based on electromagnetic bandgap (EBG), photonic bandgap (PBG), frequency selective service (FSS) fractal antenna, and many other latest technologies in Chapter 11.

The wireless communication industry is creating new products with advanced feature to support wireless services anywhere and anytime. Chapter 12 provides an idea of current research and development (R&D) trends in the design, analysis, and synthesis of broadband, multiband, and reconfigurable antennas for modern wireless communications. Automotive communication has witnessed a tremendous growth in recent years due to modern communication. Automobiles are equipped with many antenna systems such as navigation, Global System for Mobile communication (GSM), Bluetooth, satellite radio, Remote Keyless Entry Service (RKES), Tire Pressure Monitoring System (TPMS), and radars. Chapter 13 is focused on automobile antenna design.

The antenna is one of the most complex and important aspects of the RF system. Chapter 14 presents antenna design consideration in a complete transceiver system for the active phased array at C-band using multitechnology-based chips. The book is completed by Chapter 15 in which a system-level, three-dimensional, beam-steerable, high-gain phased array system for a 5G multiple-input and multiple-output (MIMO) network is designed.

All of the chapters are self-contained and include several antenna design projects, making the book suitable for self-study. A list of key references is included at the end of all chapters. In this book, the presentation principle is to explain printed antenna design concepts in simple and concise terms along with practical antenna design. Although I have avoided the textbook approach in which many equations and theories are presented with little or no explanations of actual context, a considerable amount of the material in this book is related to the design of printed antennas for both practical and educational use.

Acknowledgments

This book would not have been written without the encouragement of and interaction with many people. I thank my friends in the industry and academia for their support on projects and applications.

Much of the information contained in this book is the result of my research and investigation on printed antenna design carried out at the Keysight Technologies and Space Application Center (SAC). I would therefore like to acknowledge the support of my colleagues at the Keysight Technologies and SAC who have made various contributions.

I thank all my colleagues in Keysight Technologies for their support and collegiality thought the years. I especially thank Mohit Khanna, who worked with me on many antenna design projects and provided valuable guidance. Jan VanHese, Jack Sifri, HeeSoo Lee, Anurag Bhargava, and Marc Petersen gave much technical support on electromagnetic simulations and antenna design. In addition, I would like to acknowledge the support provided by the Boris Troyanovsky and Deepty Chauhan at Keysight Technologies.

I have benefited from many experts through their works and guidance. I would like to express my sincere thanks to them, especially to my colleagues at the Indian Space Research Organization (ISRO): S. B. Chakrabarty, V. K Singh, Sanjeev Kulshrestha, B. K. Pandey, S. B. Sharma, and Anil Solanki.

My family has also played a key role throughout the years, supporting me always when I needed it the most. Writing a book is tougher than I thought and more rewarding than I could have ever imagined. It requires significant time and effort to make complicated things easy to grasp and understood, and none of this would have been possible without my wife Shraddha Pandey and children Anushka and Atharva and I acknowledge them for patiently tolerating the extra work connected with writing a book.

I am particularly thankful to the reviewers who carefully reviewed the manuscript and gave valuable suggestions. I also offer sincere thanks to the personnel at Artech House for their help and patience throughout the preparation of the manuscript. Finally, I would like to thank my readers for their interest and passion in the subject.

CHAPTER 1

Printed Antennas

1.1 Introduction

Antennas are a fundamental component of any wireless communications systems. An antenna is a kind of transducer that converts a transmission line electrical signal into an electromagnetic wave in free space and vice versa. The technology related to antennas in the modern wireless system has been continuously improved with the corresponding increase in the number of and requirements for communications. Compared to other antenna options, printed antennas have some excellent features, such as low profile, low weight, and are easy to manufacture, along with good performance characteristics. The unique properties of printed antennas, such as mechanical conformability, durability, compactness, and cheap manufacturing costs make them suitable for many applications. Printed antennas have a range of applications in the commercial, medical, military, and aerospace sectors, and are often mounted on the exterior of spacecraft and aircraft as well as incorporated into wireless devices. In addition, the straightforward integration of printed antennas with electronics systems has opened new fields of application, such as 5G phased array and smart sensing systems.

Printed antennas are used in most classical microwave applications, including radars, telecommunications, wireless communication, satellites communication, mobile communications, aeronautical applications, the space industry, Global Positioning System (GPS), systems for detection and identification, and medical applications. In commercial sectors and industries, printed antenna uses include e-textiles, interactive point-of-sale displays, electronic toll collection, smart cards, and product packaging and equipment identification and tracking. These antennas are used at frequencies ranging from ultrahigh frequency (UHF) to millimeter waves. Printed antennas generally behave like resonators. This naturally leads to a narrow bandwidth, typically a of few percents. However, there are various techniques and design methodologies to make printed antennas behave differently and work in broadband applications.

1.2 Types of Printed Antennas

Focusing on applications, different types and technologies of printed antennas can be considered. Printed antennas originated from the use of planar microwave technologies such as microstrip, slot lines, coplanar waveguide (CPW), and customized printing. The different types of printed antennas are classified based on the shape of the radiating element, feeds, or ports that allow its excitation and radiation mechanism. Depending on their characteristics, we can find different classifications [1–25].

1.2.1 Microstrip Antenna

Among printed antennas, microstrip antennas are the most popular [1]. A microstrip antenna consists of a radiating patch with an electrically large ground plane separated by a dielectric material. For the radiating patch, different shapes are used. Rectangular [6] and circular shapes are the most commonly used. Patch antennas are comprised of a thin metallic patch placed above a conducting ground plane [7]. The patches are photo-etched on the dielectric substrate. The relative dielectric constant of a substrate is usually in the range of $2.2 < \varepsilon_r < 12$ [3]. Substrates with lower ε_r provide better efficiency, larger bandwidth, loosely bound fields for radiation into space. Higher values ($\varepsilon_r > 10$) may be used in special circumstances like for compact antenna designs. Due to its simple geometry, the half-wave rectangular patch is the most commonly used microstrip antenna [8,9]. A typical microstrip patch antenna structure is shown in Figure 1.1. Microstrip antenna analysis and design are discussed in detail in Chapter 2.

1.2.2 Slot Antenna

Printed slot antennas are formed by a dielectric substrate with a metallic plane [10,11]. The slot element is made by eliminating the pertinent metal on the metallic side; the most common shapes in slot antennas are rectangular and ring. Slot antennas have a bidirectional radiation pattern with a wider bandwidth than microstrip antennas. Their basic problem is the difficulty of integrating them into the electronics. To improve the possibility of integration, CPW feed schemes are normally used. To ensure unidirectional radiation patterns, a metallic ground plane is used as the reflector. Tapered slot antennas are used when bigger bandwidth and end-fire

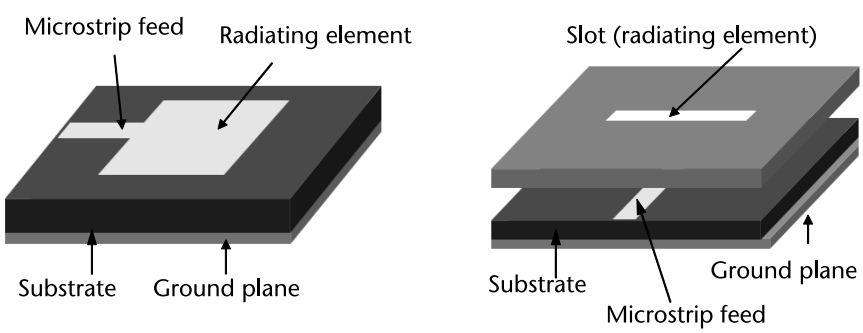

Figure 1.1 Microstrip patch antenna and slot antenna configuration.

radiation is required. Recently, slot antennas integrated into a substrate integrated waveguide (SIW) structures have attracted interest. The main advantages of slotted SIW antennas are their greater compactness and ease of integration when compared with microstrip antennas or traditional slot antennas, due to the guide wave behavior of the SIW structure.

1.2.3 Inverted-F Antenna

Inverted-F antennas (IFAs) are a very common antenna type in most smartphones and wireless devices. Visually, the antennas sometimes resemble an F shape [12–14]. The inverted-F antenna is basically a folded monopole with an inductive stub added to offset the capacitance introduced by locating to antenna element closer to the ground. The IFA can also be designed to deliver multiband operation by stacking two or more F type structures or the trace can be meandered to reduce its size.

Selective metallization is extensively used in mobile phones and is often used to combine multiple antennas onto a single plastic substrate. Other antenna types such as loops, inverted Ls, and monopoles can also be used side-by-side with the IFA to support the multiple radio technologies contained within today's mobile devices. IFAs are usually custom designed to fit within the available PCB space or product geometry. The design costs are small once amortized over the product's lifecycle and if a PCB trace-based design is selected, the IFA can be a very effective and low-cost solution.

1.2.4 Planar Inverted-F Antenna

The planar inverted-F antenna (PIFA) is a well-known variation of the classical microstrip antennas. Although it has a similar name as the IFA, the planar inverted F-antenna is, in fact, a different antenna type. Where the IFA is related to the monopole, the PIFA is related to the patch antenna [15–17]. As the name suggests, the PIFA structure is positioned planar to the PCB. This provides the antenna with an increased physical volume and hence a wider bandwidth than the IFA. In addition, as the PIFA can use air as its dielectric rather than a lossy PCB material, and it tends to be slightly more efficient. Like the off-board IFA, PIFAs can be constructed from formed metal (usually tin) or use selective metallization techniques on a plastic former. PIFA consists of a radiating patch and an electrically large ground plane. Both metallic components are connected by a metallic pin (via) or in some cases by

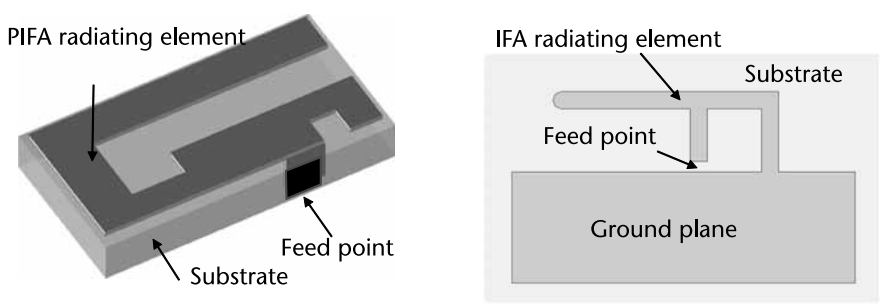

Figure 1.2 Planar inverted-F antenna and inverted-F antenna.

a metallic plane. This scheme reduces the final size of the radiating patch and avoids the use of a dielectric substrate. PIFAs have been widely used in mobile communications systems as mobile phones and laptops due to their compact design with multiband behavior capability. An electrically large ground plane is needed. The PIFA also has less radiation through the ground plane, which if used in a mobile phone or wireless headset can help reduce the amount of wasted RF energy sent toward the user's head and hence help reduce the specific absorption rate of the device.

1.2.5 Printed Dipole Antenna

Printed dipole antennas are widely used for applications based on personal wireless systems like Wi-Fi, Bluetooth, WiMAX, and WSNs based on these protocols. Such antennas consist of two radiating elements (arms of the antenna) fed in opposite phases. The antenna arms can be located on the same side of the substrate or on different sides. Depending on the location of the arms, different kinds of feeding schemes can be applied. The most used feeding schemes are coplanar waveguide lines, which are quarter-length line baluns and direct coaxial connector feed. Different shapes can be used as dipole arms [18,19].

1.2.6 Monopole Antenna

Printed monopole antennas consist of only one resonant element (one arm) directly fed with a transmission line. With an appropriate design procedure, some monopole antennas can provide a wider bandwidth than dipole antennas. This behavior makes monopole printed antennas suitable for compact and wideband applications [20]. Monopole antennas are widely used in mobile and small wireless communication devices. Design of a monopole antenna for Wi-Fi application in a mobile device is discussed in detail in Chapter 3.

1.2.7 Printed Inductor Antenna

Inductor antennas have gained high popularity due to their generalized use in radio frequency identification (RFID) applications. The working frequency of the printed inductor antenna in these cases is quite low when compared with typical

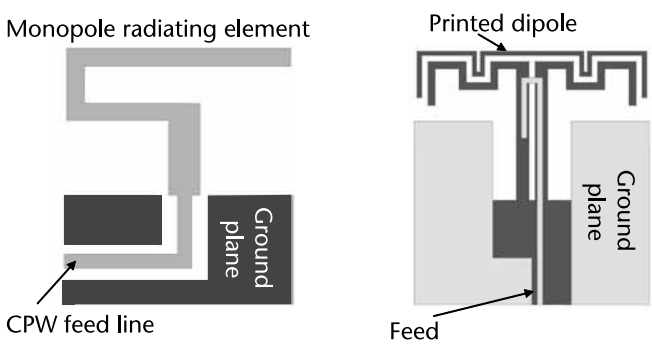

Figure 1.3 Monopole antenna and printed dipole antenna designs.

applications of printed antennas for wireless communications systems. In this sense, these can be considered electrically small antennas and they can be used in passive configurations. The antenna works in the near field region and the coupling is mainly inductive. The specific frequency depends on the application [21]. These antennas are also suitable for low-frequency RFID 13.56- and 900-MHz application. In these instances, the antenna of the tag is the main radiating element.

1.2.8 Printed Quasi-Yagi Antenna

Printed quasi-Yagi antennas are used when a directive behavior is required, by adding parasitic elements in a Yagi-Uda fashion. Printed Yagi-Uda antennas display the same structure and behavior as an original nonplanar Yagi-Uda antenna with the advantages of the printed technology. Planar quasi-Yagi antennas have several benefits compared to wire Yagi-Uda antenna, such as a simple structure, lightweight, low profile, low fabrication cost, broad bandwidth, unidirectional radiation with high gain, and appropriateness for integration with microwave circuits. For wireless sensor networks (WSNs), planar Yagi antennas are normally used to increase the communication distance [22]. The classic Yagi-Uda antenna consists of a driven element, a reflector, and one or more directors. The reflector and directors act as parasitic elements. Quasi-Yagi antennas typically have a narrow bandwidth but an end-fire radiation pattern and high gain make them suitable for many wireless applications.

1.2.9 Log-Periodic and Fractal Antenna

Log-periodic antennas are used to improve the bandwidth of printed antennas. The log-periodic dipole array (LPDA) is the most common form of log-periodic antenna. It consists of a few half-wave dipoles driven radiating elements of gradually increasing length, each consisting of a pair of metal rods. This kind of design approach has, theoretically, a frequency-independent behavior. The main disadvantage of these antennas is the size [23,24].

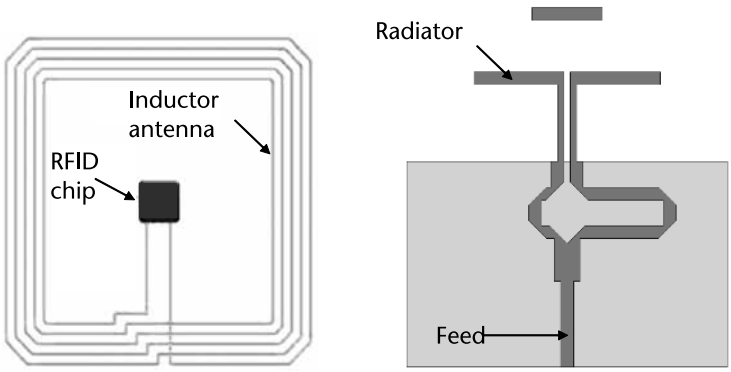

Figure 1.4 Printed inductor and quasi-Yagi-Uda antenna design.

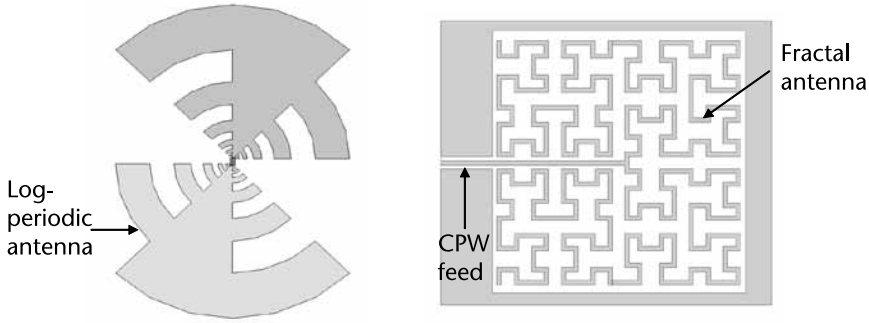

Figure 1.5 Log-periodic and fractal antenna design examples.

The fractal term was first coined by Benoit Mandelbrot in 1983 to classify the structure whose dimensions were not whole numbers. One of the properties of fractals geometry is that it can have an infinite length while fitting in a finite volume. There is an infinite number of possible geometries that are available to try as a design of the fractal antenna. The antenna size can be reduced significantly using fractal concepts, such as the Koch dipole, Koch loop, Koch monopole, and Minkowski loop. It can be also used for multiband applications and increase the bandwidth due to the self-similarity in the geometry, such as the Sierpinski dipole, fractal tree dipole, and Cantor slot patch [25–28]. In these antennas, self-similar shapes provide significant advancements than the fractal nature [28]. Fractal antenna designs are discussed in detail in Chapter 11.

1.2.10 Customized Printed Antenna

In modern wireless antenna applications, there is an increase in antenna complexity and miniaturization combined with a need to integrate many radio environments into one component. The rising adoption of customized printed antennas in the aerospace, defense, and mobile communication industry is projecting growth of this market by leaps and bounds. This is because a customized printed antenna with many resonant frequencies can be designed according to the shape and available space of the device. Customized printed antennas form an integral component of devices thereby enhancing the data transmission capabilities of these devices. Often multiple antenna structures are integrated into a single product. To achieve such a high level of integration the antenna structures are manufactured, for example, from flexible boards or via laser direct structuring (LDS), which allows the production of complex monopole or dipole antennas with a three-dimensionally curved shape.

1.2.11 Comparison of Planar Antennas

Several types of planar antennas are compared in Table 1.1. Patch and slots are resonant-type antennas that have a compact and low profile that can be readily integrated into large, active arrays. Inverted-F, PIFA, and customized antennas are appropriate choices for mobile communication as they require broadband antennas to cover all standards. Other more exotic planar antennas, such as quasi-Yagi

Table 1.1 Planar Antenna Comparison

Type	*Sketch*	*Radiation Pattern*	*Directivity*	*Bandwidth*
Microstrip Patch	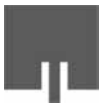	Broadside	Medium	Narrow
Slot		Broadside/ bidirectional	Low/medium	Medium
Dipole		Broadside	Low	Medium
LPDA		End-fire	Medium	Wide
Bow tie		Broadside	Medium	Wide
Circular loop		Broadside	Medium	Narrow
Spiral		Broadside	Medium	Wide
TSA		End Fire	Medium/high	Wide
Quasi-Yagi		End Fire	High	Wide
PIFA		Broadside	Medium	Medium
Monopole		Broadside	Low	Medium
Fractal		Broadside	High	Wide
Leaky wave	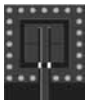	Scannable	High	Medium

antennas and microstrip leaky waves, demonstrate higher directivity and the ability for frequency scanning. Their compact size, broad bandwidth, and good patterns provide a viable alternative to antennas based on other technologies. As planar antenna technology continues to mature, the functionality of these antennas is expected to increase and drive penetration of commercial wireless communications

to even higher frequency applications. The design of many of these antennas is discussed in detail thoroughout this book.

1.3 Important Specifications of Antenna Design

There are several antenna parameters that are useful to describe for antenna design engineers [1–5]. Before beginning antenna design work, it is essential to know typical antenna design specifications. It is easy to confuse some of the antenna specifications and how to use them in antenna design. For example, the gain of an antenna and amplified gain are two very different definitions.

The primary specifications or parameters of an antenna consists of frequency, gain, bandwidth, impedance, return loss, half-power beamwidth (HPBW), sidelobes, polarization, cross-polarization, and voltage standing-wave ratio (VSWR).

1.3.1 Operating Frequency

The antenna resonant point or design frequency f_c is the specifications of the antenna at which it resonates. Antenna operating frequency (or frequency bandwidth) is the range of frequencies within which the performance of the antenna, with respect to some characteristic, which conforms to a specified standard. The antenna center frequency between a high frequency point f_H and a low frequency point f_L is calculated as shown in (1.1):

$$f_c = \frac{f_H - f_L}{2} \tag{1.1}$$

1.3.2 Impedance

The impedance of an antenna relates the voltage to the current at the input terminal and it has real resistive and imaginary reactance parts. The inductive and capacitive elements of antenna impedance changes with frequency. An antenna will have two types of resistance associated with it: radiation and ohmic resistance, as shown in Figure 1.6(b). Radiation resistance converts electrical power into radiation. Ohmic resistance is the loss of the antenna's structure that converts electrical power into heat. For effective radiation and efficiency, the radiation resistance should be much higher than the ohmic resistance. For efficient transfer of energy, the impedance of the system, the antenna impedance, and the transmission line impedance must be the same.

1.3.3 Return Loss and VSWR

Antenna return loss measures how effectively power is delivered from a transmission line to an antenna. If the power incident on the antenna under test is P_{in} and the power reflected to the source is P_{ref}, the degree of mismatch between the incident and reflected power in the travelling waves is given by the ratio P_{in}/P_{ref}. Return loss is expressed either in terms of the VSWR present on the input to the antenna because of the reflection or as the relative level of the return signal in decibels. The

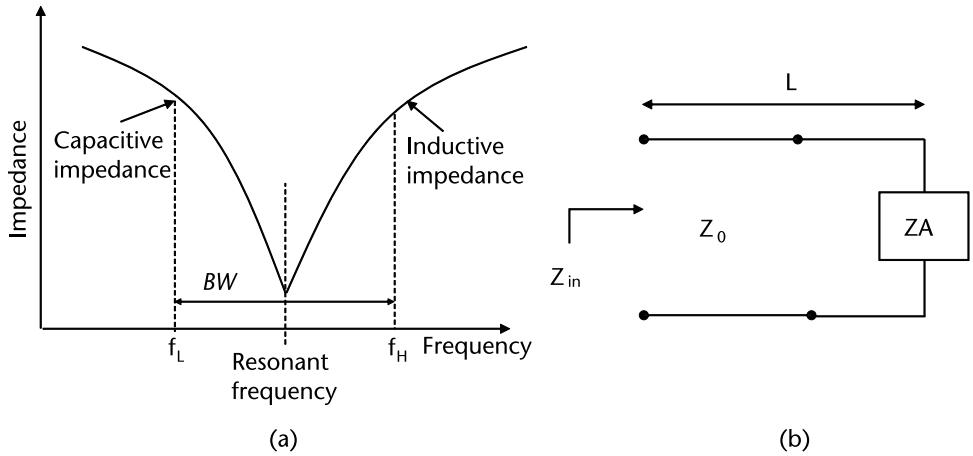

Figure 1.6 (a) Antenna impedance and bandwidth diagram, and (b) antenna resistance model.

negative of the magnitude of the reflection coefficient in decibels is return loss. Since power is proportional to the square of the voltage, return loss is given by (1.2):

$$RL(dB) = 10\log_{10}\frac{P_{in}}{P_{ref}} \tag{1.2}$$

Return loss and VSWR are related. VSWR is a measurement of reflected power from the source. It is calculated by measuring the forward voltage wave toward the load versus the voltage wave that is reflected from the load. A perfectly matched system has a VSWR of 1:1. The higher the first number, the worse the match and the more inefficient the system. In the case of antenna VSWR, this is usually 2:1; that is, 88.9% of the energy sent to the antenna by the transmitter is radiated into free space and 11.1% is either reflected into the source or lost as heat during the transmission process. Antenna bandwidth is also measured in terms of return loss, such as -10-dB return loss bandwidth.

1.3.4 Radiation Pattern

The variation of the power radiated by an antenna as a function of the direction away from the antenna at different locations in space is defined as an antenna radiation pattern. This power variation as a function of the arrival angle is measured in the antenna's far-zone. If the radiation pattern is the same in all directions, then it is called an isotropic antenna pattern. In practice, antennas with isotropic radiation patterns do not exist but an isotropic radiation pattern is used as a reference to compare gain and pattern of real antennas. For simplicity the radiation pattern can be drawn in a two-dimensional (2-D) plane for different azimuth and elevation angle referred to as azimuth plane pattern and elevation plane pattern. Radiation pattern can be a plot in polar and rectangular form. It is more informative to plot the radiation patterns in Cartesian (rectangular) coordinates, especially when the antenna radiation pattern consists of different sidelobes and where these sidelobes levels play an important role. Many antenna parameters like gain, directivity, the

direction of the main lobe, half-power beamwidth, sidelobes, and null locations are calculated from the antenna radiation pattern, as shown in Figure 1.7.

1.3.5 Directivity and Gain

The ability of an antenna to focus radiated energy in a direction is measured with directivity. Directivity measures how much an antenna's peak radiated power density is in a direction than for a reference radiator (normally isotropic radiator or dipole) with the same source power. Gain is given with respect to a standard antenna. The two most common reference antennas to measure the directivity are the isotropic antenna and the resonant half-wave dipole antenna. The isotropic antenna radiates equally in all the directions. Real isotropic antennas do not exist, but they provide simple and uniform theoretical antenna patterns with which real antennas pattern is compared. The resonant half-wave dipole is a useful standard for comparing gain of antennas. Gain is measured in decibels or dBi (relative to an isotropic source) or dBd (with regard to a dipole antenna). A dipole has a gain of 2.15 dB more than isotropic or dBi = dBd + 2.15 dB.

It is important to note whether the gain is being expressed in dBd or dBi and convert appropriately when comparing gains of multiple antenna systems. Actual antenna performance is measured by the amount of energy that the antenna radiates into free space. Antennas are not 100% efficient and have internal losses. The gain of an antenna includes these losses. Antenna gain can be calculated using (1.3):

$$Gain = 4\pi \frac{Radiated\,intensity}{Total\,power} = 4\pi \frac{U(\theta,\varnothing)}{P_{in}} \tag{1.3}$$

Gain can be a confusing specification. Most engineers are familiar with the term about amplifiers, where the gain is a measure of how much an amplifier increases the input signal. But there is a significant difference between an amplifier's

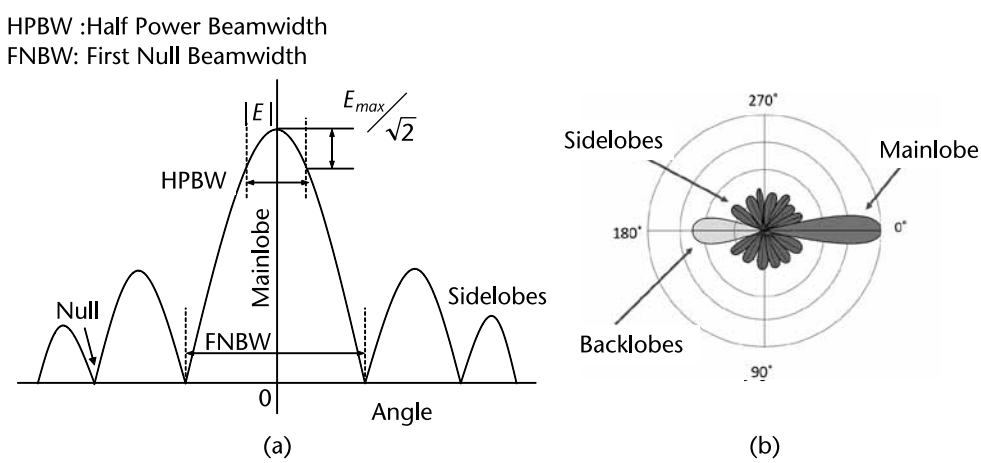

Figure 1.7 Antenna radiation pattern diagrams and parameters: (a) rectangular plot of radiation pattern, and (b) polar plot of radiation pattern.

gain and an antenna's gain. The amplifier puts energy into the system, making it an active device.

1.3.6 Antenna Efficiency

Efficiency is a measurement of how much energy put into the antenna gets radiated into free space rather than lost as heat on the antenna's structure or reflected into the source. The antenna's impedance and VSWR at the center frequency play a big role in this measurement. In a high-efficiency antenna, most of the input power delivered at the antenna terminal is radiated away while a low-efficiency antenna has most of the power lost, reflected back, or absorbed within the antenna.

1.3.7 Bandwidth

The bandwidth of an antenna is defined as the range of frequencies over which the antenna can properly radiate or receive energy. Bandwidth is typically quoted in terms of VSWR or decibels. For instance, an antenna may be described as operating at 50 to 100 MHz with a VSWR<1.5 or –10 dB. This statement implies that the reflection coefficient is less than 0.2 across the quoted frequency range. Hence, of the power delivered to the antenna, only 4% of the power has reflected the transmitter. Bandwidth can be defined in terms of radiation patterns or VSWR/reflected power. Bandwidth is often expressed in terms of percent bandwidth because the percent bandwidth is constant relative to frequency. Typically, our antennas have a nominal 10% bandwidth. This may increase or decrease depending on the antenna and performance required.

1.3.8 Half-Power Beamwidth

The beamwidth is the aperture angle from where most of the energy is radiated from the antenna. The angle over which the radiated energy falls to half (50%) its peak level is as the HPBW or the -3-dB point. The unit of HPBW is radians or degrees.

1.3.9 Sidelobes

Sidelobes are the lobes in the radiation pattern that are not the main beam. In good antenna design, the power density in the sidelobes is generally much less than that in the main beam. Sidelobe levels are measured in decibels relative to the peak of the main beam, for example -13 dB. In array antennas there are several techniques to control sidelobe levels depending on the application.

1.3.10 Polarization

All electromagnetic waves and radiation are polarized. The orientation of the electrical field or E-plane describes the polarization of an antenna. The polarization can be linear, circular, or elliptical. Linear polarization is usually horizontal or vertical. Dual-pole antennas can produce both vertical and horizontal polarization via separate ports. Circular polarization is produced when the E-plane of the antenna

radiated wave rotates along the propagation axis. Depending on the direction of spin, the polarization is right or left. Antennas are never perfectly polarized. The amount of energy in the plane perpendicular to the E-plane or opposite hand of circular polarization is measured with a cross-polarization. It is typically quoted relative to the peak gain of the antenna.

1.4 Analysis and Simulation Software for Antenna Design

The transmission line model, cavity model, and full-wave model (which include primarily integral equations/moment method) are the most popular models for the analysis of printed antennas. The transmission line model gives good physical insight and it is the simplest of all models, but it is less accurate. The cavity model is more accurate and gives a good result but is complex in nature. These techniques make a simplifying assumption about the geometry of a problem to apply closed-form solutions. However, most electromagnetic coupling problems are simply unpredictable to be modeled using this approach. As the frequency of operation is increased, it has been realized, and now it is widely known, that the quasi-static analyses of microstrip circuit elements are not accurate enough, and a more rigorous full-wave analysis is required. Full-wave techniques analyses the entire geometry provided without making a priori assumptions about which field interaction are most significant. The full wave models are very accurate, versatile, and can treat single elements, stacked elements, finite and infinite arrays, arbitrarily shaped elements, and coupling. Almost all commercial printed antennas are designed in the industry using a full-wave analysis technique. Full wave electromagnetic analysis means that the solution is obtained by solving Maxwell's equations for the electric and magnetic fields in the time domain or the frequency domain.

1.4.1 Transmission-Line Circuit Model

A microstrip patch, operating at its fundamental mode, is essentially a $\lambda/2$ long microstrip transmission line and can be represented by an equivalent circuit network [29,30]. For a rectangular patch, its radiation is basically generated from its two edges with two equivalent slots along the resonating dimension, as shown in Figure 1.8. The microstrip radiator can be characterized by these two slots separated by a transmission line, where each slot is represented by a parallel circuit of conductance (G) and susceptance (B). The complete patch antenna can be represented by the equivalent network shown in Figure 1.8.

This transmission line model is simple, computationally fast, and intuitively appealing, but it suffers from limited accuracy. For examples, this model does not consider mutual coupling between the two radiating slots and it lacks the radiation from the nonradiating edges of the patch [31].

1.4.2 Cavity Model

Microstrip radiator can be considered as an open cavity bounded by the patch element and ground plane. The open edges can be represented by radiating magnetic walls. Just like a completely enclosed metallic cavity, such a cavity will support

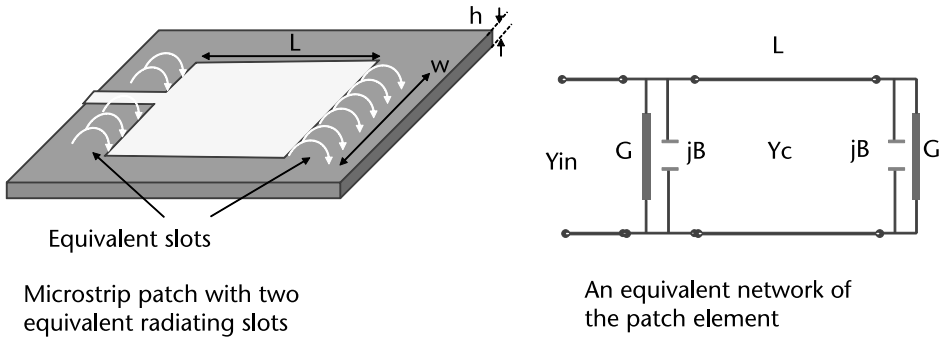

Figure 1.8 Transmission line model (TLM) of microstrip patch antenna.

multiple discrete. As shown in Figure 1.8, its total electric field in the cavity can be expressed as the sum of the fields associated with each sinusoidal mode [32]:

$$E_z(x,y) = \sum_m \sum_n C_{mn} \cos\left(\frac{m\pi}{w}\right) x \cos\left(\frac{n\pi}{L}\right) y \tag{1.4}$$

where C_{mn} is a constant that depends on the feed location, w, and L dimensions, and the dielectric constant. As substrate is considered thin, the fields are assumed to be z-directed only with no variation in the z-direction. The most important dominant mode is the TM_{10} mode, that is generated if the dimension L is approximately $\lambda g/2$. The equivalent edge magnetic currents can be determined by knowing the fields at the edges of the patch and it can be integrated to find the far-field radiation patterns. The cavity model technique permits to know the mode structure underneath the patch to understand physical radiation mechanisms, such as its resonating and cross-polarization behaviors. However, when the substrate becomes thick, because of certain assumptions the field has no z-variation, and cavity model solution is not very accurate.

1.4.3 Full-Wave Analysis Technique

There are various antenna full wave analysis and simulation tools based on different electromagnetic numerical techniques. Software for antenna design can be selected based on antenna type and size. Choosing the appropriate technique for solving an antenna problem is important, because by choosing the wrong solver one can either get incorrect results or the simulation will take excessively long to compute. Several important electromagnetic simulation technologies have developed over the years. Out of these simulations technique, the method of moments (MoM), finite element (FEM), and finite difference time domain (FDTD) solutions are used almost in all commercial electronic design automation (EDA). In principle, while these full-wave analysis technologies could be used to solve the same problems there are often good practical reasons why one simulator is better suited to solving a problem type.

While selecting a full-wave solver, the first selection criteria are based on geometry, whether antenna geometry is planar in nature or it is three-dimensional. For planar structures, MoM provides the most efficient and fastest simulation method,

and for true 3-D antenna structures, such as parabolic dish, horn, and waveguide antennas, FEM or FDTD are more appropriate. Large problems are better suited to FDTD simulation, such as an antenna placed on a vehicle or aircraft, the analysis of antenna performance in the presence of human body models, and several large array antenna simulations.

1.4.3.1 MoM

Numerical techniques based on the method of weighted residuals are called moment methods. This is mostly a frequency domain method where a single frequency is considered at a time. The current density of the antenna is the main variable used to derive other antenna parameters. It is implemented by replacing the antenna with an equivalent surface current density. The surface current density is then discretized into a set of current-density elements called basis functions or expansion with variable amplitudes. Then Green's function for the problem is used to represent the electric and/or magnetic fields everywhere in terms of current-density elements on the surface of the antenna. The boundary conditions for both fields are then enforced on the surface of the antenna using testing functions or weighted functions as pioneered by Harrington [33] for solving electromagnetic problems. MoM-based mesh on a microstrip line and current distribution on the line is shown in Figure 1.9.

All weighted residual techniques begin by establishing a set of trial solution functions with one or more variable parameters. The residual is a measure of the difference between the trial solution and the true solution. The variable parameters are obtained in a manner that guarantees the best fit of the trial functions based on a minimization of the residuals. The equation solved by moment- method technique is generally in form of electric field integral equation (EFIE) or the magnetic field integral equation (MFIE). Both equations can be derived from Maxwell's equations by considering the problem of a field scattered by a perfect conductor (or a lossless dielectric). These equations are of the form that the MoM technique can be applied to configurations of conductors only, homogeneous dielectrics only, or very specific conductor-dielectric geometries depending on the form of field integral equation used. They are not effective when applied to an arbitrary configuration with complex or inhomogeneous dielectrics and the interior of conductive enclosures or thin plates.

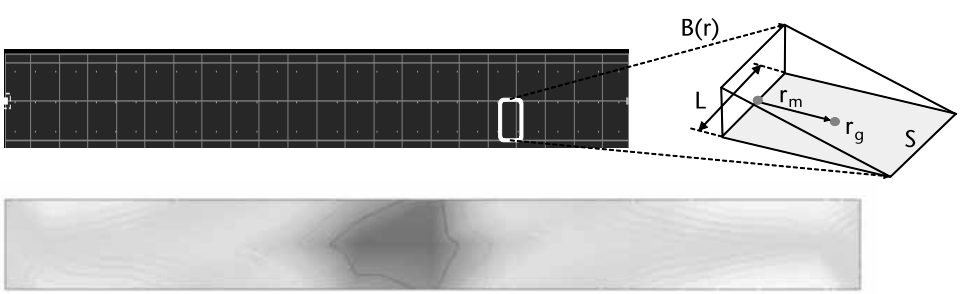

Figure 1.9 MoM mesh on a microstrip line and simulated current distribution over the line.

1.4.3.2 FEM

FEM is mainly a frequency domain method that is sometimes preferred because of its ability to model inhomogeneous media. FEM is a mathematical method of analyzing complex structures by subdividing them into many small elements (the elements can be small where geometry details exist and much larger elsewhere) and analyzing these small structures. The elements can be of many shapes such as triangles and squares for 2-D for tetrahedral and cuboids for 3-D. The field in each element is approximated using mathematical expressions (solutions of the weak form of Helmholtz equations) as described by Silvester et al. [34]. Each edge of the element is termed as a node and magnetic and electric field at each node is evaluated, and then the complete problem is solved numerically. FEM does not model unbounded radiation problems as effectively as moment method techniques.

FEM simulation uses the finite element method to calculate the electromagnetic field solution from which *S*-parameters data is computed. In the finite element method, full-problem space is divided into many smaller regions, as shown in Figure 1.10. Electromagnetic fields are calculated in each subregion (element) with a local function. In FEM-based computer-aided design (CAD) tools, the geometric model is automatically divided into many tetrahedra cells, where a single tetrahedron is formed by four equilateral triangles. An example of how a structure is discretized using finite elements is shown in Figure 1.10. The model contains information about the material constants, device geometry, excitation, and boundary constraints.

1.4.3.3 FDTD

FDTD is one of the most widely used modeling techniques in many engineering applications [35–38] introduced by Yee in 1966. The FDTD method has the advantage of being relatively simple in its formulation and its definition of the geometry (grid-layout) because no complicated and time-consuming mesh generation is needed. Just like FEM, FDTD techniques also require the complete volume to divide into the mesh. In general, the mesh must be uniform, but it can be also controlled based on geometry and applications. The FDTD technique is a time domain simulation method. FDTD methods are good numerical modeling techniques for complex

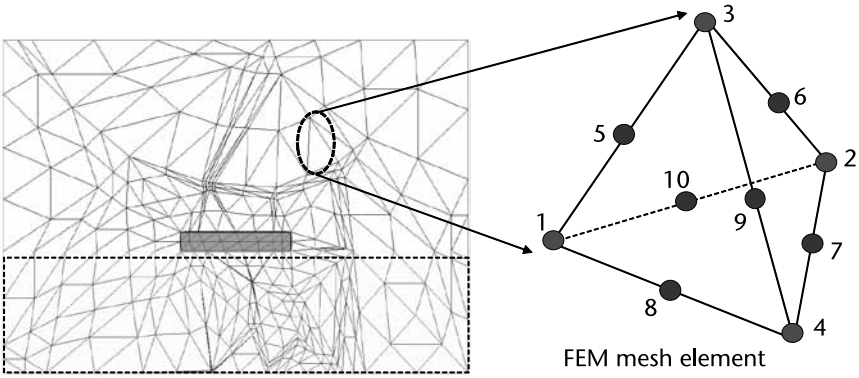

Figure 1.10 FEM mesh for a microstrip line simulation model and a tetrahedral mesh element.

inhomogeneous configurations. Many FDTD formulations and approaches model unbounded problems better than the finite element modeling technique. The FDTD method is a popular numerical technique for computer-aided printed antennas and arrays designs. Complex microstrip antenna characteristics, including the effects of parasitic elements and aperture-coupled feeds, can be solved using this technique. Figure 1.11shows FDTD mesh on a microstrip line and a Yee cell.

Mutual coupling effects between elements is a tricky problem in array antenna design, and an FDTD solver is used to model mutual coupling problems. One main advantage of the FDTD approach is that it gives broadband output from a single execution. However, the main reason for using the FDTD approach for large problem size is the excellent scaling performance of the method as the problem size grows.

1.4.4 Comparison between MOM, FEM, and FDTD

Computational electromagnetics (CEM) based on various techniques solves Maxwell's equations that satisfy a given set of boundary conditions and initial conditions. In doing so, these methods enable complex electrodynamic systems to be modeled. Among the methods used for CEM, are integral-equation (IE) solvers, differential-equation (DE) solvers, asymptotic techniques, and some other numerical methods. Most commercial electromagnetic simulation software is based on the MoM, FEM, and/or FDTD full-wave analysis techniques.

The MoM and multilevel fast multipole method (MLFMM) are based on IE-solving techniques while FEM and FDTD use differential-equation-solving techniques. Asymptotic techniques are used for large antennas based on the optical concept and include physical optics (PO), geometric optics (GO), and the uniform theory of diffraction (UTD). The FEM numerical technique, is a very popular simulation tool for high-frequency structure and antenna designs. Some CAD tools have multiple EM solvers like FDTD-, FEM-, or MoM-based simulators. A comparison among these solvers is shown in Table 1.2.

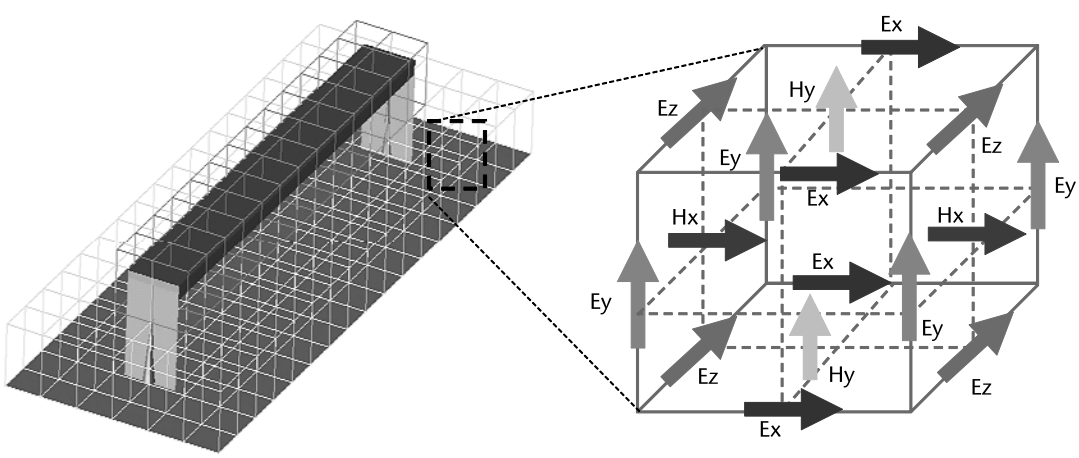

Figure 1.11 FDTD mesh for a microstrip line simulation model and a Yee cell.

Table 1.2 Comparison between MOM, FEM, and FDTD

Parameters	*MOM*	*FEM*	*FDTD*
Method	Frequency-domain	Frequency-domain	Time-domain
Principal	Need frequency-dependent Green's function	Variational principal (minimizing energy function)	A discrete solution of Maxwell's equations
Main advantage	Fast simulation	Very flexible with suitable mesh generation	Can solve electrically large structure
Equations	Integral equation	Differential equations	Differential equations
Suitable for	Wire antenna, planar antenna	Arbitrary shapes, single or few frequencies	Electrically large structures, Broadband
Not suited for	Electrically large structures, various material, broadband type	Electrically large structures, broadband investigation	Multiport structure Hight Q structures

1.5 RF and Microwave Frequency Band and Applications

RF and microwave frequency ranges have been divided into many frequency bands, each represented as shown in Figure 1.12.

Different sources define different frequency ranges as microwaves and it includes UHF and EHF (mmWave) bands also. The frequencies from 1 GHz to 100 GHz is generally defined as microwave frequency band. There are many organizations that assign these bands. The most common being the IEEE Bands followed by NATO Radio Bands and ITU Bands. These frequency bands are used in different applications as listed in Table 1.3.

Antennas, which are used to transmit and receive data, play a crucial role in most of these communication systems. Among various microwave antennas, printed antennas are the most popular and used technologies. The increasing compactness of modern microwave communication and radar equipment commonly demands that the associated antennas have flat profiles. Planar and printed monopole antennas are good candidates for use in wireless technology because of their wide impedance bandwidth and nearly omnidirectional azimuthal radiation pattern.

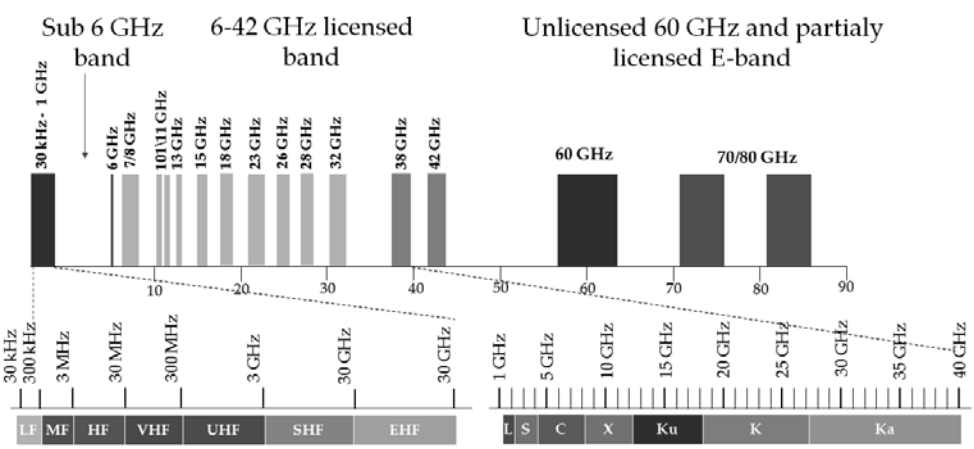

Figure 1.12 RF and Microwave frequency spectrum.

Table 1.3 RF and Microwave Frequency Spectrum and Applications

Band	*Frequency Range*	*Application*
Low frequency(LF)	30 to 300 kHz	Navigation, RFID, time standard, submarines communication
Medium frequency (MF)	300 kHz to 3 MHz	Marine/aircraft navigation, AM broadcast
High frequency (HF)	3 MHz to 30 MHz	Mobile radio, shortwave broadcasting
Very high frequency (VHF)	30 MHz to 300 MHz	Land mobile, FM/TV broadcast, amateur radio, aircraft communications
Ultrahigh frequency (UHF)	300 MHz to 3 GHz	RFID, mobile phone, wireless LAN, PAN
L	1 to 2 GHz	Mobile satellite service (MSS), GNSS/GPS, remote sensing, military telemetry, mobile phones (GSM), air route surveillance radar (ARSR), airborne warning & control (AWACS)
S	2 to 4 GHz	MSS, remote sensing, WiFi, Bluetooth, mobile communication, XM radio, airport surveillance radar (ASR), radio astronomy, wireless LAN, ZigBee, missile guidance, biomedical
C	4 to 8 GHz	satellite communication, WiMax, WLAN, DSRC, weather radar systems, WiFi and ISM band applications, radar altimeter
X	8 to 12 GHz	Radar, FSS military, fire control radars, police speed radar
Ku	12 to 18 GHz	Broadcast satellite services, VSAT, airborne Doppler navigator (ADN)
K	18 to 27 GHz	Radar, satellite communications, astronomical observations
Ka	27 to 40 GHz	Satellite communications, mapping radars
Q	30 to 50 GHz	terrestrial microwave communications, radio astronomy, automotive radar
U	40 to 60 GHz	5G cellular, intersatellite communication
V	50 to 75 GHz	New WLAN, 802.11 ad/WiGig
E	60 to 90 GHz	5G cellular
W	75 to 110 GHz	Automotive radar
F	90 to 140 GHz	Experimental, radar, radio astronomy
D	110 to 170 GHz	Experimental, radar, directed-energy weapon, millimeter wave scanner

There are many new techniques for designing printed antennas and arrays and antenna design for many of these applications will be covered in subsequent chapters.

In this introductory chapter, printed antennas and various types of printed antenna and their applications are discussed. Important antenna specifications that are basic requirements for any antenna designer are explained. For commercial antenna design and analysis, the full-wave analysis technique based on FEM, FDTD, or MoM is used. These three main simulation techniques are covered in this chapter. The next chapter focuses on microstrip antenna design, which is a frequently used printed antenna type.

1.6 Overview of the Book

Printed antennas have a variety of beneficial properties including compactness, conformability, low weight, and cheap manufacturing costs. This book offers a practical design guide to state-of-the-art printed antenna technology used for all types of commercial and industrial systems. The book is divided into six sections covering fundamental printed radiating elements, printed antennas for wireless and mobile systems, array antennas, phased array antennas, and advanced concepts and applications of printed antenna technology. Figure 1.13 shows how these sections are arranged within the book.

After introductory Chapter 1, microstrip antenna technology is discussed. Various types of printed antenna design, analysis methods, and applications are then

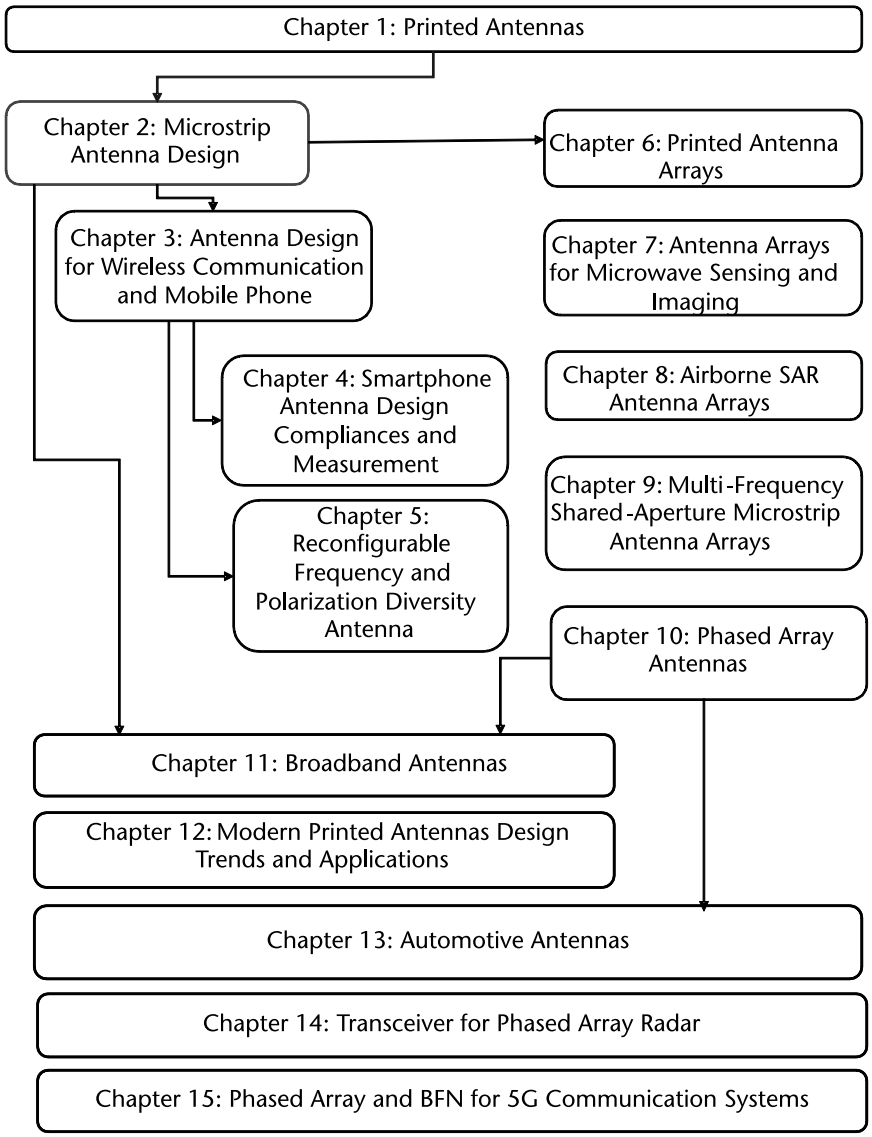

Figure 1.13 Book chapters and content arrangement.

described in detail. Three chapters are then devoted to the design and analysis of printed antennas for wireless and mobile communication systems. The following four chapters describe array antenna technology and its applications. Phased array antennas and advanced modern technologies used in printed and microstrip antennas are covered in the final four chapters. The book is then drawn together with a chapter on system-level design of printed antennas. The following is an overview of each chapter.

Chapter 1: Printed Antennas. This chapter has provided the context for printed antennas and the design process of antennas. Printed antennas have been described together with an explanation of current terminology. Likely design parameters were given together with a review of the design process in which analysis tools should serve.

Chapter 2: Microstrip Antenna Design. To design microstrip antennas, an appreciation of antenna working principle and design process is necessary. The chapter begin with a discussion of the microstrip antennas working principle, design process flow, radiating elements, substrate selection, and feeding mechanisms. Important aspects of microstrip antenna design and knowledge-based design approaches are outlined. Then the discussion converges on practical design of microstrip antenna using the electromagnetic numerical technique.

Chapter 3: Antenna Design for Wireless Communication and Mobile Phone. Printed antennas are heavily used in wireless communication and mobile phone antennas. This chapter gives an overview of antennas used in smartphone design and WLAN antennas as well as an introduction to equivalent circuit modeling of circuits and antenna. Design of GSM, Bluetooth, and MIMO antenna for mobile applications is discussed. Finally, antenna simulation and its effect on the actual environment, along with the human body and phone components, are discussed.

Chapter 4: Smartphone Antenna Design Compliances and Measurement. Smartphone designers are struggling every day with various compliance-related problems that fail critical products to pass compliance certification and causes a big loss of profit. This chapter introduces the concept of various compliance in smartphone antenna design and methodology to measure these compliances.

Chapter 5: Reconfigurable Frequency and Polarization Diversity Antenna. In wireless communication systems antennas are designed and deployed efficiently to effectively utilize the available frequency resources. In this chapter, the frequency and polarization reconfiguration of an antenna is discussed.

Chapter 6: Printed Antenna Arrays. Printed antennas are used not only as a single element but are also very popular in arrays. This chapter outlines the design of printed array antennas for several applications. Array feeding topology, broadband antenna arrays, linear and planar array, and conformal antenna arrays are discussed in detailed.

Chapter 7: Antenna Arrays for Microwave Sensing and Imaging. Large-scale airborne and spaceborne phased arrays are some of the most important enabling techniques for microwave remote sensing. Synthetic aperture radars (SARs) are widely used for remote sensing and mapping within the aerospace and defense industries. In this chapter, microwave remote sensing antennas, SAR antennas, and antenna pattern synthesis are described comprehensively using various antenna design methods.

Chapter 8: Airborne SAR Antenna Arrays. Airborne radars typically use a variation of a cosec square shaped beam, which can get the required elevation coverage when the received power is independent of the radar range for a constant height target. This chapter covers antenna array synthesis, cosec-square patterns, and high-power SAR antennas for airborne remote sensing applications.

Chapter 9: Multifrequency Shared-Aperture Microstrip Antenna Arrays. For airborne applications, multifrequency antennas are required to collect data at different frequencies without landing the aircraft for mounting of the different antenna at different frequency bands. In the chapter, a design and analysis of a multifrequency antenna using a shared aperture are presented.

Chapter 10: Phased Array Antennas. Phased array antennas are common in communications and radar and offer the benefit of far-field beam shaping and steering for specific, agile operational conditions. All design aspects of the phase array antenna with a real-world spaceborne application is discussed in this chapter.

Chapter 11: Broadband Antennas. The advent of the broadband system in the area of wireless communication has necessitated the design of antennas that must operate effectively over a wide range of frequencies. In this chapter, design of broadband antennas is discussed based on EBG, PBG, FSS fractal antenna, and many other latest technologies.

Chapter 12: Modern Antennas Design Trends and Applications. The wireless communication industry is developing new products with advanced features to support wireless services anywhere, any time. The rapid development of communication technologies such as wearable computers, cell phone technology, and personal area networks (PANs) for remote retrieval and monitoring of the surroundings requires antennas suitable to operate with multiband characteristics in wireless communication devices. This chapter provides an idea of current R&D trends in design, analysis, and synthesis of broadband, multiband, and reconfigurable antennas for modern wireless communications.

Chapter 13: Automotive Antennas. Automotive communication has witnessed a tremendous growth in recent years due to modern communication. In addition to the traditional AM/FM, present-day automobiles are equipped with many antenna systems, such as navigation, Global System for Mobile (GSM) communication, Bluetooth, satellite radio, remote keyless entry service (RKES), and tire-pressure monitoring system (TPMS). Apart from these services, higher-end cars are equipped with digital audio broadcasting (DAB), satellite in-vehicle TV, satellite digital audio radio service (SDARS), electronic toll collection (ETC), short-range and long-range radar system for adaptive cruise control (ACC), parking assistance, and collision detection and avoidance. Antenna designs for automotive applications are discussed in this chapter.

Chapter 14: Transceiver for Phased Array Radar. The antenna is one of the most complicated aspects of RF design. This chapter presents antenna design consideration in a complete transceiver system for the active phased array at the C-band using multitechnology-based chips.

Chapter 15: Phased Array and BFN for 5G Communication Sytems. The book is completed by a chapter in which a system level three-dimensional beam steerable high gain phased array system for 5G multiple-input and multiple-output (MIMO) network is designed. Phased-arrays operating at millimeter-wave or very high frequencies are already an active area of research by the emerging 5G cellular market.

The beamforming network (BFN) is the main component of multiple beams antennas. Beamforming networks are complex networks used to precisely control the phase and amplitude of radio frequency (RF) energy passing through them, which is conveyed to the radiating elements of an antenna in the 5G system. This chapter covers the design aspect of a phased array and beamforming network for a 5G communication system.

References

[1] Waterhouse, R. B., *Microstrip Patch Antennas: A Designer's Guide*, Norwell, MA: Kluwer Academic Publishers, 2003.

[2] Sangeetha, R. G., *Microstrip Patch Antenna Array with Omnidirectional Pattern*, Lambert Academic Publishing, 2015.

[3] Al-Naiemy, Y., *Design, Fabrication, and Testing of Microstrip Antennas*, Lambert Academic Publishing, 2013.

[4] Bhartia, P., I. Bahl, R. Garg, and A. Ittipiboon, *Microstrip Antenna Design Handbook*, Norwood, MA: Artech House, 2001.

[5] Kumar, G., and K. P. Ray, *Broadband Microstrip Antennas,* Norwood, MA: Artech House, 2002.

[6] Pan, B. C., and T. J. Cui, "Broadband Decoupling Network for Dual-Band Microstrip Patch Antennas," *IEEE Transactions on Antennas and Propagation*, Vol. 65, No. 10, pp. 5595–5598, October 2017.

[7] Mendes, C., and C. Peixeiro, "A Dual-Mode Single-Band Wearable Microstrip Antenna for Body Area Networks," *IEEE Antennas and Wireless Propagation Letters*, Vol. 16, pp. 3055–3058, 2017.

[8] Pandey, B K, A. K. Pandey, S. B. Chakrabarty, S. Kulshrestha, A. L. Solanki, and S. B. Sharma, "Dual Frequency Single Aperture Microstrip Patch Antenna Element for SAR Applications," *IETE Technical Review*, Vol. 23, No. 6, Noveber–December 2006, pp. 357–366.

[9] Pandey, A., "Design of a Cosecant Square-Shaped Beam Pattern SAR Antenna Array Fed with Square Coaxial Feeder Network," *2013 European Radar Conference (EuRAD),* Nuremberg, Germany, November 13, 2013, pp. 1699–1702.

[10] Antoniades, M. A., A. Dadgarpour, A. R. Razali, A. Abbosh, and T. A. Denidni, "Planar Antennas for Compact Multiband Transceivers Using a Microstrip Feedline and Multiple Open-Ended Ground Slots," *IET Microwaves, Antennas & Propagation*, Vol. 9, No. 5, 2015, pp. 486–494.

[11] Das, S., P. Chowdhury, A. Biswas, P. P. Sarkar, and S. K. Chowdhury, "Analysis of a Miniaturized Multiresonant Wideband Slotted Microstrip Antenna with Modified Ground Plane," *IEEE Antennas and Wireless Propagation Letters*, Vol. 14, 2015, pp. 60–63.

[12] Liu, Y., Y. M. Zhou, G. F. Liu, and S. X. Gong, "Heptaband Inverted-F Antenna for Metal-Rimmed Mobile Phone Applications," *IEEE Antennas and Wireless Propagation Letters*, Vol. 15, 2016, pp. 996–999.

[13] Chaabane, G., V. Madrangeas, M. Chatras, E. Arnaud, L. Huitema, and P. Blondy, "High-Linearity 3-Bit Frequency-Tunable Planar Inverted-F Antenna for RF Applications," *IEEE Antennas and Wireless Propagation Letters*, Vol. 16, 2017, pp. 983–986.

[14] Deng, J., J. Li, L. Zhao, and L. Guo, "A Dual-Band Inverted-F MIMO Antenna with Enhanced Isolation for WLAN Applications," *IEEE Antennas and Wireless Propagation Letters*, Vol. 16, 2017, p. 2270.

[15] Asadallah, F. A., J. Costantine, and Y. Tawk, "A Multiband Compact Reconfigurable PIFA Based on Nested Slots," *IEEE Antennas and Wireless Propagation Letters*, Vol. 17, No. 2, February 2018, pp. 331–334.

[16] Yan, S., V. Volskiy, and G. A. E. Vandenbosch, "Compact Dual-Band Textile PIFA for 433-MHz/2.4-GHz ISM Bands," *IEEE Antennas and Wireless Propagation Letters*, Vol. 16, 2017, pp. 2436–2439.

[17] Behdad, N., and K. Sarabandi, "A Compact Antenna For Ultrawide-Band Applications," *IEEE Transactions on Antennas and Propagation*, Vol. 53, No. 7, July 2005, pp. 2185–2192.

[18] Sim, C. Y. D., C. C. Chen, X. Y. Zhang, Y. L. Lee, and C. Y. Chiang, "Very Small-Size Uniplanar Printed Monopole Antenna for Dual-Band WLAN Laptop Computer Applications," *IEEE Transactions on Antennas and Propagation*, Vol. 65, No. 6, June 2017, pp. 2916–2922.

[19] Saghlatoon, H., T. Björninen, L. Sydänheimo, M. M. Tentzeris, and L. Ukkonen, "Inkjet-Printed Wideband Planar Monopole Antenna on Cardboard for RF Energy-Harvesting Applications," *IEEE Antennas and Wireless Propagation Letters*, Vol. 14, 2015, pp. 325–328.

[20] Ahmad, A., F. A. Tahir, and F. Khan, "A Planar GPS/GLONASS/LTE/WWAN Antenna for Ultra-Slim Smartphones," *2017 11th European Conference on Antennas and Propagation (EUCAP)*, Paris, 2017.

[21] Ghaffar, F. A., S. Yang, H. M. Cheema, and A. Shamim, "A 24 GHz CMOS Oscillator Transmitter with an Inkjet Printed On-Chip Antenna," *2016 IEEE MTT-S International Microwave Symposium (IMS),* San Francisco, CA, 2016, pp. 1–3.

[22] Tang, M. C., T. Shi, and R. W. Ziolkowski, "Flexible Efficient Quasi-Yagi Printed Uniplanar Antenna," *IEEE Transactions on Antennas and Propagation*, VOL. 63, NO. 12, December 2015, pp. 5343–5350.

[23] Booker, H. G., "Slot Aerials and Their Relation to Complementary Wire Aerials (Babinet's Principle)," *Journal of the Institution of Electrical Engineers–Part IIIA: Radiolocation,* Vol. 93, No. 4, 1946, pp. 620–626.

[24] Dyson, J., "The Unidirectional Equiangular Spiral Antenna," *IRE Transactions on Antennas and Propagation*, Vol. 7, No. 4, October 1959, pp. 329–334.

[25] Wei, X., J. Liu, and Y. Long, "Printed Log-Periodic Monopole Array Antenna with a Simple Feeding Structure," *IEEE Antennas and Wireless Propagation Letters*, Vol. 17, No. 1, January 2018, pp. 58–61.

[26] El Hamdouni, A., et al., "A Novel Design of a CPW-Fed Printed Fractal Antenna for UWB Applications," *2015 Third International Workshop on RFID And Adaptive Wireless Sensor Networks (RAWSN),* Agadir, Morocco, 2015, pp. 38–41.

[27] Sabban, A., "New Fractal Compact Printed Antennas," *2017 IEEE International Symposium on Antennas and Propagation & USNC/URSI National Radio Science Meeting*, San Diego, CA, 2017, pp. 2197–2198.

[28] Gianvittorio, J. P., J. Romeu, S. Blanc,h and Y. Rahmat-Samii, "Self-similar Prefractal Frequency Selective Surfaces for Multiband and Dual-Polarized Applications," *IEEE Transactions on Antennas and Propagation,* Vol. 51, No. 11, November 2003, pp. 3088–3096.

[29] Gianvittorio, J. P., and Y. Rahmat-Samii, "Fractal Element Antennas: A Compilation of Configurations with Novel Characteristics," *IEEE Antennas and Propagation Society International Symposium, Transmitting Waves of Progress to the Next Millennium, 2000 Digest*. Held in conjunction with USNC/URSI National Radio Science Meeting, Salt Lake City, UT, 2000, Vol. 3, pp. 1688–1691.

[30] Derneryd, A. G., "A Theoretical Investigation of the Rectangular Microstrip Antenna," *IEEE Transactions on Antennas and Propagation*, Vol. AP-26, July 1978, pp. 532–535.

[31] Pues, H., and A. Van de Capelle, "Accurate Transmission-Line Model for the Rectangular Microstrip Antenna," *Proceedings of the IEE*, Vol. 131, Part H, December 1984, pp. 334–340.

[32] Richards, W. F., Y. T. Lo, and D. Harrison, "An Improved Theory for Microstrip Antennas and Applications," *Transactions on Antennas and Propagation*, Vol. AP-29, January 1981, pp. 38–46.

[33] Harrington R. F., *Field Computation by Moment Methods*, New York, the Macmillan Co., 1968.

[34] Silvester P. P., and R. L. Ferrari, *Finite Element for Electrical Engineers*, Third Edition, Oxford, U. K., Cambridge University Press, 1991.

[35] Zhang X., J. Fang, and K. Mei, "Calculations of The Dispersive Characteristics of Microstrips by the FDTD Methods," *IEEE Transactions on Microwave Theory and Techniques*, Vol. 26, February 1988, pp. 263–267.

[36] Shibata T., T. Havashi, and T. Kimura, "Analysis of Microstrip Circuits Using Three Dimensional Full-Wave Electromagnetic Fields Analysis in the Time-Domain," *IEEE Transactions on Microwave Theory and Techniques*, Vol. 36, June 1988, p. 1064.

[37] Feix, N., M. Lalande, and B. Jecko, "Harmonical Characterization of a Microstrip Bend via the Finite Difference Time Domain Method *IEEE Transactions on Microwave Theory and Techniques*, Vol. 40, No. 5, May 1992, pp. 955–961.

[38] Taflove A., "The Finite-Difference Time-Domain Method for Electromagnetic Scattering and Interaction Problems," *IEEE Transactions on Electromagnetic Compatibility*, Vol. EMC-22, August 1980, p. 191.

[39] J. R., James, and Hall P. S. (eds.), *Handbook of Microstrip Antennas*, Stevenage, UK: IET, 1989.

Selected Bibliography

Adin, I., G. Bistue, R. Mittra, C. Quemada, and K. F. Warnick, *Numerical Analysis for Electromagnetic Integral Equations,* Norwood, MA: Artech House, 2008.

Bahl, I. J., and P. Bhartia, *Microstrip Antennas,* Dedham, MA: Artech House, 1980.

Balanis, C. A., *Antenna Theory Analysis and Design,* Fourth Edition, Hoboken, NJ: John Wiley & Sons, 2016.

Dennis, S., *Electromagnetic Simulation Using the FDTD Method*, Piscataway NJ: Wiley-IEEE Press, July 2000.

Harrington, R. F., *Field Computation by Moment Methods*, New York: The MacMillan Co., 1968.

Hubing, T. H., "Calculating the Currents on Wires Attached to Opposite Sides of a Thin Plate," Applied Computation Electromagnetics Society 1990, pp. 9–13.

Kara, M., "Design Consideration for Rectangular Microstrip Antenna Elements with Various Substrate Thickness," *Microwave and Optical Technology Letters*, Vol. 19, No. 2, October 1998, pp. 111–120.

Kin-Lu, W., *Compact and Broadband Microstrip Antennas*, New York: John Wiley & Sons, 2002, pp. 28–30.

Kunz, K. S., and R. J. Luebbers, *The Finite Difference Time Domain Method for Electromagnetics*, Boca Raton, FL: CRC Press, 1993.

Pozar, D. M., and D. H. Schaubert, *Microwave Antennas*: *The Analysis and Design of Microstrip Antennas and Arrays*, New York: IEEE Press, 1995.

Sheen, D., S. Ali, M. Abouzahra, and J. Kong, "Application of Three-Dimensional Finite Element to the Analysis of Planar Microstrip Circuits," *IEEE Transactions on Microwave Theory and Techniques*, Vol. 38, July 1990, pp. 849–857.

Stutzman, W. L., and G. A. Thiele, *Antenna Theory and Design*, Second Edition, New York: John Wiley & Sons, 1998.

Sullivan, D. M, *Electromagnetic Simulation Using the FDTD Method,* New York: IEEE Press, 2000.

Taflove, A., and M. Brodwin, "Numerical Solution of Steady State Electromagnetic Scattering Problems Using the Time Dependent Maxwell's Equations," *IEEE Transactions on Microwave Theory and Techniques*, Vol.23, No.1, August 1975, pp. 623–630.

Yee, K., *Numerical Solution of Initial Boundary Value Problems Involving Maxwell's Equations in Isotropic Media, IEEE Transactions on Antennas and Propagation*, Vol. 14, No. 3, 1966, pp. 302–307.

Yu, W., W. Li, Elsherbeni, A., and Y. Rahmat-Samii, *Advanced Computational Electromagnetic Methods & Applications,* Norwood, MA: Artech House, 2015.

CHAPTER 2

Microstrip Antenna Design

2.1 Introduction

Applications of printed and microstrip patch antennas are increasing in popularity for use in wireless applications due to their low-profile structure. Microstrip antennas are extremely compatible with embedded antennas in handheld wireless devices such as cellular phones. The communication and telemetry antennas on missiles should be thin and conformal and are often microstrip patch antennas. Satellite communication and remote sensors are other areas where microstrip antennas have been used successfully. Because of their extremely thin profile, printed antennas have found main applications in military aircraft, missiles, rockets, and satellites. There are so many systems that use this type of antenna, such as remote-controlled television, cellular phones, satellite communications, spacecraft, radars, wireless phones, and wireless computer networks. Use of antennas in the aircraft and spacecraft has also increased the demand for a low-profile antenna that can provide reliable communication. The microstrip patch is combined with electronic components and integrated circuits. Another major advantage of the microstrip patch is that it can be conformal or flush-mounted planar with other surfaces, such as an airplane radome or mobile body, with only a minimum of space required for the feed line.

2.2 Microstrip Antenna

Microstrip antennas are planar resonant cavities that leak from their edges and radiate. A microstrip patch antenna contains a metallic radiating patch on one side of a dielectric substrate that has a ground plane on the other side. The patch is made of conducting material such as gold or copper. The radiating patch and the feed lines are photoetched on the dielectric substrate. The patch shape can be square, rectangular, circular, triangular, elliptical, or some other common shape.

Low dielectric constant substrates materials are preferred for maximum radiation. Rectangular and circular microstrip patch configurations are the most commonly used configuration. Other shapes can also be designed but these are complex to analyze and require significant numerical computations. By changing the shape of the structure, flexibility in resonant frequency, pattern, polarization, and

impedance can be achieved. A microstrip antenna is characterized by its length, width, input impedance, gain, and radiation pattern. The length is a very critical parameter because it governs the resonant frequency of the antenna. Length of the patch is nearly a half wavelength in the dielectric. For compact microstrip patch antennas, substrates with higher dielectric constants are used but these are less efficient and result in a narrower bandwidth. Hence a trade-off must be realized between the antenna dimensions and antenna performance. There is no fixed rule to find the width of a patch. Normally, the width of a patch is comparable to the operating wavelength and the thickness of the substrate is kept very small compared to wavelength.

Some of the benefits of microstrip patch antennas include [1] small profile, light weight, inexpensive fabrication, and planar configuration. Many feeding configurations are possible for feeding the microstrip patch structure, such as aperture feeds, probe feeds, microstrip line feeds, inset feed, and proximity feeds, where each method has advantages depending on the application. Despite these advantages, microstrip antennas present major challenges to the designer due to an inherently narrow bandwidth, the spurious radiation, low efficiency due to dielectric losses and conductor losses, lower power handling capability, and tolerance problems [2]. Considerable research has been done to overcome these limitations, notably in increasing the bandwidth.

2.2.1 Microstrip Antenna Working Principle

A microstrip patch radiates from fringing fields around its edges, as shown in Figure 2.1. When the metallic patch is excited by feed, a charge distribution is being established between the ground plane and the underneath of the patch. There is a positive charge below the patch and the ground plane is charged to negative and because of that, attractive forces are being set up between the patch and ground plane. A general analysis of patch considers the patch as a resonant cavity with metal (electric) walls of the patch and the ground plane and magnetic or impedance walls around the edges. Impedance match happens when a patch resonates as a resonant cavity. The antenna can achieve peak efficiency with perfect impedance matching. The field lines are uniform along the width while vary sinusoidally along the length.

The current is maximum at the center of the patch, while the electric field is maximum at the two radiating edges. Unlike the patch, a normal transmission line radiates less power because the fringing fields are matched by nearby counteracting

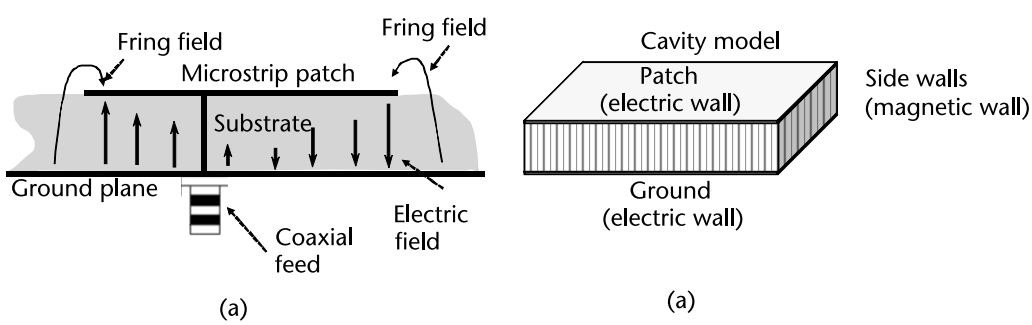

Figure 2.1 Microstrip patch (a) radiation mechanism and (b) cavity model representation.

fields. Power radiates from open circuits and from discontinuities such as transitions and corners, but the amount depends on the radiation conductance load to the line relative to the patches. The edges of a patch act as slots whose excitations depend on the internal fields of the cavity.

A thick dielectric substrate having a low dielectric constant is desirable for antenna design because this provides better efficiency, larger bandwidth, and better radiation, although such a configuration leads to a larger antenna size. To design a compact microstrip patch antenna, higher dielectric constants must be used, which are less efficient and result in a narrower bandwidth. Therefore, a compromise must be reached between antenna dimensions and antenna performance.

2.2.1.1 Cavity Model of Rectangular Microstrip Patch

In the cavity model, the microstrip patch is represented by assuming that the material of the substrate is truncated and does not extend beyond the edges of the patch as shown in Figure 2.1. The four side walls of the substrate act as the magnetic walls and these represent four narrow apertures (slots) through which radiation takes place. The inside area of the dielectric substrate is presented as a cavity limited by electric walls (conductors) on the top and bottom. The radiated field is calculated using equivalence principle. The field inside the cavity is assumed equal to zero, and its influence on the field in the infinite region outside is represented by the equivalent surface currents on the surface of the cavity [2]. Therefore, the tangential H components at the slots equal to zero:

$$J_s = \hat{n} \times H = 0 \tag{2.1}$$

Only the equivalent magnetic current density has substantial contribution to radiated field.

$$M_s = -\hat{n} \times E \tag{2.2}$$

The radiation from an (x-y) slot of constant M_s current can be found using the electric vector potential F. Since M_s has only a y component, $F = F_y$ also has only y component:

$$F_y = -\frac{\varepsilon E_0 W h}{2\pi r} . e^{-jk_0 r} . \frac{\sin X}{X} . \frac{\sin Y}{Y} \tag{2.3}$$

where

$$X = \frac{k_0 h}{2} \sin\theta \cos\varnothing$$

$$Y = \frac{k_0 W}{2} \sin\theta \sin\varnothing$$

E-plane pattern (xz plane, $\varnothing = 0°$, $0° \leq \theta \leq 180°$)

$$f_E(\theta) = \frac{\sin\left(\frac{k_0 h}{2}\sin\theta\right)}{\frac{k_0 h}{2}\sin\theta}.\cos\left(\frac{k_0 L_{eff}}{2}\cos\theta\right) \tag{2.4}$$

H-plane pattern (xy plane, $\theta = 90°$, $-90° \leq \varnothing \leq 90°$).

$$f_H(\theta) = \cos\varnothing.\frac{\sin\left(\frac{k_0 h}{2}\cos\varnothing\right)}{\frac{k_0 h}{2}\cos\varnothing}.\frac{\sin\left(\frac{k_{0W}}{2}\sin\varnothing\right)}{\frac{k_{0W}}{2}\sin\varnothing} \tag{2.5}$$

2.2.2 Microstrip Antenna Design Process

Microstrip antenna design steps are shown in Figure 2.2. The most vital step is to finalize design specifications. Design specifications are driven based on the application. Normally antenna specifications are given by the system engineer after doing the system-level analysis and simulation of a complete system such as a 5G network and radar system. A wireless mobile communication antenna has a completely different specification than that of a satellite or radar antenna system. Important antenna design specifications were covered in Chapter 1, Section 1.3. Antenna specifications such operating frequency, bandwidth, gain, radiation pattern, and polarization are driven by system requirements. The first step in designing a printed antenna is to choose an appropriate substrate. After collecting the design requirement, the next step is to select the radiating element, the size of the antenna, the feeding mechanism, and the electromagnetic simulation technique needed to get antenna performance. Proper feed selection for single-radiation element and feed network design for array antennas are another crucial design step.

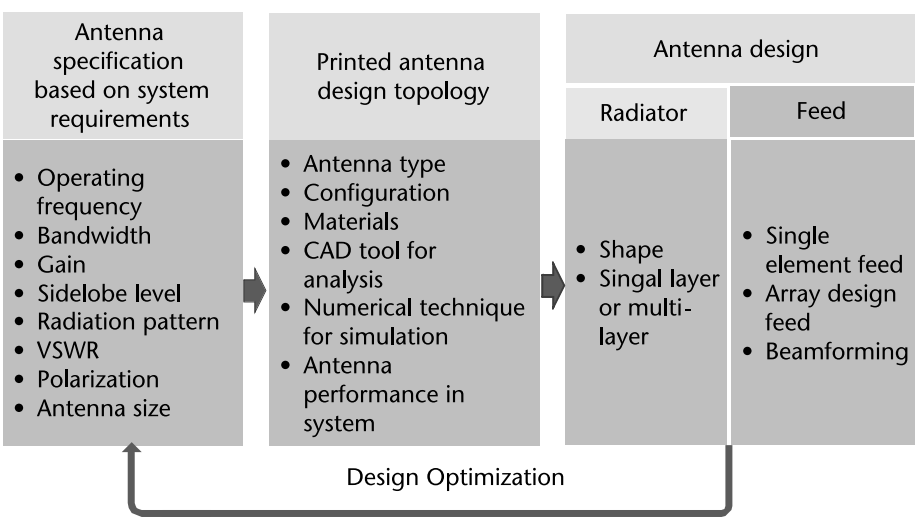

Figure 2.2 Microstrip patch antenna design flow.

2.2.3 Radiating Element Design of Microstrip Antenna

The dimensions of a single microstrip patch antenna as shown in Figure 2.3 are first calculated using approximation formulas. There are several formulas with different levels of approximation accuracy developed by various researchers [3–8] for thin substrate and effective length L less than a half-wavelength of the chosen operating frequency; however, Kara [9] developed compact formulas for thick substrates. The formulas by Kara were used to calculate the dimensions of the patch as illustrated next based on the transmission-line model of Derneryd [4].

The patch conductor can be of any shape. For a rectangular patch, the length L of the patch is usually $0.3\lambda_0 < L < 0.5\lambda_0$, where λ_0 is the free-space wavelength. The patch is very thin, so that $t << \lambda_0$ (where t is the patch thickness). The height h of the dielectric substrate is usually $0.003\,\lambda_0 \leq h \leq 0.05\lambda_0$. The dielectric constant of the substrate (ε_r) is typically in the range of $2.2 \leq \varepsilon_r \leq 12$. For efficient radiation, low dielectric constant material is preferred over high dielectric constant material. The patch width, W, is usually the first to be chosen. For thin substrates, the empirical approximation by Bahl and Bhartia [10] as shown in (2.6) is used:

$$W = \frac{\lambda_0}{2\sqrt{0.5(\varepsilon_r + 1)}} \tag{2.6}$$

where λ_0 and ε_r are the wavelength in free space and dielectric constant of the substrate, respectively. The effective permittivity in the substrate is evaluated using the formula by Schneider [11] by means of (2.7):

$$\varepsilon_{eff} = \frac{\varepsilon_r + 1}{2} + \frac{\varepsilon_r - 1}{2}\left(\frac{1}{\sqrt{1 + 12h/w}}\right) \tag{2.7}$$

where h is the thickness of the substrate and the terms are as explained above. Hall and Wood [12] give an approximation for obtaining the length L of the microstrip

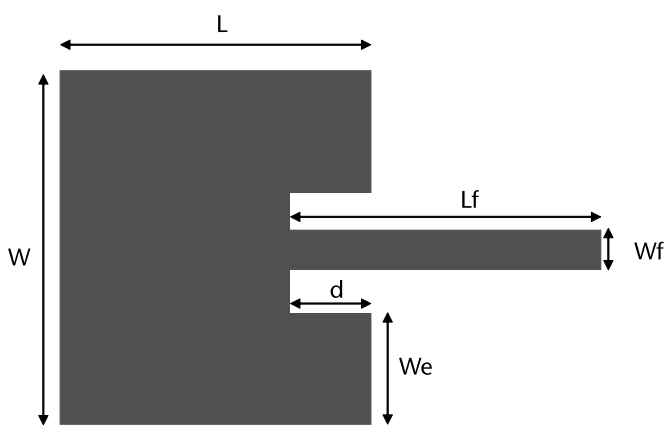

Figure 2.3 Inset fed rectangular microstrip antenna design.

patch antenna element with the substrate thickness less than $0.0815\lambda_d$ in this kind of media as

$$L = \frac{c_0}{2f_r\sqrt{\varepsilon_{eff}}} \tag{2.8}$$

with $c_0 = 2.998 \times 10^8$ meter/second being the velocity of the electromagnetic wave in free space. Because of the fringing field at the edges of the patch [13], a fringe factor, ΔL, must be subtracted from (2.8) to obtain the effective length. This fringe factor is given by (2.9):

$$\Delta L = 0.412h\frac{\left(\varepsilon_{eff} + 0.300\right)}{\varepsilon_{eff} - 0.258}\frac{\left(\frac{W}{h} + 0.264\right)}{\left(\frac{W}{h} + 0.813\right)} \tag{2.9}$$

Hence by means of (2.8) and the line extension, the effective length, L_{eff}, of a rectangular antenna element is [13–14]:

$$L_{eff} = L - 2\Delta L \tag{2.10}$$

2.2.4 Criteria for the Substrate Selection

The substrate in microstrip antennas is primarily needed for the mechanical support of the antenna. To provide this support, the substrate should consist of a dielectric material, which may affect the electrical performance of the antenna, circuits, and transmission line impedance. Some important parameters that should be considered while selecting the substrate material in the design of antennas are surface wave excitation, dispersion of the dielectric constant, loss tangent of the substrate, copper loss, effects of temperature, mechanical requirements (conformability, machinability, solderability, weight, elasticity, etc.), and cost. The criterion for the selection of substrate necessitates the following considerations:

- Substrates with higher thickness and a high dielectric constant result in smaller bandwidths and lower efficiencies due to the possibility of surface-wave excitation.
- Higher dielectric constant materials with longer lengths of feed line result in increased losses and chances of spurious radiation.
- The substrate thickness should be made as thin as possible to eliminate multiple surface waves. A height of $0.01\lambda_0$ to $0.05\lambda_0$ is considered ideal in this regard.
- It is preferable to use low dielectric constant material and a substrate of optimum thickness for containing the spurious feed radiation to a minimum.

A microstrip patch element launches surface wave modes in addition to the fields radiated into space. Surface waves give rise to end-fire radiation and it can be excited at the dielectric-to-air interface. Moreover, a surface wave can lead to unwanted coupling between array elements. The power thrown into the surface waves is a power that will ultimately be lost, and hence the excitation of surface waves lowers the overall radiation efficiency of the antenna. The phase velocity of surface waves is strongly dependent on the dielectric constant ε_r and thickness h of the substrate. The dependence of the dielectric constant ε_r and loss tangent on the frequency is referred to as frequency dispersion. Generally, the cost of printed antennas depends on the substrate material and connectors only. FR4 is one of the commercially available low-cost materials for printed antennas above the 1-GHz range. Some commonly used substrate materials in printed and microstrip antenna design are listed in Table 2.1 [2].

2.2.5 Losses in Microstrip Antennas

Losses in microstrip antennas are due to conductor loss, radiation loss, and dielectric loss. These losses affect microstrip antenna radiation efficiency. Conductor loss is calculated using (2.11):

$$\begin{aligned} \alpha_c &= 8.686 \log\left(R_s/2WZ_0\right) \text{ dB/length} \\ R_s &= \sqrt{\pi f \mu \rho} \text{ skin resistance} \end{aligned} \tag{2.11}$$

Table 2.1 Commonly used Substrates for Printed and Microstrip Antenna Design

Material	*Dielectric Constant*	*Loss Tangent*
Foam	1.08	0.0010
Unreinforced PTFE, Cuflon	2.1	0.0004
RT/duroid 5880	2.2	0.0009
Teflon-ceramic,	2.3	0.0010
RT/duroid 5870	2.33	0.0012
polyolefin-glass,	2.42	0.0010
Teflon-quartz,	2.47	0.0006
Teflon glass	2.55	0.0015
Polystyrene quartz	2.6	0.0005
RT/duroid 6202	2.94	0.0015
Fused quartz	3.78	0.0001
FR4	4.4	0.0200
Rogers TMM6	6.0	0.0023
Polyolefin-ceramic	7.5	0.0010
Alumina	9.8	0.0001
Teflon-ceramic	10.3	0.0020
RT/Duroid 6010.2LM	10.7	0.0023
Silicon	11.9	0.0400
GaAs	12.9	0.0600

Dielectric loss is calculated by using Equation (2.12):

$$\alpha_d = 27.3\left(\frac{\varepsilon_r}{\sqrt{\varepsilon_{eff}}}\right)\left(\frac{\varepsilon_{eff}-1}{\varepsilon_e-1}\right)\left(\frac{\tan\delta}{\lambda}\right) \tag{2.12}$$

where tanδ is thedielectric loss coefficient.

Low dielectric loss tangent substrate materials have less dielectric loss, which is good for antenna applications.

2.3 Feed Techniques for Single-Element

Microstrip patch antenna elements can be fed by a variety of methods. These methods can be classified into two categories: direct or indirect contact. In the direct contact technique, the power is fed directly to the radiating patch using a connecting element such as a microstrip line or coaxial connector. In the indirect contact scheme, electromagnetic field coupling is done to transfer power between the microstrip line and the radiating patch. The four most popular feed techniques used are the microstrip line, coaxial probe, proximity coupling, and aperture coupling.

2.3.1 Microstrip Line Feed

In the microstrip line feed technique, a conducting metallic strip directly connects the path element with an RF power source. This kind of feed plan has the advantage that the feed can be etched on the same substrate along with the patch element to provide a planar structure. The feed line is smaller in width as compared to the patch. As shown in Figure 2.4, there are many different configurations of microstrip line feeds.

In edge- and offset edge-fed schemes, the feed line starts from the edge of the patch, while in inset Feed, the microstrip line starts from a location inside the patch. The objective of the inset cut in the patch is to match the impedance of the feed line to the patch without the need for any additional matching element. This

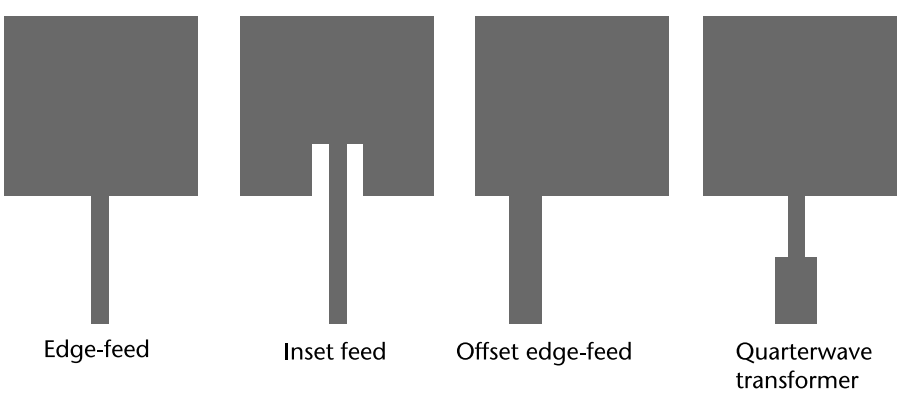

Figure 2.4 Different feeding mechanisms in a microstrip patch antenna.

is achieved by properly controlling the inset position and impedance of the line. Inset-fed is an easy feeding scheme as it provides ease of fabrication and simplicity in modeling as well as impedance matching. One disadvantage of the microstrip line feed is undesired cross-polarized radiation.

2.3.2 Coaxial Feed

The coaxial feed or probe feed for feeding microstrip patch antennas is a very common technique. The inner conductor of the coaxial feed extends through the dielectric and is soldered to the radiating patch, while the outer conductor is connected to the ground plane. The coaxial feed can be placed at any desired location inside the patch to match with its input impedance. This feed method has low spurious radiation. However, it provides narrow bandwidth and is difficult to model since a hole must be drilled in the substrate and the connector protrudes outside the ground plane, thus not making it completely planar for thick substrates ($h > 0.02\lambda_0$) and because of this, it is difficult to use this feed mechanism in array applications. Another disadvantage is for thicker substrates, which provide broad bandwidth; the increased probe length makes the input impedance more inductive, leading to matching problems. Practically, 50Ω SMA connectors are coaxial fed. The feeding probe point location can be located at the point (X_f, Y_f) in the x-y coordinates, as shown in Figure 2.5. The location points are given by (2.13):

$$X_f = \frac{L}{2} \text{ and } R\left(Y_f\right) = R\left(y = 0\right)\cos^2\left(\frac{\pi y_0}{L}\right) \tag{2.13}$$

where $R(y = 0)$ is the edge impedance of the patch.

2.3.3 Aperture-Coupled Feed

In the aperture-coupled feed technique, the radiating patch and the microstrip feed line are placed on two different layers and separated by the ground plane, as shown in Figure 2.6. Coupling between the patch and the feed line is made through an

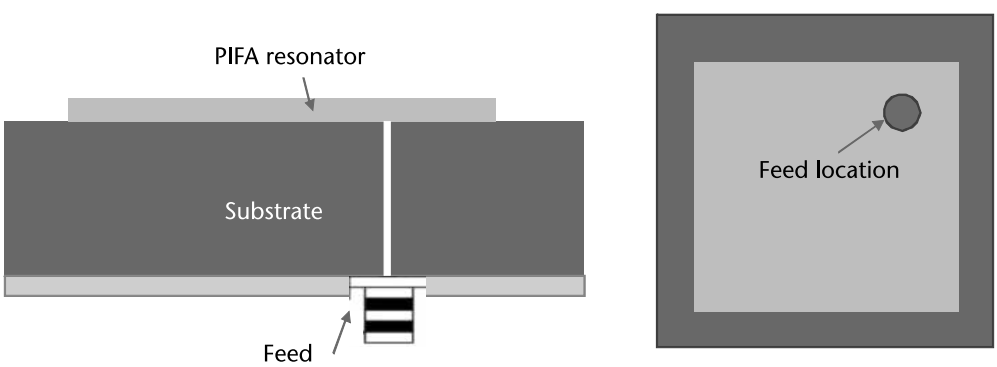

Figure 2.5 Coaxial-fed microstrip patch antenna (side and top views).

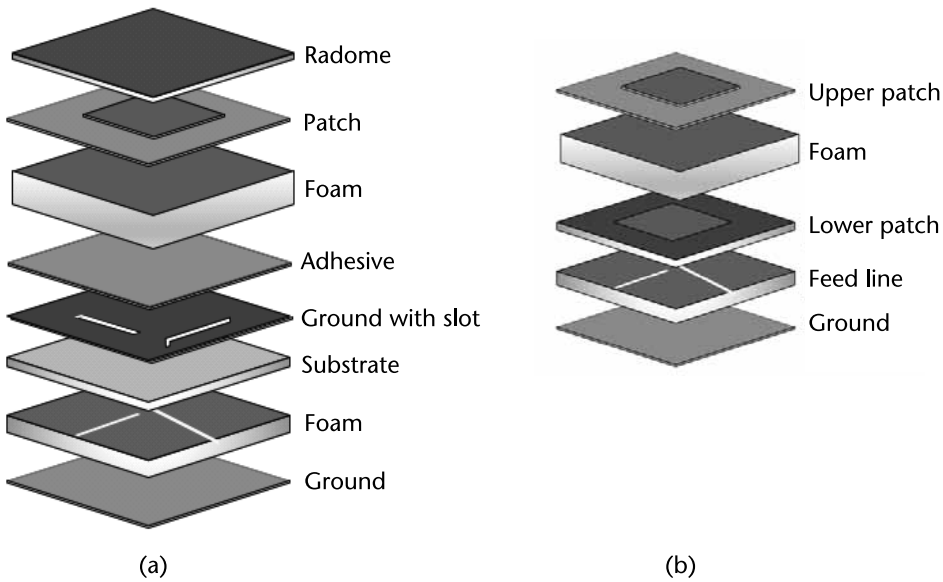

Figure 2.6 Microstrip antenna feed mechanism: (a) aperture-coupled antenna, and (b) proximity-coupled antenna.

aperture or a slot in the ground plane. The coupling slot is usually centered under the patch, leading to lower cross-polarization due to the symmetry of the configuration. In the dual-polarized antenna, there are two coupling slots, one for vertical polarization and other for horizontal polarization.

The amount of coupling from the feed line to the patch is determined by the size, shape, and location of the aperture. Since patch and the feed line are seprated by the ground plane, spurious radiation is minimized. A high dielectric material is used at the bottom for the feed line and a thick, low dielectric constant material is used for the radiator at the top substrate to optimize radiation from the patch. This feeding scheme provides narrow bandwidth.

2.3.4 Proximity- or Electromagnetically Coupled Feed

The proximity-coupled feed technique is also called an electromagnetically couple feed. As shown in Figure 2.6, the main advantage of this feed technique is that it eliminates spurious feed radiation and provides very high bandwidth (as high as 14%) due to an overall increase in the thickness of the microstrip patch antenna. This scheme also provides choices between two different dielectric material; one for the patch and another for the feed line to optimize the individual performances. Matching can be realized by controlling the length of the feed line and the width-to-line ratio of the patch. The major disadvantage of this feed structure is that it is difficult to fabricate because the two dielectric layers need a proper alignment. A comparison of all major microstrip antenna feeding structures is shown in Table 2.2.

Table 2.2 Feeding Techniques Comparison

Characteristics	*Microstrip Line Feed*	*Coaxial Feed*	*Aperture-Coupled Feed*	*Proximity-Coupled Feed*
Spurious feed radiation	More	Less	Less	Minimum
Reliability	Better	Poor due to soldering	Good	Good
Ease of fabrication	Easy	Soldering and drilling needed	Alignment required	Alignment required
Bandwidth	2%–5%	2%–5%	2%–5%	14%
Polarization purity	Good	Poor	Excellent	Poor

2.4 Design and EM Simulation of Microstrip Antennas

Design, analysis, and electromagnetic simulation of a single microstrip patch antenna analysis, design, and electromagnetics operating at 2.4 GHz is discussed in this section. The designed antenna is used for industrial, scientific, medical (ISM) applications and WLAN. Consideration is given to a practical design technique, including substrate selection and antenna measurements. The microstrip antenna is characterized by its length L, width W, and substrate thickness h.

2.4.1 Design Process

A single-element microstrip antenna design flow is shown in Figure 2.7. Design starts with antenna specification. Antenna specification is derived from the application requirement. Based on specification and cost, the substrate material is selected. Antenna radiating parameters and feed design parameters are calculated based on empirical equations (2.6 to 2.15). Antenna performance is optimized in electromagnetic simulation based EDA tools. It is important to carefully select a design and simulation EDA tool and electromagnetic simulation software for efficient antenna design as mentioned in Chapter 1.

After the antenna design parameter optimization, antenna design PCB is generated for fabrication. Finally, all antenna parameters are measured before actual use of the antenna. To design a rectangular patch antenna, its length L, width W, copper layer thickness t, and thickness of a substrate h information is needed.

2.4.2 Feed-Point Location of a Single Patch Antenna

Edge feed is used to feed the antenna. The edge impedance Z_A of the patch antenna is calculated by using (2.14):

$$Z_A = 90\left(\frac{\varepsilon_r^2}{\varepsilon_r - 1}\right)\left(\frac{L}{W}\right)^2 \tag{2.14}$$

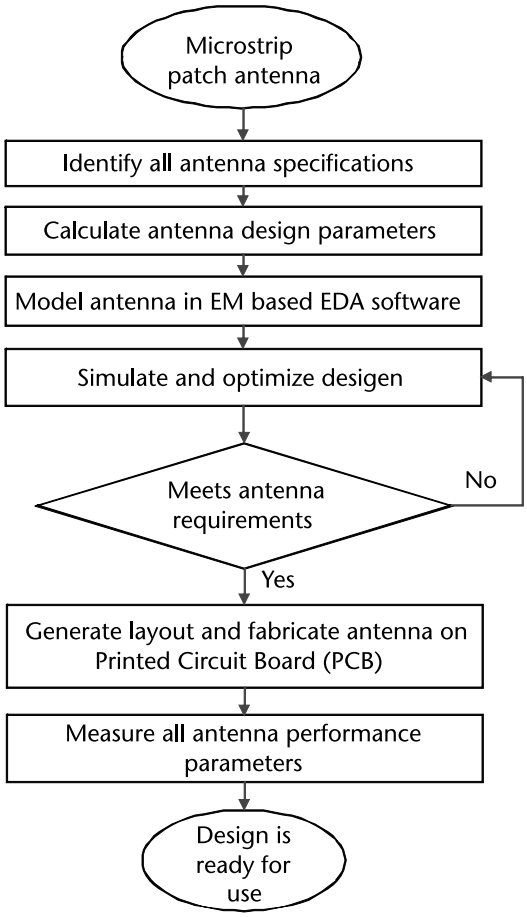

Figure 2.7 Microstrip antenna design and fabrication process.

Figure 2.8 shows a patch antenna with a quarter-wavelength matching section. Input impedance Z_{in} is matched with a 50-ohm microstrip feed line impedance Z_0. If the edge impedance of the patch antenna is Z_A, then the input impedance seen from the beginning of the quarter-wavelength line is

$$Z_{in} = Z_0 = \frac{Z_L^2}{Z_A} \tag{2.15}$$

Input impedance Z_{in} can be changed by the selection of Z_L, so that $Z_{in} = Z_0$ and the antenna is matched by impedance. The impedance Z_L value varies with the width of the quarter-wavelength strip.

2.4.3 Microstrip Patch Antenna Design Parameters

Patch antenna design parameters are shown in Table 2.3. Rogers 5870 with ε_r equal to 2.33 is used as the dielectric material. The thickness t of a metallic layer must be a substantially smaller than the wavelength of the free space ($t << \lambda_0$) for a given

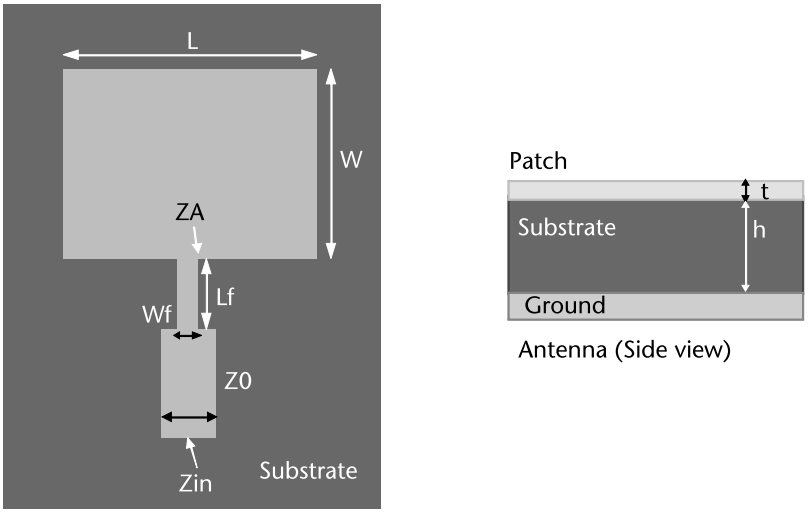

Figure 2.8 Rectangular microstrip patch antenna design parameters.

Table 2.3 Typical Design Specifications of a Microstrip Antenna

Specifications	*Parameters*	*Value*
Antenna radiating element	Patch length L	40 mm
	Patch length W	47 mm
Antenna feedline	Edge impedance (Z_A)	360
	Feedline impedance	50 ohm
	Quarter-wave transformer L	22 mm
	Quarter wave Transformer W	0.3 mm
Substrate	Dielectric constant (ε_r)	2.33
	Thickness of the substrate (h)	0.5 mm
	Loss tangent (tan δ)	0.008
	Copper metal thickness (t)	0.035 mm
Antenna specifications	Operating frequency (f_0)	2.4 GHz
	Polarization	Linear
	Feed type	Edge feed
Design requirement	Return loss	< -15 dB
	Bandwidth	10 MHz
	Gain	6 dBi
	Half-power beamwidth	71 Deg

frequency, in our case 2.4 GHz. Calculation of width W and length L for a single patch antenna is performed using (2.6) and (2.8), respectively. ΔL is the fringe factor calculated by (2.9). For an operating frequency of 2.4 GHz, the wavelength λ_0 equals 0.125m.

2.4.4 Patch Antenna Design and Analysis Result at 2.4 GHz

In a microstrip patch antenna simulation process, the first step is the creation of the layout geometry together with the definition and assignment of material. The edge-fed antenna is modeled and simulated in Advanced Design System (ADS) software.

A quarter-wave transformer is used to match patch edge impedance to 50Ω feedline impedance as shown in Figure 2.9. The next step is to define port excitation. Finally, antenna performance is optimized using the full-wave electromagnetic solver FEM. The patch antenna simulated return loss plot is shown in Figure 2.9. The obtained return loss of patch is -17 dB at 2.4 GHz. Like VSWR, return loss is indicated by how well the matching between the transmitter and antenna has taken place. The ideal value of the return loss is around –10 dB, which corresponds to a VSWR of less than 2. These results show that a microstrip patch antenna mainly radiates in the vertical direction.

The peak gain is 6.1 dBi at 2.4 GHz and with the main lobe in the direction of theta = 0 degrees and phi = 0 degrees, as shown in Figure 2.10. The half-power beamwidth of the antenna is 71 degrees.

2.4.5 Coaxial-Fed Patch Antenna for Coal Mines

In coal mines, the size of microcell zones can be efficiently increased by using bidirectional antennas, which preferentially radiate the antenna beam along the longitude. The special channel property and safety production in coal mines bring up new challenges in antenna design, such as low profile, easy fabrication, low cost, low wind resistance, antiexplosion, and good bidirectional radiation pattern. The performance of the system is degraded by severe signal attenuation inside the coal mine where the wall conductivity or dielectric constant is relatively high. Broadband VHF/UHF transmission is normally used as it is difficult to predict the polarization of the reflected component for such applications. Coaxial-fed microstrip antennas are a very suitable choice as they meet most of coal mine antenna requirements. Figure 2.11 shows a microstrip patch antenna fed with coaxial feed designed in the UHF band for such an application. This antenna is developed for end use in coal mines where the antenna is flush-mounted on coal strata. The antenna is used in determining the angle of arrival of the reflective component when RF is launched in coal strata with the antenna embedded in it. Thus, it will be able to measure the angle of arrival of any reflective component due to the presence of a waterbed at a

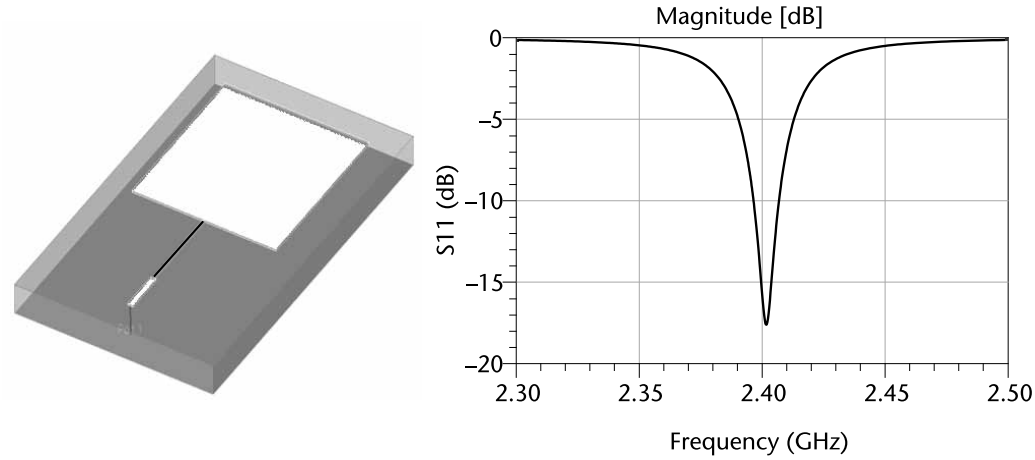

Figure 2.9 Three-dimensional model of microstrip antenna and simulated return loss plot using FEM.

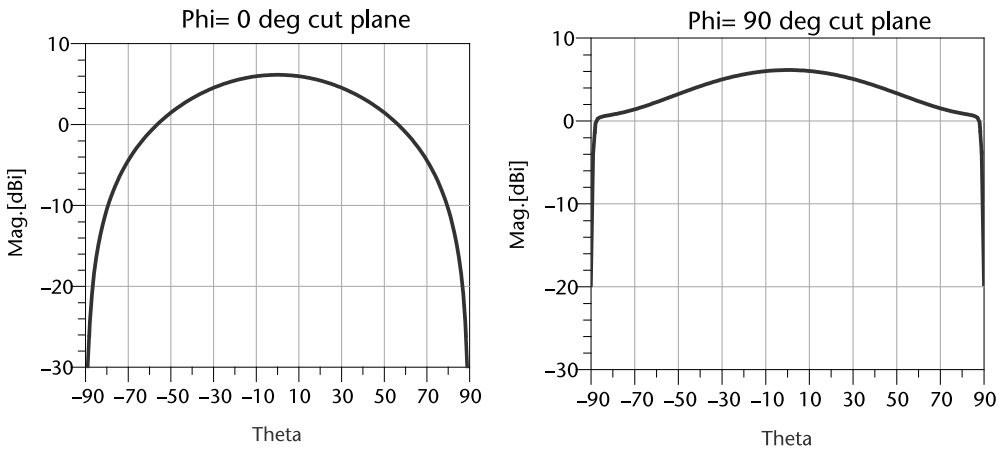

Figure 2.10 Antenna radiation patterns at phi = 0 and phi = 90-degree cuts.

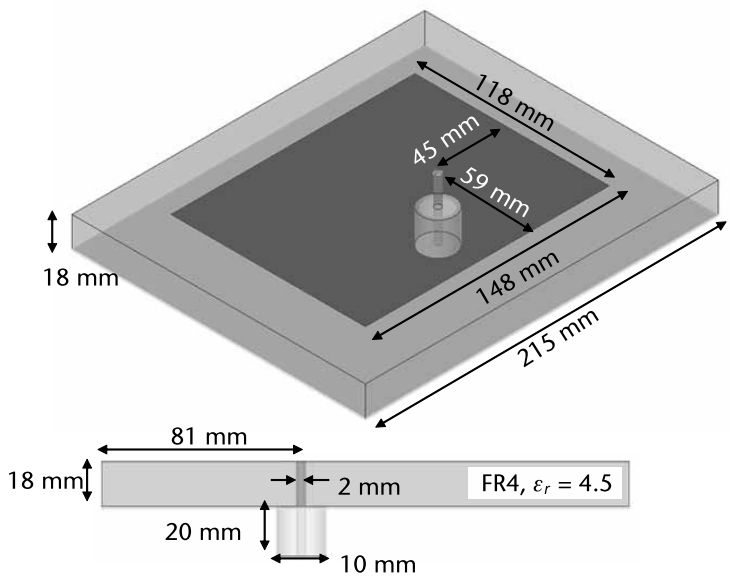

Figure 2.11 Coaxial-fed microstrip patch antenna design for coal mine.

distance. The antenna is fed with a 50Ω coaxial line at a feeding location of 59 mm by 45 mm on the patch, where patch impedance is also 50Ω. This type of feeding scheme can be placed at any desired location inside the patch to match with the desired input impedance and also has low spurious radiation.

The antenna is fabricated on an 18-mm thick FR4 substrate of 4.5 dielectric constant. Patch size is 148 mm × 118 mm. The effect of the key geometrical parameters on antenna radiation and impedance matching performance has been studied by the FEM numerical technique. The antenna operating frequency is 440 MHz, as shown in Figure 2.12. It is a 10-MHz narrowband (2.2% -10 dB bandwidth) antenna. As discussed in the previous section, coaxial feed antennas are normally

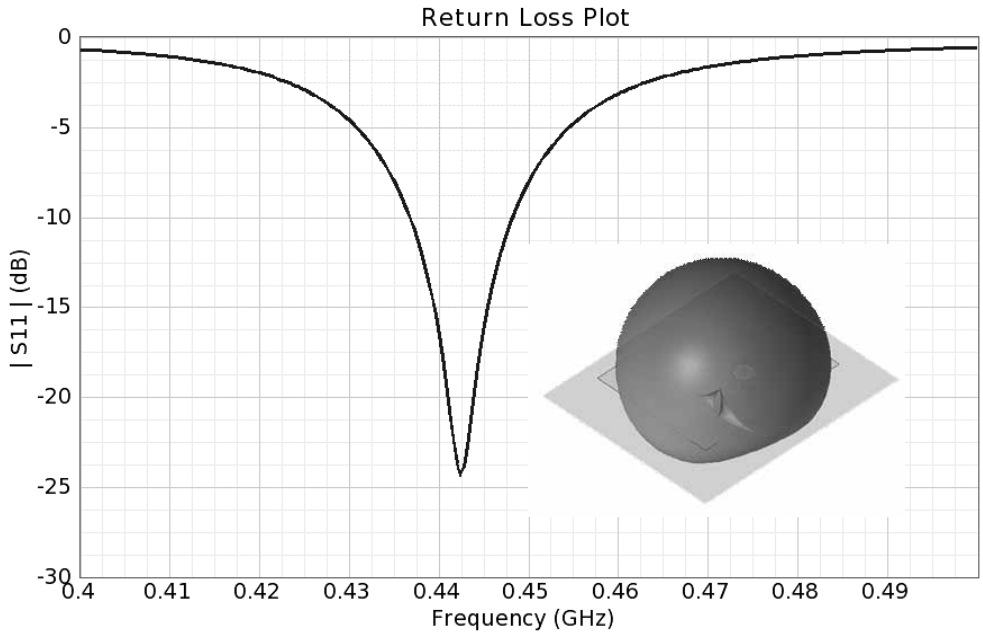

Figure 2.12 Antenna return loss plot of a coaxial-fed microstrip patch antenna.

narrowband antennas. Antenna gain is 7.1 dBi at 440 MHz and antenna radiation efficiency is nearly 60%.

2.5 Circularly Polarized Microstrip Patch Antennas

In a circularly polarized antenna, the electric-field vector at a given point in space traces a circle as a function of time. The conditions to accomplish this are if the electric field vector possesses all the following:

- The field must have two orthogonal linear components;
- The two components must have the same magnitude;
- The two components should have a time-phase difference of odd multiples of 90°.

Circular polarization (CP) in patch antennas can be achieved using either a single feed or a multifeed technique. CP designs of microstrip antennas are mainly on circular, square, and triangular microstrip patches. CP antennas are used in GPS, GNSS, and many other wireless communication applications.

2.5.1 Single-Fed Circularly Polarized Patch Antenna

Typical configurations for singly fed CP microstrip antennas are shown in Figure 2.13. Because a patch with single-point feed generally radiates linear polarization, to radiate CP it is necessary for two orthogonal patch modes with equal amplitude and inphase quadrature to be induced. This can be achieved by slightly perturbing a

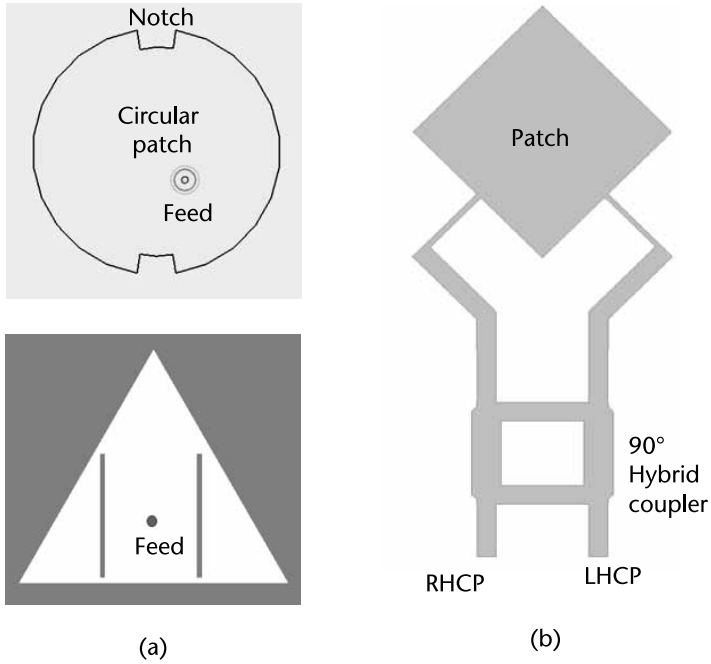

Figure 2.13 Configuration of circularly polarized patch antenna: (a) single-fed, and (b) dual-orthogonal fed.

patch at appropriate locations with respect to the feed. Perturbation configurations for generating CP operate on the principle of detuning degenerate modes of a symmetrical patch by perturbation segments, as shown in Figure 2.13.

The fields of a singly fed patch can be resolved into two orthogonal degenerate modes 1 and 2. Proper perturbation segments will detune the frequency response of mode 2 such that, at the operating frequency, the axial ratio rapidly degrades while the input match remains acceptable. CP operation of single-feed triangular microstrip antennas using a nearly equilateral triangular patch [15], an equilateral triangular patch with an inserted slit [16], or a tip-truncated equilateral triangular patch [17] has also been designed by many antenna engineers. Due to their physically smaller patch size as compared to the circular or square microstrip antennas, these circularly polarized triangular microstrip antennas are suitable for applications in systems where limited space is available.

There are several kinds of the patch elements such as square, circular, triangular, and ring shapes that have been used to realize CP radiation using a single feed [18]. The antenna shown in Figure 2.14 is a millimeter-wave CP antenna fed with a single coaxial line. The antenna finds application in 5G microcell, where a high-speed data rate is required. As frequency increases, complexities in system design also increase. Circular polarization is achieved by using two notches cut in the patch. The antenna is fabricated on Teflon ($\varepsilon_r = 2.0$) and has a substrate thickness 0.254 mm.

An antenna resonating at 29 GHz and 10 dB bandwidth of the antenna is 1.2 GHz (from 27.9 to 29.1 GHz). The designed antenna has an axial ratio (AR) value of 0.31 dB at center frequency. Single-feed microstrip antennas usually have very narrow 3-dB axial ratio bandwidth. This antenna has 0.8% 3 dB AR bandwidth.

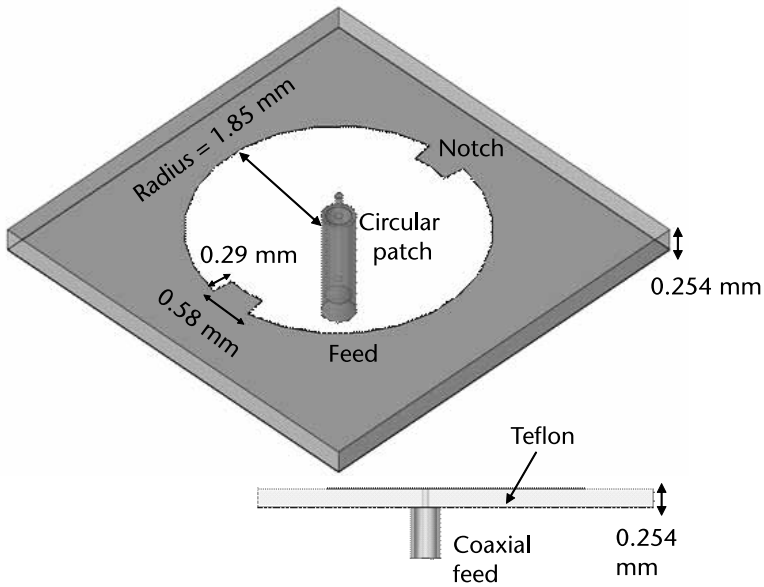

Figure 2.14 Coaxial-fed circularly polarized millimeter-wave microstrip antenna.

2.5.2 Dual-Orthogonal Fed Circularly Polarized Patch

The fundamental configurations of a dual-orthogonal fed circularly polarized patch using an external power divider is shown in the Figure 2.15. Use of a dual-feed technique in GPS and GNSS applications, is the most direct way to generate circular polarized radiation from a square patch. The two orthogonal modes required for the generation of circular polarization can be simultaneously excited using dual-orthogonal feeds. In designing, the patch is first matched to the feed lines by either properly selecting the feed locations or using impedance transformers. The two feeds are then connected to the output ports of a power divider circuit, which provides the required amplitude and phase excitations. Square patch circularly polarized antenna dimension is shown in Figure 2.15.

The dual-orthogonal feed excites two orthogonal modes with equal amplitude but inphase quadrature. The quadrature hybrid splits the input RF signal into two outputs with equal magnitude but 90° out of phase. The quadrature hybrid provides a broad axial ratio bandwidth. These power splitters can be easily constructed from various planar transmission lines. Microstrip feed lines excite the patch antenna in TM_{01} and TM_{10} modes so that it radiates both vertically polarized wave and a horizontally polarized wave simultaneously. The antenna is designed on 0.5-mm thick RT Duroid 5870 substrate with a dielectric constant of 2.33 at 2.4 GHz. The microstrip patch antenna consists of a patch and a 3-dB hybrid coupler. Figure 2.16 shows the simulated return loss and the phase difference between the two output ports, which is about to 90°.

Figure 2.17 shows the return loss, axial ratio, current distribution, antenna 3-D radiation pattern, and phi-0-degree cut pattern at 2.4 GHz. An axial ratio below 3 dB corresponds to the axial ratio bandwidth that it is extended from 2.1 to 2.7 GHz. The simulated 10-dB impedance bandwidth is from 2.2 to 2.8 GHz (about 25%). Antenna gain is 6.8 dBi.

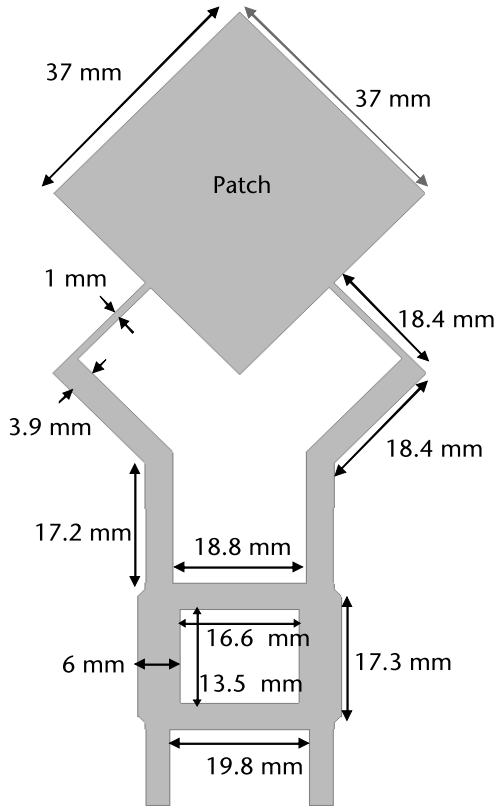

Figure 2.15 Design dimension of dual-orthogonal fed circularly polarized microstrip patch antenna.

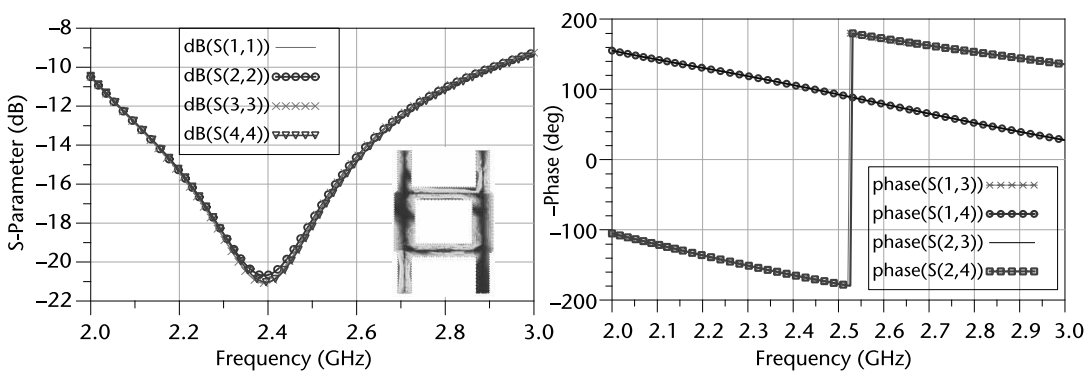

Figure 2.16 Return loss and phase plot of quadrature hybrid coupler.

2.6 Antenna Measurements

After antenna fabrication, all antenna parameters are measured to know the antenna performance. Typical parameters of antennas are resonance frequency point, bandwidth, radiation pattern, gain, directivity, beamwidth, polarization, and impedance. During antenna measurements we ensure that the antenna meets the required specifications and we can characterize the antenna parameters. The measurement

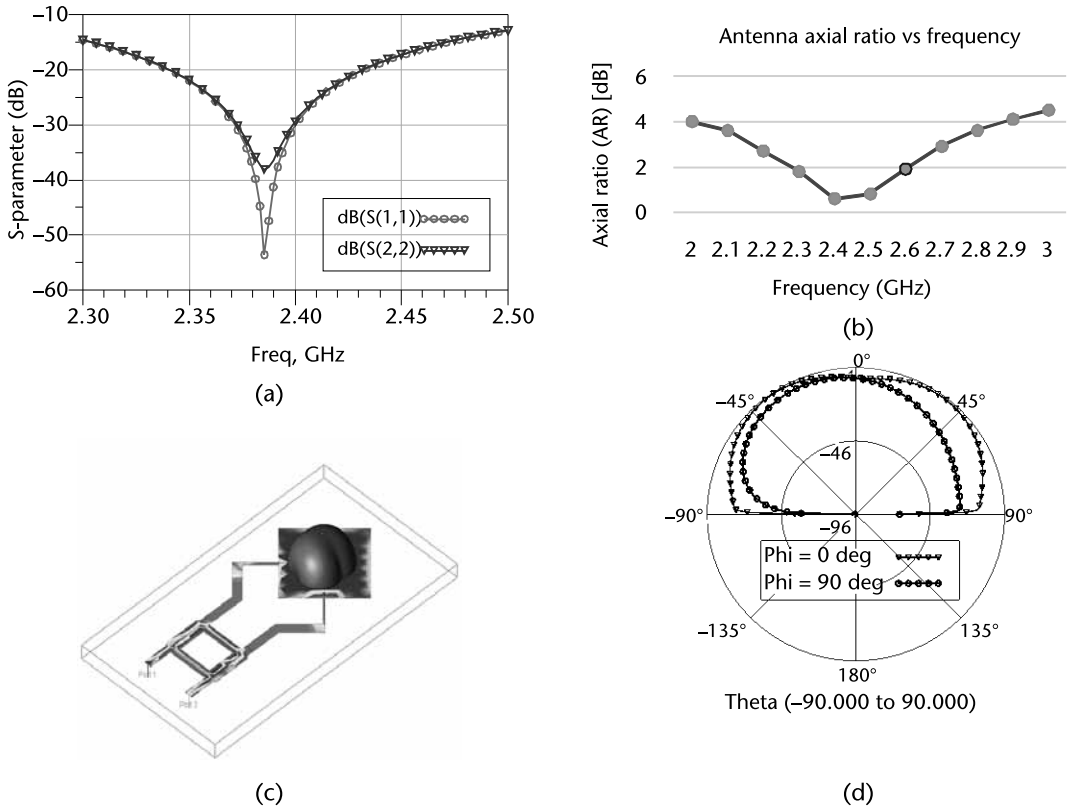

Figure 2.17 Antenna performance results: (a) return loss plot, (b) axial ratio plot, (c) current distribution over the patch, (d) radiation pattern at phi = 0 and phi = 90 degrees.

equipment includes scalar and vector network analyzers, antenna ranges, antenna positioners, pattern recorders, signal generators, and antenna gain standards. Currently, sophisticated computer systems are used to provide automated control of pattern measurements as well as fast calculations related to antenna directivity, two-dimensional to three-dimensional pattern conversion, and near-to-far field transformations (in compact antenna ranges). *S*-parameters are measured using a vector network analyzer (VNA) while antenna radiation characteristics such as far-filed patterns, gain, and efficiency are measured using different antenna pattern measurement techniques. To measure the far-field pattern, it should be illuminated with a uniform plane wave.

2.6.1 S-Parameter and Input Impedance

Antenna impedance is a fundamental parameter of all antennas operating at RF. Therefore, for the best accuracy the impedance should be measured in an environment that will most closely resemble the environment where it is intended to operate.

Impedance measurements are carried out using a VNA. This tool is used to measure the input impedance as a function of frequency. It can plot return loss (S11), and the VSWR, both of which are frequency-dependent functions of the antenna impedance. The *S*-parameter measurement setup is shown in Figure 2.18.

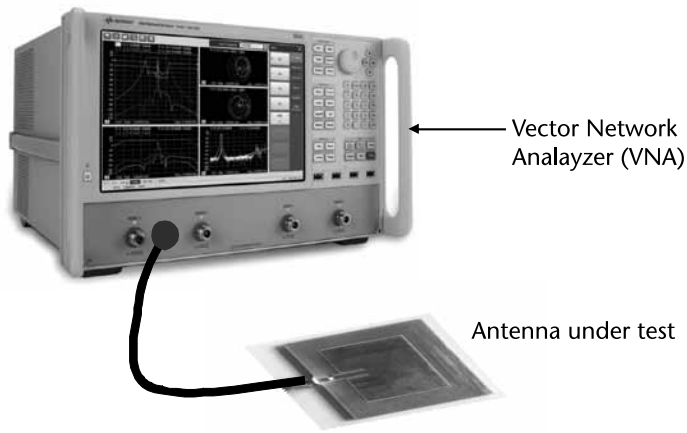

Figure 2.18 Antenna S-parameter and input impedance measurement setup using a vector network analyzer.

2.6.2 Radiation Pattern Measurements

A radiation pattern is the antenna radiated field as a function of the direction in space. The radiated field is measured at various angles at a constant distance from the antenna. Usually the antenna radiation pattern is measured in a far-field antenna range. The antenna under test is placed in the far-field distance from the transmitting antenna. Because of the size required to create a far-field range for large antennas, near-field techniques are employed. Near-field techniques allow one to measure the fields on a surface close to the antenna (usually 3–10 wavelength).

Near-field distances are transferred to far-field by using the Fourier transform. The far-field distance or Fraunhofer distance, R, is given in (2.16):

$$R = 2D^2/\lambda \tag{2.16}$$

where D is the maximum antenna dimension and λ is the antenna wavelength. The radiation pattern graphs can be drawn using Cartesian (rectangular) coordinates or as a polar plot. The antenna main beam is measured between the points that the maximum relative field intensity E decays to 0.707E. Half of the radiated power is concentrated in the antenna main beam. This antenna beam is called the 3-dB beam width. Radiation to the undesired direction is concentrated in the antenna sidelobes. The antenna radiation pattern is usually measured in free-space ranges as shown in Figure 2.19.

2.7 Summary

In this chapter, the microstrip patch antenna, which is the most popular printed antenna, was discussed in detail. A practical coaxial-fed rectangular patch antenna at the resonant frequency of 440 MHz has been designed for coal mine application

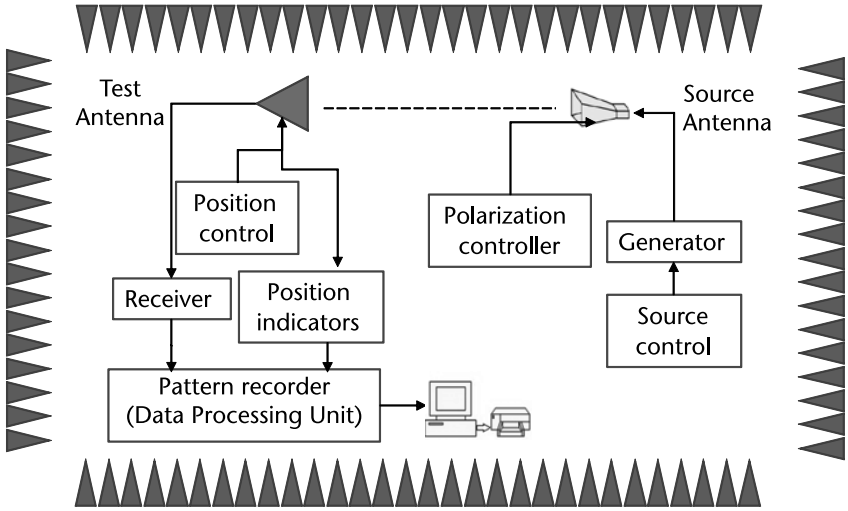

Figure 2.19 Antenna radiation pattern measurement setup in an anechoic chamber.

and simulated using an electromagnetic solver. Important antenna specifications, design parameters, and design flow were discussed through this antenna. A single microstrip antenna is the building block for complex array antennas so it very important to understand the design and working principle of the single radiator and its feeding mechanism. The radiation patterns and other important parameters of gain, efficiency, and return loss have been shown. Basic antenna parameters measurement can be done using VNA and far-field measurement ranges. In the next chapters, complex array antenna design will be presented for different applications.

References

[1] Pozar, D. M., and D. Schaubert (eds.), *Microstrip Antennas: The Analysis and Design of Microstrip Antennas and Arrays*, Piscataway, NJ: IEEE Press, 1995.

[2] Garg, R., P. Bhartia, I. Bahl, and A. Ittipiboon, *Microstrip Antenna Design Handbook*, Norwood, MA: Artech House, 2001.

[3] Kara, M., "Formulas for the Computation of the Physical Properties of Rectangular Microstrip Antenna Elements with Various Substrates Thicknesses," *Microwave and Optical Technology Letters,* Vol. 12, No. 4, 1996, pp. 234–239.

[4] Derneryd A. G., "A Theoretical Investigation of the Rectangular Microstrip Patch Antenna Element," *IEEE Transactions on Antennas and Propagat*ion, Vol. AP-26, July 1978, pp. 532–535.

[5] Lee, K. F., K. M. Luk, and H. W. Lai, *Microstrip Patch Antennas*, Second Edition, London: World Scientific Publishing Company, July 2017.

[6] Kara, M., "Closed-Form Expression for the Resonant Frequency of Rectangular Microstrip Antenna Elements with Thick Substrate," *Microwave Optical Technology Letters,* Vol. 12, No. 3, June 1996, pp. 131–136.

[7] James, J. R., and Hall P. S. (eds.), *Handbook of Microstrip Antennas*, Vols. I and II, London: Peter Peregrinus (IEE), 1989.

[8] Sainati, R. A., *CAD of Microstrip Antennas for Wireless Applications*, Norwood, MA: Artech House Publishers, 1996.

[9] Kara, M., "Empirical Formulas for the Computation of the Physical Properties of Rectangular Microstrip Antenna Elements with Thick Substrates," *Microwave Optical Technology Letters*, Vol. 14, No. 2, February 1997, pp. 115–121.

[10] Bahl, I. J., and Bhatia P., *Microstrip Antennas*, Dedham, MA: Artech House, 1980.

[11] Schneider, M., "Microstrip Lines for Microwave Integrated Circuits," *Bell System Technical Journal,* Vol. 48, 1969, pp. 1421–1444.

[12] James J. R., P. S. Hall, and C. Wood, *Microstrip Antenna Theory and Design*, Stevenage, UK: Peter Peregrinus (IEE), 1981.

[13] Hammerstad, E. O., "Equations for Microstrip Circuits Design," *5th European Microwave Conference*, Hamburg, Germany, September 1975, pp. 268–272.

[14] Bahl I. J., "Build Microstrip Antennas with Paper-Thin Dimensions," *Microwaves,* October 1979, p. 50.

[15] Suzuki Y., N. Miyano, and T. Chiba, "Circularly Polarised Radiation from Singly Fed Equilateral-Triangular Microstrip Antenna," *IEE Proceedings H-Microwaves, Antennas and Propagation*, Vol. 134, April 1987, pp. 194–198.

[16] Lu, J. H., C. L. Tang, and K. L. Wong, "Circular Polarization Design of a Single-Feed Equilateral-Triangular Microstrip Antenna," *Electronics Letters,* Vol. 34, 1998, pp. 319–321.

[17] Tang, C. L., J. H. Lu, and K. L. Wong, "Circularly Polarized Equilateral Triangular Micro Strip Antenna with Truncated Tip," *Electronics Letters,* Vol. 34, 1998, pp. 1277–1278.

[18] Wong, K. L., *Compact and Broadband Microstrip Antennas*, New York: John Wiley & Sons, 2002.

Selected Bibliography

Ahn, C. H., Y. J. Ren, and K. Chang, "A Dual-Polarized Cylindrical Conformal Array Antenna Suitable for Unmanned Aerial Vehicles," *International Journal of RF and Microwave Computer-Aided Engineering,* Vol. 21, No. 1, 2011, pp. 91–98.

Balanis, C., *Antenna Theory: Analysis and Design*, Hoboken, NJ: Wiley, 2012.

Bokhari, S. A., J.- F. Zurcher, J. R. Mosig, and F. E. Gardiol, "A Small Microstrip Patch Antenna with a Convenient Tuning Option", *IEEE Transactions on Antennas and Propagation*, Vol. 44, No. 11, November 1996.

Deshmukh A. A., and K. P. Ray, "Compact Broadband Modified Triangular Microstrip Antennas," *IET Microwaves, Antennas & Propagation*, Vol. 9, No. 11, 2015, pp. 1205–1212.

Ávila-Navarro, E., J. A. Carrasco, and C. Reig, "Printed Dipole Antennas for Personal Communications Systems," *IETE Technical Review,* Vol. 27, No. 4, 2010, pp. 286-292.

Hayes, G. J., Y. Liu, J. Genzer, G. Lazzi, and M. D. Dickey, "Self-Folding Origami Microstrip Antennas," *IEEE Transactions on Antennas and Propagation*, Vol. 62, No. 10, October 2014, pp. 5416–5419.

Iwasaki, H., "A Circularly Polarized Small Size Microstrip Antennas with Cross Slot," *IEEE Transactions on Antennas and Propagation,* Vol. 44, No. 10, 1996, pp. 1399–1401.

Javor, R. D., X. D. Wu, and K. Chang, "Design and Performance of a Microstrip Reflect Array Antenna." *IEEE Transactions on Antennas and Propagation*, Vol. 43, No. 09, September 1995, pp. 932–939.

Lee, M. S., and Y.H. Kim, "Design and Performance of a 24-GHz Switch-Antenna Array FMCW Radar System for Automotive Applications", *IEEE Transactions on Vehicular Technol*ogy, Vol. 59, No. 5, 2010, pp. 2290–2297.

Mendes C., and C. Peixeiro, "A Dual-Mode Single-Band Wearable Microstrip Antenna for Body Area Networks," *IEEE Antennas and Wireless Propagation Letters*, Vol. 16, 2017, pp. 3055–3058.

Pandey, A., "Efficient Synthetic Aperture Radar Antenna Array Design Using Multiple Electromagnetic Solvers," *Antenna System & Technology*, February 2003.

Song, Q., and X. Zhang, "A Study on Wideband Gap Coupled Microstrip Antenna Array," *IEEE Transactions on Antennas and Propagation*, Vol. 43, No. 03, Mar. 1995, pp. 313–317.

Sun, W., Y. Li, Z. Zhang, and Z. Feng, "Broadband and Low-Profile Microstrip Antenna Using Strip-Slot Hybrid Structure," *IEEE Antennas and Wireless Propagation Letters*, Vol. 16, 2017.

Xu, J., et al., "A Wideband F-Shaped Microstrip Antenna," *IEEE Antennas and Wireless Propagation Letters,* Vol. 16, 2017, pp. 829–832.

Wang Y., and Z. Du, "Dual-Polarized Dual-Band Microstrip Antenna with Similar-Shaped Radiation Pattern," *IEEE Transactions on Antennas and Propagation,* Vol. 63, No. 12, December 2015, pp. 5923–5928.

CHAPTER 3

Antenna Design for Wireless Communication and Mobile Phones

3.1 Introduction

The antenna of a mobile phone, which is a terminal equipment for transmitting and receiving electromagnetic waves, plays a vital role in mobile communication. A dramatic growth has been seen the mobile industry; it has evolved from analog to digital second generation (2G) GSM communication, then to high data rate third generation (3G) wideband code division multiple access (WCDMA), further to packet-optimized 3.5G High Speed Packet Access (HSPA) and fourth generation (4G) (Long Term Evolution (LTE) and LTE Advanced) systems and now moving towards fifth generation (5G) wireless communication system. As the smartphone era unfolds, the operating frequency band of the mobile phone is becoming wider and the space for a smartphone antenna is limited. It is very significant to design a compact wideband antenna for mobile phone application with a limited space. In recent years, the printed antenna has been widely adapted in wireless devices because it can be printed directly on the PCB along with other circuitry at a low cost. Many printed broadband antennas for the mobile phone have been proposed in the open literature [1–6]. The printed inverted-F monopole antenna designed for the multifrequency bands with compact size is one of the most used antenna choices in a cell phone.

The trend in mobile devices has been to provide more memory, faster access, improved processors, additional connectivity with Wi-Fi, GPS, 3G, and 4G world access, all with longer battery life in thinner, sleeker packages. Compound this with the desire of mobile operators to expand their available band allocations and mobile communication standards, and what results is a difficult and complex antenna design. The main design challenges of modern mobile phone antenna are the built-in structure, multisystem in multiband, including all wireless communication standards 2G, 3G, 4G, and other noncellular RF bands, and meeting all compliance standards and requirements such as specific absorption rate (SAR), over-the-air (OTA), and hearing aid compatibility (HAC). This chapter gives an overview of the design of some important antennas for mobile.

3.2 Mobile Communication Standards

In mobile communication, the common 2G, 3G, and 4G bands are GSM850 (824–894 MHz), GSM900 (890–960 MHz), GSM1800 (1,710–1,880 MHz), GSM1900 (1,850–1,990 MHz), UMTS2100 (1,920–2,170 MHz), LTE2300 (2,305–2,400 MHz), and LTE2500 (2,500–2,690 MHz) as shown in Table 3.1. The realization of the compact multiband antenna through excellent design and proper impedance matching is the main design objective of cell phone antennas. In recent years, to meet the requirements of current mobile phone built-in antennas [7–11], monopole antenna, PIFA antenna, and many other types of antennas have been designed. A navigation antenna is specially provided in most phones, which mainly covers the GPS band.

LTE provides the essential and far reaching vital solutions for wireless communication systems. It provides high-speed internet along with broader bandwidth and high throughput. During its initial stages in Europe, LTE was assigned 1.8-GHz and 2.6-GHz bands. Currently, due to the increase in the necessity of additional bandwidth, the 790–865-MHz band has been added to the LTE operating system.

The main challenges for the mobile device antenna are small size, built-in, multiband, and coexistence of a multiradio system and a multiple-input-multiple-output (MIMO) system. There have been two major requirements in the antenna design. One is that antennas for mobile terminal require small size, built-in, and multiband operation. Another is that mobile antennas should pass various compliances before production, depending on the functionality of the system, its service areas, and the quality and quantity of data to be transmitted. For a compact mobile terminal, environmental conditions are also a serious issue to be considered in the antenna design. Proximity effects due to materials near the antenna element, such as circuit components, acoustic components, camera, and printed circuit board grounding quality, may degrade antenna performance. In modern antenna design, the proximity effect is treated with the integration concept, in which nearby materials are included in an antenna system as an integral part of the radiator. For MIMO and diversity applications in Wi-Fi and 4G systems, the multi-antenna system requires low mutual coupling and low pattern correlation between antennas to realize good diversity performance. The presence of mutual coupling at the receive

Table 3.1 Mobile Communication Standards and Frequencies

Gen	*Standard*	*Band*	*Uplink (MHz)*	*Downlink (MHz)*	*Full Name*
2G	GSM	GSM850	824–849	869–894	Global System for Mobile communication
		GSM900	880–914	925–959	
		GSM1800	1,710–1,784	1,805–1,879	
		GSM1900	1,850–1,910	1,930–1,990	
3G	UMTS	UMTS Band I	1,920–1,980	2,110–2,170	Universal Mobile Teli-communication System
		UMTS Band II	1,850–1,910	1,930–1,990	
		UMTS Band V	824–849	869–894	
4G	LTE	LTE2300	2,305–2,400	2,350–2,360	Long Term Evaluation- Advanced
		LTE2500	2,500–2,690		
5G	Research is ongoing for 28-GHz and 60-GHz frequency bands.				

array antenna leads to additional correlation between spatial channels and results in a loss of MIMO system capacity [10].

Antenna modeling and simulation in handheld devices, using electromagnetic simulation tools, have improved significantly by allowing the simulation of the antenna behavior in complex environments surrounding the antenna such as the antenna along with the human head and hand and the presence of nearby components such as cameras, batteries, displays, and speakers. Some of important electromagnetic parameters to characterize antennas for mobile handheld devices are impedance mismatch, radiation efficiency, diversity gain, MIMO capacity, total radiated power (TRP), total isotropic sensitivity (TIS), SAR, average fading sensitivity (AFS), and data bit throughput (TPUT).

3.3 Mobile Phone Antennas

Smartphone antenna design is reasonably complicated because of different communication standards and regulatory requirements. In addition, there are multiple antennas on a smartphone as shown in Figure 3.1. Most of these antennas are PIFAs or a custom printed antenna. A PCB ground plane that supports the circuit board and touch screen also acts as a ground plane for all the antennas. The size of the ground plane affects antenna bandwidth, so, for better performance, the whole available size of the chassis should be used as a ground plane. PIFA bandwidth reduces with a small-size ground plane. Some important antennas used in a

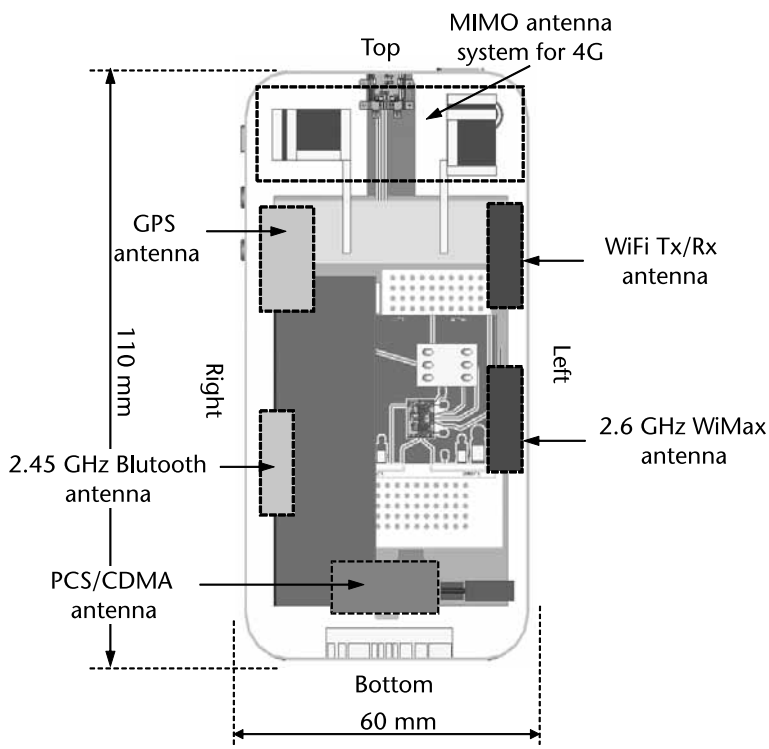

Figure 3.1 Various wireless communication antennas in a smartphone.

smartphone for various wireless standards such as GSM, LTE, WiMAX, WLAN, and Bluetooth are 2G/3G mobile antenna, 4G mobile antenna, diversity antenna, GPS antenna, Wi-Fi antenna, near-field communication (NFC) antenna, Bluetooth antenna, and 5G communication antenna.

3.4 Multiband Antenna Design for Mobile Phones

Mobile communication requires small, low-profile, and low-cost antennas. Before 1998, most of the mobile phones used the external antenna, which is simple and easy to reuse. The most popular design was the dual-band nonuniform helical antenna proposed by Egorov and Ying [12]. The Hagenuk phone, produced by a Danish company in 1996, was the first mainstream GSM phone with an internal antenna. Internal antennas are used in almost all modern smartphones. The internal antenna can increase the mechanical robustness of a mobile terminal; also, the internal antenna housing can be used as an acoustic cavity to improve the audio performance. The main types of internal antennas for mobile phone are the PIFA [13], the folded monopole antenna [14], a meander line antenna, and the loop antenna [15]. The PIFA is usually located at the top of the phone behind the printed wire board (PWB). However, the folded monopole antennas are usually used at the bottom of the handset to have less head loss and risk of high SAR. PIFA bandwidth depends on the antenna size and ground plane size. The bandwidth of the monopole is much larger than a PIFA. The monopole can be capacitive, coupled, or matched to the terminal housing to excite the chassis mode to gain some extra bandwidth when the chassis length is larger than a quarter-wavelength.

3.4.1 Feeding Structures

There are two types of feeding structures: the inductive feed and the capacitive feed. An inductive feed is a wire/pogo pin with a direct electrical connection between the PCB and the antenna. Antenna designers can fine-tune the antenna impedance matching by controlling the width and length of the feed line. A capacitive feed couples the energy to the main radiating element [16] and can also be self-resonant for matching purposes at a high-frequency band. It is either placed adjacent to the main antenna or directly underneath the antenna. Manufacturing capacitive feeds directly underneath the antenna is difficult because the feeding is highly dependent on the separation between the main antenna and the capacitive feed. This separation acts as a matching network with variable serial-capacitance loading. The antenna designs presented in this chapter used these feeding structures.

To understand the design process, design steps, optimization technique, and complexity associated with mobile antennas, four different kinds of antennas based on monopole, inverted-F, and PIFA are discussed in this chapter. These antenna designs are also applicable for any other mass wireless communication system. Practically, smartphone antenna shape and size are governed by the antenna body and available space, but the design principle and challenges are same presented in this chapter.

3.5 Dual-Band Monopole Antenna Design for WLAN

A compact planar monopole antenna with a dual band is discussed in this section. The antenna occupies an overall area of 18 × 12 mm^2. The antenna combines two folded strips and is fed by a CPW transmission line, which radiates at 2.4 and 5.2 GHz. In this antenna, by optimally selecting the antenna dimensions, dual-band resonant modes with a much wider impedance matching at the higher band can be produced. With the fast development of wireless communication systems, there is a high demand to increase the data rate of wireless communication systems [17]. Wireless local area network systems such as Bluetooth, Wi-Fi, and ZigBee always operate in the 2.4-GHz ISM band. The growing demand for WLAN technology has led to an interest in integrating the 2.4-GHz (IEEE802.11b/g) and 5.2-GHz (IEEE 802.11a) frequency bands into a single device that requires a dual-band antenna. The WLAN antenna not only has a wider frequency band, smaller size, and is easier to install, but it also has a high radiation efficiency [18]. Due to the space limitation, the WLAN antenna should be compact and should support multiband operations [19].

At present, extensive studies of dual-band microstrip antennas applied in WLAN have been performed, and various promising antennas that work in a dual-band have been put forward, such as PIFAs [20–22], planar monopole antennas [23], dipole antennas [24], dual-band monopole antennas with different lengths [25] or sleeves [26], bent folded monopoles [27], and slot antennas [28, 29]. These antennas are simple in structure and low in production cost, which is suitable for the use of WLAN devices. However, the designs of the antenna may increase cost or are complicated to be fabricated or the overall dimensions of the antenna are large in size. In the design of multiband antenna, one critical technique is to reduce the radiation caused by the currents distributed on the ground plane to improve the radiation patterns and impedance bandwidth [30]. Multiband antennas have also been greatly researched. In that, CPW-fed antennas show better antenna performance.

To cover all the three bands of WLAN (i.e., lower band of 2.4 GHz (802.11b/g standard) and upper bands of 5.15–5.35 GHz and 5.725–5.825 GHz (802.11a standard)), two monopoles are used: one working for the lower band and the other working for the higher band [31–33]. However, there is a limit in most of these antennas to obtain the wideband characteristic especially at the 5-GHz band for WLAN applications operating simultaneously at 5.2 and 5.8 GHz. Similarly, several dual-band slot antennas were proposed for wholly covering 2.4/5.2-GHz WLAN bands [34–42]. Although the reported antennas cover all 2.4/5-GHz WLAN bands, they are not very compact in size, so there is a demand for designing compact multiband antennas. Table 3.2 shows the comparison of the antenna size and the operating bands of the proposed antennas, with antennas reported in [30–42]. Antenna size variation is between 500 m^2 and 5,000 m^2.

3.5.1 Antenna Design

The geometry of the designed antenna is shown in Figure 3.2. The radiator and ground plane of the antenna are etched on a piece of PCB with an overall size of 18 × 12 × 1.6 mm^3. The antenna has two monopole arms resonating at 2.4 GHz

Table 3.2 Comparison of Designed Antenna with Other Compact Antennas

S. No.	*Published Designs* Reference	Design	*Antenna Size (mm)*	*Total Area (mm^2)*	*Frequency Bands Covered*
1	[30]		25 × 25	625	2.4/5.2/5.8 GHz
2	[31]		40 × 20	800	2.45/5.2/5.8 GHz
3	[32]		33 × 28	924	2.4/5.2/5.8 GHz
4	[33]		22 × 20	440	2.4/5.2 GHz
5	[34]		75 × 75	5,625	2.4/5.2/5.8 GHz
6	[35]		50 × 75	3,750	2.4/5.2 GHz
7	[36]		60 × 45	2,700	2.4/5.2/5.8 GHz
8	[37]		43 × 41	1,763	2.4/5.2/5.8 GHz
9	[38]		50 × 35	1,750	2.4/5.8 GHz
10	[39]		40 × 40	1,600	2.4/5.2/5.8 GHz
11	[40]		35 × 24	840	2.4/3.4/5.2/5.8 GHz
12	[41]		40 × 15	600	2.4/5.2 GHz
13	[42]		32 × 16	512	2.4/5.2/5.8 GHz
14	Designed antenna		18 × 12	216	2.4/5.2/5.8 GHz

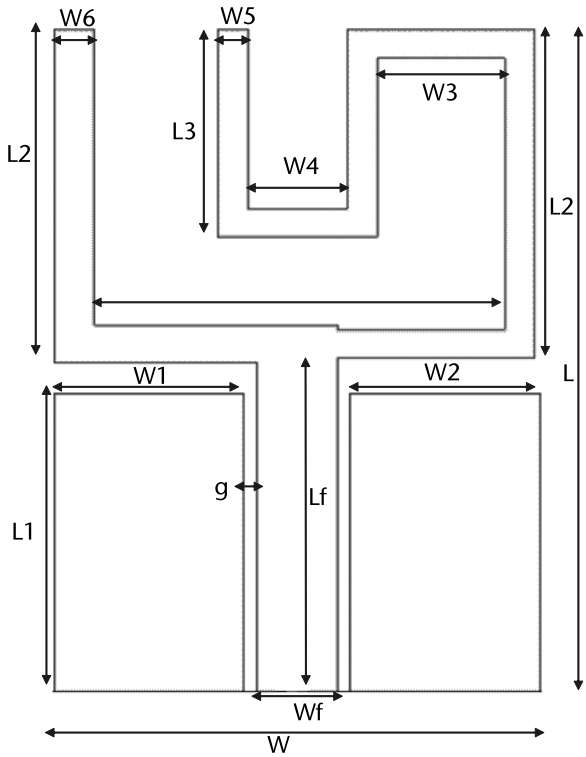

PARAMETERS	VALUE
L	12.0 mm
W	17.5 mm
Wf	2.00 mm
Lf	8.70 mm
g	0.30 mm
L1	7.90 mm
L2	8.67 mm
L3	5.49 mm
W1	4.70 mm
W2	4.70 mm
W3	3.13 mm
W4	2.45 mm
W5	0.75 mm
W6	1.00 mm

Figure 3.2 Geometry of the designed dual-band monopole antenna.

and 5.2 GHz. It consists of a coplanar ground plan, a radiation structure, and a feed line. A CPW transmission line of 50Ω, which consists of a signal strip width of 2 mm and a gap distance of 0.3 mm between the single strip and the coplanar ground plane, is used for feeding the antenna. In addition, a parametric study of the antenna might be referential for antenna engineers.

The design dimensions of the antenna are shown in Figure 3.2. It is printed on the FR4 antenna substrate with a relative dielectric constant of 4.4. The size of the substrate is W and L, and the thickness is 1.6 mm. The ground plane is printed on the same side of the radiating element, whose length and width are represented by L_1, W_1, and W_2, respectively.

The antenna is fed by a CPW line with a characteristic impedance of 50Ω, and the size of the microstrip line is $W_f \times L_f$. The radiating element of the antenna is composed of two rectangular strips. Each of the radiating element is folded and is fed with a CPW located at a distance offset from the middle of the loop. The lengths of the strips should be integer multiples of half the effective wavelength λ_{eff} at the desired frequencies to form resonant antennas. The electrical length of the whole monopole strip is equivalent to the quarter-wavelength of the lower-frequency band of 2.4 GHz, while the L-shape branch, which is a part of the folded loop, is mainly used to generate the higher-frequency band of 5.2 GHz, and the corresponding resonant quarter-wavelength is obtained by adjusting the feeding network location. Further, the antenna element has been purposely folded, not only to reduce the antenna physical dimensions but also to reduce the coupling effect between antenna elements. At the lower frequency, the quality factor Q for such a

resonator is high due to the limited size of the radiation apertures at two open ends, and the high Q leads to limited operation bandwidth.

The size of the antenna is mainly determined by the size of the monopole governing the lower band of the WLAN application. The lower-frequency band resonator has a longer arm length compared to a higher-frequency band resonator. The impedance bandwidth and resonant frequencies obtained can be varied by variation in the dimensions of folded strips. The width of the feed line has been fixed at 2 mm to provide 50Ω impedance matching.

3.5.2 Mathematical Modeling

The antenna can be characterized by an equivalent circuit of several lumped elements. This approach is based on Foster canonical forms that describe the antenna frequency characteristics [43, 44]. To represent a distributed circuit by a lumped element model, its transfer function should be first determined and then the equivalent circuit network should be found giving the same response for a required excitation as considered a distributed structure. This lumped element model provides a compact description of the distributed circuit. To establish the network model of distributed circuit, the transfer function is computed using different approaches. One such approach to perform a synthesis of compact lumped element models for linear lossy reciprocal multiport is based on the Foster canonical forms. The Foster reactance theorem states that the reactance of a passive, lossless, two-terminal (one-port) network always strictly monotonically increases with frequency. The reactance of inductors and capacitors independently increase with frequency and, from that basis, a passive lossless network can be constructed using lumped inductor and capacitors. Ronald Martin Foster presented the proof of the theorem in 1924. Generally, antennas are linear, passive elements that their input impedances can be represented by Foster canonical forms.

Normally, antennas are linear, passive elements whose input impedances can be represented by Foster canonical forms, as shown in Figure 3.3. Dipole and monopole antennas are electric antennas; this Foster canonical form is suitable for modeling electric antennas, which behave as an open circuit at the DC input signal. The antenna input impedance $Z_{in}(\omega)$ is modeled by means of the equivalent network depicted in Figure 3.3:

$$Z_{in}(\omega) \cong j\omega L_0 + \frac{1}{j\omega C_0} + \sum_{n=1}^{N_{max}} \frac{R_n}{1 + jQ_n\left(\frac{\omega}{\omega_n} - \frac{\omega_n}{\omega}\right)} \tag{3.1}$$

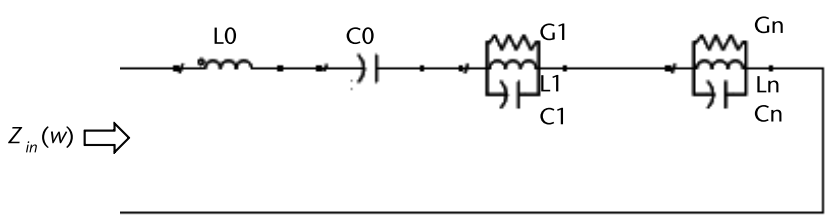

Figure 3.3 Foster canonical form of the equivalent circuit for the antenna.

where $Q_n = \omega_n R_n C_n$ and $\omega_n = (L_n C_n)^{-0.5}$. N_{max} is the number of modes needed to properly describe the frequency behavior of the antenna input impedance. Ω is the operating radial frequency, and Ω_n is the radial frequency of the nth resonant mode. C_0 is the quasi-static input capacitance, and L_0 is an inductance that considers the higher-order modes and feeding effects, while C_n, L_n, R_n, and Q_n are the capacitance, inductance, resistance, and quality factor, respectively, describing the lumped resonance processes that take place in the antenna structure [45].

The antenna equivalent circuit model with actual components is shown in Figure 3.4(a). The values of resistors, capacitors, and inductors are extracted from the Advanced Design System (ADS) schematic circuit simulation results, where these values are adjusted manually to obtain the proper response. C_0 and L_0 represent the capacitance and inductance of the monopole antenna when the antenna operates at a lower frequency and are properly chosen to resonate at the first resonance frequency of the antenna. Figure 3.4(b) shows the reflection coefficient curves of the considered antenna as obtained from an equivalent lumped element circuit model.

3.5.3 Antenna Design Parametric Study

During the antenna design phase, the antenna designers perform a series of parametric studies to achieve the desired antenna performance, particularly tuning the resonant frequencies and impedance levels. In this design, the critical antenna parameters are the resonating length of strips and the width of the strip. A complete

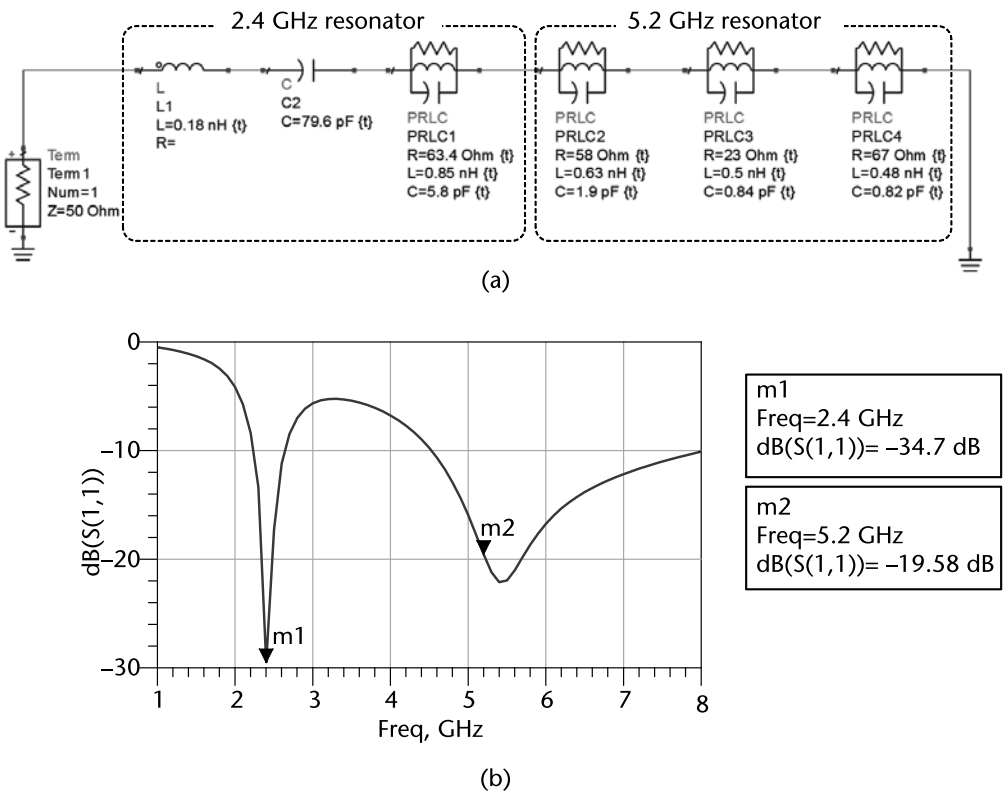

Figure 3.4 (a) Equivalent lumped-element circuit model of antenna and (b) reflection coefficient response for the antenna.

parametric analysis is performed for different parameter values by varying one parameter and keeping others constant.

3.5.3.1 Influence of the Variation of the Straight Strip Length L2

The effect of L_2 is investigated, keeping the other parameter constant. The simulation is carried out for L_2 values of 12 mm, 15 mm, 19 mm, and 22 mm. Figure 3.5 shows that the 5.2-GHz resonant frequency depends on the parameter L_2, and the second resonance frequency of 2.4 GHz is almost independent of the variation in L_2. The variation in the value of L_2 from 12 mm to 22 mm leads to shifting in first resonant frequency from 6.5 GHz to 4.5 GHz. The longer L_2 shifted the resonating frequency below 5.2 GHz, while the shorter L_2 shifted the frequency above 5.2 GHz.

3.5.3.2 Influence of the Variation of the Straight Strip Length L3 + W4 and CPW Feed Line Gap g

Figure 3.6 shows the antenna return loss (S_{11}) with a different value of length $L_3 + W_4$. The performance and antenna resonance frequency of low band change if the length ($L_3 + W_4$) is increased or decreased. However, the high band does not change much around 5.2 GHz. The 2.4-GHz frequency is mainly determined by this length ($L_3 + W_4$) of the strip.

The frequency shifts at the lower-frequency band as the length of this strip increases. A variation in the value of L_3 from 22 mm to 32 mm in step size of 3 mm leads to shifting in first resonant frequency from 3.2 GHz to 2.2 GHz. The antenna returns loss (S_{11}) with a different value of the gap between CPW feed line and coplanar grounds is shown in Figure 3.6. The variation of g is not shifting resonance frequency significantly, but the performance and antenna resonance frequency of the high band change if the g is increased or decreased. Optimum antenna perfor-

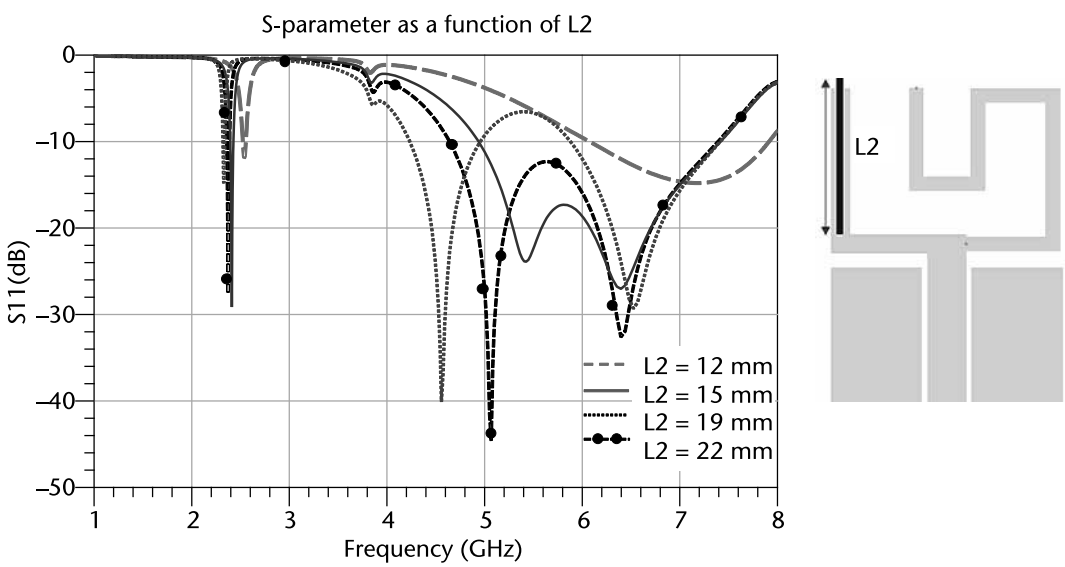

Figure 3.5 Return loss plot as a function of the length L2 variation.

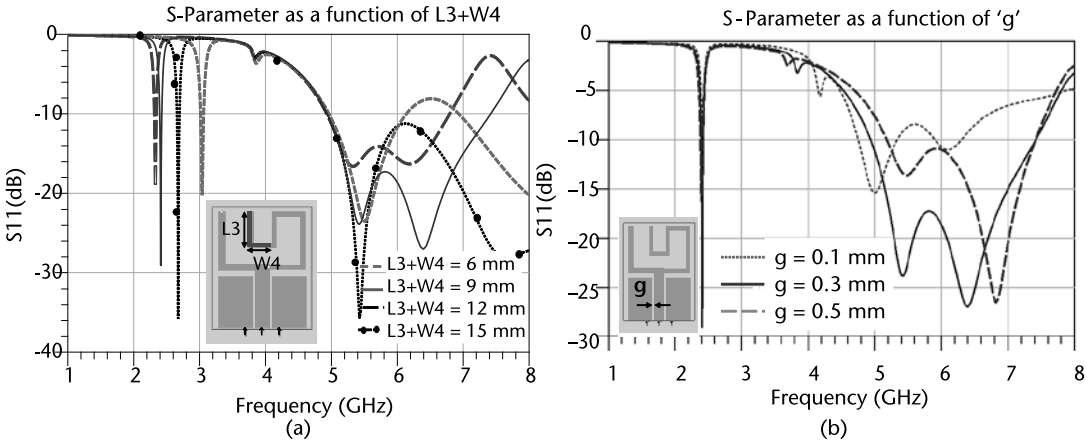

Figure 3.6 S-parameter result as a function of (a) length L3 + W4 and (b) gap g.

mance is achieved with $g = 0.3$ mm. At a higher frequency, there is more shift in resonant frequency as well as a change in the return loss value.

3.5.4 Simulated Result of the Optimized Design

After getting the optimized design parameter with parametric analysis, the antenna is simulated using an electromagnetic (EM) solver. The antenna has a bandwidth of 40 MHz at 2.4 GHz and 2,700 MHz at 5.2 GHz, and the maximum gain for a signal operating an element of the designed antenna is –0.16 dBi at 2.4 GHz and 2.1 dBi at 5.2 GHz.

3.5.4.1 S-Parameter Result of the Design

The simulated return loss of an optimized antenna shows that two operating bands are generated in 2.4 GHz and 5.2 GHz. The antenna elements resonated between 2.37–2.42 GHz and 4.9–7 GHz with a minimum $|S_{11}| < -10$ dB. The optimized antenna gives a bandwidth of about 40 MHz over a lower band of 2.4 GHz and about 2.7 GHz over an upper band of 5.2/5.8 GHz, which are very compatible with the 802.11n WLAN standard. VSWR is less than 2 obtained in the entire impedance bandwidth range. The value of VSWR at resonant 2.4 GHz is 1.09 and 1.05 at a resonance frequency of 5.2 GHz, which is well below the desired value of 2. A simulated input impedance curve as the function of frequency is shown in Figure 3.7. It is observed that at a resonant frequency of 2.4 GHz, the antenna provides an input impedance of value $(53.45 + j\,22.12)\Omega$, which is close to impedance provided by a feed line; similarly, at 5.2 GHz, this value is $(52.16 + j\,30)$. The simulated VSWR and input impedance variations indicate good impedance matching between the feed line and the antenna structure.

3.5.4.2 Electrical Field Plot

The electric field distributions with respect to the two frequencies of 2.4 GHz and 5.2 GHz are shown in Figure 3.8(a, b), respectively, At the dark region, the current

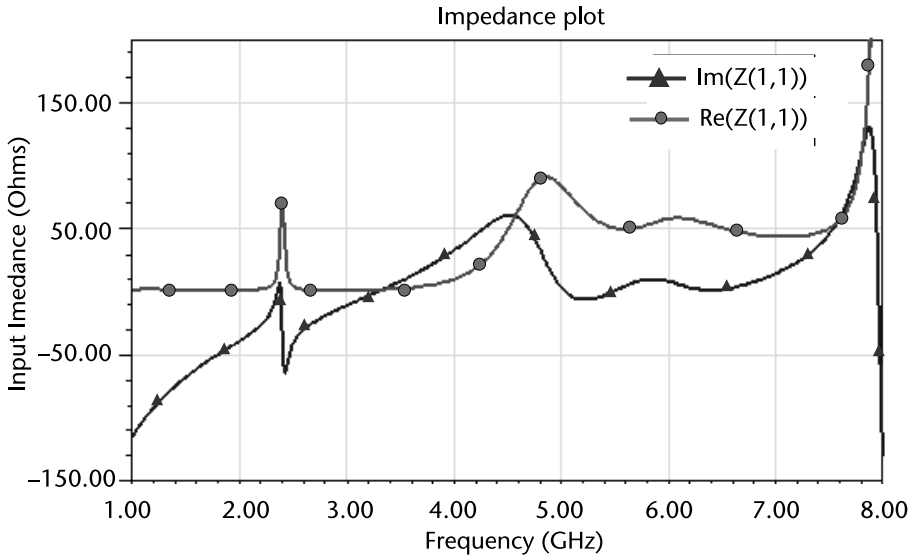

Figure 3.7 Simulated input impedance plot of a dual-band monopole antenna.

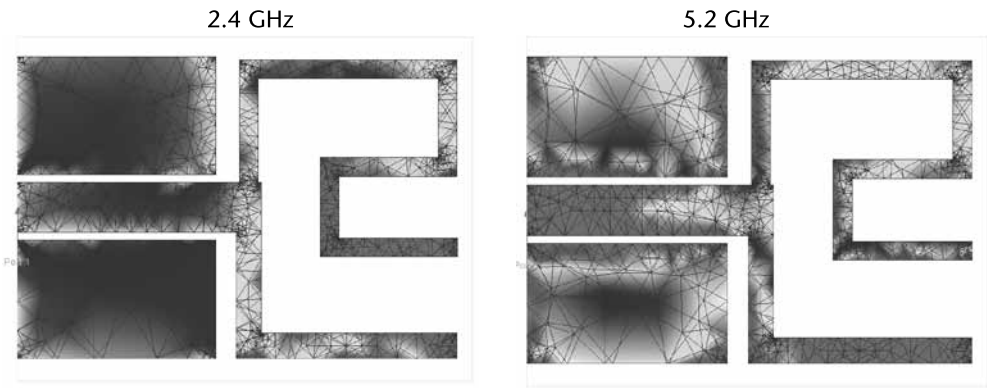

Figure 3.8 E-field distribution on antenna at (a) 2.4 GHz and (b) 5.2 GHz.

has an increasingly larger value. Conversely, moving toward the lighter region, the current has increasingly smaller value.

It is observed that, at the resonance frequency, the monopole works as an antenna generating a strong surface current, mainly on the edge of the strip. In addition, a significant current distribution is also observed along the two straight strip edges. The CPW feed line and the ground plane coupling effect may usually affect the impedance matching condition. It means that the effect of the feed line gap *g* provides impedance matching for the designed antenna. Surface currents appeared on the inner side of CPW feed line and the ground plane outer side edges. The currents on the two side edges of the ground plane have the same phase with those along the CPW feed line, thus enhancing the copolarization radiation in the far-field zone.

3.5.4.3 Antenna Radiation Pattern

The simulation result of an antenna radiation pattern is shown in Figure 3.9. In addition, simulated radiation patterns in two principal planes (*xz*-plane and *yz*-plane) at resonant frequencies of 2.4 and 5.2 GHz are presented in Figure 3.10. The radiation pattern is nearly omnidirectional for both bands that are shown in Figure 3.10 of the 2-D cut of the radiation pattern. It demonstrates that the antenna gain variation within 2.4 GHz and 5.2 GHz is minimal. The antenna radiation pattern shows a broadside pattern over the entire bandwidth with a maximum gain of about 2.1 dBi. The gain of the antenna is from –2.1 to 2.1 dBi. The peak antenna gain of 2.21 dBi is experienced at a resonant frequency of 5.2 GHz and 5.8 GHz.

3.6 Inverted-F Bluetooth Antenna

Bluetooth is a wireless technology standard for exchanging data over short distances from fixed and mobile devices, using short-wavelength radio transmissions

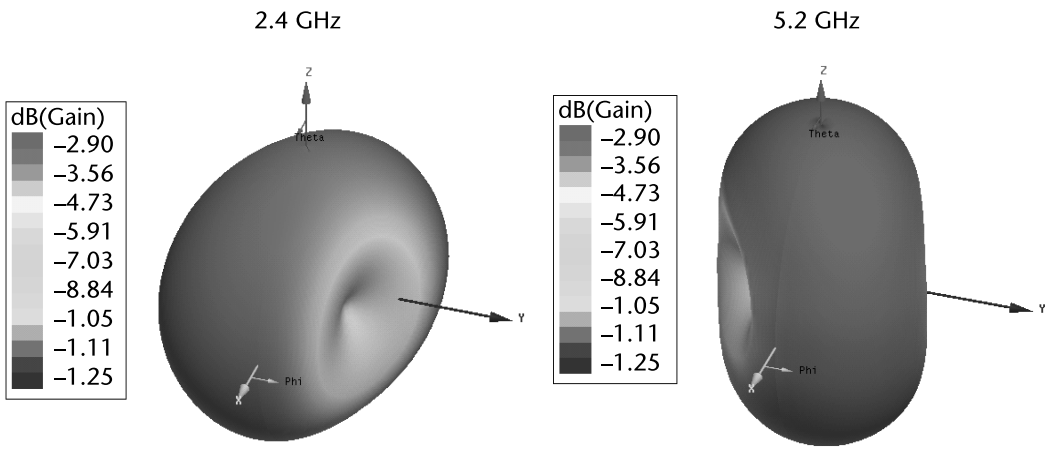

Figure 3.9 Antenna radiation pattern at 2.4 GHz and 5.2 GHz.

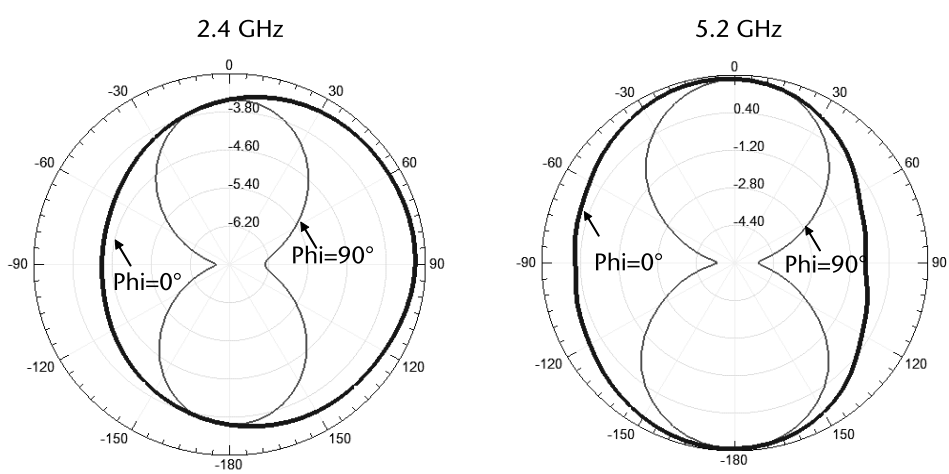

Figure 3.10 Azimuth and elevation radiation patterns at 2.4 GHz and 5.2 GHz.

in the ISM band (IEEE 802.11b and IEEE 802.11b/g standard). It creates a personal area network (PAN)with high levels of security that can connect several devices. Bluetooth technology was created by telecom vendor Ericsson in 1994 and it was originally conceived as a wireless alternative to RS-232 data cables. In a mobile phone, Bluetooth technology permits a hands-free headset for incoming voice calls, automatic synchronization of a cellphone with other devices, and the ability to print and fax. The Bluetooth antenna is designed for low-range operation because many applications only require a few meters of range.

Many compact antennas for Bluetooth have been reported in the literature [46, 47]. Some of these antennas are narrowband, while some have relatively larger dimensions. There are very compact and multiband antennas designed to be integrated into mobile terminals. These antennas have printed geometries and multiband operation is achieved by incorporating parasitic elements, slots, capacitive loading, and shorting pins. The Bluetooth antenna shown in Figure 3.11 is an IFA, employs a shunt stub for impedance matching. Four parameter variables (L, H, S, and D) control the behavior of the structure. The feed is placed from the upper arm of the IFA to the ground plane. The upper arm of the IFA has a length that is roughly a quarter-wavelength. The antenna is mounted on the plastic body of a mobile device that also acts as a substrate with dielectric constant of 2.8, and the plastic body thickness is 1.2 mm.

The resonating length of the printed antenna is 24 mm at 2.45 GHz. The antenna resonating length depends on the thickness of the substrate and the dielectric constant. Copper clearance is required around the radiating element, which is fed from a point along it. The feed position is used to control the input impedance into the antenna. The ground plane required on one side of the antenna is mobile PCB ground plane. The upper arm is shorted to the ground plane to the left of the feed. The microstrip feed line impedance is 50Ω. A PIFA can be also conformed as per a mobile housing structure as shown in Figure 3.11(b). To get the antenna performance, EM simulation is carried out using an FDTD solver. In general, the FDTD grid size should be dense where most of the electric fields are confined (edges of antenna strip). The generated electric effect is measured on other parts of the mobile phone, which is very important to meet compliance.

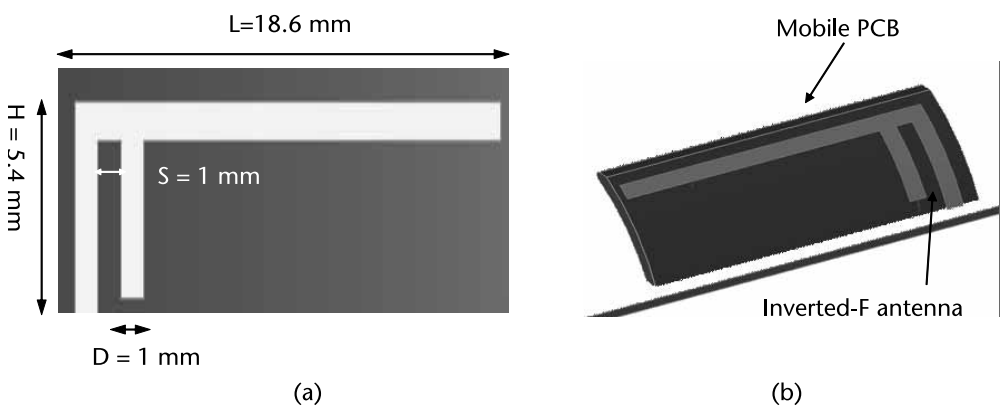

Figure 3.11 Inverted-F Bluetooth (a) antenna planar structure and (b) antenna wrapped on mobile body.

The simulated return loss S_{11} is displayed in Figure 3.12. The antenna resonating frequency is 2.45 GHz with a bandwidth of more than 100 MHz and efficiency greater than 50%. Antenna-resonating frequency depends upon the antenna-resonating length L. The variation of S-parameter data with L (1-mm variation) is shown in Figure 3.12.

The antenna is resonating at 2.4 GHz for $L = 18.6$ mm. The polarization of this antenna is vertical, and the radiation pattern is roughly donut-shaped, with the axis of the donut in the vertical direction as shown in Figure 3.13. Antenna gain is 0.27 dBi. The 2-D far-field cut plot (phi = 0°). After optimizing a stand-alone Bluetooth antenna design, it is important to simulate the antenna in the presence of other components and reoptimize the design to get the desired antenna performance.

3.7 LTE Band PIFA

As discussed in the previous section, the most popular small built-in antenna in mobile phones is the PIFA-type antenna. The PIFA radiator is mounted just above the ground layer; this ground layer acts as a metallic plate between the antenna radiation plane and the human brain when being used; thus, the impact of radiation on the human brain is reduced significantly. Typically, these antennas have good specific absorption rate (SAR) properties. The PIFA has the advantages of small size and omnidirectional pattern, and antenna production is unanimously good. Because of the shorting pin at the end, the PIFA is resonant at a quarter-wavelength; in that way, it reduces the required space needed on the phone.

To further reduce the length of a PIFA, it is common to use capacitive loading in PIFA. In this technique, a capacitance is added to the antenna between the feed point and the open edge, as shown in Figure 3.14. The impedance of the PIFA can be controlled via the distance of the feed to the short pin. Impedance decreases if the feed point is moved close to the shorting pin. The impedance can

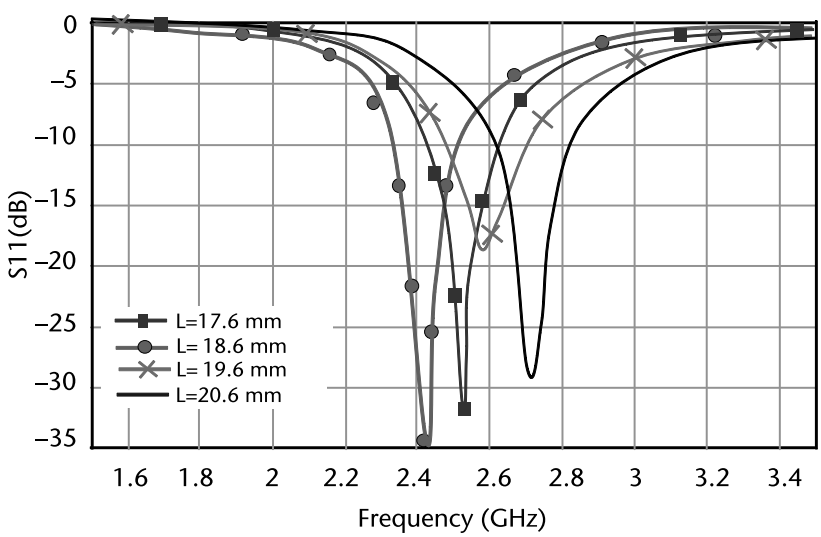

Figure 3.12 Return loss plot with length L variations.

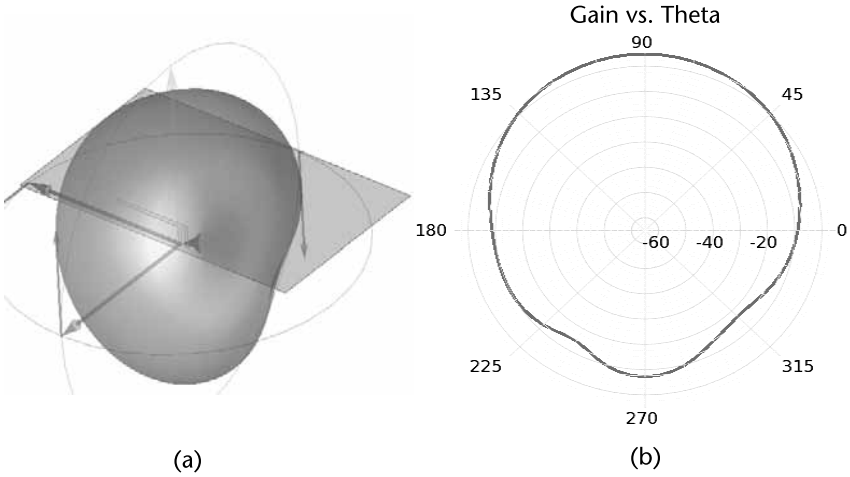

Figure 3.13 Antenna radiation pattern: (a) 3-D plot and (b) phi = 00 cut pattern plot.

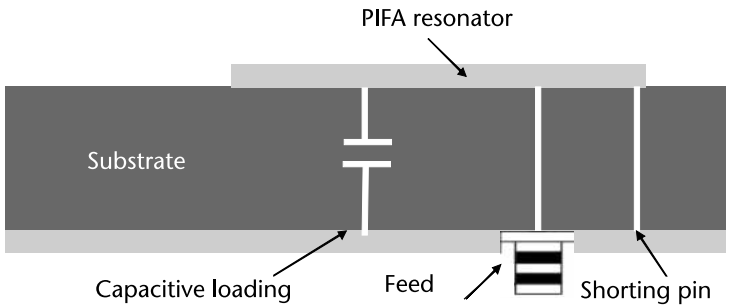

Figure 3.14 PIFA configuration.

be increased by moving it farther from the short edge. A PIFA may be in different shape. Minimal antenna size and tight integration with other device components are major challenges in LTE antennas. Due to the volume limitations, a traditional PIFA antenna solution does not meet the requirements of the LTE antenna RF and brings greater challenges to antenna designers. LTE antenna design, shown in Figure 3.15, is a customized PIFA to meet LTE band requirements. The 4G/LTE provides a comprehensive and secure all-IP based mobile broadband solution to all kinds of mobile communication devices. WiMAX and first-release LTE have been the dominant technologies in this market. These technologies have been designed for channel bandwidths of 5 to 20 MHz (optionally up to 40 MHz) and offer peak data rates of ~100 MB/sec for high mobility devices and 1 GB/s for low-mobility devices. The resonant wavelength of a PIFA can be calculated using (3.2):

$$L1 + L2 - W = \lambda_0 \tag{3.2}$$

where $\lambda_0 = c_0 / (f_0 \sqrt{\epsilon_r})$.

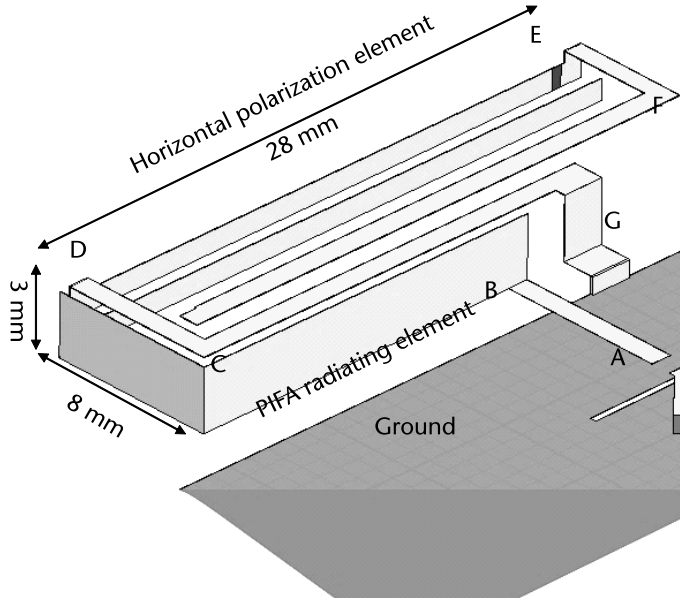

Figure 3.15 Dual-band LTE PIFA design dimensions.

A PIN diode at location E is used to control the resonating frequency of the antenna. This antenna resonates at the 800-MHz and 1,400-MHz band. The antenna is designed on FR4 with $\varepsilon_r = 4.4$ and a thickness of 0.8 mm. Isolation between both resonating bands is very high because only one band radiates at a time.

Figure 3.16 shows the simulated return loss of the LTE antenna. The antenna is tuned over 800 MHz and 1,400 MHz. The obtained simulated bands are 760–850 MHz and 1,380–1,470 MHz with a reflection coefficient better than –10 dB, covering the 800-MHz and 1,400-MHz bands. The 3-D simulated radiation patterns are at frequencies 800 MHz and 1,400 MHz, shown in Figure 3.17. Radiation patterns are nearly omnidirectional, suitable for mobile phone communication. As current nulls increase at higher frequencies, the radiation patterns show some distortions. Antenna-simulated gain varies from 3.7 dBi to 2.13 dBi.

3.8 MIMO Antenna Design for LTE Mobile Terminals

To increase the data transmission rate, MIMO technology has become an important feature in LTE communication systems. MIMO technology can linearly increase channel capacity with an increase in the number of antennas, without needing additional bandwidth or power [48]. A multiband internal antenna, including a diversity antenna in the DCS/PCS/UMTS bands and a MIMO antenna in the LTE17/LTE4 bands, is shown in Figure 3.18.

The designed antenna consists of a monopole to achieve the multiband operation. It also has a compact dimension by using 3-D, front-to-front arrangement. This antenna can cover two bands while fitting within tight volumes, providing high diversity performance and achieving reasonable mean effective gain (MEG) across both the bands of operation. The MIMO antenna, as shown in Figure 3.18,

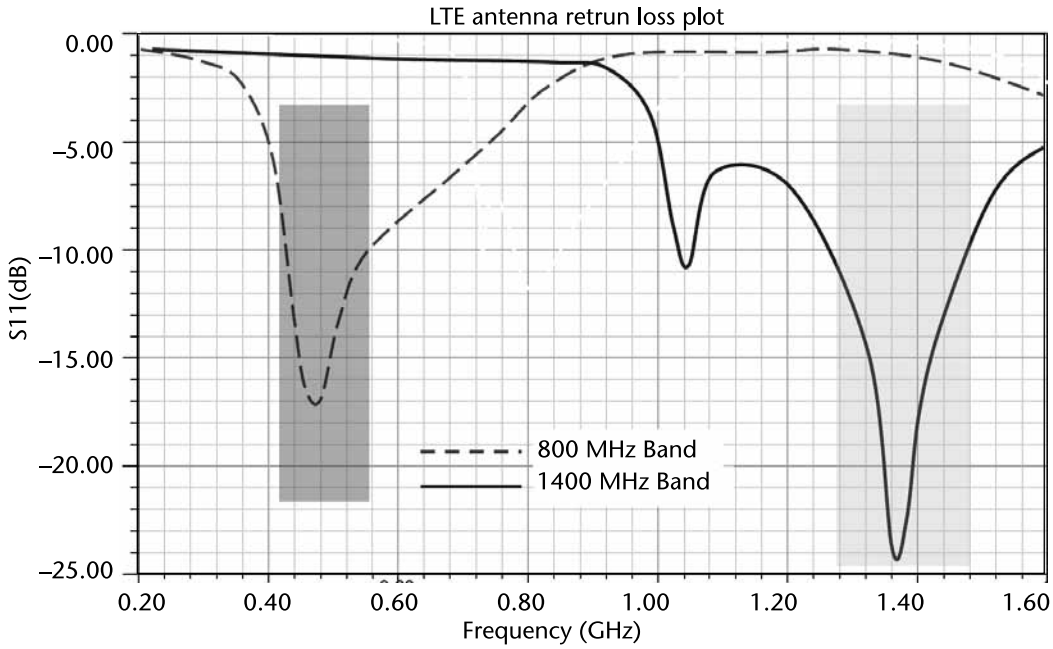

Figure 3.16 Antenna return loss plot of dual-band LTE PIFA.

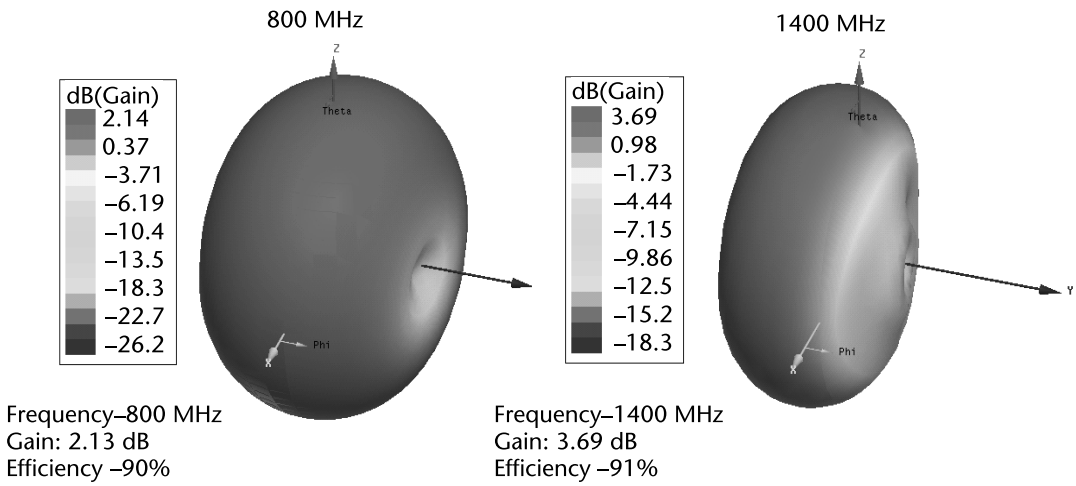

Figure 3.17 Radiation pattern plot at 800 MHz and 1,400 MHz.

has a metallic strip of a total length of 98 mm. The 2-mm-wide radiating antenna element is placed on an FR-4 substrate block of dimensions $16 \times 10 \times 5$ mm^3 and a relative dielectric constant of 4.4. The radiating bottom strip has a 2-mm feed. This multiband monopole antenna covers 890-MHz and 1,800-MHz bands. As the fractional bandwidth of an antenna is approximately the inverse of its Q [49] and bending a metal antenna to permit it to efficiently occupy a small volume can reduce its Q, a folded 3-D monopole enjoys simultaneous benefits: enhanced bandwidth and smaller required volume. Smartphone ground plane impact antenna

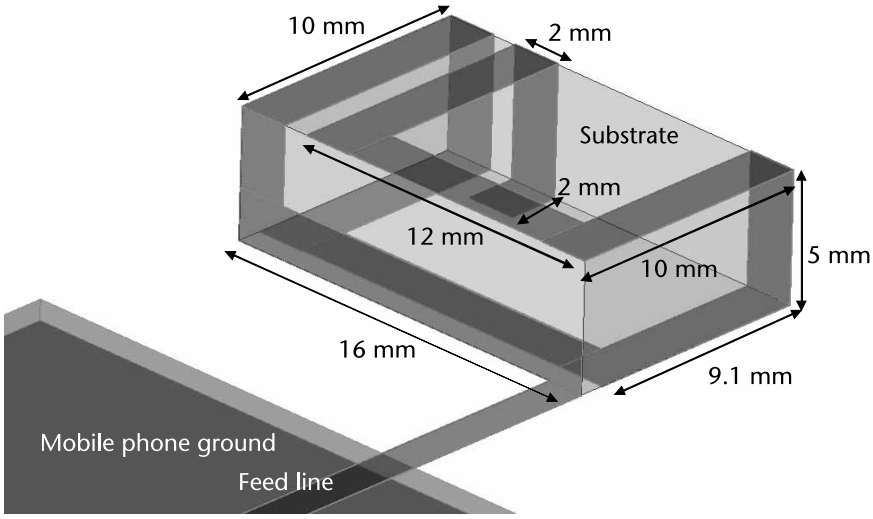

Figure 3.18 The configuration and design dimensions of the MIMO antenna.

performance must be included in the simulation and testing. The ground plane size of the antenna is 60 mm × 110 mm. For this antenna, the conductive strips are primary radiation elements and constitute two monopole radiators, identified here as monopole 1 and monopole 2. Monopole 1 is the strip length just after the antenna feed and before the strip on the substrate while the monopole 2 is the total strip length. The initial geometric parameters are optimized by using the FDTD numerical technique. The total electrical length of the monopole is set to a quarter-wavelength at the fundamental mode of 890 MHz. Figure 3.19 shows simulated reflection coefficients of the antenna. These curves indicate that the resonant frequencies of the antenna are in GSM900 and GSM1800 frequency bands.

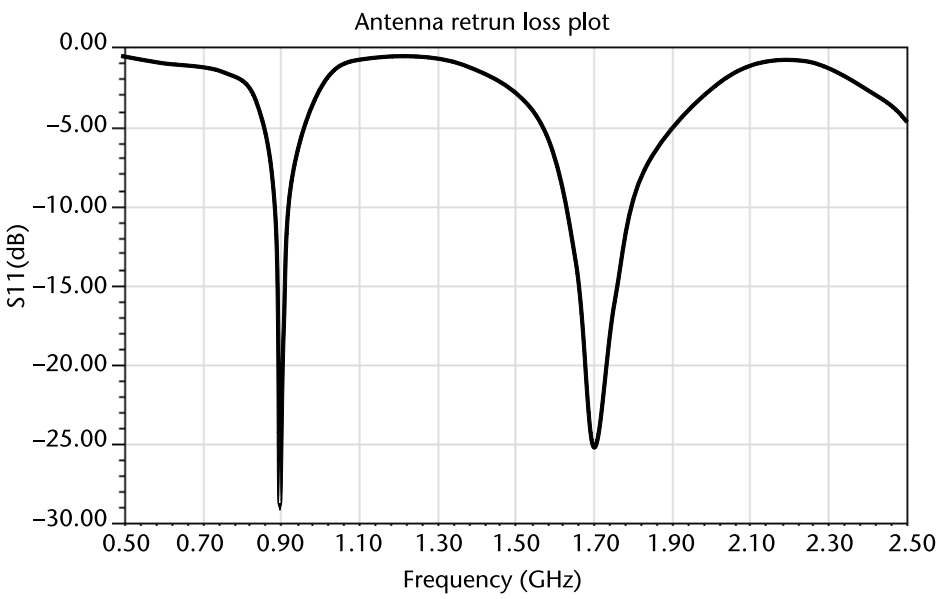

Figure 3.19 Return loss plot of a single-element LTE MIMO antenna.

To enhance the understanding of the multiband operation, the current distributions on the monopole are shown in Figure 3.20. The radiation 3-D gain patterns were simulated using FDTD. Figure 3.20 illustrates results for a 80-MHz operating frequency. After optimization of the antenna element, it is simulated along with other components of the mobile phone.

The mobile device has a maximum form factor of $115 \times 65 \times 12$ mm^3. Major electromechanical components include the other antennas radiation elements, a frame for supporting the antenna, a PCB, a plastic, mobile screen, and shielding metals. The design is slightly further fine-tuned to get optimum performance in the presence of other components of the mobile device.

3.9 Mobile Antenna Performance with Components and Standard Anthropomorphic Model Head

Antenna performance changes in the presence of other phone components and the housing structure in a smartphone. After the completion of standalone antenna design and optimization, the next step is to integrate the antenna model in a mobile phone along with other components and perform EM simulation. Integrated simulation enables the evaluation of the coupling effects of neighboring objects such as the camera, shields, traces, battery, and flash capacitors, as well as the influence of dielectric materials such as the housing and display screen. Antenna return loss, gain, and radiation pattern are affected by other electronics components of smartphone. Figure 3.21 shows electric field variation in the phone and antenna radiation pattern with other components of the mobile phone and human head model.

The smartphone performance, having a different antenna type, is analyzed in the presence of a human body, with emphasis on the head and hand to know the impact of the standard anthropomorphic model (SAM) on antenna performance. In accordance with IEEE standards, such as 1528, the SAM is used as the head model. The presence of the SAM is simulated by a head and shoulder only, since the handset antenna near-field radiation is mainly interacted with the presence of head, shoulder, and hand-hold rather than the other parts of the user's body. The frequency-dependent dielectric properties of the SAM tissue and liquid can be

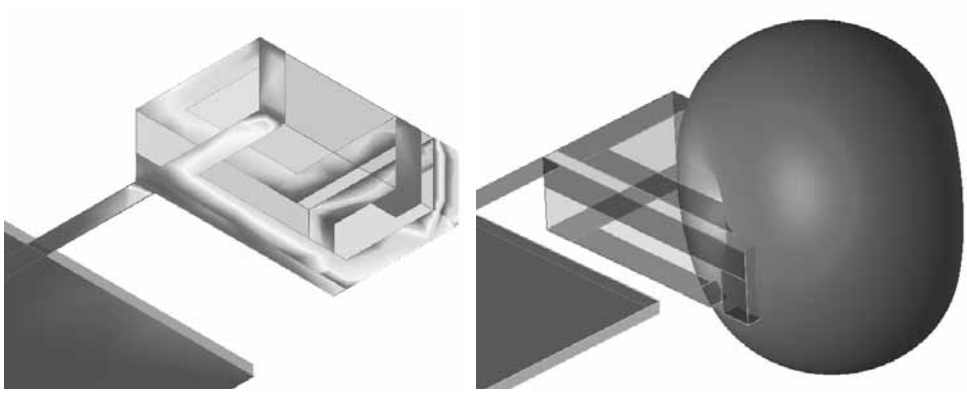

Figure 3.20 Electric current distribution on antenna and radiation pattern plot at 890 MHz.

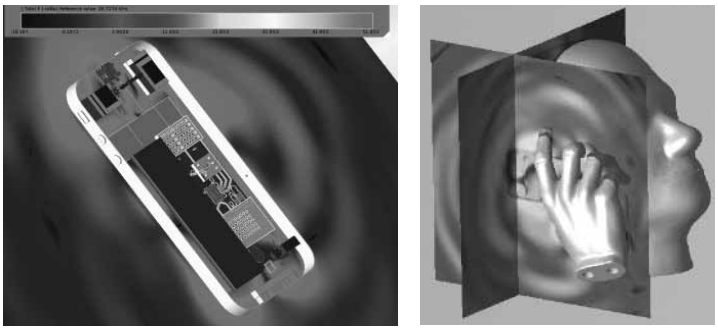

Figure 3.21 E-Field plot with phone components and SAM head model.

modeled as a dispersive material in the simulation tool. Such simulation can give important insight into how the SAM phantom or the homogeneous body models affect the performance of the mobile phone. The antenna return loss plot in Figure 3.22 indicates that deterioration is the return loss in the presence of a phone and the SAM. As can be seen, the antenna resonant frequency shifts at a higher side at 3 GHz when it is simulated with the mobile model. Reoptimization and tuning are needed to bring down Bluetooth antenna resonance at 2.45 GHz. LTE MIMO antenna behavior is different, in this case, resonance frequency shifts at a lower-frequency band as indicated in Figure 3.22(b). Antenna gain, radiation pattern, and electric field distribution are also affected by the hand and head of the human body. These simulations are a must for mobile phone antenna designers to get antenna performance in a real working environment.

In conjunction with radiation efficiency and return loss, the total radiated power (TRP) and the total isotropic sensitivity (TIS) are relevant for the complete phone. The TIS is a measure of the handset receiving performance and TIS measurements verify how the receiver antenna design performs. The objective is to measure the sensitivity of the mobile phone due to noise impairment and to find the lowest power level on which the phone can still maintain a reliable connection. A TRP measurement verifies the transmitter or transmitter antenna design. The TRP is measured by measuring the antenna radiated power at many points around the mobile phone and summing the values to the total power radiated.

The TIS and TRP together determine the effectiveness of the mobile phone and the maximum range at which the phone can operate from the base station with some given level of performance. Figure 3.23 shows the TIS values for the Bluetooth and LTE MIMO antenna in different scenarios. The lowest TIS value is measured for a mobile phone with the SAM with a tilted hand. In practice, the measurement process is often iterative: first, design all antennas separately and then simulate the antenna in the presence of other radiating elements and reoptimize the design and location of the antenna.

3.9.1 Cross-Talk of Bluetooth Antenna with MIMO Antenna

In mobile phones, several antennas are placed in a small volume. The main problem of colocating many antennas in a confined volume is mutual coupling or cross-talk between all antennas, inevitably leading to an increased design complexity.

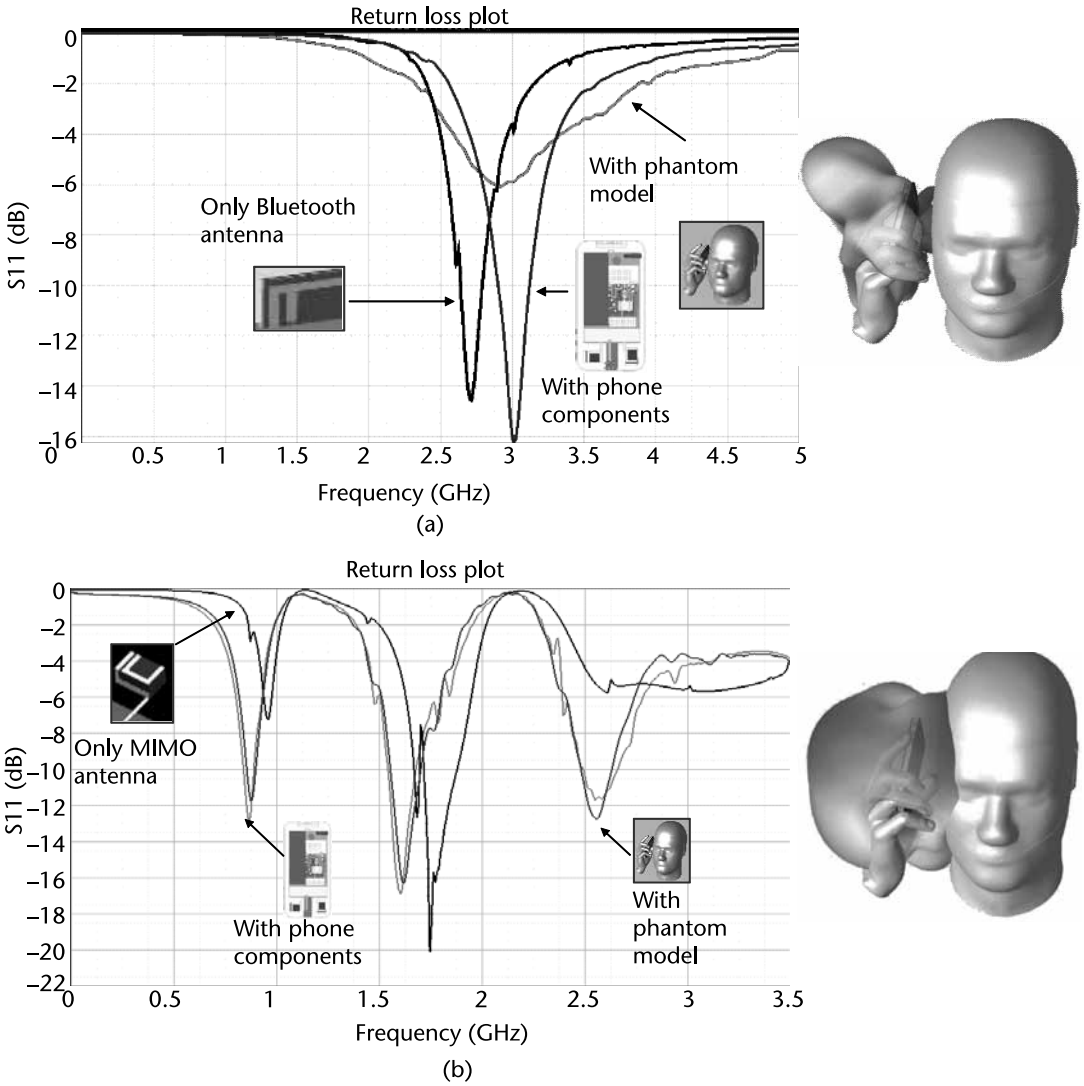

Figure 3.22 Simulated result of (a) Bluetooth and (b) LTE MIMO antenna along with phone components and the SAM head.

Designing and placing multiple antennas in a mobile phone are often extremely challenging; taking the mutual effects of other antenna elements into account can be difficult and time-consuming. Figure 3.24 shows mutual coupling better than –20 dB between Bluetooth and MIMO antenna. The mutual coupling can be reduced by the appropriate placing of the antenna, shielding, and feeding techniques.

In this chapter, basic mobile communication standards and antennas used in smartphones were discussed. Antenna design challenges and the types of antennas used in a smartphone were presented. Four different types of antennas used in modern smartphone devices are presented. Two antenna systems, one for Bluetooth and other for MIMO application, were modeled and simulated using a phone model and a SAM head and hand model. Important antenna specifications, design parameters, and design flow were discussed through these two antennas. Designing these stand-alone antennas is not sufficient to use these antennas commercially

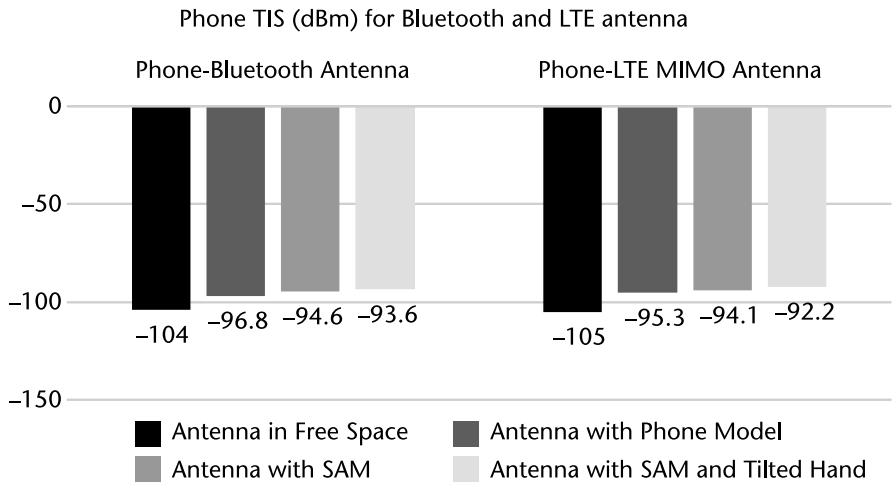

Figure 3.23 Phone TIS for Bluetooth and MIMO antenna.

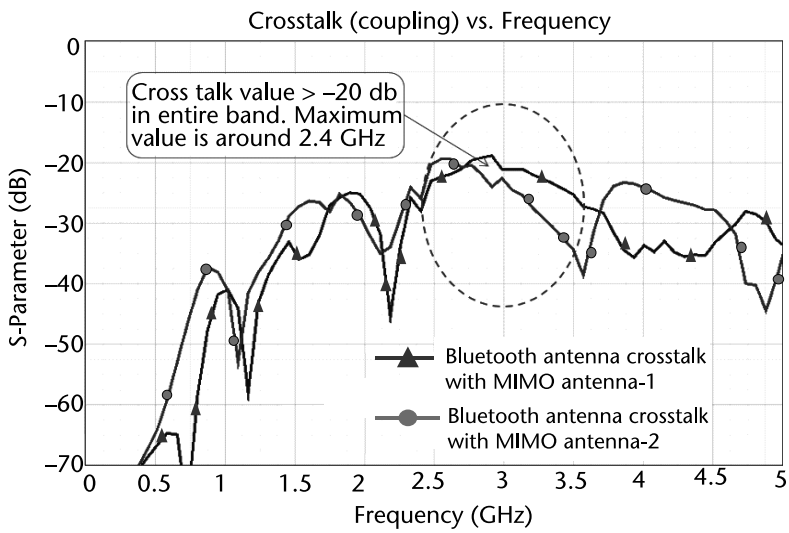

Figure 3.24 Cross-talk (coupling) between Bluetooth and MIMO antenna.

in mobile devices without meeting various mobile compliances. In Chapter 4, all these compliance and qualification processes are discussed, along with practically designed antennas.

References

[1] Ngan, T. L., et al., "The Enhanced Workflow and Efficiency of the Wireless Local Area Network (WLAN)-Based Direct Digital Radiography (DDR) Portable Radiography," *J. Digit. Imaging*, Vol. 28, 2015, pp. 302–308.

[2] Wang, Z., et al., "Embroidered Multiband Body-Worn Antenna for GSM/PCS/WLAN Communications," *IEEE Transactions on Antennas and Propagation*, Vol. 62, 2014, pp. 3321–3329.

[3] Ryu, H. K., E. Kim, and J. -M. Woo, "Miniaturization of Printed Inverted-F Antenna Using Chip Coupler for Bluetooth Applications," *Electronics Letters*, Vol. 46, No. 13, 2010.

[4] Jiang, B. T., and J. F. Mao, "Design of a PIFA-IFA-Monopole in Dual-SIM Mobile Phone for GSM/DCS/Bluetooth Operations," *ICMMT 2008 Proceedings*, 2008.

[5] Lee, E., P. Hall, and P. Gardner, "Novel Compact Wideband or Multi-Band Planar Monopole Antenna," *Proceedings of the IEEE Antennas and Propagation Society International Symposium*, Salt Lake City, UT, July 16–21, 2000, pp. 624–627.

[6] Khodabakhshi, H., and A. Cheldavi, "Irradiation of a Six-Layered Spherical Model of Human Head in the Near Field of a Half-Wave Dipole Antenna," *IEEE Transactions on Microwave Theory and Techniques*, Vol. 58, 2010, pp. 680–690.

[7] Chen, H. D., and H. T. Chen, "A CPW-Fed Dual-Frequency Monopole Antenna," *IEEE Transactions on Antennas and Propagation,* Vol. 52, No. 4, 2004, pp. 978–982.

[8] Ali, M., et al., "Dual-Frequency Strip-Sleeve Monopole for Laptop Computers," *IEEE Transactions on Antennas and Propagation*, Vol. 47, No. 2, 1999, pp. 317–323.

[9] Lu, J., and B. Huang, "Planar Multi-Band Monopole Antenna with L-Shaped Parasitic Strip for WiMAX Application," *Electronics Letters*, Vol. 46, No. 10, 2010, pp. 671–672.

[10] Fletcher, P. N., M. Dean, and A. R. Nix, "Mutual Coupling in Multi-Element Array Antennas and Its Influence on MIMO Channel Capacity," *Electronics Letters*, Vol. 39, No. 4, February 20, 2003, pp. 342–344.

[11] Teng, X. Y., et al., "A Compact CPW-Fed Omni-Directional Monopole Antenna for WLAN and RFID Applications," *Progress in Electromagnetics Research Letters*, Vol. 32, 2012, pp. 91–99.

[12] Egorov, I., and Z. Ying, "A Non-Uniform Helical Antenna for Dual-Band Cellular Phones," *IEEE Antennas and Propagation Society International Symposium*, Salt Lake City, UT, 2000, pp. 652–655.

[13] Nie, Y., and L. Song, "A Compact Triband Fractal PIFA Antenna for Mobile Handset Applications," *2013 6th International Congress on Image and Signal Processing (CISP),* Hangzhou, 2013, pp. 1468–1472.

[14] Teng, P. L., and K. L. Wong, "Planar Monopole Folded into a Compact Structure for Very-Low-Profile Multi-Band Mobile Phone Antenna," *Microw. Opt. Technol. Lett.*, Vol. 33, No. 3, 2002.

[15] Hayasida, S., H. Morishita, and K. Fujimoto, "A Wideband Folded Loop Antenna for Handset," *IEICE Trans.*, Vol. J86B, No. 9, 2003, pp. 1806–1815.

[16] Chen, H., Y. L. Ban, and L. J. Ying, "Compact PIFA Using Capacitive Coupled-Fed for LTE/GSM/UMTS WWAN Operation in the Mobile Application," *IEEE Proceedings of the Cross Strait Quad-Regional Radio Science and Wireless Technology Conference (CSQRWC '11)*, Harbin, China, July 2011.

[17] Ngan, T. L., et al., "The Enhanced Workflow and Efficiency of the Wireless Local Area Network (WLAN)-Based Direct Digital Radiography (DDR) Portable Radiography," *J. Digit. Imaging*, Vol. 28, 2015, pp. 302–308.

[18] van Rooyen, M., J. W. Odendaal, and J. Joubert, "High-Gain Directional Antenna for WLAN and WiMAX Applications," *IEEE Antennas and Wireless Propagation Letters*, Vol. 16, 2017, pp. 286–289.

[19] Mehdipour, A., T. Denidni, and A. R. Sebak, "Multi-Band Miniaturized Antenna Loaded by ZOR and CSRR Metamaterial Structures with Monopolar Radiation Pattern," *IEEE Transactions on Antennas and Propagation*, Vol. 62, 2014, pp. 555–562.

[20] Islam, M. S., et al., "Converting a Wireless Biotelemetry System to an Implantable System Through Antenna Redesign," *IEEE Transactions on Microwave Theory and Techniques*, Vol. 62, 2014, pp. 1890–1897.

[21] Choudhury, S., A. Mohan, and D. Guha, "Wideband Quasi-Omnidirectional Planar Inverted F-Antenna for Compact Wireless Systems," *IEEE Antennas and Wireless Propagation Letters*, Vol. 17, No. 7, July 2018, pp. 1305–1308.

[22] Makris, I., et al., "Modified Designs for UWB Planar Monopole Antennas," *2007 Loughborough Antennas and Propagation Conference*, Loughborough, 2007, pp. 249–252.

[23] Ghanbari, L., et al., "Planar Low VSWR Monopole Antenna for UWB and LTE Communication," *2016 16th Mediterranean Microwave Symposium (MMS)*, Abu Dhabi, 2016, pp. 1–4.

[24] Feng, B., et al., "A Dual-Wideband and High Gain Magneto-Electric Dipole Antenna and Its 3D MIMO System with Metasurface for 5G/WiMAX/WLAN/X-Band Applications," *IEEE Access*, Vol. 6, 2018, pp. 33387–33398.

[25] Xiaomu, H., S. Yan, and G. A. E. Vandenbosch, "Wearable Button Antenna for Dual-Band WLAN Applications with Combined On and Off-Body Radiation Patterns," *IEEE Transactions on Antennas and Propagation*, Vol. 65, No. 3, March 2017, pp. 1384–1387.

[26] Rahim, T., F. A. Abbasi, and J. Xu, "Dual Band Sleeve Dipole Antenna for WLAN Applications," *2016 10th European Conference on Antennas and Propagation (EuCAP),* Davos, 2016, pp. 1–3.

[27] Lin, Y. -D., and P. -L. Chi, "Tapered Bent Folded Monopole for Dual-Band Wireless Local Area Network (WLAN) Systems," *IEEE Antennas and Wireless Propagation Letters*, Vol. 4, 2005, pp. 355–357.

[28] Li, S., Y. Mao, and W. Yu, "A Novel Dual Notched UWB Antenna for Wireless Body Area Network," *2016 IEEE/ACES International Conference on Wireless Information Technology and Systems (ICWITS) and Applied Computational Electromagnetics (ACES)*, Honolulu, HI, 2016.

[29] Wen, R., "Compact Planar Triple-Band Monopole Antennas Based on a Single-Loop Resonator," *Electron. Lett.*, Vol. 49, No. 15, July 2013, pp. 916–918.

[30] Chen, Z. N., T. S. P. See, and X. Qing, "Small Printed Ultrawideband Antenna with Reduced Ground Plane Effect," *IEEE Transactions on Antennas and Propagation*, Vol. 55, No. 2, February 2007, pp. 383–388.

[31] Chang, T. N., and J. J. Jiang, "Meandered T-Shaped Monopole Antenna," *IEEE Transactions on Antennas and Propagation*, Vol. 57, No. 12, December 2009, pp. 3976–3978.

[32] Chu, Q. X., and L. H. Ye, "Design of Compact Dual-Wideband Antenna with Assembled Monopoles," *IEEE Transactions on Antennas and Propagation*, Vol. 58, No. 12, December 2010, pp. 4063–4066.

[33] Yeh, S. H., and K. L. Wong, "Dual-Band F-Shaped Monopole Antenna for 2.4/5.2 GHz WLAN Application," *IEEE Antenna Propagation Society International Symposium*, Vol. 4, June 2002, pp. 72–75.

[34] Hsiao, H. M., et al., "Novel Dual-Broadband Rectangular-Slot Antenna for 2.4/5-GHz Wireless Communication," *Microw. Opt. Technol. Lett.*, Vol. 46, 2005, pp. 197–201.

[35] Kuo, Y. -L., and K. -L. Wong, "Printed Double-T Monopole Antenna for 2.4/5.2 GHz Dual-Band WLAN Operations," *IEEE Transactions on Antennas and Propagation*, Vol. 51, No. 9, September 2003, pp. 2187–2192.

[36] Tsai, L. C., "A Triple-Band Bow-Tie-Shaped CPW-Fed Slot Antenna for WLAN Applications," *Progress in Electromagnetics Research*, Vol. 47, 2014, pp. 167–171.

[37] Liu, W. C., "Broadband Dual-Frequency Cross-Shaped Slot CPW-Fed Monopole Antenna for WLAN Operation," *Microw. Opt. Technol. Lett.*, Vol. 46, 2005, pp. 353–355.

[38] Panda, J. R., and R. S. Kshetrimayum, "A Printed 2.4 GHz/5.8 GHz Dual-Band Monopole Antenna with a Protruding Stub in the Ground Plane for WLAN and RFID Applications," *Progress in Electromagnetics Research C*, Vol. 117, 2011, pp. 425–434.

[39] Ren, W., "Compact Dual-Band Slot Antenna for 2.4/5 GHz WLAN Applications," *Progress in Electromagnetics Research B,* Vol. 8, 2008, pp. 319–327.

[40] Song, Y., et al., "Multiband CPW-Fed Triangle-Shaped Monopole Antenna for Wireless Applications," *Progress in Electromagnetics Research*, Vol. 70, 2007, pp. 329–336.

[41] Chang, M., and W. Weng, "A Dual-Band Printed Dipole Slot Antenna for 2.4/5.2 GHz WLAN Applications," *2011 IEEE International Symposium on Antennas and Propagation (APSURSI),* Spokane, WA, 2011, pp. 274–277.

[42] Zhao, G., et al., "Compact Ring Monopole Antenna with Double Meander Lines for 2.4/5 GHz Dual-Band Operation," *Progress in Electromagnetics Research*, Vol. 72, 2007, pp. 187–194.

[43] Van Valkenburg, M. E., *Introduction to Modern Network Synthesis*, New York: Wiley, 1960.

[44] Wang, S. B. T., A. M. Niknejad, and R. W. Brodersen, "Circuit Modeling Methodology for UWB Omnidirectional Small Antennas," *IEEE Journal on Selected Areas in Communications*, Vol. 24, No. 4, April 2006, pp. 871–877.

[45] Caratelli, D., et al., "Circuit Model and Near-Field Behavior of a Novel Patch Antenna for WLAN Applications," *Microwave and Optical Technology Letters*, Vol. 49, No. 1, January 2007, pp. 97–100.

[46] Jung, M., Y. Kim, and B. Lee, "Dual Frequency Meandered PIFA for Bluetooth and WLAN Applications," *Proceedings of the IEEE International Antennas and Propagation Symposium,* Vol. 2, June 2003, pp. 958–961.

[47] Naik, P. R., B. A. Singh, and S. Thakur, "Dual Band Compact Printed Monopole Antenna for Bluetooth (2.54GHz) and WLAN (5.2GHz) Applications," *2016 International Conference on Global Trends in Signal Processing, Information Computing and Communication,* Jalgaon, 2016, pp. 320–323.

[48] Wallace, J., et al., "Experimental Characterization of the MIMO Wireless Channel: Data Acquisition and Analysis," *IEEE Transactions on Wireless Communications*, Vol. 2, No. 2, March 2003, pp. 335–343.

[49] Vainikainen, P., et al., "Resonator-Based Analysis of the Combination of Mobile Handset Antenna and Chassis," *IEEE Transactions on Antennas and Propagation*, Vol. 50, No. 10, October 2002, pp. 1433–1444.

CHAPTER 4

Smartphone Antenna Design Compliances and Measurement

4.1 Introduction

The desire for internet connection anytime and anywhere has spurred cellular carriers to shift their services from voice-only networks to more data-centric services. Novel antenna technologies such as MIMO have increased data rates while improving coverage. Smartphone designers are struggling every day with various compliance-related problems that fail critical products to pass compliance certification and cause a big loss of profit. When selecting a radio technology, product designers should consider not only the performance requirements, but also the regulatory constraints. Compliance testing is testing to determine whether a product or system meets some specified standard that has been developed for efficiency or interoperability [1–10]. Standards organizations such as the American National Standards Institute (ANSI), the U.S. Federal Communications Commission (FCC), and the International Electrotechnical Commission (IEC) have certain criteria that a product must meet before compliance is recognized. A product cannot be sold unless it is known to meet those requirements specified in the standards. The first step towards regulatory compliance is to thoroughly investigate the applicable electromagnetic compatibility (EMC) specifications for the target geographic market.

Nowadays new advances in EDA technologies are providing accurate predictive simulations in a reasonable amount of time for compliance measurements [11]. With careful engineering utilizing cutting-edge, full-wave field-solvers based on MoM, FDTD, and FEM numerical techniques along with a hardware boost using heterogeneous massive CPU/GPU parallel processing (CUDA) technology, the designer can measure all compliance-related parameters such as radiations, SAR, HAC, and EMC. These simulators work as a virtual compliance test laboratory, providing the engineers with an early-stage compliance testing to find the optimum trade-off between performance and cost.

A smartphone has more advanced computing capability, connectivity and user applications than a feature phone. The smartphone combines the functions of a basic mobile phone, GPS navigation, media players, digital cameras, pocket video cameras, high-resolution touchscreens, and web browsers. Most of the operators

already switched to LTE network coverage and plans and because of that many smartphone manufacturers are switching to LTE-based phones. LTE is a radio platform technology that allows operators to achieve even higher peak throughputs than HSPA+ in higher spectrum bandwidth. The prime objective of LTE is to provide high data speed. A typical smartphone along with important electronics component is represented in Figure 4.1. Smartphone antennas design challenges, simulation flow, diversity technique, and various compliance measured in mobile devices are discussed in this chapter with practical mobile phone designs. Even all these challenges are going to increase several times when the 5G phone becomes operational in the near future.

4.2 Design Challenges in Smartphone Systems

Just designing various chips and antennas on the smartphone alone is not enough. These components, such as antennas, influence overall circuit performance. Increased digital to RF interference is required to isolate digital and RF circuits from each other and mitigate digital to RF noise interference. Even with shielding, problems can arise if the RF circuit is not properly terminated to the ground layer of the PCB. Antenna resonances and couplings are influenced by the limited size of the mobile ground plane because of the surface current flows on the ground plane. For all compliance measurement and simulation, a single EM simulation technology may not solve all problems. Both planar MoM and 3-D full-wave field-solver FDTD and FEM, along with a hardware boost using heterogeneous massive central processing unit and graphics processing unit (CPU/GPU) parallel processing (CUDA) technology, make it possible to use a simulated system in less time in the

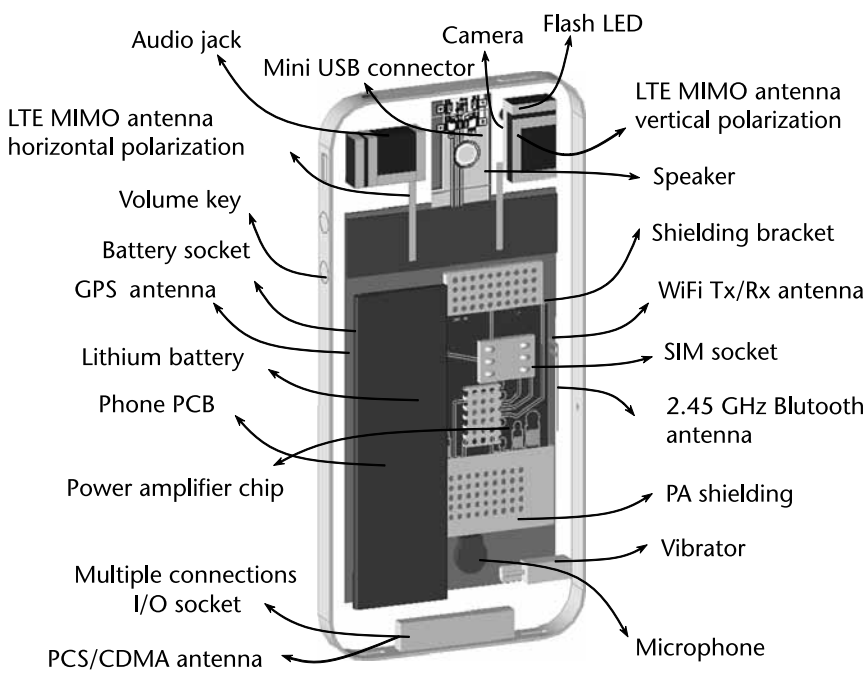

Figure 4.1 Various wireless antennas and components in smartphone.

presence of all mobile compoents. Challenging requirements such as CPU performance, wireless connectivity, memory capacity, bandwidth, display, and multimedia performance are driving new technologies in smartphone design and making a system complex. Radiation from antennas affects the performance of other electronic components in the phone as well as human tissues.

4.3 Smartphone Antenna Simulation Workflow

Antenna simulation workflow in a mobile phone is shown in Figure 4.2. The design and simulation of WLAN, GSM, Bluetooth, and MIMO antennas are discussed in Chapter 3. Mobile antennas, along with other active components of antennas such as power amplifiers, low noise amplifiers (LNAs), shields, and phone body, are simulated in a real environment. In a smartphone simulation model, the near-field environments are created using the housing and enclosed circuitry of a production-style smartphone. The major components that provide the near-field EM interaction with antennas include a liquid crystal display (LCD), a battery, a dielectric frame, phone RF board and chips, shields, and an exterior plastic shell. All individual designed components should work properly along with other devices in the phone; this is ensured with system-level simulation. Poor antenna matching can manifest itself in a high level of spurious emissions. Compliance simulation and measurement are a basic requirement to qualify a mobile device for commercial usage.

4.4 Smart Antenna System Using the MIMO and Diversity Technique

In a communication system, fading is variation of the attenuation of a signal with various variables as shown in Figure 4.3. In the case of long-distance

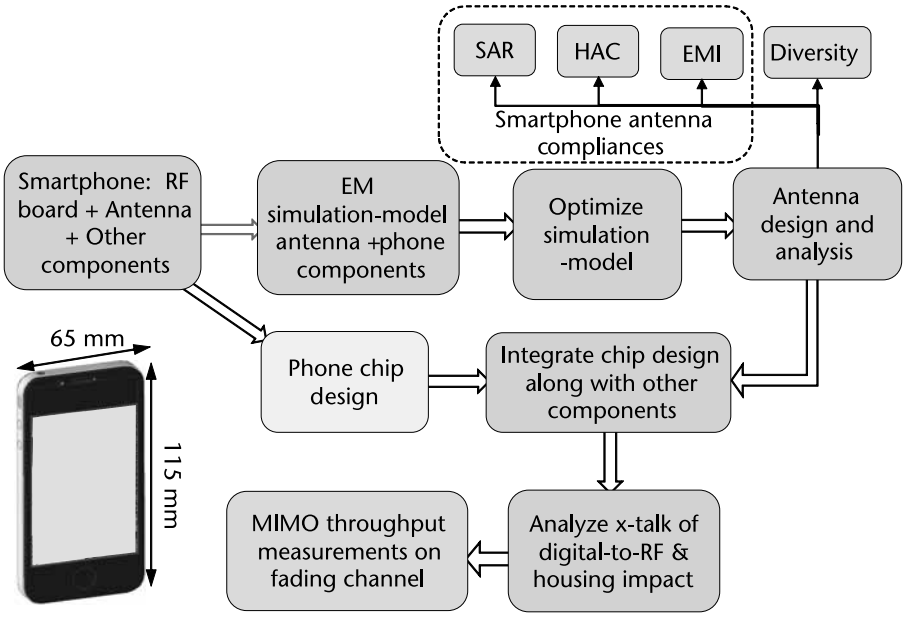

Figure 4.2 Smartphone antenna design and simulation workflow.

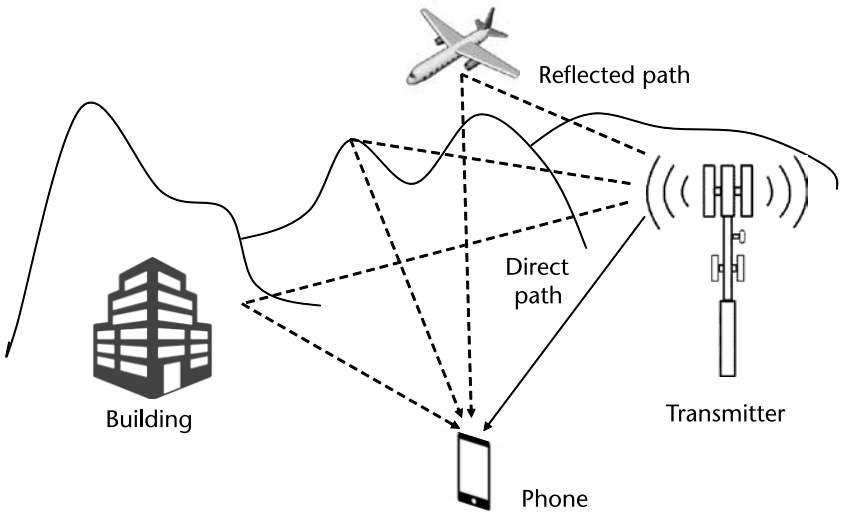

Figure 4.3 Communication signal fading environment.

communication, signal fading is a common feature for a single-input single-output (SISO) antenna system. At times, the received signal drops below the mean signal level, which ultimately leads to communication being lost. To receive the required signal strength, the power level needs to be increased, which further invites interference with other channels. To increase the power level, some active devices are used, which also introduces some nonlinear behavior into the channels. The MIMO antenna system (sometimes called smart antenna technology) using spatial diversity reception or transmission increases the probability of reception, spectral efficiency, and reliability as compared to single-antenna communication systems. Deploying multiple antennas at both transmitter and receiver ends achieves a higher data rate without increasing the total transmission power or bandwidth in a multipath wireless channel [12–16].

This antenna system is used in a wireless communication system, especially when the signal propagates through some corrupted environments. For mobile communication, the diversity scheme has already been implemented to mitigate the fading effects of multipath scenario. In a multipath rich wireless channel, deploying multiple antennas at both the transmitter and receiver achieves high data rate without increasing the total transmission power or bandwidth. In a MIMO system, the most important parameter is the increase in channel capacity because of the use of multiple transmitting and receiving antennas [17]. This antenna system is widely applicable to increase the range and reliability of Wi-Fi LAN, Bluetooth, personal digital assistants (PDAs), digital communication system (DCS), WLAN, and UMTs. It also plays a significant role in the implementation of next generation wireless equipment.

4.4.1 MIMO Antenna Configuration

Communication systems are broadly categorized into four fundamental ways in which multiple transmit and receive antennas can be used to communicate through the radio channel. Figure 4.4 shows different, general redundancy configurations:

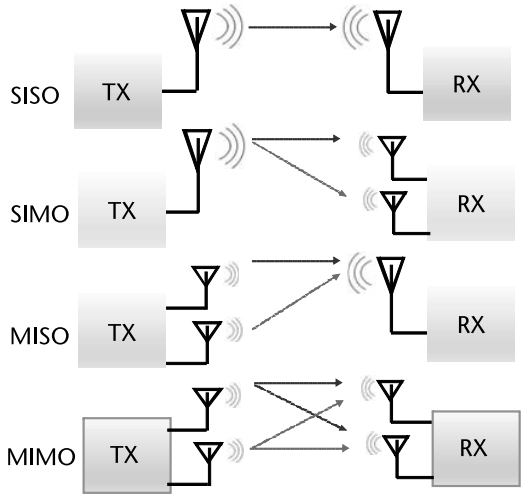

Figure 4.4 Redundancy configurations using multiple antennas.

SISO, single-input multiple-output (SIMO), multiple-input single-output (MISO), and MIMO.

SISO systems do not provide any type of robustness or capacity improvement and represent a basic wireless communication link. SIMO systems are configurations that provide receive-side diversity and provide additional robustness, but no capacity improvement. MISO provides transmitter diversity by coupling the channel at different points in space such that the links will not have the same fading characteristics and the spatial sum of the signals will be dominated by the stronger of the two signals. This configuration is better known as transmit diversity. In MIMO systems, multiple antennas are used both at transmitter and receiver ends to make use of reflected signals to provide gains in channel robustness and throughput. This provides for both redundancy and channel capacity improvement [18–22]. See Figure 4.4.

4.4.2 Antenna Diversity

Apart from the antenna configurations, there are two types of MIMO with respect to how data is transmitted across the given channel. The existence of multiple antennas in a system means the existence of different propagation paths. To improve the reliability of the system, the same data is sent across the different propagation (spatial) paths. This is called spatial diversity or simply diversity. To improve the data rate of the system, different portions of the data may be placed on different propagation paths and this is called spatial multiplexing. These two systems are listed here:

1. *Implementation using diversity techniques:* This system provides diversity gain to improve the reliability.
2. *Implementation using spatial-multiplexing techniques:* This system provides degrees of freedom or multiplexing gain to improve the data rate of the system.

In diversity techniques, the same information is sent across independent fading channels to combat fading. When multiple replicas of the same data are sent across independently fading channels, the amount of fade suffered by each copy of the data will be different. This guarantees that at least one of the data copies will suffer less fading compared to rest of the copies. Thus, the chance of properly receiving the transmitted data increases, which results in improving the reliability of the entire system as well as reducing the cochannel interference significantly. This technique is referred as spatial diversity in the communication system. To combat the fading effect, an array of antennas is used.

Diversity techniques are an effective means that enhances the immunity of the communication system to the multipath fading. A diversity antenna system provides many receiving branches or ports from which the diversified signals are derived and fed to a receiver. The receiver then combines the incoming signals from all the branches to produce a combined signal with improved quality in terms of signal strength or signal-to-noise ratio (SNR). The performance of a diversity antenna system primarily depends on the branch correlation and signal level difference between branches. There are four different diversity techniques as listed here. Spatial and polarization diversity techniques are realized through antenna systems.

- *Time diversity:* Signals transmitted at different times will get uncorrelated due to the time dependence of the multipath environment.
- *Frequency diversity:* Signals transmitted at different frequencies will get uncorrelated due to the frequency dependence of the multipath environment.
- *Spatial diversity:* Signals received at different locations can get uncorrelated due to the small-scale fading.
- *Polarization diversity:* Signals received with different polarizations can get uncorrelated due to different fading behavior for horizontal/vertical polarization.

4.4.3 MIMO Antenna Design Challenges

Despite many advantages, the MIMO antenna system suffers from a serious problem caused by strong mutual coupling between antenna elements, which causes signal interference between them and a higher value of mutual coupling lowers antenna efficiency, so that, in general, 0.5λ or more distance between antennas is needed to avoid the degradation of antenna performance. As is common in cellular phone handsets, higher levels of mutual coupling, which can easily occur in a handset, these systems can significantly degrade antenna efficiencies and produce an undesirable signal correlation between multiple antenna outputs. High signal correlation is associated with the loss of spectral efficiency and can degrade system throughput and battery efficiency. To achieve the desired low signal correlation, these communication systems require high diversity [13] and reduced coupling, which is also identified as a high port-to-port isolation.

4.4.4 Antenna Diversity Simulation and Measurement

The issue of signal fading in a multipath environment is a major problem. Using antenna diversity techniques can overcome the problem. There are two different approaches to obtain diversity gain: one is based on antenna power measurement at the receiver side, which is termed as the power-level approach, and the other is based on the analysis from both the embedded element efficiency and correlation coefficient, which is termed as the correlation approach. The second approach is described in this section to get diversity gain.

Antenna diversity always requires two far-zone patterns and two antenna systems as illustrated in Figure 4.5. For each far zone, only one antenna is fed, and the second antenna is left open. These two antennas are completely characterized by their far-zone patterns. Antenna far-zone patterns are valid for both receiving and transmitting. FDTD simulation technique is used to obtain the radiation field function and the S-parameters for calculating the correlation coefficient and embedded element efficiency. The antenna design presented in Chapter 3, Section 3.8, is used as an antenna element for a mobile terminal, which contains two PIFAs on a mobile PCB. It is discussed that the diversity antenna system can provide a good diversity performance by properly placing the two antennas through theoretical analysis and EM simulation.

4.4.5 Antenna Diversity Modeling

Using EDA tools, a complex wireless environment can never model in a deterministic way. It is even difficult to know beforehand in which environment a mobile phone antenna will be used. The complete environment (transmitter + obstacles) is described as a probability density function (PDF) that provides direction information with the highest change to receive a signal. Indoor and outdoor environments are modeled as uniform PDF and Gaussian PDF or user-defined PDF, respectively. PDF is used to model communication channels and the environment as shown in Figure 4.6. This function "weights" different directions in the far-zone sphere such that certain far-zone direction is considered more than others in the mean effective

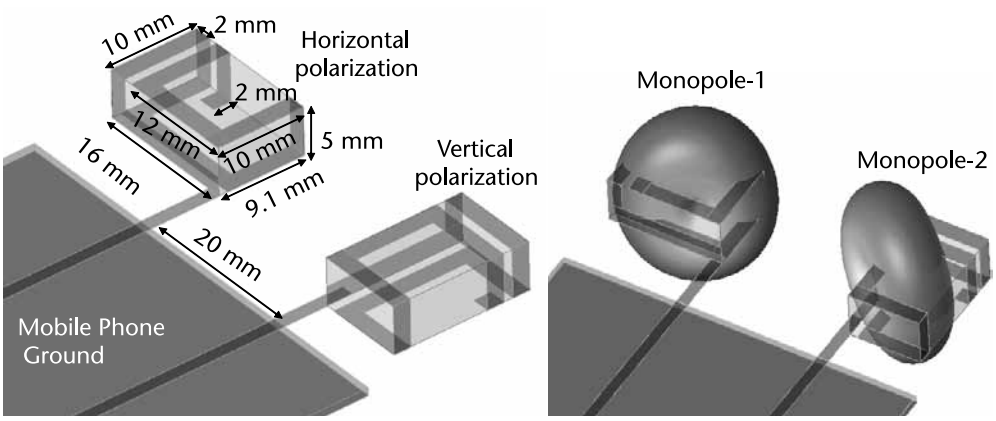

Figure 4.5 Horizontal and vertical polarization antenna elements and radiation pattern for antenna diversity system.

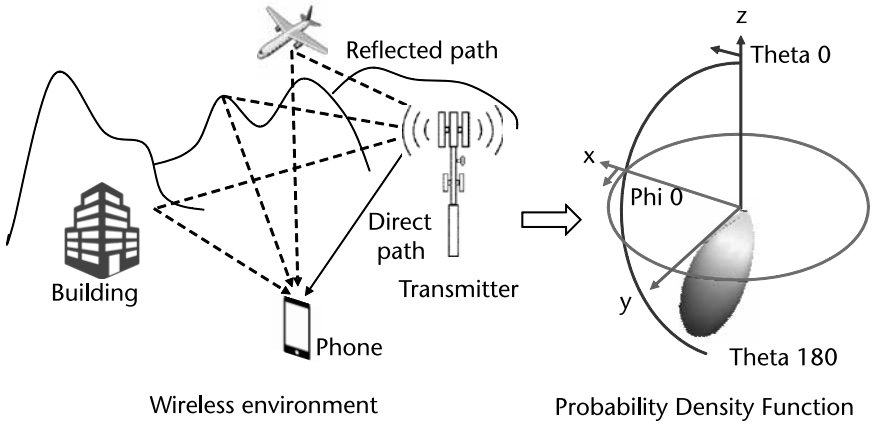

Figure 4.6 Stochastic representation of the environment.

gain and antenna diversity calculations. It has a maximum value of 1 and a minimum value of 0.

4.4.5.1 Diversity Modeling Calculations

The following are the diversity modeling calculations:

- *Complex correlation:* Given the stochastic model of the environment and antenna far-zone patterns, it gives information on how similar signals are received by the two antennas on average.
- *Complex correlation:* Real part of correlation – *j** complex part of the correlation.
- *Envelope correlation close to 1:* Very similar signals. There is no gain by using two antennas. If one signal is very weak, the other one will most likely also be very weak.
- *Envelope correlation close to 0:* Very unsimilar signals. There is significant gain by using two antennas. If one signal is very weak, the other can still be very strong with a high likelihood.
- *Rule of thumb:* Aim at an envelope correlation < 0.5.

Correlation from the 3-D pattern is given by

$$R_{ij} = \int_0^{\pi}\int_0^{2\pi} [XPD.E_{\theta i}(\theta,\varphi).E^*_{\theta j}(\theta,\varphi) + E_{\varphi i}(\theta,\varphi).E^*_{\varphi j}(\theta,\varphi)].P(\theta,\varphi)\sin\theta\, d\theta\, dd\varphi \tag{4.1}$$

On average over complete 3D sphere

Is there a preferred polarization?

Polarizations of antenna far-zone

Stochastic model for the environment

Correlation from the 2-D pattern is given by

$$R_{ij} = \int_0^{2\pi} [XPD.E_{\theta i}\left(\frac{\pi}{2},\varphi\right).E_{\theta j}^{*}\left(\frac{\pi}{2},\varphi\right) + E_{\varphi i}\left(\frac{\pi}{2},\varphi\right).E_{\varphi j}^{*}\left(\frac{\pi}{2},\varphi\right)].P(\varphi)d\varphi \tag{4.2}$$

XPD is cross-polarization discrimination of the incident multipath field. It can be expressed by the ratio of time-averaged vertical power to time-averaged horizontal power in the fading environment. Users can input a linear value or a decibel value.

- Small XPD = strong phi-polarization;
- Large XPD = strong theta-polarization.

The two antennas are completely characterized by their far-zone patterns. Two antenna patterns are always needed for diversity calculation because largest performance improvement has been observed with two antennas as shown in Figure 4.7. Only minor additional performance improvement is noticed when using more than two antennas. Antenna systems with N antennas are characterized by an $N \times N$ correlation matrix, which is built by considering the 2 2 antenna system. Complex correlations calculated from 3-D and 2-D patterns are shown in Table 4.1.

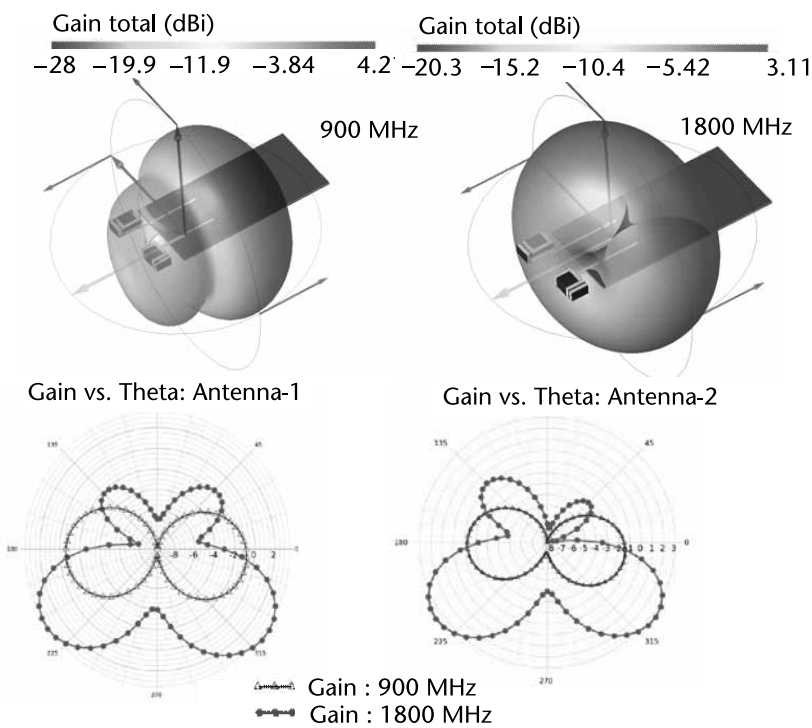

Figure 4.7 The 3-D and 2-D phi-cut radiation pattern of the antenna.

Table 4.1 Complex Correlation from 3-D and 2-D Antenna Patterns

	Envelope Correlation	*Complex Correlation*	*Complex Correlation Magnitude*
From 3-D pattern	0.1395	0.3703–0.0491*j*	0.3735
From 2-D pattern	0.1305	0.3567–0.0578*j*	0.3613

4.5 Mobile Phone Compliances and Measurement

Mobile communications devices, such as mobile phones, wireless modems, and base stations (including mobile phone towers), produce EM energy (EME) to transmit a signal. For mobile phones, HAC, SAR, EMC, and EMI compliances have been framed for serious reasons based on the context and failing to adhere to the compliance may be a violation based on the laws in the specific industry or country.

One important issue to be considered in designing antennas for a mobile phone is the reduction of SAR values, which could be caused by RF radiation from multiple radio and antennas in the mobile phone. The SAR should be as low as possible, especially when in contact with the human brain. The handset with multiple transmitters and antennas will increase the complexity of the near-field problem. In addition, HAC is required for mobile phones in some countries, which will also increase the complexity of antenna design.

4.5.1 EMC and EMI Compliance

All electronics circuits have the possibility of radiating of picking up unwanted electrical interference, which can compromise the operation of one or other of the circuit. EMC is the concept of enabling different electronics devices to operate without mutual interference, electromagnetic interference (EMI) when they are operated close to each other. The first stage in the mobile phone antenna design process is to design an antenna to meet the EMC compliance test requirements and any EMC testing that is undertaken. For good EMI performance, it is necessary to ensure that adequate filtering and shielding are in place to prevent unwanted radiation taking place or to allow in unwanted signals. Much of this can be undertaken by placing adequate filtering and metallic shielding. It is also necessary to ensure that the phone is adequately screened. Within the phone, any sources of signals or areas that are susceptible to radiation should be isolated from another component.

4.5.2 HAC Compliance

A hearing aid is an electroacoustic device that is placed in or behind the user's ear and is designed to amplify and modulate sounds for the user. When mobile phones are used near some hearing devices (hearing aids and cochlear implants), the user may detect a humming, buzzing, or whining noise. Some hearing devices are more sensitive than others to this interference noise. Similarly, cell phones also vary in the amount of interference that they generate. The FCC has approved standards and

passed regulations for digital wireless device use with hearing aids to ensure that everyone benefits from advances in technology. HAC-compliant devices carry a rating of M3, M4, T3, or T4. Cell phones that comply with the FCC's HAC rule must receive a minimum rating of M3 for RF emissions and T3 for telecoil coupling.

4.5.3 SAR Compliance

The SAR is a measure of the amount of RF energy absorbed by the human body when using a mobile phone. The SAR value is measured in terms of watts per kilogram or milliwatts per gram. The RF exposure limits are expressed in the terms of SAR, which is a measure of the electric and magnetic field strength and power density for transmitters operating at frequencies from 300 kHz to 100 GHz. The FCC and other federal governmental agencies around the world require that any wireless device is evaluated to meet the RF exposure limits set forth in the governmental SAR regulations.

SAR testing uses standardized models of the human body and head that are filled with liquids with different dielectric constants and represents the RF absorption characteristics of different human tissues. A mobile phone is tested while operating at its highest power level in all the operating frequency bands and in various specific positions against the dummy head and body. This setup represents the way that different users typically hold a cell phone, including to each side of the head to determine compliance. A robotic probe takes a series of measurements of the electric field at specific pinpointed locations in a very precise, grid-like pattern within the dummy head and torso, and this data is processed to calculate the SAR value and the compliance of the cell phone.

4.6 HAC

HAC testing includes measuring the electric and magnetic fields produced by a phone to ensure that it does not interfere with the sound quality of a hearing aid. HAC testing was originally introduced in 1970 with the purpose of making it possible to couple a wired telephone with a hearing aid. The wireless telephone industry has developed M and T ratings to assist hearing aid users in finding wireless devices that may be compatible with their hearing aids. Wireless devices with HAC compliance that are rated have the rating displayed on their box together with other relevant approval markings.

Early in 1996, the FCC called together a summit between the hearing industry, the wireless industry, and consumers to resolve the compatibility issue between hearing aids and cellular phones. Because of those efforts, in 1996, ANSI ASC 63 formed task group C63.19 to develop a measurement standard for HAC with wireless communications devices; the goal of this task group was to develop a set of tests that would evaluate the compatibility of hearing aids with cellular phones. The challenges presented to the task group were formidable. The availability of HAC handsets is observed by the FCC. The target is a market coverage of at least 50% M-rated handsets and 2 handsets with T-rating per provider. Since 2005, the FCC has required that cellular telephone providers and manufacturers offer a growing number of handsets, which are compatible with hearing aids according

to the standard ANSI C63.19. This standard specifies the audio magnetic field for T-coil coupling as well as the allowable RF interference level for E-field and H-field as a function of hearing aid RF susceptibility. In the T-coil mode, a hearing aid receives its signal not by a microphone but through an inductive pickup coil. The intended magnetic signal for the t-coil is that produced by the audio signal driving the phone receiver element or some other inductive circuit element. In the ideal case, a hearing aid delivers the same audio level whether in audio or t-coil mode.

4.6.1 M and T Ratings

These are the M and T ratings:

- *M-rating:* An M rating measures compatibility with acoustic hearing aids, and the higher the number (e.g., M3, M4, and so forth), the more compatible the handset. Usually, handsets rated M3 or T3 by the ANSI are considered compliant with FCC requirements. Wireless devices rated M3 or M4 meet FCC requirements. M4 is the better or higher of the two ratings.
- *T-rating:* A T rating measures compatibility with induction hearing aids. The higher the T number, the more likely the user will be able to use the phone with hearing aid on the telecoil setting. Wireless devices rated T3 or T4 meet FCC requirements and are likely to be more usable with a hearing device's telecoils (T switch or telephone switch) than unrated wireless devices. T4 is the better or higher of the two ratings.

4.6.2 HAC Measurement

The standardized method of measuring the HAC [23] defines the tests to be done in free-space (without the user) on a square HAC plane (50 mm × 50 mm) at a 15-mm distance from the surface of the phone. The center of the square plane is aligned with the earpiece of the mobile device. In this work, the earpiece is determined to be located at a 10-mm distance from the edge of the chassis of the terminal as shown in Figure 4.8. The HAC plane is divided into nine equal-sized subgrids. The maximum of the electric and magnetic fields is measured for each subgrid. As per the HAC standard, three adjacent subgrids (except the center subgrid) can be excluded for both electric and magnetic fields so that one of the excluded subgrids must be the same for both electric and magnetic fields. The electric and magnetic field strengths should be below the given limits to fulfill the HAC standard in the remaining six subgrids. HAC sensors gather data on a 5 cm × 5 cm arbitrarily oriented rectangle in free space. These data are used to determine if a wireless device will generate electrical and magnetic fields large enough to interfere with a hearing aid.

The maximum field limits for the HAC standard M3 (articulation weighting factor decibels for GSM systems) are shown in Table 4.2. As can be seen, the standard field values are much stricter above 960 MHz. Thus, it is assumed that it is more difficult to fulfill the standard at the upper GSM frequencies [24].

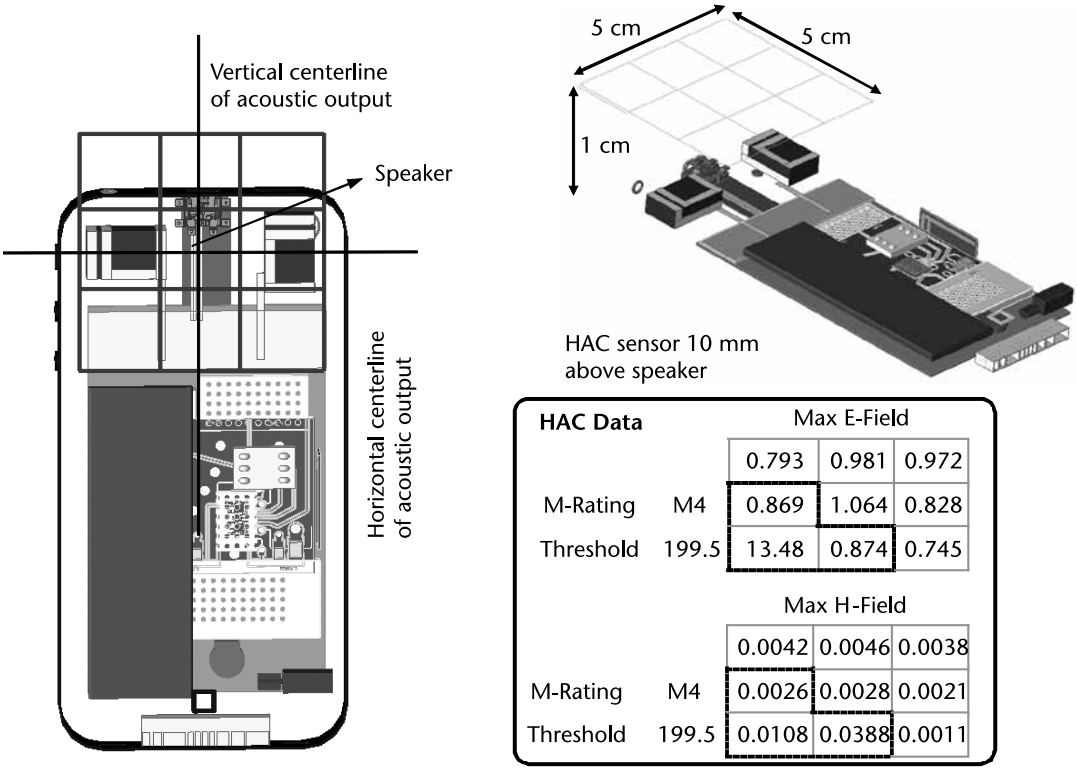

Figure 4.8 HAC sensor 10 mm above a speaker's 3 × 3 measurement grid. Simulated electric and magnetic fields of the phone on the HAC plane (peak values) with the allowed exclusions according to the HAC standard.

Table 4.2 Near-Field Limits of the HAC Standard

HAC Category M3 Limits (Articulation Weighting Factor (AWF) = −5 dB)	*Below 960 MHz*	*Above 960 MHz*
Maximum electric field	266.1 V/m	84.1 V/m
Maximum magnetic field	0.80 A/m	0.25 A/m

4.7 SAR

Mobile phones and other wireless devices emit RF. The radiation affects human health, and this has become one of the common areas of interest for both technical and medical researchers. Mobile phone users are exposed to significant amount of EM energy radiated from the transmitting antennas and directly or mutually coupled headsets, and it is seen that absorption of EM waves in the human head and other body parts causes adverse biological effects [25–28]. The phone radiation level is measured by the SAR, and it varies from device to device. To properly quantify the response of the biological structure, in terms of the incident and

induced field, of the energy absorbed and maintained inside the body, the SAR was introduced and defined.

The SAR is a measure of the rate of RF energy absorption by the body from the source being measured and it is defined as the power absorbed per mass of tissue and has units of watts per kilogram. The SAR is normally averaged either over a small sample volume or over the whole body (typically 10g or 1g of tissue). The SAR can be defined as the power absorbed in a mass of tissue as given in

$$SAR = \frac{\sigma |E_x|^2}{2\rho} + \frac{\sigma |E_y|^2}{2\rho} + \frac{\sigma |E_z|^2}{2\rho} \tag{4.3}$$

where σ = electrical conductivity, $|E_{xyz}|$ = magnitude of the electric field (V/m), and ρ = material density (kg/m^3).

Many factors can influence the SAR in a biological structure irradiated by electromagnetic energy. Among these, tissue geometry, dielectric properties, and the orientation of the body relative to the source play a vital role. The internal field and, through it, the SAR distribution are nonuniform because the RF energy induced in the body is scattered and absorbed at various interfaces. The peak spatial averages of the SAR values associated with the use of wireless handsets are mainly functions of geometry and depend on the square of the magnitude of the RF current density distribution inside the device and to the geometric position of the device relative to the head. European regulators require a 10-g cube localized peak SAR < 2 W/kg and U.S. FCC regulations require a 1-g cube localized peak SAR < 1 W/kg [24–27].

4.7.1 SAR Testing

SAR testing uses standardized models of the human head and body that are filled with liquids that simulate the RF absorption characteristics of different human tissues as displayed in Figure 4.9. Each cell phone is tested while operating at its highest power level in all the operating frequency bands and in various specific positions against the dummy head and body to determine compliance. This is the way that different users typically hold a cell phone, including to each side of the head.

In the SAR compliance test, the phone is precisely placed in various common positions next to the head and body. A robotic probe takes a series of measurements of the electric field at specific pinpointed locations in a very accurate, grid-like pattern within the dummy head and torso as shown in Figure 4.10. Only the highest SAR values for each frequency band are included in the final authorization to demonstrate compliance with the FCC's RF guidelines.

SAR is measured in three ways:

- Whole body average, which is the total amount of energy dissipated in the human body, expressed as an average of the total mass of the human body;
- A 10-g cube localized peak, which is the highest level of energy dissipation in any 10-g cube of tissue in the human body;

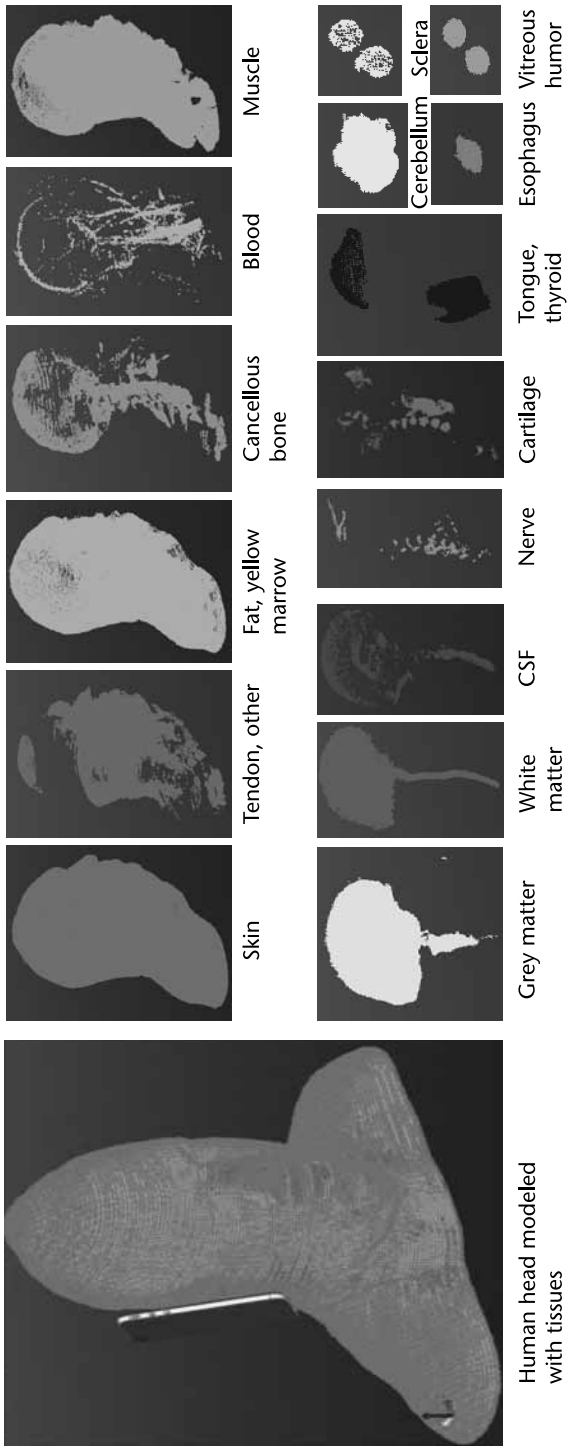

Figure 4.9 Smartphone with a human head modeled with tissues.

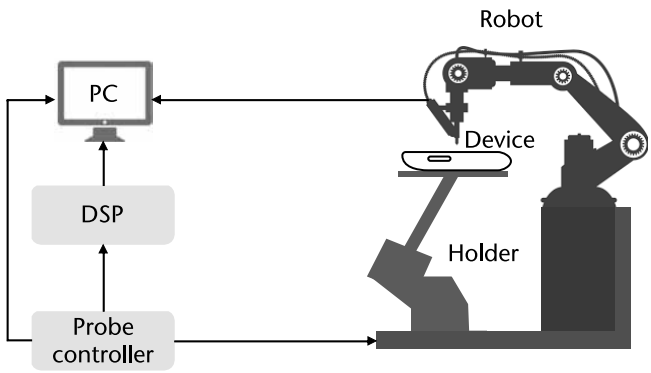

Figure 4.10 Mobile phone SAR measurement setup.

- A 1-g cube localized peak, which is the highest level of energy dissipation in any 1-g cube of tissue in the human body.

The SAR analysis and simulation flow, along with the SAM head and hand model and different antenna systems placed in a cell phone, is shown in Figure 4.10. There are various companies providing standardized models for SAR testing. For simulation, one of the most commonly used numerical models is FDTD based in the time domain because the FDTD solver can handle large simulation space and tissue material properly. The FEM or MoM can also be utilized to calculate SAR by solving Maxwell's equations in a heterogeneous electrical model of human body parts.

4.7.2 SAR Measurement

The field images of SAR values may be saved for any plane containing lossy tissue. The SAR may be adjusted for any desired input power and the peak SAR value and location are computed. The whole-body average SAR, that is, the SAR of each cell divided by the number of cells, is computed. The maximum calculated SAR value for a 10-g cube of tissue in the human body and a 1-g cube is given in Table 4.3 for the mobile phone and antenna system. Simulated peak 10-g and 1-g SAR values are compared with the corresponding measured values for two typical commercial mobile phones working at the GSM 900 band. A shown in Figure 4.11, the mobile phone is placed touching the head model.

Variations of peak 10-g and 1-g SARs with the distance measured along the Y-axis (ZX-plane) in the mid-coronal plane at 930 MHz were obtained the using

Table 4.3 Maximum Calculated SAR Value for 10g and 1g

Frequency	*Maximum SAR Value (10g)*	*Maximum SAR Value (1g)*
900 MHz	4.702e-6 W/kg	7.181e-6 W/kg
1,800 MHz	1.668e-4 W/kg	2.422e-4 W/kg
2,400 MHz	1.332e-3 W/kg	2.054e-3 W/kg

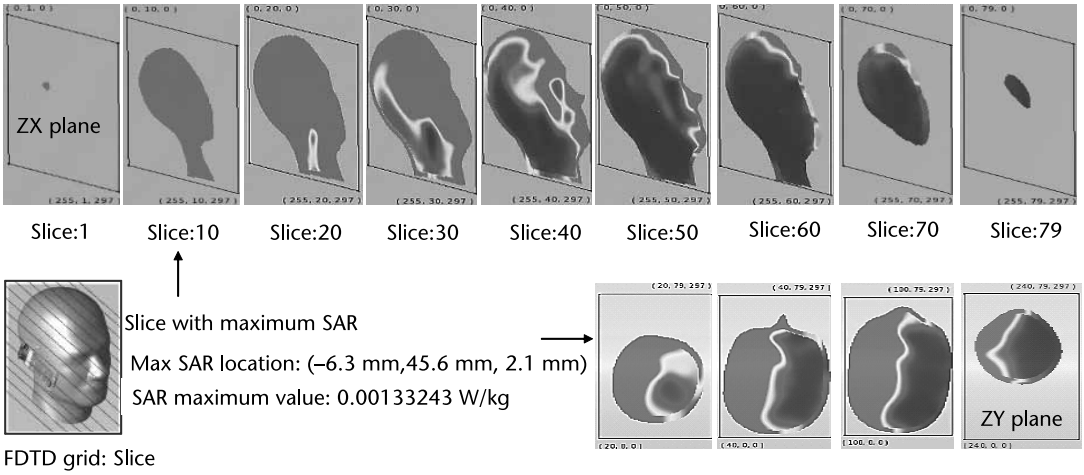

Figure 4.11 Variations of peak 10-g and 1-g SARs with distance.

FDTD solver. The stem plots of peak gram averaged SAR versus distance contain many hotspots. The density of the hotspots decreases with the increase of the SAR value and vice versa. The maximum SAR value is found corresponding to each maximum peak 10-g and 1-g SAR as shown in Figure 4.11.

4.8 EMI and EMC in Mobile Phones

The EMI and EMC are often used when referring to regulatory testing of electronic devices. As the density of wireless devices continues to increase, the concern about EM radiation and its effects from sources producing EMI also increases. The EMI and EMC can be defined as:

- *EMI:* EM emissions from a system or device that interferes with the normal operation of another device or system.
- *EMC:* The ability of equipment or system to function satisfactorily in its EM environment without introducing an intolerable EM disturbance to anything in that environment.

The EMC problem is between a source (an emission culprit) and a victim (susceptible device), which are coupled through a means, either conducted through wires or radiation through space or as shown in Figure 4.12. These electrical influences can be generated by either radiated or conductive EMI sources. Radiated sources include anything electromechanical or electrical, including power lines, antennas, traces on a PCB, motors, and even the chips on the cell phone board. Conductive EMI is a form of electrical noise pollution on the power supply traces of cell phone and this can be caused by induced voltage spikes from other devices within a system.

As shown in Figure 4.12, the radiated emission is RF energy that reaches susceptible device via radiation while conducted emission is RF energy that reaches susceptible device via conductive connections. EMI is a worldwide concern and

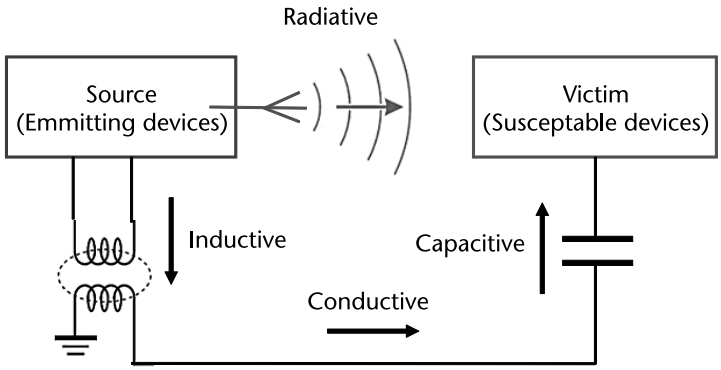

Figure 4.12 EMI coupling modes.

many governmental agencies and industry bodies have supplied specifications with which all electrical, electronic equipment and electromechanical systems must comply. These specifications are shaped to ensure that proper EMC techniques are followed by cell phone and other electronic device manufacturers during the design and fabrication of their products. Without following these specifications, even for simple appliances, the designer may be faced with unfamiliar standards governing radio interference and user safety.

EMC is becoming a critical issue within electronic components. It is needed to maintain the required level of EMC in mobile phones. With the increase of system frequencies, wireless applications and the demand for lower supply voltages, the cell phone becomes more vulnerable to the negative effects of EMI. When electronic equipment performs its designed functions without causing or suffering unacceptable degradation due to EM interference to or from other equipment, it is well designed and EM compatible. The minimization and control of EMC are out of necessity. Mobile phone manufacturers and compliance regulatory agencies are responsible to take care of EMC issue during design. Figure 4.13 shows all types of EMC tests.

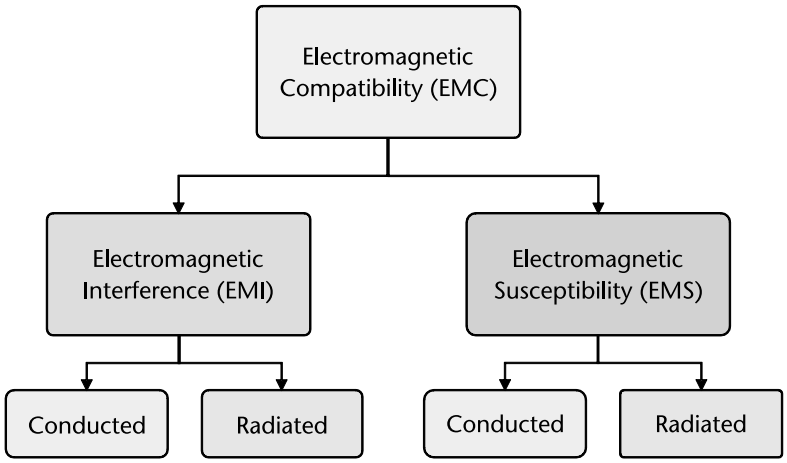

Figure 4.13 Types of EMC tests.

- *Radiated emissions test:* In radiated emission test, EM disturbances originating from an electronic device through radiation that may cause interference or malfunction to another electronic device in the same environment is measured. This is also known as EMI. Radiated emissions are propagated through the air directly from the source device to victim device. In EMC testing, radiated emissions measurements are carried out using a spectrum analyzer and or an EMI receiver and a suitable measuring antenna.
- *Conducted emissions test:* In a conducted emission test, EMI or disturbances that originate from source device and propagate along interconnected cables such as wired ports such as power conductors are measured. In this testing, conducted emissions measurements are made on an EMI receiver via an ISN (impedance stabilization network) located within the test chamber.
- *Radiated susceptibility test:* In this test, the ability of an electronic device to function normally in an EM radiation environment without experiencing interference or malfunction due to the radiation emissions emanating from another electronic device is measured. In radiated susceptibility testing, RF signal generators, amplifiers, and antennas are used to produce an EM field at varying frequencies.
- *Conducted susceptibility test:* In this testing, an EM field is generated by an RF signal generator and amplifier and then this EM field is coupled to the victim device thorough a power cable. Normally, conducted immunity testing is applicable to AC and DC ports and signal cables longer than 3m in length.

4.8.1 EMC Simulation Model

Normally, EMC testing is performed towards the end of the product development cycle that is one of the major risks to uncover an unexpected problem, forcing a design modification and a delay in the product release. EMC measurements carried out using certified test laboratories can be both time consuming and expensive that why many designers prefer to perform EMC simulation before the actual product of phones. As the design evolves, EMC aspects can be analyzed by comparing different component locations on the board or optimizing trace routing paths to minimize coupling.

EMC simulation using the FEM for mobile phone devices is performed to see the electric field level at different electronic components inside the phone [28–31] due to antennas being placed in the mobile phone. Figure 4.14 shows the E-field and H-field distribution on the smartphone board, when the Bluetooth antenna is operational at 2.4 GHz. EMC problems must be analyzed over a broad frequency range including all device components, connectors, antennas, cables, and housing. At some components, as shown in Figure 4.15, the electric field level is high, and if this value is beyond a maximum permissible limit to operate that component efficiently, then it is important to reduce the radiation level by applying different techniques such as placing a metallic shield or radiation absorbing tapes. This is important to also meet EMC compliance. Designing a shield enclosure is often a

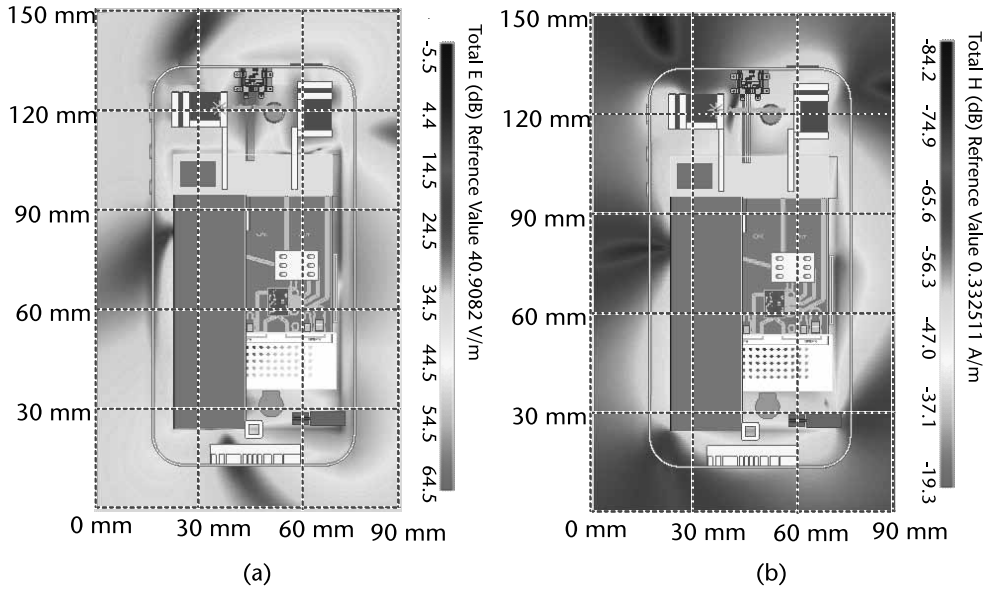

Figure 4.14 Bluetooth antenna radiation effect: (a) E-field and (b) H-field plot and values at different parts of a smartphone.

Components	Distance from antenna port	E-field value (dB)	H-field value (dB)
Speaker	49.3 mm	58.4	-38.2
Microphone	43.4 mm	43.5	-44.0
Camera	46.8 mm	31.2	-47.1
LCD	24.2 mm	34.7	-55.7
PA Chip	19.3 mm	28.9	-54.1
USB	57.0 mm	53.4	-47.5
VCO	23.1 mm	42.3	-46.6

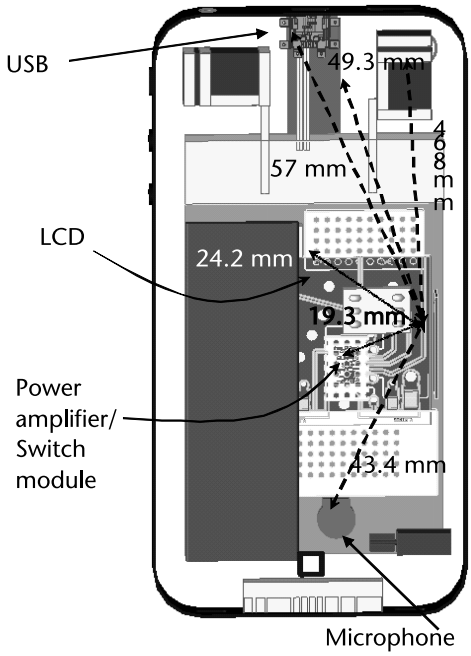

Figure 4.15 Electric field and magnetic field values at different electronic components inside a phone.

trade-off between suppressing radiation and still providing sufficient airflow for heat transportation and cooling of the electronic device.

The electric field value reduces significantly after putting a metallic shield enclosure over a power amplifier (PA) and switch module. The simulated shielding

effectiveness for a PA from 200 MHz to 10 GHz is shown in Figure 4.16. A perfectly conducting enclosure that surrounds the component prevents external radiation within that volume from electrically coupling to anything outside that volume. This type of enclosure is also called a Faraday cage.

4.8.2 EMI Simulation Model

To overcome the EMI issue, the designer must either remove the source of the interference or protect the circuit from being affected (EMC) as discussed in the previous section. EMC at the device or system level may have to comply with certain emission standards, so that the device does not affect other equipment or appliances. To meet these, the designer should think about EMI suppression starting from the board level [32]. Smartphone electronics has a strong integration of features such as high-speed digital links (such as double data rate (DDR), high-definition multimedia interface (HDMI), and USB3.1) and sensitive wireless functions (such as Wi-Fi 802.11 and Bluetooth). These digital interfaces are potential EMI aggressors. If an antenna is placed quite close to any potential EMI aggressors, Wi-Fi sensitivity can be affected and RF throughput can be significantly degraded.

Radiated EM coupling analysis is performed to investigate the EMI coupling on a component using near field EM data and then overlay this data with FCC and CISPR (International Special Committee on Radio Interference) standards for compliance measurement. In the United States, digital device regulations were established under FCC Part 15 Subpart J in 1979, internationally by the IEC standard CISPR 22 in 1985, and in the European Union under the EMC Directive in 1989 [33, 34]. The FCC has different sets of regulations for different types of digital devices. Devices that are marketed for use in commercial, industrial, or business environments are classified as Class A digital devices. Devices that are marketed for use in residential environments, notwithstanding their use in commercial, industrial, or

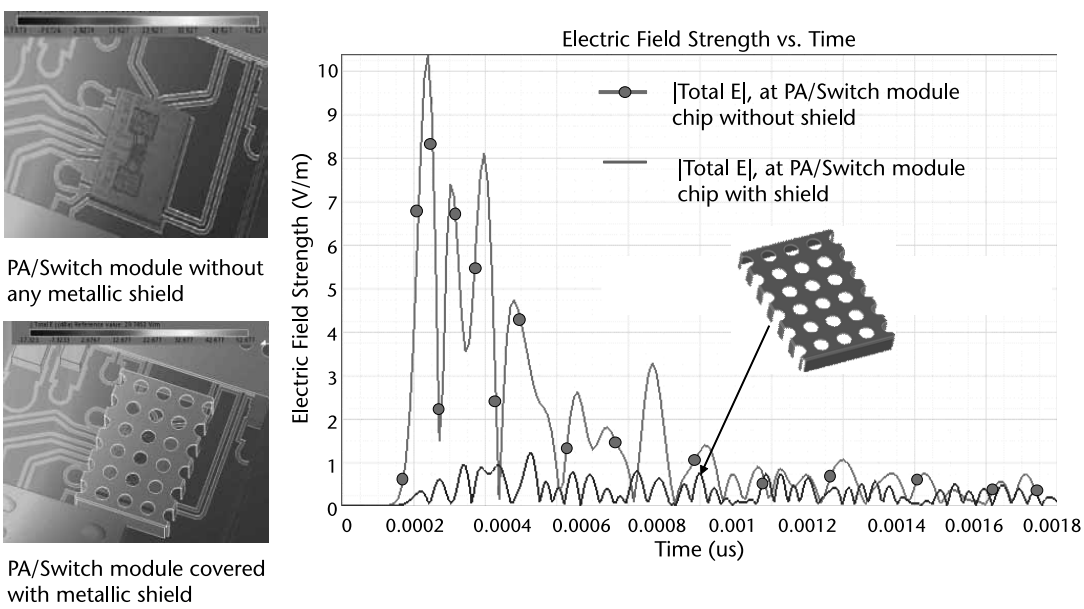

Figure 4.16 Electric field at power amplifier module with and without a shield.

business environments are classified as Class B digital devices. Radiation emission measurements at 1m, 3m and 10m are shown in Figure 4.17.

The method for measuring radiated emissions varies depending on the type of device being measured. Class A digital devices must be measured at 10m from the product and Class B devices are to be measured at 3m from the product. CISPR 22 regulations have been also adopted by several countries. CISPR 22 regulations require that radiated emissions measurements for Class A devices be measured at 30m and Class B devices be measured at 10m. Radiated emission from the Bluetooth antenna is measured at 3m and 10m as shown in Figure 4.18 using both antenna near-field and far-field approaches. Simulated data is compared with FCC

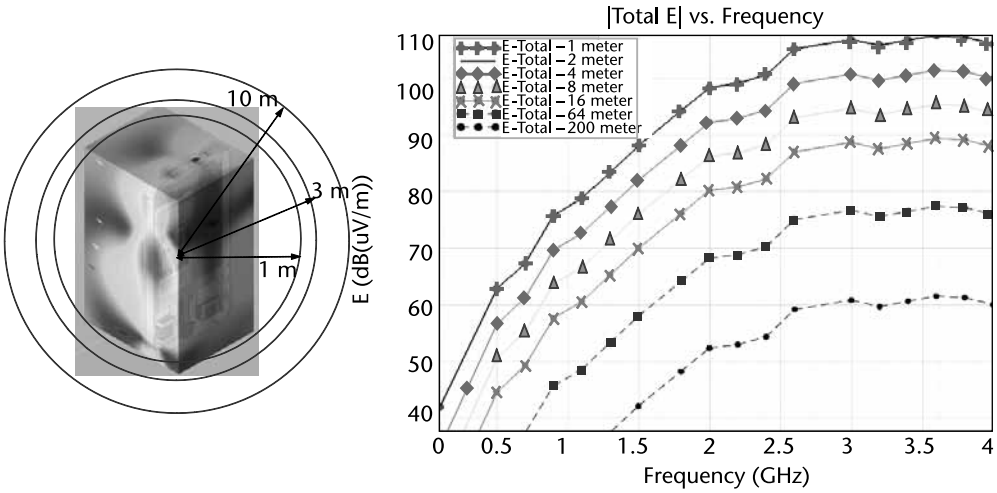

Figure 4.17 Radiation emission measurements at 1m, 3m, and 10m.

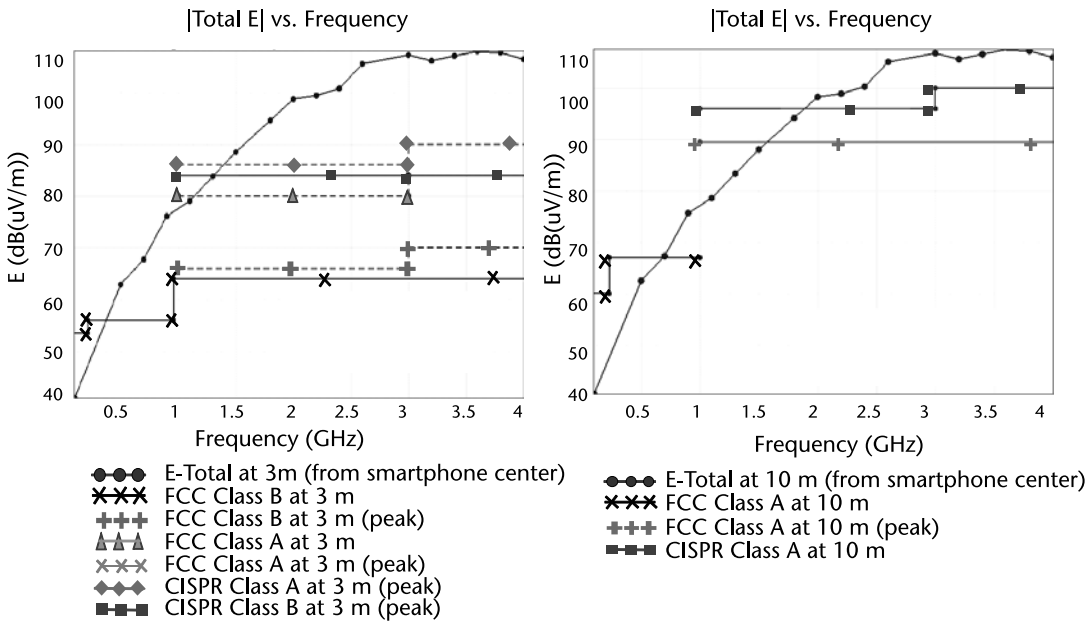

Figure 4.18 EMI limits: FCC and CISPR class A & B at 3m and 10m.

and CISPRR values. If these values are not as per compliance, then the EMI reduction technique is applied before the production of mobile devices.

4.9 Summary

In this chapter, compliance parameters and its measurement for mobile phone antennas were discussed. A product cannot be sold unless it is known to meet those requirements specified in the standards. Compliance is appreciated when a product passes a series of tests without occurring some specified mode of failure. For mobile phones, various compliances such as HAC, SAR, and EMC/EMI were discussed in detail. Antenna diversity and MIMO systems were discussed to mitigate the signal fading effect.

References

[1] Electromagnetic Compatibility (EMC)—Part 4-3: Testing and Measurement Techniques—Radiated, Radio-Frequency, Electromagnetic Field Immunity Test, *IEC Standard 61000–4-3*, Ed. 3.0, 2006.

[2] Kitchen, R., *RF and Microwave Radiation Safety Handbook*, 2nd ed., New York: Elsevier, 2001.

[3] Maeda, A., and K. Ohizumi, "A Study into the Effect of Smartphone Development on Antenna Design," *2013 IEEE Symposium on Product Compliance Engineering (ISPCE)*, Austin, TX, 2013, pp. 1–6.

[4] Durney, C. H., H. Massoudi, and M. F. Iskander, *Radiofrequency Radiation Dosimetry Handbook*, Brooks Air Force Base, Aerospace Medical Division (AFSC), 1986.

[5] Lee, A. K., et al., "Numerical Implementation of Representative Mobile Phone Models for Epidemiological Studies," *Journal of Electromagnetic Engineering and Science*, Vol. 16, No. 2, 2016, pp. 87–99.

[6] Balzano, Q., O. Garay, and T. Manning, "Electromagnetic Energy Exposure of the Users of Portable Cellular Telephones," *IEEE Transactions on Vehicular Technology*, Vol. 44, May 1995, pp. 390–403.

[7] Cicchetti, R., and A. Faraone, "Estimation of the Peak Power Density in the Vicinity of Cellular and Radio Base Station Antennas," *IEEE Transactions on Electromagnetic Compatibility*, Vol. 46, No. 2, May 2004, pp. 275–290.

[8] Tesche, F. M., M. V. Ianoz, and T. Karlsson, *EMC Analysis Methods and Computational Models*, New York: Wiley, 1997.

[9] Gosselin, M. C., et al., "Dependence of the Occupational Exposure to Mobile Phone Base Stations on the Properties of the Antenna and the Human Body," *IEEE Transactions on Electromagnetic Compatibility*, Vol. 51, No. 2, May 2009, pp. 227–235.

[10] Methods for the Assessment of Electric, Magnetic and Electromagnetic Fields Associated with Human Exposure, *IEC, Int. Electrotechnical Commission Stand*. 62209-1, 2005.

[11] Meyer, F. J. C., K. D. Palmer, and U. Jakobus, "Investigation into the Accuracy, Efficiency and Applicability of the Method of Moments as Numerical Dosimetry Tool for the Head and Hand of a Mobile," *Applied Computational Electromagnetics Society*, University of Mississippi, 2001.

[12] Björnson, E., E. G. Larsson, and M. Debbah, "Massive MIMO for Maximal Spectral Efficiency: How Many Users and Pilots Should Be Allocated?" *IEEE Transactions on Wireless Communications*, Vol. 15, No. 2, February 2016, pp. 1293–1308.

[13] Zheng, L., and D. N. C. Tse, "Diversity and Multiplexing: A Fundamental Tradeoff in Multiple-Antenna Channels," *IEEE Transactions on Information Theory*, Vol. 49, No. 5, May 2003, pp. 1073–1096.

[14] Yang, P., et al., "Transmit Antenna Selection for Multiple-Input Multiple-Output Spatial Modulation Systems," *IEEE Transactions on Communications*, Vol. 64, No. 5, May 2016, pp. 2035–2048.

[15] Larsson, E. G., et al., "Massive MIMO for Next Generation Wireless Systems," *IEEE Communications Magazine*, Vol. 52, No. 2, February 2014, pp. 186–195.

[16] Paulraj, A. J., et al., "An Overview of MIMO Communications: A Key to Gigabit Wireless," *Proc. IEEE*, Vol. 92, No. 2, February 2004, pp. 198–218.

[17] Kong, L. K., et al., "Near-Capacity Cooperative Space-Time Coding Employing Irregular Design and Successive Relaying," *IEEE Transactions on Communications*, Vol. 58, No. 2, August 2010, pp. 2232–2241.

[18] Vaughan, R. G., and J. Bach Andersen, "Antenna Diversity in Mobile Communications," *IEEE Transactions on Vehicular Technology*, Vol. VT-36, November 1987.

[19] Schwartz, M., W. R. Bennett, and S. Stein, *Communication System and Techniques*, New York: McGraw-Hill, 1965.

[20] Kildal, P. S., and K. Rosengren, "Correlation and Capacity of MIMO Systems and Mutual Coupling, Radiation Efficiency and Diversity Gain of Their Antennas: Simulations and Measurements in Reverberation Chamber," *IEEE Communications Magazine*, Vol. 42, No. 12, December 2004, pp. 102–112.

[21] Rappaport, T. S., *Wireless Communications: Principles and Practice*, Boston, MA: Pearson Education, 2002.

[22] Blanch, S., J. Romeu, and I. Corbella, "Exact Representation of Antenna System Diversity Performance from Input Parameter Description," *Electronic Letters*, Vol. 39, No. 9, May 1, 2003, pp. 705–707.

[23] American National Standard for Method of Measurements of Compatibility Between Wireless Communication Devices and Hearing Aids, ANSI C63.19-2007, *Amer. Nat. Standards Inst.*, New York, 2007.

[24] Holopainen, J., et al., "Near-Field Control of Handset Antennas Based on Inverted-Top Wavetraps: Focus on Hearing-Aid Compatibility," *IEEE Antennas and Wireless Propagation Letters*, Vol. 8, 2009, pp. 592–595.

[25] Khan, O. M., et al., "Specific Absorption Ratio Evaluation of Penta Band Antenna for LTE/GSM Mobile Handset Applications," *2017 International Conference on Electrical and Computing Technologies and Applications (ICECTA)*, Ras Al Khaimah, 2017, pp. 1–3.

[26] Wang, M., et al., "Evaluation and Optimization of the Specific Absorption Rate for Multiantenna Systems," *IEEE Transactions on Electromagnetic Compatibility*, Vol. 53, No. 3, August 2011, pp. 628–637.

[27] Zhao, K., et al., "SAR Study of Different MIMO Antenna Designs for LTE Application in Smart Mobile Handsets," *IEEE Transactions on Antennas and Propagation*, Vol. 61, No. 6, June 2013, pp. 3270–3279.

[28] Carcamo, H. K., C. Lanyon Olivares, and C. Ahumada Vera, "Numerical Finite Difference Method of Electric Field Generated to Determine the SAR Generated in a Microstrip Antenna Type Applied to a WBAN," *IEEE Latin America Transactions*, Vol. 14, No. 6, June 2016, pp. 2921–2926.

[29] Hadjem, A., et al., "Analysis of Power Absorbed by Children's Head as a Result of New Usages of Mobile Phone," *IEEE Transactions on Electromagnetic Compatibility*, Vol. 52, No. 4, November 2010, pp. 812–819.

[30] Sim, D. -U., and S. -O. Park, "A Triple-Band Internal Antenna: Design and Performance in Presence of the Handset Case, Battery, and Human Head," *IEEE Transactions on Electromagnetic Compatibility*, Vol. 47, No. 3, August 2005, pp. 658–666.

[31] Arnaut, L. R., and C. S. Obiekezie, "Stochastic Analysis of Wideband Near-Field Emissions From Dipole Antennas and Integrated Circuits," *IEEE Transactions on Electromagnetic Compatibility*, Vol. 56, No. 1, February 2014, pp. 93–101.

[32] Triverio, P., et al., "Geometrically Parameterized Circuit Models of Printed Circuit Board Traces Inclusive of Antenna Coupling," *IEEE Transactions on Electromagnetic Compatibility*, Vol. 52, No. 2, May 2010, pp. 471–478.

[33] Braun, S., "A Novel Time-Domain EMI Measurement System for Measurement and Evaluation of Discontinuous Disturbance According to CISPR 14 and CISPR 16," *2011 IEEE International Symposium on Electromagnetic Compatibility*, Long Beach, CA, 2011, pp. 480–483.

[34] Heirman, D. N., "ANSI C63.4 and CISPR 22-Harmony at Last? EMC Test Standards," *IEEE 1997, EMC, Austin Style. IEEE 1997 International Symposium on Electromagnetic Compatibility. Symposium Record (Cat. No.97CH36113)*, Austin, TX, 1997, pp. 112–117.

Selected Bibliography

Hossain, M. I., M. R. I. Faruque, and M. T. Islam, "Original Research: Analysis on the Effect of the Distances an Inclination Angles Between Human Head and Mobile Phone on SAR," *Progress in Biophysics and Molecular Biology*, Vol. 119, November 1, 2015, pp. 103–110.

Kivekas, O., et al., "Bandwidth, SAR, and Efficiency of Internal Mobile Phone Antennas," *IEEE Transactions on Electromagnetic Compatibility*, Vol. 46, No. 1, February 2004, pp. 71–86.

Lee, A. K., et al., "SAR Comparison of SAM Phantom and Anatomical Head Models for a Typical Bar-Type Phone Model," *IEEE Transactions on Electromagnetic Compatibility*, Vol. 57, No. 5, October 1, 2015, pp. 1281–1284.

Okuyucu, S., et al., "A Numerical Parametric Study of SAR from a Dual-Band PIFA Based Antenna for Mobile Communication," *2017 10th International Conference on Electrical and Electronics Engineering (ELECO)*, Bursa, 2017, pp. 1004–1008.

Park, H. H., H. B. Park, and H. S. Lee, "A Simple Method of Estimating the Radiated Emission from a Cable Attached to a Mobile Device," *IEEE Transactions on Electromagnetic Compatibility*, Vol. 55, No. 2, April 2013, pp. 257–264.

Prado, G. V., and M. A. Y. Medina, "Design and Implementation of a Non-Ionizing Radiation Measuring System Evaluated with an Unmanned Aerial Vehicle," *2015 Asia-Pacific Conference on Computer Aided System Engineering*, Quito, 2015, pp. 52–57.

Rao, Q., S. Ali, and D. Wang, "A Multi-Band Antenna for Potential 700 MHz Handheld Device Applications," *IEEE Antennas and Propagation Society International Symposium,* Charleston, SC, 2009, pp. 1–4.

Triverio, P., et al., "Geometrically Parameterized Circuit Models of Printed Circuit Board Traces Inclusive of Antenna Coupling," *IEEE Transactions on Electromagnetic Compatibility*, Vol. 52, No. 2, May 2010, pp. 471–478.

Viswanath, P., D. N. C. Tse, and R. Laroia, "Opportunistic Beamforming Using Dumb Antennas," *IEEE Transactions on Information Theory*, Vol. 48, No. 6, June 2002, pp. 1277–1294.

CHAPTER 5

Reconfigurable Frequency and Polarization Diversity Antennas

5.1 Introduction

The antenna is the most critical part of wireless communication systems and must be designed and deployed efficiently so that it can effectively utilize the available frequency resources ensuring uninterrupted concurrent multiple services to the users. In this perspective, we have three antenna methodologies: individual antennas, multiband antennas, and frequency-reconfigurable antennas. The application of these three antenna approaches on a wireless platform has its own merits and demerits [1–3]. Increased antenna complexity, large space required to accommodate multiple wireless services at a time, and coupling due to little spacing between individual antennas are major design challenges. Due to comparatively more space requirements, both single and multiband antennas are not suitable for wireless handheld devices or MIMO applications. Multiband antennas possess comparatively wide bands causing difficulty in achieving the desired antenna miniaturization. They also exhibit poor isolation between different operating bands, for which the chances of jamming or unavailability of a wireless service are increased.

Antenna reconfigurability is the capacity to change an individual radiator's fundamental operating characteristics through electrical, mechanical, or other means. Thus, as per this definition, the traditional phasing of signals between elements in an array to achieve beam steering and beamforming does not make the antenna reconfigurable because the basic operating characteristics of an antenna remain unchanged in this case. Ideally, reconfigurable antennas should be able to alter their impedance bandwidths, operating frequencies, polarizations, and radiation patterns independently to accommodate changing operating requirements. Antenna reconfigurability in many circumstances provides numerous advantages. For example, the ability to tune the antenna's operating frequency could be utilized to change operating bands, filter out interfering signals, or tune the antenna to account for a new environment. If the radiation pattern of the antenna could be changed, it could be redirected toward the access point and use less power for transmission, resulting in significant savings in battery power. The ability of reconfigurability to antenna arrays provides additional degrees of freedom that may

result in wider instantaneous frequency bandwidths, more extensive scan volumes, and radiation patterns with control on sidelobe distributions.

5.2 Reconfigurable Antennas

The reconfiguration of an antenna is achieved by altering the radiated fields of the antenna's effective aperture [4–10]. It is based on a focused rearrangement of the antenna currents or a reconfiguration of the antenna's radiating edges. This redistribution of properties results in a change in the functionalities of the antenna. These functional changes allow users to propose reconfigurable antennas for various wireless communication platforms. There are four reconfiguration properties that a reconfigurable antenna can achieve. An antenna can exhibit a reconfigurable frequency of operation, a reconfigurable radiation pattern, a reconfigurable polarization behavior, or a combination of any of these properties [4]. Based on the reconfigurable antenna property, the reconfiguration technique is selected. An antenna designer selects a technique that satisfies the imposed constraints and at the same time completes the antenna design task efficiently.

There are various techniques to implement reconfigurable antennas, as indicated in Figure 5.1. These reconfiguration techniques are divided into four major categories: electrical, optical, mechanical, and material changes. Antennas based on electronic switching components to redirect their surface currents are called electrically reconfigurable. Antenna reconfiguration is achieved using electrical switches such as varactors, pin diodes, microelectromechanical systems or recently digital tunable capacitors [11]. An antenna that depends on on photoconductive switching elements is called an optically reconfigurable antenna. By altering the structure of the antenna, physically reconfigurable antennas can be achieved. Finally, reconfigurable antennas can be realized through the use of smart materials such as ferrites and liquid crystals. Phase change materials are also extensively used for a reconfigulable antenna [12, 13]. These have advantages over ferrite and liquid crystals as they have less losses, high reliability, and excellent linearity. Also, their biasing can

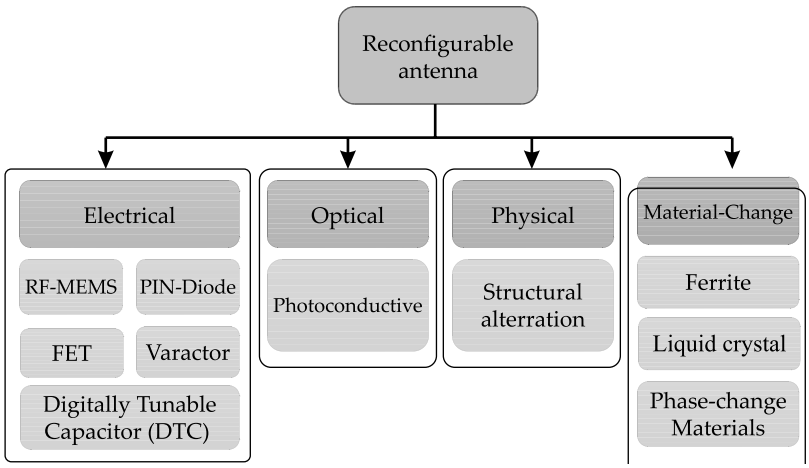

Figure 5.1 Various techniques to design reconfigurable antennas.

happen remotely so their biasing network does not affect the performance of the antenna, which is a big advantage compared to other methodologies.

In this chapter, electrical reconfiguration techniques based on the use of switches to connect and disconnect antenna parts are discussed. PIN diodes or varactors are a faster and more compact alternative to RF microelectromechanical systems (MEMS) [14–16]. RF-MEMS technology is commonly used in satellite and defense applications antenna systems and now poised to improve smartphone antenna performance in the near future by way of higher antenna efficiency [17]. MEMS-based applications need the charge pumps for high-voltage applications, which is one issue with this technology. MEMS require relatively high and variable bias voltages to be actuated [18], but recent RF-MEMS include the charge pumps on the MEMS chip and can work even with voltages as low as 3V. Reconfigurable antennas using PIN diodes [19] have a more dynamic reconfiguration ability.

5.2.1 Electrically Reconfigurable Antenna

The electrically reconfigulable antenna can be classified into four groups based on antenna reconfigurable property (e.g., frequency, radiation pattern, polarization, or combination of these):

1. Frequency-reconfigurable antennas;
2. Polarization reconfigurable antennas;
3. Radiation pattern reconfigurable antennas;
4. Hybrid reconfigurable antennas.

5.2.2 Frequency-Reconfigurable Antenna

Frequency-reconfigurable antennas have great potential to address most of the challenges coming in single and multiband antennas. They need comparatively less space to operate on multiple wireless standards with high out-of-band rejection. They are also more effective for space diversity and MIMO implementation. Cognitive radio will demand multiband reconfigurable front-end RF systems on mobile devices such as mobile phones, PDAs, and netbook computers. In this chapter, a dual-polarized frequency-reconfigurable antenna design and configuration are described for the wireless portable communication device. The antenna mathematical modeling and operating principle of the antenna is discussed. The effective length of the antenna, and hence its operating frequency, can be changed by adding or removing part of the antenna length through electronic, mechanical, or other means. There are different kinds of switching technologies. PIN diode and FET have used in frequency tunable monopole and dipole antennas for various frequency bands.

5.2.3 Polarization Reconfigurable Antenna

Antenna polarization reconfiguration can help to provide immunity to interfering signals in varying environments as well as provide an additional degree of freedom to improve link quality as a form of switched antenna diversity. The current flow direction on the antenna translates directly into the polarization of the electric field in the far field of the antenna. To achieve polarization reconfigurability, the antenna

structure and/or feed configuration should alter in ways that change the path of current flows on the antenna without significant changes in impedance or frequency characteristics. Polarization reconfigurations can take place between different kinds of linear polarizations, between right and left-handed circular polarizations, or between circular, linear, and elliptical polarizations. The mechanisms to achieve polarization reconfigurability are mainly the same as those described for frequency reconfigurability earlier, although their implementations are necessarily different. By inserting a switch (PIN diode or FET) into the antenna geometry and by controlling the current direction, different polarizations are achieved. Polarization reconfigurability is also accomplished by including switches in the feed excitation slots rather than the surface of the patch.

5.2.4 Pattern Reconfigurable Antenna

Reconfigurable antennas with its pattern selectivity can enhance system security, improving communication reliability and reducing energy loss to better the comprehensive performance of the whole system. One of the most effective and common methods to change radiation patterns independently from frequency behavior is the use of electrically tuned or switched parasitic elements. Parasitic element lengths are changed with FET or PIN diode switches or varactors, which, in turn, alter the magnitudes and phases of the currents on the parasitic elements relative to the driven element. Tilts in the main beam in one plane can then be switched or swept as the lengths of the parasitic elements are changed. These methods possess several attractive qualities: isolation of the driven element(s) from the tuned element(s) and a range of available topologies and functionalities. Fundamentally, tuning of antenna radiation patterns in this manner relies on the mutual coupling between closely spaced driven and parasitic elements, resulting in effective array behavior from a single feed point. Therefore, changes in radiation patterns are achieved through changes in the coupling between the elements, which, in turn, change the effective source currents on both the driven and parasitic elements.

5.2.5 Hybrid Reconfigurable Antenna

The ability of the antenna to reconfigure the selective operating frequency, bandwidth, radiation pattern and polarization characteristics are termed as a hybrid reconfigurable antenna. The fundamental theory of operation behind any hybrid reconfigurable antenna is the same as of an ordinary reconfigurable antenna, and design and control in this case are obviously more complex. The configuration of a hybrid reconfigurable antenna with frequency and polarization is shown in Figure 5.2.

5.2.6 Antenna Switching Techniques

The fundamental role of a switch or relay is to make or break an electric circuit. In static and quasi-static terminology, a switch operates simply as either a conduction path or a break in the conduction path. In RF antenna systems, switch function typically entails controlling and directing the flow of RF energy along a desired RF path. Usually, this path may include any of the RF subsystems leading to the

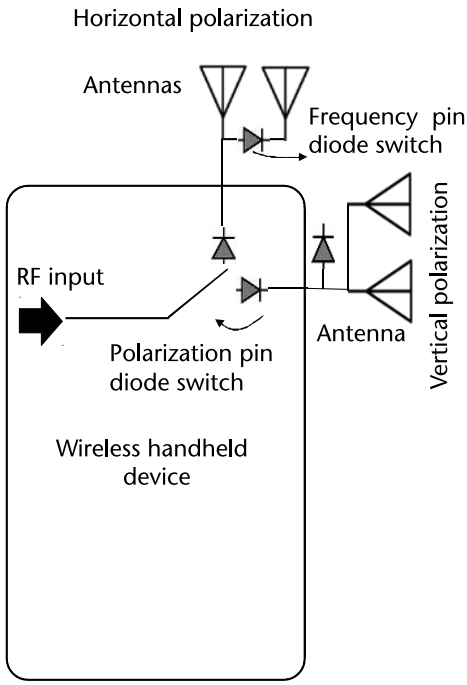

Figure 5.2 Design concept of a reconfigurable frequency and polarization antenna.

antenna feed distribution network. In reconfigurable antennas, switches are utilized to control the direction and flow of the RF current. There are several important characteristics that must be evaluated for all RF switch applications, particularly reconfigurable antenna designs. Like electrical switches, RF and microwave switches come in different configurations providing the flexibility to create complex matrices and automated test systems for many different applications. The following is a list of typical RF switch configurations and their usage:

1. Single-pole-double-throw (SPDT or 1:2) switches route signals from one input to two output paths. Using only a single-polar-double-throw (SPDT) switch, the polarization switching can be achieved.
2. Single-pole-multiple-throw (SPnT) switches allow a single input to multiple (three or more) output paths.
3. Double-pole-double-throw (DPDT) switches can be used to switch between two inputs and two outputs as a drop-out switch, for signal reversal, or to bypass a test component.

5.3 Reconfigurable Frequency and Polarization Antenna Design

Many multiband antennas have been designed to cover a wide bandwidth. However, most of them could not cover 800 MHz and 1,400 MHz with dual-polarization capability, because the antennas required significant space, as the electrical length of $\lambda_g/4$ at 800 MHz [20]. To make an antenna compact, a typical solution is to use

the coupled-feed technique [21, 22], which generates a dual resonance. In this technique, a coupled gap between the feeding line and the radiator element is essential; therefore, the ground clearance of the antenna should be increased. A couple of studies focused on a compact size [23, 24], with the designed antennas having sizes under 500 mm^2 with an efficiency around 40%. Nevertheless, they are not suitable for mobile devices because the obtained efficiency of the antennas is less than 50% in the lower band. Moreover, the antenna designed in [23] did not have a –6-dB reflection coefficient in the desired band. In [25], a printed monopole antenna with a C-shaped ground plane was introduced to improve the operating bandwidth. This antenna had a compact size of 350 mm^2, but it does not cover dual resonance and dual-polarization need. To reduce the antenna size and still cover two polarizations, novel techniques are required, such as the frequency and polarization reconfigurable technique. Until now, many reconfigurable antennas for mobile device applications have been studied. However, most of them could not cover 800 MHz and 1,400 MHz with dual-polarization capability [26–28]. The conclusion of the above discussion is that there is usually a critical trade-off between the antenna operating frequency band, antenna efficiency, antenna gain, and reduction in the antenna size.

In this design, a frequency-reconfigurable antenna with a compact size that occupies an area of 950 mm^2 is presented. Here, it is noteworthy that very few of the reported mobile antennas have a small ground clearance within 15 mm. Also, the efficiency is proportional to the size of the antenna. A small-sized antenna has a lower efficiency. Nevertheless, the efficiency of the designed antenna is more than 88% in all frequency bands. Consequently, this design has much better out-of-band rejection, radiation efficiency, reflection efficiency, and positive gain. The planar geometry of the antenna makes it suitable to find applications in thin-profile, handheld wireless devices. Two orthogonal printed PIFAs are designed [29]. As shown in Figure 5.3, two PIN diodes are used to switch between horizontal and vertical

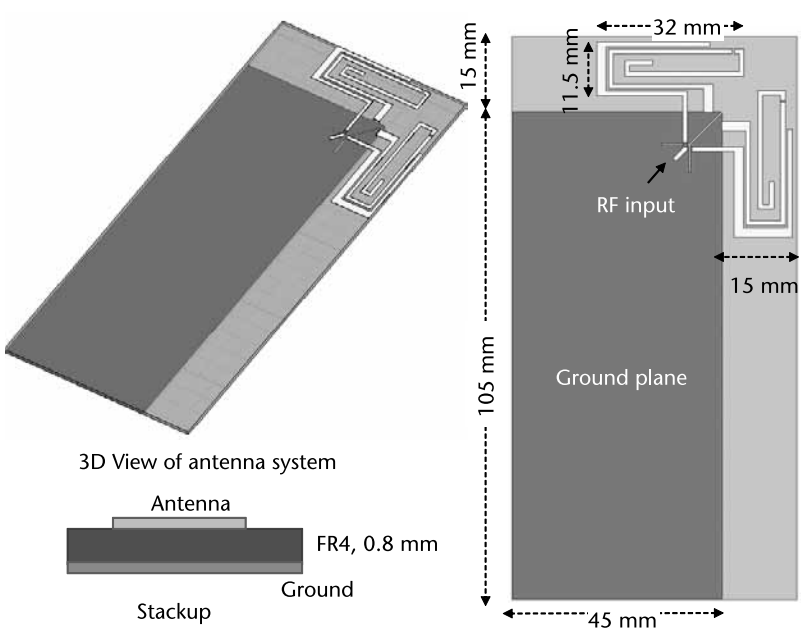

Figure 5.3 Designed antenna geometry and substrate stack-up.

polarization to select the desired polarization. Another two PIN diodes used in antenna branches are used to tune the antenna at 800 MHz and 1.4 GHz.

Figure 5.4 shows the geometry of the designed L-shaped PIFA. Planar antenna is printed over a commercially available FR-4 dielectric substrate with a permittivity of 4.4 and a thickness of 0.8 mm. The antenna has a compact design and the size of the designed structure is $32 \times 14 \times 2$ (unit) mm^2. It should be noted that this antenna differs in some important ways from a conventional PIFA. In a conventional PIFA, the short is directly connected to the feeding element; in this antenna, instead of putting the short at the feeding strip, it is placed at the end of an electromagnetically coupled strip that is parallel to the feed strip. The designed antenna mainly consists of radiating elements and four PIN diodes (part number: BAP64-03). Reconfigurability is achieved by varying the length of the parasitic shorted strip using a PIN diode with simple bias circuitry. On the back side of the main board, a ground plane of 105×60 mm^2 is printed to serve as system ground of the mobile phone. Both elements of the designed antenna are fabricated near the substrate boundary to achieve a compact structure. Antenna design dimensions are shown in Figure 5.4. Two PIN

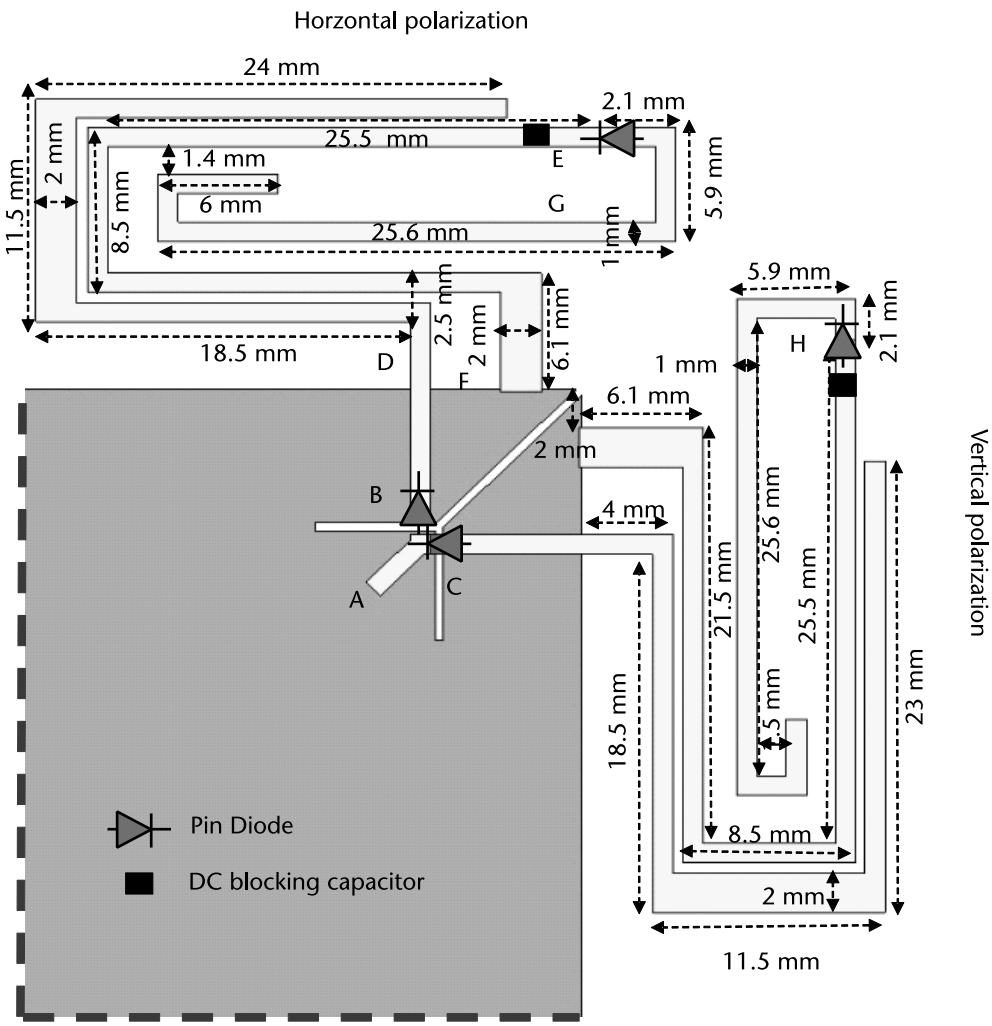

Figure 5.4 Antenna (top view) design dimensions.

diodes are placed at E and H to control resonance frequency, and another two PIN diodes are placed at B and C to control antenna polarization, The PIN diodes operate at +5V, and their consumption currents are 3 mA. The insertion loss is less than 0.5 dB in the operating band. Two RF chokes are used to improve the electrical isolation between the antenna and the bias line.

A DC block capacitor is embedded into the coupling strip to block DC in the antenna. The structure is composed of two independent elements. The driven feeding element is a monopole fed by a 50Ω microstrip line. The overall length (58 mm) of this monopole is equal to about a quarter-wavelength at 1.4 GHz. An additional resonance is created using an electromagnetically coupled strip (93 mm) using a shorted parasitic element. This shorted parasitic element is connected to the ground plane through a planar inverted via. The feeding strip is connected to a 50Ω microstrip line arranged on the front side of the main board. The shorted strip is connected to the system ground plane through a via-hole in the main board. There is a coupling gap of 0.5 mm between the feeding strip and the shorted strip. The shorted strip acts as a second radiator and generates its own resonance modes. The feeding strip has a length of about 93 mm (close to a quarter-wavelength at 800 MHz), thus generating the lowest resonant mode at about 800 MHz with reflection coefficient greater than −10 dB. The antenna operating mode and PIN diodes functions are listed in Table 5.1.

5.3.1 Antenna Mathematical Modeling

A PIFA and its supporting PCB are shown diagrammatically in Figure 5.5. This configuration can be decomposed into radiating and balanced modes as previously shown in [30]. The input impedance is given by:

$$Z_1 = \frac{(1+\alpha)^2 Z_R (Z_L + Z_B) + \alpha^2 Z_L Z_B}{(1+\alpha)^2 (Z_L + Z_R) + Z_B} \tag{5.1}$$

where Z_L is the load impedance applied to the unfed side of the strip, Z_R is the radiating mode impedance, and Z_B is the impedance of the short-circuit transmission line formed by the strip, derived from the balanced mode. The current sharing factor, α, is given by

$$\alpha = \frac{I_{R2}}{I_{R1}} \tag{5.2}$$

Table 5.1 Antenna Operating Modes and PIN Diode Function

Antenna Mode	*Polarization*	*Resonant Frequency*	*PIN Diodes*			
			B	*C*	*E*	*H*
1	Horizontal	1.4 GHz	ON	OFF	OFF	OFF
2	Horizontal	800 MHz	ON	OFF	ON	ON
3	Vertical	1.4 GHz	OFF	ON	OFF	OFF
4	Vertical	800 MHz	OFF	ON	ON	ON

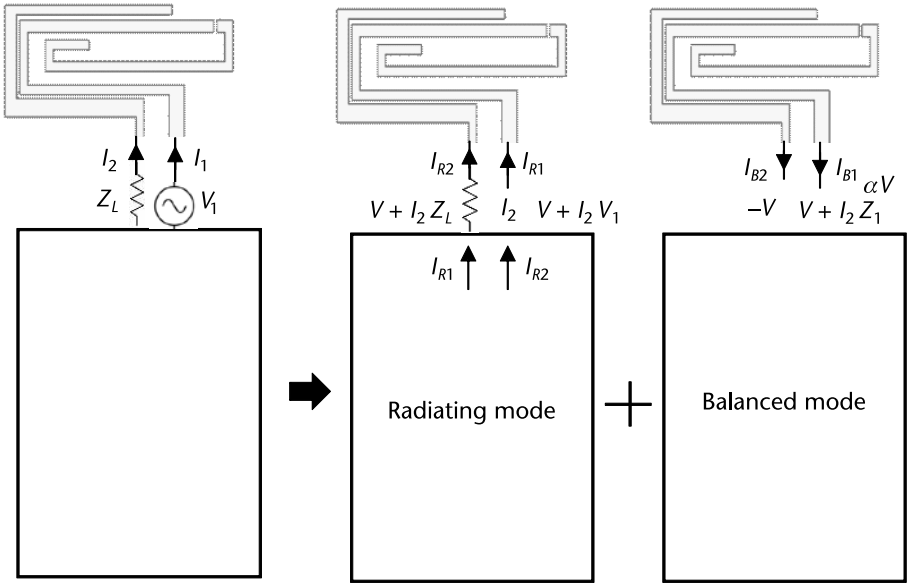

Figure 5.5 Antenna radiating and balanced mode operations.

I_{R1} and I_{R2} are the radiating mode currents at the feed and load, respectively. For the case of $Z_L = 0$, this equation simplifies to

$$Z_1 = \frac{(1+\alpha)^2 Z_R Z_B}{(1+\alpha)^2 (Z_R) + Z_B} \tag{5.3}$$

This is like the well-known expression for a folded dipole—the radiating mode is impedance transformed by a factor $(1 + \alpha)^2$ and adds in parallel with the balanced mode.

The equivalent circuit is illustrated in Figure 5.6. It should be noted that the impedance transformation in this mode is high, since I_{R2} is greater than I_{R1} due to the position of the slot. This tends to produce an impedance that is too high. It is also worthy of note that the bandwidth can be enhanced if Z_B and Z_R are resonant at the same frequency (when it becomes a double-tuning circuit). Also of interest is the open circuit case. Setting $Z_L = \infty$ gives

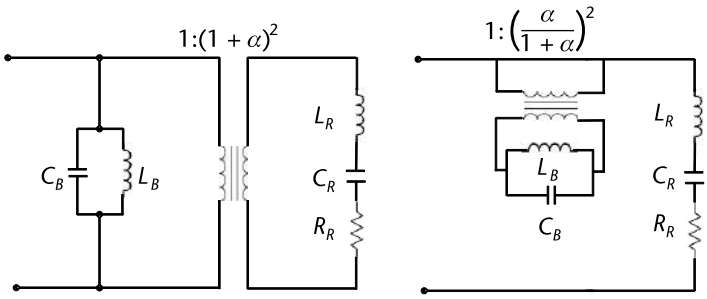

Figure 5.6 Equivalent circuit with a short-circuit load and open-circuit load.

$$Z_1 = Z_R + \left(\frac{\alpha}{1+\alpha}\right)^2 Z_B \tag{5.4}$$

The balanced mode impedance is transformed by a factor $(\alpha/(1+\alpha))^2$ and adds in series with the radiating mode. The balanced mode causes the antenna to resonate twice at lower and higher frequencies than determined by the radiating mode (controlled by L_R and C_R). The low-frequency and high-frequency resonances occur when the radiating mode capacitance and inductance are cancelled by the inductance and capacitance of the transformed balanced mode, respectively. There is no impedance transformation with an open circuit load, which tends to produce an impedance that is too low. With a reactive load, the antenna can be tuned over a wide range of impedances: from below the first resonance up to the second resonance of the open circuit mode. $Z_B = -j\Omega L_B/(1 - \Omega L_B C_B)$ and $Z_R = R_R + j\Omega L_R + (1/j\Omega C_R)$. The equivalent antenna circuit is validated using circuit simulation as shown in Figure 5.7 for 1.4 GHz.

Values used in the subsequent detailed design are $\propto = 1$, $R_R = 8.8$, $L_R = 4.6$ nH, $C_R = 1.9$ pF, $L_B = 2.3$ nH, and $C_B = 0.46$ pF. Using these values, the S-parameter for open-circuit and short-circuit loads is shown in Figure 5.7. With inductive loading, any frequency between the first resonance of the open circuit mode and the resonance of the short-circuit mode can be achieved. Capacitive tuning allows frequencies between the resonance of the short-circuit mode and the second resonance of the open-circuit mode to be covered. From the equivalent circuits with open-circuit and short-circuit loads, the open-circuit mode exhibits resonance at a lower resistance than the short-circuit mode.

For switching application, BAP64-03 PIN diode is sued in this antenna design. Equivalent circuit model of the diode in ON and OFF modes are shown in Figure 5.8. The PIN diode BAP64-03 is commonly used as the frequency-reconfigurable

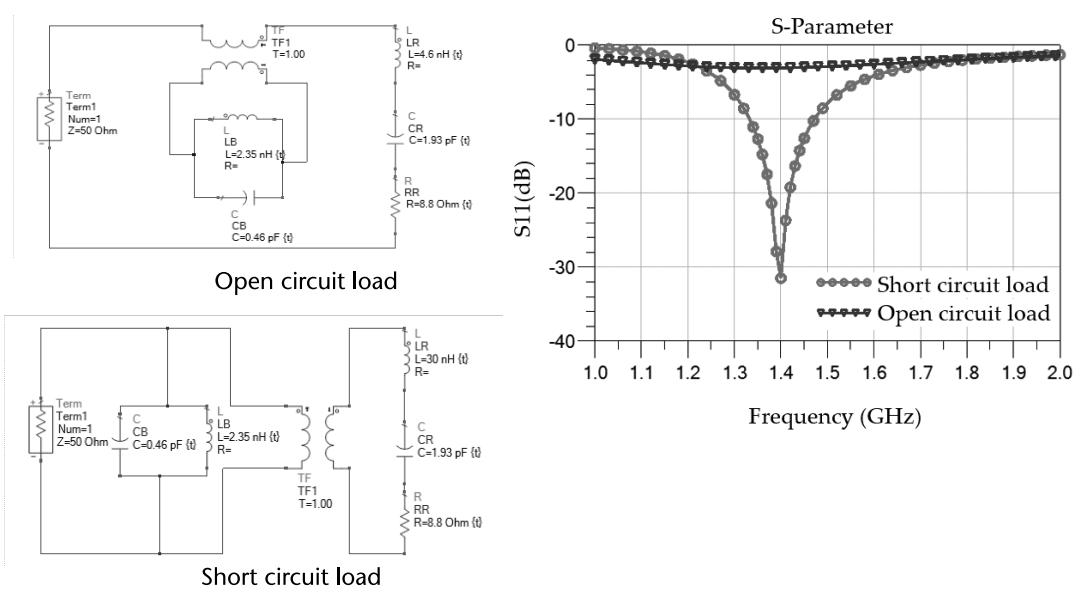

Figure 5.7 Simulation model in ADS schematic with short-circuit and open-circuit loads and simulated S-parameters.

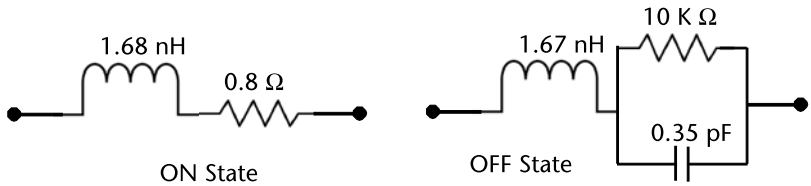

Figure 5.8 Equivalent circuit of BAP64-03 PIN diode ON state and OFF state.

antenna design. The circuit of the PIN diode switch in ON state is equivalent to a lumped element with 0.8Ω resistor series with the 1.68-nH inductor. The equivalent circuit of the PIN diode switch in the OFF state may be considered as a 1.67-nH series with a parallel circuit of 10 KΩ and 0.35 pF. A 100-pF DC block was connected to DC blocking in the antenna. When the diode is in the OFF state, the current will flow along the smaller strip. That means the resonant frequency will be at a higher frequency. When the diode is in the ON state, the major current will flow along the larger strip and then the major resonant frequency will be lower frequency. By changing the path of the current flow, the different resonant frequency can be achieved.

5.3.2 Antenna Operating Principle and Results

The horizontal antenna first resonant frequency is at 1,400 MHz, which can cover the LTE1400 bands. This resonant frequency is formed by section A-B-D-E as shown in Figure 5.4, by turning PIN diode placed at E OFF. The second resonant frequency at 800 MHz is formed by section A-D-E-F-G. To understand the operating principle of the antenna, Figure 5.9 shows the simulated reflection coefficient for different configurations of the designed antenna. As is clear from S_{11} results, the first resonant mode is centered at about 1,400 MHz. By adding an electromagnetically coupled shorted strip to the feeding strip (the designed antenna in the ON state), the antenna resonant mode shifts at about 800 MHz.

The PIN diodes are placed inside the inner strip. If the PIN diode switch is OFF, the geometrical of electrical path is small-tuned to 1,400 MHz. By changing the voltage on the PIN diode switch, it will be ON, and the electrical path of the inner strip becomes large-tuned to 800 MHz. To control the PIN diode, switch ON and OFF, a Vcc DC bias of +5V is applied through the inner strip. To have an impedance match to the desired band and reduce the RF signal to the DC source, a DC block capacitance of 100 pF is connected. The designed antenna is optimized using the FEM for the best return loss performance both for horizontal and vertical polarizations. By combining two working states of all four PIN diodes, the antenna is successfully tuned over 800 MHz and 1,400 MHz for horizontal and vertical polarization.

For horizontal polarization, the obtained simulated bands are 760–850 MHz and 1,380–1,470 MHz with a reflection coefficient better than –10 dB, covering 800 MHz and 1,400-MHz bands. For vertical polarization, the achieved bands are 760–810 MHz and 1,310–1,470 MHz, with a reflection coefficient better than –10 dB. It is always a good practice to allow the bandwidth of the antenna to operate below the –10-dB return-loss threshold. In the designed design, most of the bands are covered with a –10-dB reflection coefficient.

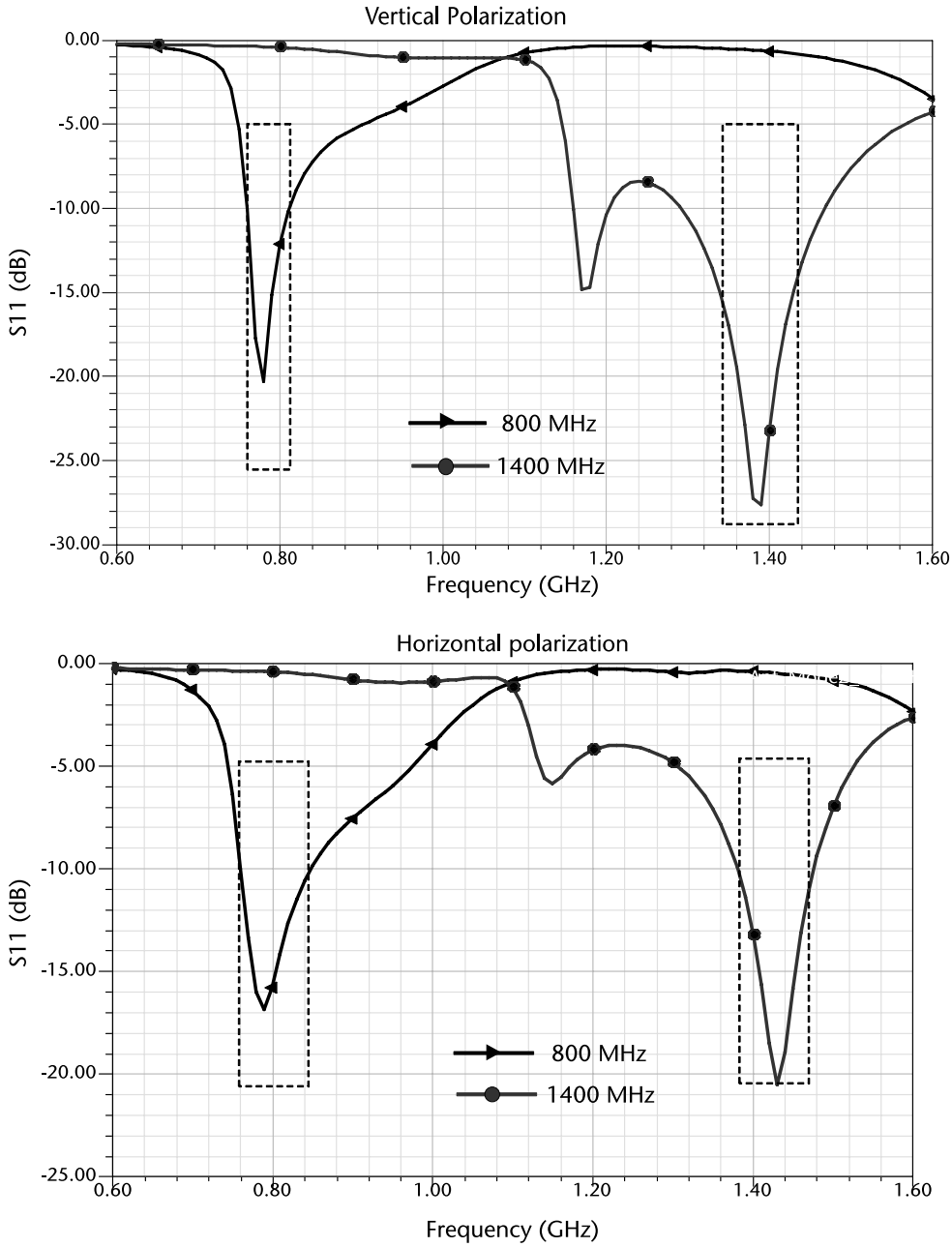

Figure 5.9 Antenna return loss plots for vertical and horizontal polarization.

Antenna 3-D simulated radiation patterns are at frequencies 800 MHz and 1,400 MHz for horizontal and vertical polarizations and are shown in Figure 5.10. Radiation patterns are nearly omnidirectionally suitable for mobile phone communication. As current nulls increase at higher frequencies, the radiation patterns show some distortions.

Table 5.2 listed simulated gain, radiation efficiency, and antenna bandwidth data. The antenna simulated gain varies from 3.7 dBi to 2.13 dBi, and the simulated

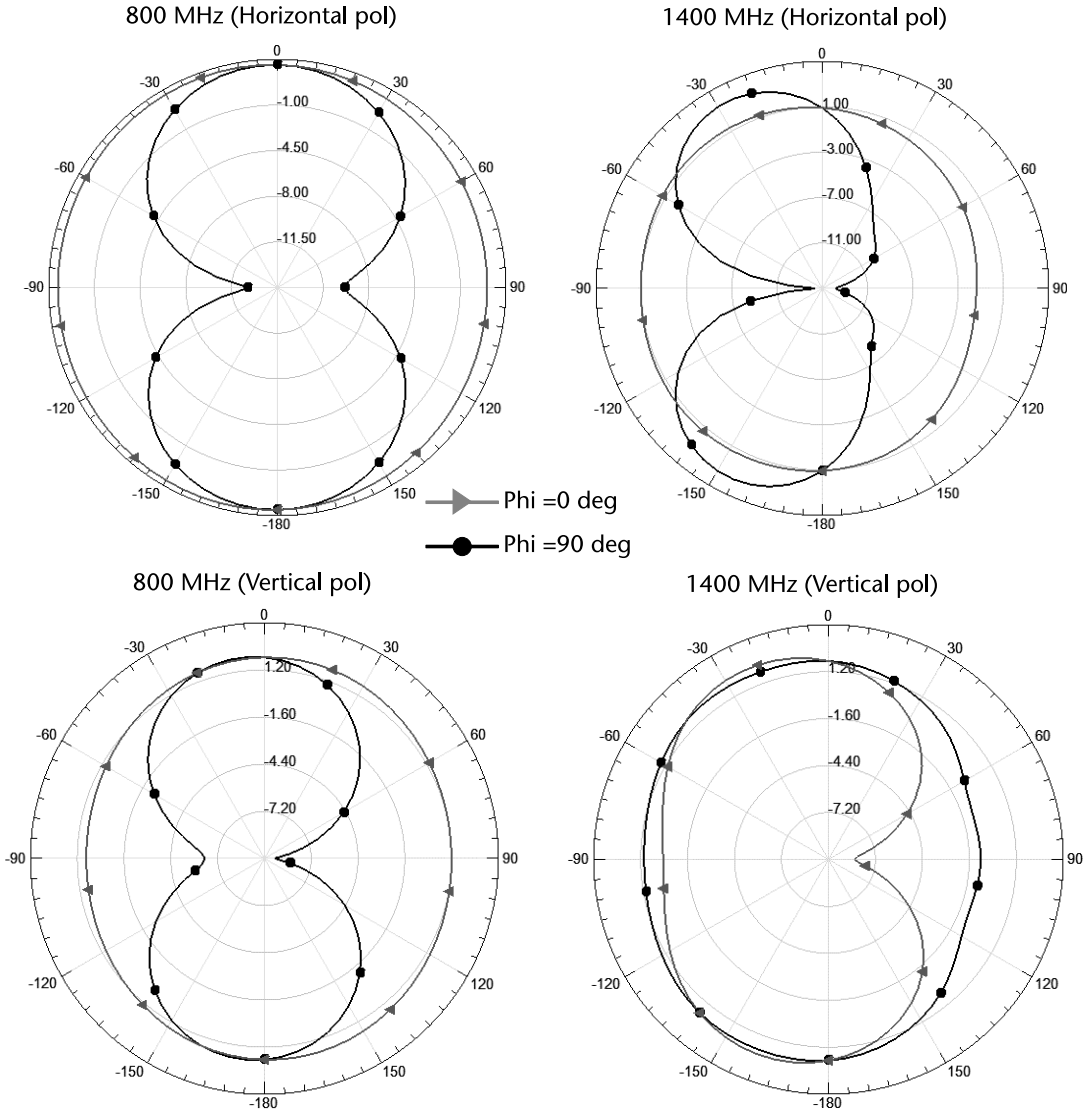

Figure 5.10 Antenna radiation patterns for horizontal and vertical polarization.

Table 5.2 Simulated Antenna Results

			Antenna Results		
Antenna Mode	*Polarization*	*Resonant Frequency*	*Gain (dB)*	*Efficiency (%)*	*Bandwidth (–10 dB)*
1	Horizontal	1.4 GHz	3.69	91	90 MHz
2	Horizontal	800 MHz	2.13	90	90 MHz
3	Vertical	1.4 GHz	2.58	92	50 MHz
4	Vertical	800 MHz	2.14	88	150 MHz

efficiency is about 88% to 92%. To further confirm the working principle of antenna and to clearly show which parts of the antennas are responsible for the radiation in the different bands, the study of the E-field distribution has been made. The surface current distribution at resonant frequencies is shown in Figure 5.11.

From the surface, the current distribution in the OFF state, and it can be observed that the resonant modes at about 1,400 MHz are mainly contributed by the feeding strip. However, due to strong coupling at higher frequencies, relatively small surface currents are also observed on the shorted strip at this band. Similarly, in the ON-state case, strong surface currents are observed on the shorted strip at about 800 MHz. At 1,400 MHz, the current is mainly located on the feeding monopole element, and at 800 MHz, strong currents appear on the coupled monopole. Antenna polarization is characterized by electric field direction.

5.4 Summary

In this chapter, various components, categorization, and the design process of printed reconfigurable antennas were presented. The various wireless applications where reconfigurable antennas are applied were discussed. A planar frequency-reconfigurable and polarization-reconfigurable antenna for two-band operation is designed to understand the working principle and design flow of such antennas. With the help of four PIN diodes, multifrequency band operation can be achieved for horizontal and vertical polarization. The modeling, control, and optimization of reconfigurable antennas were also detailed, and mechanisms were presented. This

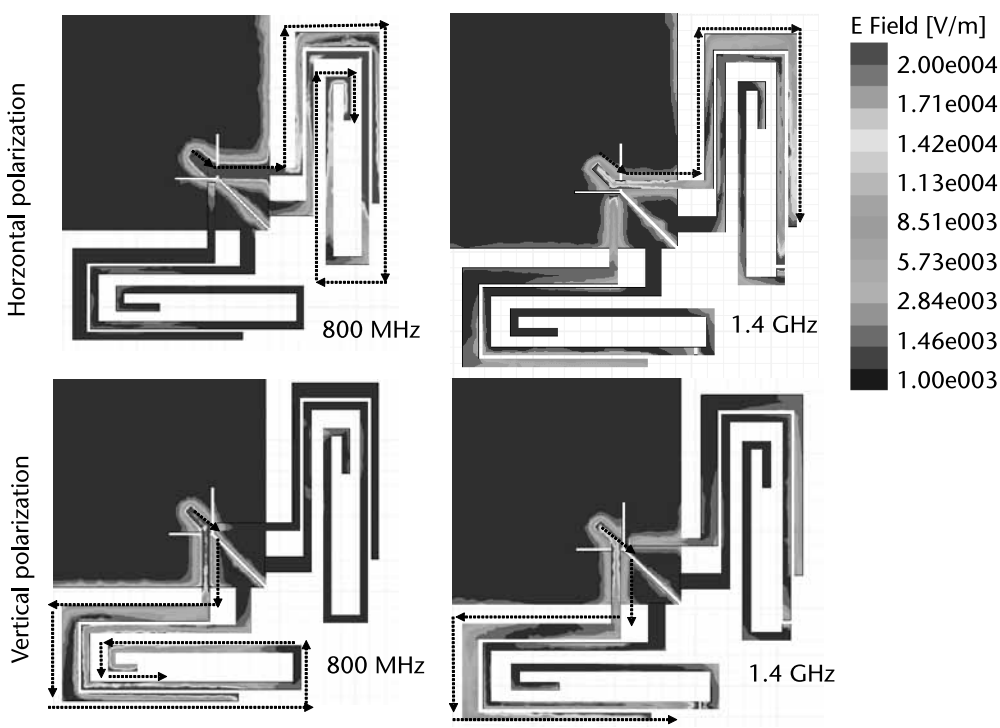

Figure 5.11 E-Field distribution in all four operating modes.

chapter emphasized the development of reconfigurable antennas to service evolving and futuristic practical wireless communication applications and proposed optimal solutions for more efficient and holistic designs.

References

[1] Park, Y. K., and Y. Sung, "A Reconfigurable Antenna for Quad-Band Mobile Handset Applications," *IEEE Transactions on Antennas and Propagation*, Vol. 60, No. 6, June 2012, pp. 3003–3006.

[2] Angus, C. K. M., et al., "Reconfigurable Multiband Antenna Designs for Wireless Communication Devices," *IEEE Transactions on Antennas and Propagation*, Vol. 55, No. 7, 2007, pp. 1919–1928.

[3] Songnan, Y., et al., "Frequency Reconfigurable Antennas for Multiradio Wireless Platforms," *IEEE Microwave Magazine*, Vol. 10, 2009, pp. 66–83.

[4] Christodoulou, C. G., et al., "Reconfigurable Antennas for Wireless and Space Applications," *Proc. IEEE*, Vol. 100, No. 7, July 2012, pp. 2250–2261.

[5] Balanis, C. A., *Modern Antenna Handbook*, New York: John Wiley & Sons, 2011.

[6] Bernhard, J. T., *Reconfigurable Antennas*, San Rafael, CA: Morgan and Claypool, 2007.

[7] Pringle, L. N., et al., "GTRI Reconfigurable Aperture Design," *IEEE Antennas and Propagation Society International Symposium (IEEE Cat. No.02CH37313)*, San Antonio, TX, 2002, pp. 473–476.

[8] Chen, R., and J. Row, "Single-Fed Microstrip Patch Antenna with Switchable Polarization," *IEEE Transactions on Antennas and Propagation*, Vol. 56, No. 4, April 2008, pp. 922–926.

[9] Erdemli, Y. E., R. A. Gilbert and J. L. Volakis, "A Reconfigurable Slot Aperture Design over a Broad-Band Substrate/Feed Structure," *IEEE Transactions on Antennas and Propagation*, Vol. 52, No. 11, November 2004, pp. 2860–2870.

[10] Behdad, N., and K. Sarabandi, "Dual-Band Reconfigurable Antenna with a Very Wide Tunability Range," *IEEE Transactions on Antennas and Propagation*, Vol. 54, No. 2, February 2006, pp. 409–416.

[11] Peregrine Semiconductor, "Digitally Tunable Capacitors," *Microwave Journal*, June 14, 2013.

[12] Ha, S. D., et al., "Quick Switch: Strongly Correlated Electronic Phase Transition Systems for Cutting-Edge Microwave Devices," *IEEE Microwave Magazine*, Vol. 15, No. 6, September-October 2014, pp. 32–44.

[13] Teeslink, T. S., et al., "Reconfigurable Bowtie Antenna Using Metal-Insulator Transition in Vanadium Dioxide," *IEEE Antennas and Wireless Propagation Letters*, Vol. 14, 2015, pp. 1381–1384.

[14] Brown, E. R., "RF-MEMS Switches for Reconfigurable Integrated Circuits," *IEEE Transactions on Microwave Theory and Techniques*, Vol. 46, No. 11, November 1998, pp. 1868–1880.

[15] Zhang, S., et al., "A Pattern Reconfigurable Microstrip Parasitic Array," *IEEE Transactions on Antennas and Propagation,* Vol. 52, No. 10, October 2004, pp. 2773–2776.

[16] Anagnostou, D. E., et al., "Reconfigurable UWB Antenna with RF-MEMS for On-Demand WLAN Rejection," *IEEE Transactions on Antennas and Propagation*, Vol. 62, No. 2, February 2014, pp. 602–608.

[17] Rebeiz, G. M., *RF MEMS: Theory, Design, and Technology*, New York: Wiley-Interscience, 2003.

[18] Nabki, F., et al., "Low-Stress CMOS-Compatible Silicon Carbide Surface-Micromachining Technology—Part II: Beam Resonators for MEMS Above IC," *Journal of Microelectromechanical Systems*, Vol. 20, No. 3, June 2011, pp. 730–744.

[19] Perruisseau-Carrier, J., P. Pardo-Carrera, and P. Miskovsky, "Modeling, Design and Characterization of a Very Wideband Slot Antenna with Reconfigurable Band Rejection," *IEEE Transactions on Antennas and Propagation*, Vol. 58, No. 7, July 2010, pp. 2218–2226.

[20] Lin, K. C., C. H. Lin, and Y. C. Lin, "Simple Printed Multiband Antenna with Novel Parasitic–Element Design for Multistandard Mobile Handset Applications," *IEEE Transactions on Antennas and Propagation*, Vol. 61, No. 1, pp. 488–491.

[21] Lee, C. T., and K. L. Wong, "Planar Monopole with a Coupling Feed and an Inductive Shorting Strip for LTE/GSM/UMTS Operation in the Mobile Phone," *IEEE Transactions on Antennas and Propagation*, Vol. 58, No. 7, July 2010, pp. 2479–2483.

[22] Lu, J. H., and Y. S. Wang, "Internal Uniplanar Antenna for LTE/GSM/UMTS Operation in a Tablet Computer," *IEEE Transactions on Antennas and Propagation*, Vol. 61, No. 5, May 2013, pp. 2841–2846.

[23] Wong, K. L., and T. W. Weng, "Small-Size Triple-Wideband LTE/WWAN Tablet Device Antenna," *IEEE Antennas Wireless Propag. Lett.*, Vol. 12, November 2013, pp. 1516–1519.

[24] Wong, K. L., and M. T. Chen, "Small-Size LTE/WWAN Printed Loop Antenna with an Inductively Coupled Branch Strip for Bandwidth Enhancement in the Tablet Computer," *IEEE Transactions on Antennas and Propagation*, Vol. 61, No. 12, December 2013, pp. 6144–6151.

[25] Lu, J. H., and J. L. Guo, "Small-Size Octaband Monopole Antenna in an LTE/WWAN Mobile Phone," *IEEE Antennas Wireless Propag. Lett.*, Vol. 13, March 2014, pp. 548–551.

[26] Sung, Y., "A Frequency-Reconfigurable Antenna for Internal Mobile Handset Applications," *Microw. Opt. Technol. Lett.*, Vol. 56, No. 6, June 2014, pp. 1366–1371.

[27] Lee, D. A., and Y. Sung, "Reconfigurable PIFA/Loop Antenna for Mobile Handset Applications," *Microw. Opt. Technol. Lett.*, Vol. 56, No. 9, September 2014, pp. 2034–2037.

[28] Lee, J. H., and Y. Sung, "Reconfigurable Hexa-Band Planar Inverted-F Antenna Using a Pin Diode for Mobile Handset," *Microw. Opt. Technol. Lett.*, Vol. 55, No. 8, August 2013, pp. 1926–1928.

[29] Chuang, H. -R., and L. -C. Kuo, "3-D FDTD Design Analysis of a 2.4-GHz Polarization-Diversity Printed Dipole Antenna with Integrated Balun and Polarization-Switching Circuit for WLAN and Wireless Communication Applications," *IEEE Transactions on Microwave Theory and Techniques*, Vol. 51, No. 2, February 2003, pp. 374–381.

[30] Boyle, K. R., and L. P. Ligthart, "Radiating and Balanced Mode Analysis of PIFA Antennas," *IEEE Transactions on Antennas and Propagation*, Vol. 54, No. 1, January 2006, pp. 231–237.

Selected Bibliography

Boukarkar, A., et al., "Compact Mechanically Frequency and Pattern Reconfigurable Patch Antenna," *IET Microwaves, Antennas & Propagation*, Vol. 12, No. 11, September 12, 2018, pp. 1864–1869.

Christodoulou, C., J. Constantine, and Y. Tawk, *Antenna Design for Cognitive Radio*, Norwood, MA: Artech House, 2016.

Jiang, Z., and F. Yang, "Reconfigurable Sensing Antennas Integrated with Thermal Switches for Wireless Temperature Monitoring," *IEEE Antennas Wireless Propag. Lett.*, Vol. 12, 2013, pp. 914–917.

Jin, G. P., D. L. Zhang, and R. L. Li, "Optically Controlled Reconfigurable Antenna for Cognitive Radio Applications," *IET Electron. Lett.*, Vol. 47, No. 17, 2011, pp. 948–950.

Xu, H., et al., "A Compact and Low-Profile Loop Antenna with Six Resonant Modes for LTE Smartphone," *IEEE Transactions on Antennas and Propagation*, Vol. 64, No. 9, September 2016, pp. 3743–3751.

Xu, Z., et al., "Reconfigurable MIMO Antenna for Integrated-Metal-Rimmed Smartphone Applications," *IEEE Access*, Vol. 5, 2017, pp. 21223–21228.

CHAPTER 6

Printed Antenna Arrays

6.1 Introduction

Printed antennas are used as a single element and are also very popular in arrays [1–16]. Microstrip antennas are well suited for arrays due to their low profile and low weight with conformability and low manufacturing cost. In various radar and communications systems, planar microstrip array antennas are greatly desired. Antenna arrays are used to increase the directivity and gain, scan the beam of an antenna, and enhance various other functions, which would be difficult with a single-element antenna. The main limitation of microstrips is that they radiate efficiently only over a narrow band of frequencies and they cannot operate at the high-power levels of the coaxial line, waveguide, or even stripline. This can be reduced with the help of various array configurations, dielectric materials, feeding methods, and ground planes.

Phased array antenna is a combination of multiple antenna systems, in which, antenna radiation pattern can be reinforced in a direction and suppressed in undesired directions [17–24]. The direction of phased array radiation can be electronically rotated, avoiding the need for any mechanical rotation mechanism. Phased arrays are used in a broad range of applications since the advent of this advanced technology because of these unique capabilities. Elements of an array may be spatially distributed to form a linear, circular, planar, or volume array. Linear arrays have antenna elements arranged in a line, while planar arrays have elements distributed on a plane. Planar array configurations are widely used in both communication and radar systems where a narrow pencil beam is required in both the azimuth and elevation planes. Individual array elements can be positioned along a rectangular grid to form a planar array for better control of the beam shape and position in space. Microstrip patch arrays are also versatile as they can be used to synthesize a required antenna pattern that cannot be achieved with a single element. The elements can be fed by a single line or by multiple lines in a feed network topology as per specifications and requirements. In this chapter, the printed array antenna working principle and designs are presented for several modern applications.

6.2 Microstrip Antenna Arrays

In an antenna array, the signals of all individual elements are coordinated to achieve better antenna gain, directivity, and SNR over those of a single antenna. The design of finite arrays demands to group several radiating elements in a symmetrical pattern so that the desired radiation is obtained in a specific direction. This can be realized only when fields due to individual patches get combined in phase in the desired direction and cancel each other in all other directions. In other words, each patch output is combined constructively to obtain the fields radiated by the array. It is important to note that radiation pattern of an individual element in the array is the same when it operates in standalone mode. The original pattern of the individual patch gets multiplied by the antenna array factor that takes into consideration the amplitudes and phases of the feed current. In the array, due to closer proximity between patches, there is an interaction between the elements. This leads to coupling among the radiating patches as each patch element induces currents to the other adjacent patches. Interelement spacing and location between the arrays affect the radiation pattern as well as antenna parameters.

6.3 Array Antenna Radiating Elements

The most basic property of the array is that the relative displacements of the antenna elements with respect to each other introduce relative phase shifts in the radiation vectors, which can then add constructively in some directions or destructively in others [25]. Many theoretical studies on antenna arrays have been published [25–28]. A linear array antenna is the primary configuration and can be applied to planar arrays. Each element is an electric or magnetic current source, which gives rise to a radiated field, the solution to Maxwell's equations [27]. In the array design below are controlling parameters that are used to shape the overall pattern of the antenna:

- The geometrical configuration of the overall array (linear, circular, planar);
- Interspacing between array antenna elements;
- Phase and amplitude of excitation to each element;
- Radiation pattern of each element.

The far-zone field of a uniform array is equal to the product of the field of a single element and the array factor. This is called pattern multiplication.

$$E_{Total} = [E_{Single\ Element}]x\ [Array\,Factor] \tag{6.1}$$

The array factor [29] is given by:

$$AF = \sum_{n=1}^{N} e^{j(n-1)}\varphi \tag{6.2}$$

where $\phi = kd\cos\theta + \beta$. The pattern for an N-element array with equal spacing and a constant phase shift between elements is given by some algebraic manipulation of (6.2) as:

$$E_{Total} = [E_{Single\ Element}]x\frac{1}{N}\frac{\sin[N(kd\sin(\theta)-\beta)/2]}{\sin[(kd\sin(\theta)-\beta)/2]} \tag{6.3}$$

The spacing should be determined such that mutual coupling among the antenna elements is minimized (often <–20 dB) and any grating lobe is invisible during beam scanning. To avoid grating lobes, the array spacing must satisfy:

$$d < \frac{\lambda}{1+|\sin\theta_{max}|} \tag{6.4}$$

where d is the array spacing and $\theta_{max}$is the maximum scan angle [30]. In array design, the interelement spacing lies between λ_g and $\lambda_g/2$. Arrays having element spacing between λ_g to $2\lambda_g$ will radiate not only a broadside beam but also two grating lobes at angles (measured from the broadside) given by:

$$\theta_0 = \sin^{-1}\left(\frac{n\lambda_0}{d}\right) \tag{6.5}$$

where $n = \pm 1$ corresponds to the appearance of the first set of grating lobes, $n = \pm 2$ corresponds to the appearance of the second set of grating lobes, and so forth. d is the element spacing.

6.3.1 Linear Microstrip Arrays

Linear arrays form a building block for planar arrays and are used for fan-shaped coverage. A linear array of a microstrip patch is shown in Figure 6.1 with equal space d between elements. All elements are exited with equal amplitude and phase to get a high gain antenna beam direction in broadside. Each patch element can be excited either individually using a separate port or with a transmission-line feed network.

The length of the microstrip feed line between patches determines the phase distribution across the antenna array elements. The separation between two array

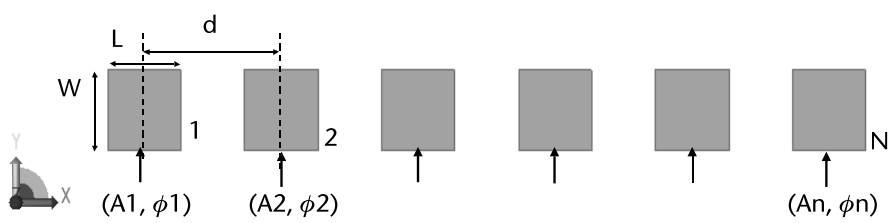

Figure 6.1 Linear microstrip antenna array configuration.

elements (i.e., an interelement spacing) is a vital parameter in array design. The closely spaced array elements suffer from strong mutual coupling effects. This affects the input and radiating characteristics of the antenna array and degrades the performance. The variation in the spacing changes the sidelobe level and the beamwidth of the main lobe. Many designs of linear array antennas are discussed in this chapter.

6.3.2 Planar Microstrip Antenna Arrays

In the planar array, all the elements are arranged in one plane as shown in Figure 6.2. In addition to placing elements along a line to form a linear array as discussed in previously, individual radiators can be placed along a rectangular grid to form a rectangular or planar array. Planar arrays provide additional variables that can be used to control and shape the pattern of the array in two directions. A planar array provides a large aperture and is used to form a pencil beam by varying the relative phase of each element. Planar arrays are also used as a reflector behind the active plane. The array factor, depending on the array geometry and excitation, is the pattern of an array of all the elements in the plane.

6.4 Feed Techniques for Array Antenna

Feed network designing is the most important part in array design. The feed network for an array application is a major design concern in terms of complexity and size. There are several kinds of feeding networks of an array antenna. Array feed network topology depends on antenna type, available space, pattern shape, sidelobe level, losses, and geometry. The efficiency of microstrip antenna arrays may

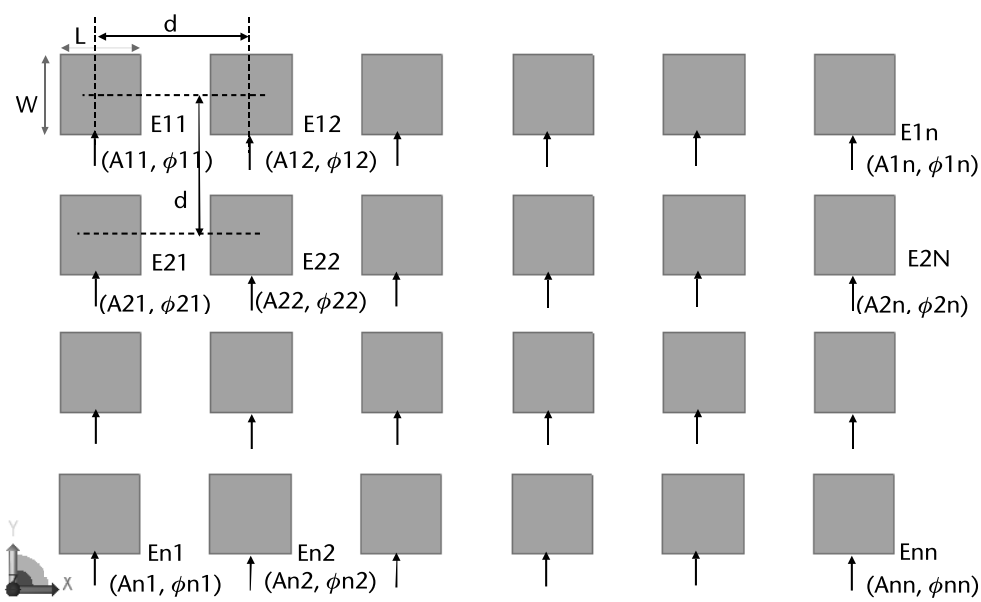

Figure 6.2 Microstrip planar antenna with equal spacing between elements.

be improved by reducing losses in the feed network. Losses in the microstrip feed network are due to dielectric loss, conductor loss, and radiation loss.

6.4.1 Corporate Feed Network

For a passive array antenna, the most common feeding network type is the corporate feed network as shown in Figure 6.3 [31–33]. This feeding technique integrates the RF feed lines with the radiating elements on the same substrate layer. As there are many microstrip lines in a corporate feed, it is lossy, particularly at high frequencies. Losses in the feed line degrade the microstrip antenna arrays' efficiency. The efficiency of microstrip antenna arrays can be improved by using a waveguide feed network. However, a waveguide-based feed network results in a significant increase in the antenna weight and dimensions. A corporate feed is also called parallel feed network. The corporate feed is composed of a power divider with transmission lines to the individual radiators. Although a corporate feed method is physically large and expensive, it is also the most broadband. The overall bandwidth of array is limited by the bandwidth of the radiators as well as feedlines. Corporate feeds are a suitable choice for phased arrays where phase shifters are inserted in the transmission lines to steer the beam direction electrically.

6.4.1.1 High Port Isolations with Wilkinson Power Divider

A Wilkinson power divider is used for high port isolation while maintaining a matched condition on all ports, especially in the case of a dual-polarized antenna. In the printed antenna array, a simple way to implement any type of uniform or non-uniform excitation is by using microstrip lines, achieving different feed amplitudes through Wilkinson or the T-junction power splitters. The T-junction is lossless and simple and takes up little area in the PCB, but its ports are not matched and there is no isolation between output ports. The Wilkinson divider divides the power in a similar way to the T-junction, but, unlike T-junctions, all ports are matched. In this power divider, reflected power is dissipated in the isolation resistor. The isolation

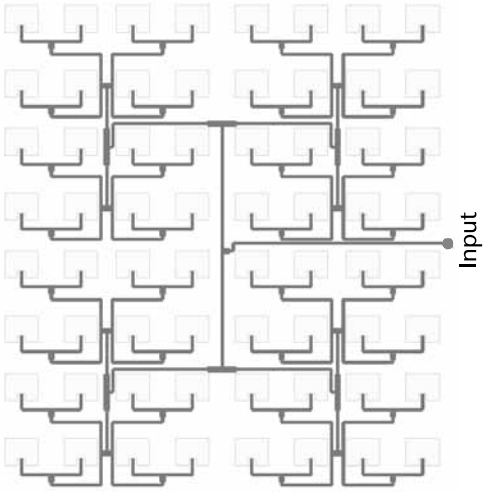

Figure 6.3 Microstrip array antenna fed with a corporate feed network.

resistor used for the Wilkinson divider introduces minimal loss, especially when microstrip transmission lines are used along with low-loss PCB substrate material.

Ernest Wilkinson invented this power divider in 1960 [34]. The S-parameter matrix for two-port equal power division is given by

$$[S] = \frac{-j}{\sqrt{2}} \begin{bmatrix} 0 & 1 & 1 \\ 1 & 0 & 0 \\ 1 & 0 & 0 \end{bmatrix} \tag{6.6}$$

The S-parameter indicates that the network is reciprocal ($S_{ij} = S_{ji}$), all ports are matched ($S_{ij} = 0$), and its lossless network is reciprocal ($[S]^H[S] = [I]$). The Wilkinson power divider is the most common topology [35–38] for the 3-dB power divider, where two parallel quarter-wavelength transmission lines are used for impedance transformation. For 50Ω input and output, the central $\lambda_g/4$ transmission line impedance is 70.7Ω. Usually, at high frequencies, the transmission lines must be separated for some distances to reduce parasitic coupling. Figure 6.4 shows a 3-dB Wilkinson power divider with a surface mount chip resistor designed for a center frequency of 7 GHz. RO 3003 of a 0.38-mm-thick substrate is used for design. This divider has a 50Ω microstrip line with a 0.96-mm width for easy fabrication. A 70.7Ω microstrip line width is 0.54 mm. The simulated S-parameter data as shown in Figure 6.4 illustrates high port isolation.

The 1:4 divider has been fabricated and measured at 7 GHz as shown in Figure 6.5. In a corporate feed network, a 1:4 Wilkinson power divider plays an important role to achieve good isolation between the output ports.

6.4.2 Inline Series Feed Network

Series-fed microstrip patch antenna arrays are used in many applications in wireless communication and radar array systems. In a series-fed array topology, the input signal is coupled serially to the antenna elements as it progresses. A series-fed network is compact as compared to corporate feed, which is one of the main

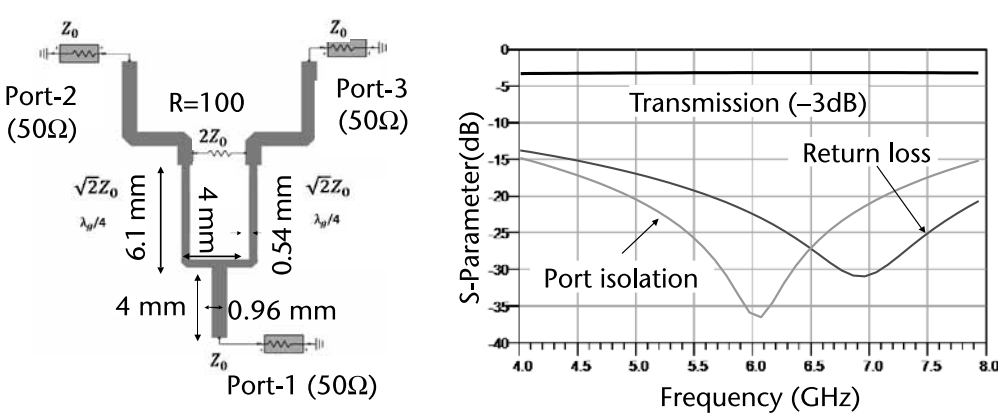

Figure 6.4 Wilkinson power divider design and S-parameter data.

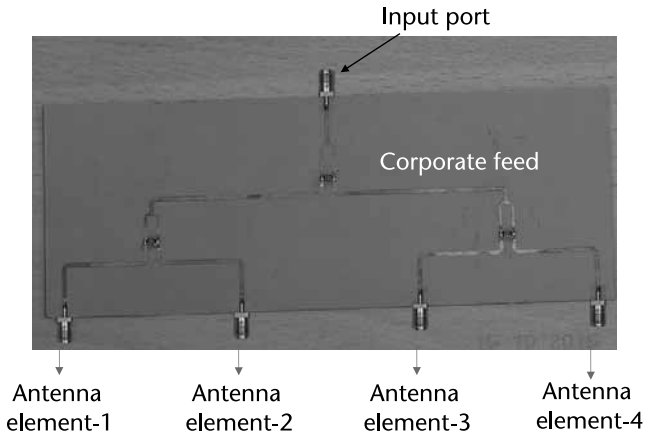

Figure 6.5 Fabricated 1:4 Wilkinson power divider.

advantages that make them more attractive than their parallel-fed counterparts. The small size of series-fed arrays results in less radiation and insertion losses, which is why, in many cases, the series-fed arrays are more efficient than corporate fed arrays. One major disadvantage of series feed configurations is narrow bandwidth and an inherent phase difference caused by the differences in the lengths of feed lines.

Figure 6.6 shows an end-fed series feed network. Radiators are coupled to a single transmission feed line and energy decays along the line length. Another configuration is a middle series-fed array as shown in Figure 6.7, in which input RF power is fed at the center of the feed network. Efficient design and fabrication of planar array antennas with low sidelobe levels are a challenging task. For reducing the sidelobe level of a uniform array, one technique utilizes amplitude tapering in which the excitation amplitudes of the array elements generally decrease with distance from the center of the array. To obtain the amplitude tapering in a linear array, a series-fed network with variable length and impendences is used.

6.4.3 Multilayer Feed Network

For broadband applications, the feeder network in the array antenna should preferably be made using a corporate network. However, for large linear arrays, the

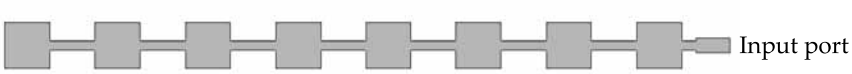

Figure 6.6 Inline end series-fed microstrip patch antenna.

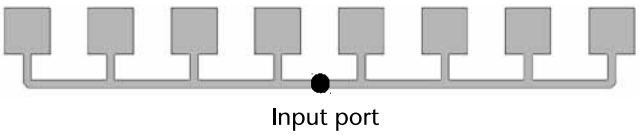

Figure 6.7 Middle series-fed microstrip patch antenna.

corporate feed network in one layer occupies a large area because the number of stages is N where 2^N is the number of output ports. For larger arrays, the number of stages increases accordingly, and thus the realization of corporate feed networks is not feasible for larger arrays. One possible solution to use the corporate feeder network for large linear arrays is to use the different stages of the feeder network in different layers, thus breaking the feed network into many parts and placing them on separate layers that can be joined by vias. An alternative solution for this is to use a series feed network, which may be realized using one stage only, but the serious limitation with this configuration of a feed network is that, when the frequency is changed, there is a progressive phase difference and the beam is scanned, resulting in frequency scanning. To solve this problem, the series and the corporate combination may be used so that the linear phase error is symmetrical about a mid-point so that the overall phase error is of quadratic nature. The quadratic phase error results in the broadening of beamwidth and the null feeling. Thus, the realization of the corporate feed network in a multilayer configuration facilitates achieving a broadband dual-polarization operation in the limited interelement space in the planar array antennas.

Printed antennas integrated with the feed network and active circuitry in a multilayer architecture as shown in Figure 6.8 are the latest technology trend. This approach allows the integration of antenna elements with complex processing circuitry maintaining the fabrication and functional modularity at different levels while overcoming some fundamental constraints. Different circuit levels are isolated from each other by placing metal planes in between, leading to parallel-plate-type circuit environments. Multilayer feed design configuration is selected according to the requirement and specifications. It depends upon available space, the power-handling capability of individual feed layers, complexity, and some critical RF parameters. The use of slot as a means of power transfer between layers makes the use of multilayer feeding networks attractive. The transfer of power between two adjacent layers in a multilayer structure can be done using either a pin, which makes an electrical contact, or via coupling apertures in the ground plane separating the layers. Aperture coupling leads to inherently symmetric feed network

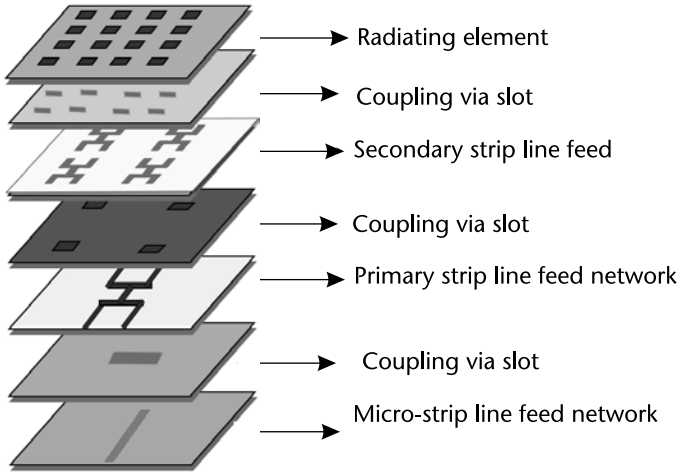

Figure 6.8 A multilayer feed architecture of the printed antenna.

layouts, which further simplify the design. Multilayer feed networks are very effective in highly integrated SiP (system-in-package) RF modules in which antenna elements are connected to the output of different components placed on the top and bottom of the chip. MMIC and LTCC-based modules along with integrated antennas use this feed network topology.

6.4.4 Feed Network for Shaped Beam Pattern Arrays

Some systems, such as airborne SAR, require a shaped antenna pattern along with dual-polarization and low cross-polarization capability. For such a requirement, the feeding network must incorporate matching circuits enabling matched wideband operation of antenna elements together with different types of power dividers and combiners providing proper, usually nonuniform, power distribution to antenna elements. A feed network called the beamforming network (BFN) is used to provide dual-linear polarization with low cross-polarization capability as well as good isolation between the individual ports. Such feed networks can be designed using a multilayer structure where different parts of BFN are placed on different layers. Sometimes special feed networks are designed to obtain shaped antenna radiation patterns like the cosec^2 radiation pattern. Each port amplitude and phase is calculated using null perturbation technique that generates the cosec^2 shape pattern. The feed network for a shaped pattern array is covered in detail in Chapter 8.

6.4.5 Feed Network for Active Antenna Arrays

Active phased arrays are usually composed of a feed network and many phase shifters. In the active phased-array antenna, transmit power is produced by many TX/RX (transceive) modules. In these antennas, each element or group of elements are connected to a separate transceiver module. Active antennas are primarily used in remote-sensing satellite, adaptive antenna, 5G phased array antennas, and radars. Feed networks are used to distribute the output signal of the transmitter to the radiation elements, and phase shifters control the phase of the signals at each radiating element to form a beam in the desired direction. Feed network design is a very critical task for such a system because of impedance matching with active components and effectively controlling amplitude and phase distribution across the network. Feed network design for active phased array radar and 5G FD-MIMO is covered in Chapter 15. In some cases, a combination of various feed networks also called the hybrid feed topology is used.

6.5 Printed Antenna Array Design for Rainfall Radar

In this section, a microstrip antenna array design is explained with a rainfall radar antenna called the Precipitation Occurrence Sensor System (POSS) design, as shown in Figure 6.9. The design has been done for the C-band application at 5.8 GHz. An array consisting of 64 elements of 8×8 is fed with the corporate feed network. RT Duroid 5870 substrate of dielectric constant 2.33 and height of substrate equal to 0.5 mm are used. The antenna gain of 25.1 dBi is achieved. The bandwidth of antenna is 150 MHz for a return loss of –10 dB. The array antenna is excited by

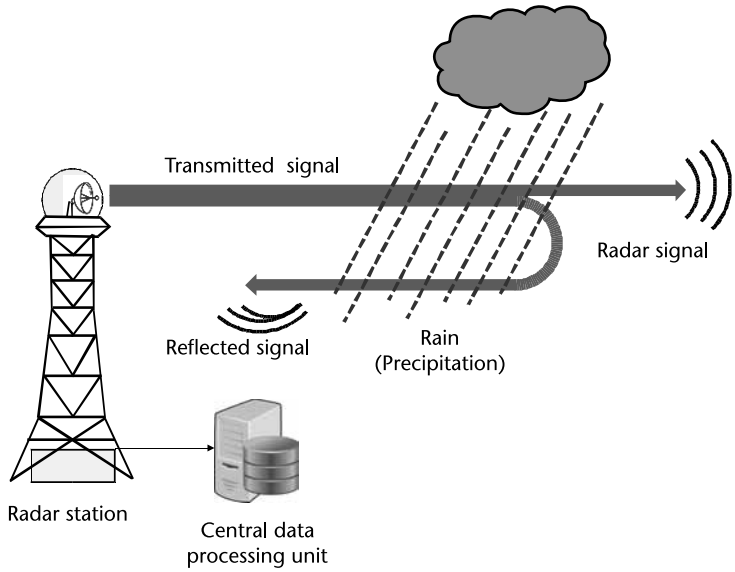

Figure 6.9 Working principle of a Doppler weather rainfall radar.

uniform amplitude and phase feeding method. In rainfall measurement, the antenna plays a critical role in terms of accuracy and performance. Such a system requires a low-cost, small-size, minimal-weight antenna capable of producing good performance at the desired frequency.

A microstrip antenna is very suitable for this application; it is very economical, is easy for fabrication, installation, and requires very little space. However, the gain of the antenna is very low; hence, to improve the directivity, antenna arrays are used. The complete design flow of an array antenna is shown in Figure 6.10. The design starts with the optimization of the single radiating element. This is a very crucial step for optimum gain and bandwidth performance of an array antenna. The array antenna feed is designed based on the available space, the power-handling requirement, and the shape of the beam and the bandwidth of the antenna as discussed in the previous section. Antenna topology decides the polarization and shape of the antenna; it may be a rectangular array, a circular array, or a customized shape. First, a linear array is optimized because it is easy to make a prototype

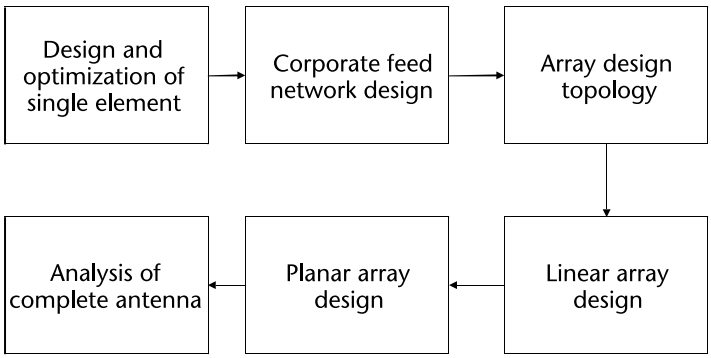

Figure 6.10 Printed array antenna design flow diagram.

of the linear array from the cost and fabrication point of view. Finally, the complete planar array is designed and simulated using EM solvers. To meet the desired bandwidth, gain, half-power beamwidth, low cross-polarization, low sidelobe levels, and antenna main lobe direction, various innovating techniques are applied. In the next section, these techniques are discussed in various presented array designs in this book.

6.5.1 Antenna Design Specifications

Rainfall antenna design specifications are driven by the gain and antenna beamwidth requirement. For a typical gain, this antenna is 35 dBi and the half-power beamwidth requirement is 1°. All important antenna design specifications are listed in Table 6.1.

6.5.2 Design and Optimization of a Single Element

The microstrip patch antenna array has been designed at 5.8 GHz on an RT Duroid 5870 substrate with the relative permittivity (ε_r) of 2.33. The antenna element is fed with 50Ω inset feed with equal power division and phase. The patch is designed using the conventional formulas mentioned in Chapter 2. The edge impedance of the patch is very high and generally varies from 100Ω to 200Ω. Impedance decreases gradually from the edge to the center of the patch and at one where impedance is 50Ω; a feed line of 50Ω with a width of 1.45 mm is used to feed the patch as shown in Figure 6.11. The size of the substrate is chosen in such a way that there remains at least $\lambda/4$ distance from the edge of the patch to the edge of the substrate.

The antenna is simulated using the full-wave analysis technique MoM. The single antenna gain and bandwidth are 6.7 dBi and 140 MHz, respectively. Microstrip antennas are a narrowband antenna. In the next section, some techniques are discussed to increase an antenna bandwidth. In any array, the single microstrip element is building a block of design; hence, it is very necessary to optimize the

Table 6.1 Antenna Design Specifications

Antenna Size	*Value*
Operating frequency	5.8 GHz
Polarization	Linear
3-dB beamwidth	1°
Gain	35 dB
First sidelobe level	–26 dB
Cross-polarization	–27 dB
VSWR	1.5
Antenna weight	80 kg
Antenna size	1.2m × 1.2m
Shape	Rectangular

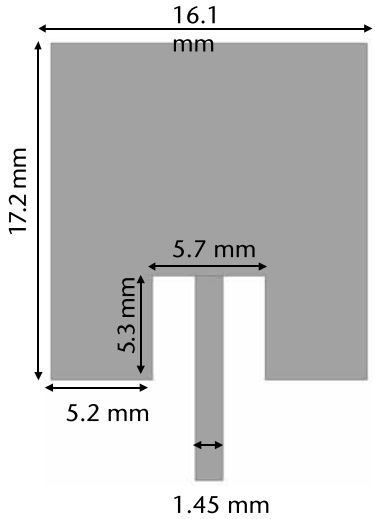

Antenna	
Patch length	17.2 mm
Patch width	16.1 mm
Width of 50 Ω line	1.45 mm
Substrate	
Dielectric constant	2.33
Thickness	0.5 mm

Figure 6.11 Single microstrip antenna element dimensions.

design for the best return loss, bandwidth, and gain before proceeding to the array design.

6.5.3 Design of the Corporate Feed Network

The array is fed with a corporate feed, in which equal power is available for each element in the array. The spacing between two elements is important, which varies from 0.5λ to λ. Spacing less than a half-frequency space wavelength is generally not used because of feed-line overcrowding. As we increase the spacing between the elements, it has been observed that the sidelobes increase significantly and the beamwidth reduces. When the spacing between the elements has reduced, the sidelobes reduce and the beamwidth increases. Thus, there is a trade-off between the sidelobe level and beamwidth of the array. If the spacing between the elements exceeds λ, then grating lobes are observed. In this design, interelement spacing of 0.75λ is selected so that we get narrow beam and sufficient space for the feed lines.

In a corporate feed network, the microstrip transmission line, bend, and junction with a quarter-wave transformer are the three main components, as shown in Figure 6.12. The width of the transmission line is calculated based on the input impedance of the antenna and the feeding location on the patch. For a bending design, there is no best way to bend a microstrip or stripline transmission line. Bend discontinuity changes the line characteristic impedance; without compensation, the bend adds shunt capacitance. However, the small capacitance usually does not change the circuit's performance very much. Another problem associated with bends is that it can cause far more damage to the intended performance of a highly tuned circuit: the effective length of the transmission line becomes shorter than the center-line length.

When a 90° bend is made of a microstrip transmission line, it adds a small amount of capacitance. Mitering the bend chops off some capacitance, restoring the line back to its original characteristic impedance. Figure 6.13 shows the important parameters of a mitered bend. The optimum mitered bend equations for a

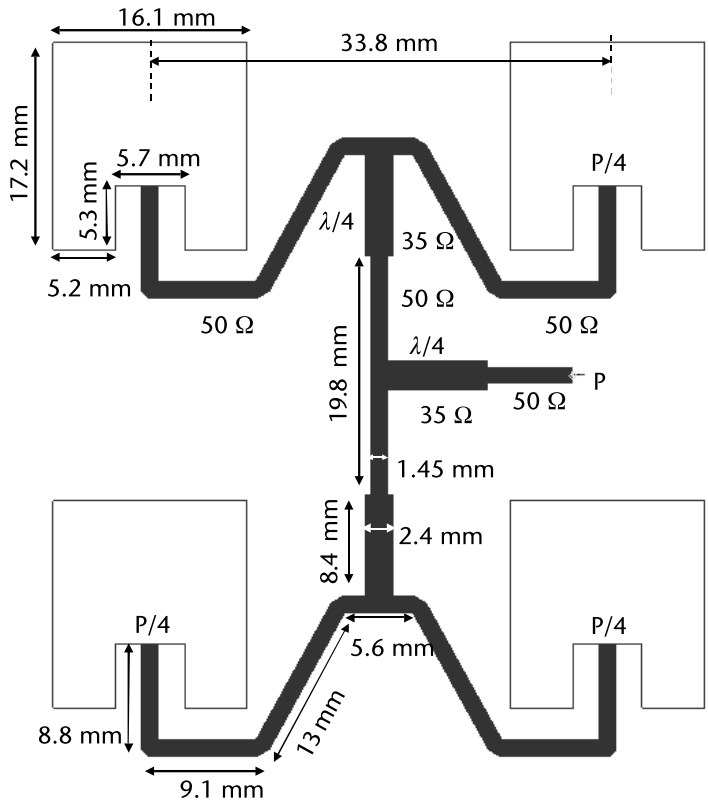

Figure 6.12 A 2 × 2 planar array fed with a corporate feed network.

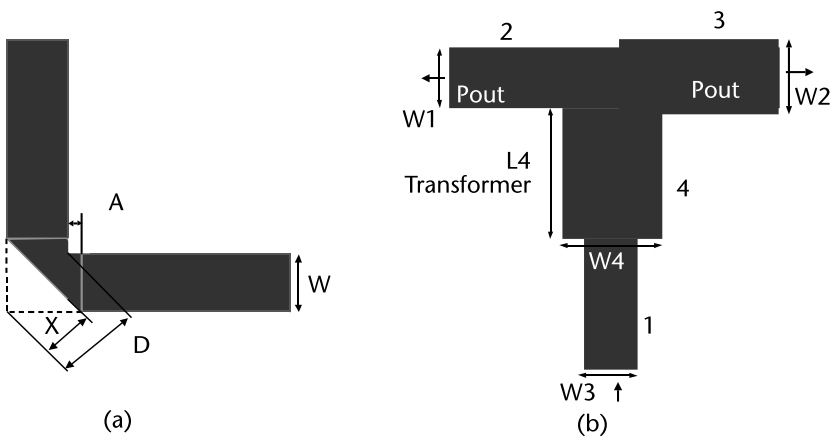

Figure 6.13 Feed network elements: (a) bend and (b) junction with quarter-wave transformer.

microstrip with a width W is given in (6.7) to (6.9). In this antenna array design, the bend has $X = D/2$ and $A = 0$. This bend gives good compensation for higher frequencies.

$$D = W\sqrt{2} \tag{6.7}$$

$$X = W\sqrt{2}\left(0.52 + 0.65e^{\left(-1.35\frac{W}{h}\right)}\right) \tag{6.8}$$

$$A = X\sqrt{2} - W \tag{6.9}$$

A junction is formed where feedlines from two patch elements meet. A junction between two dissimilar width sections introduces a large discontinuity and changes the impedance value at the junction. A standard T-junction power divider is shown in Figure 6.13. The input power P_{in} is delivered to the intersection on a microstrip of width W_1 and impedance Z_1. The line then branches into two arms with power P_{out}, width W_2 and W_3, and impedance Z_2 and Z_3. The design equations for this divider are:

$$Z_{junction} = \frac{Z_2 Z_3}{Z_{2+} Z_3} \tag{6.10}$$

A mismatch in impedance between two points on a transmission line can be compensated with a quarter-wave transformer. The quarter-wave transformer is a very suitable matching technique. In this technique, the junction impedance is matched to the characteristic feedline impedance through a quarter-wavelength of transmission. The input impedance considering the matching section of line is given by:

$$Z_4 = \sqrt{Z_{junction} Z_1} \tag{6.11}$$

To match the output port impedance line with the input port, a quarter-wave transformer with a line width W_4 and an impedance Z_4 is used. In this designed feed network, T-junction is a 3-dB power divider with $Z_1 = Z_2 = Z_3 = 50\Omega$. The junction impedance is 25Ω and the quarter-wave transformer impedance is 35.35Ω.

6.5.4 Planar Antenna Design

A linear 1 × 2 array structure is designed and then it is converted into a 4-element array as shown in Figure 6.14. The antenna center frequency is 5.8 GHz and is fed with a 50Ω impedance line. To match an antenna impedance with an input port, three quarter-wave transformers are used. The interelement spacing between antenna elements depends on the desired beamwidth and can be determined using:

$$\theta_m = 2\left[\frac{\pi}{2} - \cos^{-1}\left(\frac{\lambda}{Nd}\right)\right] \tag{6.12}$$

where θ_m is the first null beamwidth, d is the separation between array elements, and λ is the free-space wavelength. All elements are excited in phase and the beam

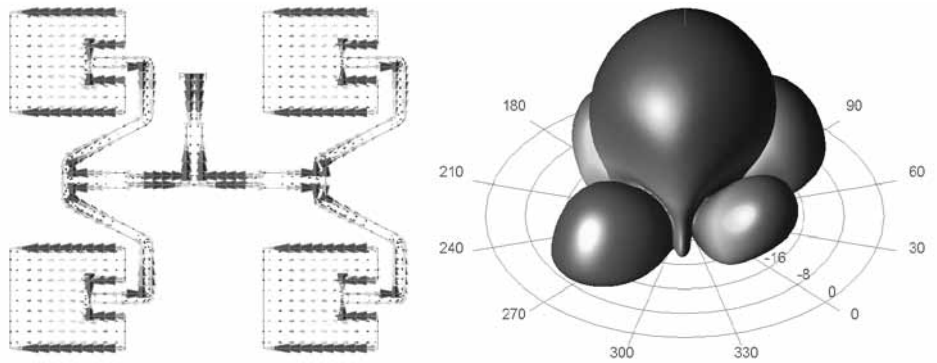

Current distribution 3D radiation pattern

Figure 6.14 The 2 × 2 microstrip antenna array and simulated 3-D radiation pattern plot.

direction is towards boresight. The current distribution and 3-D antenna radiation pattern are shown in Figure 6.14.

The antenna half-power beamwidth also reduces with array size (number of elements in an array antenna) as shown in Figure 6.15. The antenna beamwidth reduces with an increased number of elements. An array of 8 × 8 and 16 × 16 element

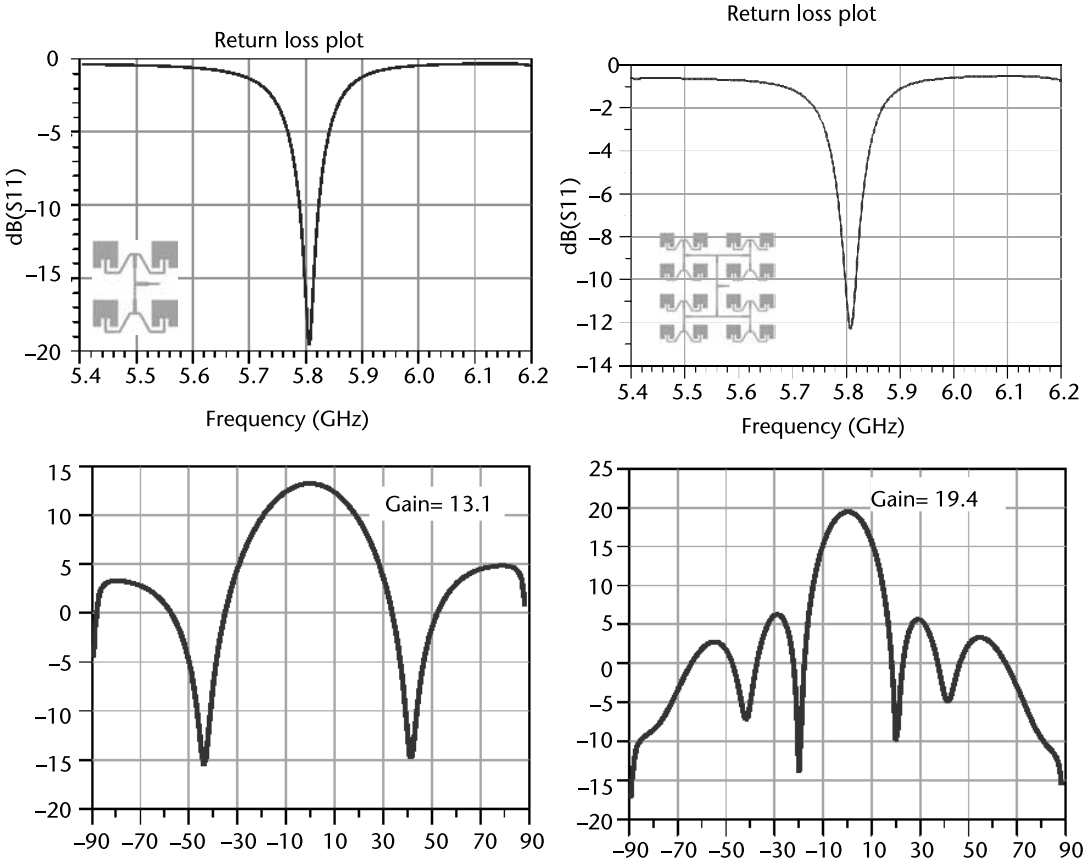

Figure 6.15 Return loss and gain pattern for 2 × 2 and 4 × 4 arrays at 5.8 GHz.

is simulated before making complete 32 × 32 element array. The gain of the 8 × 8 planar array is 26 dBi while the 16 × 16 antenna gain is 30 dBi at 5.8 GHz. The return loss plot and the radiation pattern cut of 2 × 2 and 4 × 4 antennas are shown in Figure 6.15.

6.5.5 Complete Antenna Design and Simulation

To get gain of 35 dBi and a beamwidth of 1°, a planar array of 32 × 32 is designed and simulated. The size of the complete antenna array is 1.2m × 1.2m. This antenna is placed in the weather radar radome design. All antenna performance parameters for different array sizes are summarized in Table 6.2. With an increased array size, the antenna simulation time and system memory requirement increase. Also, antenna bandwidth decreases with increased array size because of feed network losses.

The complete antenna is simulated using MoM, and this is considered a large problem to solve using the EM problem. Simulated results are shown in Figure 6.16. In the corporate feed configuration, the antenna array with *N* elements are fed by a 1:*N* power divider network with identical path lengths from the feed point to each element. The advantages of this topology include design simplicity, flexible choice of element spacing, and broader bandwidth, and they are amenable to integration with other devices such as amplifiers and phase shifters. The disadvantage of this type of feed is that it requires more space for the feed network. For large arrays, the length of feed lines running to all elements is prohibitively long, which results in a high insertion loss. The insertion loss is even more pronounced at millimeter-wave frequencies, thereby adversely degrading the gain of the array. At higher frequencies, the feed lines placed on the same plane as the patches will also radiate and interfere with the radiation from the patches.

Return loss better than –10 dB is achieved in the band. Figure 6.17 shows an antenna pattern for 256 elements. Antenna results and EM simulation time are summarized in Table 6.2. The gain of the antenna increases in an array and the beamwidth reduces. In an array antenna, the gain increase by 3 dB by doubling the number of element in the array. The 16 × 16 array has 6 dB more gain as compared to 8 × 8 array antenna because a total number of elements increased 4 times.

Table 6.2 Summary of Antenna Design Result

Array Type	*Array Size*	*Total Elements*	*Gain (dBi)*	*Bandwidth (MHz)*	*HPBW (Degree)*	*Simulation Time (Relative to Single Element)*
Single	1 × 1	1	6.7	40	78	1.0×
Linear	1 × 2	2	9.7	38	39	2.5×
Planar	2 × 2	4	13.1	35	39	5.5×
Planar	4 × 4	16	19.4	32	19	19.5×
Planar	8 × 8	64	25.1	27	10	95.0×
Planar	16 × 16	256	30.2	25	4.5	1,700×
Planar	16 × 32	512	32.8	24	2.1	7,000×
Planar	32 × 32	1,024	35.8	22	0.9	35,000×

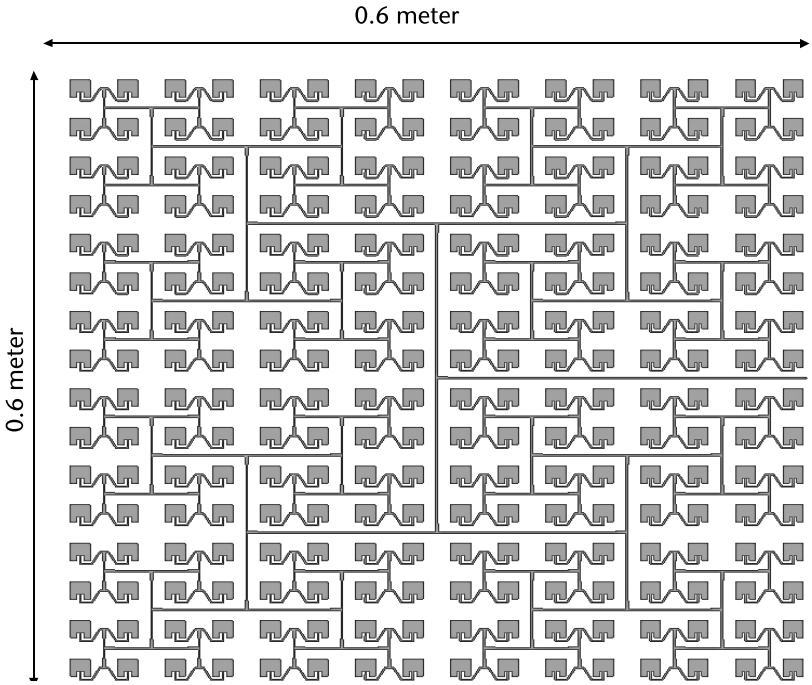

Figure 6.16 A 16 × 16 element antenna array fed with a corporate feed network.

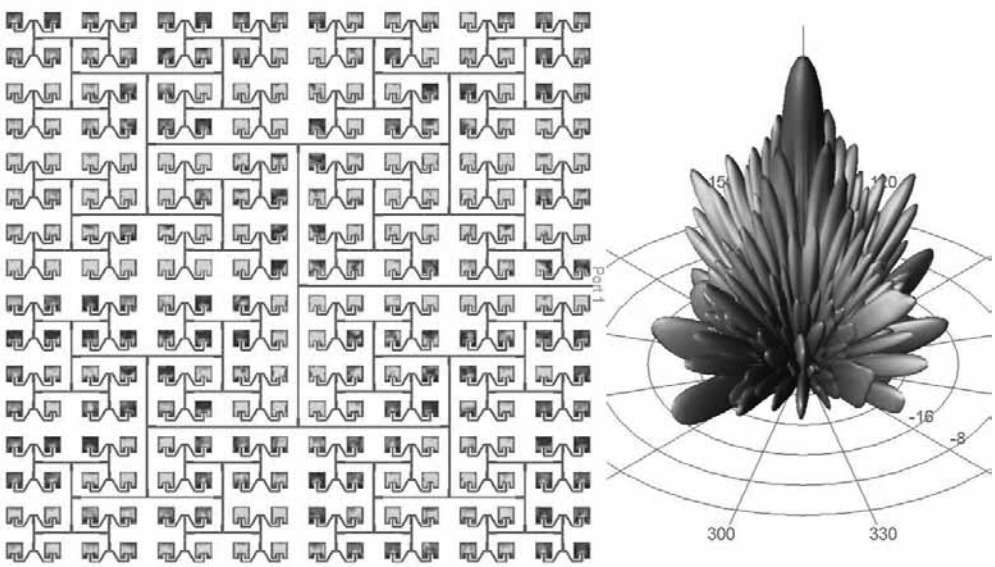

Figure 6.17 Current distribution and 3-D radiation pattern plot of a 256-element antenna array fed with a corporate feed.

6.5.6 Antenna Fabrication

The planar array antenna of 8 × 8 elements fed with a corporate feed network is printed using photolithography processes as shown in Figure 6.18. Antenna array copolarized and cross-polarized radiation patterns (E and H planes) are taken in an

anechoic chamber and are shown in Figure 6.19. Cross-polarization is better than –30 dB. Gain is measured relative to the standard horn antenna and is 25.1 dB. Minor asymmetry in the pattern is observed because of some misalignment during integration and a chance of improvement is possible. The radiation pattern is also measured using the planar near-field pattern measurement technique. Simulated data matches very well with measured data.

6.5.7 Circular Aperture Array Antenna

In many applications, the circular aperture array antenna as shown in Figure 6.20 is required based on the available system space. The symmetry method is preferred for a regular subaperture because the symmetry network is beneficial in cancelling out spurious radiation.

A circular-shaped array can be divided into regular subapertures. The number of elements is chosen to be $2N$ (N = 1, 2, 3 ...), which can be designed by symmetrical methods. A 4×4 element subarray is first designed and then, by duplicating the subarray, a larger 2^N-element array is designed. The feed network needs to be redesigned for the corner subarrays as indicated in Figure 6.20. Some antenna elements are removed to make it a circular aperture and this process feed-network

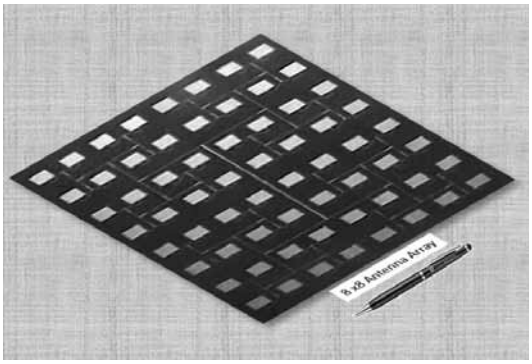

Figure 6.18 Fabricated 8×8 antenna array.

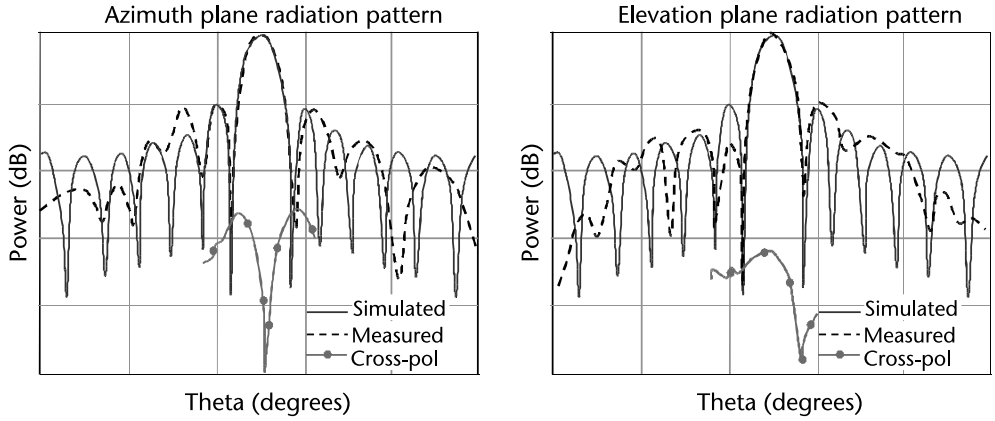

Figure 6.19 Measured azimuth and elevation plane radiation pattern of an 8×8 antenna array.

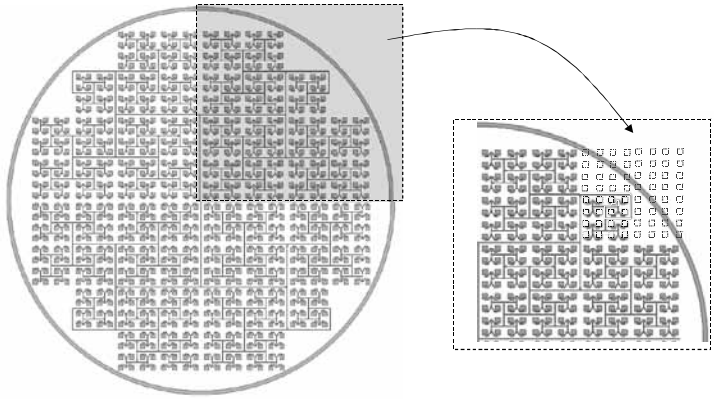

Figure 6.20 Circular aperture microstrip antenna array.

impedance for a truncated subarray is calculated based on the current division in this array segment.

6.6 Bandwidth Enhancement Technique of Microstrip Array Antenna

One of the major disadvantages of microstrip patch antenna is their narrow bandwidth. Conventional microstrip patch antennas have a small bandwidth of 1% to 3% around its resonant frequency. Many systems that could profit from the use of these radiators employ other types of elements due to the requirement for more bandwidth. Researchers have investigated techniques to improve the impedance bandwidth of this class of antennas [39, 40]. The antennas can be made of wideband aperture coupled microstrip array antennas [41], a U-slot with a designed π-shaped stub [42], a double rectangular patch with bridges [43], stacked layered structures [44], resonator antennas with capacitive coupled parasitic patch element [45], and circular edge truncation [46]. The bandwidth of microstrip radiator is directly proportional to substrate thickness h. However, if h is greater than about $0.05\lambda_0$, the probe inductance (for coaxial feed) becomes large enough for an impedance matching network. A foam substrate gives a high bandwidth; by using a thick foam substrate, a bandwidth of about 10% can be achieved. The bandwidth of a rectangular patch is also proportional to the patch width W (but we need to keep $W < 2L$).

The purpose of the design of wideband antenna elements is to arrange them into an array configuration to form a wideband array system. However, the elements in the array are fed by a feed network. Therefore, a wideband feed network is also required to match with the wideband elements and provide overall wideband array system. As discussed earlier, a corporate feed network has been proven to provide a wide bandwidth with good return loss and low transmission loss [32, 33] as compared to the series feed network. By using special feeding techniques like aperture coupling and stacked patches, bandwidths of 100% can be achieved. Edge-coupled patches and multilayer structures are two of the most widely used techniques to enhance the bandwidth of microstrip antennas. The methods devel-

oped for effective wideband patch antenna design are based on one or more of the following principles:

- Slots or parasitic elements: Additional resonances are introduced so that, in conjunction with the main resonance, an overall broader band response is obtained.
- Multilayer or thick substrates of low permittivity are used.
- Techniques to reduce the mismatch problem are associated with thick substrates.

6.6.1 Edge-Coupled Patches

Edge-coupled patches increase the impedance bandwidth of a microstrip patch through the introduction of additional resonant patches. By doing so, a few closely spaced resonances can be created. Only one of the elements is driven directly. The other patches are coupled through proximity effects as shown in Figure 6.21. With the edge-coupled approach, impedance bandwidths of up to 25% can be achieved. The advantages of the edge-coupled approach include the fact that the structure is coplanar in nature and that it can be fabricated on a single-layer substrate. However, this approach also has a few drawbacks. Because the different patches radiate with different amplitudes and phases at different frequencies, the radiation patterns change significantly over the operating frequencies and reduce operating bandwidth of the antenna. The enlarged size of the structure is also not good for array designs. The realization of the feed network in an array configuration is another challenge for this antenna kind of structure because of limited available space for feed lines.

6.6.2 Multilayer Structure

Multilayer or stacked microstrip patch is a very popular and effective technique to increase the bandwidth of a microstrip patch antenna, especially in array design. In this structure, the presence of additional dielectric substrates above the main patch causes a shift of the operating frequency. Figure 6.21(b) shows the geometry of such an antenna element where the bottom patch is driven by a feed element and the top patch, which is located on a different substrate layer, is proximity-coupled to the

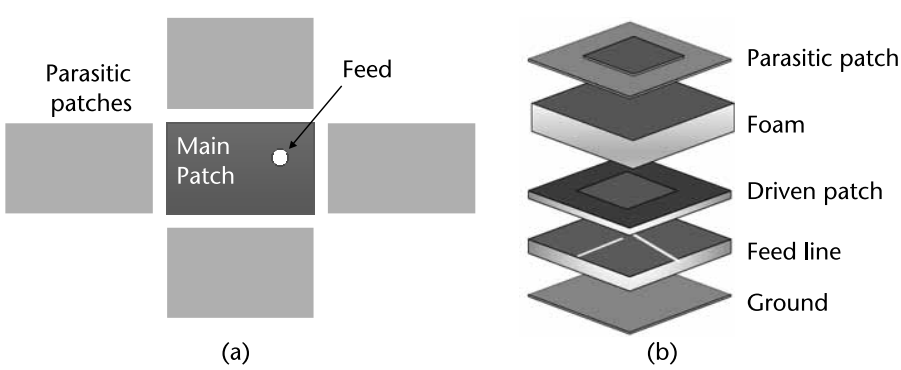

Figure 6.21 (a) Edge-coupled patches and (b) stacked patches

bottom one. In practice, the patches placed on different layers have the slightly different sizes to generate two distinct resonances.

The stacked-patch configuration has many advantages over the edge-coupled configuration. Since it does not increase the surface area of the element, it can be used in array configurations without the danger of creating grating lobes. Its radiation patterns and phase center also remain relatively constant over the operating frequency band. One drawback of stacked patches is that it requires more than one substrate layer to support the patches. This technique is used in many of designs presented in this book to get the desired bandwidth as per applications of array antennas. The rainfall antenna design presented previously is a narrowband antenna that is not suitable for many applications such as airborne SAR where a wideband antenna is required. The next designed antenna is a multilayer wideband microstrip array antenna.

6.7 Multilayer Antenna Design with Wideband Performance

The spacecraft radar antenna design should meet the requirement of high gain and wide bandwidth, keeping the weight as low as possible in the limited available space. A multilayer, lightweight direct-fed microstrip planar array antenna at 4.5 GHz is designed using foam material to meet a wide bandwidth requirement. The foam material is sandwiched between the patch and the ground plane to improve the radiation efficiency and bandwidth performance in the limited space over the single-layer conventional microstrip patch antenna. The antenna configuration is shown in Figure 6.22, where patch and feed lines are printed on the same substrate and the foam layer is placed between the patch and the ground plane to improve radiation efficiency and bandwidth performance by reducing the effective dielectric constant of the combined sandwich layer.

Terminating the patch with a high impedance line can control spurious radiation from the feed line network and cross-polar performance is improved by employing the proper phase cancellation technique. Antenna designing materials are same as used in the previous section only a foam of 2.5 mm is inserted between two 0.5-mm-thick RT Duroid 5870 dielectrics. Both patch geometry and feedline are printed on the top substrate layer, for which the bottom substrate supports the ground plane. Dielectric constant and height of individual substrate layers change the effective dielectric constant for antenna design. A low dielectric constant, which

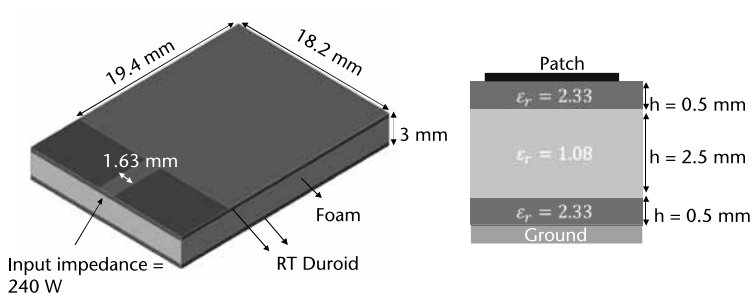

Figure 6.22 Multilayer microstrip patch antenna configuration and design dimensions.

enhances the radiation efficiency for the patch, can give rise to spurious radiation from the feed line network where high dielectric constant is generally preferred to confine the EM field. Foam material would be the best candidate for the patch, but it cannot be directly printed on foam material, which is the reason that two substrate layers are used. The single patch is optimized using the MoM EM simulation technique.

A patch antenna needs to be reoptimized because the insertion of foam and another layer of RT Duroid substrate changes the effective dielectric constant. The return loss plot of a single patch antenna with and without foam material is compared in Figure 6.23. Without foam antenna, the bandwidth is 0.6% (35 MHz) and with foam bandwidth it increased to 4.8% (280 MHz), which is an 8 times increase. This patch element is used in an array configuration to design a broadband antenna array.

6.8 Millimeter-Wave Antenna Array for Automotive Radar

The collision avoidance radar is one of the most important components of the advanced vehicle control and safety system in the future Intelligent Transport System (ITS) for the millimeter-wave ultrawideband (UWB) applications such as short-range radar (SRR) for vehicles. The radar system operating at a millimeter-wave band has the advantages of better resolution and higher data rates if compared with applications in the lower-frequency spectrum. The operation frequency of an automotive radar system is typically in the 59–61-GHz and 76–77-GHz bands for frequency-modulated continuous wave (FMCW) or pulse-Doppler operation. The higher bandwidth allows for W-band UWB systems with improved distance resolution. Microstrip antenna arrays are the most common choice in many antenna types because of their lower profile and price for automotive applications as shown in Figure 6.24.

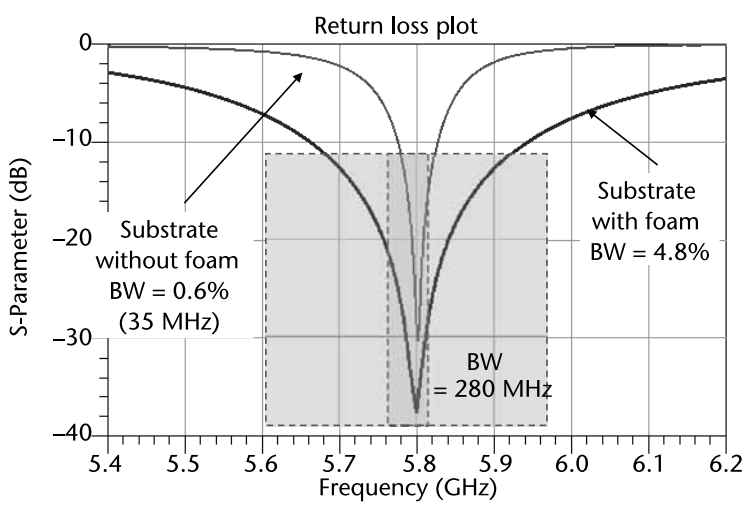

Figure 6.23 Return loss plot of antenna with and without a foam layer.

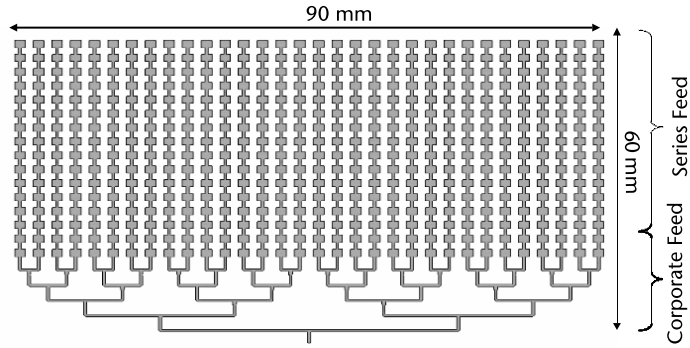

Figure 6.24 Designed millimeter-wave 32 × 16 element antenna array.

6.8.1 Equivalent Model of a Series-Fed Antenna Array

The series-fed array antenna consists of several parallel arranged and serially fed patch rows, which are supplied by a corporate feed network as shown in Figure 6.24. The linear array is composed of two components, the feedlines and the patches. This arrangement reduces the feed line lengths and parasitic radiation. Sometimes the aperture distribution is tapered to meet the desired side lobe suppression. The taper is realized by varying the patch width along the rows and using suitable power dividers in the corporate feed network. Derneryd's transmission line model of a series-fed patch array antenna is shown in Figure 6.25 [47]. In this model, the microstrip patch element is represented by two radiating slots, which are separated by a transmission line. The radiating slot is modeled as a conductance G and a susceptance B in parallel, representing the radiation and the fringing fields, although this model is not accurate when the number of patch elements in the array

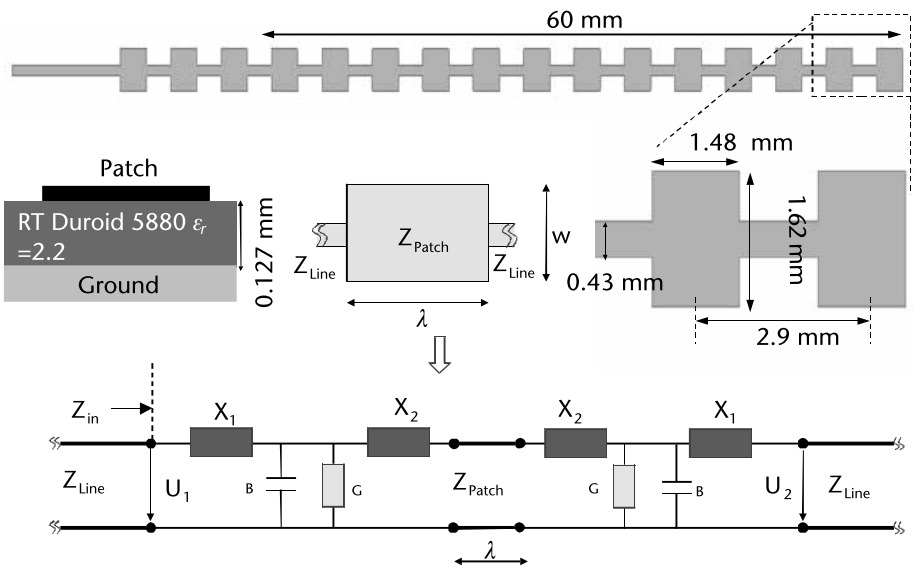

Figure 6.25 Series-fed linear array design and electrical equivalent circuit model.

is large. To improve this model, the step-in width between the feeding line and the patch is represented by two additional reactances X_1 and X_2. Using the MoM simulated scattering parameters, the parameters X_1, X_2, B, G, and λ of the mode can be extracted.

To achieve the broadside radiation pattern, the elements must be in phase, which means that the phase difference between two elements must be 360°. The array would be resonant at the center frequency, so the equivalent circuit of the array can be simplified to n radiation conductance in parallel or n radiation resistances in series (n is the number of patches).

6.8.2 Series-Fed Antenna Array Design

In the millimeter-wave frequency band, the series-fed method is better than the parallel-fed method because of the simple feeding network and low insertion loss. For that reason, the series-fed method has been more widely adopted in millimeter-wave radar. This feeding concept enables beam steering in one direction in an easy way and a minimal spacing. In the millimeter-wave band, the loss of microstrip structure becomes considerable with frequency increasing [48]. To minimize the loss at high frequency, a series-fed method is often chosen to minimize and simplify the feed network for the antenna array. Series feed network has some advantage compared to corporate feed such as compact size, low loss, and lower sidelobe level, but it also has certain disadvantages such as narrow bandwidth and antenna beam tilt with frequency.

The linear array of 16 elements with –20-dB sidelobe is designed at the desired center frequency 60 GHz according to the resonant principle [49]. A planar array of a low sidelobe level is realized with the combination of 16 linear subarrays with certain power distribution. The excitation distribution is designed by the T-junction feed network. The characteristic impedance of feedline is calculated for 50Ω line. The array is printed on the substrate Rogers RT Duroid 5880 (0.127-mm thickness and dielectric constant = 2.2). Linear array antenna dimensions are shown in Figure 6.25. A single 60-GHz radiating patch size is 1.48 mm × 1.62 mm. The series feed line width is 0.43 mm for all antenna elements. The linear array antenna performance results are shown in Figure 6.26. The antenna gain is 18.6 dBi at 60 GHz and return loss is better than –10 dB over the band. The bandwidth of antenna is 30 MHz (0.05%). The antenna half-power beamwidth in the $\varnothing = 0^\circ$ plane is 40°, while in the $\varnothing = 90^\circ$ plane the half-power beamwidth is 76°. The antenna simulation summary for different array sizes is given in Table 6.3.

The planar antenna array is constructed by using 64 linear arrays fed with a corporate microstrip feed network as shown in Figure 6.27. The antenna resonance frequency is at 60.1 GHz. The half-power beamwidth is the same in the elevation direction as of the linear array because there is no change in the number of radiating elements (16 elements) in this direction.

6.9 Conformal Printed Antennas

In many applications such as a missile, satellite, spacecraft, and aircraft, a directive antenna mounted on a curved body is required. In the case of mobile

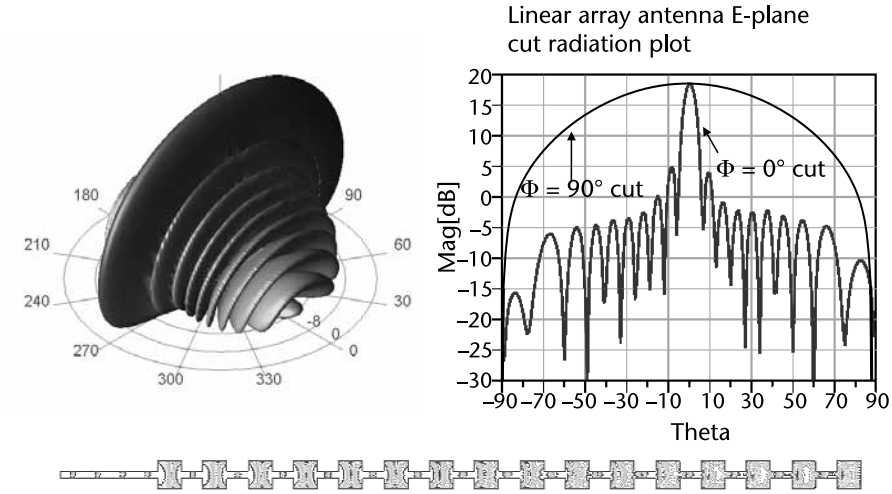

Figure 6.26 E-field and radiation pattern plot of a linear antenna array.

Table 6.3 Summary of the Antenna Array

Array Type	*Array Size (Elements)*	*Total Elements*	*Gain (dBi)*	*HPBW (Degrees)*
Linear	1 × 16	16	9.7	76 and 4
Planar	2 × 16	32	13.1	38 and 4
Planar	4 × 16	64	19.4	18 and 4
Planar	8 × 16	128	25.1	8.5 and 4
Planar	16 × 16	256	30.2	4 and 4
Planar	32 × 16	512	32.8	2 and 4

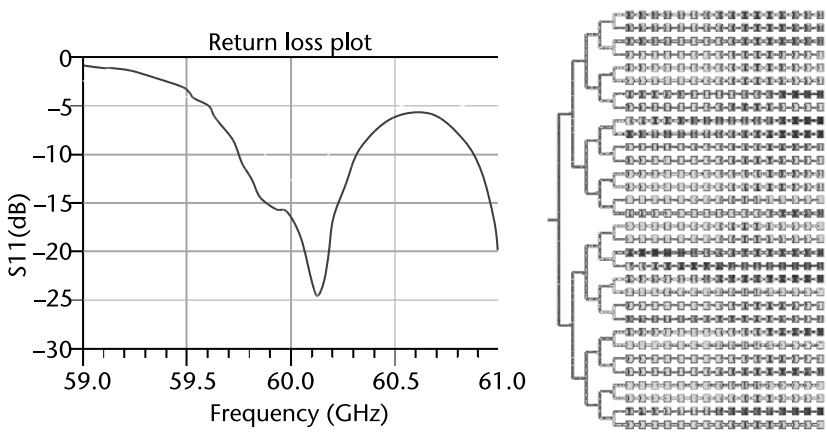

Figure 6.27 Antenna return loss plot and E-field plot on 32 × 16 element array.

communications with small vehicles, a large planar surface to dispose of microstrip array antennas is generally not available, and it is necessary to use conformal arrays. Conforming the antenna according to the application surface saves space and is often essential for structural reasons. Specifically, these radiators can become

integrated with the structures on which they are mounted and, consequently, do not cause extra drag and are less visible to the human eye. In addition, the fast-progressing development of high-frequency applications for telecommunications and navigation in automotive, aeronautics, and space increases the need for antennas, which can be integrated seamlessly into predefined structures. For both applications, conformal antenna arrays are excellently qualified. Compared to planar antennas, their steering range is significantly larger and the microstrip technology offers the possibility of manufacturing antennas as a compact building block fitting into nearly arbitrary structures. The conformal antenna can be placed in the belly of aircraft that eliminate separate radome design for the antenna. Besides this, shaping and resolution can be improved by using the conformal antenna as more elements can be accommodated. Another important feature of conformal antennas is their radiation characteristics. These antennas usually provide broader beams than their planar counterparts. This feature is an advantage when omnidirectional patterns are required, which normally are achieved by applying an array. Conformal antennas can be any geometrical shape, although the main structures investigated so far are spherical, cylindrical, and conical.

Microstrip antenna technology is the most suitable for conformal applications because of its ability to conform to nonplanar structures. Antenna patches are placed above the device's conducting plane with a dielectric substrate separating the patch from the conducting plane. The properties of conformal array depend strongly on whether it is small compared to the radius of curvature of the mounting body, in which case it behaves nearly like a planar array or whether it is comparable or large to the radius. In many conformal antennas, the resonance frequency is the same for various curvatures. However, as curvature increases, the pattern broadens.

In conformal antennas, the effect of curvature on the performance of conformal microstrip antennas on cylindrical bodies for the TM_{10} mode is very important. Curvature affects the fringing field and the fringing field affects the antenna parameters. Conformal antennas find a lot of applications in the aerospace defense system because of space limitations. The development of efficient design techniques for conformal microstrip radiators, assisted by computational EM tools, is desirable to establish clear procedures that bring about reductions in computational time, along with high accuracy results. Nowadays, the commercial availability of high-performance 3-D EM tools allows computer-aided analysis and optimization that replace the design process based on an iterative experimental modification of the initial prototype.

6.9.1 Patch Antenna Printed on Circular Cylindrical Structure

Antennas on a uniform curved surface are the simplest conformal antennas. The main objective of such an antenna is to improve the azimuth coverage, obtaining even in some cases omnidirectional coverage. The circular cylindrical antenna is frequently used in conformal antenna applications since it is one of the most straightforward nonplanar geometry. Design and analysis of radiating the microstrip patch antenna mounted on a cylindrical surface are discussed in this section. A conformal patch antenna design procedure involves parameters related to cylindrical microstrip elements to realize the desired resonant frequency, input impedance, and

radiation patterns. The analysis and synthesis of the conformal array are slightly more complicated than a linear array with uniform spacing because the array elements point in different directions.

6.9.1.1 Cylindrical Microstrip Antenna Analysis for Large Radii

The circular cylindrical microstrip patch wrapped around a grounded dielectric cylinder is shown in Figure 6.28. It is fed by an inset feedline. The antenna is optimized for 5.7 GHz. The parameters of the antenna are: relative permittivity of the substrate $\varepsilon_r = 2.2$, the diameter of the ground plane cylinder = 40 mm, and length and width of the patch = 18.27 mm. A microstrip line is used to feed the patch antenna. Antenna design specifications are given in Table 6.4.

RT Duroid of thickness 0.5 mm and relative permittivity of 2.2 are used as a substrate material for antenna design. Two options are designed, one along the curvature of the cylinder and other along the axial direction of the cylinder as shown in Figure 6.28. The antenna design was first simulated for the planer and subsequent simulation was performed for the cylindrical surface having radius of 20 mm. As for bending increases, the performance of the antenna for conformal surface degrades.

Table 6.4 Antenna Design Specifications

Design Parameters	*Value*
Design frequency	5.7 GHz
Patch antenna dimensions	18.27 × 18.27 mm
Substrate thickness	0.5 mm
Substrate permittivity	2.2
Substrate loss tangent	0.009
Radius of cylinder	20 mm

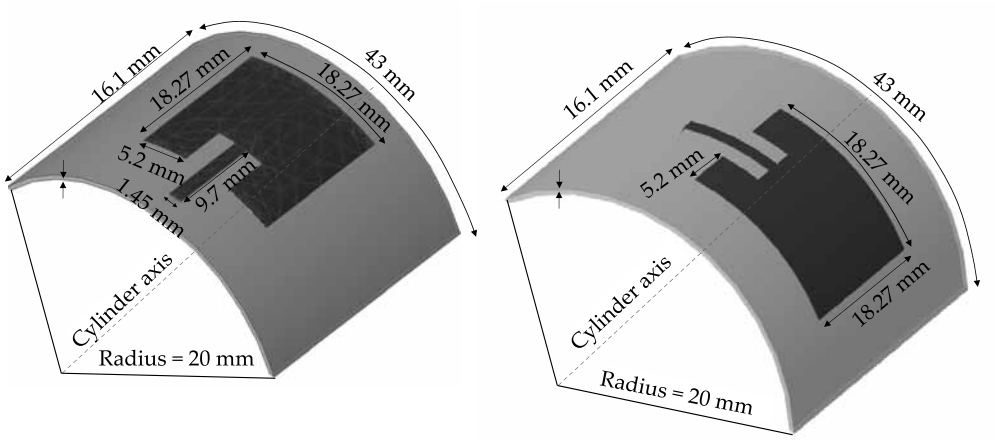

Figure 6.28 Conformal microstrip patch antenna along the axial direction and along the curvature of the cylinder.

The comparison of the return loss (S_{11}) graph shows that an increase in array size results in significant changes in frequency in conformance to the planar antenna due to the effect of curvature and mutual coupling because of interelement spacing. The effect of the curvature of the conformal antenna on resonant frequency been presented by Krowne [50] as:

$$[f_r]_{mn} = \frac{1}{2\sqrt{\mu\epsilon}}\sqrt{\left(\frac{m}{2\theta a}\right)^2 + \left(\frac{n}{2b}\right)^2} \tag{6.13}$$

where a is a radius of the cylinder, $2b$ is a length of the patch antenna, 2θ is the angle bounded the width of the patch, ϵ represents electric permittivity, and μ is the magnetic permeability as shown in Figure 6.29.

In most of the cases, the analysis of conformal antennas can be based on approximate techniques, and when the antenna has very large radii of curvature, it may be often analyzed as if it were planar. To analyze the characteristics of cylindrical patch antennas, the cavity model approach is suitable only for very thin substrate cases. Full-wave analysis is the most accurate approach for conformal antenna analysis. The knowledge of the mutual coupling among the radiating elements and the radiation patterns of individual elements are essential ingredients for conformal antenna analysis. The EM field on the surface of the antenna is calculated to find other performance parameters of the antenna, such as radiation pattern.

The simulation results are collected for different radii of the cylinder. The return loss does not have a substantial variation in the frequency band, and the overall variation is only 3 to 4 dB. The antenna gain is varying 0.8 dBi when the patch is placed along the curvature of the cylinder by increasing the cylinder radius from 15 mm to 40 mm. The gain variation is 1 dBi when the patch is placed along the cylinder axis. The simulated gain of the single element over different radii of the cylindrical surface is shown in Table 6.5.

It is observed that gain of the single radiator is more when the feed is along the axis of the cylinder. Also, there is an increase in gain with an increase in the radius of the cylinder. The antenna is simulated using FEM simulation techniques. Return loss comparison of the conformal antenna with planar antenna configuration is shown in Figure 6.30. There is slight resonance frequency shift at a higher frequency when the antenna is placed along the cylinder axis while the resonance

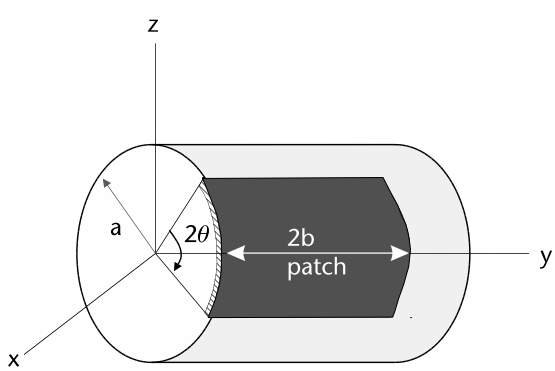

Figure 6.29 Geometry of cylindrical-rectangular patch antenna.

Table 6.5 Gain Comparison of the Antenna with Feedline Position over the Cylinder

Radius of Cylinder (mm)	*Gain of Patch Fed Along the Curvature of Cylinder (dBi)*	*Gain of Patch Fed Along the Axis of Cylinder (dBi)*
15	6.2	6.4
20	6.6	6.8
30	6.8	7.4
40	7.0	7.4

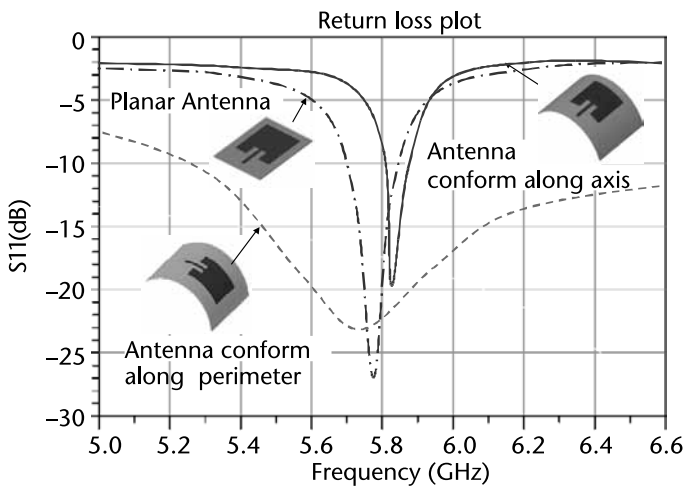

Figure 6.30 Simulated antenna return loss plot planar microstrip and conformal antennas.

frequency shifted at the lower side when the antenna was placed along the perimeter of the cylinder.

The comparison of the E-field radiation patterns can be seen in Figure 6.31. In the $\phi = 0^\circ$ plane, shown in Figure 6.31(a), the radiation from the doubly curved geometries is broader since there is a curved surface, whereas, for the singly curved geometries, it is straight. Typically, singly curved geometries are theoretically analyzed with the infinite ground plane, so it is an infinite long cylinder in the case of cylindrical antennas. In the elevation plane, the antennas are considered as an infinite planar antenna, not allowing back radiation and presenting very narrow beamwidth. In the $\theta = 90^\circ$ plane, this conformal antenna has the same curvature of $0.3\lambda_0$. As illustrated in Figure 6.31(b), that leads to approximately the same beamwidth in the hemisphere of maximum radiation. The beam in the elevation plane is narrow, while the beam is relatively broad in the plane around the cylinder axis in the hemisphere where the patch is located.

6.9.1.2 Cylindrical Microstrip Antenna Analysis for Small Radii

A conformal patch antenna has a very different performance when the radius of the cylinder is less, and the cylinder circumference is comparable to the antenna size as shown in Figure 6.32. For small radii, the size of the antenna does not match

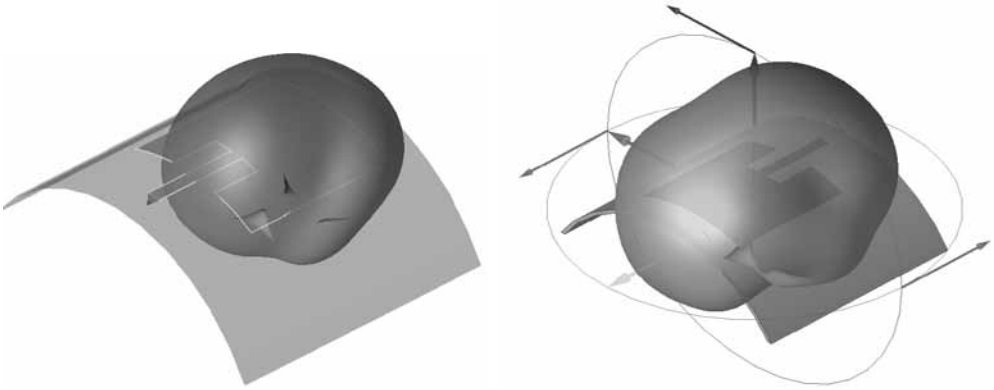

(a) (b)

Figure 6.31 Conformal microstrip patch antenna radiation pattern: (a) antenna along the axial direction of cylinder and (b) antenna along the curvature of the cylinder.

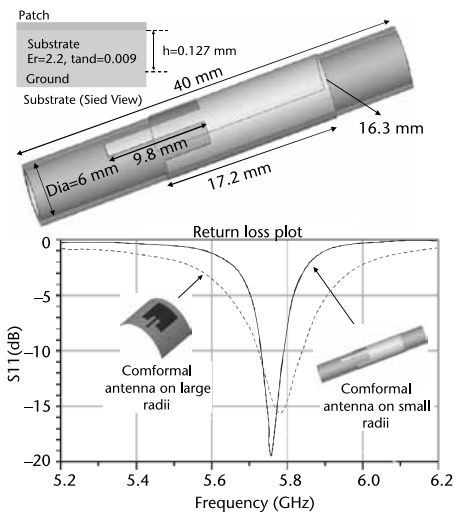

Figure 6.32 (a) Patch antenna mounted on small radii cylinder and (b) antenna return loss plot.

exactly with that of the planar since the effects of the curvature are more significant. When the radius of the curved structure is large, the antenna can be analyzed as the planar one, although for a structure with smaller radii, more rigorous analysis methods should be used. Cylindrical conformal structures, with radii greater than one half-wavelength, are used as prospective candidates for mobile communications systems, cellular base stations, and Telemetry and Telecommand (TTC) communication that is essential to maintain space missions due to their full field of view advantage [51]. The simulations for small radii antenna are performed based on the full-wave analysis.

Nearly omnidirectional patterns using a single radiating element are achieved with wraparound patch antennas in the azimuth direction, while patch has dipole-like radiation patterns in the plane that include the length of the cylinder, resulting in almost null radiation in that direction as shown in Figure 6.33.

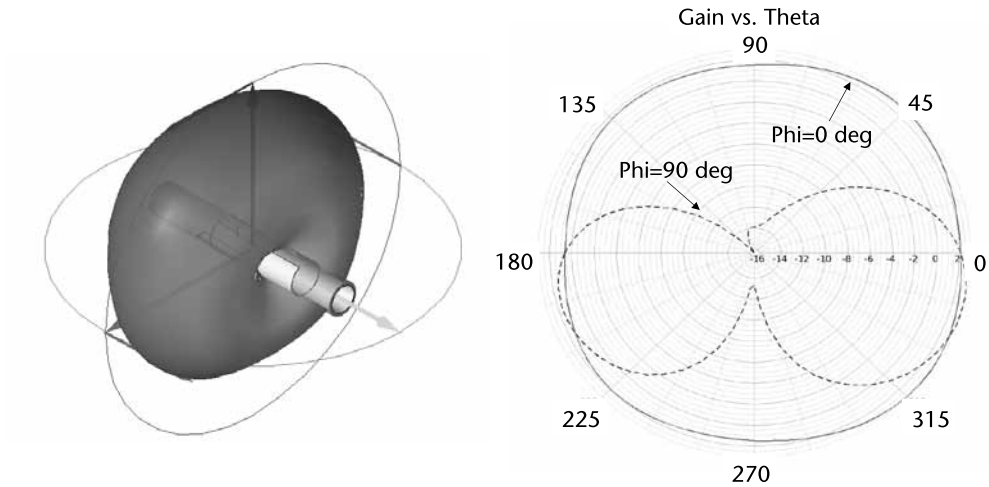

Figure 6.33 Small radii conformal microstrip antenna 3-D and 2-D radiation patterns.

6.9.2 Antenna on Missile Surface

The high-speed airborne craft, rocket, and satellite require the antenna to neither influence their air motive force performance nor destroy their mechanical structure and intensity. The moving missile is required to realize the data transmission between the missile and the launcher for the high-precision attack. It leads to how to effectively design the missile antennas when considering the least disturbance to the flight dynamics and to the air frame structure. It should have a low profile and can be mounted on the surface of a missile. Obviously, the cylindrically conformal antenna is the preferred choice. Such kinds of antennas have always been the focus of the research, and several forms of practical antennas were reported, such as the printed dipole [52], microstrip patch [53, 54], printed slot, and substrate integrated waveguide (SIW) antennas [55]. Antenna performance such as gain can be controlled by varying the shape of the conformal antennas. It is possible to reach nearly omnidirectional coverage, while, with planar antennas, the almost full coverage is limited to approximately ±60°.

Conformal antennas also have certain drawbacks. The major disadvantages are the increased design complexity and costs in the manufacturing of conformal antennas on an arbitrary shape. In addition, their size is restricted when a package of electronics is desired because they cannot be included in strongly curved structures. The technology of conformal antennas is not as fully established as it is for the planar ones, because many of their analysis tools are still in development. As discussed previously, for very large radii, conformal antennas can be considered as planar ones for analysis simplification, so their performance would be very similar to planar antennas. However, for small radii, planar design techniques cannot be applied and the designed rules are not established. Furthermore, circular polarization is more difficult to achieve in curved structures with the inconvenience that the maximum values of XPD are lower than for their planar counterparts. In a missile system, a main important characteristic of the antenna is its radiation pattern. The anti-interference and anti-multipath effect ability of antennas can be improved by utilizing the directionality.

For the high-speed whirling cylindrical carrier as the guided missile, its request for the antenna is to produce the isotropic radiation pattern in the plane that is perpendicular to the axis of the missile approximately, but in the plane that includes the axis of the missile, the radiation pattern should be offered as the hemisphere beam. For this purpose, different kinds of cylindrical conformal antennas should be adopted for different diameters of cylinders separately. The missile tracking system works at 2.4 GHz by using position data from the onboard GPS receiver and/or Inertial Navigation System (INS). Apart from the GPS antenna, the extra high gain antenna in the missile can serve many purposes. It can be used when the main guidance is not yet fully developed or when GPS is automatically cut off at any cruise speed over 1.5 mach. It can also be used for sending various missile parameter and monitoring data to the ground control station or sending the video signal from a camera attached to the head of the missile to the ground for visual guidance purposes. A microstrip conformal microstrip patch antenna array is designed at 2.4 GHz using series-fed 8 × 8 elements as shown in Figure 6.34. The antenna array is mounted on the body of 4.3-m-long missile system. The diameter of missile body is 100 mm. The antenna length is 815 mm and a total number of elements is 64 in an 8 × 8 array. The antenna simulation data and radiation pattern are shown in Figure 6.35.

6.9.3 Conformal Microstrip Antenna Array Fed with Waveguide

In high-power applications, the antenna input signal is distributed to subarrays of microstrip antennas. Among all microwave transmission lines, waveguides feature extremely low losses up to very high frequencies and can handle high power, provided that their internal surfaces are finished smoothly. Figure 6.36 shows a 220-element, waveguide-fed, microstrip patch array. To reduce the feed loss and cater to

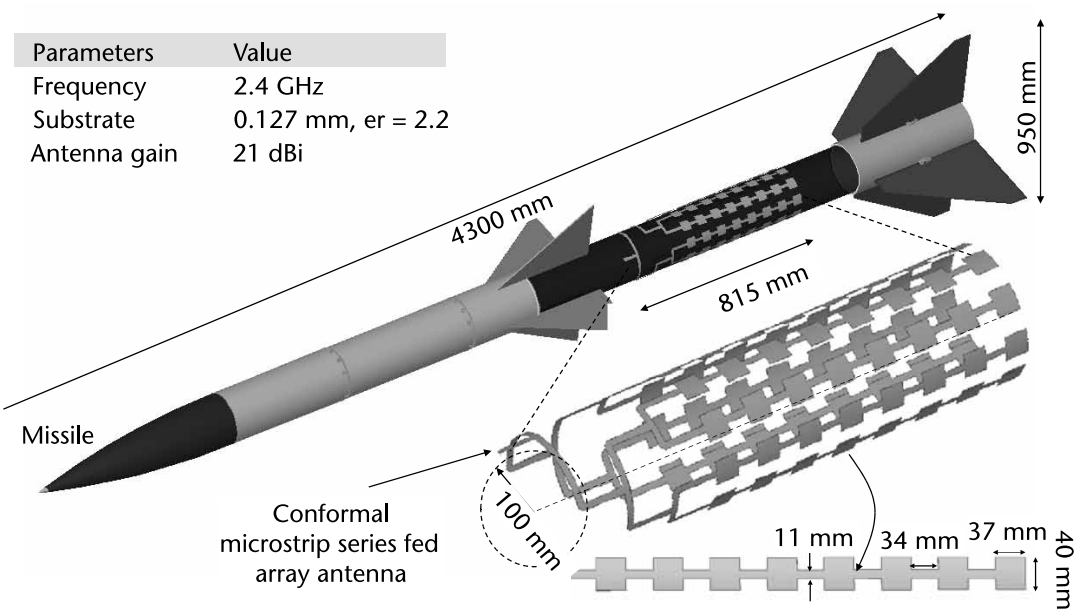

Figure 6.34 Conformal series-fed microstrip antenna array mounted on the missile.

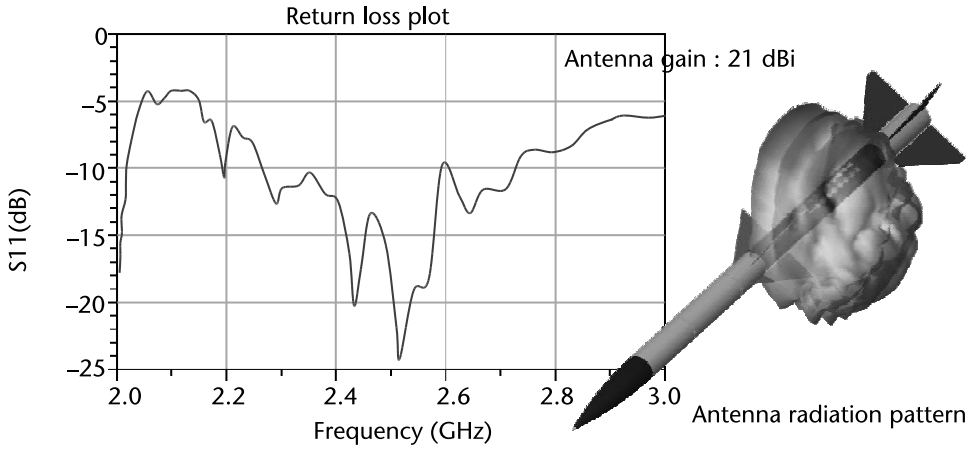

Figure 6.35 Return loss and radiation pattern plot of a conformal antenna mounted on the missile surface.

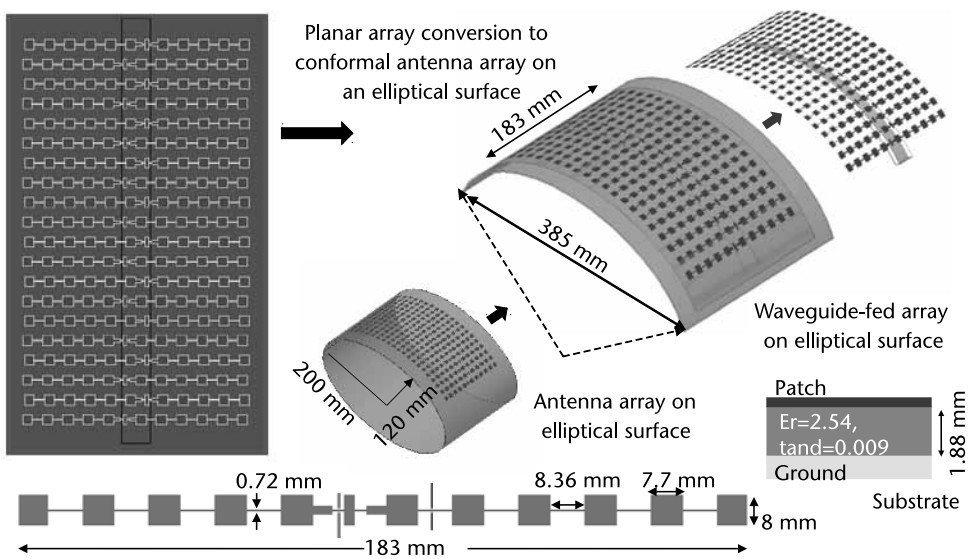

Figure 6.36 Large waveguide-fed conformal antenna array on an elliptical surface.

the high-power requirement, a slotted waveguide is used instead of the main feed line to feed the microstrip patch array. First, a rectangular microstrip patch antenna array is designed and optimized, and then this geometry is conformed over an elliptical curved surface and the design is reoptimized. As resonant frequency does not significantly change with a curved surface, the same dimensions of the patch of the planar surface are modeled over an elliptical surface. The width of the feed lines and the patch dimensions are calculated in the same way as the microstrip planar antenna array.

To simplify the manufacturing procedure, the slots of the waveguide are etched on the ground plane of the dielectric substrate, and the etched ground plane serves as the upper wall of the waveguide. A coaxial probe at the center of the bottom wall of the waveguide is used to excite the slotted waveguide. The two ends of the

waveguide are shorted. After optimizing the rectangular array, this is converted in conformal antenna array as shown in Figure 6.36.

The main advantage of this center-fed array structure is that it avoids beam squint with frequency. This array of a waveguide-fed microstrip antenna can be used in many modern communication systems, such as a mobile base station antenna. The resonant frequency is 11.5 GHz and the gain of the array is more than 30 dBi.

6.10 Summary

In this chapter, several applications of microstrip antenna arrays were presented and discussed. Microstrip antenna array concepts with an application such as rainfall and weather radar antenna, automotive antennas were covered in this chapter. One of the major benefits of microstrip antennas is the simplicity of array construction. Millimeter-wave microstrip antenna arrays with high efficiency are designed for automotive radar. A feed network is the most important design aspect in microstrip antenna. The efficiency of microstrip antenna arrays may be improved significantly by reducing losses in the feed network. Microstrip antennas are narrowband antennas, but there are several techniques to increase the bandwidth of the array antenna. The power radiated from a discontinuity may be evaluated from the computed S-parameters using the full-wave analysis technique. The gain limitation in microstrip antenna arrays can be overcome by employing active microstrip arrays. In some applications, the reflect arrays are employed. In reflect arrays, the received power is transmitted by the same antenna array. The optimization of the antenna structure and feed network dimensions allows maximizing the power rate dissipated on the load. The feed network design is the most important and critical design step in the array antenna. Depending on the application, the proper feed topology or a combination of multiple feed schemes can be selected. Several array antenna feeding techniques, including the most popular corporate and series feed, were discussed. Rainfall radar antenna array was discussed step by step to explain the complete design process and associated challenges in the planar array antenna. To overcome the bandwidth limitation of convention microstrip antennas, the broadbanding technique is applied. One such scheme is the multilayer stacking of the patch element. In the next chapter, phased array antennas are discussed.

References

[1] Pozar, D. M., "Microstrip Antennas," *IEEE Proc.*, Vol. 80, January 1992, pp. 79–91.

[2] Schaubert, D. H., "Microstrip Antennas," *Electromagnetism*, Vol. 12, 1992, pp. 381–401.

[3] Pozar, D. M., and D. H. Schaubert, *Microstrip Antennas: The Analysis and Design of Microstrip Antennas and Arrays*, New York: IEEE Press, 1995.

[4] Liu, Y., et al., "RCS Reduction of a Patch Array Antenna Based on Microstrip Resonators," *IEEE Antennas and Wireless Propagation Letters*, Vol. 14, 2015, pp. 4–7.

[5] Alhalabi, R. A., and G. M. Rebeiz, "High-Efficiency Angled-Dipole Antennas for Millimeter-Wave Phased Array Applications," *IEEE Transactions on Antennas and Propagation*, Vol. 56, No. 10, October 2008, pp. 3136–3142.

[6] Khan, O., et al., "Hybrid Thin Film Antenna for Automotive Radar at 79 GHz," *IEEE Transactions on Antennas and Propagation*, Vol. 65, No. 10, October 2017, pp. 5076–5085.

[7] Sun, D., and L. You, "A Broadband Impedance Matching Method for Proximity-Coupled Microstrip Antenna," *IEEE Transactions on Antennas and Propagation*, Vol. 58, No. 4, April 2010, pp. 1392–1397.

[8] Zhang, L., W. Zhang, and Y. P. Zhang, "Microstrip Grid and Comb Array Antennas," *IEEE Transactions on Antennas and Propagation*, Vol. 59, No. 11, November 2011, pp. 4077–4084.

[9] Li, Y., et al., "A Fixed-Frequency Beam-Scanning Microstrip Leaky Wave Antenna Array," *IEEE Antennas and Wireless Propagation Letters*, Vol. 6, December 2007, pp. 616–618.

[10] Hamberger, G. F., et al., "A Planar Dual-Polarized Microstrip 1-D-Beamforming Antenna Array for the 24-GHz Band," *IEEE Transactions on Antennas and Propagation*, Vol. 65, No. 1, January 2017, pp. 142–149.

[11] Bilgic, M. M., and K. Yegin, "Wideband Offset Slot-Coupled Patch Antenna Array for X/Ku-Band Multimode Radars," *IEEE Antennas and Wireless Propagation Letters*, Vol. 13, 2014, pp. 157–160.

[12] Shen, T. M., et al., "Antenna Design of 60-GHz Micro-Radar System-in-Package for Non-contact Vital Sign Detection," *IEEE Antennas and Wireless Propagation Letters*, Vol. 11, 2012, pp. 1702–1705.

[13] Nilsson, E., and L. Baath, "Radar Interferometric Measurements with a Planar Patch Antenna Array," *IEEE Sensors Journal*, Vol. 7, No. 7, July 2007, pp. 1025–1031.

[14] Di Bari, R., et al., "Dual-Polarized Printed S-Band Radar Array Antenna for Spacecraft Applications," *IEEE Antennas and Wireless Propagation Letters,* Vol. 10, 2011, pp. 987–990.

[15] Tanyer-Tigrek, F. M., I. E. Lager, and L. P. Ligthart, "A CPW-Fed Printed Loop Antenna for Ultra-Wideband Applications, and Its Linear-Array Performance," *IEEE Antennas and Propagation Magazine*, Vol. 52, No. 4, August 2010, pp. 31–40.

[16] Menzel, W., and A. Moebius, "Antenna Concepts for Millimeter-Wave Automotive Radar Sensors," *Proceedings of the IEEE*, Vol. 100, No. 7, July 2012, pp. 2372–2379.

[17] Chou, H. T., M. Y. Lee, and C. T. Yu, "Subsystem of Phased Array Antennas with Adaptive Beam Steering in the Near-Field RFID Applications," *IEEE Antennas and Wireless Propagation Letters*, Vol. 14, 2015, pp. 1746–1749.

[18] Haider, N., A. G. Yarovoy, and A. G. Roederer, "L/S Band Frequency Reconfigurable Multiscale Phased Array Antenna with Wide Angle Scanning," *IEEE Transactions on Antennas and Propagation,* Vol. 65, No. 9, September 2017, pp. 4519–4528.

[19] Lambard, T., et al., "Ka-Band Phased Array Antenna for High-Data-Rate SATCOM," *IEEE Antennas and Wireless Propagation Letters,* Vol. 11, 2012, pp. 256–259.

[20] Mohammed, J. R., "Phased Array Antenna with Ultra-Low Sidelobes," *Electronics Letters,* Vol. 49, No. 17, August 15, 2013, pp. 1055–1056.

[21] Chazelas, J., et al., "Potential Technological Breakthroughs for Phased Array Antennas," *IEEE Aerospace and Electronic Systems Magazine*, Vol. 24, No. 11, November 2009, pp. 22–27.

[22] Tanha, M., et al., "Overlapped Phased Array Antenna for Avalanche Radar," *IEEE Transactions on Antennas and Propagation*, Vol. 65, No. 8, August 2017, pp. 4017–4026.

[23] Babakhani, B., S. K. Sharma, and N. R. Labadie, "A Frequency Agile Microstrip Patch Phased Array Antenna with Polarization Reconfiguration," *IEEE Transactions on Antennas and Propagation,* Vol. 64, No. 10, October 2016, pp. 4316–4327.

[24] Croq, F., and A. Papiernik, "Large Bandwidth Aperture Coupled Microstrip Antenna," *Electronics Letters*, Vol. 26, August 1990, pp. 1293–1294.

[25] James, J. R., and P. S. Hall, *Handbook of Microstrip Antennas*, Stevenage, UK: IEE Electromagnetic Waves Series 28, 1989.

[26] Josefsson, L., and P. Persson, "Conformal Array Antenna Theory and Design," *IEEE Antennas and Propagation Society*, Sponsor, 2006, pp. 15–40.

[27] Orfanidis, S. J., D. Ramaccia, and A. Toscano, "Electromagnetic Waves and Antennas," Dept. of Electrical and Computer Engineering, Rutgers University, Piscataway, NJ, 2002.

[28] Balanis, C. A., *Antenna Theory: Analysis and Design*, 3rd Edition, New York: John Wiley, 2005.

[29] Stutzman, W. L., and G. A. Thiele, *Antenna Theory and Design*, New York: Wiley, 1998.

[30] Lin, Y. -D., and S. -N. Tsai, "Coplanar Waveguide-Fed Uniplanar Bow-Tie Antenna," *IEEE Transactions on Antennas and Propagation*, Vol. AP-45, 2000, pp. 305–306.

[31] Topak, E., et al., "A Novel Millimeter-Wave Dual-Fed Phased Array for Beam Steering," *IEEE Transactions on Microwave Theory and Techniques,* Vol. 61, No. 8, August 2013, pp. 3140–3147.

[32] Kim, D., et al., "4 x 4-Element Corporate-Feed Waveguide Slot Array Antenna with Cavities for the 120 GHz-Band," *IEEE Transactions on Antennas and Propagation,* Vol. 61, No. 12, December 2013, pp. 5968–5975.

[33] Vosoogh, A., and P. S. Kildal, "Corporate-Fed Planar 60-GHz Slot Array Made of Three Unconnected Metal Layers Using AMC Pin Surface for the Gap Waveguide," *IEEE Antennas and Wireless Propagation Letters,* Vol. 15, 2016, pp. 1935–1938.

[34] Wilkinson, E. J., "An N-Way Hybrid Power Divider," *IRE Trans. Microwave Theory Tech.*, Vol. 8, January 1960, pp. 116–118.

[35] Lim, J. -S., et al., "A 4:1 Unequal Wilkinson Power Divider," *IEEE Microwave and Wireless Components Letters*, Vol. 11, No. 3, March 2001, pp. 124–126.

[36] De, D., et al., "Design and Analysis of Various Wilkinson Power Divider Networks for L Band Applications," *2016 3rd International Conference on Signal Processing and Integrated Networks (SPIN)*, Noida, 2016, pp. 67–72.

[37] Tourche, K., et al., "Design and Realization of a Two-Way Microstrip Wilkinson Power Splitter," *2017 Seminar on Detection Systems Architectures and Technologies (DAT)*, Algiers, 2017, pp. 1–5.

[38] Croq, F., and A. Papiernik, "Stacked Slot-Coupled Printed Antenna," *IEEE Microwave and Guided Wave Letters*, Vol. 1, October 1991, pp. 288–290.

[39] Ning, C. Z., and Y. W. C. Michael, "Broadband Planar Antennas: Design and Applications," *Institute for Infocomm Research*, Singapore, 2006.

[40] Shavit, R., "Dielectric Cover Effect on Rectangular Microstrip Antenna Array," *IEEE Transactions on Antenna and Propagation*, Vol. 42, 1994, pp. 1180–1184.

[41] Mohanna, S., and N. Ghassemi, "Wideband Aperture Coupled Microstrip Array Antennas for Radar Applications," *18th International Conference on Radar and Wireless Communications,* June 2010, pp. 1–2.

[42] Lau, K. L., K. M. Luk, and K. F. Lee, "Wideband U-Slot Microstrip Patch Antenna Array," *IEE Proc.-Microw. Antennas Propag.*, Vol. 148, No. 1, February 2001, pp. 41–44.

[43] Jung, C. W., and F. De Flaviis, "A Dual-Band Antenna for WLAN Applications by Double Rectangular Patch with 4-Bridges," *IEEE Antennas and Propagation Society International Symposium*, Vol. 4, June 2004, pp. 4280–4283.

[44] Egashira, S., E. Nishiyama, and A. Sakitani, "Stacked Microstrip Antenna with Wide Band and High Gain," *IEEE Antennas and Propagation Society International Symposium*, Vol. 3, May 1990, pp. 1132–1135.

[45] Pues, H. F., and A. R. Van De Capelle, "Impedance Matching of Microstrip Resonator Antenna," *Proceedings of the North American Radio Science Meeting*, Quebec, 1980, p. 189.

[46] Elsherbeni, A., et al., *Wideband Slot and Printed Antennas*, New York: Wiley, 2005.

[47] Derneryd, A., "Linearly Polarized Microstrip Antennas," *IEEE Transactions on Antennas and Propagation*, Vol. 24, No. 6, November 1976, pp. 846–851.

[48] Bhartia, P., K. V. S. Rao, and R. S. Tomar, *Millimeter-Wave Microstrip and Printed Circuit Antennas*, Norwood, MA: Artech House, 1991, pp. 52–55.

[49] Freese, J., et al., "Synthesis of Microstrip Series-Fed Patch Arrays for 77GHz-Sensor Applications," *Microwave Conference*, 2000.

[50] Krowne, C.M., "Cylindrical-Rectangular Microstrip Antenna," *IEEE Transactions on Antennas and Propagation*, Vol. AP-31, 1983, pp. 194–199.

[51] Geng, J. P., et al., "The Development of Curved Microstrip Antenna with Defected Ground Structure," *Progress in Electromagnetics Research,* Vol. 98, 2009, pp. 53–73.

[52] Wang, P., et al., "A Wideband Conformal Endfire Antenna Array Mounted on a Large Conducting Cylinder," *IEEE Transactions on Antennas and Propagation*, Vol. 61, No. 9, September 2013, pp. 4857–4861.

[53] Kulshrestha, S., et al., "Rectangular-Cylindrical Conformal Printed Antenna for SAR," *International Conference on Antenna Technology ICAT 2005*, Space Applications Center, Ahmedabad, ICAT-2005, February 2005, pp. 395–401.

[54] Sriharsha, C., et al., "Synthesis of Shaped Radiation Pattern for Conformal Antenna Array on Cylindrical Surface," *International Conference on Antenna Technology ICAT 2005*, Space Applications Center, Ahmedabad, February 2005, pp. 419–422.

[55] Bayraktar, O., and O. Aydin Civi, "Circumferential Traveling Wave Slot Array on Cylindrical Substrate Integrated Waveguide (CSIW)," *IEEE Transactions on Antennas and Propagation*, Vol. 62, No. 7, July 2014, pp. 3557–3566.

Selected Bibliography

Croq, F., and D. M. Pozar, "Millimeter Wave Design of Wide-Band Aperture Coupled Stacked Microstrip Antennas," *IEEE Transactions on Antennas and Propagation*, Vol. 39, December 1991, pp. 1770–1776.

Geng, J. P., et al., "The Development of Curved Microstrip Antenna with Defected Ground Structure," *Progress in Electromagnetics Research*, Vol. 98, 2009, pp. 53–73.

Josefsson, L., and P. Persson, "Conformal Array Antenna Theory and Design," *IEEE Antennas and Propagation Society*, Sponsor, 2006, pp. 15–40.

Mueed, A., J. D. Xu, and G. Mehdi, "Cavity Backed Embedded Antenna on Cylindrical Surface for Conformal Applications," *Proc. 14th IEEE INMIC*, December 2011, pp. 351–356.

Quan, X. L., et al., "Analysis and Design of a 45° Slant-Polarized Omnidirectional Antenna," *IEEE Transactions on Antennas and Propagation*, Vol. 62, No. 1, January 2014, pp. 86–93.

Wang, P., et al., "A Wideband Conformal Endfire Antenna Array Mounted on a Large Conducting Cylinder," *IEEE Transactions on Antennas and Propagation*, Vol. 61, No. 9, September 2013, pp. 4857–4861.

CHAPTER 7

Antenna Arrays for Microwave Sensing and Imaging

7.1 Introduction

Large-scale airborne and spaceborne phased arrays are one of the most important enabling techniques for remote microwave sensing and imaging (MSI). SAR is widely used for MSI within the aerospace and defense applications. It provides day-and-night and weather-independent images for civil and military applications. The antenna plays an important role in the SAR systems, and many kinds of antennas have been applied in SAR. For example, the microstrip patch antenna array was used first in SeaSat-A, which was launched in 1978. The waveguide slots antenna array was used in SIR-C and Kosmos1870 subsequently. X-band SAR payloads with electronic beamforming system for all-weather spaceborne remote sensing or imaging are increasingly being deployed by the small satellite industry, especially with the availability of commercial off-the-shelf components [1]. Antenna researchers have been striving to develop suitable X-band wideband arrays with the dual-polarization property. One of the already-built X-band spaceborne SAR systems is TerraSAR-X [2], but the X-band dual-polarized slotted waveguide subarray employed in that system is bulky, expensive, and difficult to manufacture, thus making the subarray inappropriate for a low-cost small satellite. The use of SAR for remote-sensing applications is particularly suited for tropical countries. The microwave signal can penetrate rain, clouds, haze, fogs and precipitation with very little attenuation, thus allowing operation in unfavorable weather conditions that preclude the use of the visible/infrared system. SAR is an active sensor that provides its own source of illumination. As there is no dependency on sunlight, it can therefore operate day or night. These systems can illuminate with a variable look angle and can select wide area coverage. It has been shown to be very useful over a wide range of applications, including sea and ice monitoring, mining, oil pollution monitoring, oceanography, snow monitoring, and classification of Earth terrain. The potential of SAR in a diverse range of applications led to the development of several airborne and spaceborne SAR systems.

The spacecraft antenna design should meet the requirement of high-gain, wide bandwidth keeping weight as low as possible in the limited available space. The

necessary features of SAR devices include wide bandwidth, optimum-shaped radiation patterns, and high power. A SAR antenna system must be light-weight and low profile, so planar antennas are generally used in these systems. The bandwidth limitations of microstrip antennas can be overcome with multilayer-stacked, electromagnetically coupled printed antennas. Another limitation is associated with the power-handling capability of the microstrip patch antennas, and this cannot be overcome in the SAR system where a pulse peak power of several kilowatts is typically used. For these types of applications, a hybrid antenna where a feeder implemented in the waveguide or square coaxial line (SCL) can be used. High input power levels within the feeder networks are converted to lower-power levels by using cascaded power dividers. These distributed lower-power levels are then fed to a microstrip patch antenna. Square coaxial feed technology has volume and weight advantages over a waveguide feeder.

Medical imaging is an important tool for visualizing the interior of the body for clinical analysis and identifying any abnormality, usually in a noninvasive way. Using nonionizing EM waves at microwave frequencies for sensing and imaging for medical diagnosis is emerging as a low-cost and low health risk alternative to the imaging technologies. MSI offers a noninvasive way for the diagnosis of functional and pathological tissue conditions [3–5]. Sensing applications of microwave involve single point applications wherein microwave signals transmitted by an antenna are received by the same or a different antenna after reflection or scattering by tissues. In such a case, no 2-D or 3-D images are formed. Examples of such cases can be heartbeat detection or changes in the microwave signal caused because of the pathological accumulation of water in the brain called cerebral edema [6]. In the imaging applications, a map or an image either in 2-D or 3-D is formed that shows different tissue electrical properties or the location of strong scatterers that is usually a tumor inside the body.

7.2 Microwave Remote Sensing and Imaging

Because of their long wavelengths microwave signals have special properties that are important for remote sensing; compared to the visible and infrared, microwaves have special properties that are important for remote sensing. Longer-wavelength microwave signal can penetrate through cloud cover, dust, haze, and all but the heaviest rainfall as the longer wavelengths are not susceptible to atmospheric scattering, which affects shorter optical wavelengths. This property permits the detection of microwave energy under almost all weather and environmental conditions so that data can be collected at any time.

As shown in Figure 7.1, the two classes of sensors are passive and active. In passive sensors energy leading to radiation received comes from an external source (e.g., the Sun), and in active sensors energy is generated from within the sensor system and beamed outward, and the fraction returned is measured. Sensors can be nonimaging (measures the radiation received from all points in the sensed target, integrates this, and reports the result as an electrical signal strength) or imaging (the electrons released are used to excite or ionize a substance such as silver in film or a display). The most common form of imaging active microwave sensors is radar. The sensor transmits a microwave signal towards the target and detects

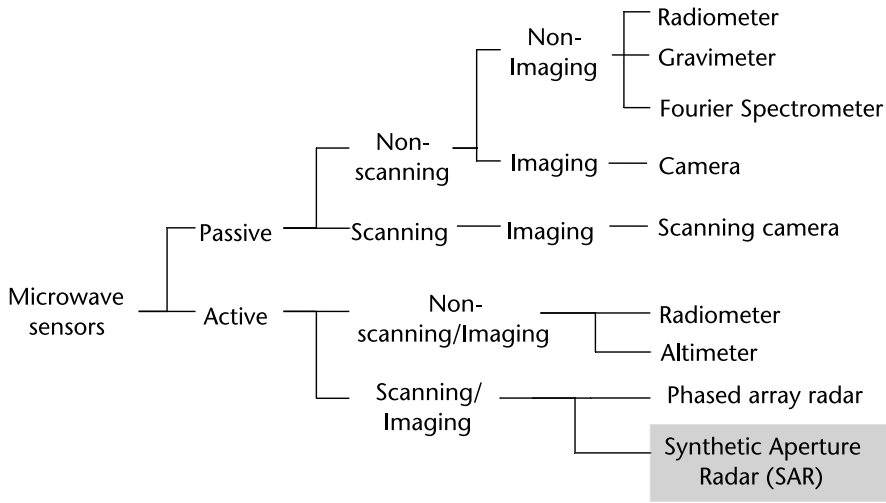

Figure 7.1 Type of microwave remote sensors.

the backscattered portion of the signal. The strength of the backscattered signal is measured to discriminate between different targets and the time delay between the transmitted and reflected signals determine the distance (or range) to the target. The SAR is an active imaging sensor.

7.2.1 Microwave Remote-Sensing Frequency Bands

As detailed in Figure 7.2, radar remote sensing uses the microwave portion of the EM spectrum, from a frequency of 0.3 GHz to 300 GHz. Microwave radars sense EM radiations in the microwave region of the EM spectrum. Most spaceborne radars operate at wavelengths between 0.5 cm and 75 cm. Shorter wavelengths such as X-band imagery are reflected from the top of the canopy, while longer wavelengths such as L-band imagery normally go down to the ground and are reflected from there.

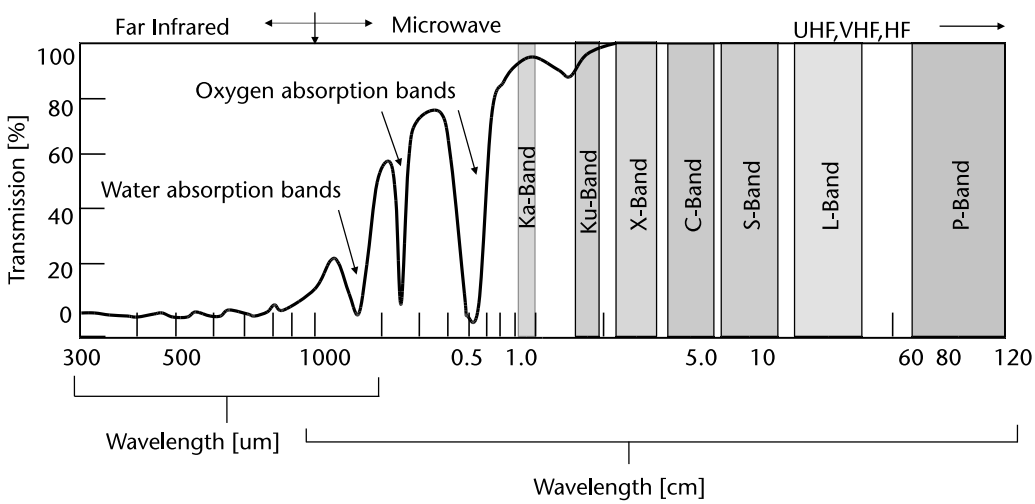

Figure 7.2 Frequency bands used in remote-sensing radars.

A remote-sensing radar system has three primary functions. It transmits microwave signals towards an area. It receives the part of the transmitted energy backscattered from the objects in that area and then it observes the strength (detection) and the time delay (ranging) of the return signals. Radar resolution is the ability of the radar to distinguish two objects in a frequency band. Spaceborne and airborne radar can collect data while flying over a large distance and then can process the data as if it came from a physically long antenna. Frequency bands commonly used in various kinds of radar applications are listed in Table 7.1

7.2.2 Antenna Polarization in Remote-Sensing Applications

Transmitted and received radar signals propagate in a certain plane called as the polarization. The propagation planes are typically horizontal (H) or vertical (V). Vertically polarized waves interact with the vertical stalks of the plant canopy, while horizontally polarized waves penetrate through plant canopy. The different combinations of the polarized wave provide different image characteristics:

- *Single polarization:* Both transmitted and received signals have the same polarization in a radar system.
- *Dual polarization:* The radar system has one polarization to transmit the signal and another polarization or both the polarizations to receive the signal.
- *Quad polarization:* Horizontal and vertical polarizations are used for alternate pulses to transmit the signal and with both simultaneously to receive the signal.

7.3 SAR

SAR is a radar system that utilizes the aircraft or satellite flight path of the platform to simulate an extremely large antenna or aperture electronically, and that generates high-resolution remote-sensing imagery. It uses polarized radiation and therefore can exploit polarization signatures of the imaged scatters for obtaining more information about the image. It has been widely used for Earth remote sensing for more than 40 years. It provides high resolution all the time and weather-independent

Table 7.1 Commonly Used Frequency Bands in Radar Remote Sensing

Band	*Frequency*	*Wavelength*	*Applications*
P	0.3–1 GHz	30–100 cm	Used for research and experimental applications; significant penetration capabilities
L	1–2 GHz	15–30 cm	Penetrates vegetation to support observations applications over vegetated surfaces for monitoring ice and glacier dynamics
S	2–4 GHz	7.5–15 cm	Used for medium-range metrological applications (e.g., rainfall measurement)
C	4–8 GHz	3.75–7.5 cm	Penetration capability of vegetation or solid is limited and restricted to the top layers; useful for sea-ice surveillance
X	8–12 GHz	2.4–3.75 cm	Widely used for military reconnaissance, mapping, and surveillance

images. These systems are used in many applications ranging from geoscience and climate change research, environmental and Earth system monitoring, 2-D and 3-D mapping, change detection, and security-related applications up to planetary exploration. SAR systems are based on a pulsed radar installed on a platform with a forward movement, and it has a side-looking imaging geometry. The radar system transmits EM pulses with high power and receives the echoes of the backscattered signal in a sequential way as shown in Figure 7.3.

The pulse repetition frequency typically ranges from a few hundred to a few thousand hertz for airborne and spaceborne systems, respectively. The swath width varies typically from a few kilometers to 30 km in the airborne case and from 30 to 500 km in the spaceborne case. The transmitted pulse interacts with the objects on the Earth's surface, and only a portion of this signal is backscattered to the receiving antenna. In a monostatic radar, the receiving antenna is the same as the transmit antenna and in a bistatic or multistatic radar, transmitting and receiving antennas are different. The microwave energy scattered back to the spacecraft is measured. The phase and amplitude of the backscattered signal depend on the physical properties (i.e., roughness, shape) and electrical properties (i.e., permittivity) of the imaged object. Depending on the operating frequency band, substantial penetration can occur to model objects as a volume (e.g., vegetation, ice and snow, dry soil). The simplest radar system provides a 2-D reflectivity map of the imaged area. High backscattered signals are identified as bright spots in the radar images and flat, smooth surfaces as dark areas. The direction of the flight is denoted as the azimuth and the line of sight is denoted as the slant range direction.

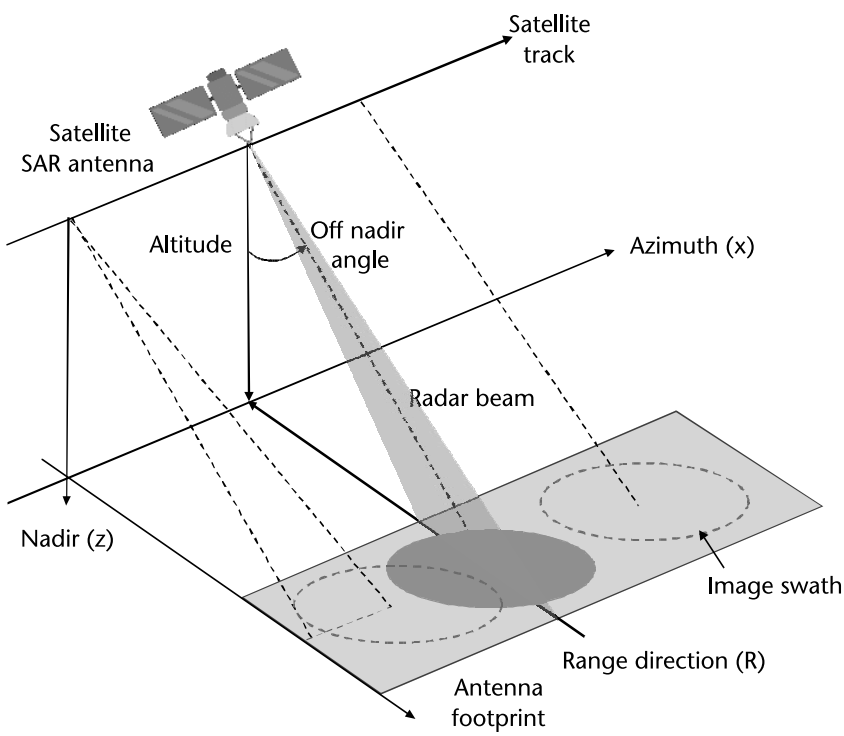

Figure 7.3 Imaging concept for a spaceborne SAR system.

The SAR makes use of the radar principle to form an image by utilizing the time delay of the backscattered signal. For high-resolution imaging of the Earth's surface, a very long antenna is required that is not feasible for a spacecraft to carry. To overcome this limitation, SAR capitalizes on the motion of the spacecraft to emulate a large antenna. The SAR processor stores all the radar returned signals as amplitudes and phases for the time T from one position to another position. With this stored data, it is possible to reconstruct the signal, which would have been obtained by an antenna of length vT, where v is the platform speed. With the changes in the line-of-sight direction along the radar platform trajectory, a synthetic aperture is produced by signal processing, which has the effect of lengthening the antenna. Making T large enough makes the synthetic aperture large, and hence a higher resolution can be achieved.

7.3.1 Antenna Types Used in SAR Systems

The antenna must be selected carefully to assure a good resolution for the SAR. Printed microstrip antennas are the most suitable choice for a SAR antenna. A variety of printed antennas, such as microstrip patch, microstrip printed dipole, and slot antennas, can be used as the radiating element. Printed antennas fulfill SAR requirements on the radiation pattern, polarization purity, return loss, and power-handling capability. A high antenna gain with a sharp pattern specification is preferable. The minimum width of the main lobe of the radiation pattern in azimuth (i.e., in the direction of flight) is determined by the required resolution. Generally, a SAR antenna would have a narrow beam in the azimuth direction and a wide-shaped beam in the elevation direction. The resolution in the azimuth direction is obtained using the Doppler shift caused by the movement of the aircraft. The radiation pattern in elevation (i.e., in the vertical plane perpendicular to the flight plane) must ensure a reasonably even illumination of the area to be mapped. Table 7.2 shows the antenna systems used in various SAR projects.

7.4 Dual-Polarized SAR Antennas Design

The design of a dual-polarized, lightweight, multilayer microstrip planar array antenna at 9.6 GHz for a remote-sensing application is discussed in this section. An 8 × 32 element dual-polarized printed planar antenna is designed using RT5870 and foam material. The foam material is sandwiched between the patch and the ground plane to improve the radiation efficiency and bandwidth performance in the limited space over the single-layer conventional microstrip patch antenna. Generally, impedance bandwidth of patch antennas varies from 2% to 3% for single-layer direct coupling or probe coupling [7–9] and can be further enhanced by coupling the power from the stripline through an aperture (slot) in the ground plane and/or printing patch effectively on the foam material whose dielectric constant is nearly equal to that of air [10–12]. In such a case, the feed network is isolated from the radiating element by a ground plane, which prevents spurious radiation. The resonant or nonresonant slot couples energy from the stripline to the patch. If the slot is resonant, it provides another resonance in addition to the patch resonance, resulting in an antenna with 10% to 15% impedance bandwidth. However, the resonant

Table 7.2 SAR Antennas Used in Various Projects

Name of the Project	*Frequency Band*	*Antenna Type*	*Gain*	*Beamwidth (Degrees)*	
				Az	*El*
NASA AIRSAR	P-band	Microstrip	14 dBi	19	38
	L-band	Microstrip	18 dBi	8	44
	C-band	Microstrip	24 dBi	2.5	50
DLR E-SAR	P-band	Microstrip	12 dBi	30	60
	L-band	Microstrip	17 dBi	18	35
	S-band	Microstrip	NA	20	35
	C-band	Microstrip	17 dBi	19	33
	X-band	Horn	17.5 dBi	17	30
CCRS C/X SAR	C-band	Horn	26 dBi	3.3	25
	X-band	Horn	28.5 dBi	1.4	26
NASDA X/L-band SAR	L-band	Microstrip	18 dBi	2.3	40
	X-band	Waveguide-slot	26.5 dBi	2.3	40
DCRS EMISAR	L-band	Microstrip	17.1 dBi	10	42
	C-band	Microstrip	26 dBi	2.4	31
Lynx	Ku-band	Dish	NA	3.2	7
PHARUS C-band SAR	C-band	Microstrip	NA	2.3	24

slot has a strong back lobe, which substantially reduces the gain of the antenna. The nonresonant slot has a better front-to-back ratio, which results in an improvement in efficiency with a narrow bandwidth. Hence, multilayer microstrip antennas are difficult to optimize when maximum efficiency is required in a limited allowable available space with the weight as low as possible.

The SAR antenna is designed as smaller units of subarrays. The typical design specification of a dual-polarized SAR antenna is given in Table 7.3. The single antenna radiating element configuration is shown in Figure 7.4, where patch and feed lines are printed on the same substrate and foam layer is sandwiched between

Table 7.3 Design Specifications of Dual-Polarized SAR Linear Antenna Array

Parameters	*Specifications*
Operating frequency	9.6 GHz
Bandwidth	200 MHz, 3.7%
Polarization	Perpendicular (VV)
Gain	14.6 dBi
Maximum antenna width	0.6m
Power	1W (continuous)
Impedance	50
Connection	Standard SMA coaxial 50Ω
Conformity	Planar surface mount
Elevation incidence	60°
Elevation beamwidth	40°–50°

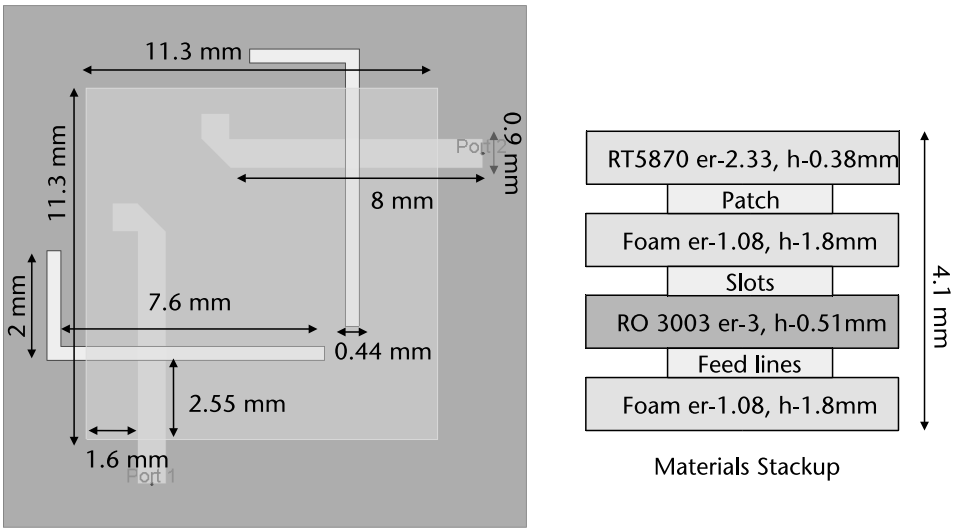

Figure 7.4 Dual-polarized multilayer microstrip antenna radiator.

the patch and the ground plane to improve radiation efficiency and bandwidth performance by reducing the effective dielectric constant of the combined sandwich layer. Terminating the patch with a high-impedance line can control spurious radiation from the feed-line network and cross-polar performance is improved by employing a proper phase cancellation technique. The design of the antenna begins with the proper selection of material, its dielectric constant, and the height of the substrate, which plays a crucial role when weight and gain should be optimized simultaneously.

A low dielectric constant, which enhances the radiation efficiency for the patch, can give rise to spurious radiation from the feed-line network where a generally high dielectric constant is usually preferred to confine the EM field. Foam material would be the best candidate for the patch, but it cannot be directly printed on foam material. The antenna is printed on RT Duroid 5870 with a dielectric constant of 2.33 and a height of 0.38 mm, while the feed line is printed on RO 3003 for mechanical rigidity and the electrical requirement of the feed line.

7.4.1 Design of Microstrip Patch Radiator

A strip-slot coupled patch has been used as a radiating element for wide bandwidth and low cross-polarization performance. The requirement of dual polarization can be fulfilled by selecting a square patch fed at two points to restore the symmetry of the structure. The MoM is used for predicting the impedance, cross-polarization, front-to-back ratio, and the bandwidth requirement to improve the efficiency of the antenna.

The propagation constant for a wave in the microstrip substrate must be accurately known to predict the resonant frequency, resonant resistance, and other antenna properties. The most sensitive parameter in microstrip antenna performance is the estimation of the dielectric constant of the substrate material, and that the manufacturer's tolerance on relative dielectric constant is sometimes inadequate.

The change in operating frequency of a thin substrate microstrip antenna due solely to a small tolerance related change of substrate dielectric constant may be expressed as:

$$\frac{\delta f}{f_0} = -\frac{1}{2}\frac{\delta \varepsilon_r}{\varepsilon_r} \tag{7.1}$$

where f_0 is the resonant frequency of a microstrip antenna assuming that a magnetic wall boundary condition, ε_r is the relative dielectric constant, and δ represents the small change. The relative frequency change for small dimensional changes may be expressed in terms of linear dimensions or in terms of temperature change as follows:

$$\frac{\delta f}{f_0} = -\frac{\delta l}{l} = -\alpha_T \delta T \tag{7.2}$$

where δ_T is thermal expansion coefficient. Polytetrafluoroethylene (PTFE) substrates reinforced with either glass woven web or glass random fiber are also very commonly used substrates because of their desirable electrical and mechanical.

The radiation of waves from the patch can be predominant when the substrate is thick and has a low permittivity. Foam materials provide very low permittivity values, very close to that of air. The surface waves become significant when the substrate is thick and has a large permittivity. It should be noted that the substrate requirement for the circuit and those needed for the antenna are contradictory. The design of a dual-polarized aperture coupled patch antenna is shown in Figure 7.5. Three different dielectric substrates are used in this design. The material properties are listed in Table 7.4.

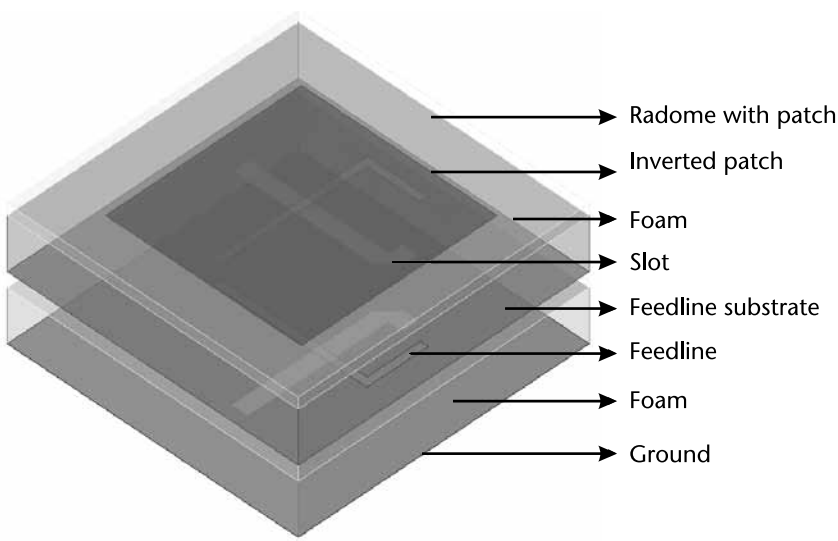

Figure 7.5 Multilayer patch antenna configuration and different layers.

Table 7.4 Material Properties of a Multilayer Antenna

Material Used	ε_r	*h (mm)*	*Loss Tangent*
RT Duroid 5870	2.33	0.38	0.001
Foam	1.08	1.8	0.008
Rogers RO 3003	3.0	0.51	0.001

Rogers RO 3003 is selected as the material for the feed line having a dielectric constant of 3, a height of the substrate of 0.51 mm, and a loss tangent of 0.001. RT Duroid 5870 material is used as radome of the antenna for environmental protection. The antenna is printed on the back side of this substrate.

7.4.2 Antenna Performance with Different Types of Slots

Antenna performance is simulated to measure coupling of the EM energy and slot-type effect on impedance variation with three different types of slots as shown in Figure 7.6. The front-to-back ratio and cross-polarization are calculated over the frequency band, and it has been found that the dog-bone slot enhances the coupled energy, but, in the case of dual polarization, the electric field vector has a higher component of cross-polarization and is not suitable for dual polarization. A thin rectangular aperture gives much stronger coupling. The coupling can be increased by using wider or longer rectangular apertures. The transverse electric field disappears at the end of the aperture for a simple rectangular slot. Coupling increases as the electrical length of the slot increases, which increases the resonant input impedance. The same concept also applies for the aperture width [13–19].

Aperture coupling using a slot is an indirect method of feeding the patch. The feed line creates an electric field in the aperture, which induces surface currents on the patch. Fringing fields are created by the patch edges perpendicular to the feed line that radiate into free space. The coupling level is mainly determined by the length of the coupling slot, as well as the back-radiation level. The slot should therefore be made no larger than what is required for impedance matching; it should be $0.25_{\lambda 0}$ and the width of the slot should be $0.1L$, where L is the length of the patch radiator. The width of the feed line affects the coupling to the slot, besides controlling the characteristic impedance of the feed line. Thinner feed lines couple

Dog bone-shape Rectangular Shape Inclined Rectangular Shape

Figure 7.6 Different shapes of the slot.

more strongly to the slot to a certain degree. For maximum coupling, the feed line should be positioned at right angles to the center of the slot [20]. Slanting the feed line from the slot will reduce the coupling, as will positioning the feed line towards the edge of the slot. The stub is typically slightly less than $\lambda_g/4$ in length; shortening the stub will move the impedance locus in the capacitive direction on the Smith chart. A summary of cross-polarization and the front-to-back ratio results for the dog bone-shaped slot, the rectangular slot, and the inclined rectangular shape slot is given in Table 7.5.

A single-element fabricated microstrip antenna is shown in Figure 7.7. Different layers of the microstrip antenna are integrated using adhesive. The measured bandwidth of the antenna is 750 MHz (7.8%). The antenna is resonating at 9.6 GHz. For maximum coupling, the patch should be cantered over the slot. Moving the patch relative to the slot in the E-plane (resonant) direction decreases the coupling level while moving the patch relative to the slot in the H-plane direction has little effect. The excess reactance of the slot coupled antenna is tuned with a tuning stub.

7.5 Array Antenna Design for X-Band SAR

Once a suitable radiating element is designed, the next step is to find an array configuration that gives satisfactory beam characteristics (direction and width). To analyze the complete radiation pattern of the SAR arrays, it is necessary to know the electrical characteristics of the single element as discussed in earlier. The design of a linear subarray antenna begins with optimization of the following parameters:

- Position of the radiating elements;
- Spacing between the elements;

Table 7.5 Results Summary of Different Slots

	Rectangular Slot		*Dog-Bone Slot*		*Tilted Slot*	
Frequency	*Cross-Polarization*	*Front-to-Back Ratio*	*Cross-Polarization*	*Front-to-Back Ratio*	*Cross-Polarization*	*Front-to-Back Ratio*
9.2	–24.25	–16.63	–24.52	–19.25	–23.40	–18.9
9.3	–23.63	–17.64	–24.0	–19.40	–23.00	–18.7
9.4	–22.47	–18.04	–24.0	–19.40	–23.05	–18.8
9.5	–22.49	–18.80	–23.7	–20.50	–22.55	–18.6
9.6	–22.40	–18.84	–23.75	–21.41	–22.52	–18.6
9.7	–22.59	–18.34	–23.7	–21.00	–22.50	–18.5
9.8	–22.59	–17.54	–24.5	–21.00	–22.49	–18.0
9.9	–22.43	–16.59	–24.7	–20.05	–22.44	–17.7
10.0	–22.40	–15.80	–25.01	–19.10	–22.40	–17.3
10.1	–22.40	–15.00	–25.2	–19.00	–22.41	–16.2
10.2	–22.0	–15.00	–25.35	–18.00	–22.41	–15.9

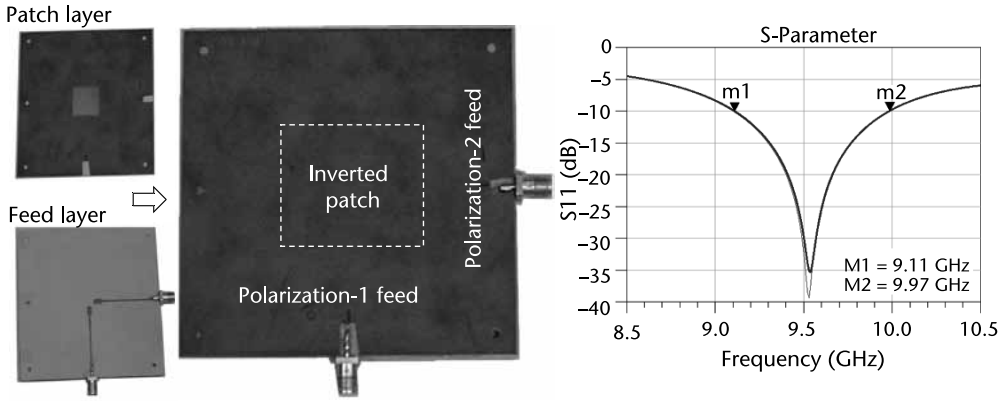

Figure 7.7 Fabricated antenna and return loss plot.

- Amplitude and phase distribution for each radiating element;
- Feed-line optimization.

A dual-polarized linear array of 1 × 8 element is shown in Figure 7.8. Interelement spacing is 0.75λ. The antenna feed network design is a most crucial step in the realization of the array antenna. For a linear array of isotropic elements as shown in Figure 7.9, the relationship of the main beam direction (θ), the distance between the elements (d), the wavelength (λ), and the phase difference ($\Delta\varphi$) are given by

$$\frac{\varnothing}{360^\circ} = \frac{d\sin\theta}{\lambda} \tag{7.3}$$

The direction in which the radiation from an array of linearly placed uniform antennas undergoes constructive interference is determined by the amount of extra

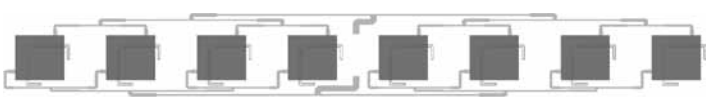

Figure 7.8 Layout design of a linear array SAR antenna.

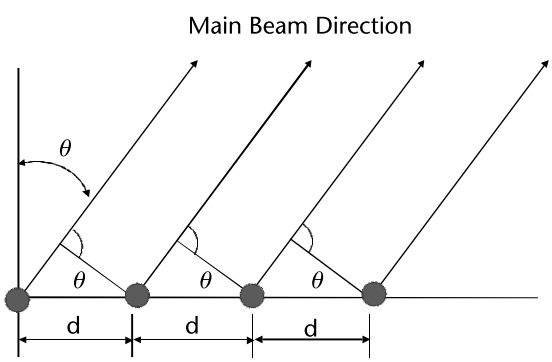

Figure 7.9 Antenna element arrangement in the linear array and beam direction.

path length that the wave needs to travel to be in phase with the wave from the adjacent antenna.

7.5.1 The Design of the Feed Network

The design of the feed network begins with the computation of the impedance that the patch offers at the point of feeding. The impedance of the patch at feeding point is 50Ω at the center frequency. This impedance value is utilized as terminating impedance for the feed network. A quarter-wave transformer is used to transform 50Ω impedance to 100Ω as shown in Figure 7.10.

Amplitude distribution can be changed by changing the impedance value of the line, hence changing the width of the line. Also, phase distribution can be changed by varying the length of the line. This high current taper ratio demands a power ratio of –9.0 dB and impedance ratio of 1:200Ω. The width of the microstrip line for 200Ω at X-band is difficult to fabricate without transformation of this impedance at a lower value impedance. Impedance transform is utilized to achieve a high current taper ratio. A MATLAB code can be developed to compute the possible impedance line width for different impedance lines, which can be printed by changing the characteristic impedance of the line of a quarter-wave transformer. A linear array of 8 elements is simulated using the MoM solver. As shown in Figure 7.11,

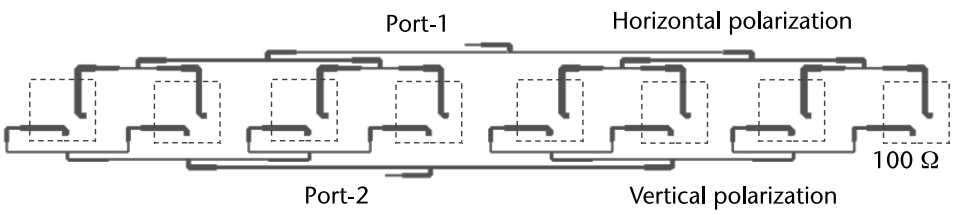

Figure 7.10 A feed network design for a dual-polarized linear array antenna.

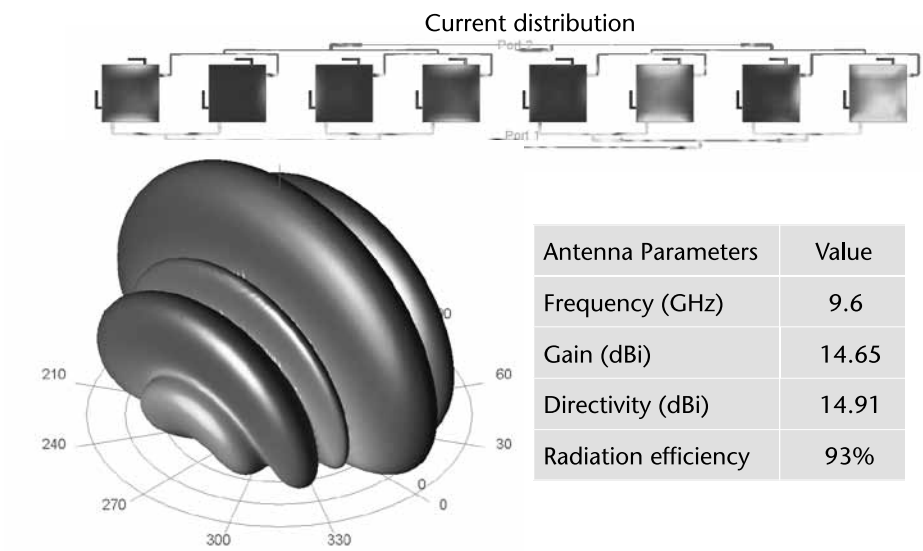

Antenna Parameters	Value
Frequency (GHz)	9.6
Gain (dBi)	14.65
Directivity (dBi)	14.91
Radiation efficiency	93%

Figure 7.11 Current distribution and antenna radiation pattern of the linear array.

the antenna has a fan beam pattern in the $\varphi = 0°$ plane while the beam pattern is narrow in the $\varphi = 90°$ cut plane. The antenna gain is 14.65 dBi, while the efficiency is 93%.

7.5.2 Antenna Performance Results

The 8-element linear array is fabricated and integrated into a multilayered configuration. Antenna return loss is measured to determine the operating bandwidth and resonance frequency. Antenna bandwidth is 700 MHz (9.2–9.9 GHz), with 9.6 GHz as the center frequency. The radiation pattern measurement of copolarization and cross-polarization for both vertical and horizontal polarization is performed at a far-field test range. A summary of the results is given in the Table 7.6 for both horizontal and vertical polarizations. As shown in Figure 7.12, ripples are high for one polarization, and the reason for this high ripple is the coupling between the coupled arm and the microstrip line that is very near to the slot, which changes the impedance of the patch antenna at the feed point.

The specification of the –20-dB sidelobe level in the azimuth plane with very little spacing between the elements makes the design of the feed network complex. This spacing is kept on the higher edge to avoid grating lobes in the visible region. While designing the feed network for the subarray, if the location of the microstrip

Table 7.6 Summary of the Linear Array Results

	Azimuth			*Elevation*		
Frequency (GHz)	*Cross-Polarization*	*3-dB Bandwidth*	*SLL (Sidelobe Level)*	*Cross-Polarization*	*3-dB Bandwidth*	*Ripple*
9.2 (H)	–28.0 dB	70°	–20.0 dB	–23.0 dB	40°	0.2 dB
9.6	–28.4 dB	65°	–19.5 dB	–22.0 dB	40°	1.0 dB
9.9	–25.0 dB	63°	–16.2 dB	–20.0 dB	37°	1.0 dB
9.2 (V)	–20.0 dB	65°	–25.0 dB	–19.0 dB	36°	2.5 dB
9.6	–25.0 dB	57°	–26.0 dB	–25.0 dB	36°	1.5 dB
9.9	–25.0 dB	56°	–22.0 dB	–20.0 dB	—	High

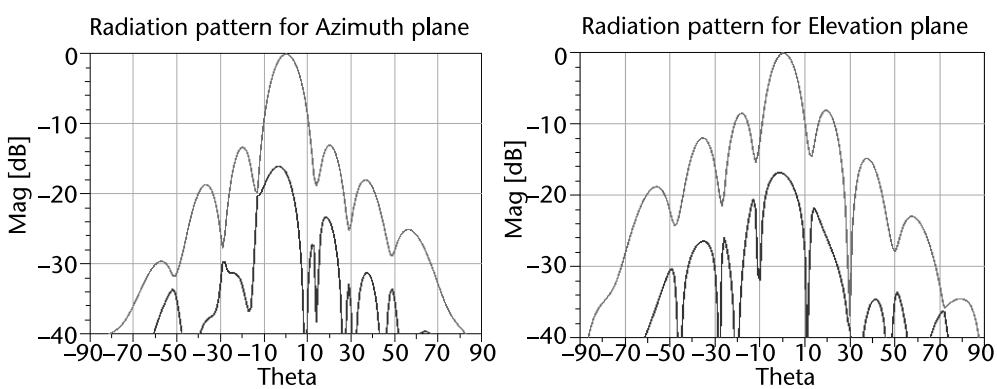

Figure 7.12 Antenna radiation pattern cuts in the azimuth and elevation planes.

line is very near to the slot for one polarization, then it might create the frequency shift. The impedance loci of the antenna do not affect only the imaginary part of the impedance but also the real part when the open stub length of the line is increased or decreased. This phenomenon is more prominent when the microstrip line is very near the slot.

7.5.3 Coupling in Feed Lines

The coupling between the feed lines of the same polarization deteriorates the excitation coefficients and hence the radiation performance of the patch antenna in an array environment. Simulation is carried out to check the coupling between the feed lines, and it was found that more spacing between the lines can reduce the problem, but an engineering compromise must be made for distance between the feed lines so that the whole feedline network for both the polarizations is accommodated in the allowed space and coupling can be reduced to a significant amount. Coupling between the feed lines is more significant in the elevation plane where shaping is stringent. In the azimuth plane, coupling can be reduced with more spacing between the lines.

7.6 Summary

In this chapter, array antennas for microwave remote-sensing application were discussed. Planar and printed antennas are very common in airborne and spaceborne SARs. The design and development of a dual-polarized antenna at X-band for SAR application were presented to prove the concept of dual polarization. Aperture coupled multilayer structures are the best choice when low cross-polarization is required over a large bandwidth. The design technique presented here will find a direct application for a dual-polarized antenna at other frequencies of interest. Also, the performance of the antenna can be improved further by taking mutual coupling effect into account within the patches, and this effect can be utilized to detune the impedance seen by the patch. In airborne, spaceborne, weather monitoring, and other high-performance applications where aerodynamic profile, cost, weight, mechanical structure, and ease of installation are important constraints, printed array antennas are preferred.

References

[1] Kramer, H. J., and A. P. Cracknell, "An Overview of Small Satellites in Remote Sensing," *Int. J. Remote Sens.*, Vol. 29, No. 15, 2008, pp. 4285–4337.

[2] Grafmuller, B., A. Herschlein, and C. Fischer, "The TerraSAR-X Antenna System," *Proc. IEEE Int. Radar Conf.*, Arlington, VA, May 2010, pp. 222–225.

[3] Semenov, S., "Microwave Tomography: Review of the Progress Towards Clinical Applications," *Philos. Trans. A Math. Phys. Eng. Sci.*, August 2009, pp. 3021–3042.

[4] Fear, E. C., et al., "Confocal Microwave Imaging for Breast Cancer Detection: Localization of Tumours in Three Dimensions," *IEEE Transactions on Biomedical Engineering*, Vol. 49, No. 8, August 2002, pp. 812–822.

[5] Semenov, S. Y., and D. R. Corfield, "Microwave Tomography for Brain Imaging: Feasibility Assessment for Stroke Detection," *Int. J. Antennas Propag.*, Vol. 8, 2008.

[6] Lin, J. C., and M. J. Clarke, "Microwave Imaging of Cerebral Edema," *Proceedings of the IEEE*, Vol. 70, No. 5, May 1982, pp. 523–524.

[7] Pozar, D. M., "Microstrip Antennas," *IEEE Proc.*, Vol. 80, January 1992, pp. 79–91.

[8] Frank, R., *Understanding Smart Sensors*, Norwood, MA: Artech House, 2013.

[9] Pozar, D. M., and D. H. Schaubert, *Microstrip Antennas: The Analysis and Design of Microstrip Antennas and Arrays*, New York: IEEE Press, 1995.

[10] Gauthier, G. P., A. Courtay, and G. M. Rebeiz, "Microstrip Antennas on Synthesized Low Dielectric-Constant Substrates," *IEEE Transactions on Antennas and Propagation,* Vol. 45, August 1997, pp. 1310–1314.

[11] Croq, F., and A. Papiernik, "Large Bandwidth Aperture Coupled Microstrip Antenna," *Electronics Letters*, Vol. 26, August 1990, pp. 1293–1294.

[12] Croq, F., and A. Papiernik, "Stacked Slot-Coupled Printed Antenna," *IEEE Microwave and Guided Wave Letters,* Vol. 1, October 1991, pp. 288–290.

[13] Sullivan, P. L., and D. H. Schaubert, "Analysis of an Aperture Coupled Microstrip Antenna," *IEEE-AP*, Vol. AP-34, No. 8, August 1986.

[14] Targonski, S. D., R. B. Waterhouse, and D. M. Pozar, "Wideband Aperture Coupled Stacked Patch Antenna Using Thick Substrates," *Electronics Letters*, Vol. 32, No. 21, October 1996, pp. 1941–1942.

[15] Edimo, M., A. Sharaiha, and C. Terret, "Optimised Feeding of Dual Polarised Broadband Aperture Coupled Printed Antenna," *Electronics Letters*, Vol. 28, No. 19, September 1992, pp. 1785–1787.

[16] Ravindra, V., et al., "A Dual-Polarization X-Band Traveling-Wave Antenna Panel for Small-Satellite Synthetic Aperture Radar," *IEEE Transactions on Antennas and Propagation*, Vol. 65, No. 5, 2017, pp. 2144–2156.

[17] Pandey, B. K., et al., "Dual Frequency Single Aperture Microstrip Patch Antenna Element for SAR Applications," *IETE Technical Review*, Vol. 23, No. 6, November-December 2006, pp. 357–366.

[18] Mao, C. -X., S. Gao, and T. Rommel, "Low-Profile Aperture-Shared X/Ka-Band Dual-Polarized Antenna for DBF-SAR Applications," *2017 International Workshop on Antenna Technology: Small Antennas, Innovative Structures, and Applications (iWAT)*, Athens, 2017, pp. 104–107.

[19] Adamiuk, G., et al., "SAR Architectures Based on DBF for C-and X-Band Applications," *Proceedings of 10th European Conference on Synthetic Aperture Radar (EUSAR 2014)*, June 2014, pp. 3–5.

[20] Heinstadtm J., "Efficient Numerical Strategies for the Computation of Microstrip-Patches and Microstrip-Arrays," Doctoral Thesis, D17, 1995.

Selected Bibliography

Akbar, P. R., et al., "X-Band Parallel-Plate Slot Array Antenna for SAR Sensor Onboard 100 kg Small Satellite," *2015 IEEE International Symposium on Antennas and Propagation & USNC/URSI National Radio Science Meeting*, Vancouver, BC, 2015, pp. 208–209.

Di Bari, R., et al., "Dual-Polarized Printed S-Band Radar Array Antenna for Spacecraft Applications," *IEEE Antennas and Wireless Propagation Letters*, Vol. 10, 2011, pp. 987–990.

Cerutti-Maori, D., I. Sikaneta and C. H. Gierull, "Optimum SAR/GMTI Processing and Its Application to the Radar Satellite RADARSAT-2 for Traffic Monitoring," *IEEE Transactions on Geoscience and Remote Sensing*, Vol. 50, No. 10, October 2012, pp. 3868–3881.

Kahrizi, M., T. K. Sarkar and Z. A. Maricevic, "Analysis of a Wide Radiating Slot in the Ground Plane of a Microstrip Line," *IEEE-MTT*, Vol. 41, No. 1, January 1993, pp. 29–37.

Kothapudi, V. K., and V. Kumar, "A 6-Port Two-Dimensional 3x3 Series-Fed Planar Array Antenna for Dual-Polarized X-Band Airborne Synthetic Aperture Radar Applications," *IEEE Access*, Vol. 6, 2018, pp. 12001–12007.

Mittermayer, J., et al., "The TerraSAR-X Staring Spotlight Mode Concept," *IEEE Transactions on Geoscience and Remote Sensing*, Vol. 52, No. 6, June 2014, pp. 3695–3706.

Mao, C., et al., "Low-Cost X/Ku/Ka-Band Dual-Polarized Array with Shared Aperture," *IEEE Transactions on Antennas and Propagation*, Vol. 65, No. 7, July 2017, pp. 3520–3527.

Pokuls, R., J. Uher, and D. M. Pozar, "Microstrip Antennas for SAR Applications," *IEEE Transactions on Antennas and Propagation*, Vol. 46, No. 9, September 1998, pp. 1289–1296.

Shafai, L. L., et al., "Dual-Band Dual-Polarized Perforated Microstrip Antennas for SAR Applications," *IEEE Transactions on Antennas and Propagation*, Vol. 48, No. 1, January 2000, pp. 58–66.

Yang, J., C. Liu, and Y. Wang, "Imaging and Parameter Estimation of Fast-Moving Targets with Single-Antenna SAR," *IEEE Geoscience and Remote Sensing Letters*, Vol. 11, No. 2, February 2014, pp. 529–533.

Ruiz Rodon, J., et al., "Geosynchronous SAR Focusing with Atmospheric Phase Screen Retrieval and Compensation," *IEEE Transactions on Geoscience and Remote Sensing*, Vol. 51, No. 8, August 2013, pp. 4397–4404.

Santosa, C. E., and J. T. S. Sumantyo, "Broadband Circularly Polarized Microstrip Antenna for Airborne X Band CP-SAR," *2017 IEEE International Symposium on Antennas and Propagation & USNC/URSI National Radio Science Meeting*, San Diego, CA, 2017, pp. 2307–2308.

CHAPTER 8

Airborne SAR Antenna Arrays

8.1 Introduction

A SAR system places a stringent requirement on its antenna radiation properties. Typically, a SAR antenna would require a high degree of polarization purity because the backscatter is a function of the wave polarization. A high degree of cross-polarization would reduce the accuracy of the ground data interpretation. The radiation pattern of a typical SAR antenna should be shaped in the main beam. An airborne radar has a range difference between the near target and the far target, within the main beam. The difference between them should be compensated in the gain of the antenna. Furthermore, the sidelobes and back lobes of the antenna should be suppressed to avoid reflection. The reflection from aircraft will result in radiation pattern distortion and gain loss, while the reflection from the opposite track will result in data corruption. The reflection from under the wing will cause multipath propagation, whereby the reflection from the ground reaches the antenna via a different path.

Airborne radars typically use a variation of a cosec square-shaped beam, which can get the required elevation coverage where the received power is independent of the radar range for a constant height target [1]. The desirable features of the antenna for airborne SAR applications include a shaped radiation pattern and a wide bandwidth capability, a good cross-polarization isolation, and a high-power capability. Shaped radiation across the track improves the target dynamic range and compensates the requirement of the sensitivity time control (STC) correction at the receiver end. Wide bandwidth performance results in finer resolution. The planar array antenna is preferred as compared to the reflector type antenna for less air drag.

Due to the project complexity and cost factor, the antenna designer first simulates the design using commercial electronic design automation (EDA) tools to get performance data before real production. The antenna design cycle time plays a big part in determining a product launch schedule. Simulation tool capability and the way that tools are used play important roles in the design cycle time and cost. Simulation technologies based on different numerical techniques can change the way that complex integrated array antennas are designed. One solution enables the use of separate solvers for the radiator and 3-D feeder networks separately.

8.2 SAR Antenna Pattern Synthesis

Antenna arrays are designed to produce desired patterns, and they are optimized under a set of specified constraints. The constraints can be sidelobe level, first null-to-null beamwidth, VSWR, and impedance. It is always possible to compute the amplitude and phase excitations for a specified radiation pattern. The process of choosing the parameters of an antenna array to produce desired radiating characteristics is known as pattern synthesis. In the array pattern synthesis, the desired output is usually the excitation of the radiating elements, which can produce an acceptable pattern shape. The synthesis of the antenna array with the desired radiation pattern is a nonlinear optimization problem.

Antenna arrays provide an efficient means to detect and process signals arriving from different directions. An array of radiating elements can have its beam pattern modified with an amplitude and phase distribution called the weights of the array. After preprocessing the antenna outputs, signals are weighted and summed to give the antenna array beam pattern. The antenna array pattern synthesis problem consists of finding weights that satisfy a set of specifications on the beam pattern. Antennas with a constant height pattern or a cosecant squared pattern are specially designed for air-surveillance radar sets as discussed previously. These permit an adapted distribution of the radiation in the space and cause a more ideal beam scanning. Such an antenna pattern can get the required elevation coverage where the received power is independent of the radar range for a constant height target. It is a mechanism to achieve a more uniform signal strength at the input of the receiver as a target moves with a constant height within the beam. The antenna pattern synthesis problem is needed in many array antenna applications. One of the key advantages of array antennas is that the array excitation can be accurately controlled to produce extremely low sidelobe patterns or very accurate approximations of chosen radiation patterns. Antenna synthesizing methods fit into three main classes of synthesis:

1. Synthesis of various antenna radiation pattern shapes;
2. Synthesis of low sidelobe;
3. Synthesis that optimizes an array parameter, such as gain and SNR.

In general, the antenna synthesis problem can be stated as the inverse of the antenna analysis problem to find out a set of design parameters that gives the desired antenna output such as the far-field pattern, sidelobe, and gain. The theory of pattern synthesis is concerned with determining the relationship between the far-field pattern of an array and the amplitude and phase distribution of the individual elements and their spacing.

To find a solution, many analytical techniques such as the Woodward-Lawson [2], Orchard-Elliot [3], Taylor method, Fourier transform method [4], Schelkunoff method [5], and Dolph-Chebyshev methods are used [6]. In general, the goal in antenna array synthesis is determining the complex excitations, amplitudes and phases of the elements for producing desired radiation pattern. The Woodward synthesis technique and power pattern synthesis methods are very appropriate for the synthesis of shaped-beam patterns. Many optimization methods such as par-

ticle swarm optimization, genetic algorithm [7, 8], and simulate annealing [9] have been useful for the synthesis of antenna array.

8.2.1 Cosecant Square Shaped Pattern

Cosecant squared pattern antennas are frequently used in the base station of wireless communication systems or surveillance radar systems to achieve an equivalent power coverage in the desired distance. Cosecant-squared pattern is one such pattern which is generally employed for long-range systems requiring higher gain near the horizon with low gain at higher elevation angles. During detection of an aircraft flying in space, it will be observed at a closer range at higher elevation angles, so use of such pattern significantly limits the power available to aircraft at higher elevation angles thereby providing a uniform signal strength to the aircraft throughout its journey. The specific gain variations [1] in the cosecant squared region compensate the propagation loss in different distances and maintain the received power unchanged.

Figure 8.1 is showing a microwave remote sensing aircraft flying at a constant height H. As it can be observed that image swath has one low gain and one high gain point. Thus, due to this variation in the range of swath angle, the antenna power distribution is different on these two points. To receive uniform power by the receiver, the radiation shape needs to be modified to cosecant-squared shape.

8.2.2 Woodward-Lawson Pattern Synthesis Technique

Woodward-Lawson pattern synthesis technique is used to compute the excitation coefficients. A pattern produced with a standard design is used in the iterative sampling method. In an iterative sampling method, correction is applied to the pattern obtained from a standard design to make the approximation pattern more nearly satisfy the specifications on the closeness fit. A correction pattern is derived by

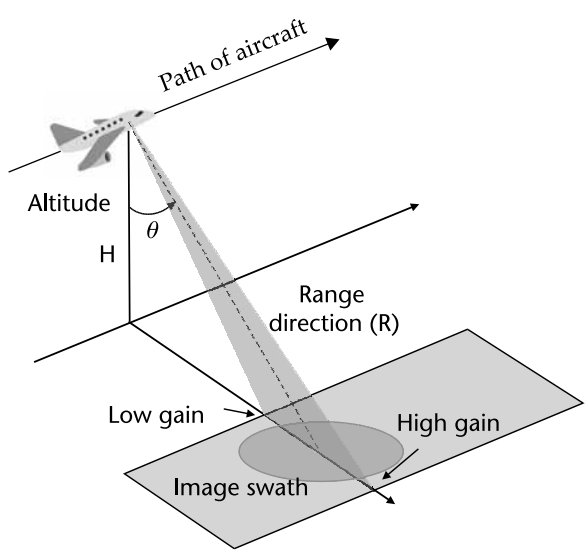

Figure 8.1 Airborne remote sensing radar system.

comparing the desired pattern with the pattern produced from synthesis method. This is the first iteration. If the resulting pattern is not satisfactory, additional corrections may be applied to the first iteration pattern. If the second iteration is also not yet satisfactory, further iterations are applied. Lastly, this iteration process converges to give the desired pattern over the region where the corrections are applied.

Iterative procedure begins with the principal plane pattern of line source of length l represented in terms of the aperture distribution $A(t)$

$$F(u) = \int_{-l}^{l} A(t) e^{iut} dt \tag{8.1}$$

where $u = (\pi l/\lambda)\sin(\theta)$, t is length normalized to wavelength and $A(t)$ is represented by the sum of uniform traveling waves with a linear phase change of $2n\pi$ radians over the length of the aperture,

$$A(t) = \frac{1}{2}\sum_{-N}^{N} b_n e^{-jn\pi t} \tag{8.2}$$

where N is the largest whole number of wavelengths contained within the length of the array, so the pattern factor is given by

$$F(u) = \sum_{-N}^{N} b_n \frac{\sin(u - n\pi)}{(u - n\pi)} \tag{8.3}$$

It can be made to coincide exactly with any given function $F(u)$ at $2N + 1$ equally spaced sampling points $u = 0, \pm\pi, \pm 2\pi, \ldots, \pm N\pi$ over the visible region by choosing each coefficient b_n to have the sample value:

$$b_n = F(n\pi) \tag{8.4}$$

The pattern of uniform linear array is given by:

$$F(\theta) = b_n \frac{\sin\left[\frac{N}{2} kd(\cos\theta - \cos\theta_m)\right]}{N \sin\frac{kd}{2}(\cos\theta - \cos\theta_m)} \tag{8.5}$$

For $2N + 1$ element, the array factor becomes:

$$AF(\theta) = \sum_{-N}^{N} b_n \frac{\sin\left[\frac{N}{2} kd(\cos\theta - \cos\theta_m)\right]}{N \sin\frac{kd}{2}(\cos\theta - \cos\theta_m)} \tag{8.6}$$

The N array amplitude weights $a(m)$ is calculated using the inverse discrete Fourier transform (DFT) formulas ((8.4) to (8.6)). Then, replace the weights by their windowed versions using any symmetric length-N window [10]. The final expressions for the windowed weights are, for odd $N = 2M + 1$:

$$a(m) = w(m)\frac{1}{N}\sum_{i=0}^{N} A(\psi_i)e^{-jm\psi_i}, m = 0, \pm 1, \pm 2, \ldots, \pm M \tag{8.7}$$

and for even $N = 2M$,

$$a(\pm m) = w(\pm m)\frac{1}{N}\sum_{i=0}^{N} A(\psi_i)e^{\pm j(m-\frac{1}{2})\psi_i}, m = 1, 2, \ldots, M \tag{8.8}$$

The power of Woodward Lawson pattern synthesis method lies in the ability to specify any shape for the array factor through its frequency samples. Woodward pattern synthesis technique is utilized to compute the complex excitation coefficients for $N = 8$ elements in a linear with $d = 0.75\lambda$. The corresponding wavenumber ψ will be $\psi = kd\cos(\theta)$. The design of the $cosec^2(\theta)$ shape pattern requires that the array factor itself have a secant dependence. As the secant pattern is defined only up to an angle $\theta_{\max}$, theoretical array factor in the normalized form can be defined:

$$f(x) = \begin{cases} \dfrac{\cos\theta_{max}}{\cos\theta} & if\ 0 \le \theta \le \theta_{max} \\ 1 & if\ \theta_{max} < \theta \le 90^\circ \end{cases} \tag{8.9}$$

A MATLAB code is written to solve these equations to get amplitude ration and phase value for each element [10].

```
%matlab code%
N=8;
K=(N-1)/2;
d=0.75;
thetamax=42;
psimax = 2*pi*d * cos(thetamax*pi/180);
Ai = ones(1,K+1);
psi = 2*pi*(0:K)/N;
j = find(psi);
Ai(j) = psimax*(psi(j)>=psimax)./psi(j) + (psi(j)<psimax);
Ai = [Ai, Ai(K:-1:1)];
a = woodward(Ai, 0) / N;
aw = a .* (0.54 - 0.46*cos(2*pi*(0:N-1)/(N-1)));
```

The required amplitude and phase distribution for the elevation plane pattern is shown in Table 8.1.

Table 8.1 Excitation Coefficients Calculated Using Woodward Lawson Pattern Synthesis Technique

Element No.	*Amplitude Ratio*	*Phase*
1	0.59	–53.7°
2	0.38	–24.8°
3	0.46	36.0°
4	2.3	52.6°
5	3.77	16.0°
6	2.70	–19.7°
7	0.91	–7.5°
8	1.00	0.0°

Elevation plane pattern requires a cosec$^2(\theta)$ shape pattern to avoid Sensitivity Time Control correction at the receiver end so that large beamwidth can be provided with higher gain. This kind of antenna will find application for the Airborne Synthetic Aperture Radar (ASAR) and other remote sensing antennas. To have the shaping pattern not only amplitude of the excitation coefficient will change, but also the phase distribution will be different to all the radiating elements to fill the nulls occurring in the visible region. Amplitude will also be tapered to suppress the sidelobe to –20 dB and hence increase the efficiency of the antenna. Hence, complex excitation coefficients make the design challenging.

8.2.3 Theoretical Predicted Patterns

After computing the aperture distribution, the radiation pattern can be obtained to compare with the required pattern as shown in Figure 8.2.

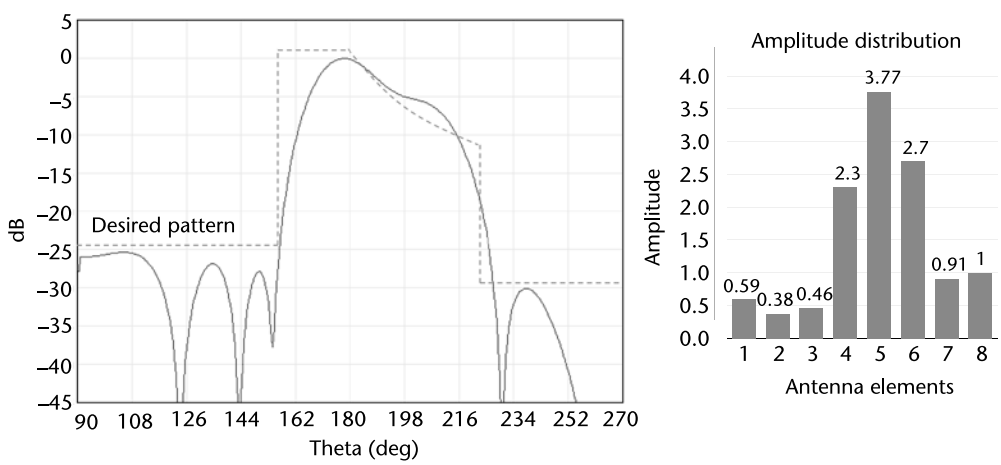

Figure 8.2 Theoretical prediction of elevation plane cosec2 antenna pattern.

8.3 Design of Airborne SAR Antenna

In the airborne application, mainly the antenna size and weight are restricted. To obtain a high-resolution image, it is required either to use an impractically long antenna or to employ wavelengths so short that the radar must contend with severe attenuation in the atmosphere. In the SAR system, the forward motion of the actual antenna is used to synthesize a very long antenna. SAR permits the possibility of using longer wavelengths and still achieving good resolution with antenna structures of a reasonable size. The antenna array design, synthesis, and simulation discussed in this section are an airborne high-power wideband cosecant squared pattern SAR array antenna with a low sidelobe level. In this antenna, a shaped radiation pattern within 35° is achieved with 8 elements. The antenna pattern ripple level is better than 0.5 dB. The feeder network for dual polarization is designed with corporate feeding for eight elements within the limited available interelement spacing. Two linear arrays (8×2) are combined at the microstrip feed network level and then it is directly fed from one of the outputs of the 1×8 square coaxial line. The input to the square coaxial line is given by the waveguide.

Normally, for remote-sensing applications, the frequency range from 1 to 30 GHz is used. In the 1–10-GHz frequency range, the transmissivity through the air is almost 100%. Therefore, a SAR operating in this frequency band is always able to image the Earth's surface independent of the precipitation or cloud cover. A SAR antenna array is designed to operate at C-band (5.4 GHz). To achieve a bandwidth of 10% at the array level, a multilayer, broadband, single-element antenna is designed. A multilayer stacked radiating array of 8×8 elements at C-band with a center frequency of 5.4 GHz for a peak power of 5 kW and a pulse repetition frequency (PRF) of 1.3% is fed with a 1:8 square coaxial feeder network. Antenna beam shaping in the elevation plane is accomplished by obtaining the complex excitation distribution employing the null perturbation technique. Many sets of coefficients giving same power patterns were obtained and the one that gave the minimum current taper ratio is selected for the realization of the antenna. This SAR system is configured with a swath of 50 km operating at an altitude of 4 km.

8.3.1 SAR Antenna Design Flow and Methodology

The high-power SAR antenna is a complex system and a single EM solver is not sufficient to design, simulate, and synthesize complete antenna. With a proper understanding, the sequence of design processes and complexity of a SAR antenna array, the simulation times and resources can be reduced significantly. The hybrid EM simulation approach is used to reduce design cycle by 50% to 60%. This high-power SAR array antenna design has been divided into two segments, the design of a multilayer planar radiating array antenna and a high-power 3-D BFN. A radiating microstrip antenna array is designed with MoM, as this is a very fast solver for the planar kind of structures. A high-power SCL feed network of the antenna is designed using the FEM-based 3-D EM solver. The complete integrated antenna simulation is carried out using the FDTD solver due to complex nature and large problem size.

8.3.2 SAR Antenna Design

The selection of radiating element for planar array is decided as per the requirement of large bandwidth, low cross-polarization with high gain. The multilayer-stacked electromagnetically coupled printed antenna overcomes the bandwidth limitation of the conventional single-layer microstrip antenna. Although the aperture coupled antenna offers the advantage of optimizing the feeder network and patch independently, the impedance matching is poor due to improper grounding when coaxial feeding below the ground is required for the array. The multilayer printed antenna as the basic radiating element is efficient for a large bandwidth. In the design discussed in this section, microstrip patch is effectively printed on the foam material whose dielectric constant is nearly equal to air to enhance bandwidth and to minimize the surface-wave propagation. Because the patch cannot be printed on the foam material, it is printed on the opposite face of the 10-mil dielectric sheet. This dielectric is also used as radome to protect the antenna against the environment.

Electromagnetically coupled feeding is used to avoid the soldering connection to patches and making it more reliable. RT Duroid material 5880 with a thickness 0.79 of mm is used for the feeder network to meet the high-power requirement. The upper patch dimensions are taken to be larger than the lower patch and are fabricated on RT5880 with h = 10 mil. The Rohacell foam, which is 5 mm thick, is placed between the upper and lower radiating patches for bandwidth enhancement. The design of a single element is optimized for a return loss better than –17 dB and cross-polarization better than –25 dB. The optimized antenna dimension and material used are shown in Figure 8.3. The measured results show VSWR (2:1) bandwidth of 800 MHz (17%, –10-dB return loss) with cross-polarization better than –22 dB.

The antenna configuration is shown in Figure 8.3. It has four layers, with an upper patch dimension of 22.6 mm by 19.6 mm and a lower patch dimension of 18.3 mm by 18.3 mm. Broadband behavior is obtained with a staggered tuning of upper and lower patch elements. Staggered tuning is a technique used in the design of broadband antennas whereby each layer is tuned to a slightly different frequency. In comparison to synchronous tuning (where each layer is tuned identically), it produces a wider bandwidth. A linear array design is created with an unequal microstrip distributed network for each of the eight antenna elements to generate a shaped antenna pattern after the single-element design is optimized. All the layers' array antennas are bonded together using nonconducting adhesive

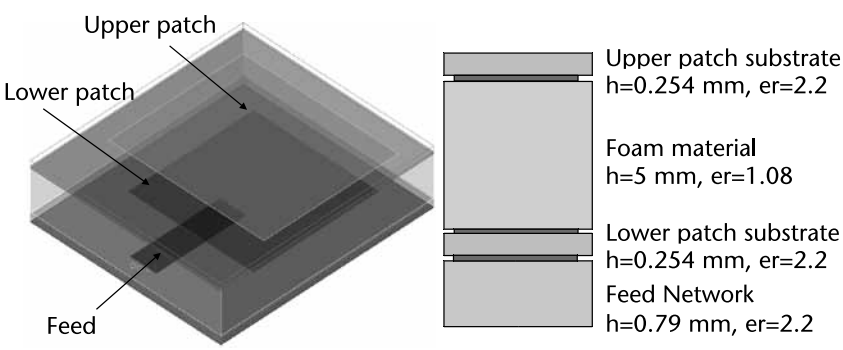

Figure 8.3 Single radiating element and substrate stack-up.

cyanate ester. In antenna simulation, it is better to take the effect of the adhesive layer for better accuracy. Antenna dimensions and simulated S-parameter data are shown in Figure 8.4.

8.3.3 Shaped Pattern BFN

In RF transceiver systems, beamformers are used between the RF signal source and the antenna radiating elements to shape the resulting radiated EM field to illuminate a target or region of space with a precisely controlled beam. To generate a cosec square antenna beam pattern, a BFN is required. The BFN controls the amplitude weight and phase of the feed arrays, which are fed to different elements of the array antenna. The BFN described in this section has a unique architecture by which excitation amplitude and phase can be controlled to shape the antenna beam.

The complex excitation coefficients for the required shape are computed using the null perturbation technique with an element spacing of 0.8λ where roots of the polynomial are moved both in the radial and angular directions in the shaped region and only angular displacement for the nonshaped region [3]. Distribution coefficients are given in Table 8.2. As shown in Figure 8.5, the microstrip feed network is first simulated and optimized by the ADS circuit simulator and optimizer by modeling an asymmetrical coupled line to consider the effect of the coupling between the lines. Because of the better phase control of the order of 5-degree, this results in fewer ripples in the shaped patterns. The design is optimized in multiple smaller parts representing T-Networks. Then all parts are combined to get overall effect of BFN.

Layout design is created for the optimized distributed network as shown in Figure 8.6. This network is simulated using EM solver MoM and a minor adjustment in length was carried out for the required phase matching. Amplitude and phase distribution at each output port are realized as per the computed value shown in Table 8.2 to get cosecant square shaped pattern. Because microstrip lines are placed close to each other in this BFN, coupling between lines affects the feed network performance.

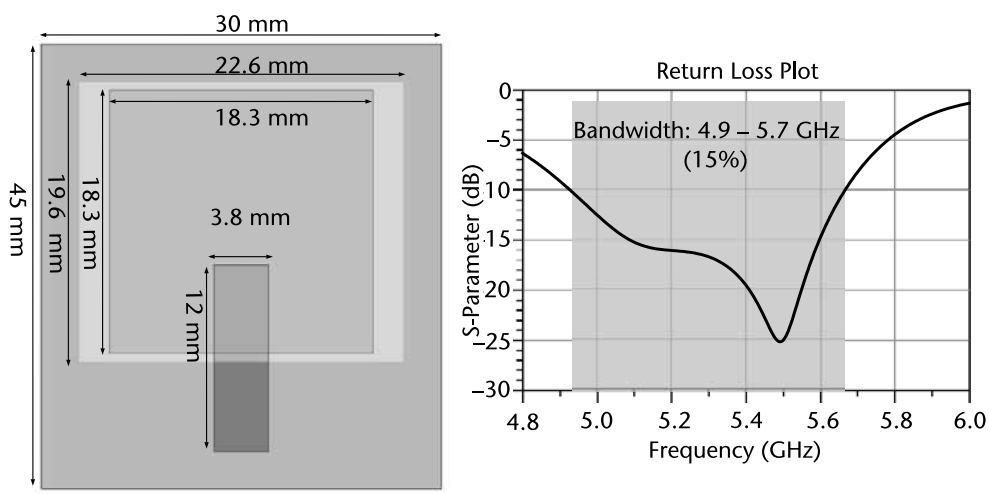

Figure 8.4 Radiating element design dimensions and return loss plot.

Table 8.2 Amplitude and Phase Distribution Coefficient of 1:8 BFN

Element Number	*Amplitude Distribution*	*1-W Power Distribution at Each Element*	*Power at Each Element (dBm)*	*Phase (Degrees)*
1	1	0.003W	–14.7	0
2	0.58	0.011W	–19.4	100.3
3	1.98	0.134W	–8.7	–107.5
4	3.37	0.380W	–4.2	–59.4
5	2.72	0.256W	–5.9	–35.9
6	2.02	0.136W	–8.6	–33.6
7	1.09	0.040W	–13.9	–21
8	0.6	0.010W	–19.3	–53.17

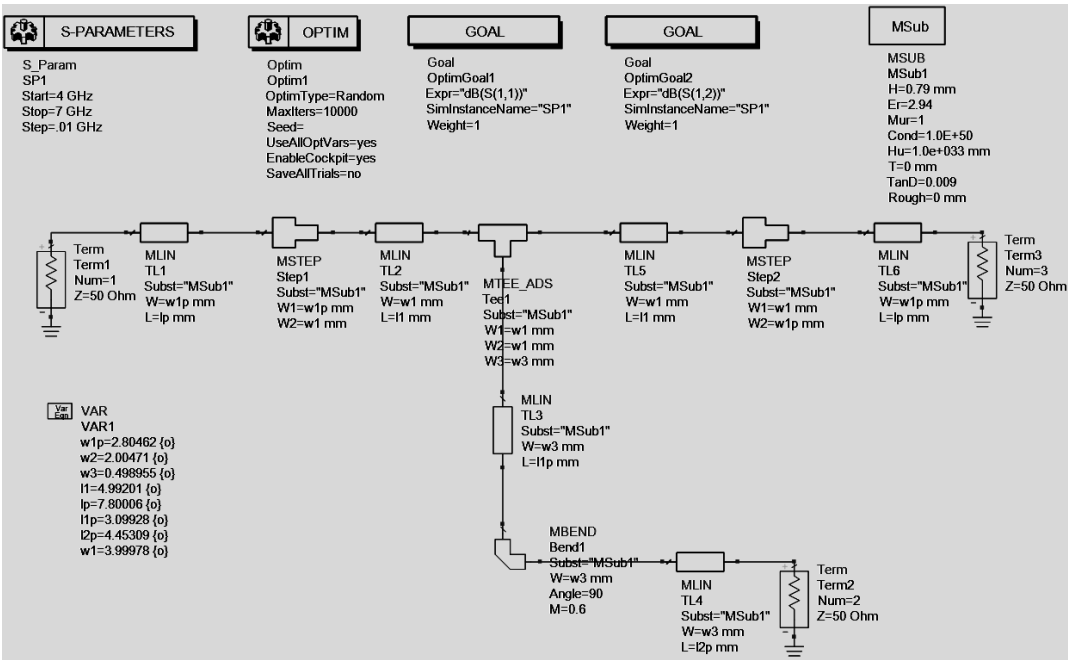

Figure 8.5 ADS circuit simulation schematic of Tee-network of BFN.

8.3.4 Antenna Array Design Realization and Simulation

First, a linear antenna array ($N = 8$, $d = 0.8\lambda$) was realized in printed microstrip technology, which works in C-band (center frequency $f_0 = 5.4$ GHz) with a frequency bandwidth of 17%. Then, using 8 optimized linear arrays, a planar array of an 8×8 element is designed with an interarray spacing of 0.8λ. A linear array antenna shown in Figure 8.7 has been simulated using MoM. The antenna pattern is a cosecant square in the elevation plane while it is a fan beam in the azimuth plane.

A planar array as shown in Figure 8.8 is formed by placing eight linear arrays with 0.8λ interarray spacing. The antenna performance is same as that of the

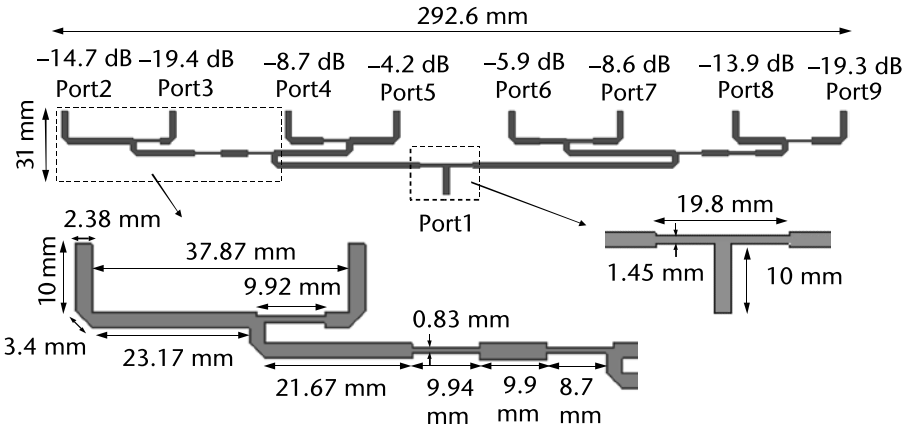

Figure 8.6 A 1:8 BFN using a microstrip line.

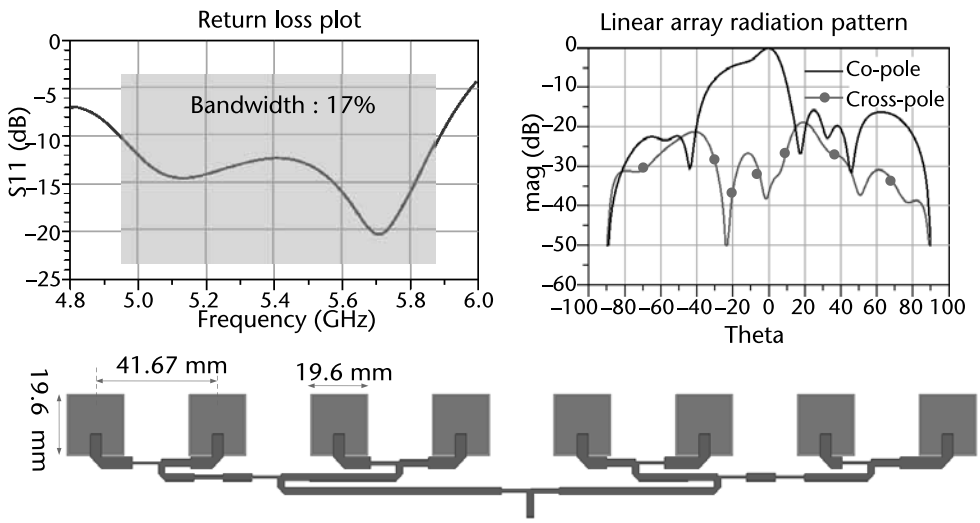

Figure 8.7 A linear antenna array with eight radiating elements.

linear-array antenna performance. All eight ports are simulated using the FEM solver. The antenna radiation pattern in azimuth and elevation plane is shown in Figure 8.9. In azimuth plane combines radiation pattern is pencil beam. More number of element in array provide sharper pattern in azimuth direction.

The antenna is fabricated layer by layer. All these layers are aligned and bonded together using a nonconducting adhesive cyanate ester. The measured return loss performance, along with the simulation of the antenna, shows the 2:1 VSWR bandwidth of the antenna is better than 350 MHz. The performance of the measured patterns and its comparison with simulated patterns are shown in Figure 8.10. A very good matching observed in the measured patterns over simulated patterns confirms the validity of the technique and shows that shaping in elevation is achieved with a 0.5-dB ripple over the frequency. This array antenna tile cannot handle the high-power (8 kW) requirement of a SAR system; for that, an SCL-based BFN design is described next.

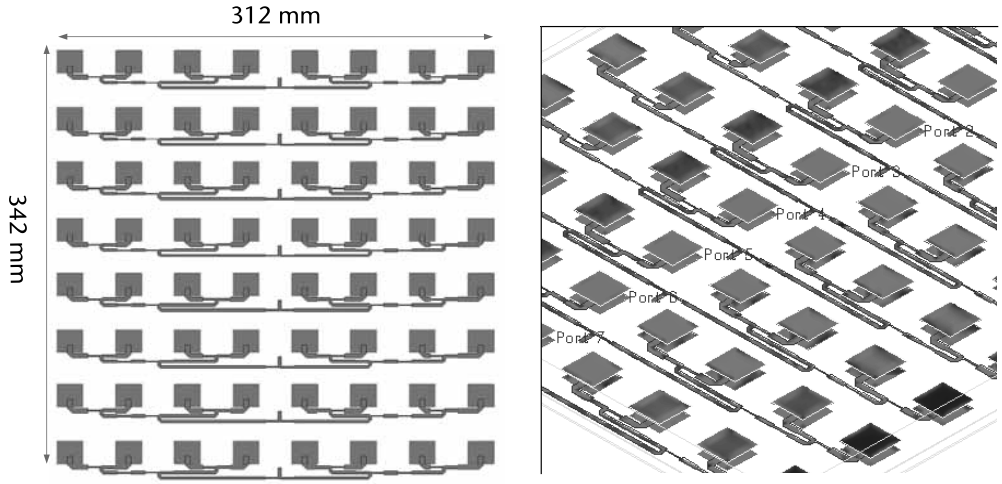

Figure 8.8 The planar antenna array (8 × 8 elements) and current distribution plot.

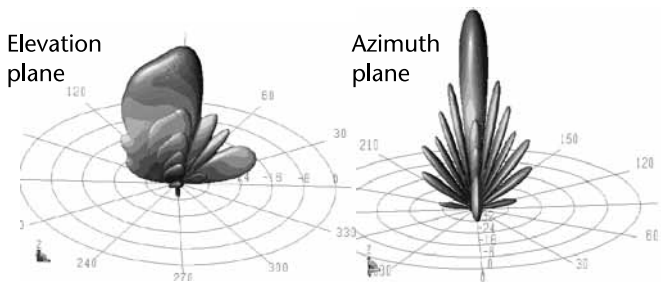

Figure 8.9 Elevation and azimuth plane radiation pattern of planar antenna array.

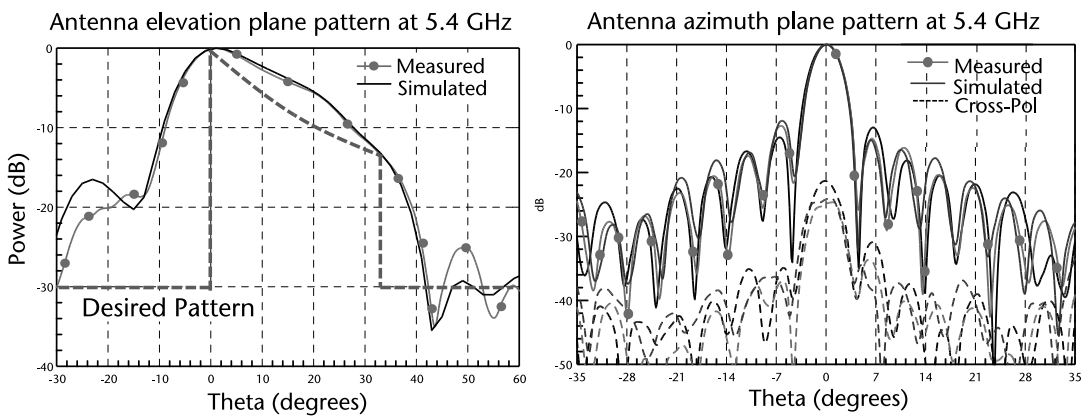

Figure 8.10 Comparison of measured and simulated azimuth and elevation plane patterns.

8.4 High-Power Feed Network Design

Microwave remote-sensing applications require antennas with shaped beams like cosecant-squared (cosec^2) sector shape, and elliptical beam. As discussed in previous sections, this requires the development of complex BFN to generate the necessary amplitude and phase distributions in the radiating elements of the antenna array to yield the desired shaped beam [11]. Usually, planar antennas are well suited for SAR applications. The most commonly used radiating element used in the planar array is the microstrip patch antenna, which is inherently low-profile and lightweight. However, there is a serious limitation with microstrip patch antennas in terms of the problem associated with the power-handling capability. Therefore, microstrip patch antennas cannot be directly used for SAR systems where a pulse peak power of several kilowatts is used. For such applications, a hybrid antenna where the waveguide feeding networks can be used to handle the high input power and proper transitions can be made to the microstrip line or directly to the microstrip patch, which can handle the split lower power. BFN represents the heart of any array antenna system. It consists of many power dividers to adjust the phase and amplitude of the signal at each feeding element. The key requirements for the BFN are wideband operation, high precision power division (typically 0.5 dB in amplitude and 5° in phase), high-power capability, and reliable technology for airborne and spaceborne applications.

Although a BFN made of a hollow waveguide is best suited from the point of view of power handling, but from the point of view of weight and compactness, the BFNs are generally not made solely of waveguides. In this case, rectangular (or, more specifically, square) coaxial lines are used as a transmission medium for the BFN in the lower-frequency range such as L-band and C-band up to X-band. While circular coaxial lines have been used extensively in the past, rectangular coaxial lines may be preferable in some applications if the presence of flat rather than circular surfaces offer mechanical advantages and it is desired to have an unambiguously defined plane of polarization. The loss characteristics and power-handling capability of rectangular coaxial line are comparable to that of circular coaxial line. However, manufacturing components with a rectangular cross-section are more economical and this type of coaxial line is predominantly used in the feed systems employing many components to form the BFN.

8.4.1 Rectangular Coaxial Line

The idea of a square coaxial radiator started in 1979 when Frank Hanna and Wilson Ishu developed the first prototype at the University of Illinois at Chicago, which, due to its symmetric aperture in theory, should have equal E and H plane patterns [12]. To obtain a low-loss coaxial transmission line, for a given operating frequency range, the cross-sectional area of the coaxial structure should be optimized [13]. Figure 8.11 shows an air-filled square coaxial transmission line.

The appropriate choice of a cross-section to be used in a specific design is a trade-off between having a low attenuation constant for the transmission line and predicting at what frequency the higher modes will start to propagate. When higher modes are present, these lead to a dispersive transmission line, so for most applications, it is desired to propagate only a TEM mode. The dominant mode in the rectangular coaxial line is TEM. For the TEM mode of propagation, the distributed

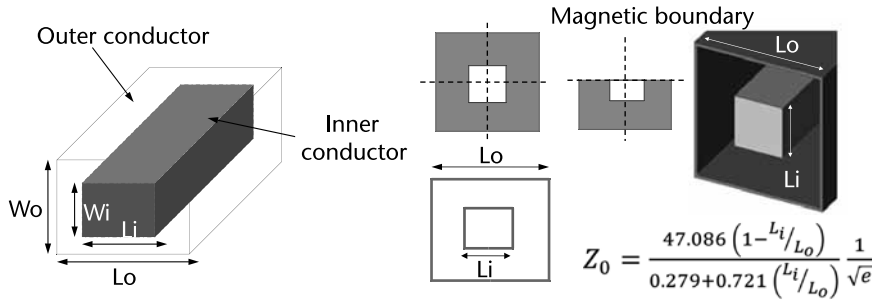

Figure 8.11 Rectangular and square coaxial line design configuration and EM simulation model.

circuit theory can be applied. The bandwidth of the rectangular coaxial line for the TEM mode propagation starts from DC to the cutoff frequencies of the first higher-order modes. Analytically, the higher-order modes in the rectangular coaxial lines can be derived using a formulation similar to that applied to the ridge waveguide [14–16].

The transverse resonance technique applied to the solution of ridge waveguide can also be used to solve the eigenvalue problems in the rectangular coaxial medium. Obviously, different boundary conditions will lead to different zeros of the system determinant and thus to different cutoff frequencies. The characteristic impedance of the rectangular coaxial line can be computed from the following equation;

$$Z_0 = 59.952 \ln\left(\frac{1+\frac{L_o}{W_o}}{\frac{L_i}{W_o}+\frac{W_i}{W_o}}\right) \tag{8.10}$$

The above equation has 10% accuracy for $\frac{W_i}{W_o} < 0.3$ and $\frac{L_o}{L_i} < 0.8$.

In the case of the SCL characteristic, impedance is calculated using the following equation, which has 1% accuracy:

$$Z_0 = \frac{47.086(1-{}^{Li}/_{Lo})}{0.279+0.721({}^{Li}/_{Lo})}\frac{1}{\sqrt{e}} \tag{8.11}$$

8.4.2 Corona and Multipaction Breakdown in the High-Power Feed Network

The corona effect can be defined as a local discharge initiated by gas ionization, when the electric field has reached a threshold [17, 18]. If gases were only composed of neutral particles, the corona effect would never occur. Electrons are necessary elements to the beginning of the discharge mechanism. Electrons absorb part of the EM energy and they start a movement of oscillation. Under certain pressure conditions, they will collide with neutral particles. Because of these collisions, the peripheral electrons are freed. They also oscillate and collide with other neutral particles. If these new free electrons are not absorbed anywhere else, their density

will increase: plasma is created, and the discharge phenomenon begins. Corona and multipaction calculations are important to determine the maximum power-handling capability of the square-coaxial feed network without any breakdown in operating frequency range.

Other breakdown phenomena exist such as the multipactor effect and the Paschen discharge. As far as a multipactor is concerned, initial electrons are also required. However, contrary to the corona effect, initial electrons will shell the metallic wall, thus starting the emission of secondary electrons. These ones are accelerated thanks to the electric field and will collide with the metallic wall on the other side. The physical quantities, which are of main importance for this effect, are the electric field magnitude, the distance between the walls, and the type of material used for the metallic wall. The mean free path of electrons helps to make the distinction between the corona effect and the multipactor, and this parameter depends on the pressure. The higher the pressure is, the more electrons have a chance to collide with molecules before reaching the wall. The two phenomena thus have their own pressure domain. The multipactor effect occurs when the ambient pressure is sufficiently low that the electron mean free path is longer than the electron separation distance. When the electron's mean free path is lower that the distance between the walls, the corona effect will occur.

Multipaction represents a possible failure mechanism of the electronic system in space in very low pressure because it can destroy RF components or it can significantly raise the system noise levels. A proper component design reduces the probability of a multipactor-free operation of an electronic system.

The air breakdown level is given by the air rigidity, which is >30 kV/mm.

- For a P power in a 50Ω impedance line, the root mean rectangular voltage is $V_{eff} = \sqrt{P.R}$V.
- For a g critical gap, the root mean rectangular field is $E_{eff} = V_{eff}/g$.
- For P = 2 kW and g = 1.8 mm, the field Eeff is 175 V/mm.

8.4.3 Design of the Feed Network

The design of SCL begins with a choice of impedance with which the patch is to be fed and it is taken as a 50Ω line and with the outer dimension $a = 9$ mm and the inner dimension $b = 3.5$ mm. The design of the feeder network requires the individual analysis of the following sections:

- 90° corner and Tee network;
- 1:2, 1:4, and 1:8 power dividers;
- SCL to microstrip transition.

The design starts with a 1:2 power divider followed by the design of 1:4 to 1:8. Power splitting to even more ratios can be accomplished in the multilayer corporate configuration to house the total feeder network in the limited available space. The coupling between different levels is done by transitions designed especially for this purpose. Using this SCL, different power dividers are designed for equal power

divisions at C-band, as shown in Figure 8.12. A 1:2 power divider is designed for equal power division (–3 dB). The input and output port impedance is 50Ω. The outer and inner conductors have dimensions of 9 mm and 3.5 mm, respectively.

8.4.3.1 Rounded Bend

The bends in the power divider can be either rounded type or chamfered bend. The design and optimization of 90° bend are important to transform waveguide impedance smoothly at bend point otherwise it will introduce mismatch. In this design bend is optimize using FEM solver as shown in Figure 8.13. It is necessary to ensure that the bending and twisting are accomplished in the correct manner; otherwise, the electric and magnetic fields will be excessively distorted, and the signal will not propagate in the way required, causing loss and reflections.

8.4.3.2 A 1:4 Power Divider

The choice of the dimension for the inner and outer conductors is based on two considerations. First is the power-handling capability of the transmission line. The gap between the inner and outer conductors should be enough to handle the transmitted power. On the other side, the second consideration is the generation of higher-order modes. A large gap between the inner and outer conductors may result

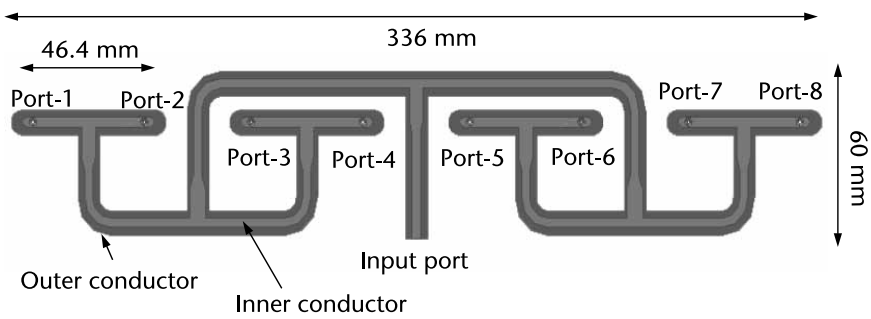

Figure 8.12 The top view of a 1:8 power divider based on SCL.

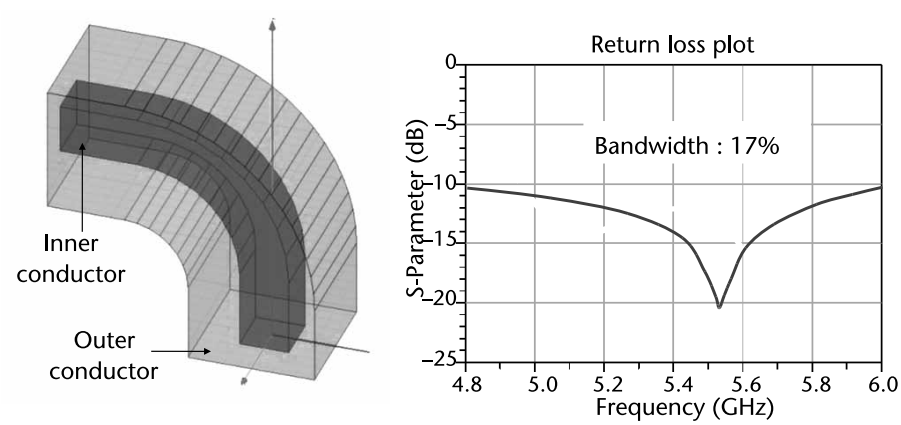

Figure 8.13 A 90° rounded bend and return loss plot.

in the generation of a higher-order mode. These modes should be avoided. Hence, the choice of dimension is a compromise between power handling and higher-order modes. A $\lambda/4$ transformer is used to match 50Ω at the input to 25Ω at the junction. The design and simulated results are shown in Figure 8.14. The simulated result shows a better than –20-dB return loss over 1 GHz.

8.4.3.3 A 1:8 Equal Power Divider

The 1:4 power divider is further progressed to 1:8 equal power division (–9 dB). The input and output sections are kept at 50Ω impedance. This power divider is designed and simulation is performed for a complete power divider with 8-port outputs. The $\lambda/4$ transformers are tuned to achieve the return loss better than –25 dB at 5.3 GHz. The Chebyshev multisection matching transformer is used for larger bandwidths. This technique provides a larger bandwidth than the binominal multisection transformer for a given number of transmission line sections but at the expense of an increased ripple over the passband of the matching network. The Chebyshev transformer is realized by equating the overall reflection coefficient to Chebyshev polynomials. Using these polynomials, matching networks are designed with a reflection coefficient at or below some prescribed level over a wide bandwidth.

The shrinkage of bandwidth is again due to transformers used at different levels. Square coaxial feeder network modules are optimized for a return loss better than –15 dB in the desired frequency band as shown in Figure 8.16. For these designs, an average of 20 to 25 design iterations is needed. A fast simulation and less memory by applying magnetic symmetry plane simply reduce design time by 50% to 60%. Optimized designed TEE, 90° bend, and transition network are integrated to form a 1:8 feeder network.

8.4.3.4 Transitions

A feeder network using an SCL is used to feed power to a radiating element such as a microstrip patch. A transition from an SCL to a microstrip line is required that will act as an interface between the two. Moreover, the power from a traveling-wave

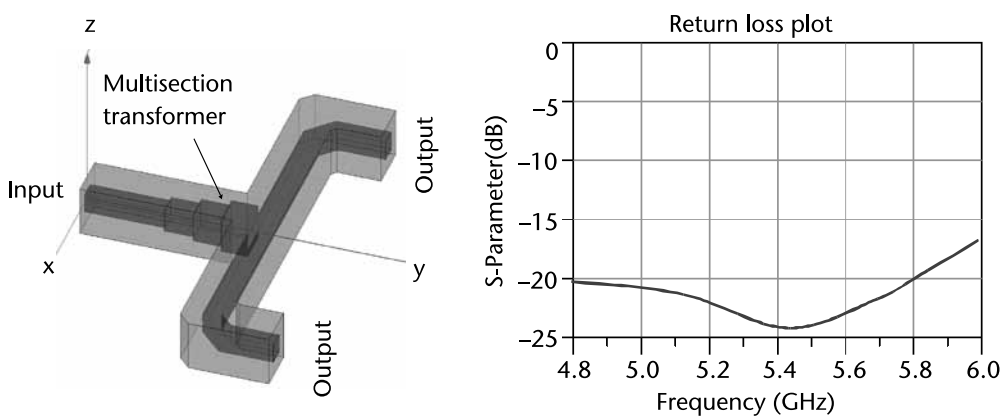

Figure 8.14 A 1:4 SCL power divider and return loss plot.

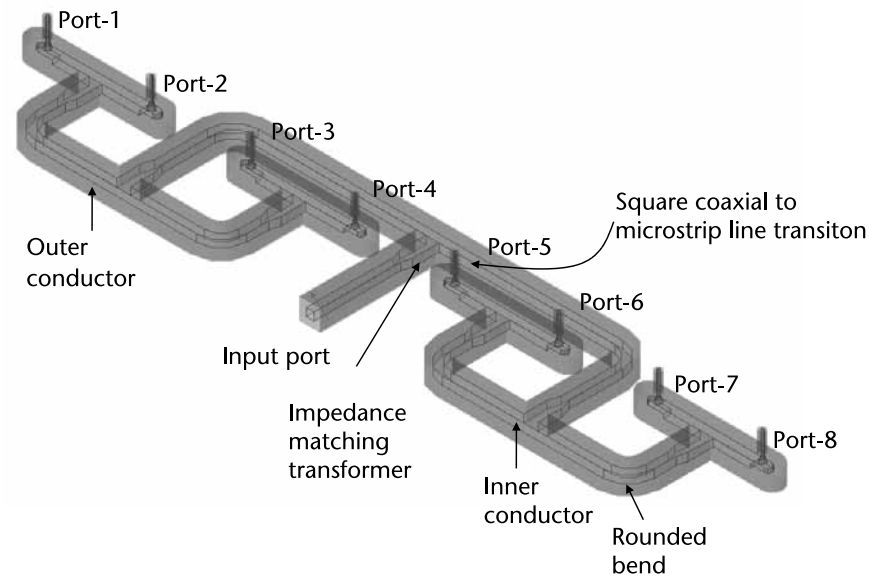

Figure 8.15 A 3-D view of a 1:8 power divider with microstrip line transition.

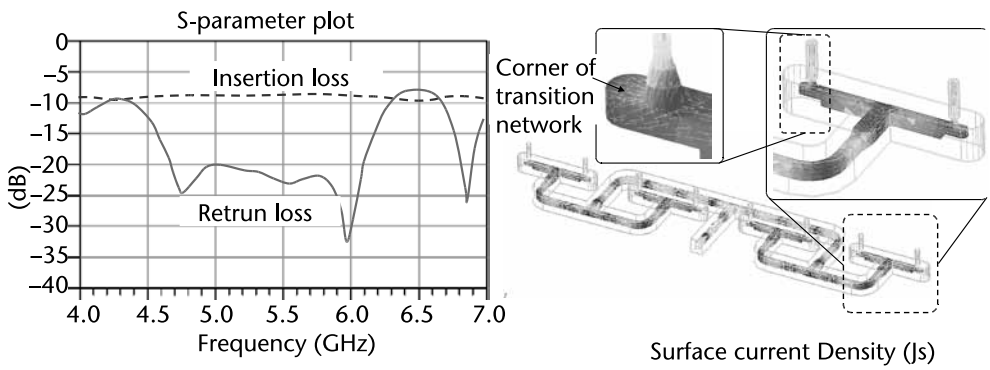

Figure 8.16 Return loss plot and surface current distribution of a 1:8 power divider.

tube (TWTA) or solid-state power amplifiers (SSPA) is to be coupled to the feed network. For high-power applications, the TWTA output is in waveguide. The transition from waveguide to SCL is required to couple power from the input to the SCL network. Sometimes it is also required to split the network into two levels so that the whole network can be accommodated in the available space. The key requirements of these transitions for practical applications would be low loss, broadband performance, tolerance to fabrication, and compact size. A transition to couple power between two levels of SCLs is also required. All these transitions are to be designed and analyzed separately.

8.4.3.5 Waveguide to SCL Transition

The coupling between waveguide and SCL is achieved by using an end launcher type of probe coupling. Numerous transition structures have been studied and now

are available for microwave and millimeter-wave transceiver applications. Among them, simple probe-type transitions providing low cost, simplicity, and broadband performances have been typically utilized for microwave and millimeter-wave applications [19, 20]. The depth of the probe and its distance from the shorted wall of waveguide are critical for the performance. These two parameters are optimized to achieve the best performance. The termination of probe in the SCL is done on the inner conductor. The aperture size of the waveguide is 40 mm × 20 mm. The simulated results show that at 5.3 GHz the return loss is better than 30 dB. The operation of the waveguide-to-coaxial line transition can be easily understood if we assume that an input power is applied to the SCL. In this transition structure, the center conductor of the coaxial line is inserted at the $\lambda/4$ distance from the waveguide wall. This transition structure can be considered as an impedance transformer structure for the impedance matching between a coaxial line and waveguide.

8.4.3.6 SCL to Microstrip Line Transition

The transition from the SCL to the microstrip line is the most critical to design. To achieve return loss and power coupling from this transition, the shape of the SCL is modified at the location of the transition. Different perturbations with the shape lead to working the transition in different frequency ranges. SCL to microstrip line transition is shown in Figure 8.17.

The transitions with short-circuited square-coaxial waveguide of $\lambda_g/4$ guided wavelength are very popular because their principle of mode transformation is almost the same with that of ordinary transitions of a waveguide and a coaxial cable. The probe transition connects a microstrip line and a waveguide and a probe at one end of the microstrip line is inserted into the SCL whose one end is short-circuited by the back-short waveguide.

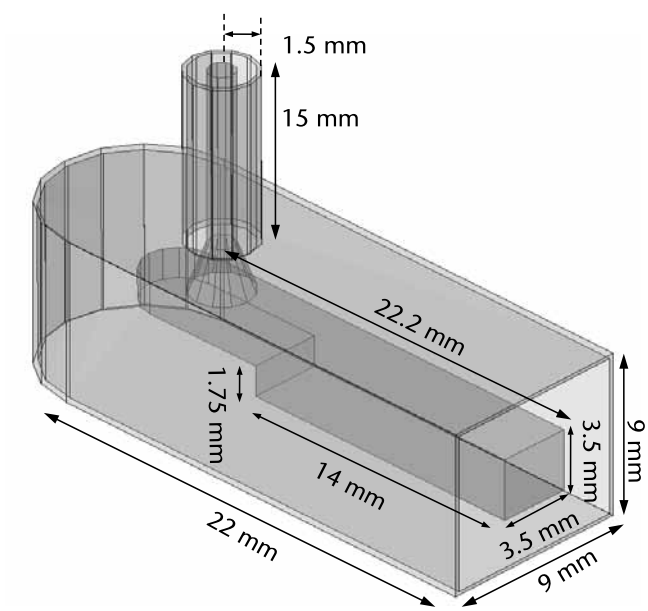

Figure 8.17 SCL to microstrip line transition design.

The performance is achieved by shaping both the outer and inner conductors. The inner and outer conductors are made circular at the end. The location of the end point of the inner conductor with respect to the end point of the outer conductor is an important parameter of optimization.

Moreover, a section of the inner conductor is cut at the end. The length and depth of the cut affect the coupling. Also, a cone-like tapered section is placed at the inner conductor, which guides the impedance transformation from a 50Ω SCL to a 50Ω circular coaxial line. The location of the center of the cone on the inner conductor affects the matching of two sections. This location can be optimized for return loss improvement. The other end of the 50Ω circular coaxial line is directly fed to the microstrip patch feed line. This transition is the most versatile of all the transitions. The simulated return loss of this transition works very well from 2 GHz to 7 GHz for a return loss better than –20 dB in this frequency band as shown in Figure 8.18.

8.4.4 High-Power Calculation of the SCL

In square-coaxial feed network design, a sufficient margin is taken in the design to avoid any damage because of the high-power operation. The electric field strength in the SCL is evaluated by modeling the complete network using the FEM. The electric field strength is computed at the junction where the minimum gap has been created because of the change in the inner conductor dimension for the required impedance transformation. The following shows the result of the calculation for a typical 8 kW of peak power and 72W of average power:

- Electric field strength in square coaxial line = 63.92 V/cm (from the FEM solver).
- Average voltage for 1-W average power = 17.75V.
- Average voltage for 72-W average power = 150.67V.
- Peak voltage for 8-kW peak power with 0.90 duty cycle = 1.588 × 103V.
- Peak electric field strength for rectangular coaxial dimensions = 577.532 V/mm.

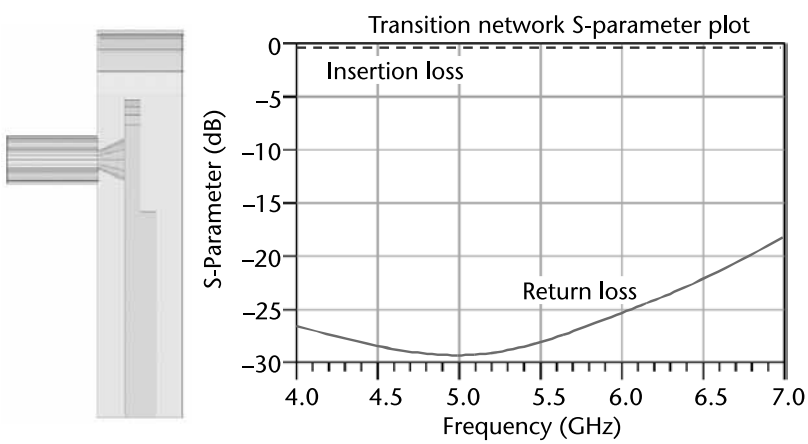

Figure 8.18 S-parameter plot of the SCL to microstrip line transition.

- Peak electric field strength for air breakdown = 3,000 V/mm.
- Peak electric field strength for dielectric breakdown = 2,000 V/mm.
- Breakdown margin for air = 14.31 dB.
- Breakdown margin for dielectric = 10.789 dB.

The gap gives around 10-dB margin and the cutoff frequency for dominant higher-order TE10 mode is 10 GHz.

8.5 Integrated Array Antenna Design

Complete SAR antenna design is designed by integrating planar microstrip radiating array with high-power square-coaxial feed network. All layers and components are shown in Figure 8.19. A complete antenna system is simulated using the FDTD technique. This is one panel of the antenna, for high gain antenna multiple panels are used on top of the SCL feed network.

SCLs are designed on aluminum by cutting grooves and placing the inner conduct metal with the help of PTFE spacers. The printed antenna is placed on top of this aluminum block and coaxial pins of each 8-output port is fed to the microstrip antenna array.

8.6 Summary

In this chapter, the airborne SAR antenna system was discussed. Antenna pattern synthesis is very important in these types of antennas. A multilayer printed antenna with EM coupling is designed and developed in C-band for wide bandwidth and low cross-polarization. Beam shaping in the elevation plane is realized by obtaining the complex excitation distribution employing the null perturbation technique.

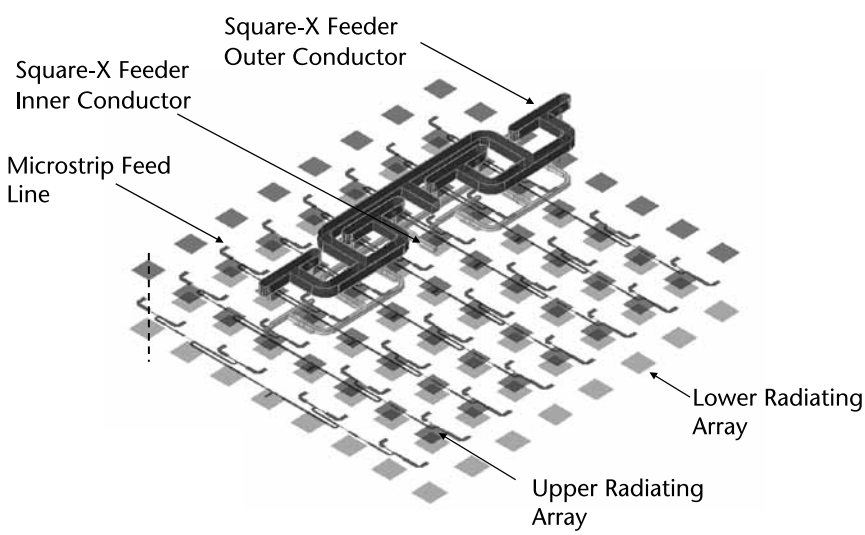

Figure 8.19 Complete 64-element array antenna integrated with a 1:8 power divider.

The design of a wideband aperture coupled microstrip linear array antenna that consisting of eight elements in the elevation plane and another eight elements in the azimuth plane has been described. The complete antenna design with MoM, FEM, and FDTD with efficient techniques reduces the design cycle by 60% compared to the traditional single solver approach.

References

[1] Rengarajan, S. R., and A. G. Derneryd, "Application of Compound Coupling Slots in the Design of Shaped Beam Antenna Pattern," *IEEE Transactions on Antennas and Propagation*, Vol. 41, No. 1, January 1983, pp. 5–9.

[2] Woodward, P. M., and J. D. Lawson, "The Theoretical Precision with Which an Arbitrary Radiation-Pattern May Be Obtained from a Source of Finite Size," *Journal of the Institution of Electrical Engineers - Part III: Radio and Communication Engineering*, Vol. 95, No. 37, September 1948, pp. 363–370.

[3] Orchard, H. J., R. S. Elliott, and G. J. Stern, "Optimizing the Synthesis of Shaped Beam Antenna Patterns," *Proc. IEE*, Vol. 132-H, No. 63, February 1985.

[4] Steyskal, H., "On the Problem of Antenna Power Pattern Synthesis for Linear Arrays, FDA Reports," *Research Institute of National Defence*, Stockholm, Sweden, Vol. 5, No. 3, May 1971, pp. 1–16.

[5] Schelkunoff, S. A., "A Mathematical Theory of Linear Arrays," *Bell Syst. Tech. J.,* Vol. 22, No. 1, January 1943, pp. 80–107.

[6] Dolph, C. L., "A Current Distribution for Broadside Arrays Which Optimizes the Relationship Between Beam Width and Side-Lobe Level," *Proc. IRE*, Vol. 34, June 1946, pp. 335–348.

[7] Marcano, D., and F. Duran, "Synthesis of Antenna Arrays Using Genetic Algorithms," *IEEE Antennas and Propagation Magazine*, Vol. 42, No. 3, 2000, pp. 328–332.

[8] Donelli, M., et al., "Linear Antenna Synthesis with Hybrid Genetic Algorithm," *Prog. Electromagn. Res.*, Vol. 49, 2004, pp. 1–22.

[9] Farhat, N. H., and B. Bai, "Phased-Array Antenna Pattern Synthesis by Simulated Annealing," *IEEE Proc.*, Vol. 75, No. 6, 1987, pp. 842–844.

[10] Orfanidis, S. J., *Electromagnetic Waves and Antennas*, Rutgers University, 1999.

[11] Pandey, A. K., "Design of a Cosecant Square-Shaped Beam Pattern SAR Antenna Array Fed with Square Coaxial Feeder Network," *2013 European Microwave Conference*, Nuremberg, 2013.

[12] Lee, C. Q., et al., "Design of a Square Waveguide Feed," *Proceedings of USNC/URSI Meeting*, Boulder, CO, November 1979, p. 134.

[13] Pandey, B. K., et al., "Square Coaxial Beam Forming Network for Multilayer Microstrip Antenna," *2007 Asia-Pacific Microwave Conference*, Bangkok, 2007, pp. 2477–2480.

[14] Yubo, T., Z. Bing, and W. Xin, "Numerical Method for Solving Characteristic Parameters of Square Coaxial Line," *2007 IEEE Antennas and Propagation Society International Symposium,* Honolulu, HI, 2007, pp. 73–76.

[15] Hurtado, M., H. E. Lorente, and C. H. Muravchik, "Analysis of a Square Microstrip Antenna with an Eccentric Slot," *IEEE Antennas and Propagation Society International Symposium*, Boston, MA, 2001, pp. 498–501.

[16] Oikawa, N., et al., "Coaxial-Line Connection of a Circularly-Polarized Patch Array Antenna on the Thick Resin and a 60 GHz-Band Quadrature Oscillator Chip," *2014 IEEE iWEM*, Sapporo, 2014, pp. 169–170.

[17] Woode, A., and J. Petit, "Diagnostic Investigations into the Multipactor Effect, Susceptibility Zone Measurements and Parameters Affecting a Discharge," *ESTEC Working Paper*, Vol. 1556, November 1989.

[18] Vaughan, J. R. M., "Multipactor," *IEEE Transactions on Electron Devices*, Vol. 35, No. 7, July 1988, pp. 1172–1180.

[19] Ko, D. H., et al., "V-Band Waveguide-to-Coplanar Waveguide Transition for 60 GHz Wireless LAN Application," *IEEE MTT-S Int EUMC*, 2004, pp. 641– 644.

[20] Kim, K. W., C. H. Na, and D. S. Woo, "New Dielectric-Covered Waveguide-to-Microstrip Transitions for Ka-Band Transceivers," *IEEE MTT-S Int. Microwave Symp Dig.*, Vol. 2, Philadelphia, PA, 2003, pp. 1115–1118.

Selected Bibliography

Alessandri, F., M. Mongiardo, and R. Sorrentino, "Computer Aided Design of Beam Forming Networks for Modern Satellite Antennas," *IEEE Transactions on Microwave Theory and Techniques*, Vol. MTT-40, No. 6, June 1992, pp. 1117–1127.

Angeletti, P., G. Toso, and G. Ruggerini, "Array Antennas with Jointly Optimized Elements Positions and Dimensions Part II: Planar Circular Arrays," *IEEE Transactions on Antennas and Propagation*, Vol. 62, 2014, pp. 1627–1639.

Bucci, O. M., et al., "Antenna Pattern Synthesis: A New General Approach," *Proc. IEEE*, Vol. 82, March 1994, pp. 358–371.

Buckley, M. J., "Synthesis of Shaped Beam Antenna Patterns Using Implicitly Constrained Current Elements," *IEEE Transactions on Antennas and Propagation*, Vol. 44, February 1999, pp. 192–198.

Deshpande, M., and N. Das, "Rectangular Microstrip Antenna for Circular Polarization," *IEEE Transactions on Antennas and Propagation*, Vol. 34, No. 5, May 1986, pp. 744–746.

Elliot, R. S., "Antenna Pattern Synthesis," *IEEE Antenna and Propagation Society Newsletter*, October 1985, pp. 5–9.

Guo, J., and Y. Lu, "Novel Aperiodic Phased Array with Reduced Number of Active Chains for Space-Borne SAR," *IEEE Fifth Asia-Pacific Conf. Synthetic Aperture Radar*, 2015, pp. 20–23.

Hu, Y., et al., "Characterization of the Input Impedance of the Inset-Fed Rectangular Microstrip Antenna," *IEEE Transactions on Antennas and Propagation*, Vol. 56, No. 10, October 2008, pp. 3314–3318.

Kumar, G., and K. P. Ray, *Broadband Microstrip Antenna*, Norwood, MA: Artech House, 2003.

Mailloux, R. J., *Phased Array Antenna Handbook*, Norwood, MA: Artech House, 1994.

Milovanovic, A., and B. Koprivica, "Analysis of Square Coaxial Lines by Using Equivalent Electrodes Method," *Proceedings of the Joint INDS'11 & ISTET'11*, Klagenfurt, 2011, pp. 1–6.

Sharma, P., and K. Gupta, "Analysis and Optimized Design of Single Feed Circularly Polarized Microstrip Antennas," *IEEE Transactions on Antennas and Propagation*, Vol. 31, No. 6, November 1983, pp. 949–955.

Sharma, S. B., et al., "Dual-Polarized Shaped-Beam Printed Antenna for Airborne SAR Applications," *Microwave Opt. Technology Letter,* Vol. 44, 2005, pp. 383–385.

Uher, J., J. Bornemann, and U. Rosenberg, *Waveguide Components for Antenna Feed Systems: Theory and CAD*, Norwood, MA: Artech House, 1993.

Zhang, X. -M., et al., "Cosecant-Square Pattern Synthesis with Particle Swarm Optimization for Nonuniformly Spaced Linear Array Antennas," *2008 8th International Symposium on Antennas, Propagation and EM Theory*, 2008, pp. 193–196.

Zurcher, J. F., and F. E. Gardiol, *Broadband Patch Antennas*, Norwood, MA: Artech House, 1995.

CHAPTER 9

Multifrequency Shared-Aperture Microstrip Antenna Arrays

9.1 Introduction

High-resolution airborne and spaceborne imaging of the Earth is often carried out using SAR techniques, as discussed in the previous chapter. Early synthetic aperture radar (SAR) systems were single-frequency and single-polarization systems, but time has seen a growing interest in multifrequency, dual-polarization SAR systems. The reason for this drift is the additional amount of geophysical information, possibly to extract from multifrequency, polarimetric SAR data [1]. Multifrequency systems such as tactical radar systems and SAR systems are common in both military and civil applications because their information capacity is significantly higher than single-frequency counterparts. A multiband antenna array can be realized by simply positioning several single-band antenna arrays side by side. However, this approach is not desirable because it significantly increases the aperture size and antenna weight. The multifrequency shared aperture antenna arrays can minimize the array size and weight by sharing the same aperture for each band. Therefore, this approach is very attractive for compact systems like space-borne SAR and vehicle-based tactical radars.

An antenna array that operates in multifrequency bands with dual-polarization capability in each band and whose elements are integrated together into a common physical space by sharing the single aperture falls into the category of multiband dual-polarized shared-aperture (MBDP-SA) array. In the multifrequency shared aperture array design, antenna designers face some design challenges such as the following:

- In multifrequency antenna array design, the requirement of avoiding grating lobes at the higher frequency dictate the interelement spacing. This condition unnecessarily increases the number of elements at the lower-frequency band [2].
- Moreover, only a moderate-frequency ratio between the operating frequencies can be achieved by this approach. For frequency ratios on the order of

4:1 or more, designing a multifrequency microstrip antenna is a complex matter.

- Antenna design becomes more challenging, especially if other spaceborne SAR critical issues such as size, system bandwidth, beam scanning, and polarization purity come into the picture.

In multifrequency SAR, the higher-band wave reflects primarily at the crown of the tree, while the lower-band wave can penetrate the leaves and reflect at the root of the forest as shown in Figure 9.1. Longer wavelength bands (L-bands) can penetrate forest canopy. These wavelengths are used to estimate forest biomass and detect the amount of wood in a forest. The shorter wavelengths (X-bands) are used to detect smaller features like leaves and twigs. The longer the microwave wavelength, the greater the penetration of canopy. The back-scattering matrix of a ground target depends on frequency, polarization, and incidence angle of the incident wave.

Theoretically, an ultrawideband (UWB) array such as a Vivaldi antenna can also be employed to minimize the aperture size, because it can cover multibands with only a single aperture [3]. However, these arrays are less suitable for the SAR applications because the element spacing is based on the smallest wavelength in the operating bandwidth to avoid the grating lobes at a higher frequency. So at a lower frequency, the elements are too densely distributed. More elements and corresponding transceiver (T/R) modules are therefore required as compared to the single frequency microstrip patch antenna. Hence, UWB arrays are less feasible due to the high cost, large weight, and difficulties in the heat control of a large amount of T/R modules. The MBDP-SA array is more suitable for the multiband SAR antenna than the UWB.

9.1.1 SAR Imaging

In SAR imaging, a very long aperture is synthesized through the integration of the magnitude and phase information of the returned echoes from an object over the entire time it is in view of the radar. Because comparatively long-wavelength radar energy penetrates through (even dense) water vapor, radar imaging is often possible in situations where optical sensing is severely limited or even impossible due to persistent cloud cover. The strength of the signal received by the antenna for a given ground resolution cell (represented by the radar backscatter coefficient σ) is

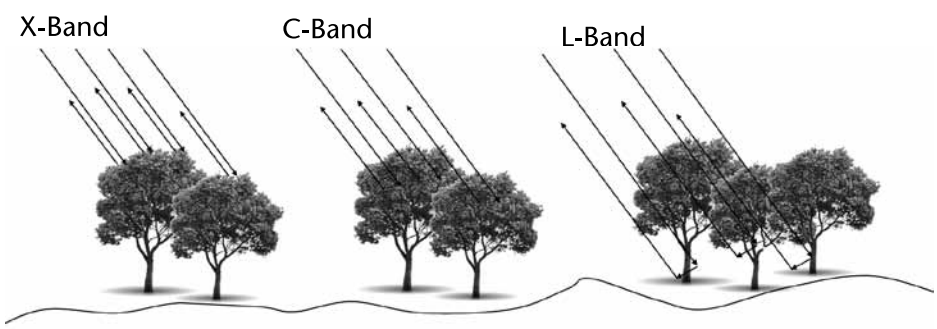

Figure 9.1 Short-wavelength X-band radar energy reflects from canopy surface while long-wavelength L-band energy penetrates through canopy and reflects from stems and terrain surface.

mainly a function of the wavelength of the characteristics of the imaged feature, the microwave energy, and the geometry of the image acquisition.

In the context mapping, the wavelength of the radar determines whether the SAR backscatter is dominated by surface scattering or volume scattering. In the case of a relatively short wavelength (for example, X-band), the microwave energy interacts with the surface of the Earth and the energy is scattered by small-scale components on the surface, such as the foliage and small branches or trees. In contrast, radar energy with relatively long wavelengths (like 24 cm for L-band) will penetrate deep and reflect from large-scale components including large objects and the terrain surface. The SAR signal logged from a surface is proportional to the surface roughness. High-frequency X-band is very sensitive to even a small-scale roughness. The same surface is much flatter by the L-band SAR due to the difference in wavelength. The penetration of the microwave signal in terrain is directly dependent on wavelength. This means that longer-wavelength SAR has more signal or sensitivity to the volume content of terrain (e.g., soil moisture). This interprets that while X-band can detect even slight details, L-band is suitable to observe larger objects, which would be unclear with X-band. Combining the two is possible to monitor both geometrical objects and small details.

Many SAR systems have the capability to send and receive energy with different polarizations. Because radar signal can be depolarized upon interaction with various surface objects, independently recording the reflection of like-polarized energy (e.g., horizontal send – horizontal receive (HH) or vertical send – vertical receive (VV)) and cross-polarized energy (e.g., horizontal send – vertical receive (HV) or vertical send – horizontal receive (VH)) can yield valuable information regarding the characteristics of imaged features and can be particularly useful in the analysis of vegetation type and structure. Commonly applied bands for radar applications and bands and polarizations for different applications are listed in Table 9.1.

Most of the current space-borne SAR systems operate from L-band to X-band due to the atmosphere attenuation. The operating frequency below L-band will suffer reflections from the ionosphere, while radiated energy higher than the X-band radiation is increasingly absorbed by water and oxygen molecules in the atmosphere and thus becomes sensitive to weather condition. Ka-band is also frequently used for SAR applications (climate surveillance or fine imaging), as it offers less

Table 9.1 Commonly Applied Bands for Radar Applications

			Applications			
Band	*Frequency Range (GHz)*	*Radar Frequency (GHz)*	*Geology and Water*	*Agriculture and Ocean*	*Forest*	*Soil*
L	1–2	1.215–1.4	L	—	L	—
S	2–4	2.3–2.5 and 2.7–3.7	—	—	—	—
C	4–8	5.25–5.925	C	C	C	C
X	8–12	8.5–10.68	—	X	X	—
Ku	12–18	13.4–14 and 15.7–17.7	—	—	—	—
K	18–26	24–24.25	—	—	—	—
Ka	26–40	33.4–36	—	—	—	—

attenuation to signal due to its location between the water and oxygen absorption peak at 23 GHz and 63 GHz, respectively.

9.2 Dual-Frequency Shared Aperture Antenna Array

The antenna plays a very important role in determining the overall system performance of airborne and spaceborne SAR systems. SAR system performance such as azimuth and elevation resolution, imaging ambiguity, and the width of the mapping area is directly determined by the performance of its antenna. The main driving force for frequency and polarization selection of a SAR system is the application targeted for. For most the applications, SAR systems generally operate at L-band, C-band, and X-band. There is an increasing demand for simultaneous multifrequency SAR systems to get images of targets of different signatures during one visit to a region of the Earth. Additionally, for airborne applications, SAR data at different frequencies like C-band and X-band can be recorded without landing the aircraft for the mounting of the different antenna at different frequency bands if a multifrequency SAR system is used onboard the aircraft. Antennas at different frequency bands will occupy a larger area, which may be prohibited by the available space in the radome of the aircraft. Thus, there is a strong need to develop antennas that fulfill the requirement of multifrequency operation for SAR applications [4].

In this chapter, the design and development of a dual-frequency shared aperture antenna array is discussed [5–15]. Rectangular slots are used as a radiator at X-band, and the inset fed patch has been used as radiating elements at C-band. A parametric study by varying various dimensions of the slot and simulated return loss curves are also presented in this chapter. The dual-band operation of an antenna has been applied in a lot of systems, such as wireless communications, radars, deep space communications, and radio astronomical telescopes. The requirements for antennas are varied in different missions.

9.3 Design of C-Band and X-Band Radiating Element

A dual-frequency antenna with a shared aperture places a severe constraint on space for the elements and the associated feed networks and makes a multilayer geometry a necessity. The C-band and X-band radiating elements and the pertinent feed networks are placed on separate layers. The design dimensions of the single C-band and X-band radiating elements are shown in Figure 9.2.

The bottom layer is a substrate material of Rohacell foam of 6.71-mm thickness with a dielectric constant of 1.08 backed by a ground plane. The foam material has low dielectric constants close to 1 because they are filled with small gas bubbles. This allows for the designing of antennas with high efficiency [16]. The ground plane serves as an effective shield between the radiating patches and the feed network improving polarization purity. Above this foam layer, there is a layer of the substrate material of 0.79-mm thickness of RT-Duroid5880 with a dielectric constant of 2.2 for the electromagnetically coupled antenna feed network for X-band antenna.

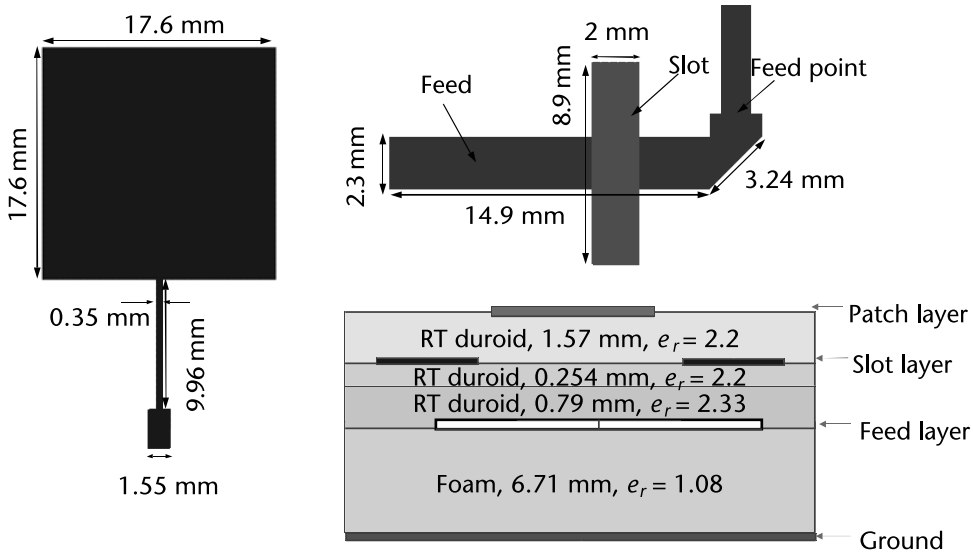

Figure 9.2 C-band and X-band antenna configuration, design dimensions, and substrate stackup.

Slots are cut at the top side of this substrate and feedlines are etched on the bottom side to excite the slots. Above the slot, there is another substrate layer of 1.57-mm thickness of RT-Duroid5880 for the C-band microstrip patch that is etched on the top side of this substrate. The patch antenna at C-band is edge-fed by a microstrip line. The slot at X-band is fed by the microstrip line beneath the slot layer. Feed for the slot is isolated from the patch by a ground layer. Thickness and permittivity of the substrate are determined as a trade-off between cross-polar radiation and bandwidth. The bottom ground layer is required to avoid radiation in the undesired direction as the slot has the characteristic of bidirectional radiation. Complete assembly is sharing a common aperture with the slot and patch radiating in the presence of each other without affecting their individual radiation pattern.

9.3.1 Design of Patch Antenna at C-Band

Microstrip edge-fed patch is selected as radiating element at C-band. In edge-fed patch configuration, the input impedance of the patch is very high at the edge because of which the width of the microstrip line feeding the patch becomes very small. In this design, the width of the 180Ω line is 0.35 mm, which is transformed into 100Ω impedance using a $\lambda/4$ transformer. The antenna design parameters have been optimized using the finite element method (FEM) solver. The final design dimensions of the patch, which yields the desired RF performance in the presence of the X-band slots cut in the ground plane of the patch, are shown in Figure 9.2. The simulated gain of the single patch is 7.1 dBi at 5.3 GHz.

9.3.2 Design of the Slot Antenna at X-Band

At X-band, the printed slot is employed as a radiating element. This slot is cut in the ground plane of the C-band patch and it is fed by a microstrip line below a dielectric thickness of 0.79 mm and a relative permittivity of 2.2. The microstrip line of 50Ω

impedance and a width of 2.3 mm is used as a slot feedline. Below this microstrip feedline, another ground plane at the separation of 5.0 mm is used to avoid radiation from the slot in the lower half plane. The RF performance of the slot must be optimized in the presence of the C-band patch which acts as a parasitic element for slot radiator. For the dual-polarized antenna, rectangular shape slot is a preferred option as it yields better cross-polar performance.

Figure 9.3 shows the simulated return loss performance of a single slot radiator at X-band. Return loss bandwidth is 800 MHz at a center frequency of 9.6 GHz for the voltage standing wave ratio (VSWR) of 2:1. At 9.6 GHz, the simulated gain of a single slot is 4.5 dBi. After designing a single radiating element at X-band, its sensitivity analysis is carried out for various dimensional tolerances. The length and width dimensions of the rectangular slot as shown in Figure 9.2 are varied, which results in a frequency shift in the return loss performance. Good impedance matching is obtained on wide bandwidths around the working frequency.

9.4 Array Design

Integrated antenna array structure using both C-band and X-band linear arrays are shown in Figure 9.4. For eight linear arrays (each having 4 C-band and 16 X-band elements), the total array size is 17.6 cm × 36 cm.

Both C-band and X-band radiating elements are arranged in such a way that these do not block each other's radiation pattern. One C-band patch radiator is placed between four X-band slot radiators. This topology helps to avoid placing two antennas for C-band and X-band separately and gives real estate to the system in which they are used.

9.4.1 Design of the C-Band Linear Array

In the C-band linear array, all four elements placed in one row and are fed through a series feed network. The entire row is then fed in the center by a corporate feed network. The design dimensions of the series feed network are shown in Figure 9.5. Multiple $\lambda/4$ transformers are used to transform 50Ω input impedance to the impedance of the patch at the edge. Figure 9.5 shows the simulated result of the linear

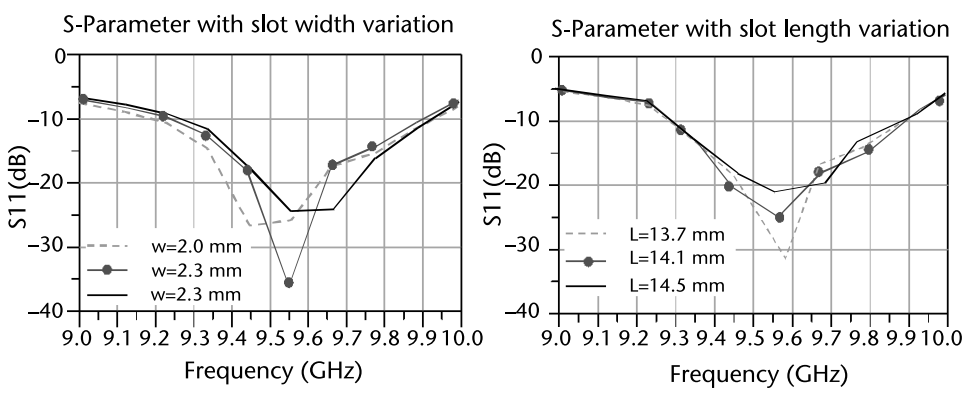

Figure 9.3 Return loss plot of the X-band antenna with the width and length variation of the slot.

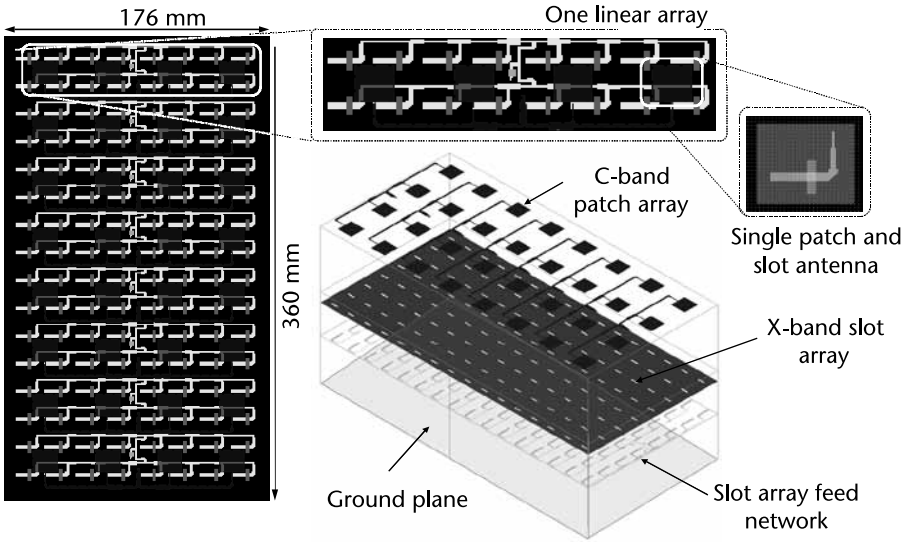

Figure 9.4 The C-band and X-band shared aperture antenna array configuration.

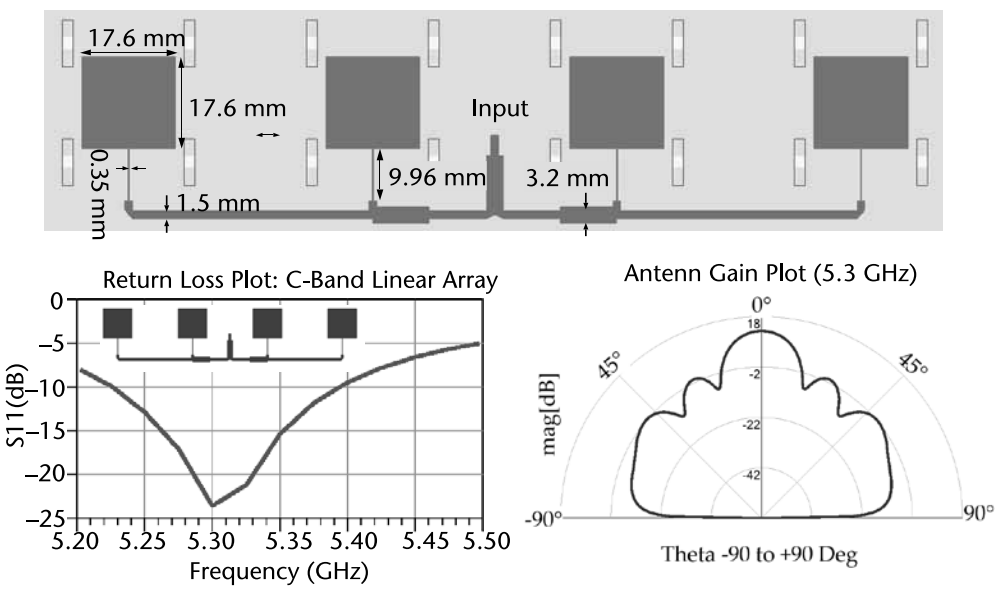

Figure 9.5 The C-band linear array antenna and simulated results.

array. The antenna is resonating at 5.3 GHz, and the operating bandwidth is 180 MHz (5.22–5.4 GHz) and gain of the linear array antenna is 13 dBi.

9.4.2 Design of the X-Band Linear Array

In the X-band linear array, eight elements placed in one row are fed through a series feed network. Two rows are combined in the center and fed with corporate feed network as shown in Figure 9.6. Such an antenna feeding mechanism is called a

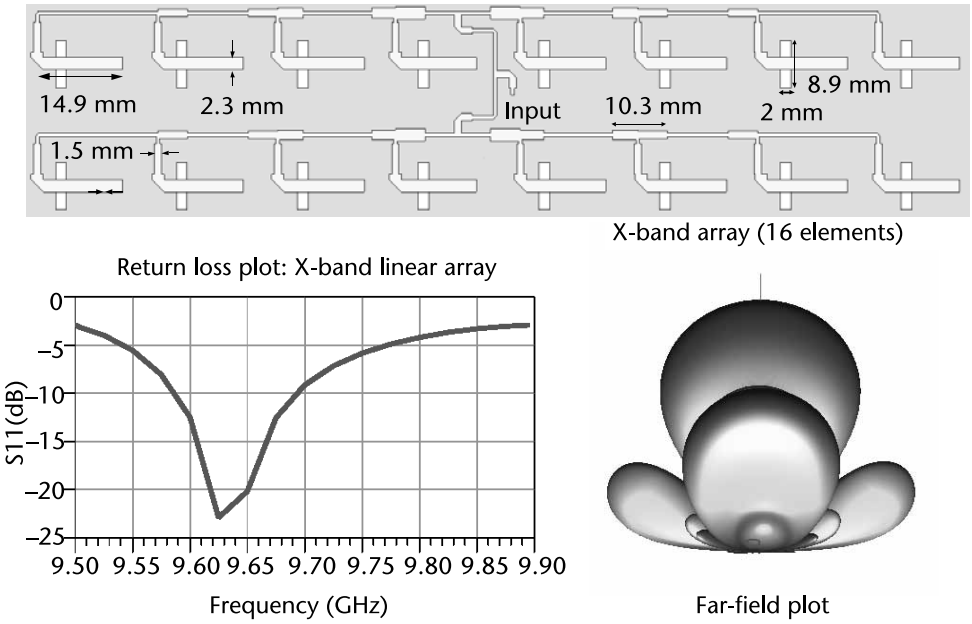

Figure 9.6 The X-band linear array antenna and simulated results.

hybrid feed network, which is a very efficient way to combine multiple antenna elements in a limited space in an array design. The simulated performance of X-band linear antenna, in the presence of the C-band linear array, is shown in Figure 9.6. The antenna is resonating at 9.63 GHz and the operating bandwidth is 120 MHz (9.58–9.7 GHz). The 16-element antenna gain is 15.6 dBi.

9.4.3 Integrated Array

A single linear array is duplicated in Y directions to form a planar array as shown in Figure 9.7. The spacing between patch elements is 0.8λ in both the X and Y directions. The interelement spacing between patches is optimized for the maximum gain of the array. The spacing between slots is subjected to a condition that the slot array is within the inner periphery of the patch array. Slots are spaced at 0.8λ in the X direction and 0.6λ in the Y direction. The total aperture of the patches is square in geometry, while that of slots is rectangular. In a planar antenna array, the total number of elements in C-band is 32 (4×8 elements), while total number of elements in X-band is 128 (8×16 elements).

A simulated return loss plot of a planar array is shown in Figure 9.7. The 10-dB bandwidth of a 4×8 planar array is 100 MHz at C-band and 300 MHz at X-band. Isolation between two antennas is better than 27 dB over the entire operating frequency band. The fabricated antenna is shown in Figure 9.8. The radiation pattern of the antenna is measured at the anechoic chamber. The measured gain of a patch array is 13.5 dBi at a center frequency of 5.3 GHz, and the gain of a slot array is 14.8 dBi at a center frequency of 9.6 GHz.

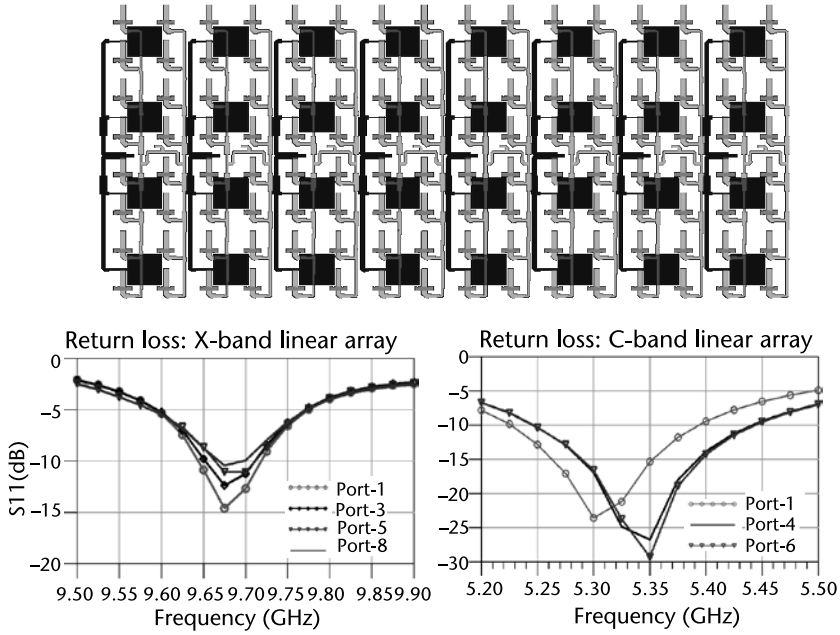

Figure 9.7 Dual-frequency shared-aperture planar antenna array and return loss plot.

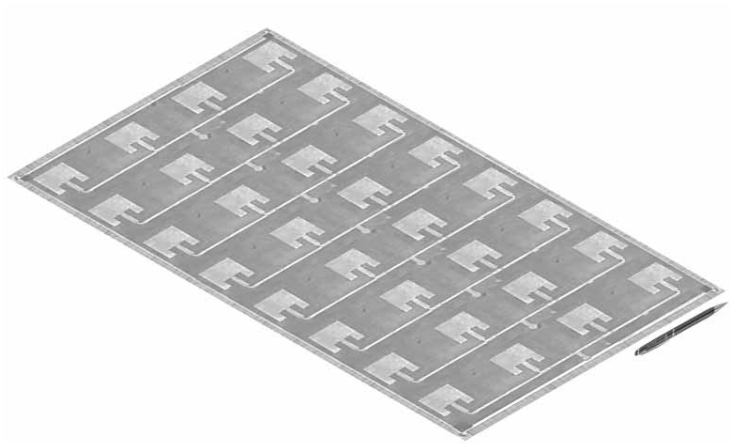

Figure 9.8 Fabricated planar antenna array.

9.5 Summary

In this chapter, the method of assembling two frequency band shared-aperture subarrays to form a large shared-aperture array was introduced. The planar array for the SAR application was constructed from microstrip patches at the C-band slots at X-band in a single aperture. An array prototype was fabricated and measured to validate the method. This array design method can be extended to the shared-aperture arrays with more than two frequency bands. The advantage of this configuration is that the isolation between the two frequency bands is better than 27 dB, which ensures proper functioning of the system at an individual frequency band.

References

[1] National Aeronautics and Space Administration, "Spaceborne SAR: Current Status and Future Directions," NASA Technical Memorandum 4679, April 1995.

[2] Shafai, L. L., et al., "Dual-Band Dual-Polarized Perforated Microstrip Antennas for SAR Applications," *IEEE Transactions on Antennas and Propagation*, Vol. 48, January 2000, pp. 58–66.

[3] Loui, H., J. P. Weem, and Z. Popovic, "A Dual-Band Dual-Polarized Nested Vivaldi Slot Array with Multilevel Ground Plane," *IEEE Transactions on Antennas and Propagation*, Vol. 51, No. 9, September 2003, pp. 2168–2175.

[4] Pokuls, R., J. Uher, and D. M. Pozar, "Dual Frequency and Dual Polarization Microstrip Antennas for SAR Applications," *IEEE Transactions on Antennas and Propagation*, Vol. 46, September 1998, pp. 1289–1296.

[5] Pandey, B. K., et al., "Dual Frequency Single Aperture Microstrip Patch Antenna Element for SAR Applications," *IETE Technical Review*, Vol. 23, No. 6, November-December 2006, pp. 357–366.

[6] Uher, R. P. J., and D. M. Pozar, "Dual-Frequency and Dual-Polarization Microstrip Antennas for SAR Applications," *IEEE Transactions on Antennas and Propagation*, Vol. 46, No. 9, September 1998, pp. 1289–1296.

[7] Pozar, D. M., and S. D. Targonski, "A Shared-Aperture Dual-Band Dual Polarized Microstrip Array," *IEEE Transactions on Antennas and Propagation*, Vol. 49, No. 2, February 2001, pp. 150–157.

[8] Zhong, S. -S., et al., "Tri-Band Dual Polarization Shared-Aperture Microstrip Array for SAR Applications," *IEEE Transactions on Antennas and Propagation*, Vol. 60, No. 9, September 2012.

[9] Wong, H., K. -L. Lau, and K. -M. Luk, "Design of Dual-Polarized L-Probe Patch Antenna Arrays with High Isolation," *IEEE Transactions on Antennas and Propagation*, Vol. 52, No. 1, January 2004, pp. 45–52.

[10] He, S., and J. Xie, "Analysis and Design of a Novel Dual-Band Array Antenna with a Low Profile for 2400/5800-MHz WLAN Systems," *IEEE Transactions on Antennas and Propagation*, Vol. 58, No. 2, February 2010, pp. 391–396.

[11] Qu, X., et al., "Design of an S/X Dual-Band Dual-Polarised Microstrip Antenna Array for SAR Applications," *IET Microw. Antennas Propag.*, Vol. 1, No. 2, 2007, pp. 513–517.

[12] Hsu, S. -H., Y. -J. Ren, and K. Chang, "A Dual-Polarized Planar-Array Antenna for S Band and X-Band Airborne Applications," *IEEE Transactions on Antennas and Propagation*, Vol. 51, No. 4, August 2009, pp. 70–78.

[13] Rahmat-Samii, Y., et al., "Advanced Precipitation Radar Antenna: Array-Fed Offset Membrane Cylindrical Reflector Antenna," *IEEE Transactions on Antennas and Propagation*, Vol. 53, No. 8, August 2005, pp. 2503–2515.

[14] Naishadham, K., et al., "A Shared-Aperture Dual-Band Planar Array with Self-Similar Printed Folded Dipoles," *IEEE Transactions on Antennas and Propagation*, Vol. 61, No. 2, February 2013, pp. 606–613.

[15] Pokuls, R., J. Uher, and D. M. Pozar, "Dual-Frequency and Dual- Polarization Microstrip Antennas for SAR Applications," *IEEE Transactions on Antennas and Propagation*, Vol. 46, No. 9, September 1998, pp. 1289–1296.

[16] Rostan, F., and W. Wiesbeck, "Aperture-Coupled Microstrip Patch Phased Arrays in C- and X-Band: A Contribution to Future Multi-Polarization Multi-Frequency SAR Systems," *Proceedings of International Symposium on Phased Array Systems and Technology*, Boston, MA, 1996, pp. 141–146.

Selected Bibliography

Chiou, T. W., H. C. Tung, and K. L. Wong, "A Dual-Polarization Wideband Circular Patch Antenna with Hybrid Feeds," *Microwave Opt. Techno. Lett.*, Vol. 26, July 5, 2000, pp. 37–39.

Krishna, D., et al., "Compact Dual-Polarized Square Microstrip Antenna with Triangular Slots for Wireless Communication," *IEE Electronics Letters*, Vol. 42, No. 16, August 2006, pp. 894–895.

Lindmark, B., et al., "Dual Polarized Array for Signal-Processing Applications in Wireless Communications," *IEEE Transactions on Antennas and Propagation*, Vol. AP-46, No. 6, June 1998, pp. 758–763.

Nystrom, I., and D. Karlsson, "Reduction of Back Radiation and Cross-Coupling in Dual Polarized Aperture Coupled Patch Antennas," *IEEE Antennas Propagat. Soc. Int. Symp. Dig.*, 1997, pp. 2222–2225.

Skora, J., A. Sanz, and R. Fabbra, "Dual Polarized Phased Array Antenna for Airborne L-Band SAR," *IEEE MTT-S International Conference*, Long Beach, CA, July 2005, pp. 192–196.

Vallecchi, A., and G. B. Gentili, "Design of Dual-Polarization Series-Fed Microstrip Arrays with Low Losses and High Polarization Purity," *IEEE Transactions on Antennas and Propagation*, Vol. 53, No. 5, May 2005, pp. 1791–1798.

CHAPTER 10

Phased Array Antennas

10.1 Introduction

The phased array antenna is a multi-element antenna system in which the radiation pattern can be reinforced in a direction and suppressed in undesired directions by controlling the phase of individual elements. The direction of phased array radiation can be electronically steered avoiding the need for any mechanical rotation. These specific capabilities have found a broad range of applications for phased arrays since the arrival of this technology. In a phased array antenna with a very large number of regularly spaced radiating elements along with phase shifters, the gain realized at the beam peak is equal to the number of antenna elements times the gain realized in the same direction when only one element is excited. Antenna beams are formed by shifting the phase of the signal emitted from each radiating element to provide constructive/destructive interference to steer the beams in the desired direction. Thus, in the phased array, the main beam of the array is steered by applying a progressive phase shift across the array aperture by exciting all the antenna elements simultaneously.

Phased array radars are distinguished from other radars by phased array antennas that can steer the beam electronically in space. This provides a greater flexibility, makes the system much more versatile by being able to radiate the signal in the volume of space, and optimizes the search and track functions. Alhough scanning antenna arrays had been developed for various electronic communications applications, it was the radar system for which the phased array was broadly used for the first time. Radars demand fast beam scanning, wideband performance, and the ability to adapt the beam patterns to avoid jammers that could be addressed by phased array antennas. Recent growth in communication systems and civilian radar-based sensors has drawn increasing interest in utilizing phased array technology for commercial applications.

Phased array antennas are becoming popular for various applications such as automotive driver assist systems, satellite communications, and advanced radar. These antennas are widely used in communication and radar systems. They offer the benefit of far-field beam shaping and steering as per the requirements of agile operational conditions. Phased array antennas have been used for military radar applications for many decades. Another important use of phased arrays is

in automotive collision avoidance radar or ACC technology [1]. These arrays are also used in base stations to enhance the signal coverage in an area while minimizing interference to other areas [2]. In the healthcare sector, satellite biomedical applications are among the emerging applications that take advantage of phased arrays [3–10]. These arrays are used in microwave imaging to detect early-stage breast cancer. In this system, a wideband impulse is emitted by an antenna array placed at the breast surface. The receiver uses beamforming technique to focus the backscattered signal from the malignant tumor and compensate for the frequency-dependent propagation effect.

The performance of phased array antennas is limited by the characteristics of antenna arrays and the beam-scanning effects. The work on phased array technology was initiated more than four decades ago, but the development of the array technology was slow primarily because of the high cost of the components. The cost per active array element is still not low, but in the last 15 years, the demands for phased array radar systems have significantly increased. Many new technologies for better performance have resulted in the incorporation of features such as beam agility, multitarget tracking, antenna pattern control, electronic countermeasures, and multimoding in these systems. The complexity and cost issues involved in developing phased array antennas are being addressed through new functionalities in electronic design automation (EDA) software that supports antenna designers with the means to develop new antenna system architectures and component specifications, as well as implement the physical design of individual components and verify performance prior to prototyping.

10.2 Phased Array Types

In general, there are two types of phased arrays: passive and active. Passive arrays use a central transmitter and receiver but have phase shift capability at each radiating element or subarray. In active arrays, the high-power generation for transmit and low-noise amplification on receive are distributed as well as the phase control at each radiating element. Active arrays provide added system capability and reliability, but they did not receive much attention until the last 15 years because they were too expensive and complex. Active arrays are becoming the preferred approach for many radar systems and communication systems requiring rapid scanning, with the advent of relatively low-cost GaAs monolithic microwave integrated circuits (MMICs), automated assembly of microwave components, and low-cost, high-speed, high-throughput digital processor [11, 12].

10.2.1 Passive Phased Arrays

In passive phased arrays, the power from a single transmitter is distributed to the array elements through a passive beamformer network. Usually, in a passive array, there is no element amplitude control; only bilateral phase shifters are used at each radiating element to provide the required phase shift for scanning. These phase shifters are situated directly behind the antenna elements (i.e., they transfer the

full transmit power and the raw receive signals). Therefore, the phase shifter losses increase antenna losses, which reduce the overall system efficiency and increase the system noise figure. The design challenge in a passive array is to minimize the losses in the feed network and the phase shifters to increase the system efficiency and sensitivity. This necessity often limits the type of RF feed network to the waveguide that increases the weight of an array system appreciably. If very low sidelobe levels are required, a separate receive feed network with the appropriate amplitude weighting is used in a passive phased array.

A block diagram of a typical passive phased array system is shown in Figure 10.1. A centralized high-power transmitter, which generally consists of microwave tubes such as traveling-wave tubes or crossed-field amplifier tube (CFA or amplitron), provides the power to the radiating antenna elements through a BFN. High-power ferrite or diode phase shifters are controlled at each radiating element to electronically steer the beam to the desired direction. In the receive mode, the outputs of the antenna elements and phase shifters are combined using a low-power BFN.

In the receive mode, LNAs are used to amplify the signal at the output of the beamformers. Passive array systems have some inherent performance limitations and inefficiencies. For instance, the transmit beamformer typically has significant losses, and the transmitter must generate a large amount of power to overcome these losses. Because of losses, a significant portion of the RF power generated by the transmitter is dissipated as heat before being radiated. A high-power centralized transmitter generally employs a microwave tube. These tubes operate at lower duty factors and have limited waveform flexibility. High receive feed network losses, particularly when low sidelobes are required, significantly degrade receive sensitivity. Also, the transmit noise from a centralized source is often a limitation in clutter-driven radar applications.

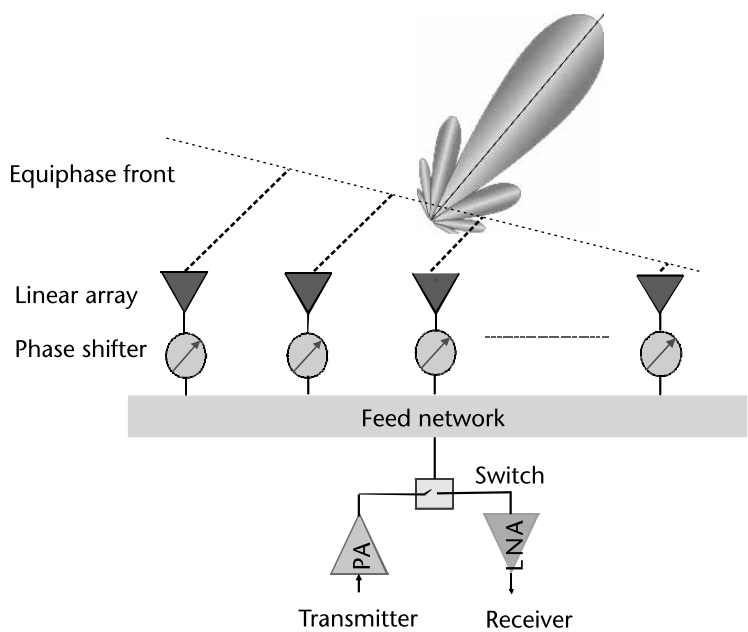

Figure 10.1 Passive phased array antenna system.

10.2.2 Active Phased Arrays

In an active phased array system, a transmit/receive module (TRM) is used at each antenna element to provide both amplitude and phase control. The central transceiver module used in a conventional passive array is replaced by the distributed TRM as shown in Figure 10.2. The main advantage of an active array is that the system sensitivity is increased because the system noise figure is set, and the RF power is generated at the aperture. Another advantage is that the TRMs provide complete flexibility in amplitude and phase control for both the transmit and receive signals. Also, in an active phased array, the feed networks need not be optimized for minimum losses, thereby allowing design flexibility and the ability to minimize size and weight.

The active phased array has gained importance in the past 5 years mainly because, with this technology, it is possible to realize affordable electronic scanning radar sensors. TRMs are main elements in any active phased array radar system. RF transmit power and received low-noise amplification in an active phased array are distributed at the aperture, which reduces the effect of losses in the transmit/receive (T/R) BFNs. Adequate transmit gain in the TRM allows a low RF input power to the antenna. In the receive mode, a high-gain LNA reduces the noise contribution from secondary stages of the TRMs and beamformers. By reducing the impact of transmit and receive feed network losses, large active phased array antennas provide increased radar sensitivity in the range of 8–12 dB compared to passive arrays. In addition, TRMs provide wider bandwidth and higher average transmit power as compared to passive phased arrays.

Because active phased array antennas contain large numbers of active components, the antenna performance degrades gracefully as components fail over time. The electrical block diagram of an active phased array antenna is shown in Figure 10.3. The system-level analysis to cross-check antenna performance along with other electronic components is very important in such a complex system.

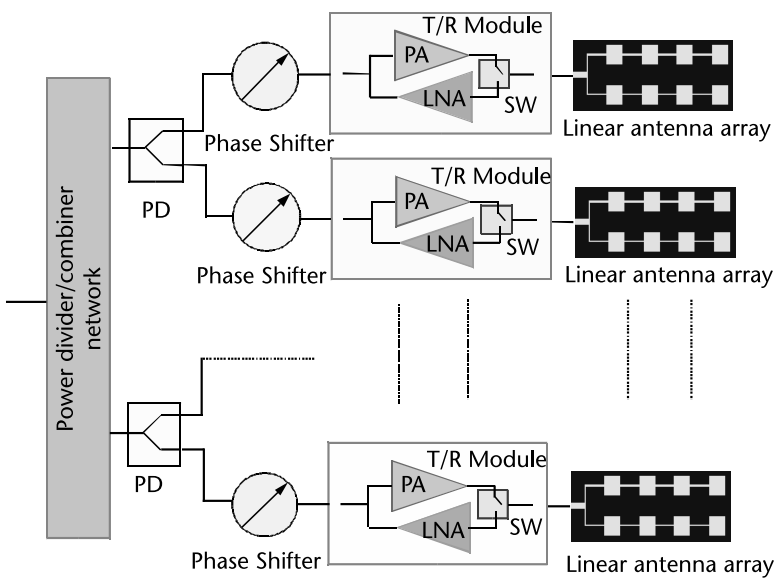

Figure 10.2 Active phased array antenna system.

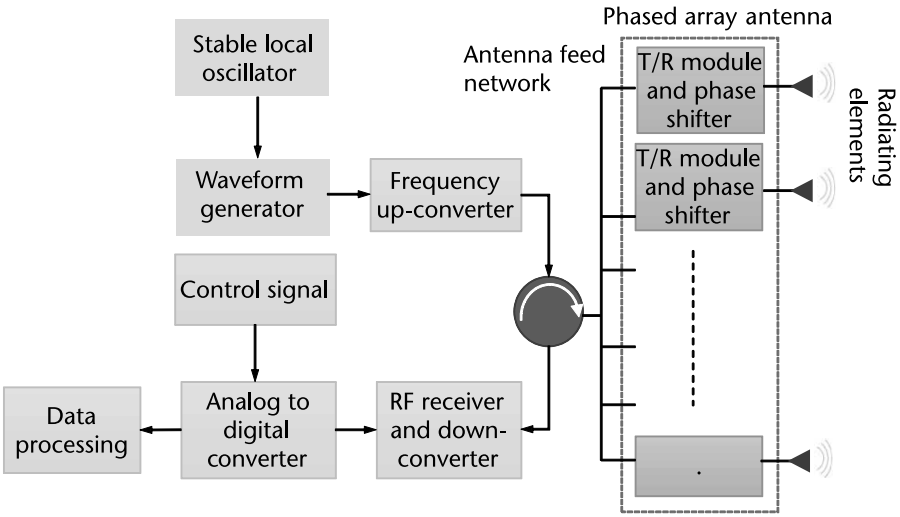

Figure 10.3 Electrical block diagram of an active phased array radar system.

The operating frequency, bandwidth, waveform parameters, and array performance requirements will vary depending on the applications served by the radar. The effective isotropic radiated power (EIRP) and antenna beamwidth determine the total number of antenna elements and the required TRM output power. The sidelobe levels determine the amplitude and phase characteristics of the TRMs and feed network. The phase noise, reliability, stability, and maintainability requirements all influence the array architecture as well as the characteristics of the TRMs and power supplies.

Table 10.1 lists the key parameters of an active phased array system. Nearly all high-performance radars under development today employ an active array antenna. Active phased array antennas are going to play big role in 5G communication system. For current and next-generation advanced spaceborne SAR antennas, high-speed beam steering, high gain, and precise beam shaping are mandatory. Compared to other antenna options such as multifed reflector antenna or passive phased arrays, the active phased array antenna provides the only practical solution to all these requirements, with successful applications in a series of spaceborne SAR systems. One notable disadvantage of space SAR active phased array antenna is the great power consumption. To compensate extreme high path loss, the transmitting RF power of the SAR antenna must be on a very high level. This power consumption usually exceeds the maximum power generated by the solar array onboard spaceborne SAR satellites.

10.2.3 Hybrid Phased Arrays

A hybrid phased array combines features of both passive and active phased arrays. A central transmitter feeds the array as in a conventional passive phased array, but an LNA is placed at each element in front of the phase shifters to improve the overall system noise figure. A limiter may be required in front of the LNA for protection,

Table 10.1 Typical Specification of an Active Phased Array

Specification	*Value*
Electronic specification	
Antenna type	Microstrip phased array antenna
Operation frequency	Tx: 14.2 GHz, Rx: 12.5 GHz
Bandwidth	500 MHz
Antenna gain	35 dBi
Beamwidth	Azimuth: 1.2°, elevation: 4°
Polarization mode	Linear (H, V)
G/T	9.6 dB/K (without radome)
Cross-pol isolation	≥25 dB
EIRP	>49/1 beam dBW
Phase shifter bit number	6
Operating mode	Satellite-switched time division multiple access (SS-TDMA) continuous-wave mode
VSWR	<2 (50Ω reference)
Efficiency	60%
Mechanical specification	
Antenna size	1,200 × 900 × 120 mm (length * width * height)
Aperture size	1,200 mm × 900 mm
Number of radiating elements	256
Weight	25 kg
Operation temperature	–40°C~65°C
Scanning	Electronics
Scanning range	Azimuth: 360° continuous Elevation: 20°– 60°
Max. steering step size	5°
Electrical specification	
Power consumption	<700W
Power supply	AC220V ± 10%, 50 Hz ± 2 Hz
Rated consumption	120W (without block upconverter (BUC))

as in an active phased array. A separate receive feed network is used for sidelobes. In a hybrid array, it is also possible to distribute medium power transmitters (e.g., in each column of the array) to provide increased system reliability. For very large phased arrays systems with wide instantaneous bandwidths, array architecture with true time delay (TTD) is required to prevent signal distortion and beam squinting. In these arrays, the length of the transmission line feeding each element provides the differential phase shift. However, to scan the beam, the effective line length of the feed lines to each element must be changed accordingly [13].

10.3 Phased Array Theory

The radiation pattern of linear and planar phased arrays is a function of each element's physical structure, interelement distance, excitation, and array lattice.

Typically, similar radiating elements are arranged in a linear, rectangular, circular, triangular, or customized lattice with periodic spacing between antenna elements. When similar radiators are used in a large rectangular array, the radiation pattern is the product of two factors: first is the element factor that is a function of the radiating element physical realization; and second is the array factor that is a function of the array geometry and the element excitations. The radiation pattern of phased array is the product of the element and array factor. Antenna arrays with the radiators arranged in concentric circles have certain advantages such as lower first sidelobes compared to a rectangular array lattice.

To understand the array factor, consider an array of identical radiators as shown in Figure 10.4. The $2N + 1$ elements, equally spaced by a distance d along the z-axis, are arranged in a line. All elements have same current distributions that differ only in magnitude and phase. In is the magnitude of the current on the nth element. For this linear array, the array factor $F_a(\theta, \varnothing)$ is proportional to the radiated field at a point in space described by $(\theta, \varnothing)$.

$$F_a(\theta,\varnothing) = \sum_{n=-N}^{n=N} \frac{I_n}{I_0} e^{jnkd\cos\theta} \tag{10.1}$$

where $k = 2\pi/\lambda$ and λ is the wavelength. For a linear array, $F_a(\theta, \varnothing)$ is rotationally symmetric about the z-axis (independent of $\varnothing$).

If the currents are equal and in phase, (10.1) reduces to (10.2):

$$F_a(\theta,\varnothing) = \sum_{n=-N}^{n=N} e^{jnkd\cos\theta} \tag{10.2}$$

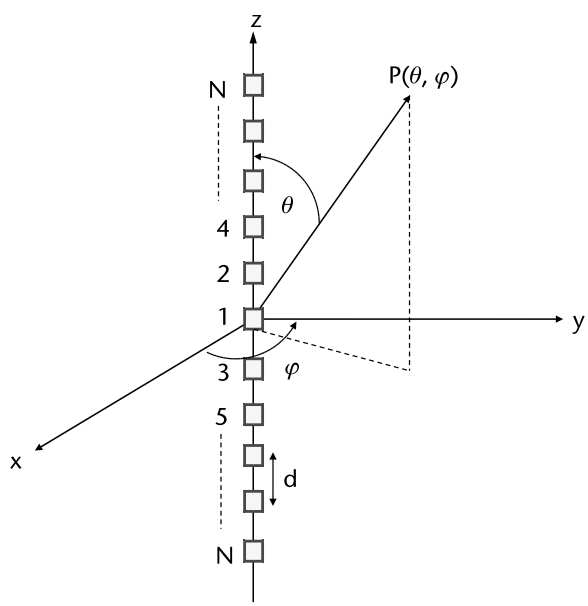

Figure 10.4 A linear array with the radiating elements equally spaced along the z-axis.

The array factor is equal to a sum of phasors of unity magnitude with progressive multiples of the basic angle φ:

$$\varphi = \frac{2\pi d}{\lambda}\cos\theta \tag{10.3}$$

If the array length L is very large compared to a wavelength ($L>>\lambda$) and the element spacing d is less than a wavelength ($d<\lambda$), then the array pattern gives a narrow beam broadside to the array axis ($\theta = \pi/2$) with several sidelobes.

In the linear array, the first sidelobe is 13.5 dB below the peak of the main beam, and the peak of each successive sidelobe is even lower as its distance from the main beam increases. Tapering the magnitude of the currents across the array elements can decrease the sidelobes. The central element is fed with the largest current and the magnitudes of the currents in the other elements are symmetrically tapered. As a result, the sidelobes are reduced, but the width of the main beam (beamwidth) is increased.

The directivity of a uniformly weighted linear array of N isotropic radiators spaced $\lambda/2$ apart is equal to N independent of the main beam scan angle. For non-uniformly weighted linear arrays, the directivity is given by:

$$D = \frac{2d}{\lambda}D_0 \tag{10.4}$$

where D_0 is given by

$$D_0 = \frac{\left[\sum_{n=-N}^{n=N} I_n\right]^2}{\sum_{n=-N}^{n=N} I_n^{\,2}} \tag{10.5}$$

In a linear array, elements with currents all have equal amplitudes and a uniform progressive phase as follows:

$$F_a(\theta,\Phi) = \sum_{n=-N}^{n=N} e^{jn(kd\cos\theta-\alpha_z)} \tag{10.6}$$

The uniform progressive phase factor α_z changes the peak beam position from broadside to another angle in space θ_0 given by

$$\theta_0 = \cos^{-1}\left(\frac{\alpha_z}{2\pi}\frac{\lambda}{d}\right) \tag{10.7}$$

10.3.1 Grating Lobes

The active impedance of each radiating antenna element in a phased array varies with the scan angle, because of mutual coupling between the elements. Mutual coupling is fundamentally unavoidable in a closely spaced infinite array of elements. Mutual coupling reduces antenna efficiency and coupling increases with closer spacing. Another phenomenon associated with a phased array is that grating lobes can exist when the antenna elements are not closely spaced; for example, in a linear or planar array with more than $\lambda/2$ spacing, there is high chance of grating lobe occurrence as shown in Figure 10.5. In this case, the array will have equally strong radiation in other directions. These unintentional beams of radiation are known as grating lobes.

If the element spacing d is too large compared to a wavelength, the grating lobe will appear in the radiation pattern. This will happen at an angle θ [13], where

$$kd\cos\theta - \alpha_z = \pm 2\pi \tag{10.8}$$

$$\cos\theta = \cos\theta_0 \pm \frac{\lambda}{d} \tag{10.9}$$

To prevent a second main beam, the spacing must be chosen to satisfy the following condition:

$$\frac{d}{\lambda} < \frac{1}{1+|\cos\theta_0|} \tag{10.10}$$

The equation for the maximum interelement spacing is a function of the wavelength of operation and the maximum look angle θ.

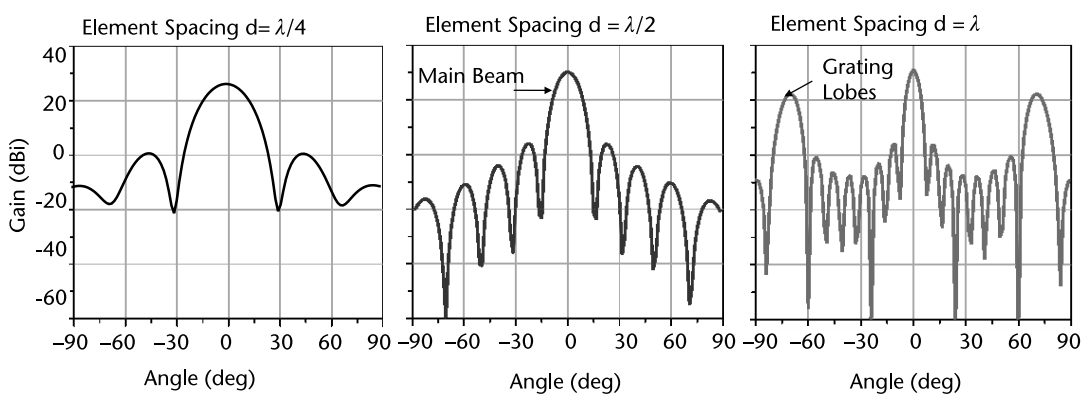

Figure 10.5 Linear antenna array radiation pattern with different interelement spacing.

$$d_{max} = \frac{\lambda}{1 + \sin\theta} \tag{10.11}$$

Thus, for 45° scan angles, the maximum interelement spacing is 0.59λ. The elements must be spaced one half-wavelength apart to prevent a second main beam when scanning close to endfire ($\theta = 0$ or π). Figure 10.5 shows a grating lobe appearing in real space when the beam of a 16-element array with elements equally spaced at $d = \lambda$ of a wavelength is scanned off broadside.

10.4 Active Phased Array Antenna Design

In a phased array radar, the antenna is one of the most critical components from a design point of view due to the requirement of enhanced capabilities in terms of dual polarization, beam agility, high gain, and reliability. Because of the size and weight constraints, the printed multilayer planar array antenna is the most popular choice in a phased array system. The challenges in active array antenna design are to achieve high gain, dual linear polarization with low cross-polar radiation, and accommodation of dual feed networks within the limited space. In the case of a dual-polarized phased array, the most critical aspect of design is the realization of dual-polarized feed networks, which require an innovative design approach. Apart from the complexity of electrical design, modeling, and simulation using EDA tools, the fabrication of antenna with required tolerance, assembly, and alignment of various layers are of paramount importance [14–19]. A phased array antenna design operating in X-band is discussed in this section. This design covers antenna specifications for active phased array, different options of multilayer radiators, array antenna feed network configuration, design sensitivity analysis, and measurement philosophy.

Phased array antenna design starts with the antenna design specification provided by the system engineer. Based on the system-level requirement, the system engineer provides the design requirement specification for antennas such as the maximum available space to mount the antenna, gain, beamwidth, bandwidth, cross-polarization level, sidelobe level, and some other parameters as listed in Table 10.2.

10.4.1 Antenna Configuration

The physical aperture size of an active phased array antenna is determined based on the required antenna beamwidth in the principal planes. Form an antenna design fabrication and assembly point of view, an antenna is divided into multiple panels and then each panel consists of several linear arrays as shown in Figure 10.6. This antenna consists of 4 foldable panels of a size of 0.37m × 0.53m. To scan the beam in the elevation plane, 16 linear arrays each having 24 elements are designed with a distributed power scheme. Linear arrays are fed at the center by T/R (transceiver) modules for digital phase control. Several types of antennas such as the open-ended waveguide horn array, slotted array, and printed microstrip array can be used to meet antenna specification requirements. The horn antenna array is not suitable

Table 10.2 Design Specifications of X-Band Active Phased Array Antenna

	Specifications		
Parameters	*Linear Array*	*One Tile*	*Complete Antenna*
Size ($L \times W$)	0.53m 0.02m	0.53m × 0.35m	1.5m × 0.52m
Antenna beamwidth	2.7° × 73°	2.7° × 2.7°	0.6° × 1.6°
Gain	20.7 dB	35.3 dB	43.4 dB
Gain bandwidth	1.1 dB	1.1 dB	1.1 dB
Antenna bandwidth	50 MHz	47 MHz	45 MHz
Return loss	–10 dB	–10 dB	–10 dB
Cross-polarization	–21 dB	–20 dB	–20 dB
Frequency	9.5 GHz (X-band)		
Polarization	Dual linear polarization		

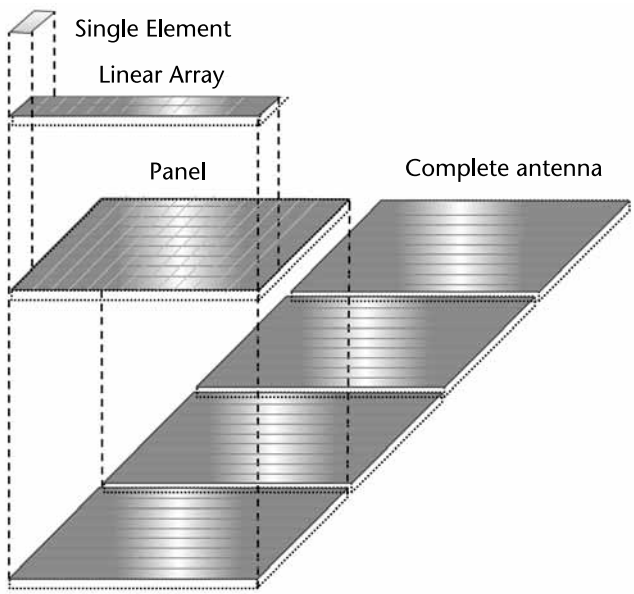

Figure 10.6 Designed X-band phased array antenna configuration and assembly.

due to its large size and weight. The slotted waveguide antenna array has narrow bandwidth characteristics and, because of that, it is also not feasible. A low-profile and low-weight printed multilayer planar array antenna configuration is the best option for this spaceborne SAR application due to the weight constraints in the satellite payload.

A single element of the phased array antenna should be broadband and high gain so that the overall antenna gain requirement can be met with fewer elements. In an array antenna, the antenna gain increases about 3dB when the number of elements doubles. For such a bandwidth requirement, the conventional direct fed microstrip patch cannot be used. Multilayer microstrip patch antennas are suitable

to meet the functional requirements. Two options of multilayer microstrip patch antennas can be used to increase antenna bandwidth and gain:

1. Aperture-coupled microstrip antenna (ACMA);
2. Proximity EM coupled microstrip antenna (PECMA).

10.4.1.1 Aperture Coupled Microstrip Antenna

In the aperture coupled microstrip antenna configuration, the radiating element and the feed line are separated by a ground plane layer that consists of slots to couple power from the feed line to the radiator as shown in Figure 10.7(a). The feed line is isolated from the radiator to avoid spurious radiation from the feed line, which would otherwise distort the radiation pattern of the radiator. Different substrate material can be selected for radiator and feed line to optimize the performance in terms of gain, bandwidth, isolation, and front-to-back ratio of the radiator. The optimum performance is obtained by putting the radiator on a substrate of lower dielectric constant as near to that of air and the feed line on a substrate of a higher dielectric constant. The preferred configuration for a feed line is to have an asymmetric stripline configuration. In this arrangement, the feed line is sandwiched between two ground planes where the upper ground plane contains coupling slots and the lower ground plane acts as a ground plane for the feed line. The ground

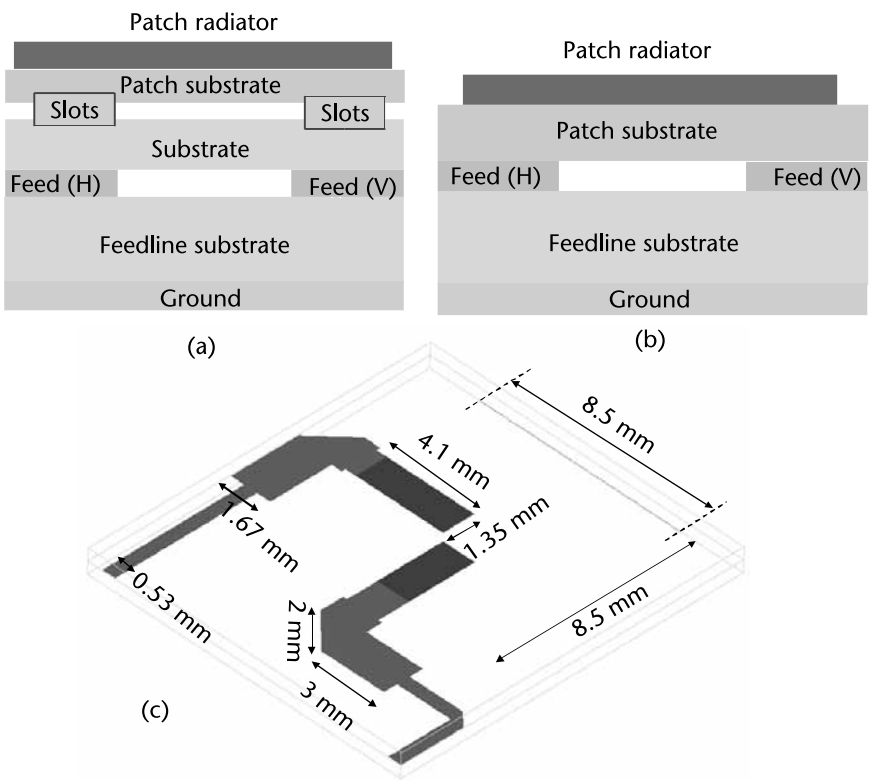

Figure 10.7 (a) Aperture-coupled and (b) electromagnetic microstrip antenna stack-ups; and (c) single-element electromagnetically coupled dual-polarized radiator.

plane slot and patch center are positioned above the microstrip feed line $\lambda_g/4$ from the open termination. On microstrip lines above a ground plane, a voltage null and current maximum occur $\lambda_g/4$ from an open termination.

A major problem in this configuration is the impedance matching of a 50Ω coaxial line with the microstrip feed line when coaxial connector pins protrude from below the ground plane as required. Using shorting pins connecting the lower and upper slot ground planes near the coaxial connector probe solves this matching problem, but this results in a very unreliable configuration due to the enormous number of shorting pins and problems associated with their soldering and assembly.

The equivalent circuit model of an aperture-coupled microstrip patch antenna is shown in Figure 10.8. The antenna ground plane slot acts as an impedance transformer and parallel LC circuit ($L_{aperture}$ and $C_{aperture}$) in series with the microstrip feed line [20]. The ground plane slot resonant behavior is represented with the LC circuit. The 1:N impedance transformer represents the effects of the impedance of the patch antenna being coupled through the ground plane slot. The patch antenna is modeled as two transmission lines terminated by parallel RC components (C_{fring} and R) due to patch edge fringing fields.

10.4.1.2 Proximity EM Coupled Stacked Patch Antenna

In a proximity EM coupled stacked patch configuration, the patch is excited through an EM coupled feed line. In this configuration, two dielectric substrates are used such that the feed line is in the interior of the substrates and the radiating patch on top of the other substrates shown in Figure 10.7(c). Decoupling is obtained by placing the patch and feed at different levels as shown in Figure 10.7(b). It offers better port isolation between the feed lines for vertical and horizontal polarizations. In the case of the broadband array requirement, two stacked radiating patched are separated by a thick layer of foam of low permittivity to enhance the radiation efficiency and bandwidth performance. Compared to aperture-coupled configuration, this configuration has been found to be optimum from the design and realization point of view and has been preferred for the development of the antenna. A single radiating antenna is optimized for a minimum gain of 7.7 dB. The optimization was carried out in terms of the patch dimension, substrate thickness, and dielectric

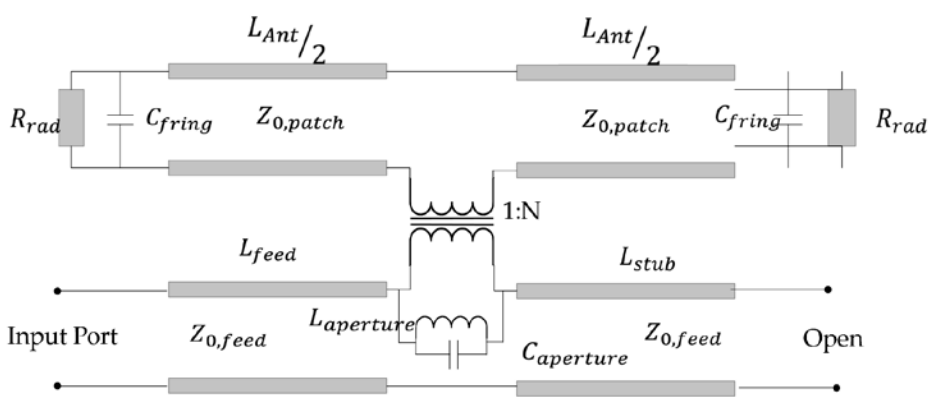

Figure 10.8 Equivalent circuit of aperture-coupled patch antenna.

constant and dielectric loss tangent. The optimized electrical performance of the various options of single radiating elements is given in Table 10.3.

Of these two single radiating element options, the stacked EM coupled patch is preferred because of the following advantages:

1. This configuration meets the antenna array bandwidth requirement.
2. The center pin of the 50Ω coaxial line can be matched with the printed feed line without any spurious radiation issue.
3. This configuration is slightly less sensitive to fabrication errors and misalignment errors as compared to the aperture-coupled configuration.

One disadvantage of this configuration is that the feed lines are not isolated from the radiating patches and the radiation from the feed lines can result in a degradation in cross-polarization. However, cross-polarization can be further improved in the planar array environment using cross-polarization suppression techniques. Beside these two configurations, it is possible to increase the absolute bandwidth of the microstrip antenna by simply using thicker substrates. However, thick substrate introduces several problems such as the excitation of surface waves, which distorts the normal radiation pattern and introduces additional loss, and the excitation of higher-order modes with Z-dependence, which introduces further distortions on the pattern and impedance characteristics. The RT Duroid 6002 substrate (thickness of 15 mils and dielectric constant of 2.94) is used both for the radiating element and the feed line substrate material.

10.4.2 Dual-Polarized Feed Network

The array feed network design begins with the optimization of a 1:2 feed followed by 1:6, 1:12, and finally 1:24 to feed all the 24 elements of the linear array as shown in Figure 10.9. The feed network design is the most complex part in an array dual-polarized array antenna design. Before the start of the design, the current distribution is calculated at the input of each element and, based on this, the microstrip line width is calculated for each value of impedance. Then these lines are combined to form a feed network and optimization is carried out to find out optimal dimensions of these lines. In this design, one major design constraint is that the feed line networks for both the polarizations should be accommodated within limited interelement spacing. The spacing between the lines is as close as 0.9 mm at some points. The coupling between the feed network lines should be considered during the design of the complete feed network, as these lines run very close to each other. Feed network design is optimized using ADS optimization and the MoM simulation technique is applied for the EM analysis of the feed network. A corporate feed

Table 10.3 Performance of a Single Radiating Element

Configuration	*Return Loss Bandwidth*	*Isolation (dB)*	*Gain (dB)*
Aperture coupled	80 MHz	–30.0	7.5
Proximity EMC patch	90 MHz	–24	7.7

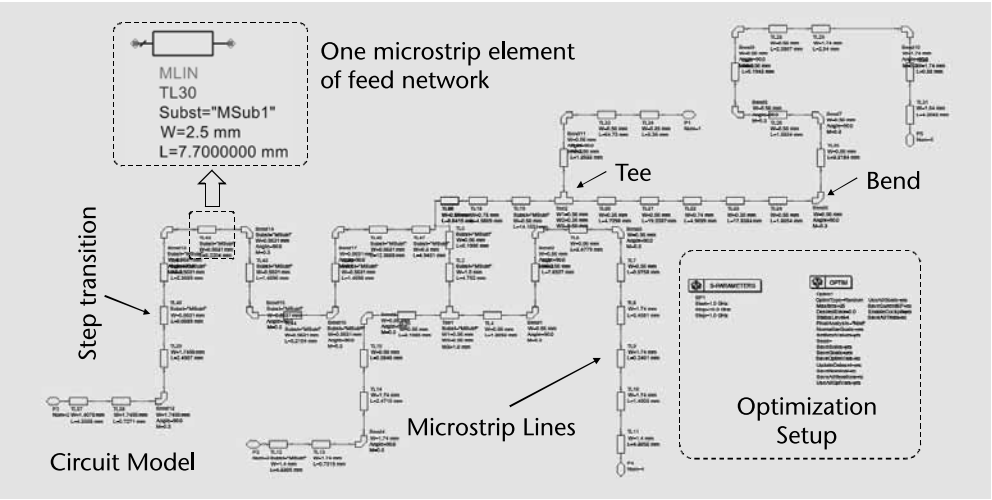

Figure 10.9 Feed network design and simulation in ADS.

network is a better choice from a bandwidth point of view, but it was not possible to realize such a feed due to the limited available space for the dual linear networks. The series feed networks can be easily accommodated within the given space, but they result in phase spreading over the bandwidth. Therefore, a combination of corporate and series feed is used in the design of 1:24 dual-polarized feed networks. The layout diagram of the dual polarized feed network is given in Figure 10.10.

It is shown that input power is divided using both corporate and series power dividers. Additional line lengths are added to achieve equal phase at all the 24 ports of the power divider at the center frequency. The feed network has been optimized for an equal amplitude at all 24 ports within ±0.3 dB at the center frequency and ±0.6 dB at the band edges.

In addition to this, the feed network of the linear array was designed using the cross-polarization suppression technique to reduce cross-polarization radiation in the planar array environment [21] compared with that of single radiator as shown in Figure 10.11. Option-3 is applied in this antenna array design. In this configuration, the antenna element mirroring is performed in both the horizontal and vertical planes. With this arrangement, the array cross-polarization is improved significantly, but sometime undesired sidelobes will appear in the horizontal and vertical planes. A complete linear antenna array is simulated using MoM-based electromagnetic simulation. A return loss plot for horizontal and vertical polarizations is shown in Figure 10.12. Linear array resonance is at 9.47 GHz and –10-dB bandwidth of antenna is 50 MHz.

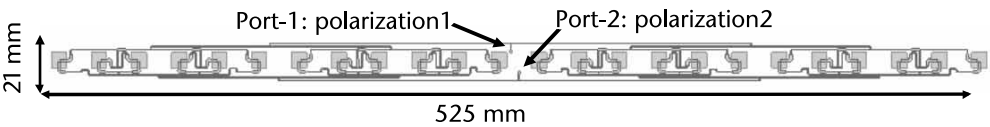

Figure 10.10 Dual-polarized linear array design with a hybrid feed network.

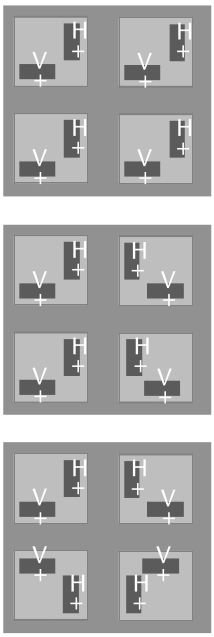

Option-1

- Individual elements have same orientation
- Array x-Pol suppression poorer than single element

Option-2

- Two rightmost element mirrored wrt vertical plane x-pol improves significantly(~8-10db)
- Improvement in vertical plane than horizontal.
- Undesired sidelobes in horizontal planes

Option-3

- Element mirroring in both planes
- Significant improvement in X-Pol in both planes
- Undesired sidelobes in both planes

Figure 10.11 Cross-polarization suppression techniques.

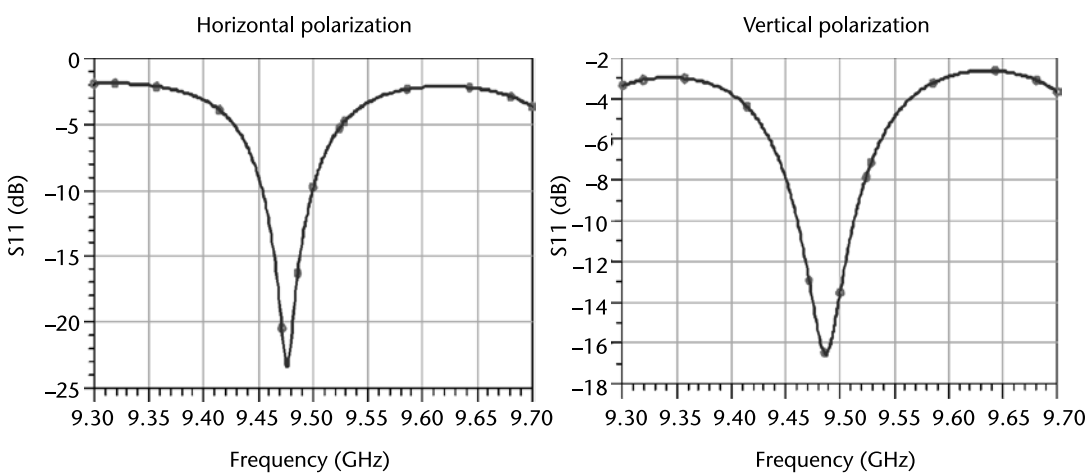

Figure 10.12 Return loss plot of horizontal and vertical polarization linear array.

This is a narrowband array meeting the system design requirement, but, in many cases, broadband array antenna is needed for spaceborne SAR application. Port isolation between horizontal and vertical polarization is better than 35 dB across the operating frequency band.

The radiation pattern plot of a linear array antenna at three different frequencies (9.45, 9.48, and 9.50 GHz) in the antenna band is shown in Figure 10.13. The peak gain of array is 21.1 dBi. The sidelobe variation is within 1.5 dB. The gain variation obtained over the frequency band was within 0.6 dB.

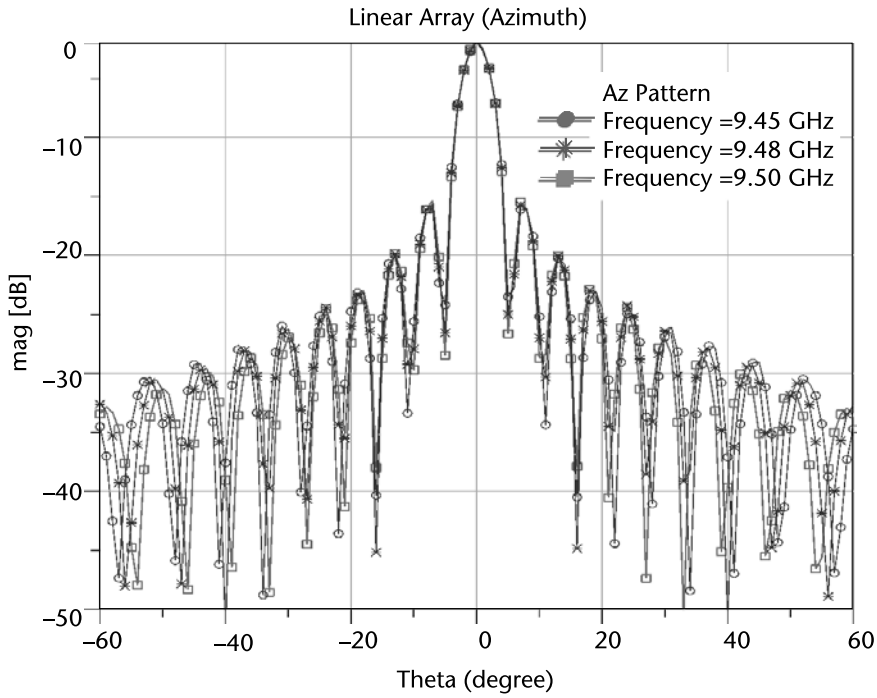

Figure 10.13 Azimuth pattern plot of linear array antenna.

10.5 Planar Array Antenna Design

A planar array is formed by placing 16 linear arrays at the required interelement spacing to get the beamwidth in the elevation plane as shown in Figure 10.14. The cross-polarization of the planar array gets further deteriorated as compared to a single linear array. The major challenge of the planar array design is to control the isolation between two linear arrays to improve the cross-polar radiation

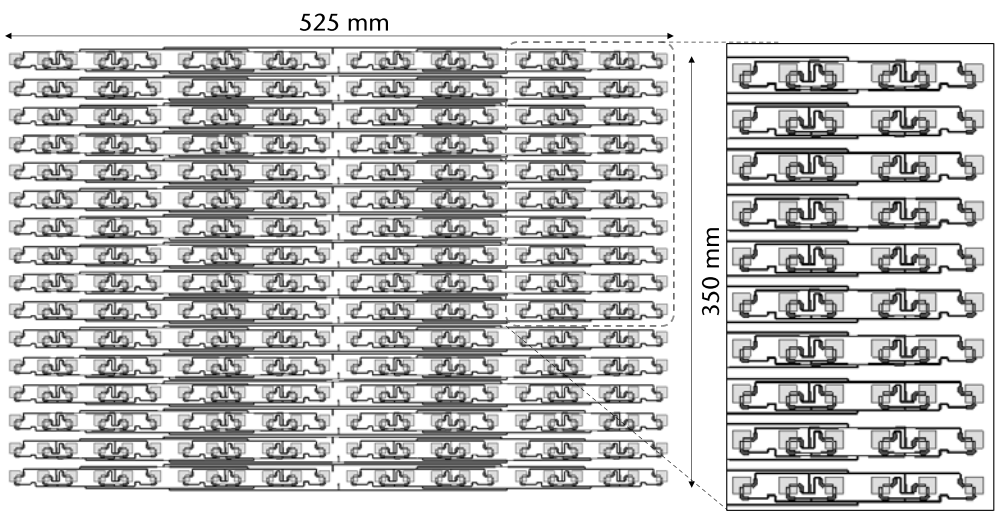

Figure 10.14 Planar antenna array (20 × 16 elements) design.

performance. Option-3 of cross-polarization suppression is also applied in the planar antenna array design.

Using this technique, the cross-polar radiation is further reduced by –9 dB than that of a single linear array. Planar antenna return loss and radiation pattern are shown in Figure 10.15. By combining four planar antennas, a complete dual-polarized active phased array antenna is constructed as shown in Figure 10.16. The peak gain at 9.5 GHz of this antenna is 43.4 dBi. A total 128 TRM (64 for horizontal polarization and 64 for vertical polarization) is required to drive the antenna and scan the antenna beam.

10.6 Measurement of Phased Array Antenna

The radiation pattern measurement of the antenna can be measured either using far-field measurement techniques or a planar near-test facility (PNF). The return loss and isolation between ports are measured using a vector network analyzer (VNA). To test antenna beam scanning, T/R with automated test setup consisting of digital control unit (DCU) and control computer are used. The TRMs are controlled to

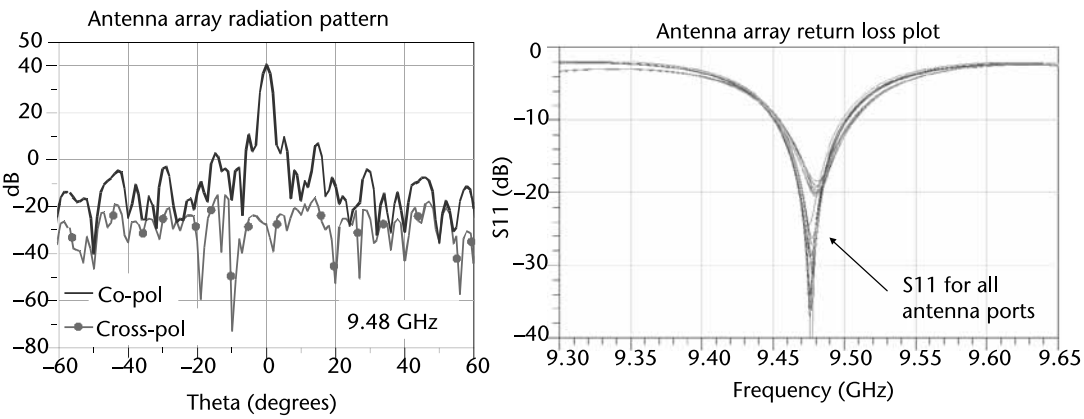

Figure 10.15 Return loss and radiation pattern plot of planar array antenna.

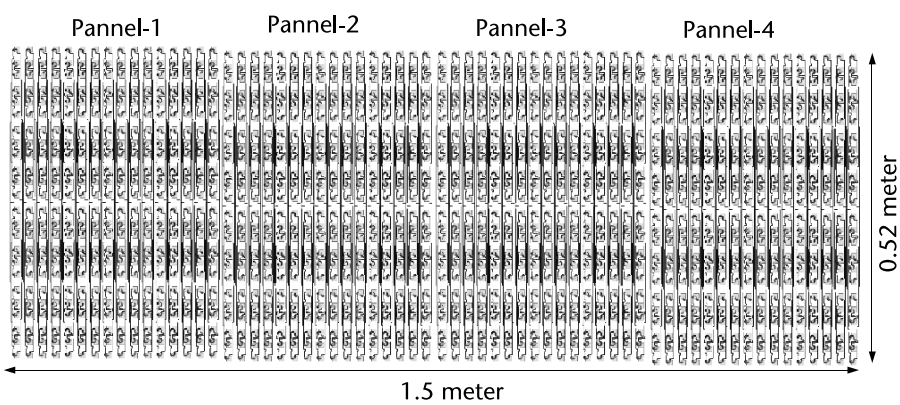

Figure 10.16 Layout of complete dual-polarized phased array antenna design.

get amplitude and phase. In this case, 16 TRMs are connected to 16 linear arrays for either vertical or horizontal polarization. To control the phase and amplitude between linear arrays for beam scanning, DCU controls the phase and amplitude of T/R. This DCU will feed 6-bit phase and amplitude information to R-modules. Extensive testing is required to characterize antenna for all possible beam locations. The performance of the antenna is checked over the complete operating bandwidth with a center frequency of 9.5 GHz. Continuous beam scanning can be achieved using amplitude and phase only control required for beam location. It has a DCU to cater to any amplitude and phase combination for each linear array fed at the center with maximum of 16 such arrays. A 6-bit phase shifter meets the minimum phase step criteria of 5.6° with a maximum of 360. Any phase beyond 360 repeats the cycle again.

10.6.1 Microwave Holography

Microwave holography is a method for the diagnosis and alignment of phased array antennas. The microwave holography measurement is conducted using near-field measurement (PNF) technique. This technique is also known as back-transformation. Microwave holography [22] is a fast inversion technique that relies on the measurement of the magnitude and phase of the wave scattered from the phased array antenna. In this technique, far-field data is back-projected using the inverse Fourier transformation to compute amplitude and phase at the aperture. A microwave sensor scans completely the array antenna aperture and collects electromagnetic field data at each location along the *X*-axis and *Y*-axis. The scanning data gives a 2-D power plot as shown in the Figure 10.17. This aperture distribution is compared with the given amplitude and phase distribution to locate the faulty array

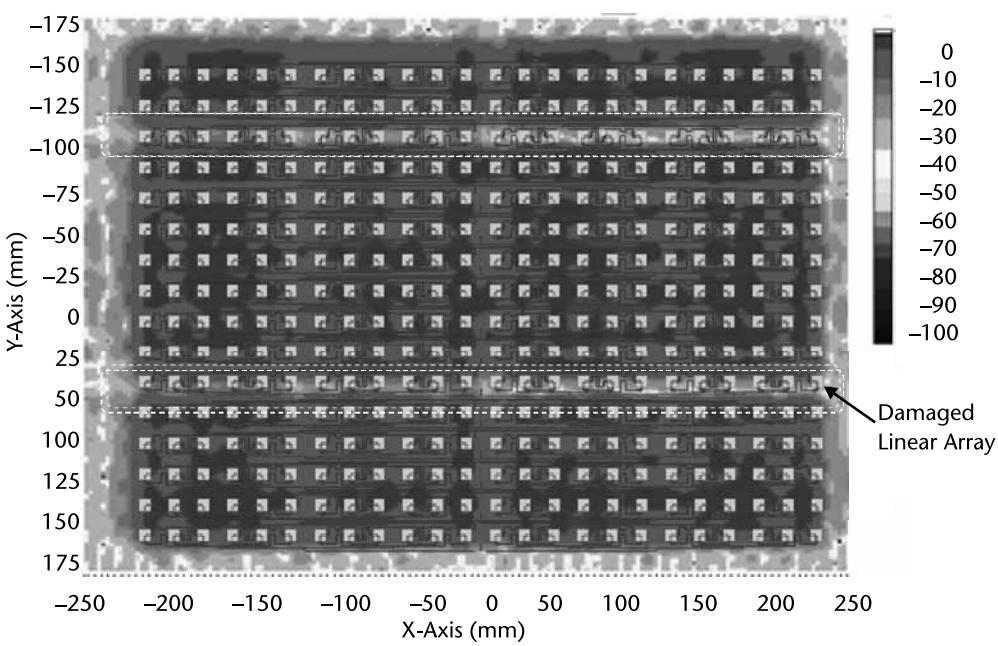

Figure 10.17 Microwave holography of a planar antenna array showing two faulty linear arrays in the design.

element. In this example, there are two faulty array elements as shown in Figure 10.17. The plot clearly shows a sudden drop of power in the form of a line that shows a faulty element of the array. Thus, this technique is very useful to locate faulty elements of the larger arrays. This analysis ascertains that back-projected data can be used for aperture distribution analysis.

10.7 Summary

Phased array radar technology has been traditionally used mainly in military or remote-sensing applications. Due to the proliferation of new consumer and commercial applications such as Internet of Things (IoT) and smart city and smart home applications, the demand on radar technology continues to grow, as it can enhance the product features and increase the product's competitiveness. Such features may include occupancy detection, gesture detection and motion, and speed detection for smart home applications. In this chapter, phased array antenna technology was discussed that is applicable for various applications. In future 5G systems, to handle the bandwidth needed for greater than 10-Gbps data rates, the millimeter-wave spectrum along with massive MIMO phased array is going to be a driving technology. There are many phased array antennas that do everything required, for example, the fire control radar and an active electronic scanning array (AESA). Phased array antennas are used in missile guidance systems to control the flight path. In this chapter, phased array antenna design was discussed for spaceborne remote sensing.

References

[1] Kolak F., and C. Eswarappa, "A Low Profile 77 GHz Three Beam Antenna for Automotive Radar," *2001 IEEE MTT-S International Microwave Symposium Digest*, Phoenix, AZ, 2001, pp. 1107–1110.

[2] Sawahashi, M., et al., "Coordinated Multipoint Transmission/Reception Techniques for LTE Advanced," *IEEE Wireless Communications Mag.*, Vol. 17, No. 3, June 2010, pp. 26–34.

[3] Irishina, N., N. Moscoso, and N. Dorn, "Microwave Imaging for Early Breast Cancer Detection Using a Shape-Based Strategy," *IEEE Transactions on Biomedical Engineering*, Vol. 56, No. 4, April 2009, pp. 1143–1153.

[4] Klemm, M., et al., "Radar-Based Breast Cancer Detection Using a Hemispherical Antenna Array Experimental Results," *IEEE Transactions on Medical Imaging,* Vol. 28, No. 7, 2009, pp. 969–981.

[5] Wo, J. Y., et al., "Effect of Very Small Tumor Size on Cancer-Specific Mortality in Node-Positive Breast Cancer," *J Clin. Oncol.*, Vol. 29, May 2011, pp. 2619–2627.

[6] Rosen, A., M. A. Stuchly, and A. V. Vorst, "Applications of RF/Microwaves in Medicine," *IEEE Transactions on Microwave Theory and Techniques*, Vol. 50, No. 3, March 2002, pp. 963–974.

[7] Fenn, A. J., *Adaptive Phased Array Thermotherapy for Cancer*, Norwood, MA: Artech House, 2008.

[8] Nikolova, N., "Microwave Imaging for Breast Cancer," *IEEE Microwave Magazine*, Vol. 12, No. 7, 2011, pp. 78–94.

[9] Balanis, C. A., *Antenna Theory Analysis and Design*, New York: Wiley-Interscience, 2005.

[10] Mailloux, R. J., *Phased Array Antenna Handbook*, Norwood, MA, Artech House, 2005.

[11] Livne, A., "System Design Considerations in Fiber-Optic Networks for Active Array Antennas." *Proc. 19th Europe, Microwave Conf.*, 1989.

[12] Lockerd, R. M., and G. E. Crain, "Airborne Active Element Array Radars Come of Age," *Microwave Journal,* January 1990.

[13] Hansen, R. C., *Significant Phased Array Papers*, Dedham, MA: Artech House, 1973.

[14] Jyoti, R., et al., "Multilayer Printed Active Phased Array Antenna for Radar Imaging Satellite," *2014 IEEE International Microwave and RF Conference (IMaRC)*, Bangalore, 2014, pp. 205–208.

[15] Tapan, M., et al., "Synthetic Aperture Radar Payload On-Board RISAT-1: Configuration, Technology and Performance," *Current Science*, Vol. 104, No. 4, February 25, 2013, pp. 446–461.

[16] Woelder, K., and J. Granholm, "Cross-Polarization and Sidelobe Suppression in Dual Linear Polarization Antenna Arrays," *IEEE Transactions on Antennas and Propagation*, Vol. 45, No. 12, December 1997, pp. 1727–1740.

[17] Serra, A. A., et al., "A Wide-Band Dual-Polarized Stacked Patch Antenna," *IEEE Antennas and Wireless Propagation Letters*, Vol. 6, 2007, pp. 141–144.

[18] Chang, F. S., et al., "Compact Vertical Patch Antenna for Dual-Band WLAN Operation," *IEE Electronics Letters*, Vol. 44, No. 10, 2008.

[19] Jackson D. R., and P. Manghnani, "Analysis and Design of a Linear Array of Electromagnetically Coupled Microstrip Patches," *IEEE Transactions on Antennas and Propagation*, Vol. 38, May 1990, pp. 754–759.

[20] Civerolo, M., and D. Arakaki, "Aperture Coupled Patch Antenna Design Methods," *2011 IEEE International Symposium on Antennas and Propagation (APSURSI)*, Spokane, WA, 2011, pp. 876–879.

[21] Woelder, K., and J. Granholm, "Cross-Polarization and Sidelobe Suppression in Dual Linear Polarization Antenna Arrays," *IEEE Transactions on Antennas and Propagation*, Vol. 45, No. 12, December 1997, pp. 1727–1740.

[22] Farhat, N. H., and W. R. Guard, "Holographic Imaging at 70 GHz," *Proc. of the IEEE*, Vol. 58, No., 12, 1970, pp. 1955–1956.

Selected Bibliography

Aboserwal, N. A., et al., "Source Current Polarization Impact on the Cross-Polarization Definition of Practical Antenna Elements: Theory and Applications," *IEEE Transactions on Antennas and Propagation*, Vol. 66, No. 9, September 2018, pp. 4391–4406.

Brookner, E., "Phased-Array and Radar Breakthroughs," *Proc. IEEE Radar Conf.*, 2006, pp. 37–42.

Cesario, J., "Electromagnetic Coupling Between a Metal Nanoparticle Grating and a Metallic Surface," *Optics Letters*, Vol. 30, No. 24, December 15, 2005, pp. 3404–3406.

Hong, L., et al., "Design and Implementation of an Active Array Antenna with Remote Controllable Radiation Patterns for Mobile Communications," *IEEE Transactions on Antennas and Propagation*, Vol. 62, No. 2, February 2014, pp. 913–921.

Ip, K. H. Y., T. M. Y. Kan, and G. V. Eleftheriades, "A Single-Layer CPW FED Active Patch Antenna," *IEEE Microwave and Guided Wave Letters*, Vol. 10, No. 2, 2000, pp. 64–66.

Kang, M., et al., "Efficient Synthesis of Antenna Pattern Using Improved PSO for Spaceborne SAR Performance and Imaging in Presence of Element Failure," *IEEE Sensors Journal*, Vol. 18, No. 16, August 15, 2018, pp. 6576–6587.

Kasemodel, J. A., C. Chen, and J. L. Volakis, "Wideband Planar Array with Integrated Feed and Matching Network for Wide-Angle Scanning," *IEEE Transactions on Antennas and Propagation*, Vol. 61, No. 9, September 2013, pp. 4528–4537.

Kumar, C., et al., "Dual Circularly Polarized Spherical Phased-Array Antenna for Spacecraft Application," *IEEE Transactions on Antennas and Propagation*, Vol. 61, No. 2, February 2013, pp. 598–605.

Landsberg, N., and E. Socher, "Design and Measurements of 100 GHz Reflectarray and Transmitarray Active Antenna Cells," *IEEE Transactions on Antennas and Propagation*, Vol. 65, No. 12, December 2017, pp. 6986–6997.

Pokuls, R., J. Uher, and D. M. Pozar, "Dual Frequency and Dual Polarization Microstrip Antennas for SAR Applications," *IEEE Transactions on Antennas and Propagation*, Vol. 46, September 1998, pp. 1289–1296.

Rowe, W. S. T., and R. B. Waterhouse, "Broadband Microstrip Patch Antennas for MMICs," *Electronics Letters*, Vol. 36, No. 7, March 30, 2000, pp. 597–599.

Talukder, P., et al., "A 24 GHz Active Antenna in Flip Chip Technology with Integrated Frontend," *IEEE MTT-S Int. Microw. Symp. Dig.*, June 2000, pp. 1776–1779.

Talisa, S. H., et al., "Benefits of Digital Phased Array Radars," *Proceedings of the IEEE*, Vol. 104, No. 3, March 2016, pp. 530–543.

Yan, J., et al., "A Dual-Polarized 2–18-GHz Vivaldi Array for Airborne Radar Measurements of Snow," *IEEE Transactions on Antennas and Propagation*, Vol. 64, No. 2, February 2016, pp. 781–785.

CHAPTER 11

Broadband Antennas

11.1 Introduction

The arrival of broadband systems in the wireless communication area has demanded the design of antennas that must operate effectively over a wide range of frequencies. The broadband antenna is an antenna with a wide bandwidth. The definition of a broadband antenna is somewhat arbitrary and depends on the type of the antenna. If the impedance and pattern of an antenna do not change significantly over about an octave ($f_U/f_L = 2$) or more, the antenna is classified as a broadband antenna. Broadband antennas are generally made of structures that do not change abruptly in their physical dimensions, but instead utilize materials with smooth boundaries. Smooth physical geometry tends to produce antenna patterns and input impedance that also change smoothly with frequency, which is very important for a broadband antenna operation.

Typical broadband antennas include the log-periodic antenna, traveling-wave antenna, helical antenna, biconical antenna, frequency-independent antenna, spiral antenna, and complementary antenna. However, most of these existing broadband antennas are nonplanar and may not be directly mounted on a metallic platform. Many new technologies have emerged in recent years and, for such emerging technologies, printed antennas and antennas in the package are preferred. The fundamental and basic principles of broadband design of microstrip and printed antennas are [1–5]:

1. Low Q-factor of the magnetic wall cavity under the patch that can be achieved with low dielectric constant or larger thickness of the substrate.
2. Multiple resonances: Various geometries and perturbations to introduce multiple resonances as well as input impedance matching such as reactive loading by shaped slot, notch, cuts, pin, or post.
3. Customized patch geometry: Very irregular and unconventional patch shape optimized using the Genetic Algorithm.
4. Suppression of surface waves in a thick substrate: Periodic patterns on the ground plane or on any substrate produce an EBG structure on one face of which the microstrip element or arrays are printed.
5. Frequency-dependent substrate or ground plane: Multiple layers of FSS can reflect at respective frequency bands.

In this chapter, the designs of printed broadband antennas are discussed based on EBG, PBG, FSS fractal antenna, and many other latest technologies.

11.2 Metamaterials

In 1968, Veselago [6] hypothesized the possibility of having simultaneous negative values for permittivity and permeability. Thereafter, he also delved into the physical realization of $-\mu$ and $-\varepsilon$. Materials that display these properties are known as a metamaterial. Metamaterials are material that has properties that are not found in nature. Metamaterials possessing these properties are also frequently named double negative (DNG) material and Negative Refractive Index (NRI).

In addition to the materials with simultaneously negative permeability and negative permittivity, the single negative metamaterials have also drawn a great interest as shown in Figure 11.1. Over the years many researchers worked on microwave antenna composites with metamaterials [7–9].

11.3 Antenna Designs Based on EBG

In broadband antenna applications, the antenna cavity is usually loaded with absorbers to eliminate the backward radiation, but in doing so the radiation efficiency of the antenna is reduced. To enhance the radiation efficiency of such antennas, EBG structures are used. EBG structures that exhibit metamaterial behavior are researched intensively in the application of microstrip antennas. The magnetic conductors improve the radiation efficiency of antennas, but do not exist. One method to create an artificial magnetic conductor (AMC) is to design periodic structures that have electrical characteristics such as a magnetic conductor in the desired frequency band; one such example is an EBG structure. When EBG structures interact with EM waves, different electrical properties are observed at different frequencies. Periodic structures pass certain frequency bands, reject some frequency bands, and behave like a magnetic conductor in a band of frequencies, known as the bandgap [10, 11]. The EBG terminology came from the photonic bandgap (PBG) phenomena in optics that are realized by periodical structures. EBG structures are equivalent to

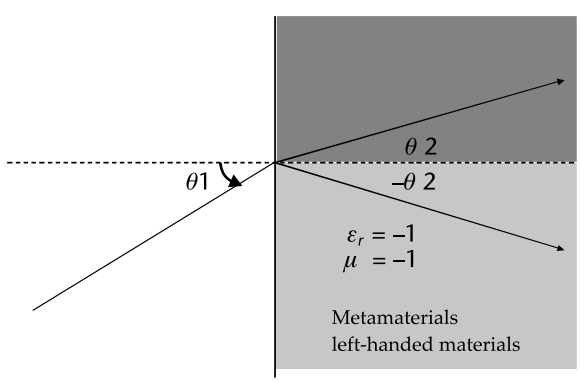

Figure 11.1 Negative refraction occurring at the interface between air and NRI metamaterials.

a tank circuit with capacitance represented by the gap between the patches and the inductance represented by the distance between the patches and the ground plane. EBG structures are usually compact and have low loss and can be easily integrated with antennas but operate over a narrow band of frequencies.

The EBG of a structure can be determined from the reflection phase, the dispersion diagram, and the transmission characteristics. The EM nature of a surface is predictable from the reflection phase characteristics, such that a 180° reflection phase implies a perfect electric conductor (PEC) surface and a 0° reflection phase resembles a perfect magnetic conductor (PMC) surface. EBG structures can be classified based on reflection phases for the same reflection magnitude. These structures can be designed to have a reflection phase of 0° for a specific frequency, which makes EBGs behave like a magnetic conductor, hence the name AMC. The bandgap of EBG structures is defined as the band of frequencies where the reflection phase from the EBG surface is between 90° and –90°.

EBG structures exhibit unique EM properties that have led to a wide range of applications in antenna and propagation fields [12–17]. There are two major advantages associated with EBG ground planes. First, these structures exhibit the possibility of creating a PMC because of in-phase reflection phase characteristics. This feature can cause efficient radiation for antennas laid adjacent to the EBG ground plane [12]. Second, such structures prevent the propagation of EM waves in a certain frequency band. Therefore, these can be used to block surface waves that usually corrupt antenna performance. Bandgap features are revealed in two ways: the in-phase reflection coefficient and the suppression of surface-wave propagation. The surface-wave suppression feature helps to improve an antenna's performance such as increasing the antenna gain and reducing back radiation.

Depending on the applications and geometries as shown in Figure 11.2, many other different names have been used for periodic structures. These applications include FSS, filtering, and EBGs. EBG structures are adopted to reduce surface waves and increase the gain of antennas and they were first introduced as FSS. In an antenna system that operates at multiple frequency bands, EBG structures (FSS layers) can be used to isolate bands.

The performance of an antenna is significantly affected by the surrounding medium and the presence of conducting ground planes. A conducting surface close

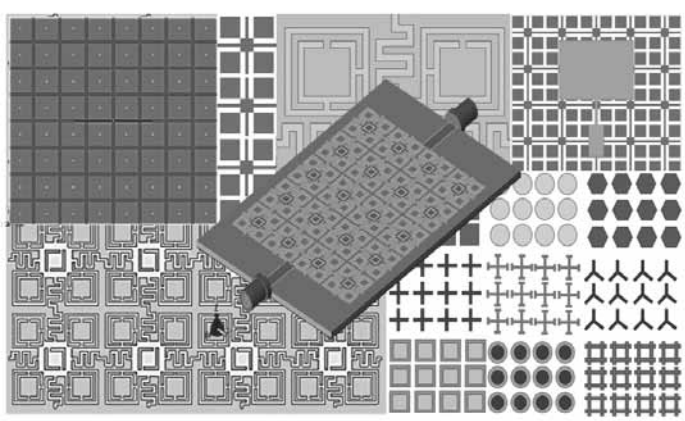

Figure 11.2 Various configurations of EBG structures [12–17].

to a radiating antenna typically degrades the performance of the antenna. From the conducting surface, a parallel electric field is reflected out of phase. When this current interacts with the forward propagating EM wave, they often add destructively and thus affect the radiation characteristics of the antenna. A tangential current close to a conducting plane is equivalent to two current elements, which are in opposite directions, as compared with the current in free space without the conducting plane. This property of the current causes the radiation from the current elements to cancel each other, thus affecting the radiation characteristics of the antenna. However, when an antenna is placed close to a parallel magnetic conductor, the electric field is reflected in phase and thus interacts constructively with the forward propagating electric field, which enhances the radiation in the forward direction instead of completely cancelling it. A tangential current element close to the magnetic conducting plane is equivalent to two electric current elements, in the same direction for the free space equivalent without the magnetic conducting plane. This behavior causes the radiation from the current elements to add constructively, thus enhancing the radiation characteristics of the antenna.

EBG structure classification is shown in Figure 11.3. Uniform EBG (U-EBG) structures are typically periodic structures consisting of metal patches that are separated by small gaps and vias that connect the patches to the ground plane. U-EBG structures are equivalent to a magnetic surface at the frequency of resonance and thus have very high surface impedance; this makes the EBG structures useful when mounting an antenna close to the metallic ground plane, provided that the antenna currents are parallel to the EBG structure. These structures can also be used between antennas in an array to decrease coupling between adjacent antenna elements, helping to eliminate blind scan angles. Utilizing EBG in a patch antenna with an air gap appears to perform five key functions:

1. Increase operation bandwidth;
2. Reduce sidelobe levels;
3. Increase front-to-back ratios;
4. Increase directivity and consequently gain improvement;

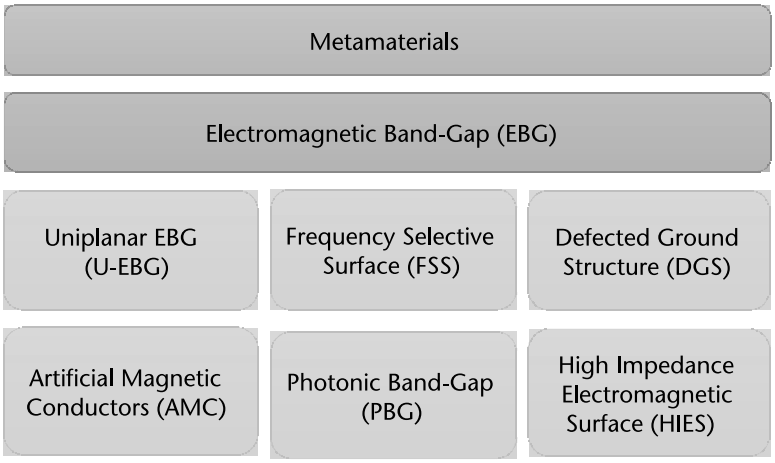

Figure 11.3 EBG structure types and classifications.

5. Harmonic control (suppression of resonance at the harmonic frequencies of the antenna).

Because of rapid progress in computational EM techniques various computational methods have developed for EBG analysis. These analyses are accurate, but very time-consuming, as Maxwell's equations need to be solved inside the unit cell by applying appropriate boundary conditions on unit cell walls. One of the advantages of using existing full-wave solvers is that the results allow the extraction of the properties of the EBG structure (surface impedance, reflection phase, dispersion diagram).

11.3.1 Microstrip Patch Antenna on Mushroom-Like-EBG Structure

There are many forms of periodic EBGs such as mushroom-like EBG, uniplanar EBG (UC-EBG), fork-like EBG, and spiral-like EBG. The mushroom-like EBGs known as high impedance surface (HIS) were initially proposed by Sievenpiper [12] and they are made up of metal patches, dielectric substrate, and vias connected with patches and ground plane, as shown in Figure 11.4. The mushroom-like EBG has a frequency bandgap and very high surface impedance characteristics, which is generally called the in-phase reflection band [13]. This conventional mushroom-like EBG structure can be used in antenna design to suppress the propagating of surface wave, but the cell size is still too large to be used in some practical applications. Thus, it is necessary to investigate the smaller EBGs for wide use in antenna fields.

The mushroom-like EBG structure is a 2-D EBG surface that consists of a metallic patch and a via that connects the patch to the ground as shown in Figure 11.4. The operating mechanism of the structure can be explained using an effective medium model with equivalent lumped LC elements. The shorting vias have an equivalent inductive effect, while the gaps between the patches have an equivalent capacitive effect. At its resonant frequency, the impedance is very high, and the structure impedes any surface waves, resulting in a frequency bandgap.

A unit cell EBG structure is composed of a metallic patch, a substrate, a ground plane, and a metallic via connecting the patch to the ground plane. The gap between adjacent patches has the effect of capacitance while the current flowing through the metallic via has an inductive effect. For an EBG structure with patch

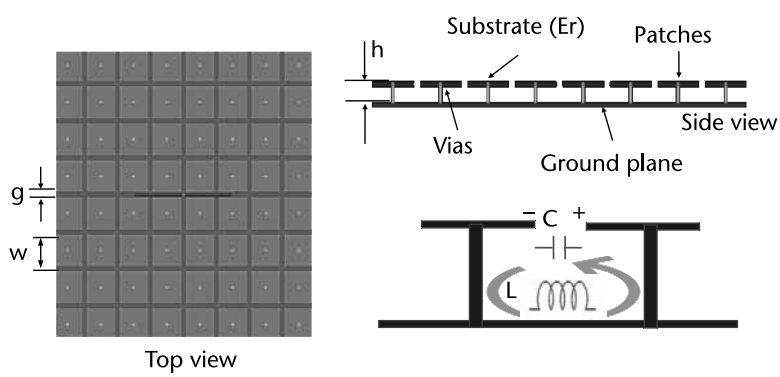

Figure 11.4 Mushroom-like EBG structure and equivalent circuit model of the conventional EBG unit cell [15].

width W, patch gap width g, dielectric constant ε_r, and substrate thickness h, the values of the inductor L and the capacitor C can be predicted with the following equations [13].

$$L = \mu h \tag{11.1}$$

$$C = W\varepsilon_0 \frac{1+\varepsilon_r}{\pi} \cosh^{-1} \frac{2W+g}{g} \tag{11.2}$$

$$f_0 = \frac{1}{2\pi\sqrt{LC}} \tag{11.3}$$

$$f = \frac{1}{\eta} f_0 \sqrt{\frac{L}{C}} \tag{11.4}$$

where μ is the free space permeability, ε_r is the substrate dielectric constant, and ε_0 is the free-space permittivity. The bandgap of such a structure can be determined by f_0, which is the central bandgap frequency, and Δf, which is the bandgap width. η is the free-space impedance, which is equivalent to 120π.

The surface impedance and reflection coefficient for the uniplanar compact EBG structure can be estimated based on this parallel LC equivalent circuit configuration. Hence, the surface impedance may be represented as

$$Z_s = \frac{j\omega L}{1-(\omega/\omega_0)^2} \tag{11.5}$$

where ω_0 is given by

$$\omega_0 = \frac{1}{\sqrt{LC}} \tag{11.6}$$

The bandgap of a periodic structure is calculated from its dispersion characteristics [14], which can be obtained by an eigenmode solver. In a structure, the eigenmode solver determines the resonant frequency for a given wavenumber, which is an important parameter to describe the propagation property of EM waves. There may be several different propagation constants at the same frequency. Each propagation constant is known as a specific mode with its own phase velocity, group velocity, and field distribution. The relation between phase constant and resonant frequency is referred to as the dispersion diagram.

A patch antenna design with an inset feed on the 1.6-mm-thick ($h = 0.026\,\lambda_{4.9\ \mathrm{GHz}}$ FR-4 substrate with a dielectric constant of 4.5 and a loss tangent of 0.025 is shown in Figure 11.5. The dimensions of the patch are 18.5 mm × 14.4 mm ($L = 0.29\lambda_{4.9\ \mathrm{GHz}}$, $W = 0.230\lambda_{4.9\ \mathrm{GHz}}$). The feed has a length of 5.3 mm from the edge and a notch width of 0.3 mm. The microstrip line width has a 1.5-mm EBG structure. The bandgap of the EBG structure was adjusted by tuning its width to 7.5 mm and its gap to 0.5 mm to cover the frequency of 4.9 GHz. The via diameter connecting the EBG patch and the ground plane is 1 mm. The number of columns of mushroom-like EBG structures placed around the patch antenna was varied to determine the number of columns required to effectively suppress the surface waves. The EBG structures were placed at least one period away from the edges of the patch antenna. Simulations were done for a different number of EBG columns. The patch antenna of the same ground size without EBG is also simulated for comparison purposes.

The simulation results are tabulated in Table 11.1. A patch antenna with 11 columns exhibited noticeable improvements in terms of the antenna bandwidth and gain of the antenna.

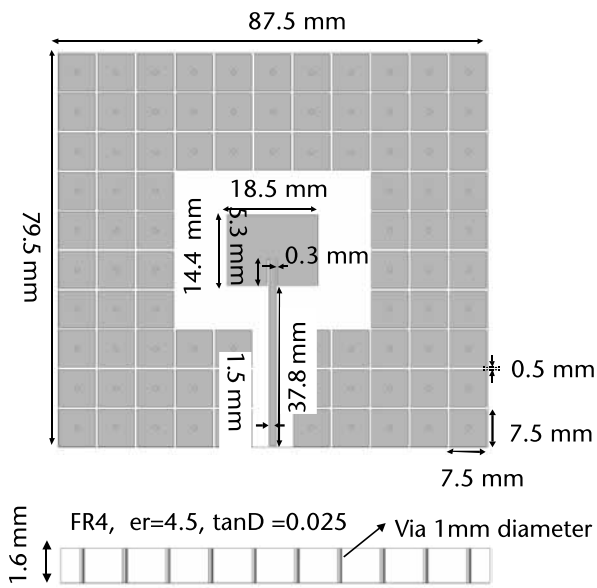

Figure 11.5 Microstrip patch antenna design using mushroom-like EBG structure.

Table 11.1 Antenna Performance with and without EBG

EBG Structure Size (Columns)	*Resonant Frequency (GHz)*	*Bandwidth (MHz)*	*Bandwidth Percentage*	*Gain (dBi)*
Without EBG	4.86	56	1.15%	6.20
7	4.88	185	3.79%	6.05
9	4.89	205	4.19%	6.76
11	4.91	227	4.60%	7.24

The S-parameter comparison of the antenna with the same size of the ground plane only and with the EBG structure is shown in Figure 11.6. An antenna with an EBG structure has around 4 times the bandwidth as compared to an antenna without any EBG structure. Unlike uniplanar and other EBGs, mushroom-like structures do not have any interconnecting microstrip lines that restrict their placement periodically. The electric field distribution over the patch antenna and the radiation pattern is shown in Figure 11.7. The gain improved from 6.2 dBi to 7.24 dBi, with the EBG structure.

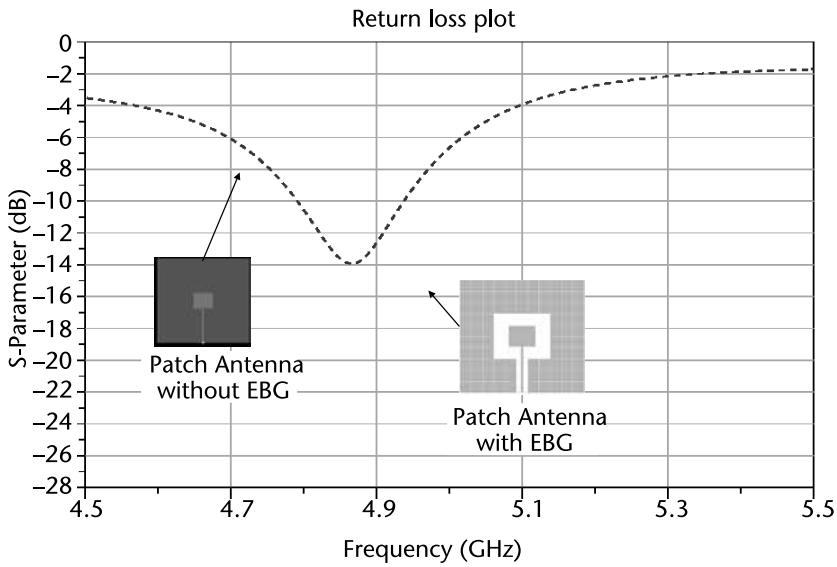

Figure 11.6 Microstrip patch antenna result with and without EBG.

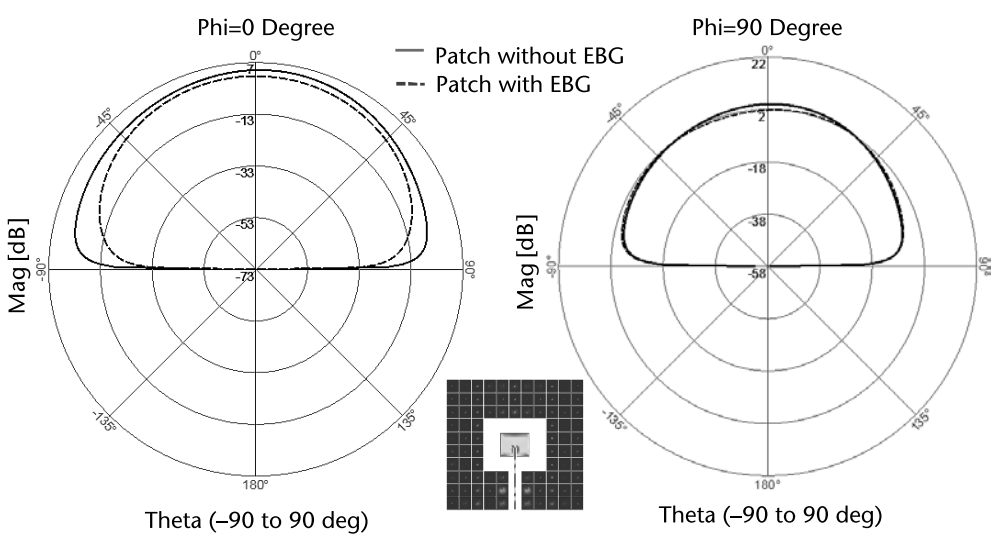

Figure 11.7 Radiation pattern of a mushroom-like EBG patch antenna.

11.3.2 Uniplanar EBG Cells with a Rectangular Microstrip Antenna

The design of a rectangular microstrip antenna based on the EBG cell-loading technique is shown in Figure 11.8. By incorporating the U-EBG cells on the ground plane of the rectangular microstrip antenna, the performance of the antenna can be enhanced. An important feature in the U-EBG design is the removal of vertical vias. Thus, it simplifies the antenna fabrication process and is compatible with microwave and millimeter-wave circuits. There are numerous configurations of EBG structures according to their application in the antenna. In this design, a square EBG periodic structure with stripline is used in the ground plane of the microstrip patch antenna. In the microstrip antenna design, an EBG structure can be used to design a high impedance ground plane that acts as a thin AMC metamaterial capable of reducing surface waves near resonance.

The zero-order bandwidth for an antenna over a magneto-dielectric substrate with thickness can be approximated by [18]:

$$BW \approx \frac{96\sqrt{\mu_r t / \varepsilon_r \lambda_0}}{\sqrt{2}\left[4 + 17\sqrt{\mu_r \varepsilon_r}\right]} \tag{11.7}$$

Thus, for a given miniaturization factor (constant $\sqrt{\mu_r \varepsilon_r}$) the antenna bandwidth can be enhanced by increasing μ_r/ε_r.

The rectangular microstrip antenna is designed and fabricated on low-cost glass epoxy substrate of relative permittivity of 4.4 and a substrate height of 1.6

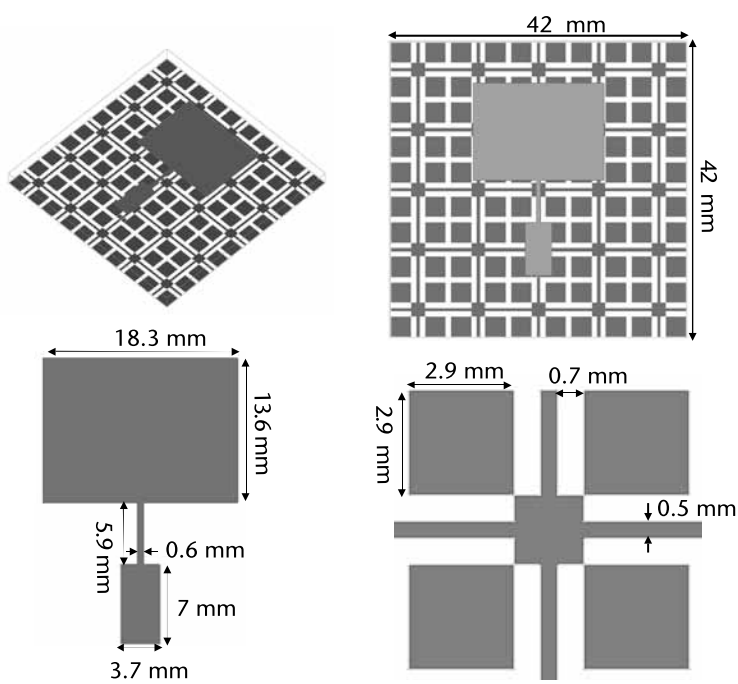

Figure 11.8 Design of a rectangular microstrip antenna based on the EBG cells as a ground plane.

mm. The rectangular microstrip patch length is 13.6 mm and the width is 18.3 mm. The enlarged view of the EBG cell is also shown in Figure 11.8. There are 5 × 5 EBG cells with a dimension of 7.7 mm × 7.7 mm. The total size of the ground plane is 42mm × 42 mm for the design. U-EBG microstrip antenna performance is compared with microstrip patch antenna with metallic ground plane without EBG structure. The return loss versus frequency characteristics of the antenna is shown in Figure 11.9.

The antenna bandwidth is 34% with a U-EBG structure that is almost 4 times more than the bandwidth of patch antenna without EBG as listed in Table 11.2.

11.3.3 Bowtie Antenna with EBG Cells

The ultrawideband (UWB) antenna designs may be broadly divided as traveling-wave structures such as the Vivaldi antenna [19, 20], frequency-independent structures such as the biconical antenna or the bowtie antenna [21, 22], self-complementary antennas that are characterized by a self-complementary metallization such as the logarithmic spiral antenna and fractal antennas [23], and combinations of these such as the log-periodic antenna [24–26]. The bowtie antenna, first proposed by Lodge and later reexamined by Brown and Woodward, demonstrates its benefits. There are various shapes of bowtie antenna such as the triangular shape, rounded edge, or slotted shape.

A bowtie antenna design is shown in Figure 11.10. This is printed on a 0.64-mm-thick dielectric substrate with a 10.2 (Rogers RT6010) dielectric constant. The feeding structure consists of a microstrip line continued by the transmission line formed by two parallel strips. One side of the feed consists of a microstrip

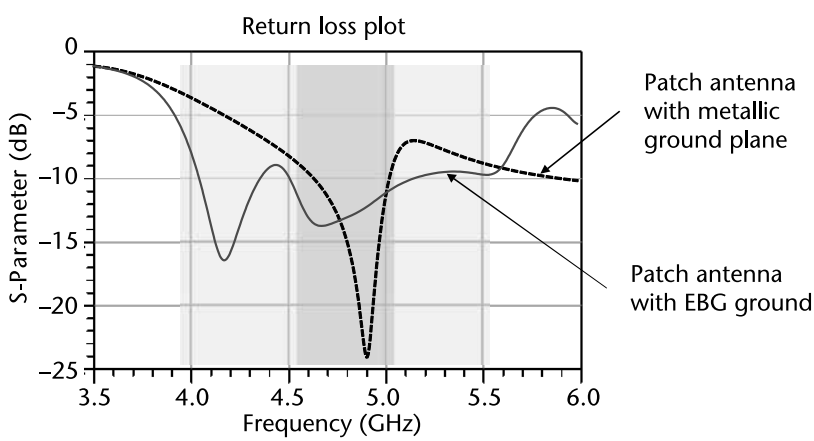

Figure 11.9 Antenna return loss plot with metallic and with EBG ground plane.

Table 11.2 Antenna Bandwidth with and without EBG

Antenna	*Bandwidth (–9 dB)*	*Bandwidth in %*
Rectangular microstrip patch antenna with ground plane	425 MHz	8%
Patch antenna with EBG	1,575 MHz	34%

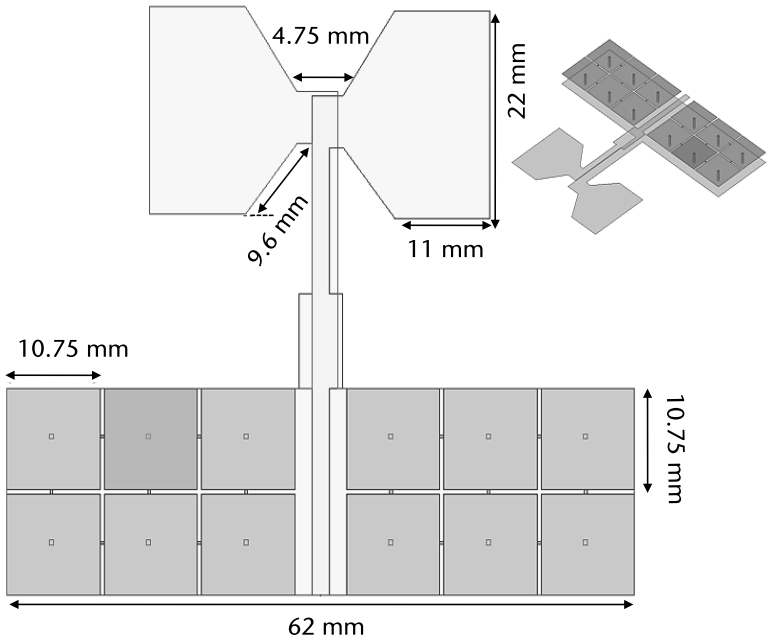

Figure 11.10 Double bowtie antenna design over a rectangular EBG structure.

line, one of the parallel lines, and one arm of the printed bowtie antenna. The other side consists of a truncated ground plane, the other line of the parallel strip transmission line, and the second arm of the bowtie antenna. The microstrip line is designed with a characteristic impedance of 50Ω. The parallel strips are selected based on some parametric studies and optimization procedures for the best antenna performance.

The truncated ground plane acts as a reflector; thus, the radiation patterns are expected to peak in the opposite direction of the ground plane edge. The dimensions used for this printed bowtie antenna are shown in Figure 11.10. The total area of the substrate is approximately 1,300 mm^2 at the central frequency. The antenna was built and tested. The computed and measured reflection coefficients and 3-D radiation at 2.5 GHz are shown in Figure 11.11. An antenna with a –10-dB bandwidth is 21%.

11.3.4 Array Antenna Design Using EBG

There are many frequency bands for different communication systems, and these are allocated to serve different purposes in modern life. Many of these applications and devices mainly operate in Ka-band, which is allocated in the microwave radio region of the EM spectrum.

For high gain, printed array antennas are used in these applications. Mutual coupling is one major issue in printed array antenna design. This coupling becomes especially critical in arrays of patch antennas where coupling comes from two paths. The first path is due to the free-space radiation, which is present in all types of array antennas. The second path comes from surface waves and it constitutes a very important factor in patch antennas. In these types of antennas, surface waves

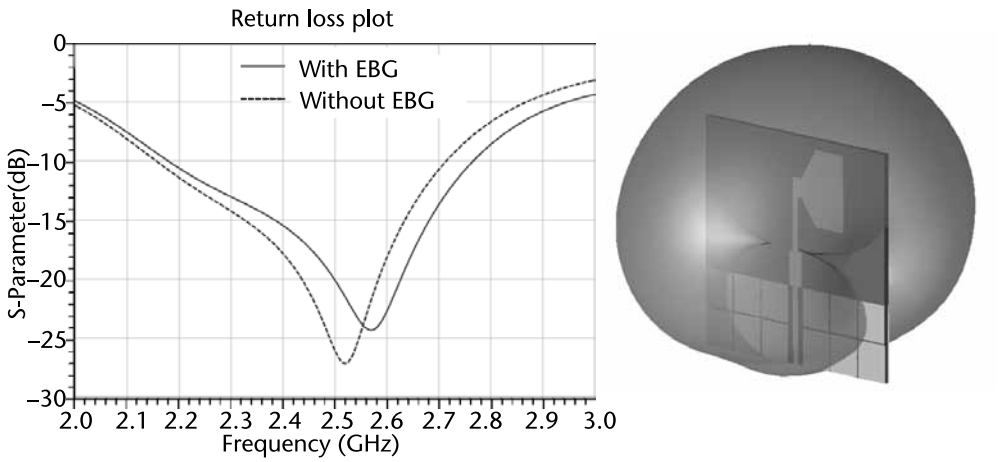

Figure 11.11 Bowtie antenna return loss and 3-D radiation pattern plot.

are strongly excited in E-plane when the antenna is operated in the fundamental mode (TM_{10} for rectangular patches). In this mode, the field distribution inevitably excites the first propagating mode of surface waves in E plane, given that this mode has no cutoff frequency.

Array antennas with a periodic structure like EBG, as shown in Figure 11.12, have the ability to suppress surface-wave propagation in a frequency band. The EBG structure is made of rectangular metallic elements (patch type) whose size to suppress surface-wave propagation is related to (usually smaller than) $0.5\lambda_{er}$. The simulated antenna return loss plot is shown in Figure 11.13. The antenna resonates at 28.8 GHz.

The lower cutoff frequency of this structure to behave as an EBG is related to the periodicity (here, 1.65 mm) in the direction of propagation (E-plane). Simulations were carried out using the FEM. The mutual coupling in the E-plane is shown

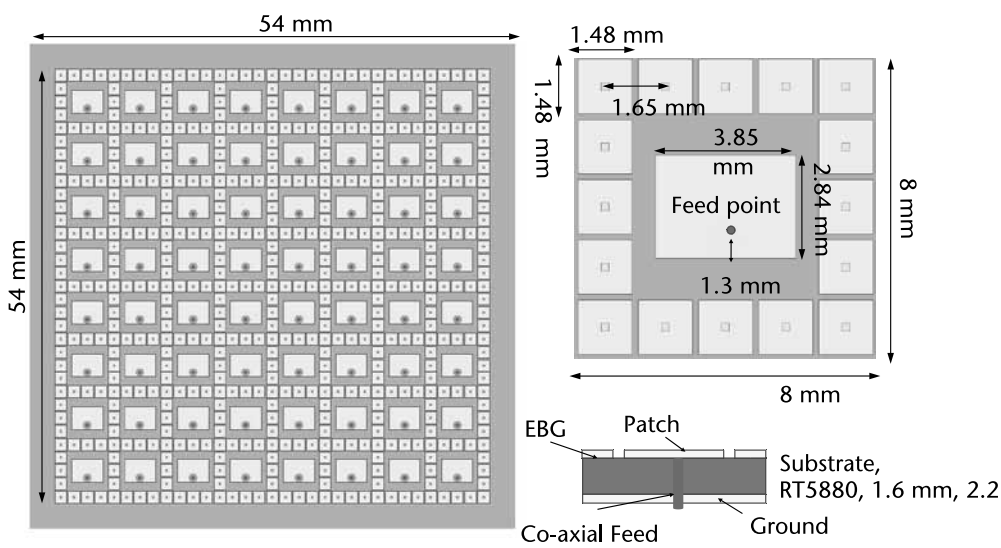

Figure 11.12 Ku-band microstrip patch antenna array using a rectangular EBG structure.

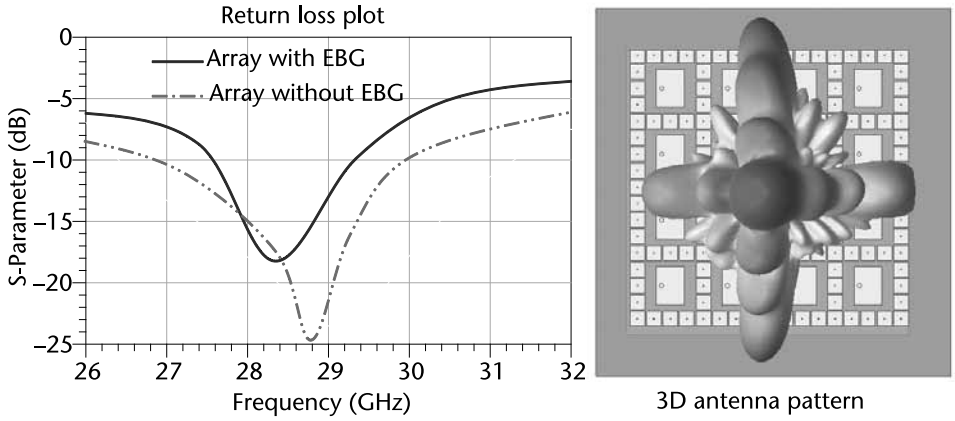

Figure 11.13 A 4 × 4 antenna array return loss and radiation pattern (top view).

in Figure 11.14. In the frequency band where the antenna is matched (with an S_{11} smaller than 10 dB), the maximum coupling level is –22 dB.

11.4 FSS

FSS is another area of interest to broadband antenna researchers. The FSS comprises periodically arranged metallic patch elements or aperture elements within a metallic screen and exhibits total reflection (patches) or transmission (apertures) about the element resonance. A periodic surface is basically an assembly of identical elements arranged in a 1-D or 2-D infinite array. Its basic characteristic is to scatter or reflect certain frequencies of EM waves incident on it. The FSS is used in

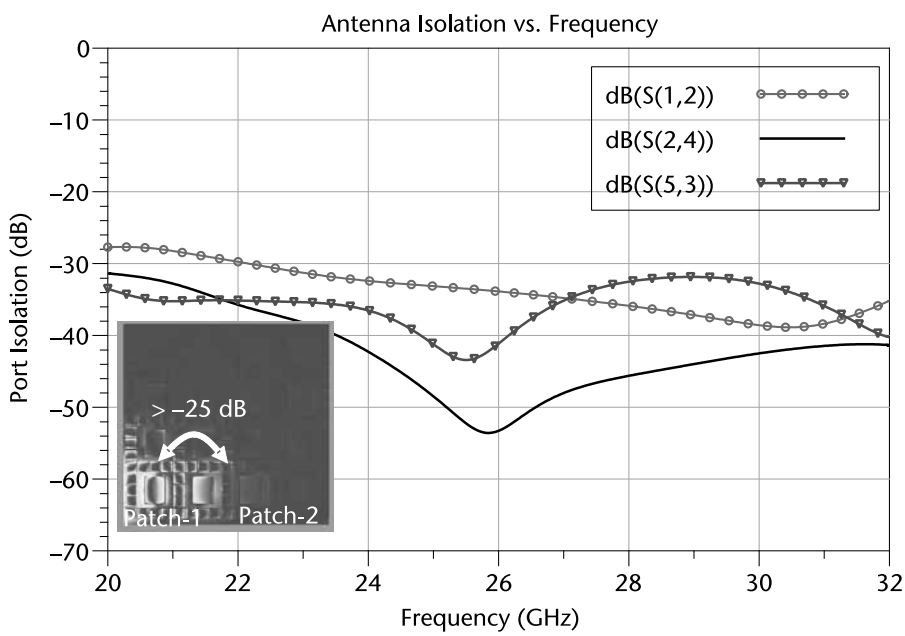

Figure 11.14 Simulated mutual coupling between antenna elements is greater than –25 dB.

various applications such as aerospace, antenna design, medical, and microwave devices. In microwave and medical applications, FSS technology is used to reduce the leakage of power and to prevent EMI. In aerospace applications, it is used to reduce the radar cross-section (RCS) of various devices such as radome, antennas, and microwave circuits. Sometime FSS is placed on top of the microstrip patches to reduce the cross-polarization level of the antenna [27].

High-performance, low observable antennas can be designed using the FSS structure to the planar antenna, where the FSS is employed either as superstrate or high-impedance ground plane of the antenna. The incorporation of the FSS to the antenna mainly enhances its gain and bandwidth. In printed antennas, to reduce the scattering component outside the operating bandwidth, the conventional metallic ground plane can be replaced with a stopband FFS of the antenna, because it largely reflects the energy of incident waves.

There are four different types of possible element-type FSS arrays: plate, center connected, loop, and combination. Figure 11.15 shows some examples of each element type. These elements vary from narrowband to wideband structures. In the first group, the plate group, the FSS elements in general do not have very desirable characteristics. Primarily, the elements have x and y dimensions around a half-wavelength, which limits how closely these elements can be placed next to one another. In addition, plates are highly inductive elements with small capacitances between them, leading to issues regarding achieving resonance. It is impossible to achieve perfect reflection if the FSS does not resonate. This is because, at resonance, the FSS becomes a short circuit and thus acts as a PEC ground plane.

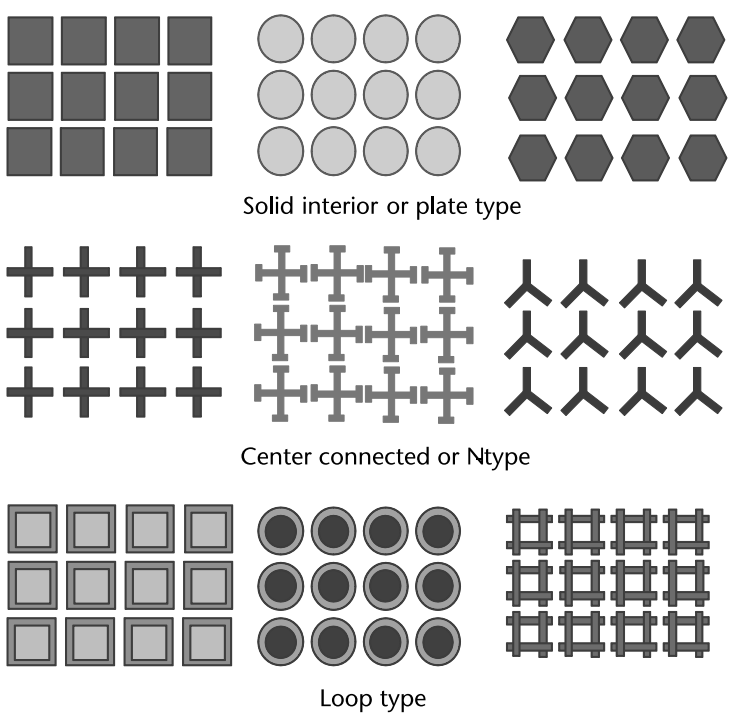

Figure 11.15 The three major groups of FSS elements.

The second group, the center-connected elements, is a viable candidate for both radiating and nonradiating arrays. The most recognizable from the center-connected group is the dipole. This is by nature a narrowband element, but when it is placed in a well-designed array this element can reach a bandwidth ratio of 4:1 without the addition of a dielectric matching section added in front of the array. The third group, the loop elements, is, in general, an excellent choice for nonradiating element FSS arrays. These FSS elements are typically smaller in the x and y directions than the center-connected elements with respect to a wavelength and thus can be spaced close to one another. As will be discussed in more detail later, this leads to a delayed onset of grating lobes and generally wider bandwidth.

An FSS pattern on a 2-mm-thick RO3003 substrate is shown in Figure 11.16. Periodic boundary conditions are used on four sides of the unit cell to simulate the infinite 2-D array. Perfectly matched layers (PMLs) on the top and bottom of the unit cell absorb the excited mode from the input port and any higher-order modes generated by the periodic structure. Unit cell simulation setup is shown in Figure 11.17.

An EM simulation model of a unit cell is shown in Figure 11.18. This structure acts as a passive resonant absorber. The FSSs have found applications in multiband reflector antennas and radome such as the Cassegrainian subreflectors in parabolic dish antennas, especially in communications and defense applications. The simulation transmission loss and the electric field are shown in Figure 11.19.

11.5 Antennas on PBG

Microstrip planar antennas fabricated on a substrate with a high dielectric constant (GaAs, Si, and InP) are strongly preferred for easy integration with the MMIC RF front-end circuitry. However, it is well known that patch antennas on high dielectric constant substrates are inefficient radiators due to surface wave losses and have very narrow (1%–3%) frequency bandwidth. This situation becomes very severe

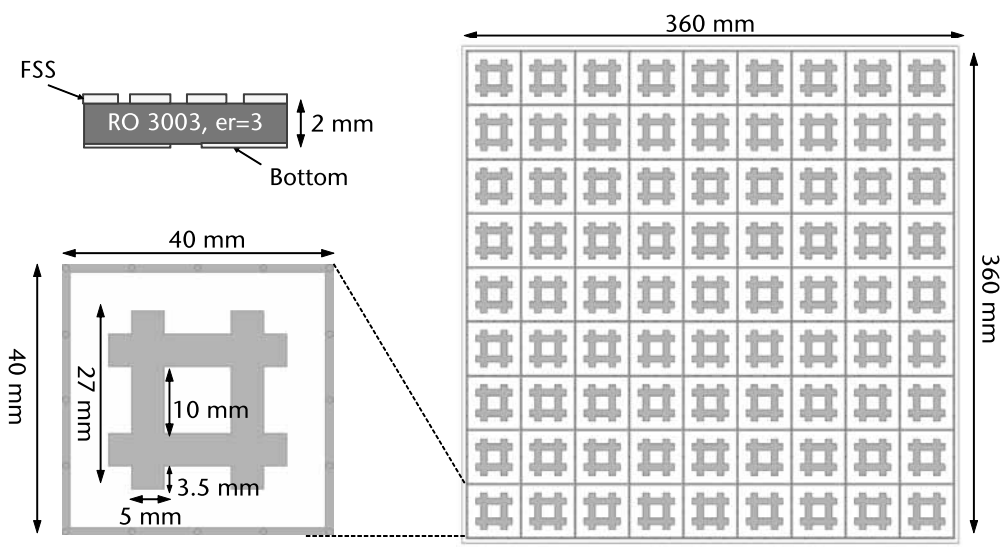

Figure 11.16 FSS array with rectangular strips pattern and FSS unit element.

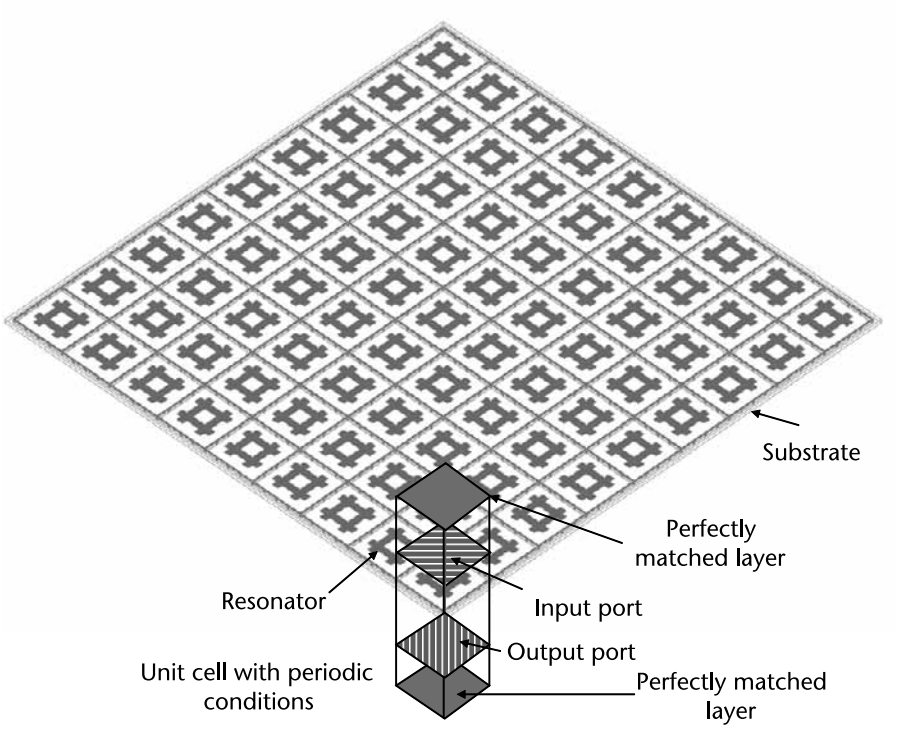

Figure 11.17 Layout geometry of the FSS and EM simulation setup for a unit FSS cell.

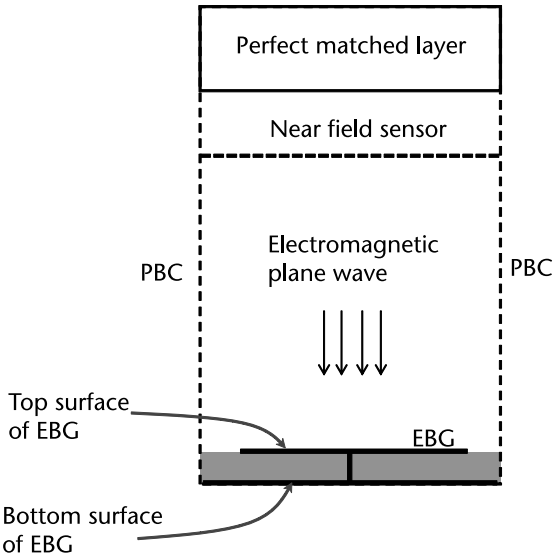

Figure 11.18 Unit cell model of FSS with boundary conditions and plane-wave excitation for EM simulation.

as applications move to higher frequencies, resulting in microstrip patch antennas with reduced efficiency and gain as well as an unacceptably high level of mutual coupling and cross-polarization within an array environment. PBG technology has been applied as a new promising solution to these problems. Another way to get

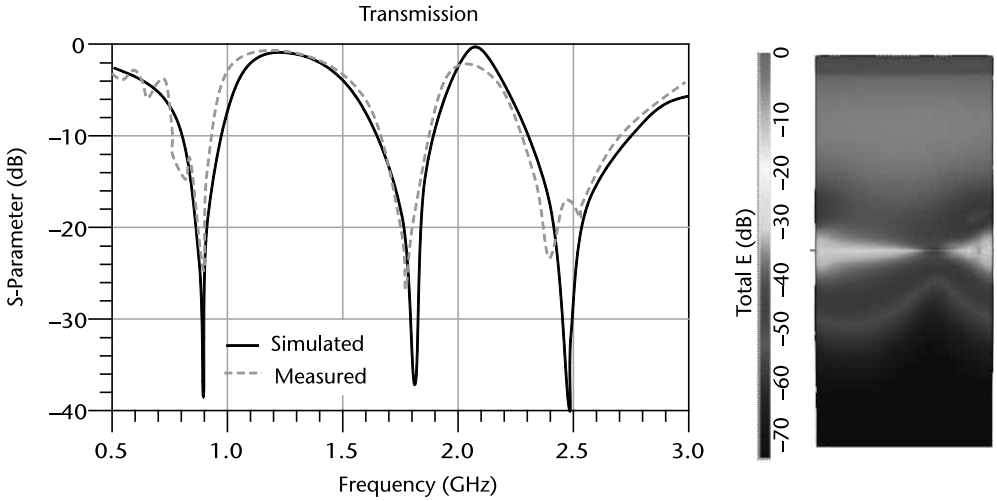

Figure 11.19 Simulated and measured reflection coefficient and E-field profiles in the xz-plane, the unit cell cavity.

broadband antenna performance is increasing the substrate thickness that introduces the low Q-factor of the cavity below the patch. However, this technique is restricted by the surface-wave generation leading to low gain and low efficiency of the antenna.

The PBG structure is basically a periodic metallic pattern printed on a dielectric substrate for microwave and millimeter-wave applications as shown in Figure 11.20. This technique provides a stopband of EM waves propagating through it, called the bandgap. The frequency range of the stopband depends on the geometry dimensions and its pattern. The wave is attenuated during propagating through the substrate if the antenna operating frequency falls within this stopband. In this way, the generation and propagation of the surface wave are stopped, which increases antenna efficiency. The PBG structure can be formed by using metallic, dielectric, ferroelectric, or ferromagnetic implants. Dielectric PBG structures have been used

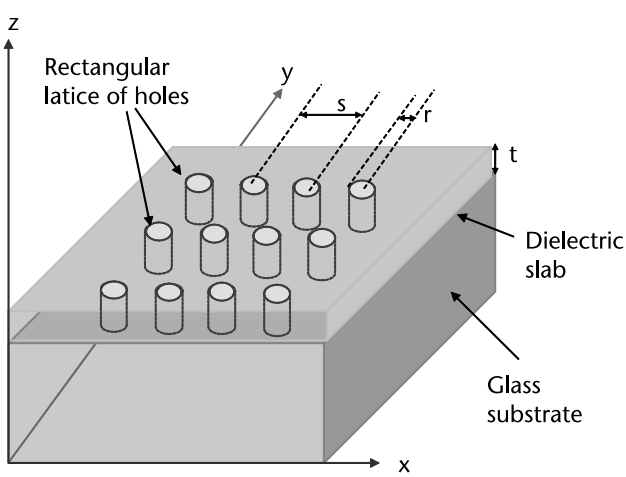

Figure 11.20 A PBG structure with a periodic metallic pattern printed on a dielectric substrate.

for microstrip circuits [10]. These require drilling of a periodic pattern through the substrate. A PBG structure that requires only partial etching of the ground plane is compatible with monolithic circuit technology. Photonic structures have been applied to the study of the microwave frequency ranges [10, 11].

A microstrip planar antenna design that uses photonic crystals as a substrate to enhance the antenna performance at the terahertz frequency regime is shown in Figure 11.21. The dominant surface wave in microstrip patch antennas on a dielectric substrate with the ground is the TM0 mode, which has no cutoff frequency. A 2-D PBG lattice can prohibit the propagation of the TM0 mode along the dielectric substrate. The incorporation of PBG unit cells in the dielectric substrate volume reduces the effective dielectric constant and refractive index and improves the gain and radiating efficiency of the antenna. The effective dielectric constant and refractive index of the PBG material depends on the dimension and periodicity of the PBG unit cell. The microstrip patch antenna basic structure consists of a conducting patch and a ground plane separated by 5-μm-thin glass substrate. This is the terahertz antenna with thin substrate and high dielectric constants, which results in tightly bound fields within the dielectric material. The end of the microstrip feed line is connected with a coaxial line for impedance transition. The antenna input impedance can be matched by tuning the length, width, and position of the microstrip feed line.

The PBG is used to control the refractive index of the substrate material to be less than 1. The refractive index of the PBG material depends on the lattice factor (k), where k is the ratio of the radius of the cylindrical air cavity unit cells to the PBG unit cell interspacing distance. PBG is also used for filtering, as they block certain bands; these structures can be used to block undesired frequencies. The antenna is simulated using the FEM solver. Antenna return loss plot and mesh data are shown in Figure 11.22. Antenna resonance frequencies are 2.24 THz and 2.61 THz.

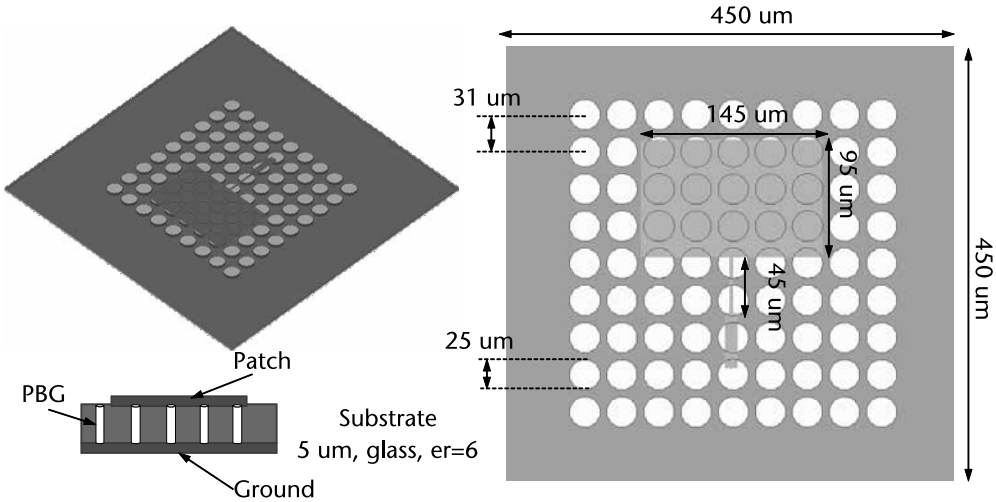

Figure 11.21 Microstrip patch antenna design with photonic crystals in the ground plane. The PBG is constructed on a grounded dielectric substrate by drilling holes in the substrate.

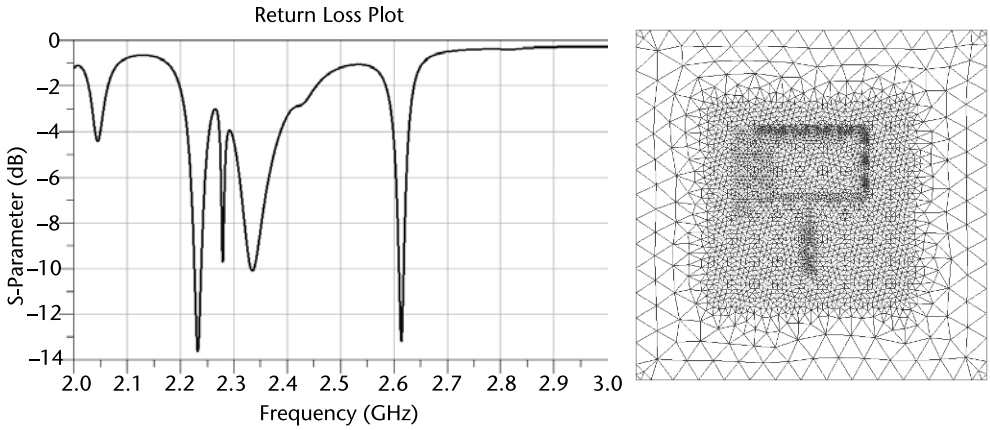

Figure 11.22 Computed return loss plot using the FEM technique and FEM mesh.

11.6 Fractal Antennas

Miniature antennas are of prime importance due to the available space limitation on the user equipment and the oncoming deployment of diversity and MIMO systems in many applications. The major antenna miniaturization techniques include material loading, lumped element loading, the use of ground planes, short circuits, and the antenna's environment and geometry optimization. Among these miniaturization techniques, geometry optimization has gained much interest with the introduction of fractals in antenna engineering due to their inherent miniaturization ability. The term fractal, which means irregular fragments or broken, was originally coined by Mandelbrot [28] to describe a family of complex shapes that possess an inherent self-similarity or self-affinity in their geometrical structure. The original motivation for the development of fractal geometry came mainly from the study of the patterns of nature. For example, fractals have been effectively used to model complex natural objects such as galaxies, cloud boundaries, mountain ranges, snowflakes, coastlines, ferns, and much more. By using fractals in antennas, some of the unique properties can be achieved:

- Reduction of physical radiator size;
- Multiband behavior is a result of self-similarity;
- Self-similar radiation pattern;
- Consistence performance over the huge frequency range;
- Added inductance and capacitance without components.

To overcome narrow bandwidth and low gain limitation of conventional microstrip patch antennas, these antennas are designed with fractal geometries. Broadband antennas, logarithmic spiral, and log-periodic structures can be considered as fractal antennas, and these antennas can be also analyzed based on fractal antenna theory. Frequency independence in antennas starts with Rumsey's principle [29]. As per Rumsey's principle, the impedance and pattern properties of an antenna will be frequency-independent if the shape is specified only in terms of angles. The spiral

antenna can be considered as a smoothly self-symmetric structure. Similarly, in the log-periodic antenna, various performance properties repeat in the same geometric ratio as its element size and spacing.

11.6.1 Fractal Antenna Geometries

There are some common fractal geometries that have been found to be useful in developing new and innovative designs for antennas such as the Sierpinski gasket, Sierpinski carpet fractal structure, Koch snowflake, fractal rectangular curve (FRC), and Hilbert curve as shown in Figure 11.23. A few of the other fractal geometry types are Cantor's comb, the Mandelbrot set, and the Lorenz attractor.

Nathan Cohen, a radio astronomer at Boston University, was a fractal antenna innovator who experimented with wire fractal antennas (von Koch curves) and fractal planar arrays (Sierpinski triangles). In 1988, he built the first known fractal antenna. Fractal antenna geometries have two common properties: self-similarity and space-filling. While the self-similarity property is successfully applied to design multiple band fractal antennas, the space-filling property can be used to compact the antenna size.

11.6.2 Sierpinski Gasket Fractal Antenna

The Sierpinski gasket is named after the Polish mathematician Sierpinski, who described some of the main properties of this fractal shape in 1916 [30]. The original gasket is constructed by subtracting a central inverted triangle from the main triangle shape as shown in Figure 11.24. After the removal, three equal triangles remain on the structure, each one being half of the size of the original one. The same

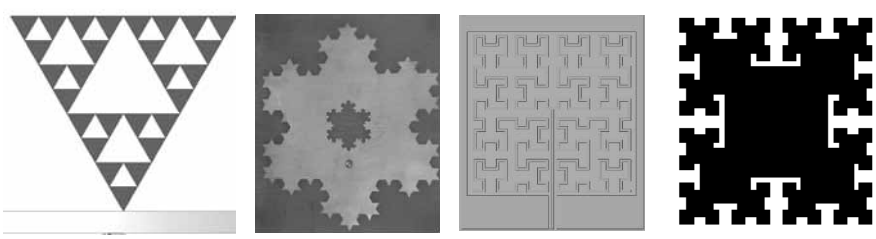

Sierpinski gasket Koch snowflake Hilbert curve FRC

Figure 11.23 Common fractal antenna geometries, Sierpinski gasket, Koch snowflake, Hilbert curve, and FRC.

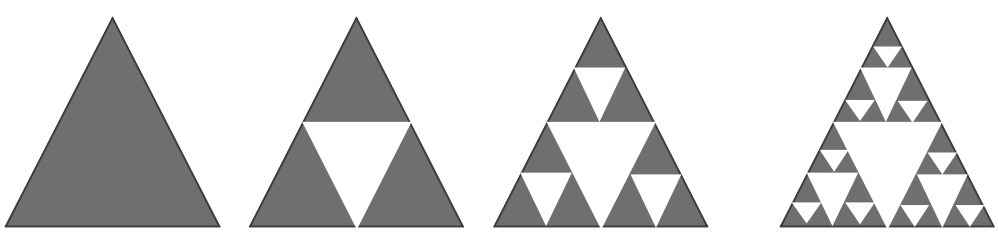

Stage 0 Stage 1 Stage 2 Stage 3

Figure 11.24 Several stages in the construction of a Sierpinski gasket fractal.

subtraction procedure can be iterated on the remaining triangles and, if the iteration is carried out an infinite number of times, the ideal fractal Sierpinski gasket is formed. In this ideal structure, each shape of its three main parts is exactly equal to the whole object but scaled by a factor of 2 and so is each of the three gaskets that compose any of those parts.

The first few stages in the construction of the Sierpinski gasket are shown in Figure 11.24. The Sierpinski gasket is an example of a self-similar fractal. The procedure for geometrically developing this fractal begins with an equilateral triangle contained in the plane, as shown in stage 0. The next step is to remove the central triangle with vertices that are located at the midpoints of the sides of the original triangle, shown in stage 1. The same process is then repeated for the three remaining triangles, as illustrated in stage 2. The next two stages (i.e., stages 3 and 4) in the construction of the Sierpinski gasket are also shown in Figure 11.24. A Sierpinski triangle antenna design is shown in Figure 11.25.

The antenna is printed on a 1.6-mm-thick RT Duroid substrate with a dielectric constant of 2.3. The structure is fed through a 1.5-mm diameter, 50Ω coaxial probe with a SubMiniature version A (SMA) connector on the bottom side of the plane. The size of the antenna is 10 cm × 10 cm. The sides of the initiator equilateral triangle are 6 cm. The antenna has been constructed through four iterations in this design, so four-scaled versions of the Sierpinski gasket are found on the antenna (circled regions), the smallest one being a single triangle. The antenna is analyzed using the MoM. The return loss against frequency and 2-D radiation patter=n plots at two frequencies are shown in Figure 11.26 for different iterations. For the first iterations of the antenna, the resonant frequencies observed are 4.3 GHz, 7 GHz, 8.3 GHz, and 9.8 GHz, respectively, with the prominent frequencies being 4.3 GHz and 7 GHz. The second iteration resonates at 3.1 GHz, 6.6 GHz, and 9.2 GHz.

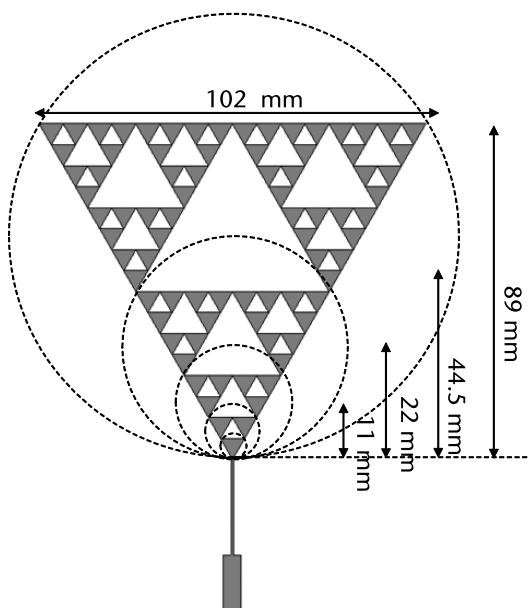

Figure 11.25 Sierpinski monopole antenna and design dimensions.

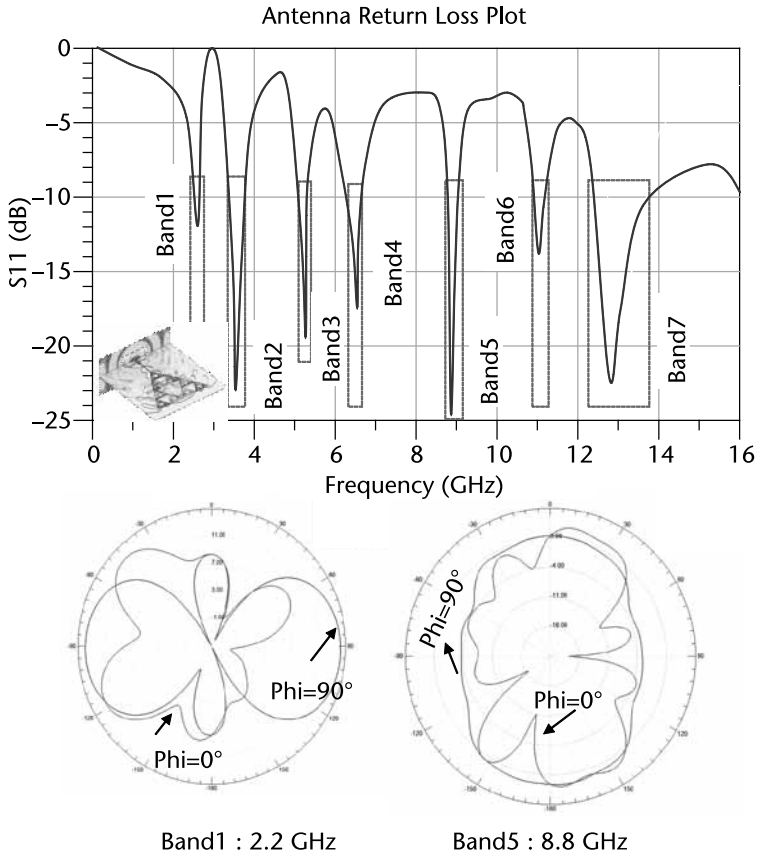

Figure 11.26 Sierpinski monopole antenna return loss and 2-D radiation pattern plot at 2.2 GHz and 8.8 GHz.

It is seen that the lower resonant frequencies are less emphasized in case of the single-layered structures of the Sierpinski geometry. Thus, the true multiband character is not so emphasized by this single-layered design approach.

11.6.3 Square Shape Fractal Antenna Design

The UWB fractal antennas with a notch are used in many broadband systems. In applications such as Wi-Fi and GPS, operation at two or more subbands is necessary. A valid alternative to the broadening of total bandwidth is the use of a multifrequency fractal antenna in a single radiator. A square shape fractal geometry with four stages is shown in Figure 11.27.

A square shape fractal antenna design and dimensions are shown in Figure 11.28. At the initial stage, antenna geometry looks like a simple square patch designed on the RT Duroid substrate with ε_r= 2.2 and a substrate thickness of 1.57 mm.

The square patch has a dimension of 25 mm × 25 mm. The first iteration of the fractal antenna has been constructed by inscribing the circular patch of diameter of 24 mm and subtracting it from the square. The second iteration has been

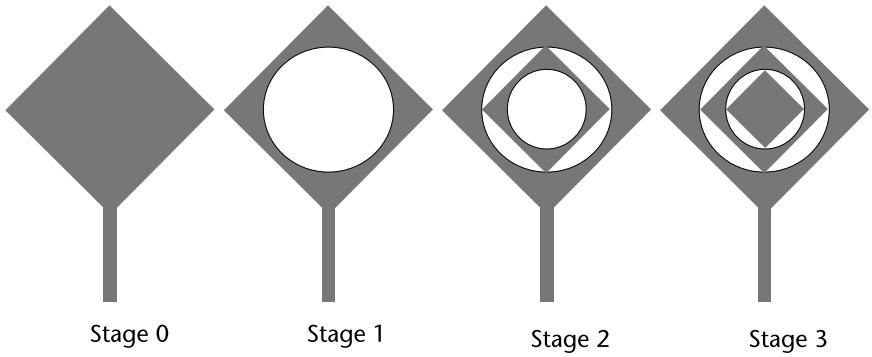

Figure 11.27 Square shape fractal geometry with four stages in the construction.

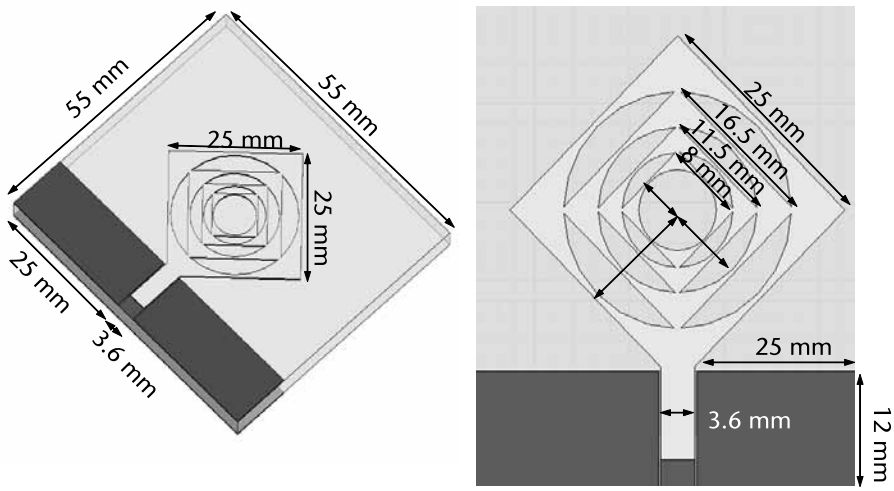

Figure 11.28 Square shape microstrip fractal antenna geometry and design dimensions.

constructed by making the square of the dimension 16.5 mm × 16.5 mm and an inscribed circle with a diameter of 15.5 mm and subtracting it from the square. Likewise, the third iteration is constructed by making a square of 11.5 mm × 11.5 mm and inscribing the circle with a diameter of 10.5 mm and subtracting it from the square. In the fourth iteration, a square of dimension of 8 mm × 8 mm is made, and an inscribed circle of a diameter of 7.5 mm is subtracted from it. This fractal antenna has been fed with a CPW feed line.

After simulating this fractal antenna, it is noticed that the operating resonant frequency of the antenna depends on patch size and substrate thickness. So, for better performance of the antenna, these parameters should be optimized. The simulated return loss of the antenna is shown in Figure 11.29. Antenna 2-D radiation patterns at 4 GHz and 8.5 GHz are shown in Figure 11.30.

The antenna has an operational resonant frequency at 2.1 GHz, 4.4 GHz, 5.4 GHz, 6.4 GHz, and 7.7 GHz normalized to a 10-dB return loss value, which is covered in WLAN and Wi-Max bands for communication.

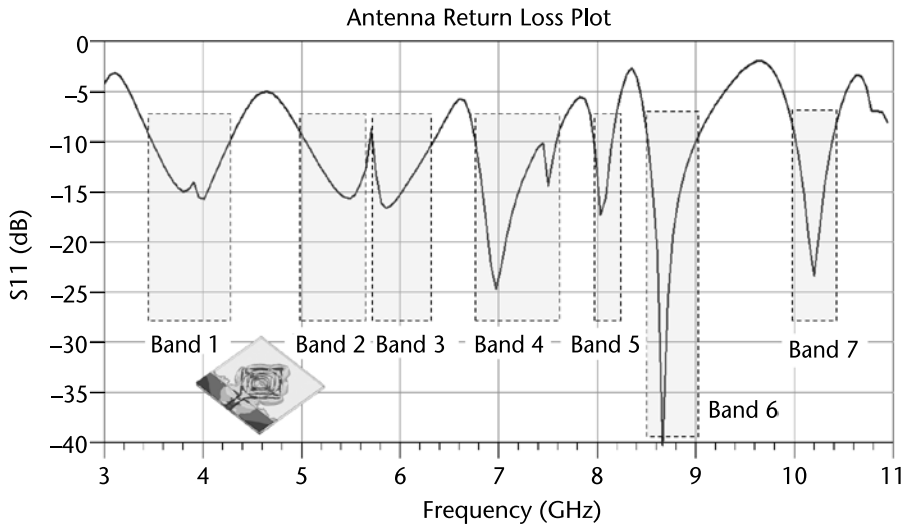

Figure 11.29 Return loss plot of the square shape fractal antenna.

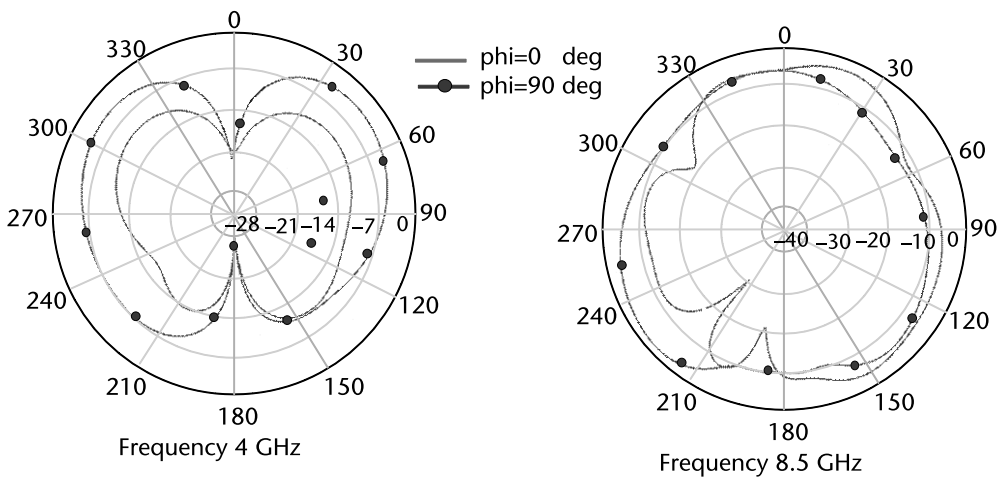

Figure 11.30 Antenna radiation pattern at 4 GHz and 8.5 GHz in the antenna operating frequency band.

11.6.4 Koch Snowflake Fractal Antenna

The Koch snowflake is another popular fractal antenna. The creation of the Koch fractal starts with a straight segment with a length L, and then this initiator line segment is divided into three parts of equal length (i.e., $L/3$ each). Next, the middle segment is replaced with other two segments of the same length, with 60° as intersection angle. This geometry is called the generator and is the first iterated version of fractal geometry. By repeating this process further, higher iterations are generated. This fractal also starts out as a solid equilateral triangle in the plane, as illustrated in stage 0 of Figure 11.31. However, unlike the Sierpinski gasket fractal, which is formed by systematically removing smaller triangles from the original structure,

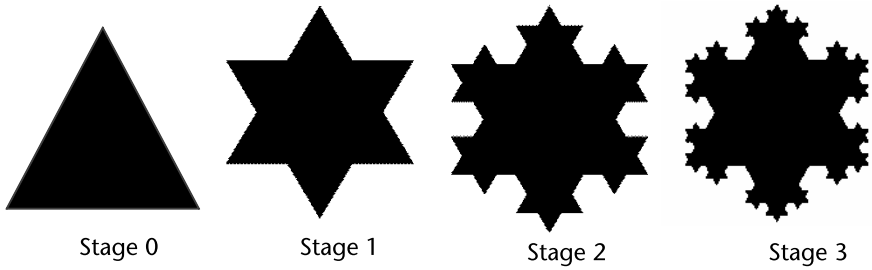

Figure 11.31 Four stages in the construction of a Koch snowflake fractal.

the Koch snowflake is constructed by adding smaller triangles to the structure in an iterative fashion. This process is clearly represented in Figure 11.31, where the first four stages in the geometrical construction of a Koch snowflake are shown.

For the design of triangular patch antenna, there are three important parameters: resonant frequency (f_r), dielectric material of the substrate (ε_r), and thickness of the substrate (d). The resonant frequency of the fundamental mode of such an antenna is given as:

$$f_r = \frac{2c}{3a\sqrt{\epsilon_r}} \tag{11.8}$$

where c is the speed of light, ε_r is the relative permittivity of the substrate, and a is the patch side length. The first iteration of the Koch fractal antenna is obtained by replacing the sides of an equilateral triangle by a Koch curve. After the first iteration of the Koch fractal, the resulting shape is a star shape patch, as shown in Figure 11.31. After the second iteration of the Koch fractal antenna, the resulting shape is as shown in stage 2. In each new iteration, the area of the geometry increases.

If $A_k$is the area at one iteration, then the area A_{k+1} of the next iteration can be computed:

$$A_{k+1} = A_k + \frac{\sqrt{3}}{12}\left(\frac{4}{9}\right)^{k-1} a^2 \tag{11.9}$$

where a is the side length of the initial triangle that has an area of:

$$A_0 = \frac{\sqrt{3}}{4}a^2 \tag{11.10}$$

Figure 11.32 shows a microstrip Koch snowflake fractal antenna operating at multiple frequency bands between 2 GHz and 16 GHz. Some fractal shapes are not broadband structures like Koch is narrowband, but this is good for miniaturization.

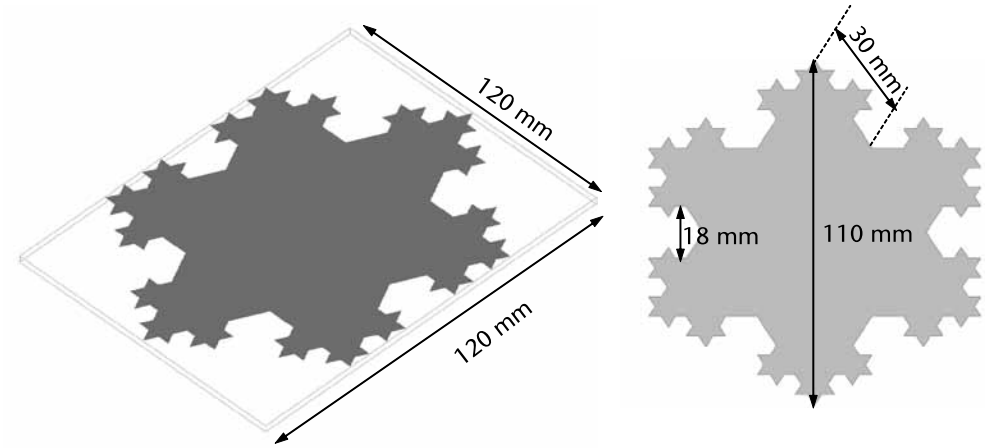

Figure 11.32 Koch snowflake fractal microstrip antenna geometry and design dimensions.

11.6.5 UHF Hilbert Antenna Array for Partial Discharge (PD) Detection

PD is a common local dielectric breakdown phenomenon of an electrical insulation system, and it often takes place in gas-insulated switchgears, power transformers, switches cabinets, and power cables [31, 32]. A PD is normally accompanied by EM and acoustic emissions [31]. A PD online monitoring system, as shown in Figure 11.33, is an effective method in inspecting insulation defects and fault diagnosis in electrical apparatus. Compared with ultrasonic detection and pulse current detection, the UHF method possesses the advantage of high sensitivity and strong anti-interference capability. The design of the UHF antenna is the key technology in the UHF detection approaches because the performance of UHF antenna determines the ability of the PD online detection systems. In general, the frequency of EM waves arising from PD varies from 300 MHz to 3 GHz, and the ratio bandwidth reaches up to 10:1. To cover the entire frequency band, several broadband antennas (e.g., planar equiangular spiral antenna, Hilbert fractal antenna, horn antenna, and biconical log-periodic antenna) are employed. However, these antennas suffer from

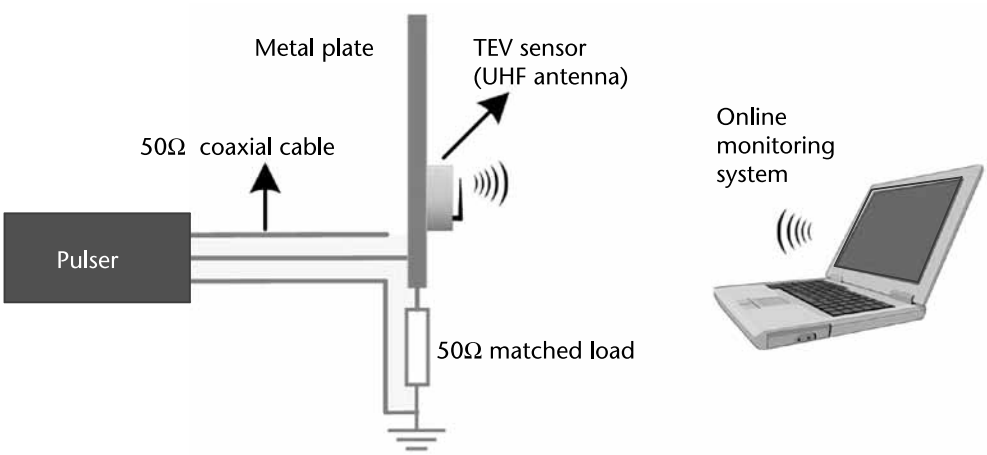

Figure 11.33 PD detection system and detection process.

excessive size, and it is inconvenient for the internal installation. The space-filling property of fractal antenna helps to lengthen the effective current path within the limited area and the self-similar property aids the generation of multiple resonant modes [33].

A UHF Hilbert antenna array for PD monitoring is designed. The first four steps in the construction of the Hilbert curve are shown in Figure 11.34. The Hilbert curve is a space-filling fractal curve that is self-avoiding (i.e., has no intersection points). The performance of the Hilbert fractal antenna can be affected by numerous factors, such as the order, side dimension, width of the conductor, and thickness of the substrate and feed point. The increasing number of order corresponds to the increasing number of resonant frequencies of a Hilbert fractal antenna and decreasing first resonant frequency.

Considering the size and resonant frequencies of the Hilbert fractal antenna, the optimal design is based on the third-order Hilbert curve, as shown in Figure 11.35. The Hilbert fractal antenna is designed synthetically through simulations. The simulation model includes conductor patch, substrate, ground plane, and probe feed. The conductor patch is filled with the third Hilbert curves, and the material of the substrate is FR4 epoxy with a dielectric constant of 4.4. The total

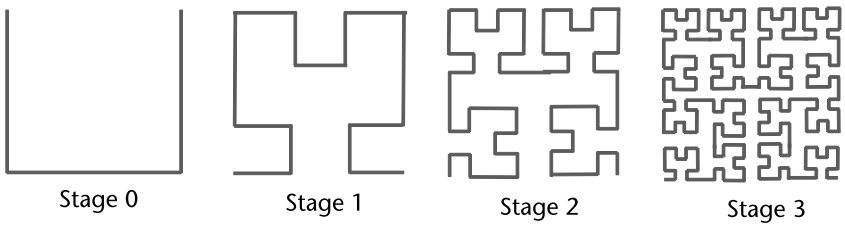

Figure 11.34 The first four stages in the construction of a Hilbert curve.

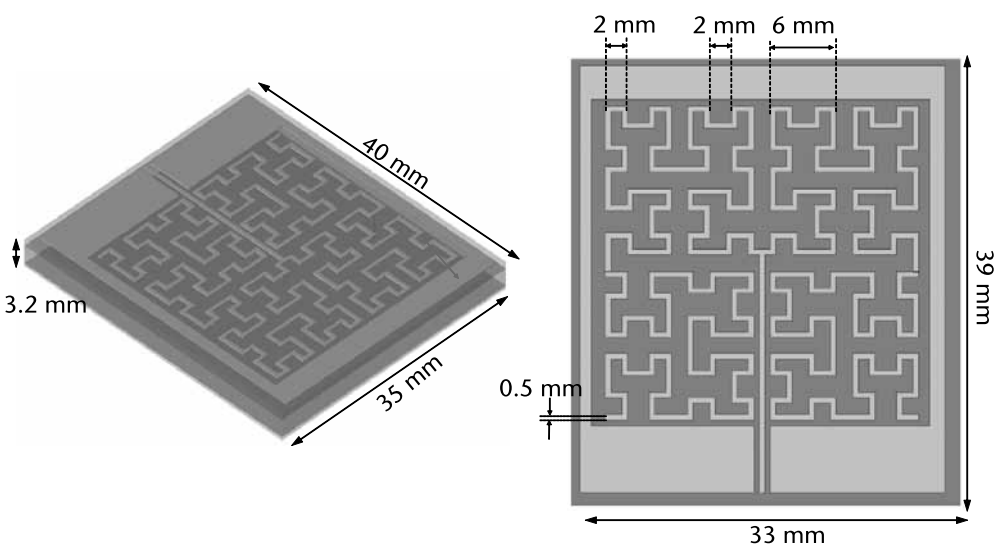

Figure 11.35 Microstrip Hilbert antenna structure and design dimensions.

antenna size is 40 mm × 35 mm, which is very compact in the 2.4-GHz frequency band. The impedance bandwidth of the Hilbert fractal antenna is narrow in the range of 2 GHz to 2.41 GHz as shown in Figure 11.36. The gain of the antenna at 2.4 GHz is 3 dBi.

11.7 UWB Antenna

The commonly used frequency band allocated for UWB applications is 3.1–10.6 GHz, although lately there appear to be systems with operation bands started from 300 MHz and sometimes up to 20 GHz, depending on the fields of use and the applications. Due to the FCC and ITU regulations, the UWB assigned an unlicensed band in the range of 3.1–10.6 GHz with the transmitted power emission limitation of –41.3 dBm/MHz, and the other frequency range with as low power as –75 dBm/MHz as shown in Figure 11.37.

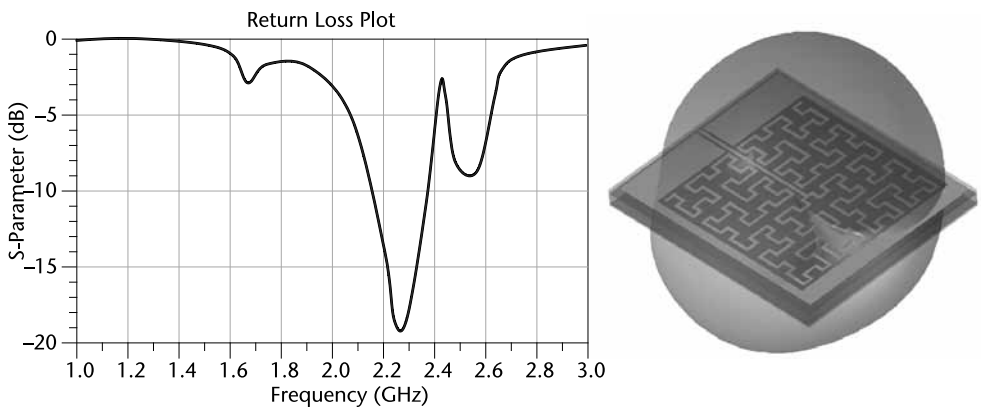

Figure 11.36 Antenna return loss and radiation pattern plot.

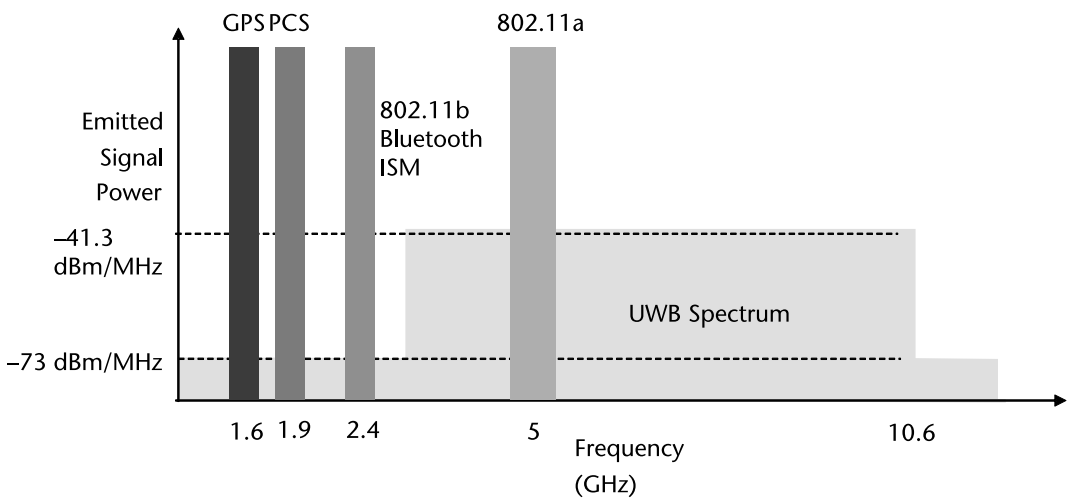

Figure 11.37 UWB spectrum.

11.7.1 UWB Hexagonal Printed Monopole Antenna for GPR Systems

Ground-penetrating radar (GPR) systems are used for subsurface investigations. These are used for the detection of objects buried beneath the Earth's surface such as landmines, pipes, cables, and hidden tunnels. GPR uses a high-frequency microwave signal that is transmitted into the ground, and reflected signals are returned to the receiver as shown in Figure 11.38. The reflected signals are processed to get information. The transmit and receive antennas are one important component in any GPR system [34].

The desired features of a GPR antenna include UWB operation capability and good impedance matching. One of the problems found in the impulse radar system is the generation of short pulses. Stepped frequency continuous wave (SFCW) ground penetration radar (SFCW-GPR) normally use inverse discrete Fourier transform (IDFT) to transform the frequency-domain data into time-domain pulse data. For UWB operation, some of the required properties of an antenna are compact size, wide impedance bandwidth, unidirectional radiation pattern, low-power operation, ease of manufacturing, and unipolar configuration. Printed monopole antennas with a very large bandwidth are a popular antenna design choice as they meet most of the above requirements. For SFCW-GPR applications, it is also vital that the antenna has a flat transfer function in the frequency domain.

A hexagonal UWB antenna is designed for transmitting a monocycle pulse generated by a 100–1,000-MHz SFCW system. As per requirement, the antenna has a low VSWR (≤ 2), the flat transfer function in the entire bandwidth, and exhibits very small late-time ringing (in the time domain).

A hexagonal monopole UWB antenna for a 3–10-GHz frequency band is designed as shown in Figure 11.39. For UWB antennas, instead of resonance or operating frequency, the lower band-edge frequency and total bandwidth become the design parameters. The lower frequency depends mainly on the maximum height of the substrate, while the bandwidth of the antenna depends on how the impedance

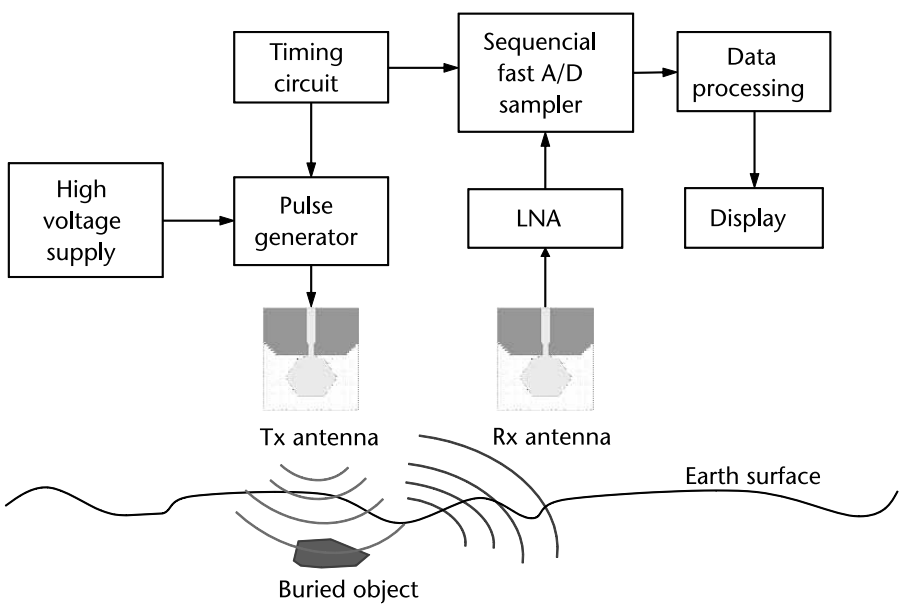

Figure 11.38 SFCW-GPR system.

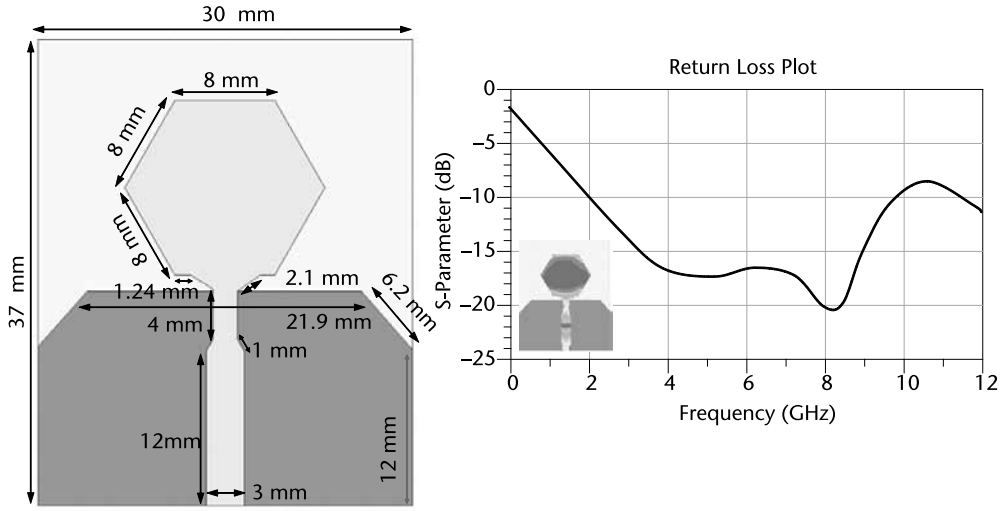

Figure 11.39 UWB hexagonal patch antenna design and return loss plot.

of various modes of the patch is matched with the feed line. The substrate used is FR4 of a 1.6-mm thickness and a dielectric constant (ε_r) of 4.4. The antenna size is 30 mm × 37 mm. In this design, truncated ground structures are used. Usually to reduce the size of the antenna without affecting the bandwidth, gain, and other antenna parameters, various methods such as using high-permittivity dielectric material and magneto-inductive waveguide loaded slots on the patch can be used. The antenna performance is analyzed using the FEM simulation technique. The simulation results are shown in Figure 11.39. Antenna return losses are lower than –10 dB for the entire frequency band (2.95–10 GHz) and the VSWR is also less than 2 for the entire frequency. The bandwidth of the antenna meets the requirement of the 100–1,000-MHz SFCW-GPR application.

11.7.2 Broadband Rectangular Patch

To improve the antenna bandwidth, several techniques are used such as partial ground plane feeding structure, inserting a capacitor between the patch and the ground plane, inserting a chip resistor between the patch and the ground plane, and inserting a chip inductor that broadens impedance bandwidth. A broadband monopole rectangular patch antenna with the partial ground plane is designed as shown in Figure 11.40. The antenna design is optimized for the frequency range from 1.9 GHz to 9 GHz. This design can be used for various applications operating in this frequency range.

A Teflon-based dielectric substrate with a relative permittivity ε_r of 2.65, a thickness of 0.8 mm, a length of 15 mm, and a width of 13 mm is used. The radiating patch element and ground plane are on the top and bottom of the dielectric substrate, respectively, and are made of copper material with a thickness t of 0.035 mm and a conductivity σ of 5.96e 7 s/m. The ground plane length and width are 28 mm × 9 mm. To achieve 50Ω output impedance matching with the SMA connector, a transmission line fed with a width of 2 mm and a length of 13 mm is used. The

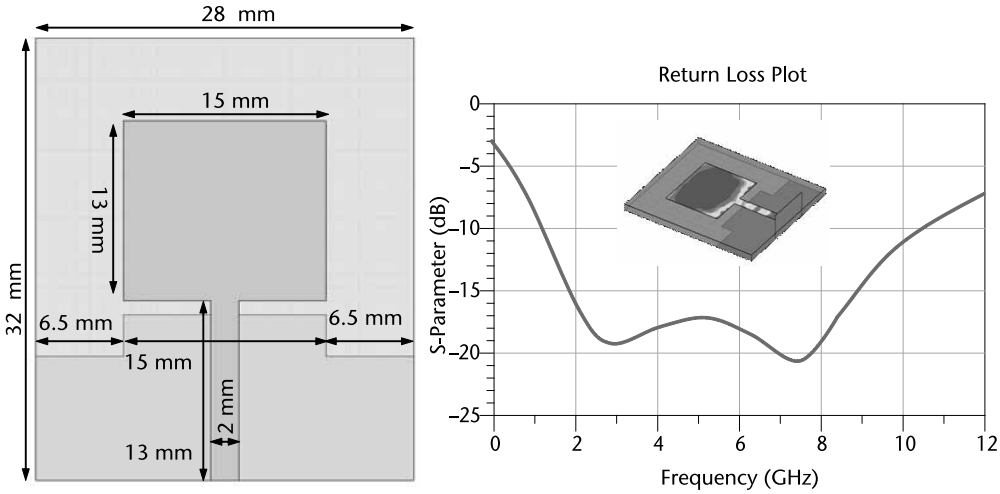

Figure 11.40 Broadband rectangular patch antenna design and simulated return loss and E-field plots.

antenna 2-D radiation pattern and gain versus frequency plots are shown in Figure 11.41.

11.7.3 Slot-Loaded Patch

One technique to improve the bandwidth of the microstrip patch antenna is to cut a half-wavelength-long slot in the patch at a desired resonant frequency as shown in Figure 11.42. Slots are embedded in the printed patch. Their dimensions and positions are properly selected to the first two broadside-radiation modes of the patch to be perturbed such that their resonance frequencies get close to each other to form a wide impedance bandwidth [1, 2]. Slots cut into the patch are of different types (e.g., commonly used slots are the E-slot, U-slot, and H-slot). The antenna performance of the U-slot patch antenna is shown in Figure 11.43.

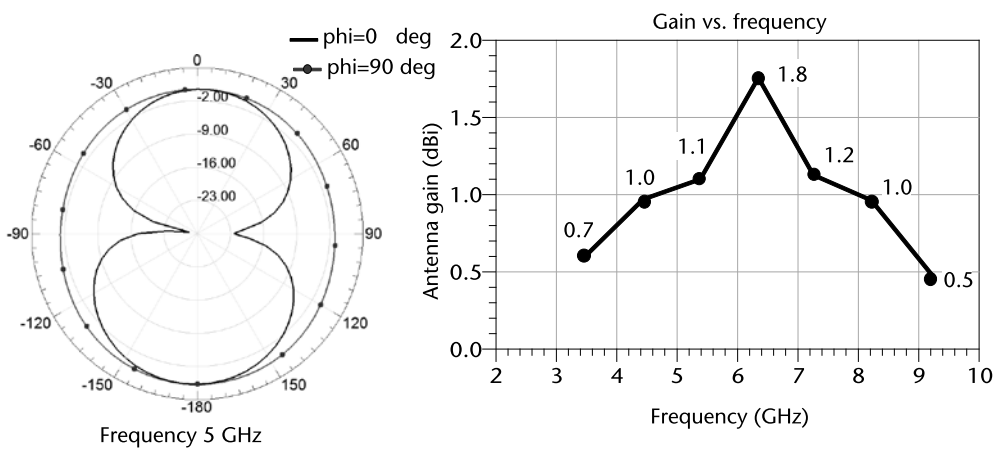

Figure 11.41 The 2-D radiation pattern at 5 GHz and gain versus frequency plot of the broadband rectangular patch.

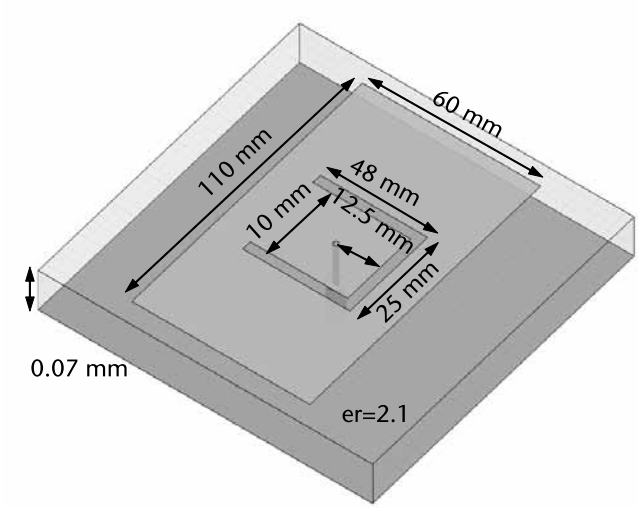

Figure 11.42 U-Slot patch antenna structure and design dimensions.

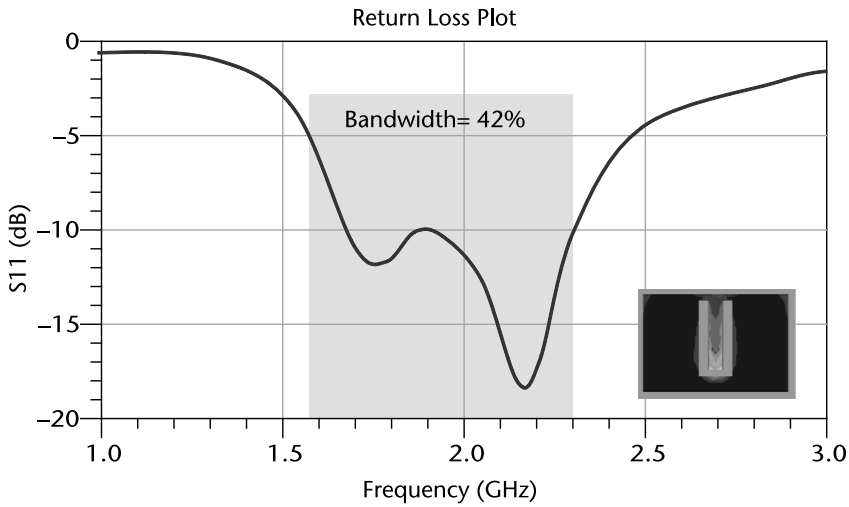

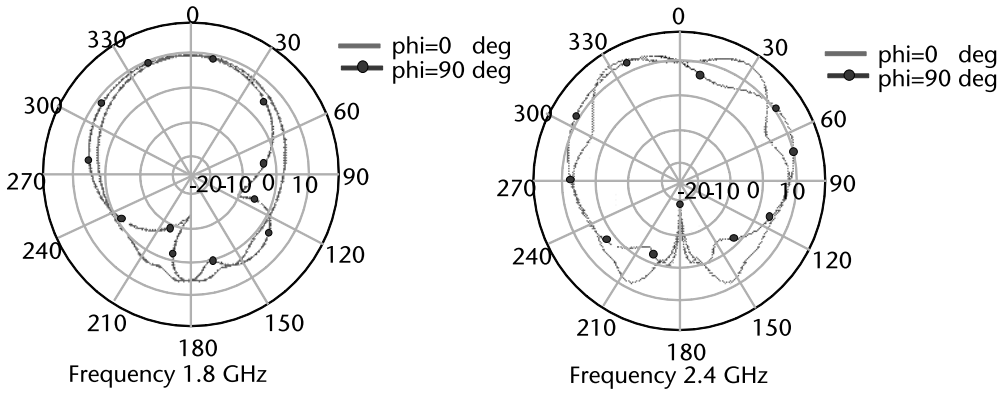

Figure 11.43 U-slot patch antenna simulated return loss and 2-D cut pattern plot at 1.8 GHz and 2.4 GHz.

11.7.4 Wideband Spiral Antenna for Software-Defined Radio-Based Radar

Software-defined radio (SDR)-based radar finds many applications in modern electronics systems such as air traffic radar controls, real-time processing FMCW radar for target detection, and even space communications. SDR has many advantages such as a multipurpose system with the ability to reuse the hardware and signal processing algorithms, low cost, and faster development. In this system, a wideband antenna is applied to scan over all the frequencies. The spiral antenna belongs to the class of frequency-independent antennas and has a radiation pattern, impedance, and polarization that remain virtually unchanged over a large bandwidth. A perfect spiral antenna that radiates a circularly polarized wave will not receive the wave reflected from the interface, because it is predominantly cross-polarized. A broadband two-arm logarithmic spiral antenna as shown in Figure 11.44 is designed for 3–6-GHz frequency band.

The spiral antenna consists of two identical arms that are shifted by 180° with respect to each other. The shape of the spiral arm is like a filling of two identical curves shifted by 90°. The curve is described by the function [29]:

$$r = r_0 e^{a(\varnothing+\varphi)} \tag{11.11}$$

where r_0 is the starting distance at $\varphi = 0°$, a determines the increasing rate of radius r, $\varnothing$ is the variable angle, and φ determines rotation of the curve. The outer antenna curve is set up for $\varphi = 0°$ and inner antenna curve is set up for $\varphi = 90°$.

11.7.5 UWB Vivaldi Antennas

The important parameters for the UWB antennas are the impedance bandwidth, the radiation efficiency, usable gain, the directivity, the beamwidth of the main lobe, and the minimization of the sidelobes and back lobes. Vivaldi antennas are the microstrip type of traveling-wave UWB antennas, which carries all the benefits

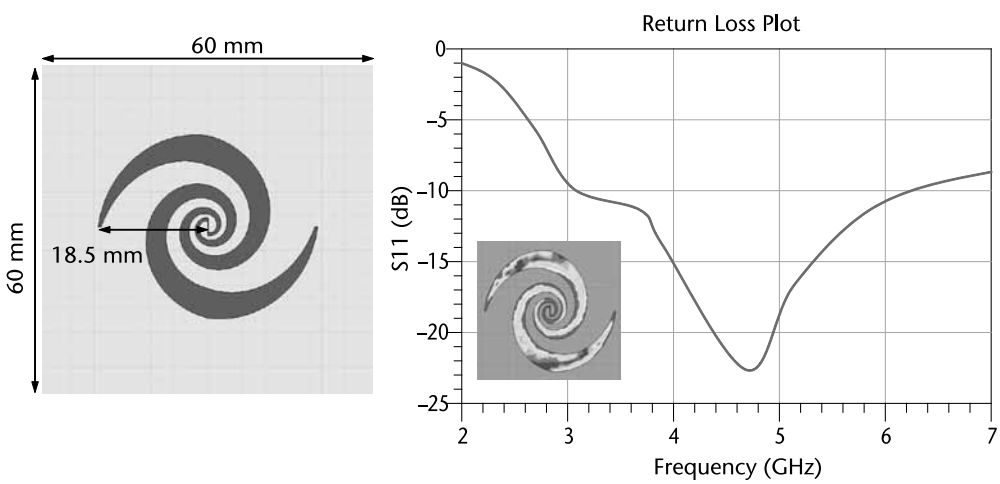

Figure 11.44 Two-arm logarithmic spiral antenna with self-complementary pattern and antenna return loss plot.

that microstrip designs have. Like all other microstrip antennas, the Vivaldi antenna design consists of two parts: the radiator (the part of the antenna body shape responsible for generating radiation by the currents flowing through it), and the matching element (the part of antenna that makes impedance transition from the radiator to the system impedance for which the antenna is designed as shown in Figure 11.45). The radiator part also acts as matching between the transmission line and the free space. The radiator part of antenna is made of copper layers or any other conducting material. The radiator shape is limited by the surrounding curves. One curve, called the inner or radiation curve, looks inside towards the body of the substrate, and the second one is placed close to the side edge of the substrate and can be called the outer or directivity curve. The radiator plates are followed with the transmission line, which provides impedance matching between radiator plates and the system. Radiation curves are the main contributors of antenna radiation; they act as a load in an antenna circuit and provide radiation resistance R_R. Directivity curves are responsible for radiation beam formation, controlling the main beam width and its direction.

The antenna current distribution at the edges of the conductor plate is much higher than the current in the middle; thus, the curves through the edges take most of the responsibilities for the radiation. The shapes of inner curves are crucial for antenna performance, because they are the main contributors of the radiation. The current strength through the inner curve is the highest.

11.7.5.1 Antipodal Vivaldi Antenna for the GB-SAR System

Subsurface radar including GPR is used to observe and detect anomalies beyond the surface. One of the applications is the through-the-wall radar, where the key objective is the detection of moving targets behind the wall. The monitoring of moving targets as well as static objects behind the wall can be done by ground-based SAR (GBSAR). These radars find applications to inspect the structure of building walls. Damages on building walls are sometimes obvious from the outside; however, in

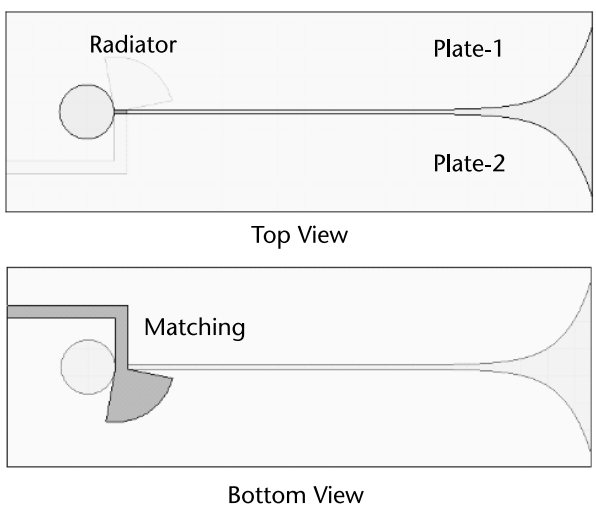

Figure 11.45 Vivaldi antenna design (top and bottom views).

many cases, damages are hidden inside the structures of the walls, and they cannot be found from the outside.

One of the main features of the GB-SAR system is radar polarimetry. To have a higher resolution of the radar image, a very wide frequency range for improving the range resolution is used. However, even with higher resolution, it is not easy to observe very small details of the structures. Radar polarimetry is a technique that can overcome this specific problem. To achieve a wide-frequency range and full polarimetric radar data acquisition, two antenna types, antipodal Vivaldi and spiral antennas, are used. Both these antennas are for wide frequency range operation, but the Vivaldi antenna is for linear polarization, and the spiral antenna is for circular polarization.

A wideband antipodal Vivaldi antenna design to achieve UWB performance is shown in Figure 11.46. The total size of the antenna was 12.4 mm × 12.4 mm. Between different substrate materials, different thicknesses of the substrate, and different shapes of antenna flare, the widest usable bandwidth was achieved for the 3–18-GHz frequency range. The high dielectric material of 6.15 is used for the substrate (RO3006). The main purpose is to improve the usable gain in a frequency. For constructing antenna design, an elliptical flare is used.

11.8 Substrate-Integrated Waveguide Microstrip Patch Antenna for Radar Applications

In the early 2000s, SIW was invented, and it offers an approach of the highly efficient driving patch antenna and array for linear polarizations [35–38] and circular polarizations [39]. In high-frequency applications, microstrip devices are not very efficient because of losses; also, microstrip device manufacturing requires very tight tolerances. Waveguide devices are less lossy at high frequency and less lossy compared to microstrip; however, these are bulky, and their manufacturing process is difficult. Therefore, a new concept emerged: SIW, which is a transition between dielectric-filled waveguide (DFW) and microstrip. The DFW is converted to SIW with the help of vias for the side walls of the waveguide. Another potential use case of

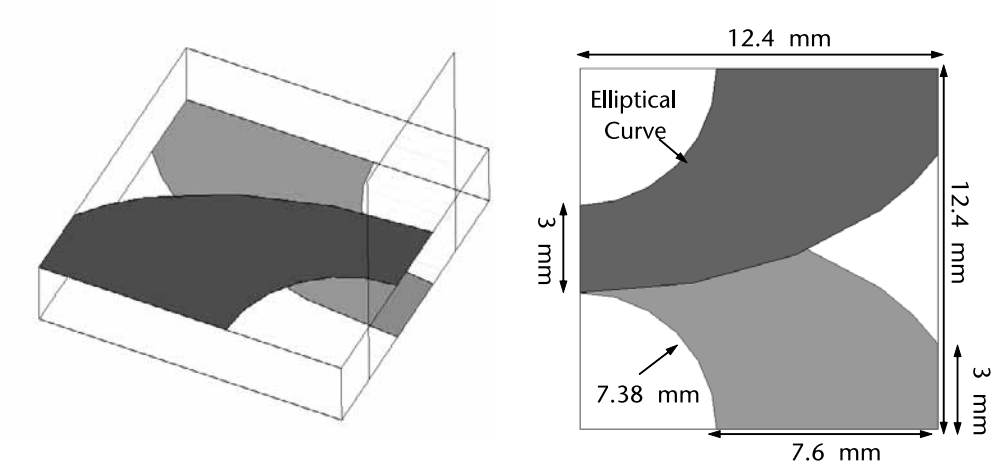

Figure 11.46 Design dimensions of the antipodal Vivaldi antenna for the GB-SAR system.

SIW-based antenna is the integration of microwave active devices with an antenna on the same board to reduce the overall physical volume and cost in the RF front-end subsystems. There has been growing interest in implementing SIW technology in active circuits and complete systems, including active integrated antennas.

SIW technology is basically a hybrid of microstrip and DFW technologies. Starting with a PCB substrate, the top and bottom metal layers provide two of the waveguide walls. Then two parallel rows of vias are placed, forming the side walls of the waveguide. Microstrip antennas designed with SIW technology have excellent performance because they suppress the propagation of surface waves, increase the bandwidth, and decrease both end-fire radiation and cross-polarization radiation. SIW-based microstrip cavity-backed antenna design is shown in Figure 11.47. The cavity-backed antenna has better performance because of the suppression of the propagation of the surface wave. This increases the bandwidth, decreases end-fire radiation, decreases cross-polarization radiation, and increases the applicable frequency range.

Table 11.3 shows the dimensions of the antenna. Arlon 25N material with a dielectric constant of 3.38 and a loss tangent of 0.025 is used as antenna substrate. To design and analyze an antenna, a full-wave FEM solver is used before fabrication. Antenna length and slot length control the resonance frequency. The physical length and width of the SIW square patch antenna is 6.6 mm, while the via-hole diameter is 1 mm and the inter-via distance is 2 mm. A patch with a 2-mm slot length resonates at 10.15 GHz as shown in Figure 11.48. Resonance frequency shifted at a lower frequency if there was an increase in antenna length and slot length.

The electric field for the TE10 mode on the SIW antenna at 10.1 GHz is shown in Figure 11.48. The simulation result shows that the magnitude of E-field is concentrated in the center of the SIW cavity. In this condition, the array of via-holes of the SIW is used as a boundary to prevent the EM fields from escaping from the SIW cavity.

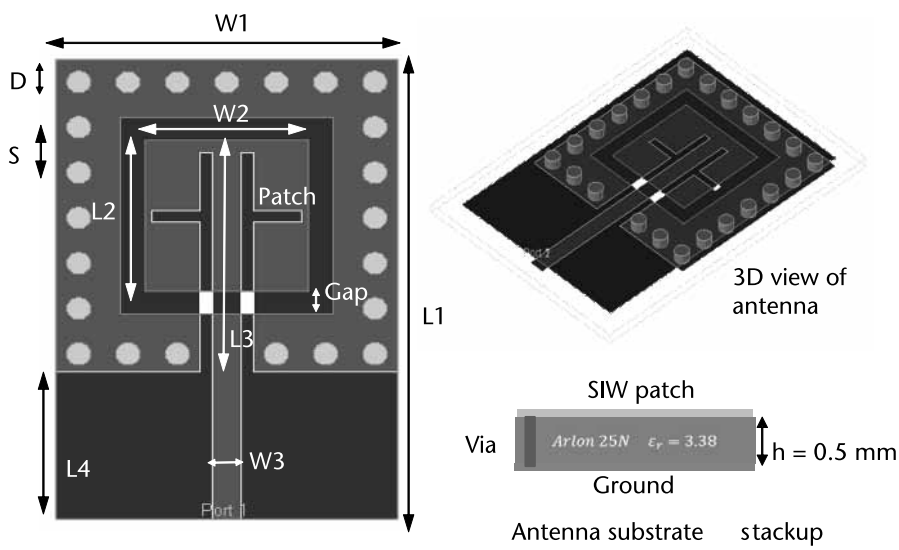

Figure 11.47 SIW patch antenna structure, substrate stack-up, and design dimensions.

Table 11.3 Antenna Dimensions

Symbol	*Value (mm)*	*Symbol*	*Value (mm)*
W1	14	W3	1.15
L1	21	L4	7
D	1.1	Slot L	2
S	2	Slot W	0.5
L3	9.6	W2	6.6
Gap	1	L2	6.6

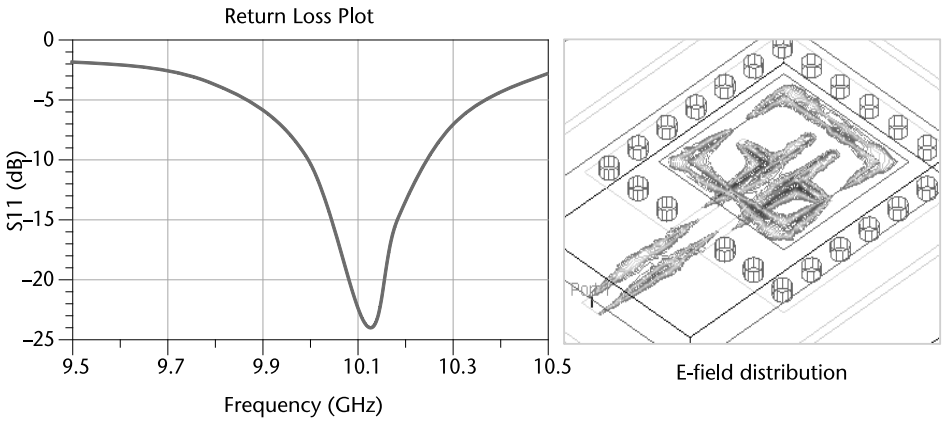

Figure 11.48 SIW patch antenna return loss plot and E-field for the TE10 mode.

Figure 11.49 shows the radiation pattern for the single-mode antenna at 10.15 GHz. The pattern represents the main lobe magnitude of 4.6 dBi at a 5.0° direction from the origin point. The $\varphi = 0°$ cut radiation pattern at 10.15 GHz of the fabricated and simulated design is shown is Figure 11.49. SIW structures show propagation characteristics like the ones of classical rectangular waveguides, including the field pattern and the dispersion characteristics.

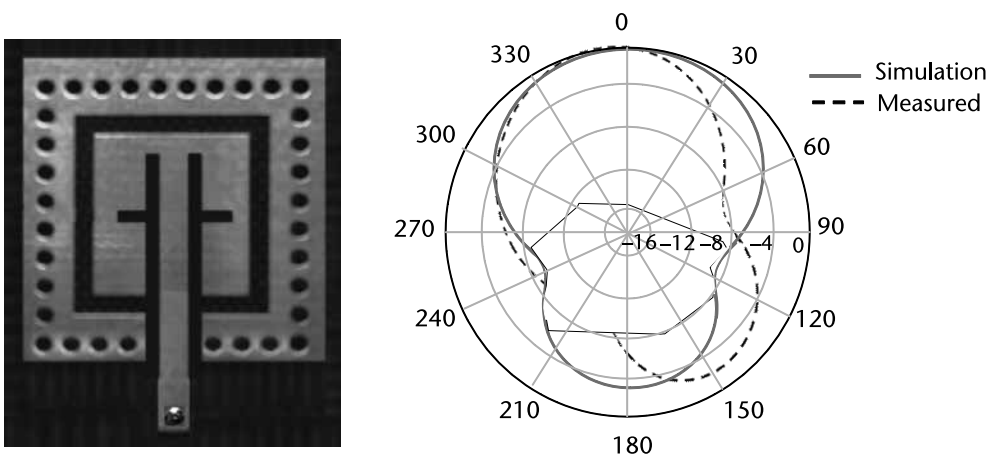

Figure 11.49 Fabricated SIW patch antenna and 3-D and $\varphi = 0°$ cut patterns at 10.15 GHz.

11.9 Summary

In this chapter, various broadband and UWB designs and applications were discussed. The design of broadband antennas based on EBG, PBG, FSS fractal, and many other latest technologies were presented with antenna performance results. Antenna geometries, materials, design solutions, and numerical tools adopted for the analysis and design have been explained. Several classes of broadband antennas have been identified. The EM performances, the dimensions, and the materials, as well as the design solutions useful to improve the antenna bandwidth of printed monopoles, metamaterials, and fractals, have been covered. The advent of the broadband system in the wireless communication area has demanded the design of antennas that must operate effectively over a wide range of frequencies. The widespread commercial deployment of UWB systems has sparked a new interest in UWB antennas.

References

[1] Kumar, G., and K. P. Ray, *Broadband Microstrip Antennas*, Norwood, MA: Artech House, 2002.

[2] Gardiol, F. E., and J. -F. Zurcher, *Broadband Patch Antennas*, Norwood, MA: Artech House, 1995.

[3] Wong, K. L., *Compact and Broadband Microstrip Antennas*, New York: Wiley, 2002.

[4] Pozar, D. M., and D. H. Schaubert, *Microstrip Antennas: The Analysis and Design of Microstrip Antennas and Arrays,* New York: IEEE Press, 1995.

[5] Bhartia, P., et al., *Microstrip Antenna Design Handbook*, Norwood, MA: Artech House, 2000.

[6] Veselago, V. G., "The Electrodynamics of Substances with Simultaneously Negative Values of ε and μ," *Soviet Physics Uspekh.*, Vol. 10, No. 4, January-February 1968, p. 509.

[7] Pendry, J. B., et al., "Low Frequency Plasmons in Thin Wire Structures," *J. Phys.: Condens. Matter*, Vol. 10, March 1998, p. 4785.

[8] Smith, D. R., and N. Kroll, "Negative Refractive Index in Left Handed Materials," *Physical Review Letters*, Vol. 85, No. 14, October 2000, pp. 2933–2936.

[9] Ziolkowski, R. W., "Design, Fabrication, and Testing of Double Negative Metamaterials," *IEEE Transactions on Antennas and Propagation*, Vol. 51, No. 7, July 2003, pp. 1516–1529.

[10] Radisic, V., Y. Qian, and T. Itoh, "Broadband Power Amplifier Using Dielectric Photonic Bandgap Structure," *IEEE Microwave Guided Wave Lett.*, Vol. 8, January 1998, pp. 13–14.

[11] Kesler, M. P., J. G. Maloney, and B. L. Shirley, "Antenna Design with the Use of Photonic Bandgap Materials as All Dielectric Planar Reflectors," *Microwave Opt. Tech. Lett.*, Vol. 11, No. 4, March 1996, pp. 169–174.

[12] Sievenpiper, D., et al., "High-Impedance Electromagnetic Surfaces with a Forbidden Frequency Band," *IEEE Transactions on Microwave Theory and Techniques*, Vol. 47, 1999, pp. 2059–2074.

[13] Sievenpiper, D. F., "High-Impedance Electromagnetic Surfaces," UCLA, Ph.D. dissertation, 1999.

[14] Toyota, Y., et al., "Stopband Analysis Using Dispersion Diagram for Two-Dimensional Electromagnetic Bandgap Structures in Printed Circuit Boards," *IEEE Microwave and Wireless Components Letters*, Vol. 16, No. 12, 2006, pp. 645–647.

[15] Yang, F., and Y. Rahmat-Samii, "Microstrip Antennas Integrated with Electromagnetic Band Gap (EBG) Structures: A Low Mutual Coupling Design for Array Applications," *IEEE Transactions on Antennas and Propagation*, Vol. 51, No. 10, October 2003.

[16] Yang, L., et al., "A Novel Compact Electromagnetic Band Gap (EBG) Structure and Its Application for Microwave Circuits," *IEEE Transactions on Microwave Theory and Techniques*, Vol. 53, No. 1, January 2005.

[17] Yang, F., and Y. Rahmat-Samii, "Reflection Phase Characterizations of the EBG Ground Plane for Low Profile Wire Antenna Applications," *IEEE Transactions on Antennas and Propagation*, Vol. 51, No. 10, October 2003, pp. 2691–2703.

[18] Hansen, R. C., and M. Burke, "Antennas with Magneto-Dielectrics," *Microwave Opt. Tech. Lett.*, Vol. 26, No. 2, July 2000, pp. 75–78.

[19] Hood, A. Z., T. Karacolak, and E. Topsakal, "A Small Antipodal Vivaldi Antenna for Ultrawide-Band Applications," *IEEE Antennas and Wireless Propagation Lett.*, Vol. 7, 2008, pp. 656–660.

[20] Ying, L., and A. -X. Chen, "Design and Application of Vivaldi Antenna Array Antennas," *8th International Symposium Propagation and EM Theory 2008 (ISAPE2008)*, November 2008, pp. 267–270.

[21] Kiminami, K., A. Hirata, and T. Shiozawa, "Double-Sided Printed Bow-Tie Antenna for UWB Communications," *IEEE Antennas and Wireless Propagation Lett.*, Vol. 3, No. 1, 2004, pp. 152–153.

[22] Ito, Y., et al., "Unidirectional UWB Array Antenna Using Leaf-Shaped Bowtie Elements and Flat Reflector," *IEE Electron Lett.*, Vol. 44, No. 1, January 2008, pp. 9–11.

[23] Naghshvarian-Jahromi, M., "Novel Wideband Planar Fractal Monopole Antenna," *IEEE Transactions on Antennas and Propagation*, Vol. 56, No. 12, December 2008, pp. 3844–3849.

[24] Chen, S. Y., P. H. Wang, and P. Hsu, "Uniplanar Log-Periodic Slot Antenna Fed by a CPW for UWB Applications," *IEEE Antennas and Wireless Propagation Lett.*, Vol. 5, No. 1, December 2006, pp. 256–259.

[25] Pantoja, R., A. Sapienza, and F. M. Filho, "A Microwave Printed Planar Log-Periodic Dipole Array Antenna," *IEEE Transactions on Antennas and Propagation*, Vol. AP-35, October 1987, pp. 1176–1178.

[26] Calmon, A., G. Pacheco, and M. Terada, "A Novel Reconfigurable UWB Log-Periodic Antenna," *IEEE Antennas and Propagation Society International Symposium 2006*, July 2006, pp. 213–216.

[27] Sung, Y. J., "Bandwidth Enhancement of a Wide Slot Using Fractal-Shaped Sierpinski," *IEEE Transactions on Antennas and Propagation*, Vol. 59, No. 8, August 2011, pp. 3076–3079.

[28] Mandelbrot, B. B., *The Fractal Geometry of Nature*, New York, W. H. Freeman, 1983.

[29] Rumsey, V. H., *Frequency Independent Antennas*, New York: Academic Press, 1966.

[30] Sierpinski, W., "Sur une courbe dont tout point est un point de ramification," *C. R. Acad.*, Paris, Vol. 160, No. 302, 1915.

[31] Li, J., et al., "UHF Stacked Hilbert Antenna Array for Partial Discharge Detection," *IEEE Transactions on Antennas and Propagation*, Vol. 61, No. 11, November 2013, pp. 5798–5801.

[32] Hai-Feng, Y., et al., "Development of Multi-Band Ultra-High-Frequency Sensor for Partial Discharge Monitoring Based on the Meandering Technique," *IET Sci., Meas., Technol.*, Vol. 8, No. 5, September 2014, pp. 327–335.

[33] Li, T., et al., "Development Simulation and Experiment Study on UHF Partial Discharge Sensor in GIS," *IEEE Transactions on Dielectr. Electr. Insul.*, Vol. 19, No. 4, August 2012, pp. 1421–1430.

[34] Daniel, D. J., *Ground Penetrating Radar*, 2nd ed., IEE Radar Sonar, Navigation and Avionics Series, London, UK: Institution of Engineering and Technology, 2004.

[35] Wahab, W. M. A., S. Safavi-Naeini, and D. Busuioc, "Wide-Bandwidth 60-GHz Aperture-Coupled Microstrip Patch Antennas (MPAs) Fed by Substrate Integrated Waveguide (SIW)," *IEEE Antennas Wireless Propag. Lett.*, Vol. 10, 2011, pp. 1003–1005.

[36] Mikulasek, T., et al., "2 × 2 Microstrip Patch Antenna Array Fed by Substrate Integrated Waveguide for Radar Applications," *IEEE Antennas Wireless Propag. Lett.,* Vol. 12, 2013, pp. 1287–1290.

[37] Ghassemi, N., and K. Wu, "High-Efficient Patch Antenna Array for E-Band Gigabyte Point-to-Point Wireless Services," *IEEE Antennas Wireless Propag. Lett.*, Vol. 11, 2012, pp. 1261–1264.

[38] Li, Y., and K. M. Luk, "60-GHz Substrate Integrated Waveguide Fed Cavity Backed Aperture-Coupled Microstrip Patch Antenna Arrays," *IEEE Transactions on Antennas and Propagation*, Vol. 63, No. 3, March 2015.

[39] Li, Y., et al., "Axial Ratio Bandwidth Enhancement of 60-GHz Substrate Integrated Waveguide-Fed Circularly Polarized LTCC Antenna Array," *IEEE Transactions on Antennas and Propagation*, Vol. 60, No. 10, October 2012, pp. 4619–4626.

Selected Bibliography

Caloz, C., and T. Itoh, *Electromagnetic Metamaterials: Transmission Line Theory and Microwave Applications*, New York: Wiley-IEEE Press, 2005.

Cheype, C., et al., "An Electromagnetic Bandgap Resonator Antenna," *IEEE Transactions on Antennas and Propagation*, Vol. 50, No. 9, September 2002, pp. 1285–1290.

Chung, K. B., and S. W. Hong, "Wavelength Demultiplexers Based on the Superprism Phenomena in Photonic Crystals," *IEEE Transactions on Antennas and Propagation*, Vol. 81, August 2002, pp. 1549–1551.

El Hamdouni, A., et al., "A Novel Design of a CPW-Fed Printed Fractal Antenna for UWB Applications," *2015 Third International Workshop on RFID and Adaptive Wireless Sensor Networks (RAWSN)*, Agadir, 2015, pp. 38–41.

Engheta, N., and R. W. Ziolkowski, *Metamaterials Physics and Engineering Explorations*, New York: Wiley, 2006.

FCC 02-48, Revision of Part 15 of the Commission's Rules Regarding Ultra-Wideband Transmission Systems, First Report & Order, Washington DC, Adopted February 14, 2002, Released April 22, 2002.

Jang, Y. W., "Characteristics of a Large Bandwidth Rectangular Microstrip-Fed Inserted Triangular Patch in a Circular Slot Antenna," *Microwave Journal*, Vol. 45, No. 5, May 2002, pp. 288–298.

Kaneko, S., et al., "Detecting Characteristics of Various Type Antennas on Partial Discharge Electromagnetic Wave Radiating Through Insulating Spacer in Gas Insulated Switchgear," *IEEE Transactions on Dielectrics and Electrical Insulation*, Vol. 16, No. 5, October 2009, pp. 1462–1472.

Amiri, N., and K. Forooraghi, "Dual-Band and Dual-Polarized SIW-Fed Microstrip Patch Antenna," *IEEE Antenna and Wireless Propagation Letters*, Vol. 13, 2014, p. 1605.

Park, J. S., et al., "A Novel Resonant Microstrip RF Phase Shifter Using Defected Ground Structure," *30th European Microwave Conf.*, France, 2000, pp. 72–75.

Radisic, V., et al., "Novel 2-D Photonic Bandgap Structure for Microstrip Lines," *IEEE Microw. and Guided Wave Lett.*, Vol. 8, No. 2, 1998, pp. 69–71.

Sabban, A., "New Fractal Compact Printed Antennas," *2017 IEEE International Symposium on Antennas and Propagation & USNC/URSI National Radio Science Meeting*, San Diego, CA, 2017, pp. 2197–2198.

Yang, L., et al., "A Novel Compact Electromagnetic Band Gap (EBG) Structure and Its Application for Microwave Circuits," *IEEE Transactions on Microwave Theory and Techniques*, Vol. 53, No. 1, January 2005.

CHAPTER 12

Modern Printed Antennas Design Trends and Applications

12.1 Introduction

The world is undergoing a major wireless revolution in terms of both mobile technology and wireless systems that are also leading new trends and technologies in antenna design world. The wireless communication industry is bringing new products with advanced features to support wireless services anytime and anywhere. The fast development of the communication technology such as wearable devices, cell phone technology, 5G, and personal area networks (PANs) for remote retrieval and monitoring of surrounding information has demanded that antennas should be able to operate with multiband characteristics in wireless communication devices. There is tremendous research interest in designing the compact size of antennas to offer more space to integrate other electronic components. All these needed attributes push the antenna researcher into challenges in designing new broadband, multifrequency, compact, low-cost, and reconfigurable antennas for the new generation of mobile communication devices, as well as for UWB communication systems. This chapter provides an idea of the latest antenna design trends for modern wireless communications.

In this chapter, printed antennas used in many wireless communication devices are discussed to facilitate the idea of current research and development trends towards different antenna applications. RFID antennas and its applications are covered in Section 12.2. Low-profile RFID tag and reader antenna design is presented to cover the operation bands of low-frequency and high-frequency bands. For navigation applications, antenna designs are presented in Section 12.3. Section 12.4 describes the features of the most recent antennas for medical applications. In addition, this chapter also describes wearable antennas. The wearable antennas find potential applications in healthcare, entertainment, identification systems, sport, smart home, and space.

12.2 RFID Antennas

RFID technology is one of the major methods for object identification purposes. It provides a unique identifier for objects and, just like a bar code or magnetic strip, the RFID device must be scanned to retrieve the identifying information [1–6]. RFID systems are also used in health monitoring with wearable devices [2]. It is also an important technology in the Internet of Things (IoT) that communicate with different sensors. The integration of RFID systems in production chains and process management is common. Antenna designs for RFID tags and readers are very specific and are a challenging topic. This section presents some advanced antenna design methods that can help RFID designers to reach good performance in many cases. Several realistic examples are considered with design and antenna performance data.

12.2.1 RFID System Working Principle

The principle of operation of a passive RFID system is illustrated in Figure 12.1. It typically contains three parts: a scanning antenna, also called the RFID reader, a transponder that is an RFID tag, and a transceiver with a decoder to interpret the data. The tag consists of an antenna and an application specific integrated circuit (ASIC) chip.

Both tag and reader exhibit complex impedances Z_a and Z_c, respectively. The RFID tag can operate in the interrogation zone of the reader. When it receives the modulated signal with sufficient power from the reader (downlink), the tag switches the chip impedance between two states Z_c^0 and Z_c^1. At these two impedance states, the RFID tag presents a specific complex RCS. The tag generates the information back by varying its input impedance and thus modulating the backscattered signal (uplink).

In most of the RFID systems, tags are attached to all items that need to be tracked. These tags are made from a small tag chip that is connected to an antenna. The tag chip contains a memory module that stores the electronic product code (EPC) and other variable information so that it can be read and tracked by RFID readers anywhere. An RFID reader system is a network-connected device (fixed or mobile) with an antenna that sends power as well as data and commands to the tags.

Fundamentally, RFID devices are categorized as either active or passive. Active RFID uses tags that need a power source for operation. They are either connected to a battery or some other power source. Having a battery embedded on the RFID system makes the product bulky, which is why active tags are impractical for retail trade. As compared to the active ones, passive tags do not require a power source or battery for operation. They absorb the EM energy propagated from a reader's

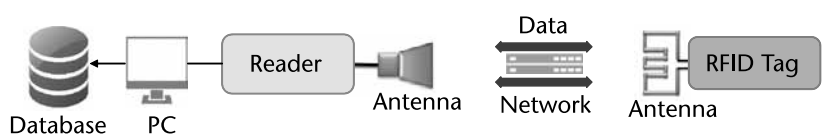

Figure 12.1 Block diagram of a typical RFID system.

RF field to supply all the needed power to operate. Passive tags are commonly used because these are cost-effective and small enough to fit into a practical adhesive label.

12.2.2 RFID Frequency Band Allocation

There are many different RFID frequency bands or RFID frequencies that are used around the globe listed in Table 12.1.

12.2.3 RFID Antennas

For any RFID antenna, there are two operating regions: near field and far field depending on the communication distance between the reader and the tags. Normally, if an antenna has a small loop-shaped antenna in the middle, it usually has near-field capabilities. Many RFID antennas use a near-field coupling mechanism (i.e., inductive coupling). When RFID antennas work based on near-field effects, the reader and the tag are relatively closely coupled to each other, which affects the bandwidth and performance of the antenna. In the RFID design, coupling must be considered when designing the antennas. For the RFID antenna design, parameters such as bandwidth, the radiation resistance, efficiency, and Q all need to be considered to

Table 12.1 RFID Frequency Band/Spectrum Allocation

Frequency Band	*Description*	*Typical Range*	*Typical RFID Application*
125–134.2 kHz and 140–148.5 kHz	Low frequency	Up to 0.5m	These frequencies can be used globally without a license; often used for vehicle identification
6.765–6.795 MHz	Medium frequency	Up to 0.8m	Inductive coupling is used
13.535–13.567 MHz	High frequency also called 13.56 MHz	Up to 1m	These RFID frequencies are typically used for electronic ticketing, contactless payment, access control, garment tracking, and so forth
26.957–27.283 MHz	High frequency	Up to 1m	Inductive coupling only, and used for special applications
433 MHz	Ultrahigh frequency (UHF)		These RFID frequencies are used with backscatter coupling for applications such as remote-control car keys
858–930 MHz	UHF	1 to 20 meters	These RFID frequencies cannot be accessed globally, and these are significantly restricted on their use; when they are used, they are often used for asset management, container tracking, and baggage tracking and often in conjunction with Wi-Fi system
2.400–2.483 GHz	SHF		Backscatter coupling (only available in the United States and Canada)
2.446–2.454 GHz	SHF	3m upwards	These RFID frequencies are used for long-range tracking and with active tags, RFID, and automatic vehicle identification (AVI)
5.725–5.875 GHz	SHF		Backscatter coupling, not widely used for RFID

meet the system requirements. RFID antennas are designed to resonate only to a narrow frequency band that is centered on the designated RFID system frequency.

12.2.4 RFID Tag Antenna Design

The role of the tag antenna and its impact on the RFID system performance is very critical. A passive tag is activated shortly by the RF scan of the reader. The generated small electrical current is just enough for transmission of an ID number. Passive RFID tags use an induced antenna coil voltage for operation. The tag antenna not only transmits the radio wave carrying the information stored in the tag, but it also needs to catch the EM wave from the reader to generate energy for the tag operation. Tag antennas gather energy and channel it to the chip to turn it on. Usually, the larger the tag antenna's area, the more energy it will be able to collect and channel toward the tag chip. Tag antennas can be made from a variety of materials; these can be printed, stamped with conductive ink, etched, or even vapor-deposited onto labels. A tag antenna should be compact, low-cost, and easy to fabricate for mass production. In most cases, the tag antenna should have hemispherical coverage or omnidirectional radiation. Usually, the impedance of the tag chip is not 50Ω, so the antenna impedance is realized for the conjugate match with the tag chip impedance to supply the maximum power to the tag chip.

Passive UHF RFID tag antennas are widely used for inventory tracking and sensing in various applications. The tag cost is an important factor in antenna design and it should be as low as possible. From tag cost point of view, chipless approach is an interesting option. Chipless RFID tags, also called Beacon Range Factor (BRF) barcodes, are an emerging area of RFID technology for ultralow-cost RFID applications. Cost and application also play an important role in material selection for tag antenna design.

The meandered dipole antenna is most used tag antenna type in RFID because of the size and tunability requirements. A thin flexible polyester substrate with a dielectric permittivity of 3.5 and a thickness of 2 mils (0.051 mm) is used for the tag antenna presented in this section. The top antenna trace is made of copper and had a thickness of 0.7 mil (0.018 mm). The antenna geometry and design parameters are shown in Figure 12.2 at 915 MHz (860–960 MHz UHF band). The typical tag antenna design specifications are listed in Table 12.2.

A traditional printed dipole antenna size is large, and it will exceed the maximum allowed dimension of the tag. Thus, a meander-formed dipole antenna is designed to decrease the antenna's size as much as possible with respect to the matching impedance. Meandering allows the antenna to be compact and to provide omnidirectional performance in the plane perpendicular to the axis of the meander. A loading bar with the same width as the meander trace is added to have

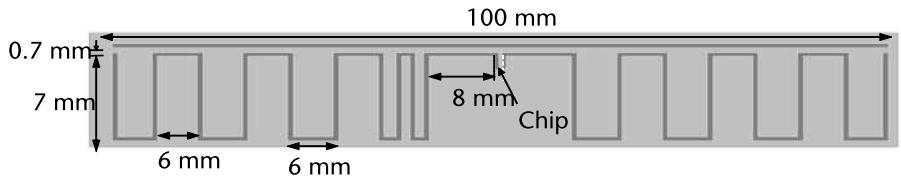

Figure 12.2 UHF RFID tag antenna design dimensions.

Table 12.2 Typical Specifications of RFID Tag Antenna

Parameters	*Typical Value*
Frequency	915 MHz
Maximum dimension	110 mm × 15 mm × 0.05 mm
Maximum area	16.5 cm^2
Gain	1.2 dBi
Range	10m

a better control over the antenna resistance. To provide a better match for the tag chip capacitive impedance, one meandered section is further meandered to obtain additional inductance.

The loaded meander antenna has several key variable parameters: loading bar width, length, spacing, meander step width, and meander step height. These parameters influence antenna gain and impedance, which determine tag resonance, peak range, and bandwidth. The maximum allowed antenna length is decided by the size requirements. The read range is calculated using the Friis free-space formula:

$$R = \frac{\lambda}{4\pi}\sqrt{\frac{P_t G_t G_r \tau}{P_{th}}} \tag{12.1}$$

where λ is the wavelength, P_t is the power transmitted by the reader, G_t is the gain of the transmitting antenna, G_r is the gain of the receiving tag antenna, P_{th} is the minimum threshold power necessary to provide enough power to the RFID tag chip, and τ is the power transmission coefficient given by

$$\tau = \frac{4R_c R_a}{\left|Z_c + Z_a\right|^2}, 0 \le \tau \le 1 \tag{12.2}$$

where $Z_c = R_c + jX_c$ is the chip impedance and $Z_a = R_a + jX_a$ is the antenna impedance.

Thin planar tag antenna is optimized using the MoM-based EM solver. The tag range is computed from (12.1) using simulated values of antenna gain and impedance and known values of chip impedance at the threshold power. A figure of merit (FoM) of RFID tag is calculated, with $P_{\min}$ as the minimum power necessary to activate the chip and the area defined as the substrate area of the entire design:

$$FoM = -P_{min}(dBm)10.\log_{10}\left(\frac{Area(cm^2)}{20}\right) \tag{12.3}$$

The simulated result of the antenna for different dipole lengths is shown in Figure 12.3. This antenna can be easily tuned by trimming. Loading bar length and lengths of the meander trace can be varied to obtain optimum reactance and resistance matching. The trimming is obtained by punching holes through the antenna

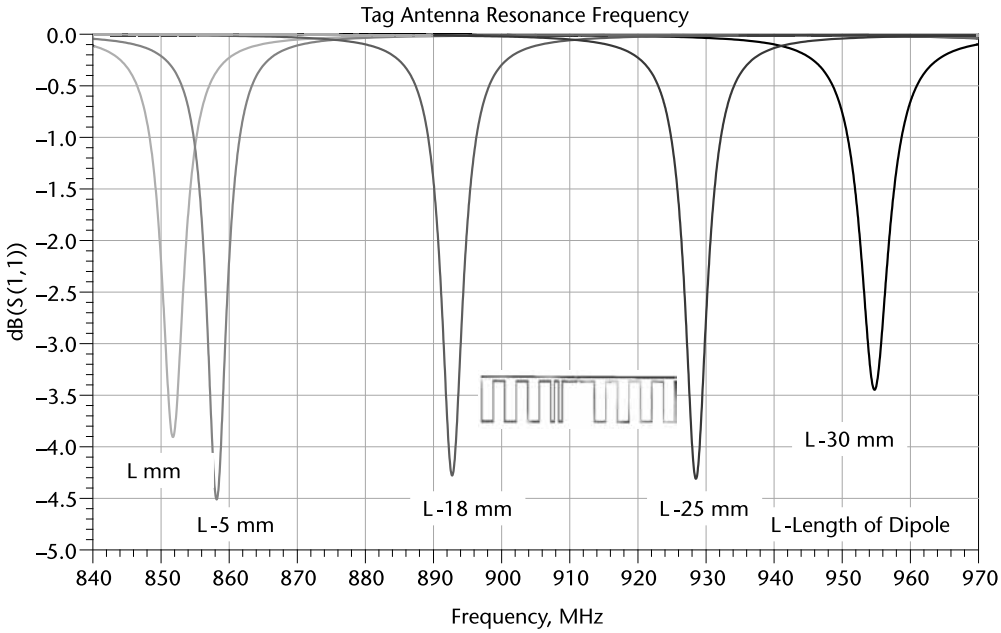

Figure 12.3 Simulated result of a tag antenna for different dipole lengths.

trace at defined locations. Such a tunable design is desirable where it is often needed to provide a solution for an application with a minimum lead time. The antenna resonance frequency shifts at a higher value with a reduced dipole length.

12.2.5 Fat-Tag or Dog-Bone RFID Antenna

Fat-tag RFID dipoles, also known as broadband dipoles, are characterized by having the maximum amount of metal on the tag face. Increasing the amount of metal on the tag is achieved by the etching process or with silver ink printing. By increasing the wire thickness, inductance value is reduced, and the increased metal surface produces a large capacitance.

Since these tags have a lot of metal, they are often best used on high dielectric surfaces like wood, glass, and plastic. Figure 12.4 is showing one such RFID tag antenna designed in UHF (860–960 MHz) band. In this tag, the EPC C1G1 memory chip is used. EPC is used for RFID in today's global, information-hungry trading networks. Gen2 or EPC global Class1 Generation2 defines the physical and logical requirements for a passive-backscatter, RFID system operating in the 860–960-MHz frequency range. EPC C1 Gen2 represents a major step in performance, standardization, and quality. This tag is modeled and simulated using the FEM EM solver. The antenna radiation plot is shown in Figure 12.5.

12.2.6 RFID Printed Tag Antenna on Hydrophobic Paper

Paper-based electronics find application in RFID tag antenna design. Paper is considered one of the best organic substrate candidates for UHF and microwave applications. Inkjet-printing using conductive silver ink is used to print electronics on the

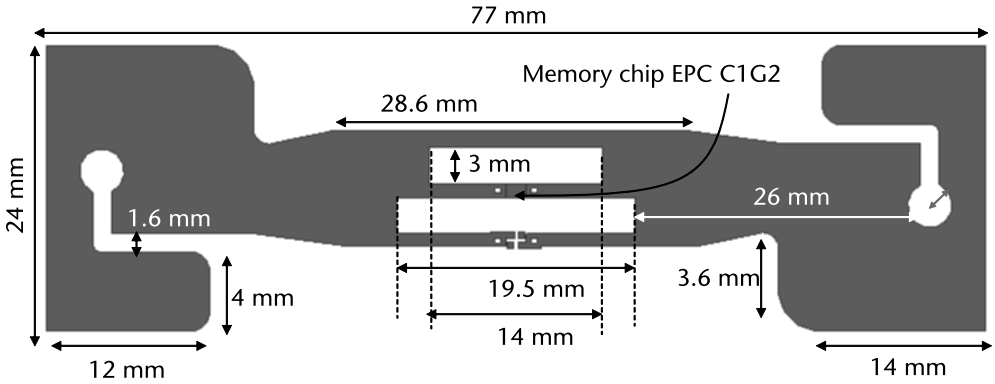

Figure 12.4 Fat-tag RFID antenna design in the UHF band.

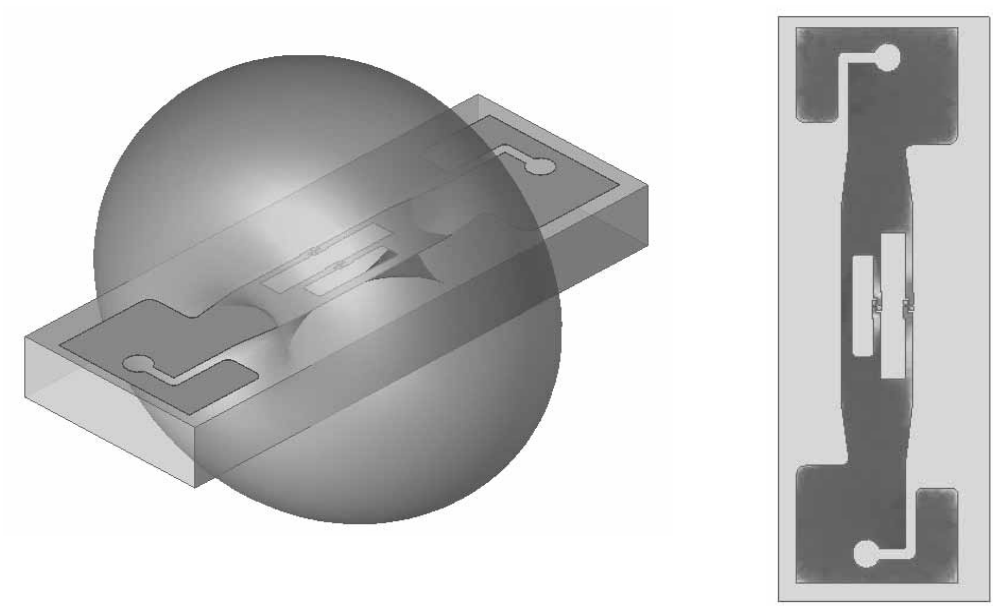

Figure 12.5 Fat-tag RFID antenna radiation pattern and E-field plot.

surface of a paper substrate. In addition, paper can be made hydrophobic by adding certain textiles; thus, mass-fabricating RFID inlays on paper becomes more feasible.

12.2.7 Reader Antenna

The reader antenna produces RF energy to activate the RFID tag, which modulates the information and reflects the remaining energy back to the reader antenna; this is called backscatter coupling. These antennas convert electrical current into EM waves that are then radiated into space where they can be received by a tag antenna and converted back to electrical current. In a near-field RFID system, the performance of the RFID system depends on the type of the reader antenna employed, which is viewed as a near-field reader antenna. Designing a reliable near-field reader

antenna is an engineering challenge. In the UHF RFID near-field systems, two coupling mechanisms are employed between tags and reader antennas and capacitive and magnetic coupling. In most of the near-field RFID applications, the interaction between the reader and tag antennas is based on magnetic coupling, in which the magnetic field stores most of the reactive energy. Usually, electrically small loops can produce a strong magnetic field over the near-field region [7, 8]. These magnetic coupling-based antennas can detect large numbers of loop-like tags, but their short reading distance limits the scope of their applications.

The second mechanism is capacitive coupling, in which most of the energy of reader antenna is stored in the electric field. The electric coupling reader antennas can be assessed using the leaking wave of a microstrip transmission line. The reader antenna can be a signal turn or a multiple turn as shown in Figure 12.6. The RFID near-field reader antennas can be designed based on loop structure. An EM E-field plot on a loop-based RFID reader antenna at 12.5 MHz is shown in Figure 12.7.

12.2.7.1 Far-Field Reader Antenna Design

In some actual application scenarios, UHF near-field RFID reader antennas with given radiation patterns are desired. Far-field patterns are often used to achieve a

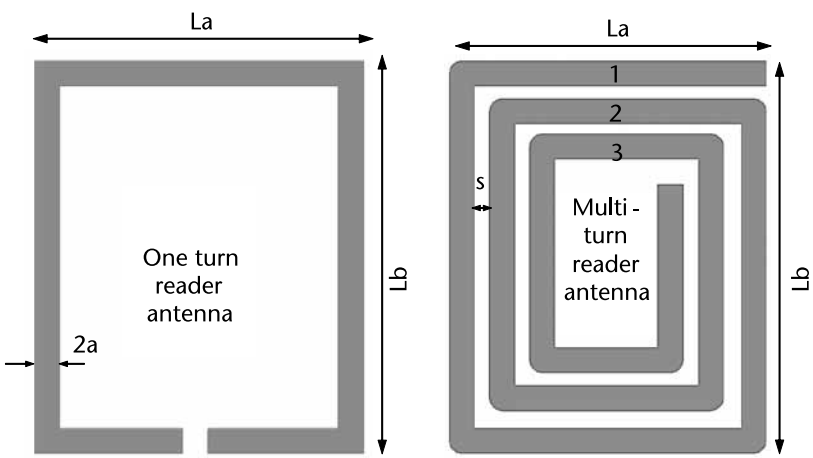

Figure 12.6 Signal-turn and multiple-turn RFID reader antennas.

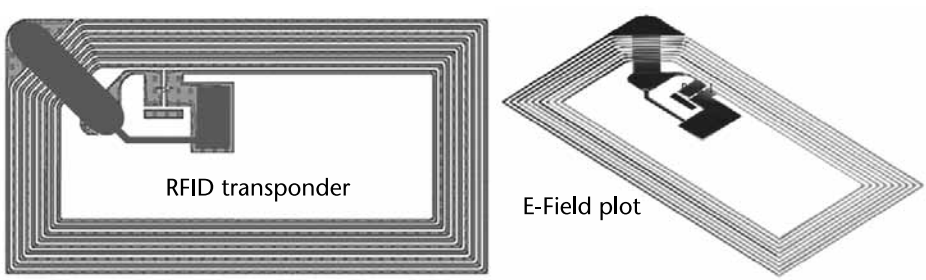

Figure 12.7 RFID reader antenna design at 13.5 MHz.

long-read range; for example, in a medication-monitoring management system, a reader antenna needs to detect near-field tags to realize medical product tracking while reading a far-field tag. Here, the far-field tag might serve as an environment monitor through offering the environment parameters (e.g., temperature) collected by sensors embedded in the far-field tag antenna or work as an identification of the operators.

A far-field-based reader antenna is designed for UHF RFID application at 915 MHz (902–928 MHz frequency range). The design parameters (all dimensions are in millimeters) of this planar antenna is shown in Figure 12.8.

The antenna consists of a microstrip-to-coplanar strip line, Marchand balun, a meandered driven dipole, a folded finite-size ground plane, and a closely coupled parasitic element. This antenna is appropriate for RFID handheld readers [9]. A microstrip-to-coplanar stripline (CPS) Marchand balun, which works as a matching network, is inserted between the feed line and the dipole element. The lengths of the parasitic element and driven dipole are optimized for simultaneously achieving excellent input impedance matching and high antenna front-to-back ratio. The dipole arms are meandered to reduce the antenna size. A tuning stub is added near the microstrip feed line, which is electrically connected to the top ground plane and provides a capacitive loading between the feed line and the ground plane. It further improves the antenna input impedance matching. The antenna is designed on a 1-mm-thick FR4 epoxy substrate with a dielectric constant of 4.4 and a loss

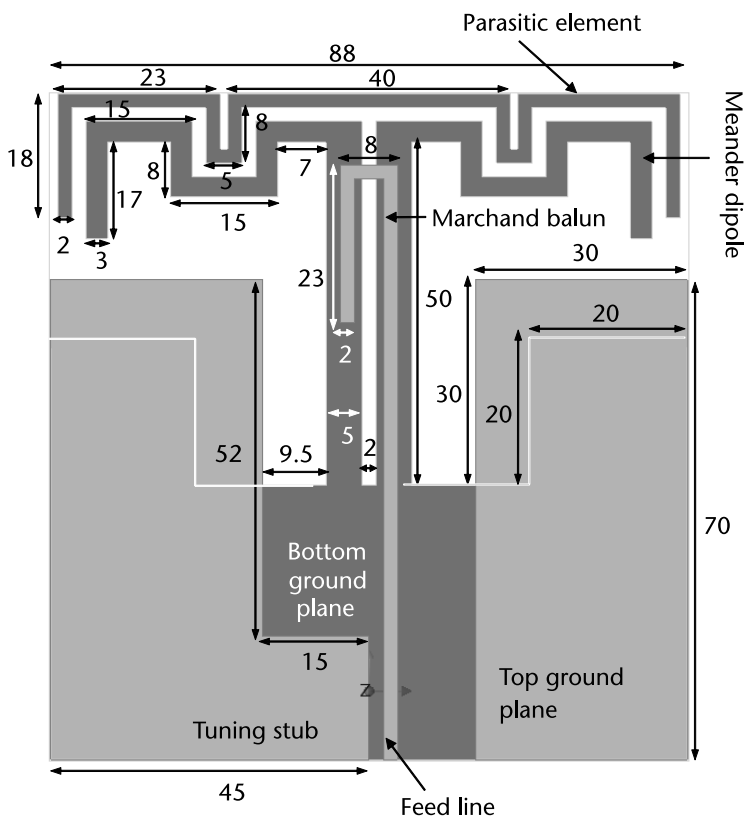

Figure 12.8 Far-field RFID reader antenna dimension (in millimeters) at 915 MHz [9].

tangent of 0.02. Normally, the conductors used in tags are copper, silver, or aluminum. The simulated antenna return loss, E-field plot, and radiation pattern are shown in Figure 12.9. The simulation was performed using the FEM.

The simulated center frequency is at 915 MHz. The slight frequency shift between the results can be mostly attributed to the fabrication tolerance, especially the electrical connection between the top and bottom ground planes. The simulated 10-dB return loss bandwidths are from 885 to 985 MHz. Antenna gain is 3.7 dBi at 915 MHz. Strong near-field coupling between the driven dipole and the parasitic element gives rise to the relatively high current densities along both elements and, in turn, helps further broaden the impedance bandwidth of the reader antenna. As the parasitic element is placed further apart from the driven dipole, the magnitude of the near-field coupling decays dramatically and has less influence on the impedance matching.

12.2.8 RFID Read Range Calculation

Operating range or RFID read range is one of the most significant criteria for evaluating the performance of RFID systems, especially UHF RFID systems. A longer operating range system finds more potential application opportunities and ensures a more reliable performance. The read range is the maximum distance at which the RFID reader can detect the backscattered signal from the tag. Because reader

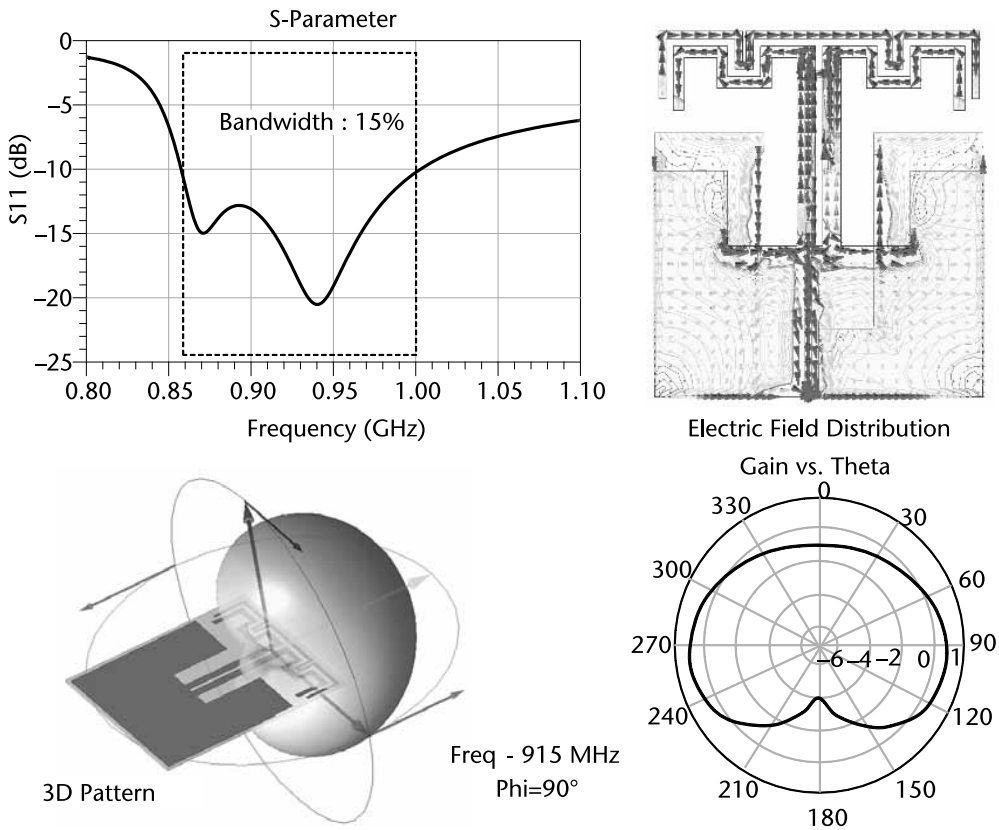

Figure 12.9 Reader antenna return loss, E-field, and radiation pattern plots at 915 MHz.

sensitivity is typically high as compared to tag, the read range is defined by the tag response threshold. Read range is also sensitive to the material on which the tag is placed, the tag orientation, and the propagation environment. The read range measurement is conducted in a controlled environment, such as anechoic chamber or transverse EM (TEM) cell.

In both methods, the tag position is fixed, and transmitter output power is varied by controlled attenuation. This setup allows one to carry accurate tag range characterization and avoid using large and prohibitively expensive chambers or cells. A compact TEM cell is a suitable tool for measuring small tags while a larger anechoic chamber can be used to measure tag performance on various objects. In the anechoic chamber, the tag is placed at a fixed distance from the reader antenna as illustrated in Figure 12.10. The operating range is determined by the whole RFID system design including RFID reader and tag antennas. Theoretically, read range can be calculated using the Friis equation (12.1). Experimental or simulation setup to calculate read range is shown in Figure 12.10. Complete simulation is carried out using FEM to find electric field strength at a different distance at the tag antenna when the reader is excited.

12.3 Radio Navigation Satellite System Antennas

Radio navigation satellite system antennas (RNSS) is a system that uses satellites to provide autonomous geospatial positioning. It permits small electronic receivers to determine their location (longitude, latitude, and altitude) to high precision (within a few meters) using time signals transmitted from satellites. A satellite navigation system with global coverage is called GNSS. At present, the United States' GPS, the European Union's Galileo, and Russia's GLONASS are global operational GNSSs. Navstar GPS of the United States is an operational, 31-satellite GNSS with

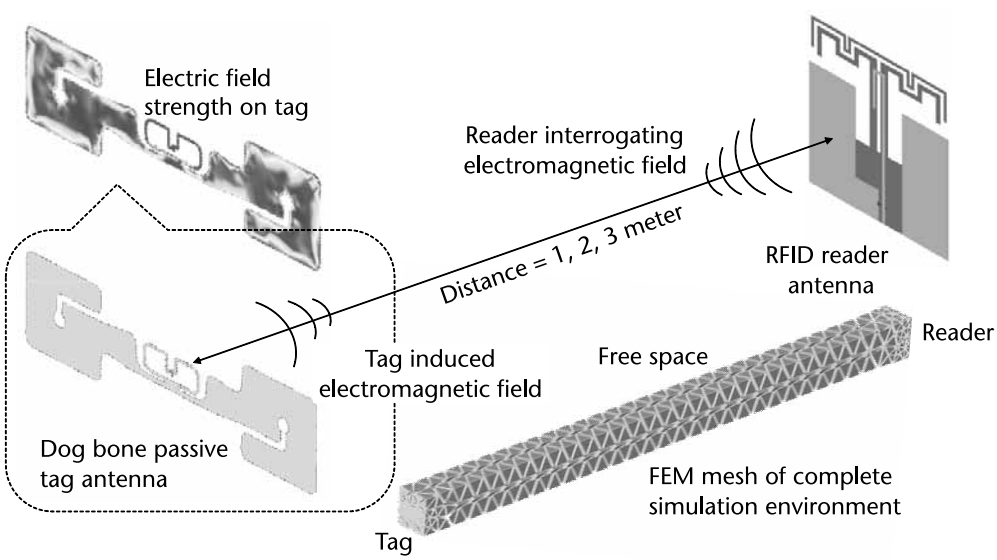

Figure 12.10 RFID read range simulation environment.

downlinks in the L1, L2, and L5 bands. The typical position accuracy available to a user is better than 30m. The Russian GLONASS has 24 satellites currently, and it provides a civilian radio navigation-satellite service. The Galileo system has been under planning by the European Commission since 2008. The Galileo system created by the European Union (EU) went live in 2016. Galileo is intended to provide horizontal and vertical position measurements within 1m precision and better positioning services at higher latitudes than other positioning systems. The Chinese COMPASS navigation system consists of a constellation of 30 nongeostationary satellites and five geostationary satellites. The integration between GNSS and other related technologies, such as telecommunications (GSM, GPRS, UMTS), the Geographic Information System (GIS), and the Inertial Navigation System (INS), has created numerous applications.

GNSS receivers include frequency bands such as GPS L5, Galileo E5/E6, and the GLONASS bands in addition to the legacy GPS bands, and the antenna feeding a receiver may need to cover some or all these bands as shown in Table 12.3.

12.3.1 RNSS Frequency Bands

Figure 12.11 shows the different frequency bands for modern RNSS [10]. The two primary Aeronautical Radio Navigation Service (ARNS) bands are allocated for safety applications, which includes the upper L-band (1,559–1,610 MHz) with GPS L1, Galileo E1, BeiDou B1, and GLONASS G1 and the lower L-band (1,164–1,214 MHz) with GLONASS G3, GPS L5, and Galileo E5. The remaining GPS L2, GLONASS G2, and Galileo E6 signals are in the bands allocated for radiolocation services and RNSS on a primary basis.

12.3.2 Antennas for RNSS

The antenna is a critical component of GNSS receiver system. The signals received from GNSS satellites are very weak and they can arrive from virtually any direction with signals from different satellites arriving simultaneously. GNSS antennas are typically GPS antennas as GPS has been the navigation system for years, but other

Table 12.3 GNSS Frequency Band Allocations

RNNS	*No. of Satellites*	*Frequency Band*	*Country*	*Band*
GPS	32	1.57542 GHz (L1 signal), 1.2276 GHz (L2 signal), 1.164 GHz (L5)	United States	L1, L2, L5
GLONASS	24	Around 1.602 GHz (SP), around 1.246 GHz (SP)	Russia	L1, L2, L3, L5
Galileo	30	1.164–1.215 GHz (E5a and E5b), 1.260–1.300 GHz (E6), 1.559–1.592 GHz (E2-L1-E11)	Europe	L1, L2
COMPASS (Beidou)	30	1.561098 GHz (L1), 1.589742 GHz (B1-2), 1.20714 GHz (B2), 1.26852 GHz (B3)	China	L1, L2, L5
NAVIC	8	1,176.45 MHz (L5 band) 2,492.028 MHz (S-band)	India	L5, S

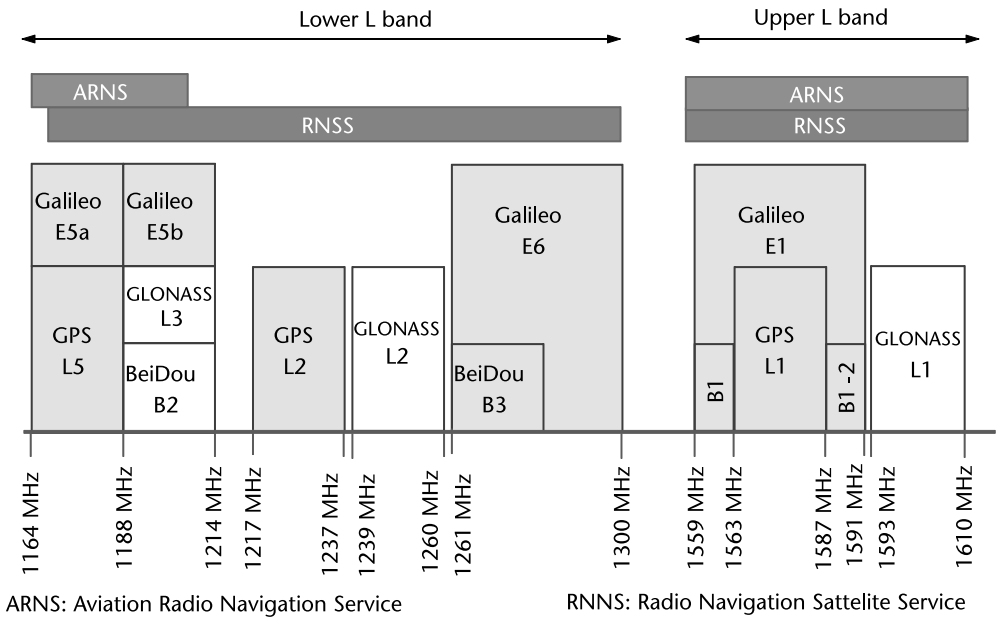

ARNS: Aviation Radio Navigation Service RNNS: Radio Navigation Sattelite Service

Figure 12.11 RNNS frequency bands.

systems have been and are being developed. Many important properties of GNSS antennas affect functionality and performance, including frequency coverage, gain pattern, circular polarization, and interference handling.

Spaceborne systems at L-band normally use circular polarization (CP) signals for transmitting and receiving. The changing relative orientation of the transmitting and receiving CP antennas as the satellites orbit the Earth does not cause polarization fading as it does with linearly polarized signals and antennas. Also, CP does not suffer from the effects of Faraday rotation caused by the ionosphere in the Earth's environment. Due to the Faraday rotation, an EM wave from space arrives at the Earth's surface with a different polarization angle than it would have if the ionosphere was absent. This results in signal fading and potentially poor reception of linearly polarized signals.

The antenna gain pattern optimizes gain and coverage for satellites over $0° < \theta < \theta_c$ as shown in Figure 12.12 and mitigates problems due to multipath from satellite platform, ionosphere, troposphere, and platform environment, as well as interferences. The ideal gain pattern and spatial coverage vary from application to application. Before 2010, conventional GPS generally called for $70° < \theta_c < 80°$ for terrestrial applications and $70° < \theta_c < 100°$ for airborne applications. After 2010, GNSS applications were expected to move toward a higher cutoff elevation angle, probably about $50° < \theta_c < 70°$ for terrestrial applications and $60° < \theta_c < 80°$ for airborne applications. A GNSS antenna with a higher cutoff angle θ_c above the horizon and good axial ration (or low cross-polarization) would have a higher antenna gain over noise temperature to detect the low line-of-sight CDMA signal desired.

GNSS receive antenna design challenges basically come from two major areas: the large bandwidth requirement and the constraints by the platform on which the antenna operates. Feed network and cost are other major challenges. Because the GNSS antenna needs to detect extremely low GNSS signals, about 25 dB below

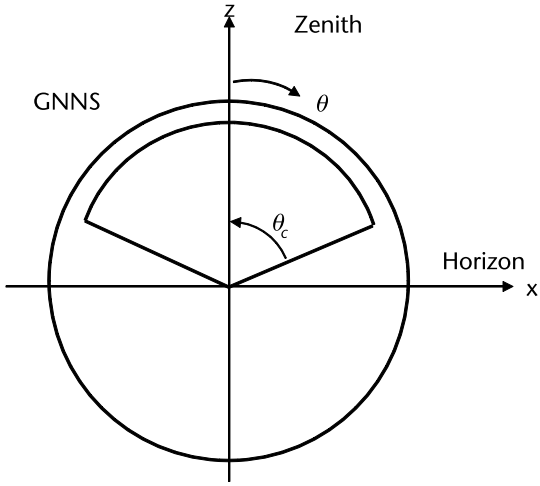

Figure 12.12 Ideal antenna gain patterns for GNSS antennas.

the noise level on Earth, the use of LNA close to antenna is highly desirable. The design cost of a GNSS antenna is a fundamental design consideration driven by the market. A testimony is the printed antennas, whose widespread use is due not only to its low profile but also for its low cost enabled by its simple feed.

GNSS satellites use right-hand circular polarization (RHCP), and therefore a GNSS antenna receiving the signals must also be designed for RHCP. The quality of the circular polarization is defined by specifying the axial ratio (AR). AR is the measure of the polarization ellipticity of an antenna designed to receive circularly polarized signals. An AR close to 1 (or 0 dB) is best (indicating a good CP). AR< 3 dB or cross-polarization (LHCP) of <10 dB is desired over $\theta < \theta_c$ for a medium-quality GNSS antenna. A minimum antenna gain $G_{\min}$ in RHCP is desired over the band. Generally, $G_{\min} > -10$ dBic in RHCP is needed to provide sufficient SNR for detection. However, this low gain requirement can be further relaxed by up to 10 dB or so by using various software and hardware techniques for applications with lower precision requirement.

12.3.3 GPS Spiral Antenna Design

Spiral antennas operate over a wide range of frequencies, and these belong to the class of frequency independent antennas. The main characteristics of spiral antennas are CP, broadband, and low directivity. The antenna impedance, polarization, and radiation pattern of such antennas remain unchanged over a large bandwidth. Spiral antennas are compact antennas because of their windings. A bandwidth of 5:1 or 10:1 comfortably can be obtained, and a stable input impedance is achieved through a self-complementary geometry. This wideband characteristic of the spiral antenna makes it an attractive choice for GNSS where a single antenna is required to transmit and receive over multiple channels.

Figure 12.13 shows a single-arm rectangular spiral antenna. It includes a conductive arm extending from the center outwards. This antenna radiates an axial beam with its outer rectangular periphery loop length being approximately one guide wavelength. The antenna is designed and simulated using the FEM for the L1

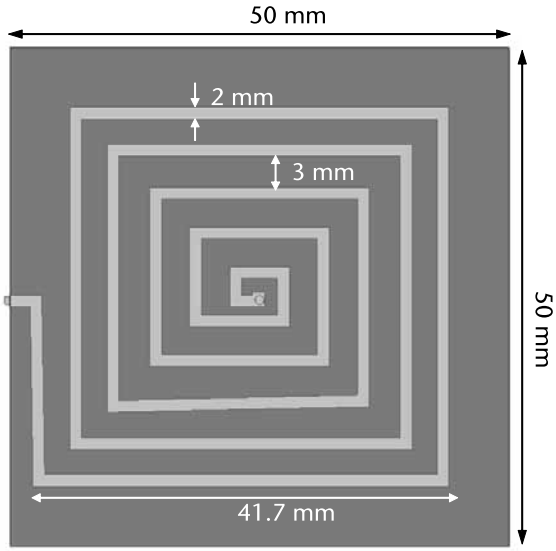

Figure 12.13 Rectangular spiral antenna for the GPS L1 band.

band of GPS. The length of spiral (L), width (W), spacing between turns, and width of stripline (w) parameters control the spiral geometry and its performance. The antenna is designed on a 1.1-mm-thick FR4 substrate with a dielectric constant of 4.24 and a loss tangent of 0.015. This is a bidirectional antenna and here substrate thickness plays a major role in controlling antenna behavior.

Important antenna performance parameters such as gain, radiation patterns, and impedance of the antenna are shown in Figure 12.14. The antenna has dual resonance frequency at 1.508 GHz and 1.576 GHz. The antenna gain is 1.2 dBi. This antenna is covering only the L1 band; hence, this has a very limited application for GPS.

For broadband GPS covering multiple bands, the Archimedean spiral antenna as shown in Figure 12.15 is used. The spectra of GPS, GLONASS, Beidou, and Galileo spread densely across 1.15–1.62 GHz, covering a frequency bandwidth of 446 MHz or an octave bandwidth of 1.383:1. For performance and redundancy, it

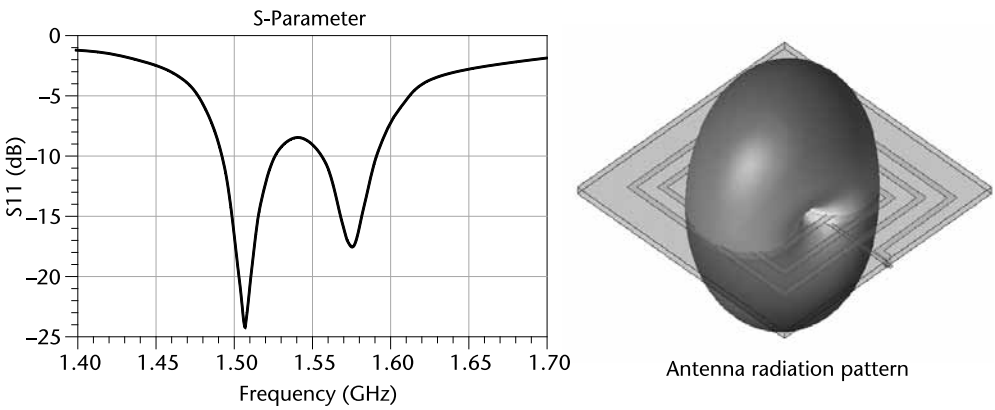

Figure 12.14 GPS L1 band rectangular spiral antenna performance results.

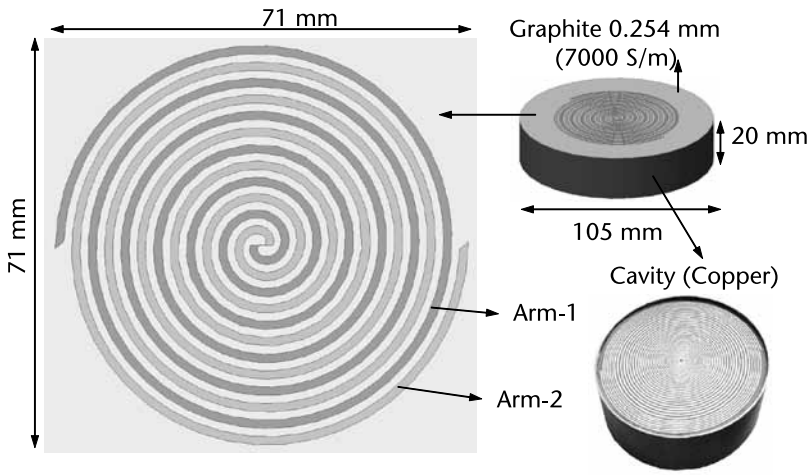

Figure 12.15 Two-arm Archimedean spiral antenna design.

is highly desirable for a GNSS receiver to cover more than one of these GNSSs. The Archimedean spiral antenna [11, 12] can be classified as a frequency-independent antenna in the sense that its input impedance and gain remain almost constant throughout the bandwidth. At low frequencies, the radiation zone is close to the outermost part of the spiral, while at high frequencies it is near the center. Therefore, the lowest cutoff frequency of the spiral antenna is associated with its outer radius and the highest cutoff frequency is related to its inner radius. This is the reason that spiral antenna bandwidth can be very large, only depending on size and printing accuracy. Figure 12.15 shows a two-arm Archimedean spiral antenna.

The arm of the Archimedean spiral is defined by the equation:

$$r = a\varphi \tag{12.4}$$

Equation (12.4) states that the radius r of the antenna increases linearly with the angle θ. The rate at which the spiral flares out is controlled by the parameter a. Arm 2 of the spiral is the same as arm 1 but rotated at 180°. Both arms are 1.4 mm wide. The direction of rotation of the spiral arms defines the direction of antenna polarization. Extra arms may be included to form a multiband spiral antenna. These antennas operate in three ways: traveling wave, leaky wave, and fast wave. The traveling wave, formed on spiral arms, allows for broadband performance. Fast wave is due to the mutual coupling phenomenon occurring between the arms of the spiral. The leaky wave leaks the energy during propagation through the spiral arms to produce radiation. Typically, the spiral is cavity-backed, and the conductive cavity changes the antenna pattern to a unidirectional pattern.

The spiral antenna shown in Figure 12.15 is excited in a balanced mode. In this mode excitation amplitudes are same but there is 180° phase difference between the two arms. This spiral antenna radiates a circularly polarized wave in the antenna-axis direction normal to the antenna plane over a wide frequency range. For exciting the antenna, a coaxial line is used with a wideband balun circuit, which transforms the unbalanced mode of the coaxial line into the balanced mode required for the spiral antenna. The simulated antenna result using the FDTD solver

is shown in Figure 12.16. The AR of this GNSS antenna is an important parameter in enhancing SNR and suppression of interference such as those due to multipath scattering and propagation. The result shows that its maximum AR is about 0.4 dB on boresight, slowly increasing to 3.8 dB at 70°, over 1,100–1,700 MHz.

12.3.4 Sine-Wave Meander Archimedean Spiral Antenna

The size of the Archimedean spiral antennas is determined by the lowest operating frequency, the depth of the cavity, and the length of the feed balun. Many techniques have been applied to overcome these size limitations by reducing the aperture and/or by decreasing the profile [13, 14]. An efficient way to miniaturize the antenna aperture is by meandering the spiral antenna arms, which extends the electrical length of arms and lowers the operating frequency [15]. A sinuous meander Archimedean spiral line is used to miniaturize the aperture and a controlled-width exponential spiral line that helps to minimize the input impedance [16]. Such antennas have been used for circularly polarized broadband communications and can be easily flush-mounted in many systems. They are characterized by radiation characteristics and stable input impedance over several octaves.

This section presents a sine-wave meander Archimedean spiral antenna (SMARSA) operating over a frequency range from 1.05 GHz to 1.95 GHz, as shown in Figure 2.17, where the ARSA lines are inserted with a sine wave. With the same amplitude, the sine curve is longer than both the rectangle curve and the sawtooth curve in the same period; additionally, the sine wave is continuous and derivable in the whole period. So it is better for a SMARSA to hold the fine radiation characteristics of a typical ARSA. For getting a unidirectional operation, the antenna is backed by an absorber-loaded cavity. This eliminates back-side radiation without decreasing the frequency band of operation, but at the cost of an efficiency reduction. The exponentially tapered microstrip balun is used as a wideband balun necessary for the balanced feeding of the antenna.

A SMARSA operating over a frequency range from 1.05 GHz to 1.9 GHz is shown in Figure 12.17. With the same amplitude sine curve is longer than both the rectangle curve and the sawtooth curve in the same period. This eliminates back-side radiation without decreasing the frequency band of operation, but at the cost of an efficiency reduction.

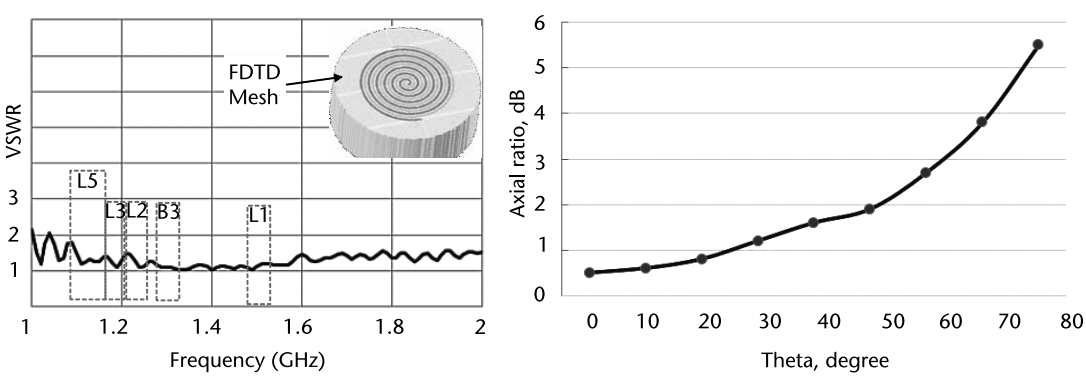

Figure 12.16 Archimedean spiral antenna VSWR and AR plot.

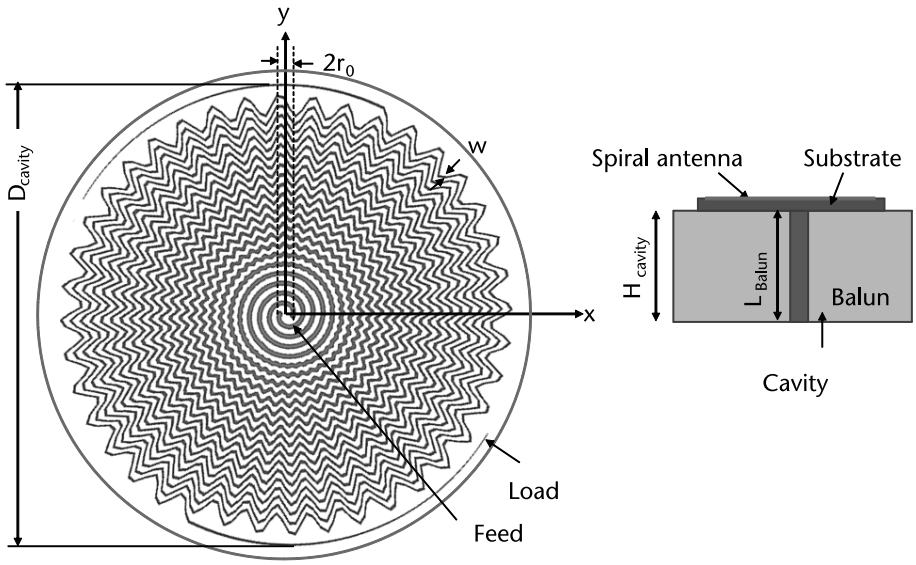

Figure 12.17 Configuration of SMARSA.

The spiral line is defined by the function

$$r = r_0 + a\varnothing + m.\left(\frac{\varnothing - \varnothing_{start}}{\varnothing_{end} - \varnothing_{start}}\right).\sin(n\varnothing) \tag{12.5}$$

where r_0 is the original radius of the spiral line, a is the spiral constant, and $\varnothing$ is the winding angle rising from the starting angle $\varnothing_{start}$ and the ending angle $\varnothing_{end}$. In addition, m and n are the amplitude and the angular frequency of the sine wave, respectively. The antenna is backed by an absorber-loaded cavity, whose depth H_{cavity} is equal to the length of the balun (L_{balun}) decided by the lowest frequency of the band. R is the radius of the final antenna and R_{inner} is the inner radius of the ring-shaped parasitic antenna. The cavity diameter D_{cavity} is 105 mm while antenna diameter is 95 mm. The cavity height H_{cavity} is 30 mm.

The antenna is printed on RT5880 with a dielectric constant of 2.2 (thickness of 1 mm). The simulated antenna return loss plot is shown in Figure 12.18. The RHCP antenna AR is from 0.22 dB (L5 band) to 4.9 dB (L1 band). The antenna gain also varies from 1.12 dB to 1.9 dB. This antenna covers all frequency bands of GNSS. A tapered microstrip is placed in the end of the antenna arm to weaken the terminal reflection.

12.4 Printed Antennas for Medical Applications

Biomedical engineering is involved for improving medical diagnosis and treatment. Insulin pumps, glucose monitoring, deep brain simulations, and endoscopy are a few examples of the medical applications that are based on a remote monitoring system and a body implantable unit. Body implantable devices are generally used in applications such as monitoring temperature and blood pressure, wirelessly transferring

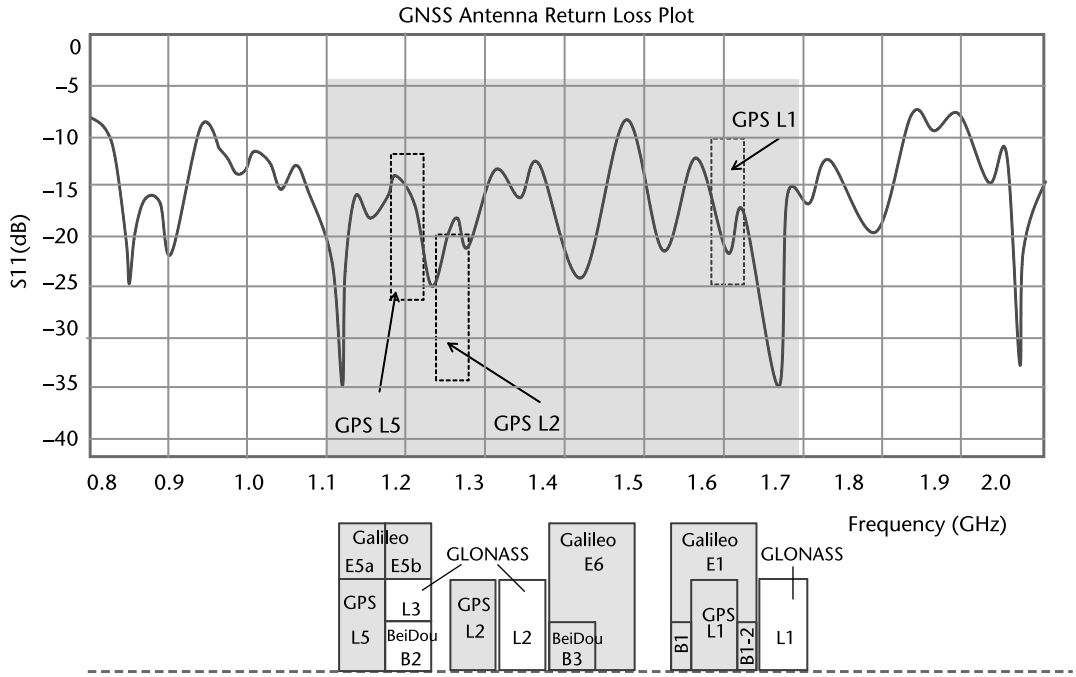

Figure 12.18 SMARSA return loss plot.

diagnostic data from an electronic device implanted in the human body for human safety, and care such as a pacemaker to an external RF receiver and tracking nonindependent people or lost pets. In medical therapy, local and/or whole-body hyperthermia provides successful modality in treatment of some malignant tumors. Microwave energy is one of the operative ways of inducing rapid hyperthermia, but there are certain issues like heating of a relatively large volume of tissue and deep laying tissues. In general, the required characteristics of a microwave radiator include an effective deposition of the energy in a defined tissue volume, minimum leakage of microwave energy into the outside of the treated area, proper impedance matching, lightweight system, and easy-to-handle design. The antenna plays a key role in such system designs to meet these requirements.

Because of different electrical properties of human tissue, designing an antenna for an implanted application is challenging. Implantable medical devices can communicate wirelessly with an external monitoring device. Biomedical telemetry is either in real time or stored physical signals are communicated to the receiver. As per the recommendation of FCC, the Medical Implant Communication Services (MICS) band of 402–406 MHz is suggested for implantable antennas. The MICS frequency band has replaced a previously used low-frequency inductive link, which suffers from short-range communication and slow data rate. The maximum transmit power requirement at this band is very low, about 25 μW. This minimizes the risk of interference with other users of the same band. The maximum bandwidth utilization at a time is 300 kHz, which makes it a low bit rate system compared with Bluetooth or Wi-Fi. Implanted devices are placed into human body and implantable antenna ensures wireless biotelemetry. These antennas can be implanted either into human bodies or can just be mounted over the torso (skin-fat-muscle)

to form a biocommunication system between medical devices and exterior instruments for short-range biotelemetry applications.

Printed and microstrip radiators offer the advantage of being small, lightweight, and capable of conforming to the shape of the human body, but the electrical performance of antenna is altered significantly in vicinity to the human body. These facts make the biomedical antenna design complicated. The electrical performance of a new class of wideband wearable printed antennas for medical applications is presented in this section. Low-profile, compact tunable antennas are important in the development of wearable human biomedical systems. The antenna resonant frequency can be tuned by using a varactor to compensate variations in antenna resonant frequency at different locations on the body. A conformal applicator employing a radiator consisting of a few printed dipoles was previously used for inducing hyperthermia at 2.45 GHz [17]. RF transmission properties of human tissues have been investigated in several articles [18, 19]. Several wearable antennas have been designed in the past decade [20–23].

12.4.1 Antenna Design for Wireless Body Area Network (WBAN)

WBAN is widely utilized in the fields of medical and motion monitoring, personal entertainment, modern wars, and virtual reality games [18]. Wearable antennas are crucial for WBAN applications [19]. These can be divided into three common modes: in-body mode [20–23], on-body mode, and off-body mode [22, 23]. In-body mode, the antenna is implanted into human body, which needs to consider the body tissue's influence on antenna performance. On-body mode shows that the wearable antenna can communicate with other wearable antennas located at other positions along the body surface, which demands maximum directivity along the body surface. Off-body mode represents that the antenna can communicate with a medical base station or other devices far away from the body, which requires maximum radiation in the broadside direction.

Figure 12.19 shows the design of a wearable antenna at ISM frequency band at 2.45 GHz for wireless vital signs monitors (VSMs). VSMs generally measure temperature, respiration, heart rate, and, more recently, blood oxygen saturation levels. To do this, the sensor device mainly incorporates an integrated antenna, a low-power digital processing technology and RF circuitry. A repeatable simulation phantom model (human body model) is required to overcome predictable variations in human test subjects and to comparatively analyze the performance of different VSM systems. An ideal phantom has a variable tissue model. In this design, a tissue phantom model as shown Figure 12.19 is used that is electromagnetically representative of the spread in tissue properties of the thorax region of a wider range of the human population [24].

The design of this antenna is discussed in Chapter 3 (Section 3.5) in detail. The antenna is printed on flexible substrate, which conforms to the surface of the human body. The EBG structure is used as shown in Figure 12.20 to increase the impedance bandwidth of the antenna to be relatively large, which will mitigate against resonant frequency shifts and detuning when mounted on variable tissue morphologies. Furthermore, to fully characterize the performance of the antenna, it is wrapped and placed on the chest. The return loss ($|S_{11}|$) and the radiation efficiency of the antennas are simulated on the physical tissue phantom.

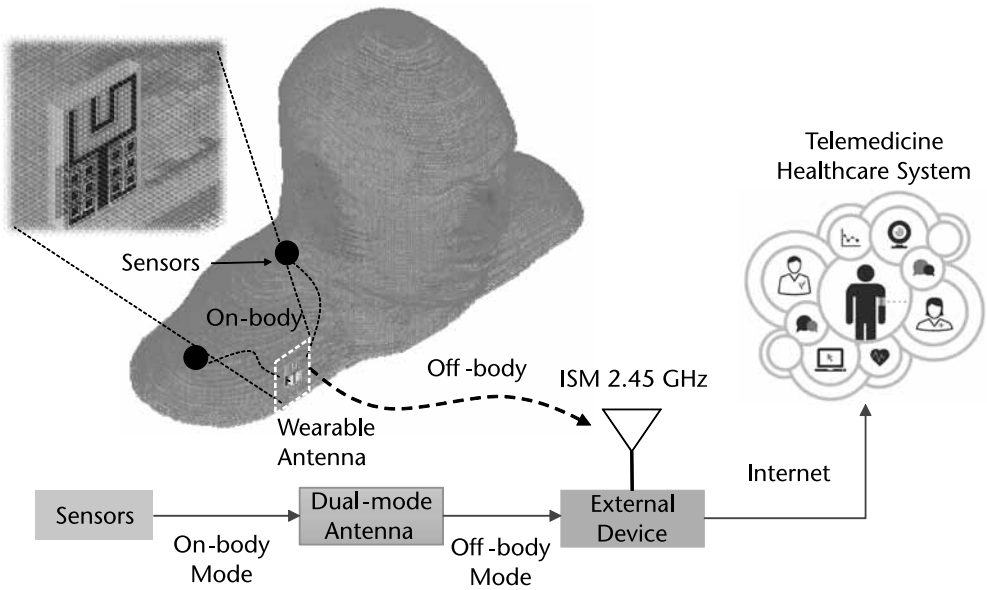

Figure 12.19 Dual-band wearable antenna design and on-body and off-body systems.

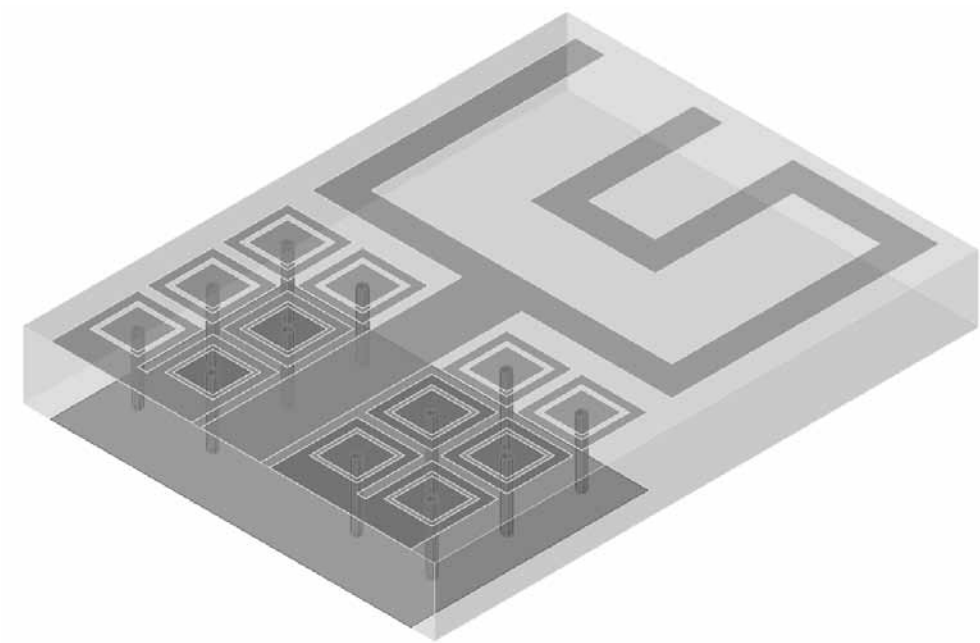

Figure 12.20 Dual-band wearable antenna with EBG structure.

The return loss plots for the antenna are shown in Figure 12.21. The total radiation efficiency of the antennas is measured on each side of the tissue phantom, composed of a thick side with a relatively larger tissue layer and a lean side with a thin tissue layer. The measured radiation efficiency is between 8% and 30%. The maximum total radiation efficiency is achieved on the phantom side with the thickest tissue layer. The minimum performance is achieved where the tissue layer

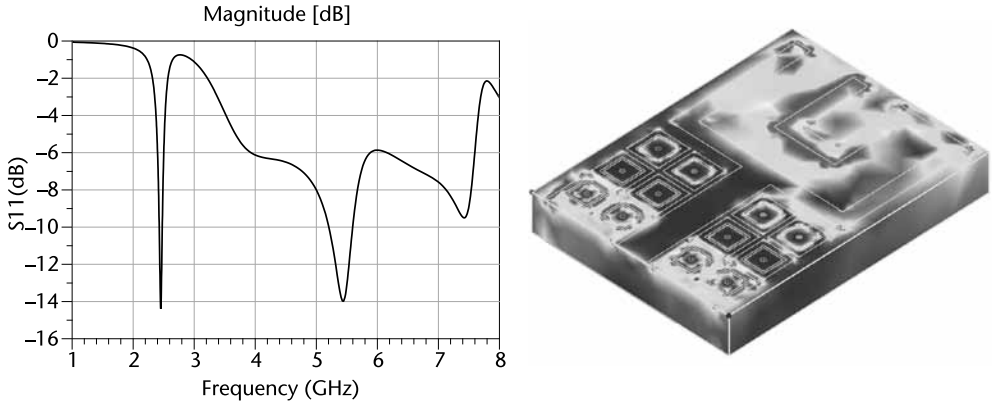

Figure 12.21 Dual-band wearable antenna return loss and E-field plots.

is thinnest, which means that the antenna is position closer to the inner phantom tissue layer, which has a relatively larger electrical conductivity.

12.5 IoT Antennas

IoT applications are extensively used for consumer and industrial markets for various purposes such as computations and sensing as well as connecting things within the region. IoT is a booming market; gradually, IoT modules are becoming compact and demand for incorporating more than one wireless technology is increasing. These requirements have increased the demand for IoT antennas compliant to IoT modules. IoT devices are commented using wireless communications links to other devices. Driven by the demands of the IoT, more antennas are required to be integrated into devices to make all wireless interconnectivity possible. IoT systems shall be able to incorporate many different and heterogeneous end systems for the digital services including everything from smart health, smart homes, smart retails, smart wearables, smart agriculture, smart factories, smart cities, and the smart grid. As fundamental units of machine-to-machine (M2M) communications which is the basis for IoT, the performance of microwave antennas directly affects the performance of IoT devices.

Antenna design challenges related to the IoT include providing reliable connectivity and maintaining a reasonable performance within an ever-smaller footprint. Many devices will need to operate in an increasingly crowded radio spectrum with the possibility of co-site conditions, operation near the human body, and other challenging installed environments. Antenna placement is crucial in these cases.

The choice of an antenna system for is a critical component of all these node-end smart devices. Designing an antenna with an effective performance in IoT devices requires engineers to examine several factors including antenna size, from what is needed to what is possible, antenna shape, and placement. Therefore, IoT module antenna designers face the restrictions of maintaining good antenna performance in ever-shrinking volumes and under extreme interference conditions. The major types of IoT antennas are chip, wire, whip, PCB, and proprietary, as shown in Figure 12.22.

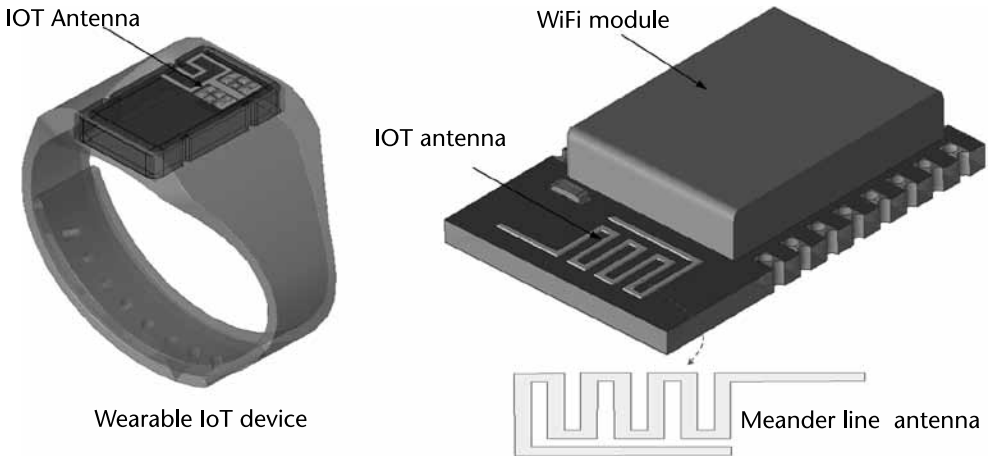

Figure 12.22 IoT device and integrated printed antennas.

12.5.1 Low-Power Wide Area Network (LPWAN) IoT Antenna Design

IoT systems are characterized by the transmission of small amounts of data and low transmission rate, which drastically reduce the bandwidth requirements. Usually, less than 1-MHz bandwidth is enough for most of the IoT applications. New wireless standards for LPWANs, such as LoRa or Sigfox, well match the low data rate needed by IoT applications. Compact antennas allow for easier integration within IoT devices, but miniaturization is strictly connected to the antenna radiation efficiency η_r through the lower bound limit on the antenna quality factor Q [25]

$$Q_{lb} = \eta_r \left(\frac{1}{ka} + \frac{1}{(ka)^3} \right) \tag{12.6}$$

where k is the wavenumber and a is the radius of the sphere enclosing the antenna.

Figure 12.23 is showing IoT antenna design covering 2.2–6-GHz frequency band. The printed antenna is designed using a flexible substrate of ULTRALAM 3850 by Rogers consisting of 100-μm-thick LCP substrate [26]. The substrate has a dielectric constant of 3.14 and a loss tangent of 0.0025. These materials satisfy robustness, flexibility, and thermal conditions in which the antenna can perform effectively under extreme bending.

The antenna design is initiated from a circular monopole radiator with the addition of a circular slot ground that surrounds the radiator. The rectangular slots present on the radiator and partially filled gaps in the ground slot help the generation of CP radiation for a certain frequency range. The antenna is fed with a 50Ω CPW transmission line. It has a compact size with a total area of 46 × 46 mm^2. The resulting reflection coefficient confirms that the antenna maintains less than –10 dB within bandwidth starting from 2.2–4.5 GHz and 5.1–5.9 GHz. At a lower frequency, the antenna has an omnidirectional pattern that tends to deform as the frequency increases, which is observed at 5.8 GHz.

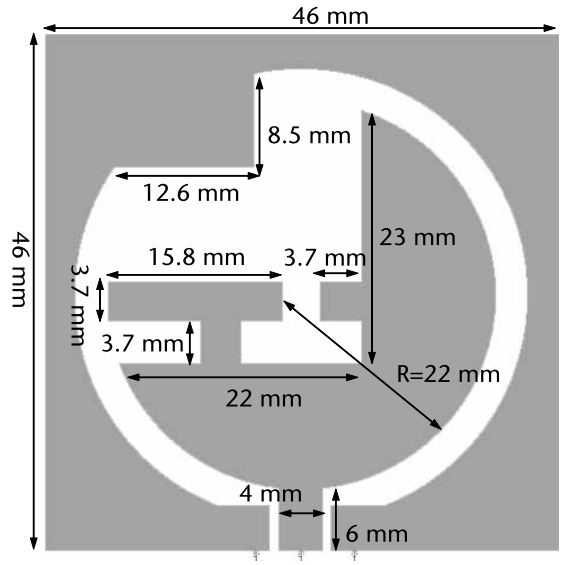

Figure 12.23 IoT antenna design dimensions.

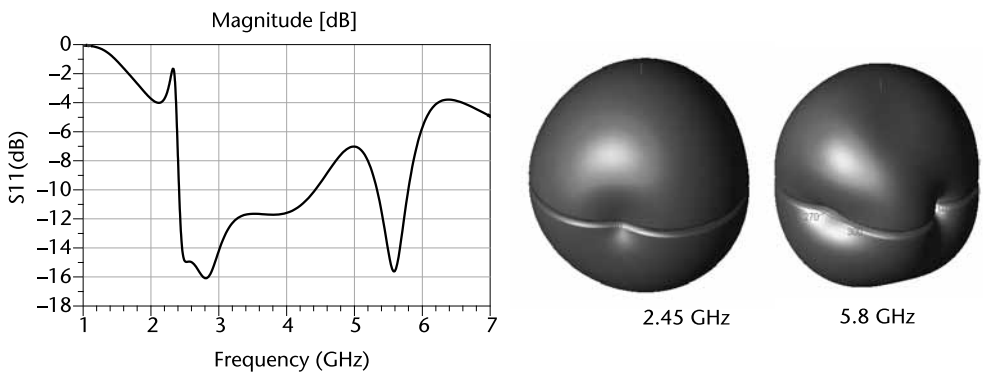

Figure 12.24 IoT antenna return loss and radiation pattern plots.

12.5.2 Quasi-Yagi IoT Antenna Design

Quasi-Yagi antennas are used for IoT device communications for their properties, such as compact size, easy fabrication process, light weight, and end-fire radiation pattern [26–31]. A traditional Yagi-Uda antenna has a dipole driver in the center, a single reflector on one side, one or more directors on the other side, and a feeding structure. The directivity of a microstrip Yagi antenna significantly depends on the number of directors. There is always a trade-off between the bandwidth and antenna gain. Bandwidth gets narrow as more elements are used to increase the gain. The design parameters of a quasi-Yagi antenna for X-band IoT applications are shown in Figure 12.25.

In a microstrip Yagi-Uda antenna, EM energy is coupled from the driven element dipole through space into the parasitic dipoles and then gets reradiated to form a directional beam. This process is analogous to the conventional Yagi antenna, but the slight difference is that the substrate also plays some role in coupling by

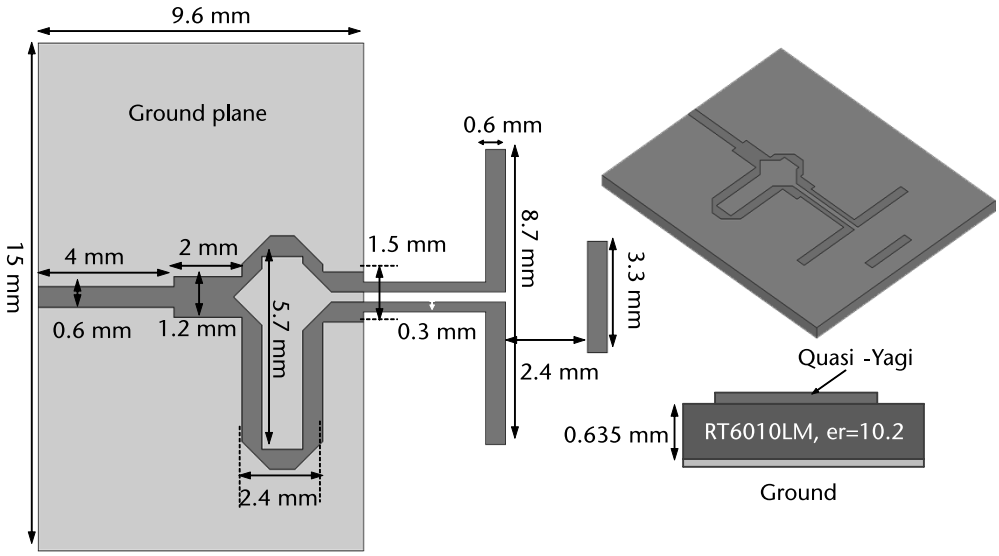

Figure 12.25 Quasi-Yagi antenna design parameters.

surface waves. The microstrip patch antenna normally couples very little energy as it radiates largely in broadside and slightly along the direction of the ground plane. The field radiated by the driven element is reflected by the long reflector element positioned at the reverse end-fire direction. The parasitic director elements help to improve further the radiation in the end-fire direction. The basic design parameters are the length of driven element (0.45λ–0.49λ), the length of directors (0.4λ–0.45λ), and the separation between directors (0.3λ–0.4λ). The separation between the directors and the length of the directors need not be uniform.

The antenna is fabricated on a 0.635-mm-thick RT6010LM substrate with metallization on both sides. The top metal layer consists of a microstrip feed, a broadband microstrip-to-coplanar stripline (CPS) balun, and two dipole elements, one of which is the driver element fed by the CPS and the other of which is the parasitic director. The bottom metal plane is a truncated microstrip ground, which serves as the reflector element for the antenna. The parasitic director element on the top plane simultaneously acts as an impedance-matching parasitic element and directs the antenna propagation toward the end-fire direction. One of the most effective features of this antenna is the use of the truncated ground plane as the reflector element.

In the quasi-Yagi antenna, the simplest method to enhancement the bandwidth is to increase the distance between the ground plane and radiator, but it will increase substrate thickness. The main limiting factor of bandwidth in the quasi-Yagi antenna is its feed. A broadband microstrip-to-CPS transition structures is used to enhance the impedance bandwidth of the quasi-Yagi antenna in [28], although the delay line used in the balun structures still restricts the antenna's bandwidth. UWB balun or coplanar waveguide feeding has been used in many designs to enhance the bandwidth [29, 30]. Approximately 40% bandwidth is achieved using this technique as shown in Figure 12.26.

The FEM-based simulation results of the antenna are shown in Figure 12.26. The simulated bandwidth (–10 dB) is 40%. The radiation patterns are measured

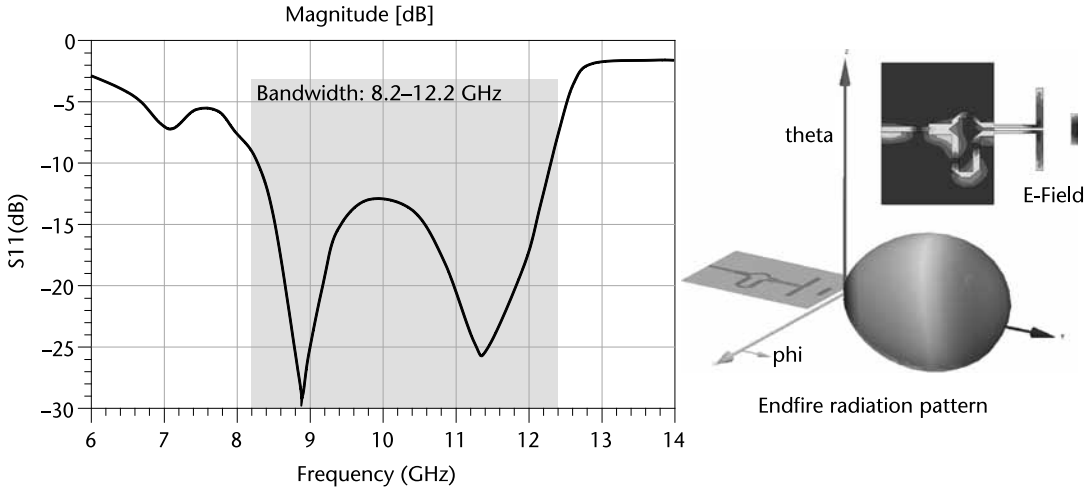

Figure 12.26 Quasi-Yagi antenna return loss, E-field, and radiation pattern plots.

across the bandwidth, the antenna gain is better than 5.6 dB, and the measured front-to-back ratio is better than 8.1 dB within the operating band. The front-to-back ratio is a critical parameter for a unidirectional antenna. The directivity of the one director Yagi antenna can be increased by adding extra metallic strips acting as directors, but it will reduce the bandwidth of antenna.

12.6 Summary

The fast development in the field of wireless communications demands that compact devices be capable of operating in more than one frequency band. The design of innovative compact and high-performance printed antennas with multiple communications protocols, for example, ISM band (2.4 GHz), the IEEE 802.11b/g, and the IEEE 802.11a, is a challenge for the designers. In this chapter, modern application-based printed antenna design was discussed covering antennas for RFID, GPS, IoT, and printed antennas for medical applications. Printed antenna design techniques were presented that make them suitable for modern communications applications. Printed antennas are also used as a part of the power supply block in sensor systems. Low-power sensor systems work by harvesting energy from the ambient in different environments. These systems are usually called rectennas. Printed antennas are good candidates for this purpose due to the availability of broadband design and ease of integration with the required electronics.

References

[1] Azzouzi, S., et al., "New Measurement Results for the Localization of UHF RFID Transponders Using an Angle of Arrival (AoA) Approach," *Proc. IEEE RFID*, April 2011, pp. 91–97.

[2] Amendola, S., L. Biachi, and G. Marrocco, "Movement Detection of Human Body Segments," *IEEE Antennas and Propagation Magazine*, Vol. 57, No. 3, June 2015, pp. 23–37.

[3] Finkenzeller, K., *RFID Handbook: Fundamentals and Applications in Contactless Smart Cards, Radio Frequency Identification and Near-Field Communication*. New York: Wiley, 2010.

[4] Perret, E., et al., "BRF and THz Identification Using a New Generation of Chipless RFID Tags," *Radio Engineering*, Vol. 20, Special Issue: Emerging Materials, Methods, and Technologies in Antenna & Propagation, No. 2, June 2011, pp. 380–386.

[5] Marrocco, G., L. Mattioni, and C. Calabrese, "Multiport Sensor RFIDs for Wireless Passive Sensing of Objects-Basic Theory and Early Results," *IEEE Transactions on Antennas and Propagation*, Vol. 56, No. 8, August 2008, pp. 2691–2702.

[6] Lee, B., and B. Yu, "Compact Structure of UHF Band RFID Tag Antenna Mounted on Metallic Objects," *Microw. Opt. Technol. Lett.*, Vol. 50, No. 1, January 2008, pp. 232–234.

[7] Qing, X. M., C. K. Goh, and Z. N. Chen, "A Broadband UHF Nearfield RFID Antenna," *IEEE Transactions on Antennas and Propagation*, Vol. 58, No. 12, December 2010, pp. 3829–3838.

[8] Shi, J., X. Qing, and Z. N. Chen, "Electrically Large Zero-Phase-Shift Line Grid-Array UHF Near-Field RFID Reader Antenna," *IEEE Transactions on Antennas and Propagation*, Vol. 62, No. 4, April 2014, pp. 2201–2208.

[9] Hua, R., and T. Ma, "A Printed Dipole Antenna for Ultra High Frequency (UHF) Radio Frequency Identification (RFID) Handheld Reader," IEEE Transactions on Antennas and Propagation, Vol. 55, No. 12, December 2007, pp. 3742–3745..

[10] Subirana, J. S., J. J. Zornoza, and M. Hernandez-Pajares, *GNSS Signal*, University of Catalunia, Spain, 2011, https://gssc.esa.int/navipedia/index.php/GNSS_signal.

[11] Kaiser, J., "The Archimedean Two-Wire Spiral Antenna," in *IRE Transactions on Antennas and Propagation,* Vol. 8, No. 3, May 1960, pp. 312–323.

[12] Wang, Y. -W., G. -M. Wang, and H. -Y. Zeng, "Design of a New Meander Archimedean Spiral Antenna," *Microwave and Optical Technology Letters*, Vol. 52, No. 10, 2010, pp. 2384–2387.

[13] Filipovic, D. S., and J. L. Volakis, "Broadband Meanderline Slot Spiral Antenna," *IEE Proc. Microw. Antennas Propag.*, Vol. 149, No. 2, April 2002, pp. 98–105.

[14] Kramer, B. A., C. -C. Chen, and J. L. Volakis, "Size Reduction of a Low-Profile Spiral Antenna Using Inductive and Dielectric Loading," *IEEE Antennas Wireless Propag. Lett.*, Vol. 7, February 2008, pp. 22–25.

[15] O'Brien, J. M., et al., "Miniaturization of a Spiral Antenna Using Periodic Z-Plane Meandering," *IEEE Transactions on Antennas and Propagation*, Vol. 63, No. 4, April 2015, p. 1843.

[16] Gao, X., and Z. Shen, "UHF/UWB Tag Antenna of Circular Polarization," *IEEE Transactions on Antennas and Propagation*, Vol. 64, No. 9, September 2016, pp. 3794–3802.

[17] Sterzer, F., et al., "Microwave Apparatus for the Treatment of Cancer," *Microwave J.*, Vol. 23, 1980, pp. 39–44.

[18] Hall, P. S., and Y. Hao, *Antennas and Propagation for Body-Centric Wireless Communications*, Norwood, MA: Artech House, 2006.

[19] Xiaomu, H., S. Yan, and G. A. E. Vandenbosch, "Wearable Button Antenna for Dual-Band WLAN Applications with Combined On and Offbody Radiation Patterns," *IEEE Transactions on Antennas and Propagation*, Vol. 65, No. 3, March 2017, pp. 1384–1387.

[20] Liu, C., Y. -X. Guo, and S. Xiao, "Capacitively Loaded Circularly Polarized Implantable Patch Antenna for ISM Band Biomedical Applications," *IEEE Transactions on Antennas and Propagation*, Vol. 62, No. 5, May 2014, pp. 2407–2417.

[21] Liu, C., Y. X. Guo, and S. Xiao, "Compact Dual-Band Antenna for Implantable Devices," *IEEE Antennas Wireless Propag. Lett.*, Vol. 11, 2012, pp. 1508–1511.

[22] Liu, Z. G., and Y. X. Guo, "Dual Band Low Profile Antenna for Body Centric Communications," *IEEE Transactions on Antennas and Propagation*, Vol. 61, No. 4, April 2013, pp. 2282–2285.

[23] Liu, Z. G., and Y. X. Guo, "Compact Low-Profile Dual Band Metamaterial Antenna for Body Centric Communications," *IEEE Antennas Wireless Propag. Lett.*, Vol. 14, December 2015, pp. 863–866.

[24] Conway, G. A., et al., "Layered RF Phantom Characterisation for Wireless Medical Vital Sign Monitors," *IEEE International Symposium on Antennas and Propagation*, 2013.

[25] Best, S. R., "Low Q Electrically Small Linear and Elliptical Polarized Spherical Dipole Antennas," *IEEE Transactions on Antennas and Propagation*, Vol. 53, No. 3, 2005, pp. 1047–1053.

[26] Zahran, S. R., Z. Hu, and M. A. Abdalla, "A Flexible Circular Polarized Wide Band Slot Antenna for Indoor IoT Applications," *2017 IEEE International Symposium on Antennas and Propagation & USNC/URSI National Radio Science Meeting*, San Diego, CA, 2017, pp. 1163–1164.

[27] Yen, C. C., and P. Nysen, "Broadband Quasi-Yagi Antenna with Enhanced Radiation Pattern for MIMO Applications," *IEEE International Symposium on Antennas and Propagation Society International Symposium*, 2013, pp. 880–881.

[28] Sor, J., et al., "A Broadband Quasi-Yagi Antenna Array," *European Microwave Conference,* 1999, pp. 255–258.

[29] Tzyh-Ghuang, M., et al., "A Modified Quasi-Yagi Antenna with a New Compact Microstrip-to-Coplanar Strip Transition Using Artificial Transmission Lines," *IEEE Transactions on Antennas and Propagation*, 2009, pp. 2469–2474.

[30] Kan, H. K., et al., "Simple Broadband Planar CPW-Fed Quasi-Yagi Antenna," *IEEE Antennas and Wireless Propagation Letters*, Vol. 6, 2007, pp. 18–20.

[31] Kwangseok, H., et al., "Broadband CPS-Fed Yagi-Uda Antenna," *Electronics Letters*, Vol. 45, No. 24, 2009, pp. 1207–1209.

Selected Bibliography

Fujita, K., et al, "UWB Circularly Polarized Planar Antenna on Flexible Substrate," *Microwave Workshop Series on RF and Wireless*, 2013.

Jeong, S. H., and H.-W. Son, "UHF RFID Tag Antenna for Embedded Use in a Concrete Floor," *IEEE Antennas Wireless Propag. Lett.*, Vol. 10, 2011, pp. 1158–1161.

Liang, W., et al., "A Novel Simple and Compact Microstrip-Fed Circularly Polarized Wide Slot Antenna with Wide Axial Ratio Bandwidth for C-Band Applications," *IEEE Transactions on Antennas and Propagation*, Vol. 64, No. 4, 2016, pp. 1552–1555.

Lin, K. H., S. L. Chen, and R. Mittra, "A Capacitively Coupling Multifeed Slot Antenna for Metallic RFID Tag Design," *IEEE Antennas Wireless Propag. Lett.*, Vol. 9, 2010, pp. 447–450.

Tran, H. H., S. X. Ta, and I. Park, "A Compact Circularly Polarized Crossed-Dipole Antenna for an RFID Tag," *IEEE Antennas Wireless Propag. Lett.*, Vol. 14, 2015, pp. 674–677.

Zahran, S. R., A. Gaafar, and M. Abdalla, "A Flexible UWB Low Profile Antenna for Wearable Applications," *IEEE Int. Ant. & Prop. Symp.*, 2016, pp. 1931–1932.

CHAPTER 13

Automotive Antennas

13.1 Introduction

Modern vehicles are fitted with multiple antennas to enable communication and allow a moving vehicle to connect with the outside world. In automobiles, many electronic devices are usually designed to increase safety or enhance the driving experience, and most of them depend on wireless communication to perform their task to the roadside environment. Antennas on a vehicle form the basis of navigation, telemetry, and all kinds of onboard communication. Systems such as Bluetooth, satellite navigation, radio, vehicle tracking, collision notification, and remote diagnostics all depend on high-performance antennas that perform as intended in challenging environments. Automobile manufacturers have been looking to create cost-effective, fuel-efficient vehicles with attractive designs. This leads to a focus on lightweight vehicles with reduced aerodynamic drag, and sleek and improved styling. Many significant innovations in the world of vehicular antennas are driven by these market preferences along with the technological factors.

Automotive communication has witnessed a tremendous growth in recent years due to modern communication. In addition to the traditional amplitude and frequency modulation (AM/FM), the present-day automobiles are equipped with multitude of information and entertainment systems such as navigation, GSM, Bluetooth, satellite radio, RKES, and TPMS. Apart from these services, higher-end cars are equipped with DAB, satellite in-vehicle TV, SDARS, ETC, short-range and long-range radar system for ACC, parking assistance, and collision detection and avoidance. In the present scenario, premium cars are integrated with at least 10 to 30 dedicated antennas.

Driverless cars will rely on radar to a much higher degree. These cars will have to autonomously keep a safe driving distance from other vehicles, exit and enter highways, change lanes safely, and make many other driving decisions that are now handled by human drivers. Vehicles are becoming ever more connected to other cars using V2X (vehicle to everything) communication, to transport infrastructure, to pedestrians, and to data centers. V2X is the umbrella term for the car's communication system, where information from sensors and other sources travels via low-latency, high-reliability links and high bandwidth, paving the way to fully autonomous driving.

Simulation techniques are critical in automotive antenna design because the range of antenna types and principles of operation, as well as the range of geometric scale involved, means that no single numerical technique will be suitable for all simulation cases. Because of antenna shape and operating frequency, simulating an FM windscreen antenna should use a different approach than simulating a roof-mounted integrated shark-fin antenna, which is again different from simulating a 77-GHz bumper-integrated collision avoidance system antenna. The choice of numerical method depends on the frequency of operation, geometrical complexity, materials used, and overall electric size of the model being studied. A strong trend currently is to combine multiple numerical approaches to provide a hybrid solution. With EM simulators such as MoM, FDTD and FEM automotive engineers can analyze radar system performance in complex, dynamic environment with improved accuracy. EM and system-level simulations are important in designing, testing, and validating many aspects of automotive radar systems. High reliable parametric antenna arrays design and their performance analysis by mounting them on vehicle bumpers are possible with EM simulations. Strong vehicle scattering can cause antenna radiation pattern sidelobes to rise and multiply; such a problem is solved by modeling the array interaction with the vehicle and predicting the installed antenna pattern. The main antenna beam shift, gain loss, shape distortion, depolarization, and sidelobe levels are all critical metrics in modeling the performance of an LRR and can be analyzed and studied thoroughly using simulations. In this chapter, antenna designs and the frequencies that are commonly used in the automotive environment are discussed.

13.2 Frequency-Modulated Continuous-Wave Automotive Radar System

Modern automobiles are equipped with radar and proximity sensors. Radar is prevalent in safety, navigation, and driver assistance systems. The radar systems in the 24-GHz and 77-GHz frequency bands are used for functions such as autonomous cruise control, collision avoidance, blind spot detection, cross-traffic alerts, parking assistance, pedestrian detection, and emergency braking. Automotive frequency-modulated continuous-wave (FMCW) radar needs target elevation angle information not only in azimuth angle but also in range and velocity. The automotive radar can detect moving objects including vehicles and pedestrians or some static objects as shown in Figure 13.1.

In an FMCW radar, the transmitted signal is a linear frequency-modulated continuous-wave (L-FMCW) chirp sequence, whose frequency versus time characteristic follows a sawtooth pattern, as shown in Figure 13.2. A local oscillator generates the L-FMCW signal, also known as the chirp signal, for amplification and transmission from the transmit antenna. Any object presents in the coverage of the radar signal, reflect the transmitted signal back. Mixing the reflected signal with the local oscillator signal produces an intermediate frequency (IF) output, which is digitized and subsequently processed in a digital signal processing. In the case of moving objects, the IF signal also has a Doppler component that depends on the relative velocity between the radar and the target. Looking at the phase shift of the IF signal from one chirp to the next chirp provides an estimate of the Doppler and

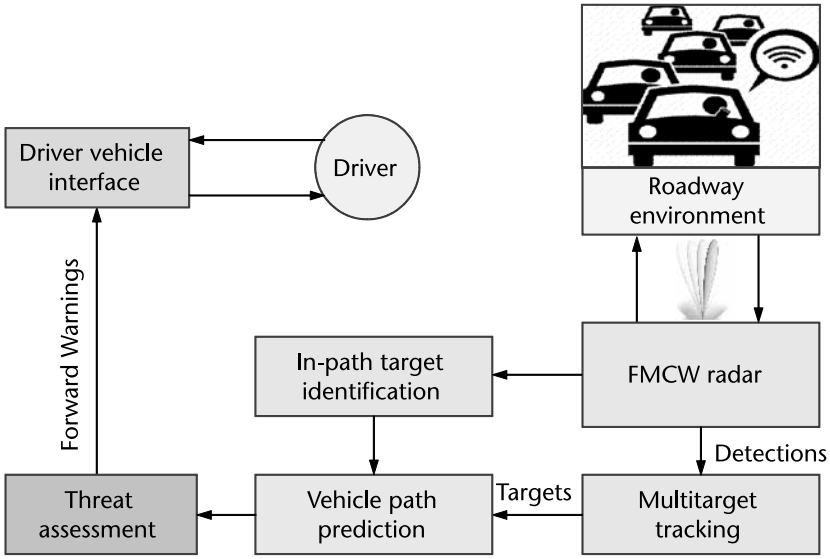

Figure 13.1 A basic FMCW radar system.

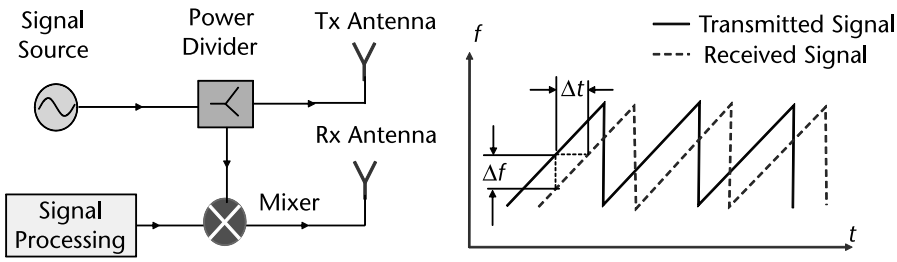

Figure 13.2 Block diagram of the FMCW automotive radar and the frequency-time relationships of transmitted and received signals.

hence the relative velocity. This is typically accomplished by performing a second FFT across chirps.

Figure 13.2 is the general block diagram of a FMCW automotive radar, and it is capable of measuring both the distance and velocity of a moving object. The time delay can be calculated by

$$\Delta t = \frac{\Delta f}{k} \tag{13.1}$$

where Δf is the frequency difference between the transmitted and received signals, which could be measured from the mixer output and k is the frequency sweep rate. The distance between the observer and target is then given by

$$d = \frac{c.\Delta t}{2} \tag{13.2}$$

Frequency bands 24 GHz and 77 GHz are two specific frequency bands for automotive radar applications. The high-frequency 77-GHz solution offers advantages such as broader bandwidth and a smaller dimension, but there are more challenges in design and implementation. The 77-GHz band could be divided into two subbands: 76–77 GHz and 77–81 GHz (also called the 79-GHz band). The former has been approved by most countries, while the latter is only available in Europe so far but has been under discussion in other countries. The functions of automotive radar sensors vary with their maximum ranges. Three major classes of radar systems are typically employed in automotive safety systems:

- *Short-range radar (SRR):* SRR is mainly used for collision proximity warning and safety and to support parking assist features.
- *Medium-range radar (MRR):* MRR is used to watch the corners of the vehicle, perform blind spot detection, observe other-vehicle lane crossover, and avoid side/corner collisions.
- *Long-range radar (LRR):* LRR is for forward-looking sensors, ACC, and early collision detection functions.

LRR is usually mounted in the front grill of the vehicle to measure the distance of objects ahead (up to 200m) and it has a narrow beam. SRR offers a broader beam and is used to monitor the vicinity of a vehicle (within 30m). MRR, which can be installed on the front, the rear, or the side area of the vehicle, is used for different applications as shown in Figure 13.3. Detailed comparisons of the three radar types are given in Table 13.1.

13.3 Automotive Antenna Design Requirements

The antennas used for automotive communication and its radiation performance depend on the type of application. Table 13.2 gives the list of services available in

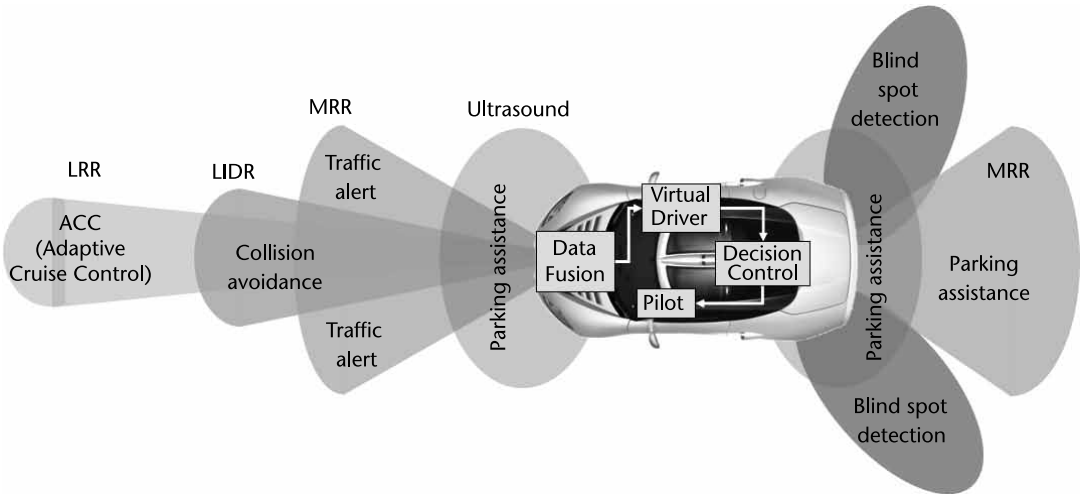

Figure 13.3 Various types of radars in automobiles.

Table 13.1 Automotive Radar Classifications

Radar Type	*LRR*	*MRR*	*SRR*
Range (m)	100–200	60–150	30
Applications	ACC	Cross-traffic alert (CTA), ACC	Blind spot detection, parking aid
EIRP	55 dBm	–9 dBm/MHz	–9 dBm/MHz
Frequency band	76–77 GHz	77–81 GHz	77–81 GHz
Distance resolution	0.5m	0.5m	0.1m
Velocity resolution	0.6 m/s	0.6 m/s	0.6 m/s
Velocity accuracy	0.1 m/s	0.1 m/s	0.1 m/s
3-dB beamwidth (Az)	±15°	±40°	±80°
3-dB beamwidth (El)	±5°	±5°	±10°

Table 13.2 Automotive Applications and Antenna Requirements

Serial Number	*Application*	*Frequency*	*Type of Radiation Pattern*
1	AM	1 MHz	Omnidirectional
2	FM	88–110 MHz	Omnidirectional
3	In-vehicle TV	50–400 MHz	Omnidirectional
4	DAB	100–400 MHz	Omnidirectional
5	GSM, 3G, and LTE	800/900 MHz	Omnidirectional
		1,800/1,900 MHz, 2,600 MHz	Omnidirectional
6	Wi-Fi and WiMAX	2.4 GHz and 2.3, 2.5, and 2.7 GHz and 3.5 GHz	Omnidirectional
7	V2V	5.9 GHz	Omnidirectional
8	RKES	315 MHz/413 MHz/434 MHz	Omnidirectional
9	Navigation system (GPS)	1.176 GHz, 1.382 GHz, 1.575 GHz	Directional
10	Satellite radio	1.472 GHz	Directional
11	SDARS	2.3 GHz	Directional
12	ETC	5.8 GHz	Directional
14	Automotive radar	24 GHz and 77 GHz	Directional
15	TPMS	315 MHz/413 MHz/434 MHz	Isotropic
16	Bluetooth	2.45 GHz	Isotropic
17	Wi-Fi (internal)	2.45 GHz	Isotropic

modern automobiles and the corresponding antenna radiation requirements. The radiators used in vehicles are grouped into three major categories, namely, omnidirectional, directional and isotropic. The choice of antenna technology depends on the antenna's performance with respect to the intended application and the location where the antenna is to be placed in the vehicle. Some of the technologies are rod

antennas, printed antennas, on-glass antennas, and glued foil antennas. Automobile antennas should have following characteristics:

- Multiband capability and good spatial coverage;
- Compact design;
- Fits into the overall picture of the car body;
- High flexibility with a minimum number of antenna modules;
- Diversity and MIMO capability;
- Extremely cost-effective;
- Low in-car SAR exposure.

13.4 Antennas for Automotive Radars

As an indispensable part of the automotive radar system, the antenna is the main component in radar. The structure of antenna should be as compact as possible for easy integration into the vehicle and it must be suitable for mass production to minimize the average cost per unit. An automotive system, performance-wise, is required to maintain a low sidelobe level, so that misdetections could be avoided. All these facets pose challenges to the antenna design for automotive radars. In the earliest days of automotive radar, the horn antenna or parabolic antenna was often chosen for the system [1, 2]. However, these antennas are too large to fit in the modern vehicle; also due to the high cost, they are very impractical for commercial use. Revolution happens when the development of printed technology makes planar antennas available even at millimeter-wave frequencies. Planar antennas could be mass-produced at a very low cost because these are more compact and more appropriate for commercial applications. Based on the vehicle design, these antennas are placed at various locations in cars as shown in Figure 13.4.

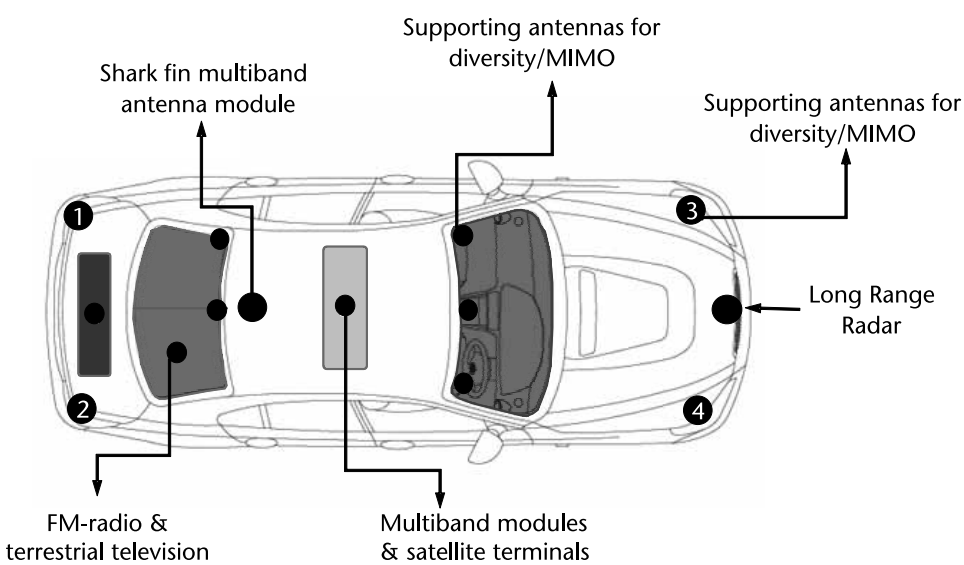

Figure 13.4 Antennas placement in car system.

13.4.1 Low-Frequency Automobile Antennas

AM/FM antennas used in automobiles are low-frequency antennas. AM radio works in the frequency band between 535–1,605 kHz, while FM radios function from 88–108 MHz [3]. This makes AM/FM radio communications the two lowest-frequency forms of wireless communications in vehicles. Because many antenna dimensions correspond to the electrical length at the desired frequency of operation, antennas that operate at lower frequencies tend to be larger than those that operate at higher frequencies. Blade, or shark-fin, antennas represent most of the radio antennas in modern vehicles [4, 5]. These are composed of vertically oriented PCBs covered with a radome. Their appearance and small size allow them to be mounted on the roof of the vehicle, which limits the interference that the antenna experiences from the vehicle itself. A vehicle designer wanting to avoid a shark-fin antenna may go with antennas printed onto the windshield and/or the rear windshield. These on-glass antennas have received much interest in recent years due to the immense number of potential designs that can be implemented on the large glass surfaces found in automobiles [6, 7].

DAB is another low-frequency antenna used in vehicles. These antennas may be like AM/FM antennas, as the DAB band (100–400 MHz) overlaps the FM band (88.0–108.0 MHz). Just as the DAB band overlaps the AM/FM radio at the lower frequencies, it also overlaps RKES and TPMS at the higher frequencies of the band. RKE is a wireless communication system in which a driver utilizes a transmitter attached to their key ring to communicate with a receiver on their vehicle. This can provide several convenient functions, such as locking and unlocking doors, opening automatic doors from a distance, and starting the vehicle. The TPMS comprises air pressure sensors on all four tires paired with wireless transmitters. These communicate with a receiver mounted near the center of the vehicle, which relays the information to an electronic control unit (ECU) mounted in the instrument panel. The ECU uses the data from the receivers to calculate the tire pressure, and it alerts the driver if an irregular tire pressure is detected. The TPMS and RKES both operate between 300 and 400 MHz. Also, both systems are designed to work only at a short range in and around the vehicle. Because of this feature, these antennas are different from dedicated short-range communications (DSRC) antennas that must operate at medium to long ranges strictly outside the vehicle.

13.4.2 High-Frequency Automobile Antennas

Satellite navigation antennas communicate with GPS satellites to calculate the vehicle's location and velocity and provide the user with directions to their destination. These systems operate with a center frequency of 1.575 GHz [7]. When GPS antennas are discussed, they are often mentioned in conjecture with Satellite Digital Audio Radio Service (SDARS) antennas. Although there is a sizable gap between the center frequency of GPS systems (1.575 GHz) and that of SDARS antennas (2.3 GHz), their operation requirements are similar [8]. Bluetooth technology (2.4 GHz) is often used inside vehicles to create a link between passengers' mobile phones and the vehicle's onboard audio and navigation system. Some vehicles employ Wi-Fi to communicate with passengers' wireless devices within the vehicle cabin, although this is less common (2.4 GHz). Vehicle detection radar systems typically

use antenna arrays to detect large metallic objects. The system detects not only the presence of the object, but also the speed of the object relative to the speed of the vehicle to which the radar is attached. Radar antenna arrays operate at very high frequencies (~74 GHz) and are attached to the front and rear bumpers of the host vehicle. Because of this, they have minimal interference from other wireless.

13.5 Automotive Glass-Mounted FM/DAB Antennas

The lowest frequencies used in vehicles are often for AM and FM radio as shown in Figure 13.5. At the beginning of car radio history, a quarter-wavelength FM rod antenna played the major role in automotive radio reception. Over the years, new antenna concepts, such as a windscreen-printed antenna, have emerged [9]. These antenna structures, inconspicuously embedded into the windscreen of a car, offer several significant advantages over standard rod antennas on a vehicle. Another trend is represented by the integration of as many services as possible in a single antenna. Nowadays, there is a steadily increasing demand towards DAB (1,452–1,492 MHz), which offers better audio quality than FM and is more suitable for mobile scenarios.

Many glass-mounted antennas are based on wire geometry, although the antenna may or may not be an actual wire. A glass wire antenna is formed by using the wire of a very thin diameter or a silk-screened film that is laminated between layers of glass in the vehicle windows. No additional aerodynamic drag is provided by glass-mounted antennas and it also creates no wind noise, which is a significant advantage over mast-type designs. Glass antennas are more directional than mast antennas, which can lead to nulls in the reception on certain angles around the vehicle. Different shapes are used for wire glass antennas, often forming a grid or

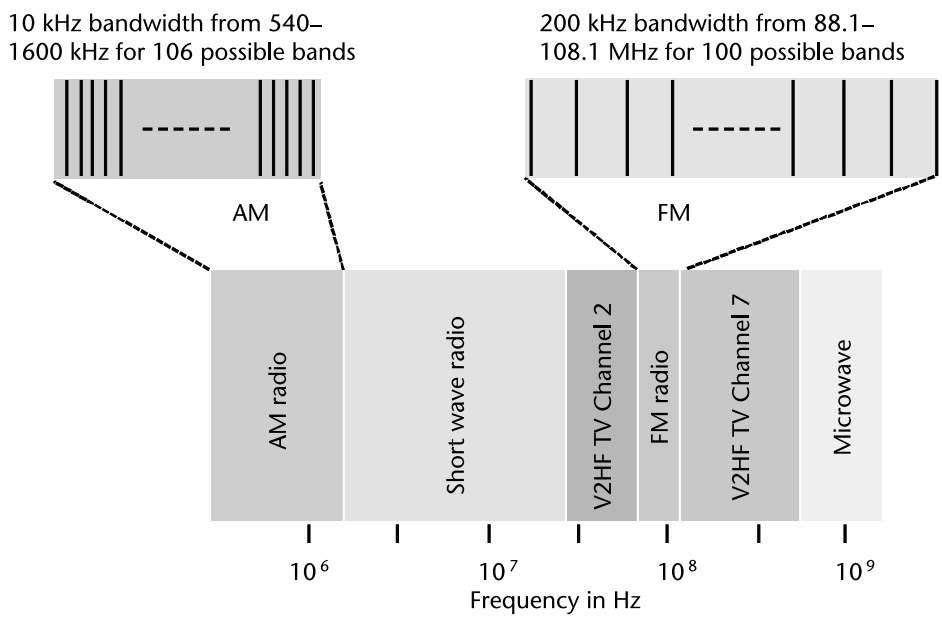

Figure 13.5 AM and FM frequency bands in radio communication.

meandering geometries, with a shape that works well on one vehicle not necessarily performing well on other vehicles. No universal glass-mounted antenna has yet been discovered. This is because of the vehicle body on the antenna's impedance and radiation, which is significant for on-glass antennas. Antennas oriented vertically may provide better reception of vertically polarized signals.

A windscreen antenna is designed for the services FM 88–108 MHz and DAB in the VHF-band (174–240 MHz) as shown in Figure 13.6 with a 1.5-mm metallic copper strip.

The heater-grid antenna is more effective at AM frequencies than the standard whip monopole antenna. The reason that the heater-grid antenna is more effective is that it has a larger effective height than the whip antenna. A preamplifier is used to compensate for poor radiation performance of the heater-grid antenna. The distance between the horizontal lines on the heater-grid is electrically small (at AM/FM frequencies), such that the RF current flow in the horizontal direction is the same as it would be on an equivalent conducting plate. To allow the RF current to flow vertically, as it would on a conducting plate, 1 to 3 additional vertical lines must be added to the heater grid. The antenna copper structures are placed on the windscreen of the car. This adaptive windscreen antenna consists of multiple FM and DAB antenna structures. The different frequency bands are combined by means of filter circuits. Glass thickness is 3.2 mm, and permittivity is 7.4. Figure 13.7 shows the simulated result of the antenna using the MoM.

13.6 Shark-Fin Antenna

Shark-fin antennas have gained considerable attention, to meet the demands of built-in system to support Wi-Fi and LTE inside the automobile. Low-profile design is necessary as several dedicated antennas are placed inside a small shark-fin module [10–12]. As a result, antenna performance can be largely affected by the

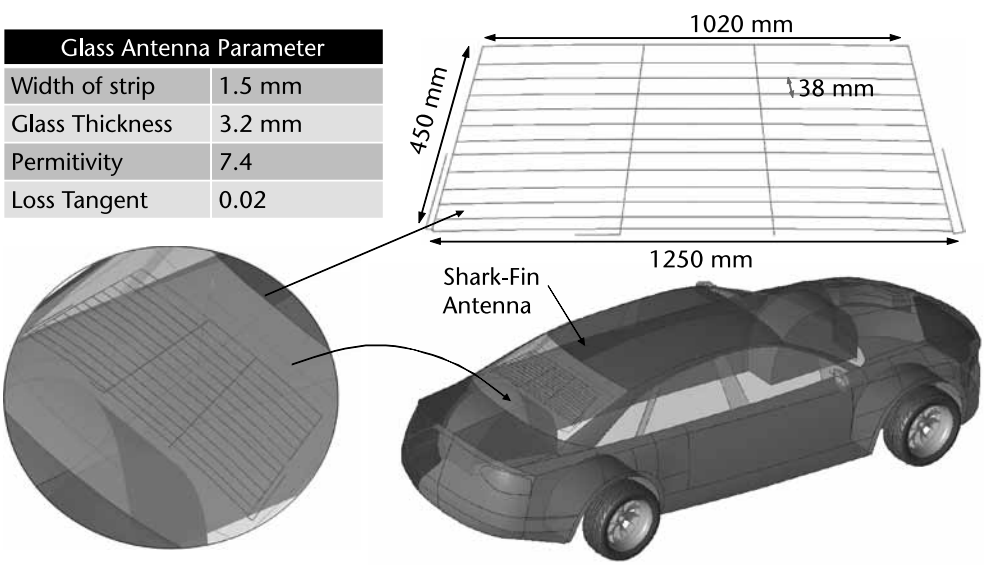

Glass Antenna Parameter	
Width of strip	1.5 mm
Glass Thickness	3.2 mm
Permitivity	7.4
Loss Tangent	0.02

Figure 13.6 Antenna placement on the car and glass antenna design parameters.

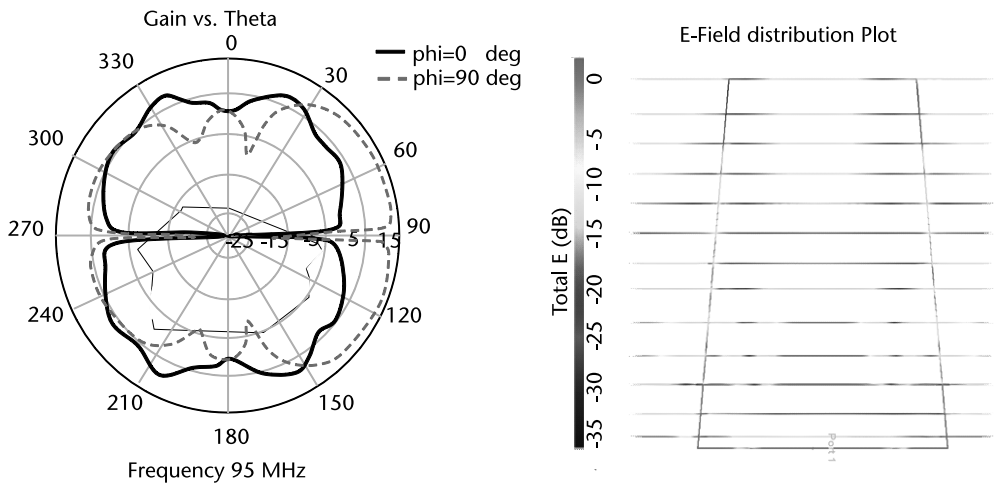

Figure 13.7 Antenna radiation patterns and current distribution over the antenna.

limited space available in typical shark-fin modules. This module is typically shaped like a blade or dorsal fin and is usually located on the roof towards the rear of the vehicle as shown in Figure 13.8. One of the main challenges is the antenna integration in a small-form factor such as the shark-fin case on the roof of a vehicle and its multiband behavior between antenna elements. Antenna elements placed closely should be highly isolated within a small volume for covering simultaneous multiband operations. In automobiles, several cellular and ad hoc-based communication standards are under consideration for offering a safe, efficient, and comfortable driving environment. For LTE, GPS, WLAN, and car-to-car (C2C) communications, antenna design becomes challenging in terms of compactness, bandwidth, efficiency, and mutual coupling. Cellular bands such as LTE700, LTE750, LTE800 MHz, LTE1800 MHz (1,710–1,880 MHz), LTE2600 MHz (2,520–2,690 MHz),

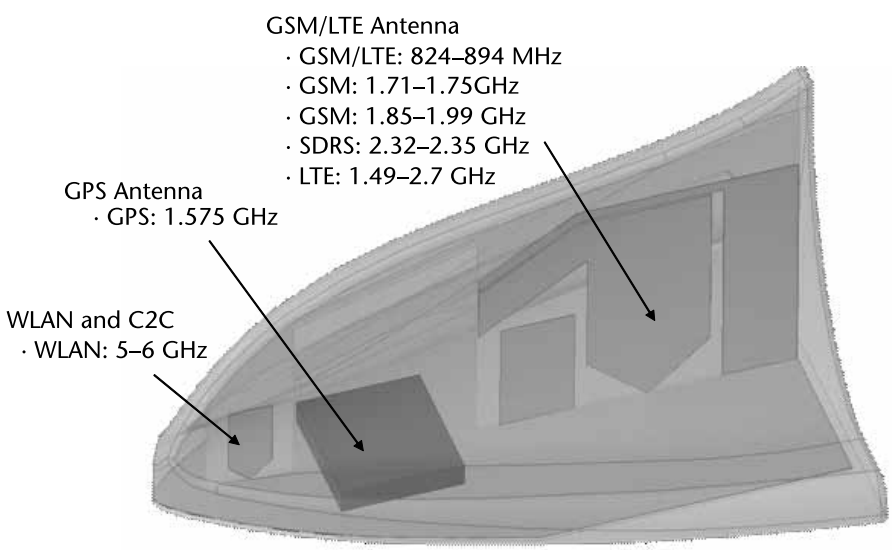

Figure 13.8 Designed shark-fin antenna covering several cellular and ad-hoc-based communication standards.

and GSM900 require the operation along with many other standards, for example, DCS1800 and PCS1900 (from 1,710–2,700 MHz). The DSRC system working in 5,850–5,925-MHz frequency band is a new standard intended for intervehicular communications to improve traffic safety for Intelligent Transportation Systems (ITS). A Wireless Access in the Vehicular Environment (WAVE) protocol, the IEEE 802.11p standard at 5.9-GHz band, can be a great candidate for vehicle-to-vehicle communication due to its real-time operation when anticollision messages and safety information must be provided to vehicles.

A shark fin antenna as shown in Figure 13.8 is designed to cover the frequency range of 698–2,700 MHz (VSWR < 3), which would serve major GSM/LTE standards. A GPS antenna for 1.575 GHz and one-tab monopole antenna covering the frequency range of 5–6 GHz is integrated into the shark-fin module and provide services for WLAN and C2C. Three antenna elements are used to cover all frequency bands and applications: one element for the low LTE band, the second element for GPS, and the third element for the WLAN band. In the case of multiple antennas placed side-by-side, high mutual coupling between the two antenna elements is a serious issue. Additional filters are needed to mitigate mutual coupling but with extra fabrication costs. In this design, low mutual coupling (lower than –22 dB) between the two antennas is achieved in the frequency range of 698–6,000 MHz without any additional filters.

13.6.1 LTE/GSM Antenna Design

A monopole antenna has an omnidirectional radiation pattern and it radiates with equal power in all azimuthal directions perpendicular to the antenna, which is why it is a suitable antenna choice for LTE frequency bands. It is possible to reduce the antenna height using an L-shaped monopole as shown in Figure 13.9. For conformal placement of the LTE antenna, the tail of the monopole is bended as per shark-fin geometry [13]. The length of the L-monopole determines the lower resonance. The first resonance of the monopole antenna is mainly determined by the length of

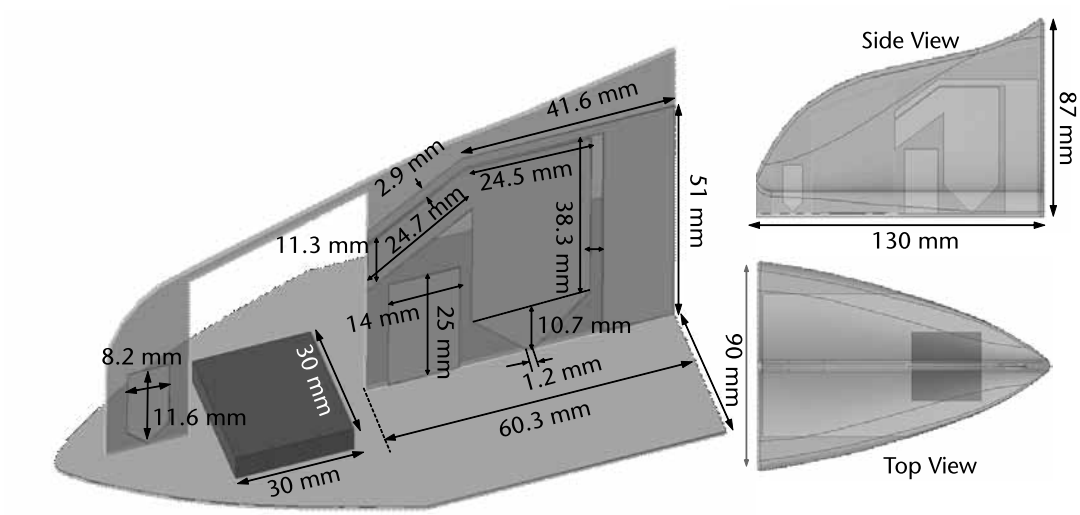

Figure 13.9 Design dimensions of LTE/GSM and WLAN shark-fin antenna.

the right-side sleeve, and the second resonance is attributed mostly to the length of the main central monopole. As both the left sleeve and the monopole have similar L-shape structures, their lengths are about 0.3λ. The VSWR plot is shown in Figure 13.10 for all antenna resonance frequency in GSM/LTE band. Bluetooth is incorporated into many present-day vehicles to allow hands-free calling and the operation of an equipped mobile through the vehicle's multimedia system.

To depict the working principles of the LTE and WLAN antennas, its E-field distributions are shown in Figure 13.11. This antenna can be used for the 2.4-GHz ISM band, which has seen enormous growth in the past decade due to the ubiquitous application and implementation of Wi-Fi and Bluetooth, which occupy part of this band.

13.6.2 GPS Antenna

Guidance and navigation facilities are becoming more cost-effective and are seeing a large uptake in the modern market. These navigation systems usually rely on the constellation of approximately 30 GPS satellites to determine the location of the vehicle before plotting it on a map. The GPS L1 band is received in a narrow 20-MHz channel centered at 1.575 GHz. The GPS antenna is placed between LTE and WLAN antennas. A square patch of 30 mm × 30 mm with a diagonal probe feeding as shown in Figure 13.12 is used as radiating elements. The patch is printed on an Arlon1000 substrate (with a relative permittivity of 10.2, a loss tangent of 0.003, and a thickness of 1 mm).

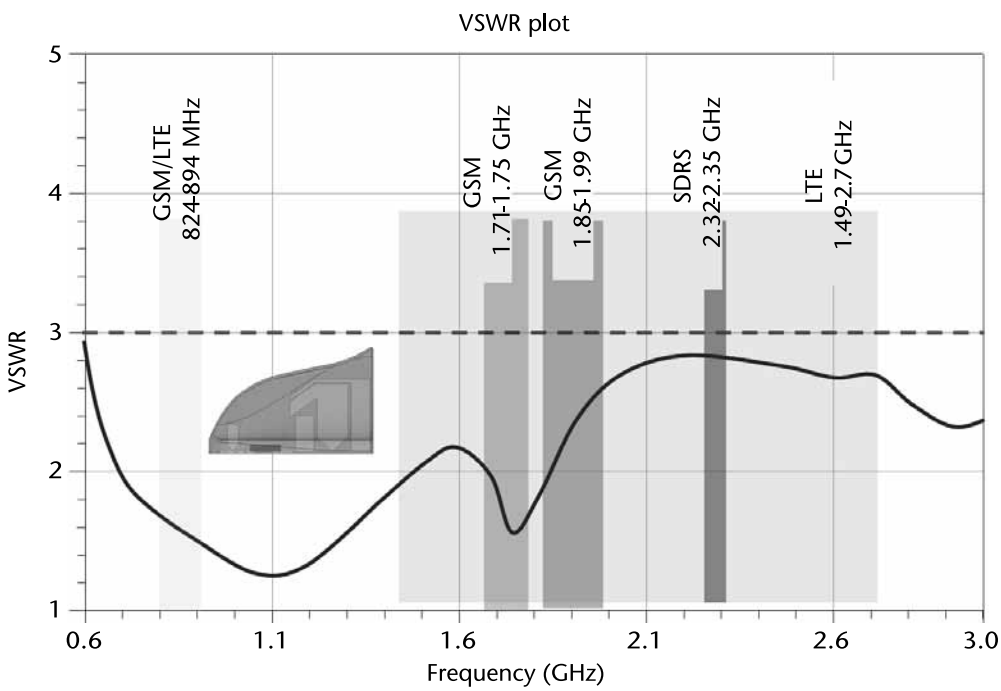

Figure 13.10 GSM/LTE antenna result (VSWR < 3).

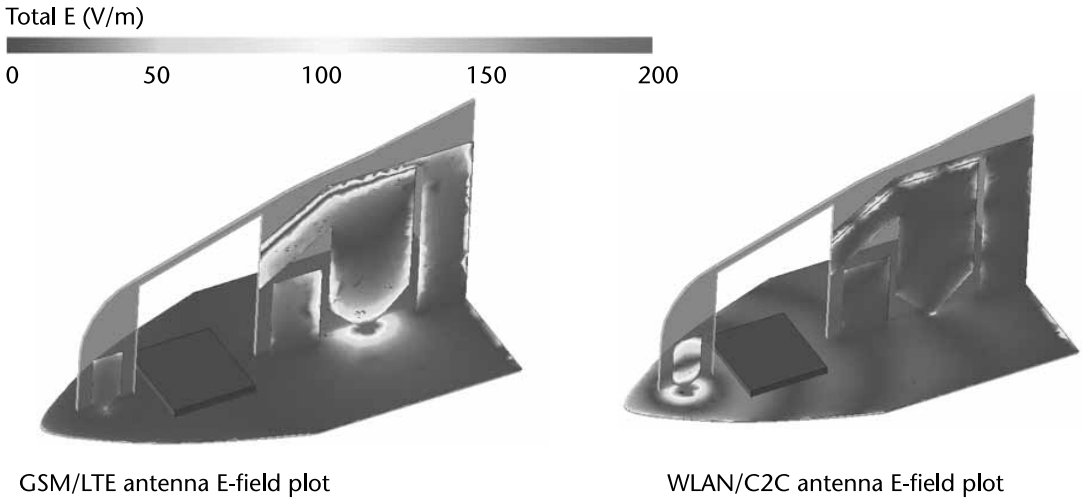

Figure 13.11 E-field distribution on LTE and WLAN antenna.

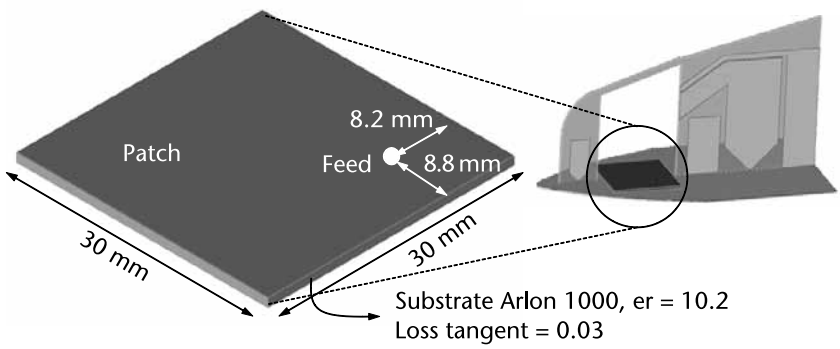

Figure 13.12 GPS microstrip patch antenna design dimensions.

The simulated gain of the antenna is 2.1 dBi as shown in Figure 13.13 at 1,575 MHz, a reasonable value for the square patch on a high permittivity dielectric substrate.

Sometimes GPS antennas are designed for circular polarization by truncating a corner of a square patch or with one or two feed points. Based on application and design, a circular polarization can also be obtained from a single-point square or a circular patch.

13.6.3 WLAN Antenna

A WLAN antenna provides services to high-band WLAN (IEEE 802.11n, 802.11ac) and C2C communications (IEEE 802.11p). For the WLAN antenna, a tab monopole with dimensions of 11.6 mm × 8.2 mm is used to cover the frequency range of 5–6 GHz [14]. It fits the shark-fin module. As it is electrically small and impedance=mismatched in the working frequency range of the LTE antenna (i.e. 698–2,700 MHz), low mutual coupling levels between them are expected in this

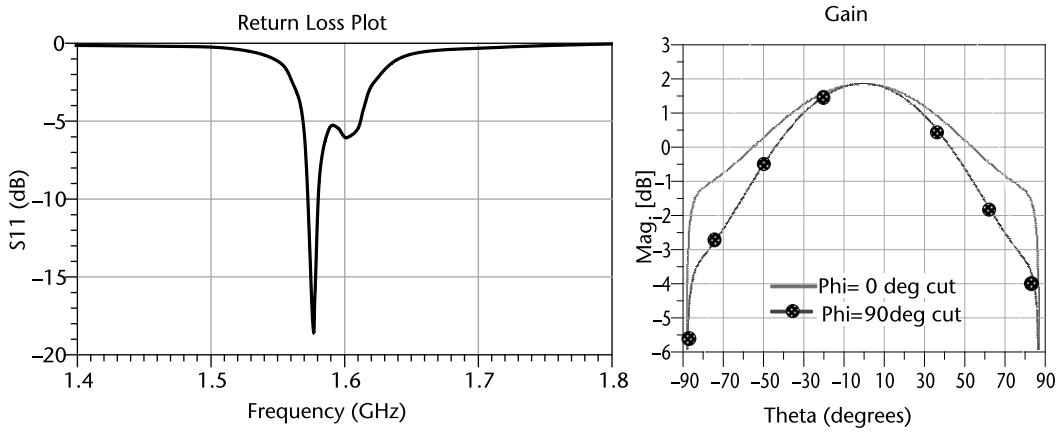

Figure 13.13 Simulated return loss and antenna gain plot of the GPS antenna.

range. The antenna resonating frequency range is between 5 GHz and 6.5 GHz, as shown in Figure 13.14.

13.7 Grid Array Antenna for 24-GHz Automotive SRR

The two most popular millimeter-wave automotive radars are LRR and SRR systems. The LRR operating at the 24/77-GHz frequency spectrum is characterized by narrow beams to control the driving path in the front of the car and to estimate the relative distance between the car and the vehicle ahead of it. This ensures a minimum safety distance between the vehicles and hence reduces the accident risk. The LRR can range up to 250m and requires a bandwidth of less than 1 GHz with a typical spatial resolution of 0.5m [15]. However, the SRR gives a wide field of view for target detection near the car, typically around 30m. The modern vehicles are fitted with at least 10 SRRs to ensure the safety aspects of the vehicle. In this section, an antenna design is discussed for the SRR that requires a wideband operation for

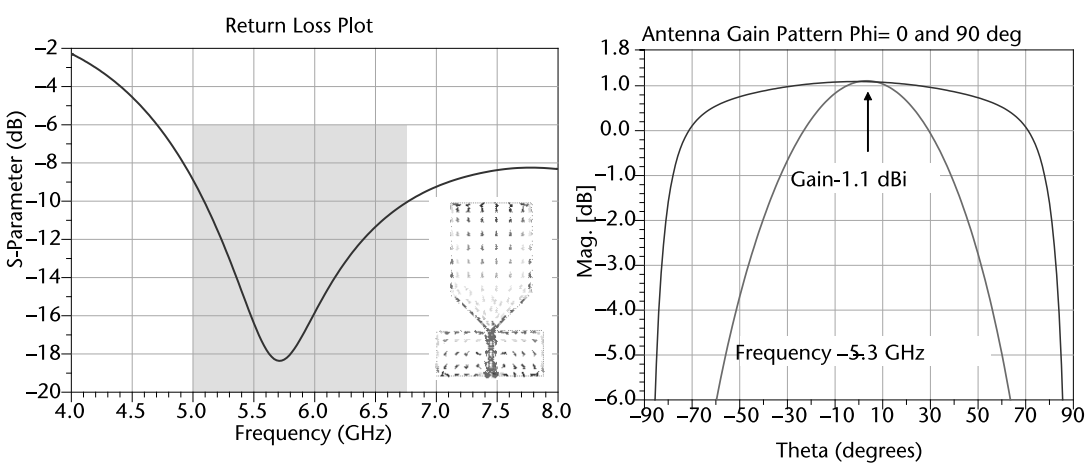

Figure 13.14 WLAN and C2C antenna return loss and radiation pattern.

interference-free target detection. A very specific type of antenna array called the grid array antenna (GAA), which has gained recent research interest for automotive radar antenna development, is designed.

GAA was proposed by Kraus [16] in 1964. He found that the performance of the GAA depends largely on the synchronization of surface currents. In 1981, Conti et al. [17] adopted it as a monopulse antenna. The GAA for 24-GHz automotive radar sensor applications was first studied by Zhang et al. [18, 19]. A GAA, which is backed by many grid cells, is a low-profile, flat antenna consisting of numerous radiation and transmission-line elements. The microstrip GAA has all the usual benefits of conventional printed radiators along with broad bandwidth, high gain, adequate cross-polarization control, and beam scan ability with frequency. The grid is a periodic structure of rectangular frames with dimensions equal to about one wavelength by one-half wavelength.

The GAA consists of horizontal transmission lines and vertical radiating elements. The radiation originates from the short edges, while long edges act as transmission-line feed elements. The width and length of the transmission line control the impedance and frequency specifications, respectively. There is no beam scanning in GAA, but it is designed to radiate a narrow beam along the elevation plane and a broad beam along the azimuth plane to enhance the lateral coverage of the automotive radar system. In the GAA, the current on the vertical radiating sections are aligned in phase and constructively interfere to produce radiation at the far-field distance, whereas the current in the transmission line, which is separated by a full wavelength, changes phase and interferes destructively. Therefore, the horizontal sections contribute only to a small radiation. Hence, the GAA produces a narrow beam along the elevation plane and a broad beam along the azimuth plane. This antenna is positioned vertically in the front side of the car beneath the plastic bumper to achieve the lateral coverage.

Figure 13.15 shows geometries of the 24-GHz microstrip GAA. It comprises a radiating grid, a substrate, a metalized ground, and one feed probe. The radiating grid with 61 meshes is etched on the top surface of the substrate. The length of the short side is 4.6 mm, which is approximate to half of the guided wavelength at 2 GHz, and the length of the long side is 9.23 mm (7 mm +2.23 mm), which is approximate to one of the guided wavelengths. The width of the short side is 2.23 mm, while the width of the long side is 0.38 mm. The substrate is a 65 mm × 65 mm square. A coaxial probe is drilled through the ground and the substrate to feed the radiating element. Rogers 5880 with an ε_r of 2.2 and a tangent loss of 0.001 with a thickness of 0.787 mm is chosen as the board material.

To monitor blind spots, 24-GHz automotive radars are used that require the maximum directivity of the antenna to be larger than 20 dBi, the impedance and radiation bandwidth to be larger than 0.25 GHz [18]. The radiation characteristics are evaluated using MoM based on the obtained current distribution along the GAA. Figure 13.16 shows $|S_{11}|$ as a function of frequency. The input impedance bandwidth is 2.4 GHz. The simulated 3-dB gain bandwidth is 1.54 GHz from 22.8 GHz to 25.2 GHz with a maximal directivity of 20.21 dBi at 24 GHz. The radiation patterns at 24 GHz in phi = 0° and 90° cut-planes are shown in Figure 13.16.

Another configuration of the 24-GHz microstrip GAA is shown in Figure 13.17. It is composed of 25 grids. This antenna can fit in the circular aperture radar.

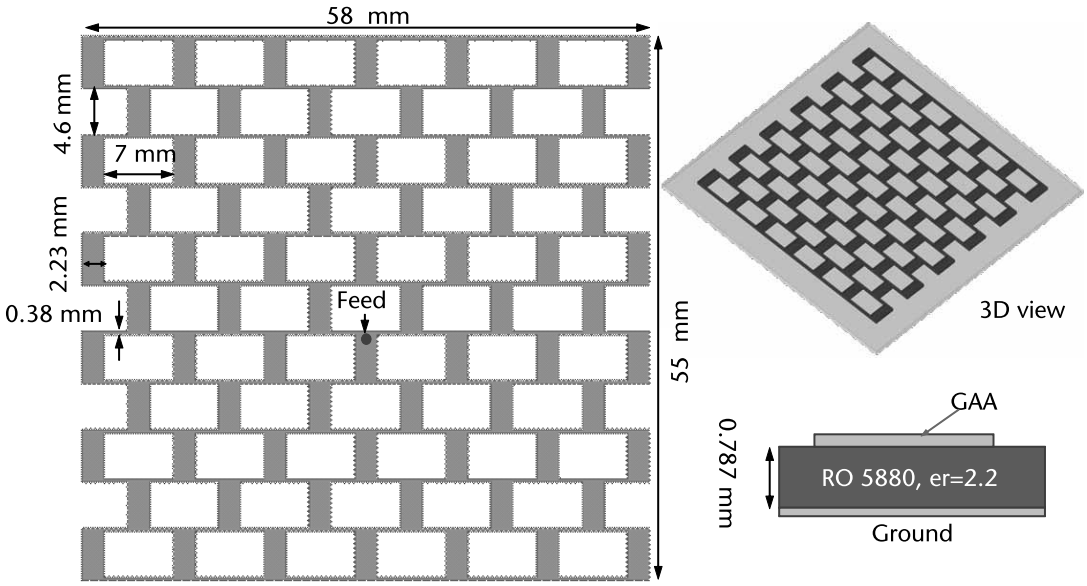

Figure 13.15 Design dimensions of a 24-GHz microstrip GAA.

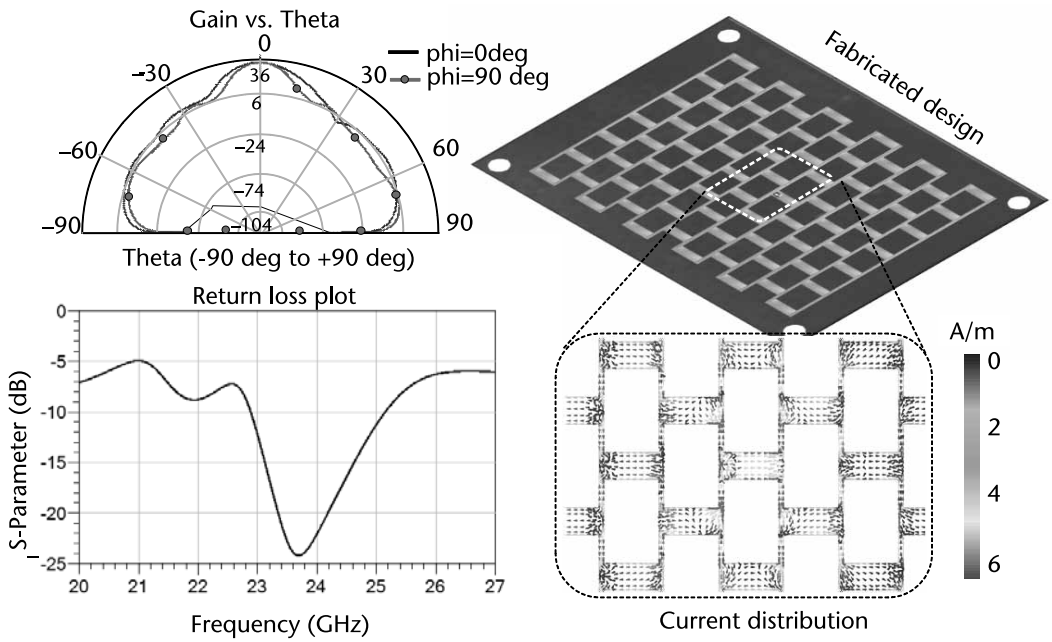

Figure 13.16 Fabricated 61-grid microstrip GAA and results.

13.7.1 Microstrip Comb-Line Antenna Arrays for LRR

The microstrip comb-line antenna array is a form of GAA discussed previously. As shown in Figure 13.18, if we remove the top and bottom conducting lines from the GAA, then it becomes a comb-line antenna.

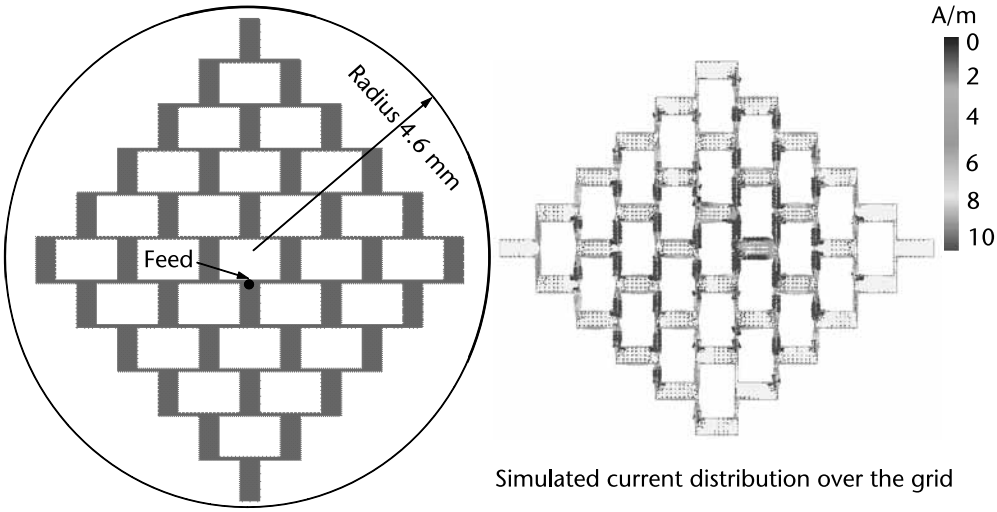

Figure 13.17 GAA for circular aperture.

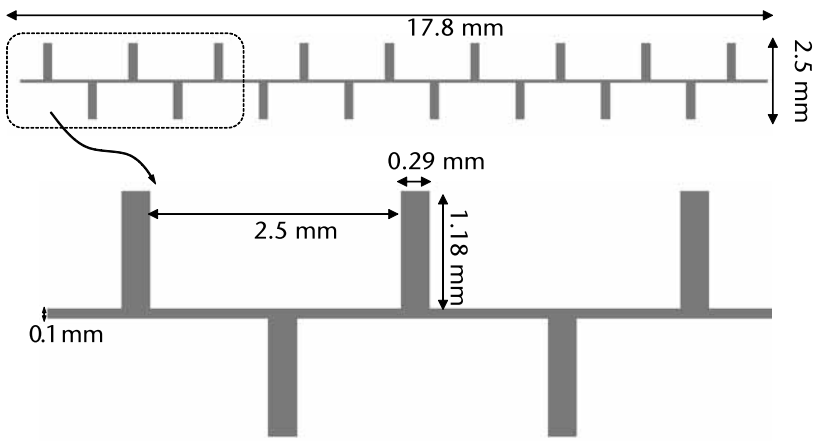

Figure 13.18 Microstrip comb-line antenna array for LRR.

The comb-line array should be realized in a standing-wave configuration with 45° polarization orientation for an automotive LRR application. To begin with, 90° linearly polarized arrays are first designed. Figure 13.18 shows a 90° uniform comb-line antenna array in a standing-wave configuration. The length of open stub and the spacing between adjacent stubs both equal a half-wavelength; the amplitude distribution of the array is controlled by the open stub width. In the simplest case of uniform array, the width of each stub is the same, so power will be evenly spread over the aperture. A 5-mil-thick Rogers RO3003 substrate with an ε_r of 3.2 and a loss tangent of 0.016 is used for antenna design. The length and width of a 50Ω half-wavelength stub are 1.18 mm and 0.29 mm, respectively. The feedline of 0.1-mm width with the distance between adjacent stubs of 1.48 mm is used to feed the signal.

The simulation results of the reflection coefficient from 74 to 84 GHz and radiation patterns at 77 GHz are presented in Figures 13.19 for 17 elements. The

return loss is better than 10 dB from 75.5 to 78.2 GHz. The 3-D radiation pattern demonstrates a broadside beam with a fan-shaped main lobe. Peak radiation occurs and the maximum gain is 13.1 dBi. In the $\theta = 0°$ plane radiation pattern, the half-power beamwidth (HPBW) is approximately 12° and the sidelobe level is –12.5 dB.

13.7.2 Amplitude Tapered Antenna Array

Theoretically, the best sidelobe level that a uniform linear array could obtain is about –13.46 dB. To accomplish better sidelobe suppression, nonuniform amplitude distribution is formed on the array by applying several amplitude tapering methods. In this design, Taylor distribution is selected as this technique offers an optimal balance between beamwidth and sidelobe level. A compromise between the Dolph-Chebyshev and the Taylor one-parameter distribution was developed by Taylor and called the $\bar{n}$ distribution [20]. This method offers a modest improvement in efficiency over the one-parameter distribution by making the first few sidelobes at an equal level. The radiation pattern of a Taylor weighted array exhibits the following properties: the first $\bar{n}$ sidelobes near the main lobe are at the same level $1/R_0$, while the rest decrease monotonically. Both parameters $\bar{n}$ and $1/R_0$ are specified by the designer. The value of $\bar{n}$ should be carefully determined, as it will influence the peak positions of amplitude distribution on the array. Generally, for –25 dB, the sidelobe level should be no less than 3 [21]. To improve the sidelobe suppression, the uniform array is modified with a 20-dB ($\bar{n}$=3) Taylor amplitude taper [22]. The corresponding voltage ratio is

$$R_0 = \cosh(\pi.X) = 10 \tag{13.3}$$

The constant X can be calculated by

$$X = \frac{1}{\pi}\text{sech}^{-1}(R_0) = 0.95 \tag{13.4}$$

The scaling factor σ is given by

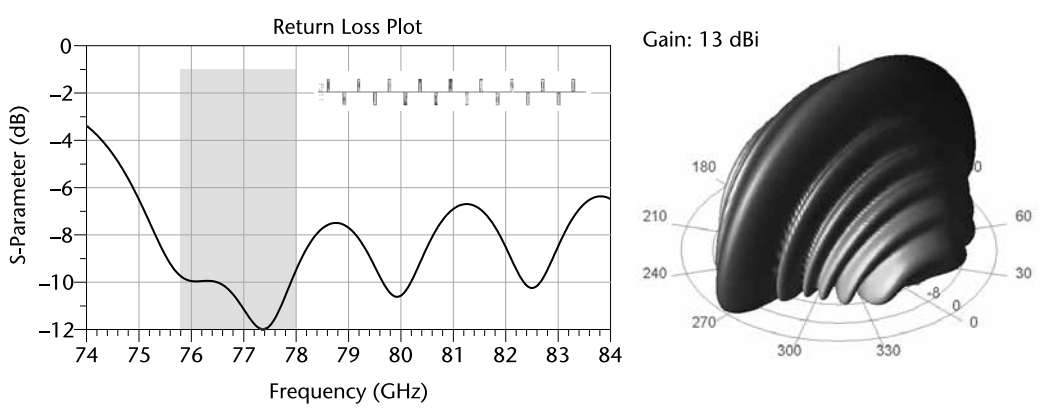

Figure 13.19 Antenna performance results of the comb-line array.

$$\sigma = \frac{\overline{n}}{\sqrt{X^2 + \left(\overline{n} - 1/2\right)^2}} \tag{13.5}$$

and the normalized current distribution over the array can be expressed as

$$I(z) = \frac{\lambda}{l}\left[1 + 2\sum_{p=1}^{\overline{n}-1} SF(p, X, \overline{n})\cos\left(2\pi p\frac{z}{l}\right)\right] \tag{13.6}$$

where Taylor space factor SF(p, X, ($\overline{n}$) is given as

$$SF(p, X, \overline{n}) = \begin{cases} \dfrac{\left[(\overline{n}-1)!\right]^2}{(\overline{n}-1+p)!(\overline{n}-1-p)!}\displaystyle\prod_{m=1}^{\overline{n}-1}\left[1 - \left(\frac{\pi p}{z_m}\right)^2\right], |p| < \overline{n} \\ 0, |p| \geq \overline{n} \end{cases} \tag{13.7}$$

where zeros z_m are

$$z_m = \pi\frac{l}{\lambda}\cos\theta_m = \begin{cases} \pm\pi\sigma\sqrt{X^2 + \left(m - \dfrac{1}{2}\right)^2}, 1 \leq m < \overline{n} \\ \pm m\pi, \overline{n} \leq m \leq \infty \end{cases} \tag{13.8}$$

and θ_m is the location of the mth sidelobe in the radiation pattern. The $\overline{n}$ distribution gives a narrower beamwidth and higher efficiency, without significantly degrading its robustness. Normalized current levels on the 90° comb-line antenna array with a 20-dB ($\overline{n}$ = 3) Taylor amplitude taper are given in Figure 13.20. Only half of the values need to be calculated because the distribution is symmetric. Once the current distribution is established, the following task is to decide the corresponding stub widths.

The stubs at two ends of the array (stub 1 and stub 13) will carry the lowest currents, so their characteristic impedances are the highest among all stubs. Stub 1 and stub 13 are assigned the minimum manufacturable line width of 0.11 mm, which corresponds to the characteristic impedance of 87Ω. The characteristic impedances of other stubs can be obtained by

$$Z_{0,i} = Z_{14-i} = \frac{I_1 Z_1}{I_i} = \frac{0.53x87}{I_i} = \frac{46.11}{I_i} \tag{13.9}$$

The –10-dB impedance bandwidth is from 74 to 78.4 GHz. As shown in Figure 13.21, a 77-GHz elevation plane radiation pattern has a –4-dB less sidelobe label compared to an array with equal amplitude distribution, the HPBW is about 12°, and the sidelobe suppression is better than 16.3 dB. The sidelobe suppression has been improved 4 dB after applying the amplitude taper, and the differences in the

Element No.	Normalized Current	Z_0 (Ohm)	Line Width (mm)
1 & 13	0.53	87.00	0.11
2 & 12	0.56	82.33	0.13
3 & 11	0.64	72.04	0.17
4 & 10	0.76	60.67	0.23
5 & 9	0.88	52.39	0.29
6 & 8	0.97	47.53	0.34
7	1.00	46.11	0.36

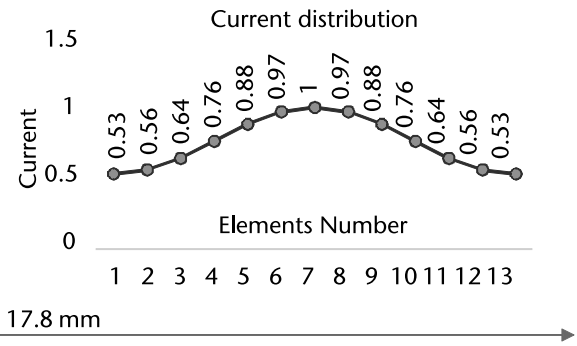

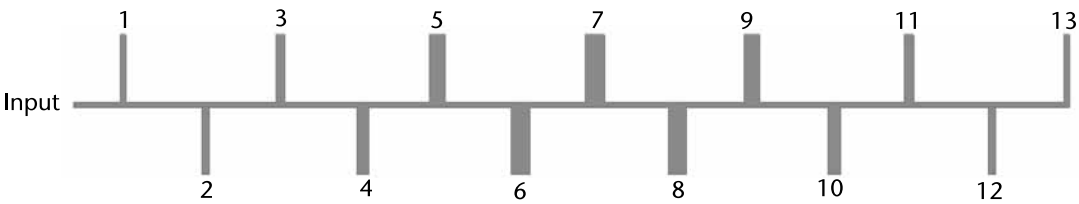

Figure 13.20 Normalized current distribution for the Taylor method with $N = 13$ and the sidelobe level 18 dB and ($\overline{n} = 3$) and the line width of each element's stub.

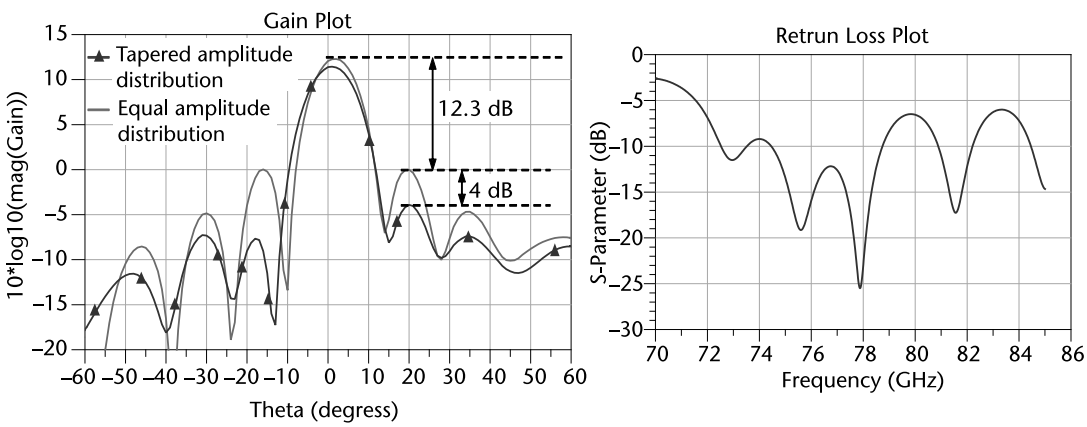

Figure 13.21 Phi = 0° plane radiation pattern (at 77 GHz) and return loss plot.

first three sidelobes' power levels of the Taylor array are much smaller than those of the uniform array, as it is expected.

13.7.3 Amplitude Tapered 45° Antenna Array

In a 90° comb-line antenna, all open-circuit stubs are perpendicular to the main feed line, so those arrays are 90° linearly polarized. The disadvantage of this configuration is that automotive radars equipped with such antennas cannot distinguish between the reflected signals and signals transmitted by vehicles from the opposite directions.

One solution is to create a 45 linearly polarized array by tilting the orientation of stubs to 45°, and then signals from vehicles traveling in opposite directions are orthogonal (assuming that 45° antennas are installed on both vehicles) and the

interferences will be minimized. The design principle of 45° comb-line antenna array is very similar to that of a 90° array.

Figure 13.22 shows a 45° 13-element comb-line array with an 18-dB ($\bar{n}$ =3) Taylor amplitude taper. The stub widths are the same as the 90° array. The antenna results of the 45° amplitude tapered array are shown in Figure 13.22. The reflection coefficient is below 10 dB from 76.4 to 79 GHz. Using 8 linear arrays, a phased array as shown in Figure 13.23 is realized. This phased array antenna can communicate with multiple targets on the road. An antenna simulated radiation pattern is shown with a 20-dBi gain.

13.8 Planar Array for Millimeter-Wave Automotive Radar

Planar antennas are commonly used in sensing applications at frequencies as high as 77 GHz and above, for example, in automotive sensing. Early vehicular radar development was in the microwave frequency range of 10–24 GHz [23–30]. To reduce the physical size of the radar sensors for use on automobiles, the frequency of operation had to be increased to the millimeter-wave range. At those frequencies, the radar antenna can be made electrically large to produce the required high directivity and narrow beamwidth, while keeping the physical size small enough for installation on an automobile. Typical antenna requirements for millimeter-wave automotive radar are multibeam or scanning capability, high gain up to 35 dBi, and moderate to low sidelobes.

Radar technology has been investigated for use on automobiles since the 1970s and has been employed for various functions on automobiles since the early 1980s [31, 32]. The initial usage of microwave radar was for collision warning applications on commercial vehicles, such as ambulances, buses, and trucks. Now these

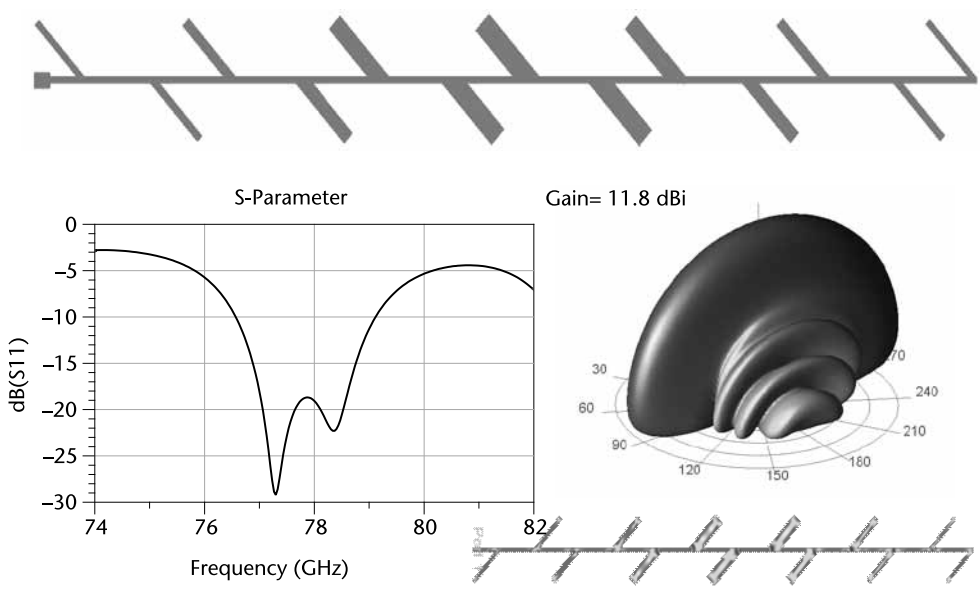

Figure 13.22 Layout design, reflection coefficient, and radiation pattern of the 45 amplitude tapered comb-line array.

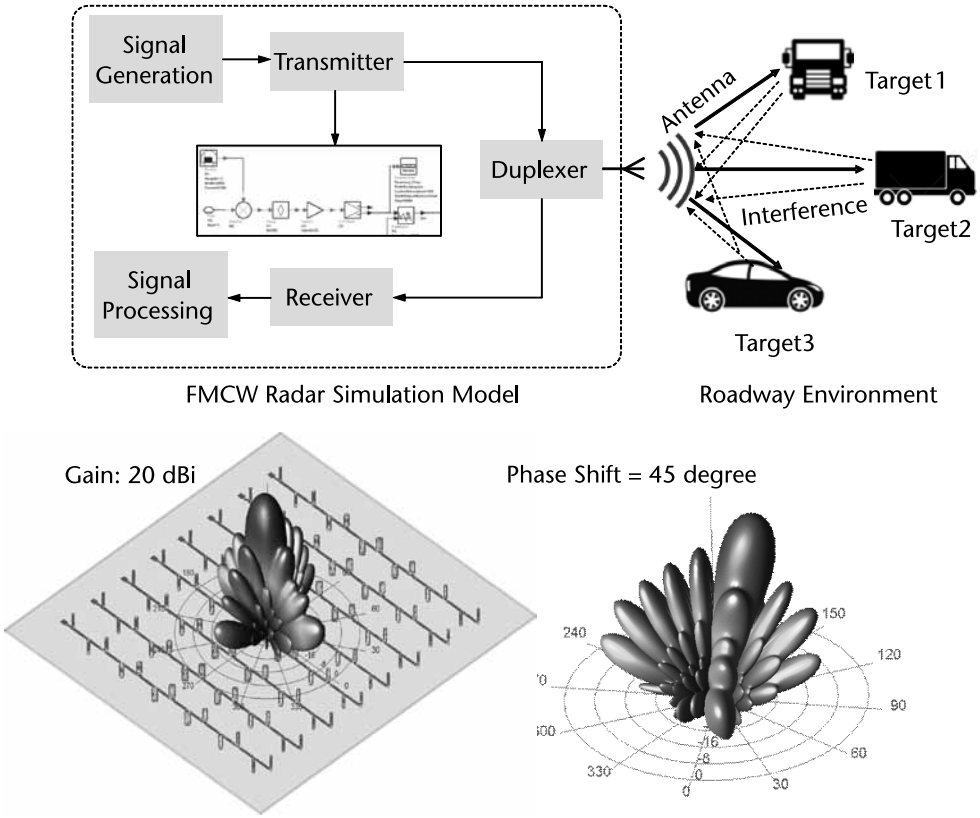

Figure 13.23 FMCW radar simulation model and antenna array 3-D radiation pattern.

radars are aimed to improve vehicle safety, efficiency, and economy. Radar can also be used for target identification and for detecting road conditions by making use of scattering signature information.

Automotive radar sensors are making it to the broader automobile market as part of ACC. ACC radar sensors provide range and closing-rate information to the cruise control system, which can control the brakes, throttle, and automatic transmission of the vehicle. The ACC system adapts the speed of the vehicle according to the speed of the vehicle ahead, to maintain a separation time interval between the two vehicles. The driver sets the minimum separation desired and the maximum speed. The radar system can also be used to locate and track multiple targets on the road ahead to anticipate traffic conditions in the driving lane. The same radar sensors used for ACC can also be used in pre-crash sensing, parking aid, and collision warning/avoidance (CW/A) systems, as shown in Figure 13.24. When used in a CW/A application, the radar sensors allow for warning signals to be given and for air bags to be activated. CW/A systems can also be designed to take control of a vehicle when a collision is anticipated.

13.8.1 ACC Radar System Requirements

The ACC radar must be able to detect targets of varying sizes up to 200m ahead. These targets could be moving relative to the radar at speeds of up to 250 km/h.

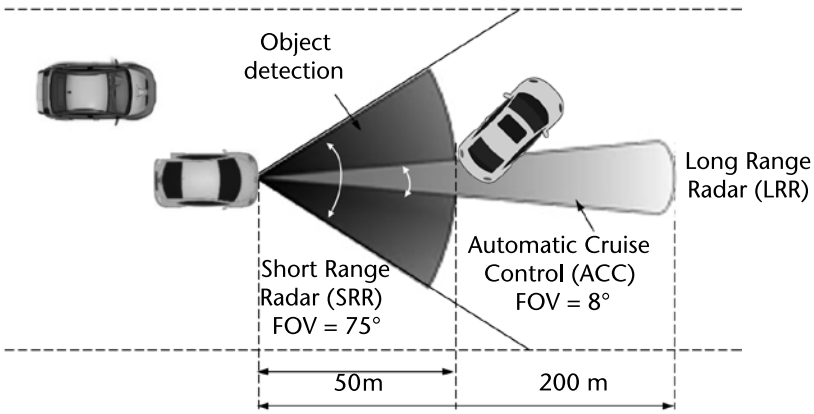

Figure 13.24 Precollision systems in vehicular radar to detect potentially dangerous crashes.

The radar must have an angular coverage of at least ±8° in the azimuth plane. Table 13.3 summarizes the typical performance specifications of ACC radar modules.

13.8.2 ACC Radar Antenna Design

A multimodal radar for an ACC system based on FMCW radar driving multiple antenna arrays is discussed in this section. This multibeam radar with an electronic antenna scanning technique operates at 77 GHz for long-range, narrow-angle coverage (200m, ±10°). This example illustrates the use of tapered series fed antenna array (15 × 16 elements) and Rotman lens for beam scanning. One of the primary requirements of ACC radar is low sidelobe levels. In a microstrip antenna array, the most commonly used approach for reducing the sidelobe level of a uniform array involves amplitude tapering, in which the excitation amplitudes of the array elements generally decrease with distance from the center of the array. To obtain the amplitude shading coefficients for a linear array of uniformly spaced point sources, several techniques [33, 34] have been developed.

The series-fed taper antenna array shown in Figure 13.25. The array mounted on the top of RT5880 dielectric substrate of 0.787-mm thickness and a relative

Table 13.3 Typical Specifications of ACC Radar

Parameters	*Typical Value*
Transmit frequency	76–77 GHz
Transmit frequency	>10 dBm
Target detection range	2m to 200m
Relative velocity	Up to 250 km/h
Angular coverage, azimuth	8.5° wide coverage with 3° minimum resolution
Angular coverage, elevation	3° to 4° single beam
Antenna gain	26–34 dBi
Antenna sidelobe level	>20 dBc

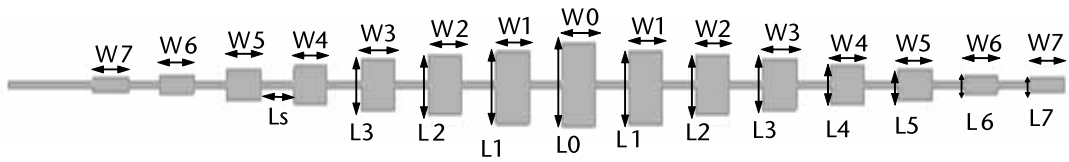

Figure 13.25 Tapered series fed microstrip antenna array design at 77 GHz.

dielectric constant $\varepsilon_r = 2.2$. The design parameter of antenna array is given in Table 13.4.

With end-fed arrays, the elements nearest the feed couple only a small amount of power and therefore must be narrow. The feed line (0.155 mm) is small compared to the narrowest patch. The radiating patches themselves are resonant so that the input line to a patch is matched. Each patch element is tapered according to the excitation current amplitude obtained from the Chebyshev synthesis method.

The antenna is simulated using the FEM full-wave analysis technique. The 1-D linear array has a –10-dB bandwidth of about 0.5 GHz, and the return loss at 77 GHz is –20 dB, the gain is 17.2 dB, the sidelobe level is approximately –24 dB, which meets the antenna sidelobe-level requirements for ACC radar, and the width of the E-plane is 7.2°. The planar antenna array is designed by using 16 linear antenna arrays as shown in Figure 13.26. The element spacing between the antenna elements is 0.5λ. The size of a 15×16 element antenna array is 41×43 mm.

The maximum array scan angle is ± 30°. The simulation result of its pattern is shown in Figure 13.27 for E-plane and H-plane. The sidelobe reduction technique is applied only in the E-plane direction. By comparing the 1-D linear array pattern, we can find that the E-plane pattern has not changed substantially, the beamwidth was compressed to 6.8° in the H-plane pattern, and the sidelobe level is –13.1dB.

13.8.3 Rotman Lens Design for Electronic Scanning of the Antenna Beam

The electronic scanning antenna (ESA) can position the antenna beam instantaneously to any position, but phase shifters for the millimeter-wave frequency range are pricey or for many frequencies not available. Rotman lenses offer a compact alternative for antenna scanning technologies. Multibeam concepts used the Rotman

Table 13.4 Tapered Series Fed Microstrip Antenna Dimensions

Parameter	*Value (mm)*	*Parameter*	*Value (mm)*
L0	2.205	L5	0.830
W0	1.255	W5	1.332
L1	1.874	L6	0.488
W1	1.306	W6	1.289
L2	1.546	L7	0.415
W2	1.264	W6	1.342
L3	1.314	Ls (spacing)	1.297
W3	1.131	Feed line *W*	0.155
L4	0.9776	W4	1.281

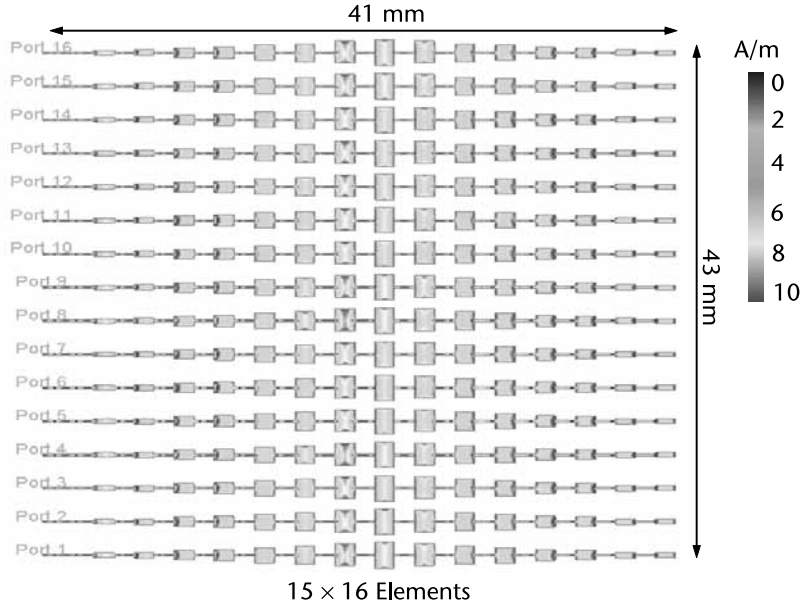

Figure 13.26 Current distribution in tapered series fed microstrip antenna array.

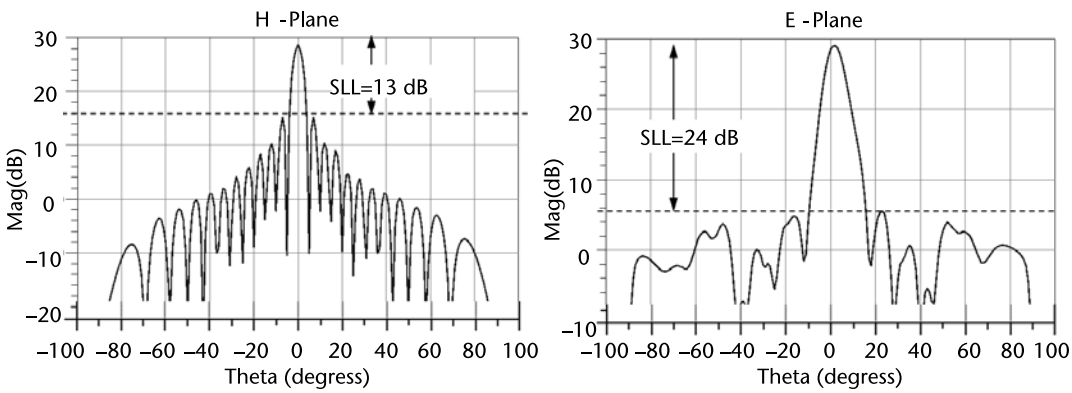

Figure 13.27 Tapered series fed antenna array radiation pattern at 77 GHz.

lens for the frequency range between 6 GHz and 94 GHz [35–38] and are used in many applications. A microstrip line connects each antenna input port with one antenna element as shown in Figure 13.28.

Based on the different lengths inside the Rotman lens, the radiated energy from the antenna elements will produce a beam along a defined direction. The Rotman lens equations include the design parameter for the parallel plate region and the length differences for the connecting lines between antenna port and antenna element. For a lens design based on solving Rotman's design equations, the output parameters contain the x, y-coordinates for the positions of the array and focal ports and the different length between the array ports and the antenna elements.

For the realized lens designs, nine main input parameters are used: focal angle, focal ratio, focal length, beam angle to ray angle ratio, maximum beam angle, number of beams, number of array elements, array element spacing, and design

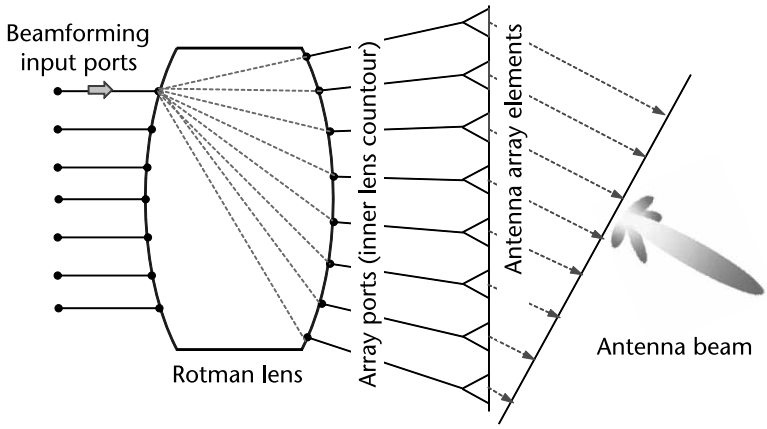

Figure 13.28 Sketch of the functional principle of a Rotman lens.

frequency. Figure 13.29 shows the complete antenna system along with a Rotman lens with 7 beam ports for the scan range ±25° and 15 × 16 antenna elements. As a compromise between the overall size of the lens and the phase aberrations of the beamforming system, a focal length of 8λ was chosen. By optimizing the ratio between the on-axis focal length and the symmetrical off-axis length f/g = 1.13, the residual phase errors remain <1° over the array antenna elements. Rotating the beam ports pointing towards the center of the output arc avoids asymmetrical illumination of the array ports.

Figure 13.30 shows a pattern of scanning beam at ±25° in the H-plane of the phased array antenna. As can be seen from the figure, when the scanning angle is 0, the gain is 29.5 dB, the sidelobe level is –24.2 dB, and the beamwidth is 6.8°. With the increase of the scanning angle, the sidelobe level increased gradually, and the gain also decreased slightly, as shown in Figure 13.31.

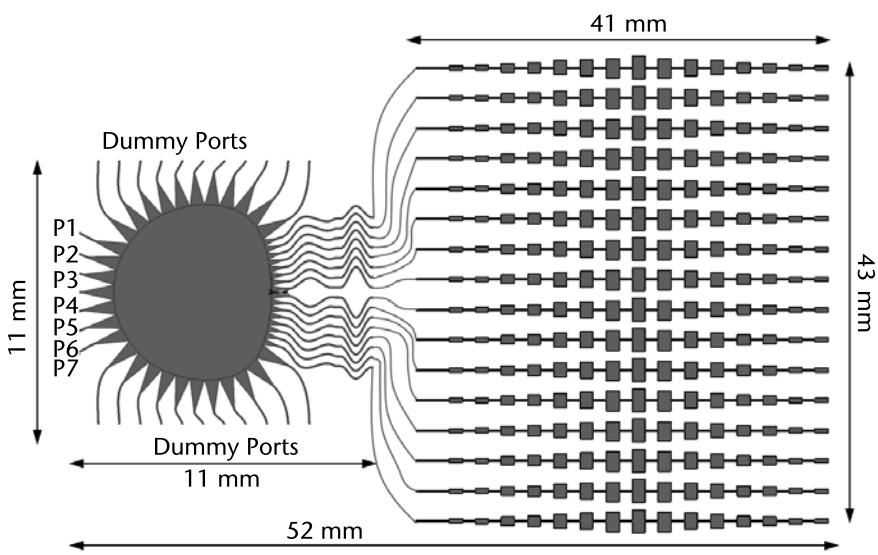

Figure 13.29 Microstrip antenna array design with Rotman lens.

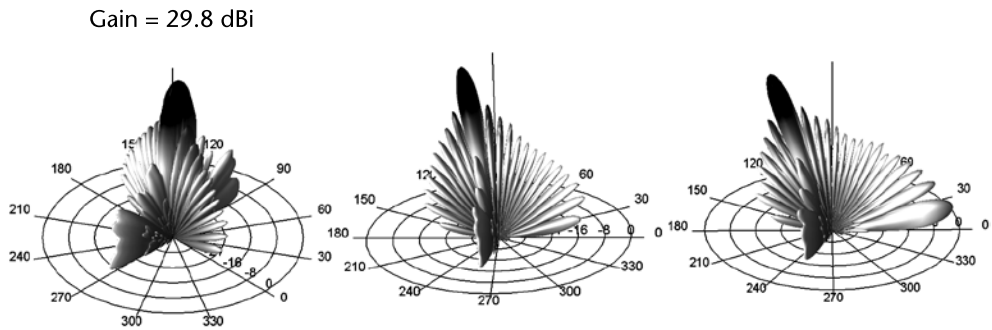

Figure 13.30 Antenna beam direction for phase differences 0°, 45°, and 90°.

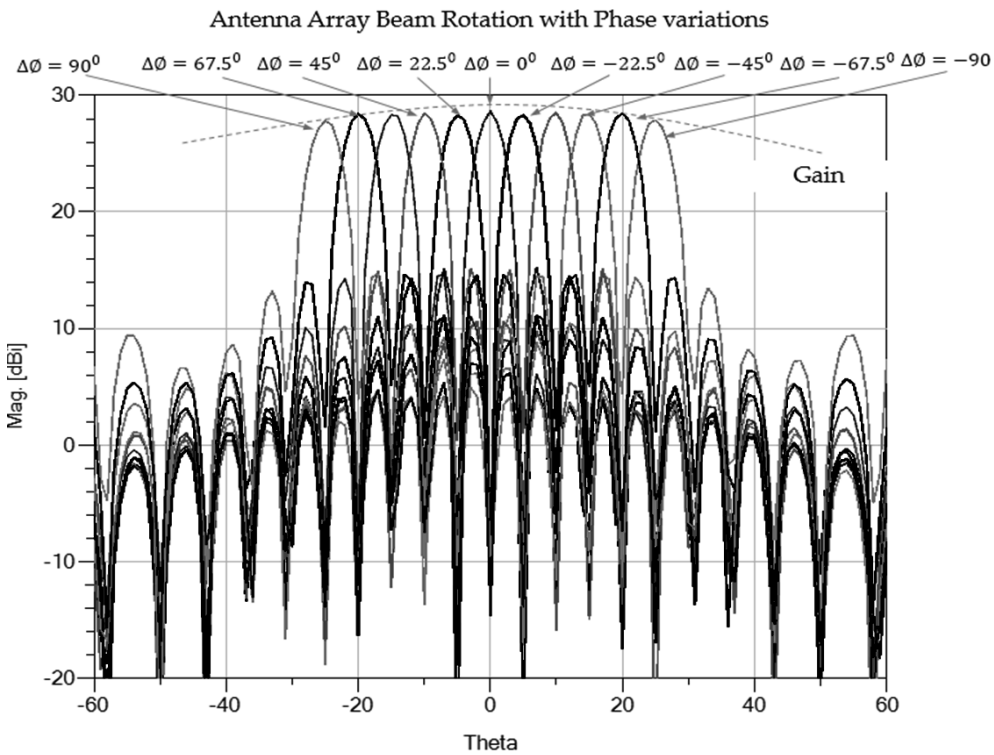

Figure 13.31 A 2-D antenna beam direction for different phase angle.

13.9 Automotive System-Level Simulation

Automotive system-level simulation includes comprehensive tools of FMCW radar waveform generation, signal modulation, antenna modeling, channel simulation, and signal processing to establish the unique automotive radar simulation scenarios. System-level simulation is important to validate the automotive radar at microwave and millimeter-wave frequency bands with various simulation scenarios such as evaluating the effect of the transmit and receive antenna channel number, weather, and clutter and verifying the unique radar waveform design, direction of angle (DOA) degree calculation, micro-Doppler effect detection, and more as shown in Figure 13.32.

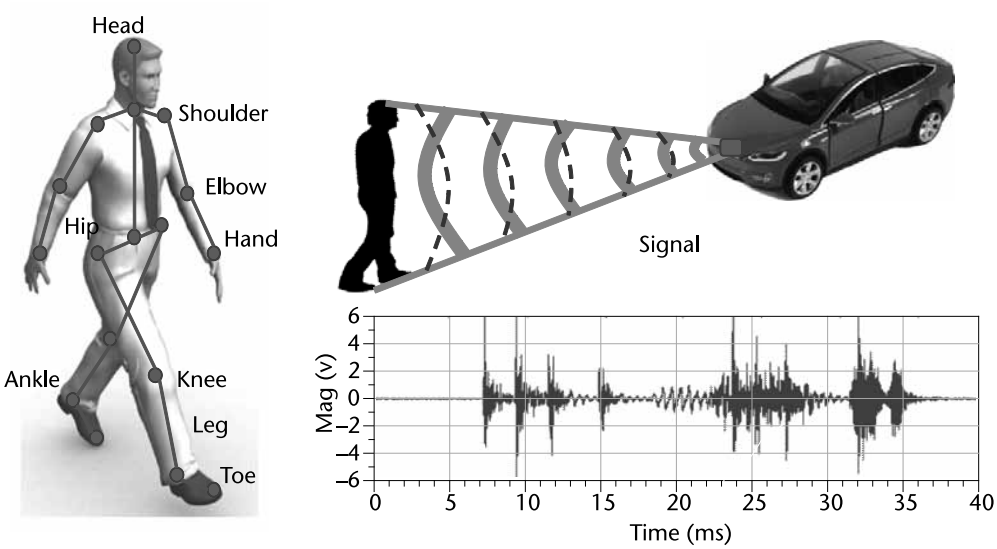

Figure 13.32 Walking passenger modeling and detection simulation.

The system-level simulation integrates critical, safety-conscious, and complicated scenarios into a reliable, leading-edge design of automotive radar. It provides solution under cost and time-constrained projects to design and develop an algorithm such as DOA and phase comparison. System simulations have proven to be a valuable aid during the development process, keeping costs for prototyping small and enabling development engineers to gain substantial insight into the circuits and investigate different conceptual approaches. The radar system-level simulator has been created in ADS to simulate the RF front end, including all nonlinear effects, target model, and antenna effect as shown in Figure 13.33.

Simulation setup consists of three main building blocks: the transmitter and receiver subcircuits and the channel cosimulation (including the antenna characteristics) that are all embedded in a dataflow simulator called Ptolemy, which is steering the whole simulation process from ramp generation to the back-end signal processing. All simulations are performed in a technique called Circuit Envelope (CE) in ADS. The equivalent simulation model of system-level simulation is shown in Figure 13.33.

13.10 Antenna Array for the ETC System

ETC, which enables the electronic collection of toll payments, is applied in different contexts (e.g., highways, bridges, tunnels) [39, 40]. ETC systems are usually developed by means of RFID technology. Passive tag systems are usually preferred due to their main advantage of being cheaper. The reader is placed at a certain height above the lane and irradiates energy toward the tag (placed on a vehicle) to enable a communication link.

A unique identification number that is embedded on the tag is read by the roadside RFID reader, as the vehicle reaches the toll plaza. This unique number is sent to a central computer. An applicable toll amount is deducted from a prepaid account

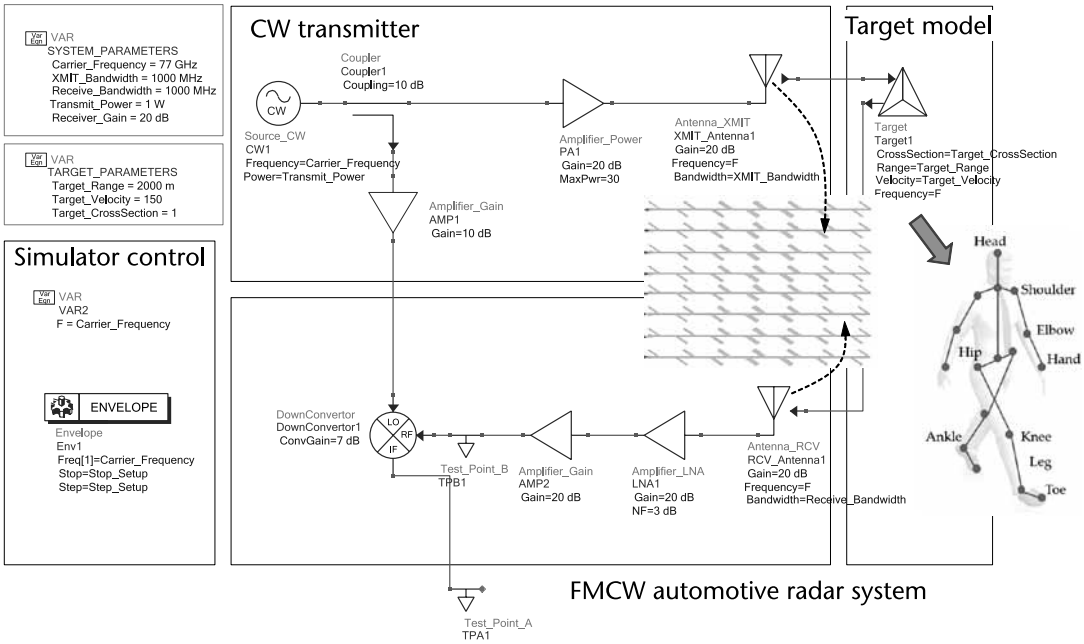

Figure 13.33 System-level simulation setup of radar including target model and antenna.

that is linked to that tag. The main objective of ETC is to eliminate the delay on toll roads. In 1986, ETC was first introduced in Bergen, operating together with traditional tollbooths. The world's first use of completely unaided full-speed electronic tolling was introduced by Trondheim in 1991. Any ETC system must address four aspects: vehicle identification, classification, transaction processing, and violation handling. Vehicle identification is usually implemented by means of opening a communication channel between the vehicle and the roadside unit (RSU), leading to an automatic vehicle identification (AVI) system. There are different AVI systems that can be categorized according to the employed communication technology: GPS, GSM, Wi-Fi, and DSRC in the UHF and microwave frequency spectra, as well as infrared [2]. Among them, DSRC is probably the most consolidated technology for road toll applications, as also demonstrated by the proliferation of numerous communication standards (IEEE 802.11p, ETSI, and so forth).

13.10.1 Phased Array Antenna for ETC Application at 5.8 GHz

In automatic toll collection and access control systems, an exact allocation between the transmitted data and the position of the communicating vehicles is important for an enforcement of unauthorized ones. A phased array antenna is a more flexible solution and is well suited to substitute several fixed beam antennas. The phased array antenna with a steerable narrow main lobe to cover four lanes for 5.8-GHz DSRC is shown in Figure 13.34. By using the microwave DSRC between the tag or the onboard unit (OBU), which is installed on the front window of vehicles and the reader or roadside unit (RSU) on the ETC road of toll collection station, the passing vehicles' toll could be collected automatically without stopping.

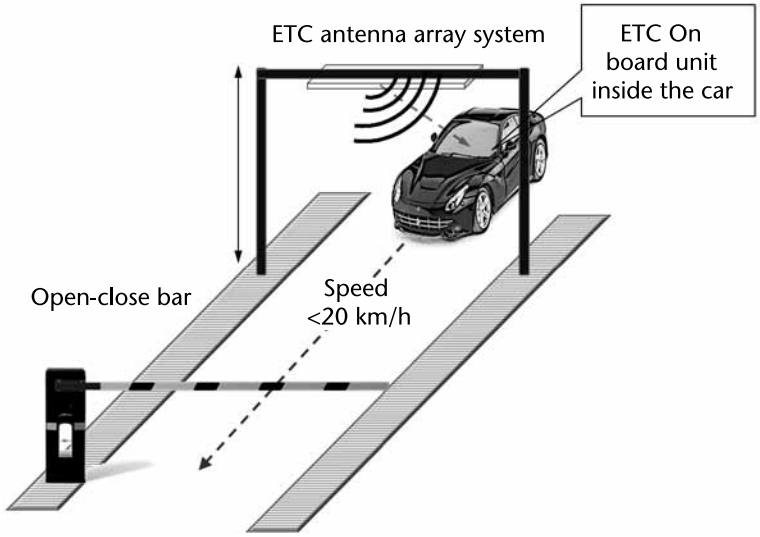

Figure 13.34 Antenna array system for RFID-based ETC.

For 5.8-GHz DSRC, an antenna must have a high gain, a low profile, a compatibility with a monolithic microwave integrated circuit (MMIC) as well as being simple and low-cost to manufacture. Planar microstrip patch arrays for left-handed circular polarization (LHCP), with 1×4 elements, is suitable for this application as shown in Figure 13.35. One of the advantages in the adoption of CP is its capability to achieve a good immunity to multipath propagation. In a vehicular environment, particularly rich of scatterers, this is an important advantage. Phase-shifter modules are designed using a 4×4 Butler matrix connected to each element of the antenna.

Microstrip array antenna resonating at 5.8 GHz provides a peak gain of about 13.2 dBi at the center frequency. It radiates a beam with a half-power lobe width of 18° in the horizontal plane and 34° in the vertical plane. The patch is printed on the Rogers 4003 substrate with the thickness h of 0.8 mm and ε_r of 3.38. It is easy to get CP of this type of antenna by trimming the opposite corners of a square patch and exciting at the feed point as in Figure 13.35. This single patch antenna has the dimensions 14.1×14.1 mm^2. A common measure for the quality of the achieved circular polarization is the AR.

$$\mathrm{AR}(\text{Axial ratio}) = {E_{max}}/{E_{min}} \tag{13.10}$$

This feed of antenna arrays is well matched with the array of 4 patch antennas at 5.8 GHz. The gain of this antenna arrays is 13.2 dB as shown in Figure 13.36.

The phased array antenna (reader antenna) and tag antenna installed in car are shown in Figure 13.37. The advent of autonomous vehicles will drive the need for multiple sensors, spanning microwave and millimeter-wave radar, as well as visible and infrared spectra.

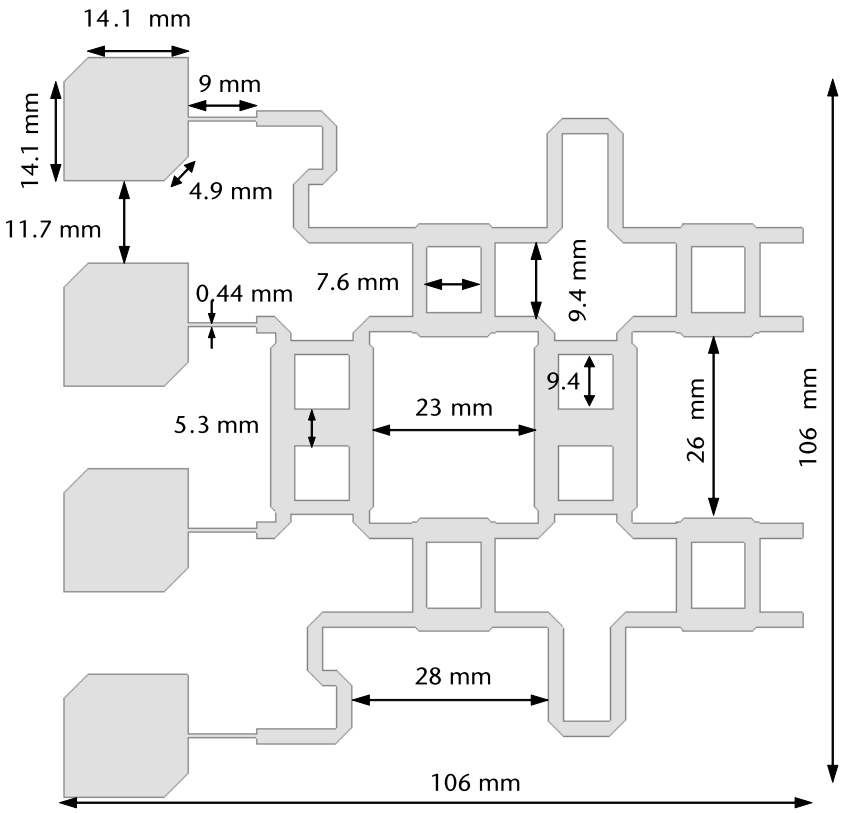

Figure 13.35 Phased array antenna design for ETC.

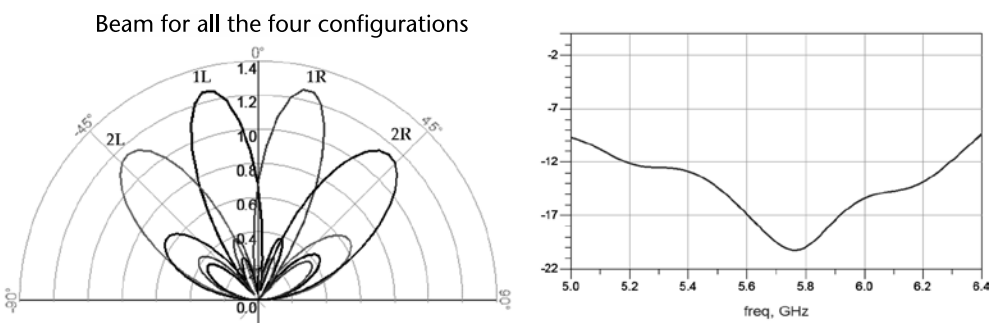

Figure 13.36 Antenna beam scanning and return loss plot.

In addition, radar sensors in the future are likely to have a significantly higher degree of functionality, with the ability to image the road scene, detect and track objects and obstructions, and locate safe paths through unfolding hazards. These radars will be able to monitor road conditions, even locating and reporting potholes and debris on the road. Modeling the installation effects of the radar antenna, including the defocusing effect of bumpers, fascia, and grills, is important. Analysis of the radar module and its installation location can affect the radar's ability to detect the direction of an object, as well as to reduce the radar's sensitivity to objects

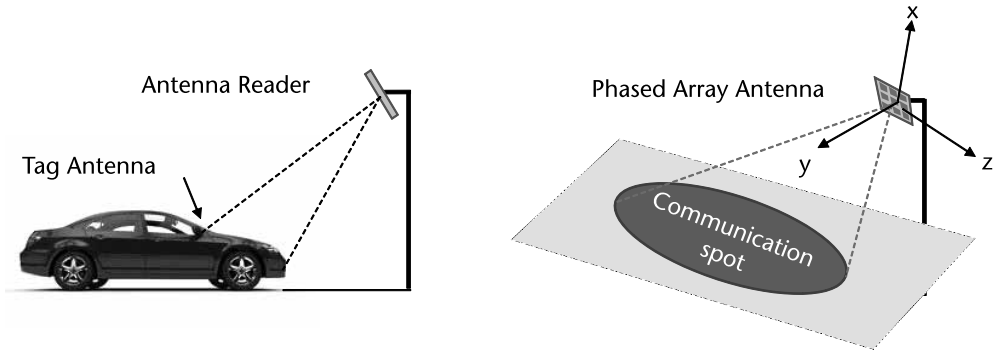

Figure 13.37 Antenna array and propagation model with a car.

that are more difficult to detect. The antenna design must tightly control the distribution of radiation energy, focusing it on the areas of the road under observation and minimizing energy broadcast to locations that are not of interest to the sensor. The antenna array is then placed on a virtual vehicle in a virtual world and evaluated as a complete radar system.

13.11 Summary

In this chapter, various antenna designs for automotive applications were discussed. Automotive antennas have seen significant advancements in recent years. Various services and requirements in automotive applications demand multiband antennas. In the near future, MIMO diversity and beamforming will become more important due to bandwidth-hungry multimedia applications. Future automotive developments will likely focus on two key areas: further integration of the antenna components with the vehicle structure, and new antenna configurations for radar and vehicle-to-vehicle communication services.

References

[1] Meinel, H. H., "Evolving Automotive Radar – From the Very Beginnings into the Future," *8th European Conf. Antennas and Propagation*, 2014, pp. 3107–3114.

[2] Rohling, H., "Milestones in Radar and the Success Story of Automotive Radar Systems," *11th Int. Radar Symp.*, 2010.

[3] "United States Frequency Allocations: The Radio Spectrum," *U.S. Department of Commerce, National Telecommunication and Allocations Information Administration*, Office of Spectrum Management, October 2003.

[4] Jairam, H., "Novel Blade Antenna Using Microstrip Patch Elements," *Microwave Conf., 19th European*, London, UK, 1989, pp. 1118–1122.

[5] Walbeoff, A., and R. Langley, "Multiband PCB Antenna," *Proceedings of IEE Microwaves*, Antennas and Propag., Centre, Sittingbourne, UK, December 2005, pp. 471–475.

[6] Lindenmeier, H., J. Hopf, and L. Reiter, "Active AM-FM Windshield Antenna with Equivalent Performance to the Whip Now as Standard Equipment in Car Production," *IEEE AP-S Int. S.*, Munich, Germany, June 1985, pp. 621–624.

[7] Murakami, et al., "Glass Antenna for Automobile," U.S. Patent No. 5,334,988, 1994.

[8] Heidari, A. A., M. Heyrani, and M. Nakhkash, "A Dual-Band Circularly Polarized Stub Loaded Microstrip Patch Antenna for GPS Applications," *Progress in Electromagnetics Research*, Vol. PIER 92, 2009, pp. 195–208.

[9] Fujimoto, K., and J. James, *Mobile Antenna Systems Handbook*, Norwood, MA: Artech House, 1994.

[10] Geissler, M., K. Scharwies, and J. Christ, "Intelligent Antenna Systems for Cars," *Proc. German Microw. Conf.*, 2014, pp. 1–3.

[11] Ghafari, E., A. Fuchs, and D. Eblenkamp, "A Vehicular Rooftop, Shark-Fin, Multiband Antenna for the GPS/LTE/Cellular/DSRC Systems," *Proc. IEEE-APS Top. Conf. Ant. Prop. Wirel. Comm.*, August 2014, pp. 237–240.

[12] Gallo, M., S. Bruni, and D. Zamberlan, "A Novel Fully Integrated Fin Antenna for Automotive Application," *Proc. Europ. Conf. Antennas Propag. (EuCAP),* 2014, pp. 2986–2989.

[13] Gavilanes, G., et al., "Comparative Characterization of Four Antennas for VANETs by On-Field Measurements," *Proc. Int. Conf. Antennas Electron. Syst.*, Tel Aviv, Israel, 2013, pp. 1–5.

[14] Johnson, J. M., and Y. Rahmat-Samii, "The Tab Monopole," *IEEE Transactions on Antennas and Propagation*, Vol. 45, No. 1, January 1997, pp. 187–188.

[15] Malley, O., et al., "Rear-Lamp Vehicle Detection and Tracking in Low-Exposure Color Video for Night Conditions," *IEEE Transactions on Intelligent Transportation Systems*, Vol. 11, 2010.

[16] Kraus, J. D., "A Backward Angle-Fire Array Antenna," *IEEE Transactions on Antennas and Propagatation*, Vol. 12, January 1964.

[17] Conti, R., et al., "The Wire-Grid Microstrip Antenna," *IEEE Transactions on Antennas and Propagation*, Vol. 29, January 1981, pp. 157–166.

[18] Zhang, L., W. Zhang, and Y. P. Zhang, "Microstrip Grid and Comb Array Antennas," *IEEE Transactions on Antennas and Propagation*, Vol. 59, pp. 4077–4084, November 2011.

[19] Zhang, B., L. Zhang, and Y. P. Zhang, "Design of Low-Cost Linearly-Polarized Microstrip Grid Array Antenna for 24 GHz Doppler Sensors," *IEEE Topical Meeting on Microwave Photonics*, Singapore, October 18–21, 2013.

[20] Taylor, T. T., "Design of Line-Source Antennas for Narrow Beamwidth and Low Side Lobes," *Trans. IRE*, Vol. AP-3, 1955, pp. 16–28.

[21] Balanis, C. A., *Antenna Theory: Analysis and Design*, 3rd ed., New York: Wiley-Interscience, 2005.

[22] Wu, D., et al., "A 76.5 GHz Microstrip Comb-Line Antenna Array for Automotive Radar System," *2015 9th European Conference on Antennas and Propagation (EuCAP)*, Lisbon, 2015, pp. 1–3.

[23] IEEE Standard for Information Technology – Telecommunications and Information Exchange Between Systems – Local and Metropolitan Area Networks – Specific Requirements, Amendment 6: Wireless Access in Vehicular Environments, 2010.

[24] Mariottini, F., et al., "Design of a Compact GPS and SDARS Integrated Antenna for Automotive Applications," *IEEE Antennas and Wireless Propag. Lett.*, Vol. 9, May 2010, pp. 405–408.

[25] Eom, S. Y., et al., "Design and Test of a Mobile Antenna System with Tri-Band Operation for Broadband Satellite Communications and DBS Reception," *IEEE Transactions on Antennas and Propagation*, Vol. 55, 2007.

[26] Mousavi, P., et al., "A Low-Cost Ultra-Low Profile Phased Array System for Mobile Satellite Reception Using Zero-Knowledge Beamforming Algorithm," *IEEE Transactions on Antennas and Propagation*, Vol. 56, No. 12, 2008, pp. 3667–3679.

[27] Kilian, A., and L. -P. Schmidt, "Conformal Superstrate Loaded Automotive Radar Antenna for Integration in Polymer Car Body Panels," *2010 Proceedings of the Fourth European Conference on Antennas and Propagation (EuCAP)*, 2010, pp. 1–5.

[28] Mariottini, F., et al., "Design of a Compact GPS and SDARS Integrated Antenna for Automotive Applications," *IEEE Antennas and Wireless Propagation Letters,* Vol. 9, 2010, pp. 405–408.

[29] Baek, S., and S. Lim, "Low-Profile Internal Automotive Antenna for WiBro Vertical Polarized Signal Reception," *2010 IEEE Antennas and Propagation Society International Symposium (APSURSI)*, 2010, pp. 1–4.

[30] Koch, N., "Triple-Service GPS-DAB/DMB-WiMAX Patch Antenna for Automotive Applications," *Loughborough Antennas & Propagation Conference 2009 (LAPC 2009)*, 2009, pp. 605–608.

[31] Belohoubek, E. F., "Radar Control for Automotive Collision Mitigation and Headway Spacing," *IEEE Transactions on Vehicle Technology*, Vol. 31, May 1982, pp. 89–99.

[32] Brus, E., "Vehicular Radar: The Ultimate Aid for Defensive Driving?" *Microwaves & RF*, September 1987, pp. 53–58.

[33] Riblet, H. J., "Discussion on 'A Current Distribution for Broadside Arrays Which Optimizes the Relationship Between Beamwidth and Side-Lobe Level'," *Proc. IRE*, Vol. 35, June 1947, p. 489.

[34] Pritchard, R. L., "Optimum Directivity Patterns for Linear Point Arrays," *J. Acoust. Soc. Amer.,* Vol. 25, September 1953, pp. 879–891.

[35] Rotman, W., and Turner R. F, "Wide-Angle Microwave Lens for Line Source Applications," *IEEE Transactions on Antennas and Propagation*, November 1963, pp. 623–632.

[36] Rausch, E. O., A. F. Peterson, and W. Wiebach, "Electronically Scanned Millimeter Wave Antenna Using a Rotman Lens," *Radar 97*, Publication No. 449, October 1997, pp. 374–379.

[37] Fuchs H. -H., and D. Nüßler, "Design of Rotman Lens for Beam-Steering of 94 GHz Antenna Array," *Electronic Letters,* Vol. 35, No. 11, May 27, 1999.

[38] Metz, C., et al., "Fully Integrated Automotive Radar Sensor with Versatile Resolution," *IEEE Transactions on Microwave Theory and Techniques*, Vol. 49, No. 12, December 2001, pp. 2560–2566.

[39] Li, M. W., et al., "On the Feasibility of Using 802.11p for Communication of Electronic Toll Collection Systems," *Proc. International Conference on Network-Based Information Systems (NBiS),* 2011.

[40] Fuxjaeger, P., et al., "Towards Privacy Preserving Wi-Fi Monitoring for Road Traffic Analysis," *IEEE Intell. Transp. Syst. Mag.*, Vol. 8, No. 3, 2016, pp. 63–74.

Selected Bibliography

Eibert, T. F., et al., "Electromagnetic Field Transformations for Measurements and Simulations (Invited Paper)," *Progress in Electromagnetics Research*, Vol. 151, 2015, pp. 127–150.

Guan, N., et al., "A Roof Automobile Module for LTE-MIMO Antennas," *Proc. IEEE-APS Topical Conf. Antennas Propag. Wireless Commun.*, Turin, Italy, 2015, pp. 387–391.

Gulam, M., N. Alsath, and M. Kanagasabai, "Ultra-Wideband Grid Array Antenna for Automotive Radar Sensors," *IET Microwaves, Antennas & Propagation*, Vol. 10, No. 15, October 12, 2016, pp. 1613–1617.

Ku, B., et al., "A 77–81-GHz 16-Element Phased-Array Receiver with ±50° Beam Scanning for Advanced Automotive Radars," *IEEE Transactions on Microwave Theory and Techniques*, Vol. 62, No. 11, November 2014, pp. 2823–2832.

Ku, B., et al., "A High-Linearity 76–85-GHz 16-Element 8-Transmit/8-Receive Phased-Array Chip with High Isolation and Flip-Chip Packaging," *IEEE Transactions on Microwave Theory and Techniques*, Vol. 62, No. 10, October 2014, pp. 2337–2356.

Mailloux, R. J., *Phased Array Antenna Handbook*, 3rd ed., Norwood, MA: Artech House, 2017.
Rabinovich, V., N. Alexandrov, and B. Alkhateeb, *Automotive Antenna Design and Applications*, Boca Raton, FL: CRC Press, 2010.
Rabinovich, V., and N. Alexandrov, *Antenna Arrays and Automotive Applications*, New York: Springer, 2013.
Xu, J., Z. N. Chen, and X. Qing, "CPW Center-Fed Single-Layer SIW Slot Antenna Array for Automotive Radars," *IEEE Transactions on Antennas and Propagation*, Vol. 62, No. 9, September 2014, pp. 4528–4536.
Yeap, S. B., X. Qing, and Z. N. Chen, "77-GHz Dual-Layer Transmit-Array for Automotive Radar Applications," *IEEE Transactions on Antennas and Propagation*, Vol. 63, No. 6, June 2015, pp. 2833–2837.

CHAPTER 14

Transceiver for Phased Array Radar

14.1 Introduction

The antenna is one of the most complicated aspects of RF design, but it is probably also the most ignored part of an RF system design. The performance, range, and legality of an RF link are critically dependent upon the antenna. However, antenna placement and analysis in RF system are often left until the end of the design and are expected to fit into whatever space is left, no matter how that location may affect the antenna performance. Many of these RF system designs ultimately go with degraded performance or multiple redesigns are carried out. Engineers designing an RF transceiver for the first time can quite easily confuse or misunderstand the meaning of antenna specifications and how to apply them in system-level analysis. For example, the gain of an antenna is very different from the gain of an amplifier.

This chapter presents the antenna design consideration in a complete transceiver system for the active phased array radar at C-band. The heart of an active phased array radar is the TRM. The TRMs provide power amplification during transmit and LNA during receive, as well as amplitude and phase control for beam steering and sidelobe reduction. Generally, complex RF and microwave transceiver chips are based on different fabrication technologies such as MMIC, LTCC, microwave integrated circuit (MIC), RF integrated circuit (RFIC), RF MEMS, and various packaging technologies on same RF board. Design and performance optimization of a complete transceiver system, along with an antenna system, are challenging due to the presence of a component based on multiple technologies in a single TRM. A low-power phased array transceiver that includes LNA, PA, single-pole-double-through (SPDT) switch, and lowpass filter (LPF), along with an antenna array is designed at 5.4 GHz to explain the design process of a transceiver integrated with an antenna system. This system-level design uncovers the key design challenges and techniques in implementing an integrated phased array transceiver.

14.2 TRM Architecture

TRMs are key elements in any active antenna aperture system. The transmit power is distributed at the aperture, eliminating the central high-power transmitter needed in passive phased array antennas [1]. A system-level block diagram of the transceiver (T/R) module is shown in Figure 14.1.

A transceiver module contains a transmit path and a receive path. The transmit path consists of a phase shifter, a driver amplifier, and a power amplifier (PA). A SPDT switch is used to provide the duplexing function between transmit and receive paths. The receive path consists of a limiter, an LNA, and a phase shifter. Active phased arrays use an individual solid-state T/R microwave module at each of their radiating elements. This way avoids the distribution and phase shifter losses encountered in the passive array design. Additionally, the active aperture array techniques help to generate very large power for long-range surveillance and tracking radar systems.

The concept of an active phased array is highly dependent on the availability of compact, low power consumption, and high-reliable TRMs. The large number of individual TRMs integrated with the respective radiating elements of the active array ensures a great degree of redundancy in case of the failure of the elements (graceful degradation). Compared to passive array systems, due to the close connection of the TRMs to the radiating elements, the losses are low. This results in a low receive noise figure and a high transmit efficiency. The main functions of a TRM are the generation of transmit power, LNA of received signals, and phase shift in the transmit and receive chain for beam steering.

To fulfill the demands on bandwidth, power, robustness, weight, and requirement of the TRM, new emerging semiconductor and packaging technologies are implemented for the next generation TRMs. The fast development of technology, especially in MMIC, SiGe, CMOS, and GaN, has enabled the integration of most of the components of TRMs into one small chip commonly called a multicore chips (MCC). Small chips (<20 mm^2) enable the possibility of integrating the electronics in the back of the antenna and reduce the cost of the phased array antenna system. As active phased array antennas consist of hundreds, thousands, or even tens of

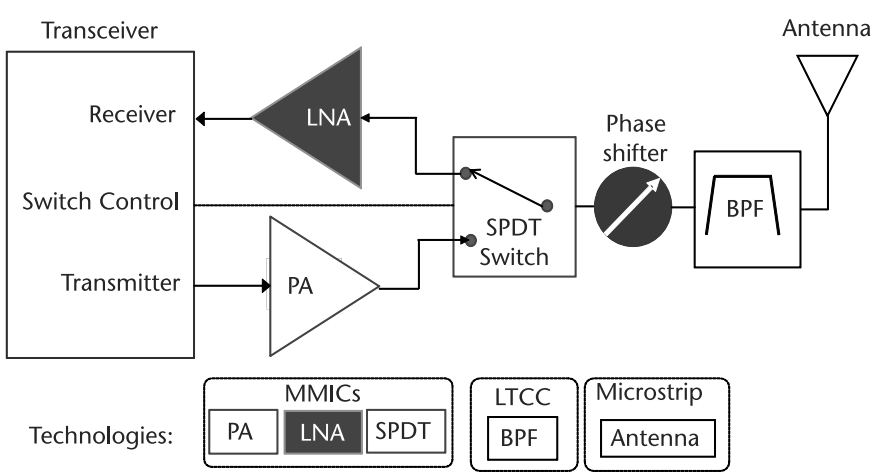

Figure 14.1 Block diagram of active phased array TRM.

thousands of elements per aperture, the TRM has a big impact on the cost and weight of the entire antenna system. The constraint aiming for the cost and weight reduction is the trend towards higher integration both on the module level and on the chip. TRM components for active phased array radar, as shown in Figure 14.1, are designed using three different major technologies listed here.

- MMIC technology: SPDT switch, LNA, and PA;
- LTCC technology: LPF, 3-pole LPF based on a 6-layer LTCC technology;
- Microstrip technology: Antenna, C-band microstrip patch antenna array.

TRM requirements are derived from the phased array antenna requirements and can vary significantly depending on the application. The following key parameters are typically specified for a TRM:

- Operating frequency and bandwidth;
- Beamwidth in azimuth and elevation;
- Maximum output power;
- Power-added efficiency (PAE);
- Spurious and harmonic output;
- Receive noise figure;
- Receive gain and third-order intercept;
- Number of amplitude and phase bits;
- Amplitude and phase root-mean-square (rms) errors;
- Mean time between failure (MTBF);
- Azimuth and elevation steering angles;
- Size of TRM.

These modules are sized to fit within the lattice of a phase array, which is a function of operating wavelength. A good rule of thumb is that, within the plane of the array, the modules must stack together to meet a half-wavelength spacing. Typically, the spacing between modules is chosen to be around 0.5–0.8λ_0 for wide antenna scanning beam performance. At C-band (5.4 GHz), the spacing between modules is 2.5 cm. All these modules are integrated into a single system-on-package (SoP) chip as shown in Figure 14.2.

The SoP module has a highly integrated transceiver MMIC mounted on thick anodized aluminum. Using a selectively anodized aluminum substrate, high-power Tx MMICs are mounted on the bottom aluminum layer. With this arrangement, heat can be easily dissipated from bare chips. The Rx MMICs are mounted on the top aluminum layer with embedded passives such as a microstrip line, a meander line inductor, and a metal-insulator-metal (MIM) capacitor for the bias circuit. To provide isolation and minimize the possibility of oscillation, the LNA is gated off in the transmit mode while the driver amplifier and PA are off in the receive mode.

PAE is a vital parameter for minimizing the prime power requirements and cooling load of the active array. Depending on the technology used, transmit PAEs on the order of 20% to 25% are typically achieved. For a high-power TRM package,

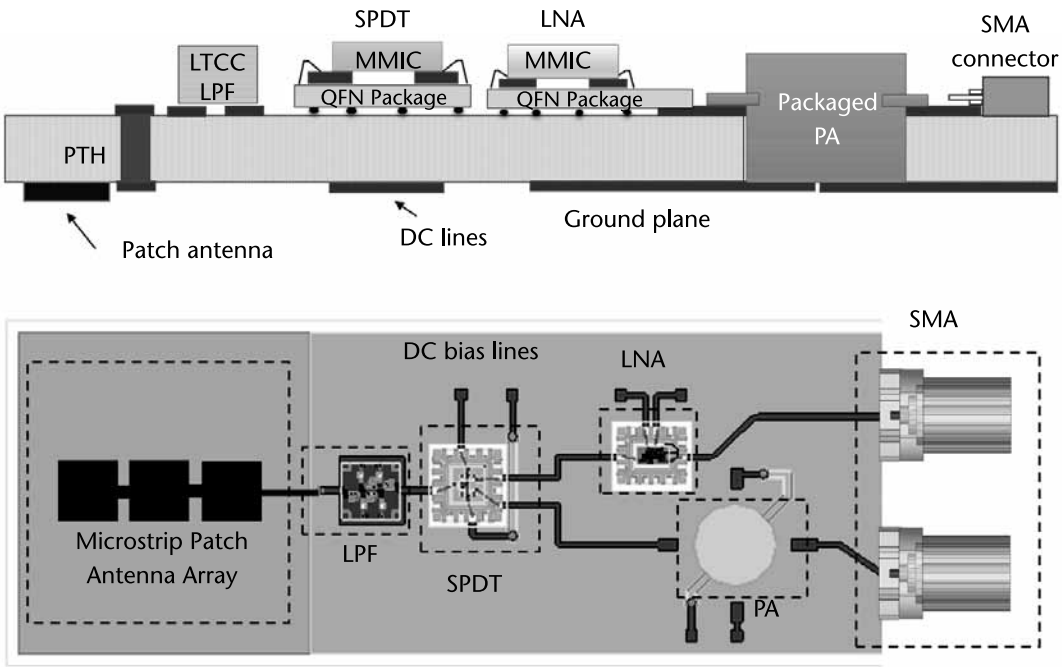

Figure 14.2 Cross-section (side and top) view of a transceiver system.

thermal conduction is a major parameter because it determines the operating temperature of the GaAs, SiGe, and GaN MMICs [2]. The amplitude weighting is essential to control the sidelobe performance of the beams, whereas proper phase shifting enhances the reception from the desired direction and rejects emissions from other directions, increasing SNR at the receiver output [3].

Because all the layers of the TRM include RF components, there is a need for efficient via-interconnects between the components placed on both side of the substrates. The important properties of the vertical via interconnects are the low insertion loss, sufficient electrical shielding, high mechanical stability, compactness, compatibility with multilayer structures, and easy assembly. Over the years, various researchers and companies developed several TRMs at different frequency bands and using multiple technologies.

14.3 TRM Design and Simulation

In the first phase of design, all individual transceiver components are modeled and optimized to meet design specifications separately. Individual components of the T/R model are simulated using circuit simulations, and then these chips are integrated on a PCB. The FEM solver has been used for complete chip and board-level simulation of the layout design to extract the couplings and parasitic parameters of TRM. EM simulation is carried out without active components (like FETs) for a complete system. The design is then simulated for the S-parameter using circuit simulators along with active components. The typical design specifications of a TRM are listed in Table 14.1.

Table 14.1 Design Specifications of Transmit and Receive Channels

	Specifications	
Parameters	*Tx*	*RX*
Frequency	5.2–5.4 GHz	5.2–5.4 GHz
Gain	20 dB	19 dB
Power output per channel	30 dBm	2.4 dB
Beamforming	Electronics	
Efficiency	>40%	
Insertion loss	3 to 6 dB	
Phase shift	360°	
Antenna gain	16–20 dBi	3–10 dBi
Power (T/R)	30 dBm	–50 dBm
P1dB	29 dBm	
OIP3	35 dBm	

A complete design flow diagram of the designed transceiver is shown in Figure 14.3. The design process of the individual components of PA, LNA, LTCC filter, and antenna module is discussed in this section.

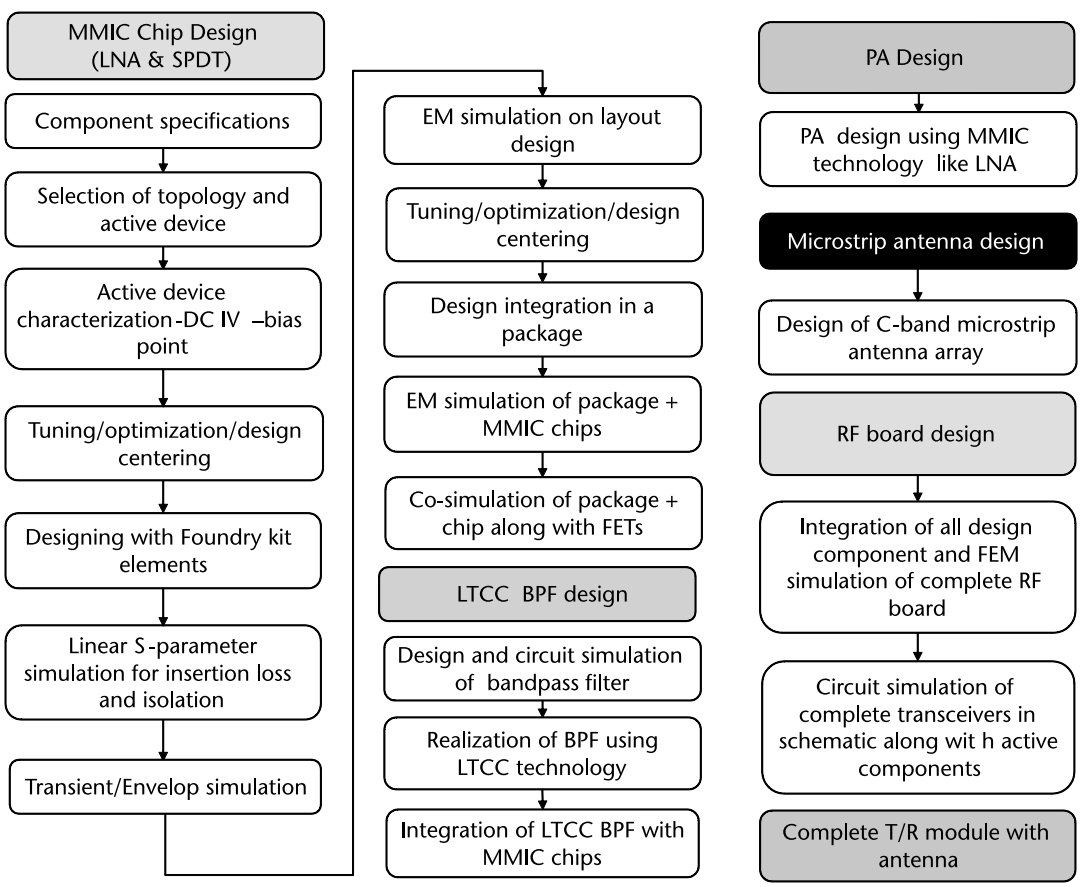

Figure 14.3 Design flow diagram of the complete transceiver system.

14.3.1 MMIC LNA Design

An LNA is used to amplify signals of very low strength, usually from an antenna where signals are barely recognizable and should be amplified without adding any noise. The LNA is a key component of any receiver system. The main function of a LNA is to amplify the small signal received from the antenna without adding too much noise signal. By using an LNA, the effect of noise from subsequent stages of the receiving chain is diminished by the gain of the amplifier. It is placed at the front end of a receiving system to improve the noise figure (NF) of the total system as well as providing the initial boosting of signal. LNAs with higher gain, lower NF, and wider bandwidth are desirable in most of the communication systems.

In the LNA design, the goal is to realize an NF as low as possible while surviving a large input signal. The first step in designing the LNA is to decide which profile provides the best combination of features and performance. The next step is to choose the device size. The selection of active device depends on the requirement of gain and NF of the amplifier. The progress in physics of semiconductors have been the origin of a new generation of components, called heterojunction transistors such as high electron mobility transistors (HEMTs). Another family of HEMTs, named pseudomorphic HEMT (pHEMT), offers better noise performance. The pHEMT process is selected based on high maximum available gain (MAG) and low NF. Device size affects the performance of LNAs such as bandwidth, DC power consumption, NF, and nonlinear performance [4].

In this section, the design and development of a single-stage MMIC LNA using 0.1-μm GaAs pHEMT process in microstrip architecture as shown in Figure 14.4 are discussed. A wideband bias decoupling circuit is designed at C-band, which also suppresses low-frequency bias-induced oscillation to stabilize the amplifier from dc to 8 GHz.

The operating point must provide a compromise between a minimal noise factor (NF_{min}) and a high gain (MaxGain). The operation point (V_{ds} = 3V, V_{gs} = –0.5V) on a biased curve is selected as the biasing point. $\lambda/4$ tramsmission lines are

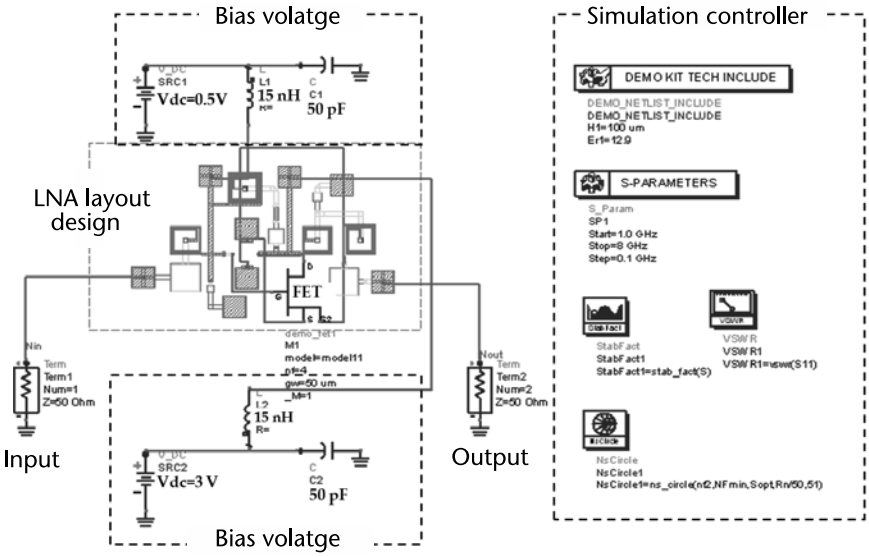

Figure 14.4 Single-stage LNA design using GaAs.

implement and folded in the biasing circuit to minimize the resistive loss adding to the signal.

In a multistage LNA design, a good compromise between each stage's noise and gain performance is made to meet the NF and gain specifications of the LNA. According to Friis' formula [5]:

$$N_f = N_{f1} + \frac{N_{f2} - 1}{G_1} + \frac{N_{f3} - 1}{G_1 G_2} + \ldots \tag{14.1}$$

So, to obtain low noise behavior from the overall amplifier not only the noise figure of the single stage must be considered but also its available gain, as shown in (14.1). When an amplifier is unstable, there is a risk of oscillations, due to reflection coefficients at the input and at the output of the transistor that are greater than unity. Stability is the most important factor that should be considered when designing LNA; the K-B factor is always used to determine if the amplifier is unconditionally stable [6]:

$$K = \frac{1 - |S_{11}|^2 - |S_{22}|^2 + |\Delta|^2}{2|S_{12}S_{21}|} \tag{14.2}$$

$$B = 1 + |S_{11}|^2 - |S_{22}|^2 - |\Delta|^2 \tag{14.3}$$

$$\Delta = S_{11}S_{22} - S_{12}S_{21} \tag{14.4}$$

When considering the stability of the amplifier, not only the stability in the operating frequency range should be checked, but also stability in the whole band (from DC to f_{max}) should be checked to make sure that it is unconditionally stable. Conditional stability (Stability Factor below 1) is when the stability of the quadruple is checked only for certain source impedance and load values at the operating frequency. If the stability conditions are satisfied whatever the impedance of the source and the load, the quadruple is then unconditionally stable (stability factor over 1).

In the design and optimization process, first LNA is realized using ideal components based on behavioral models. After design optimization for the desired performance, these idle components are replaced with actual MMIC component models provided by foundries. EM simulation is the performance along with trace routing and a chip-package model. Figure 14.5 shows the LNA design and matching networks.

Simulated results from 1 to 8 GHz are shown in Figure 14.6. LNA gain is 6.7 dB and the NF value is 2.64 at 5 GHz. The NFs in the microwave regime typically range from 1 to 2 dB. Including losses and other effects, module NFs in the 3 to 4-dB range are generally good.

In Figure 14.6, NF and gain of a GaN-based MMIC low noise amplifier are shown. The obtained NF is very close to the expected one over the whole frequency

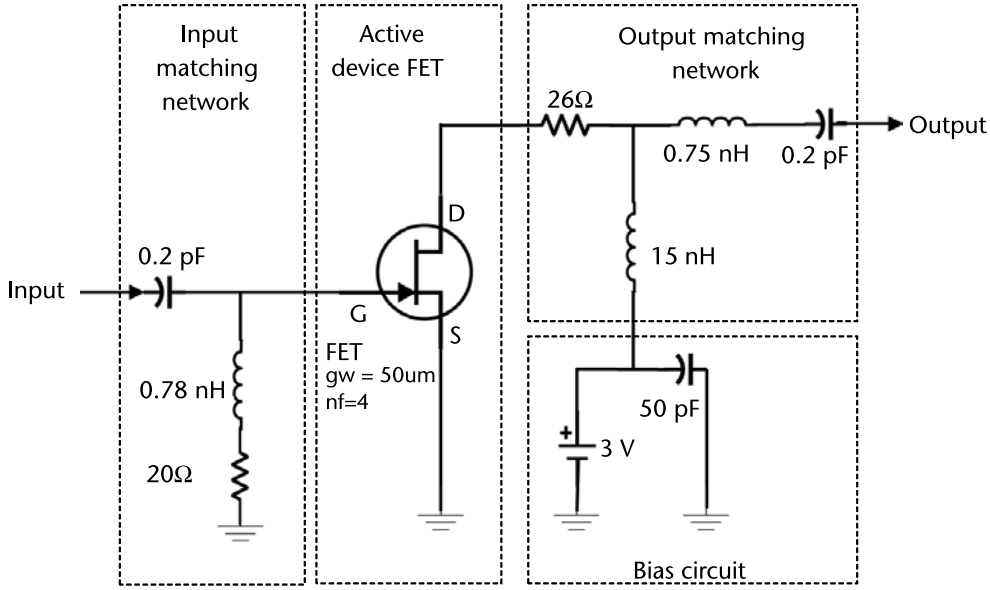

Figure 14.5 LNA layout design and matching networks.

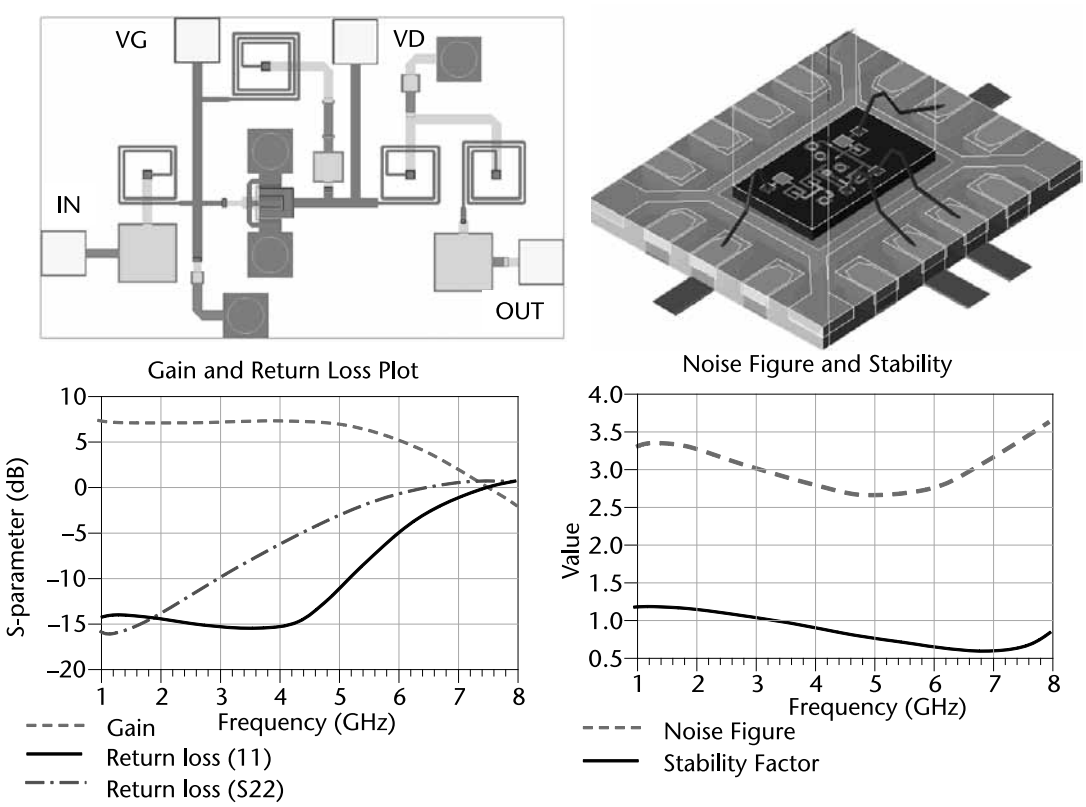

Figure 14.6 Layout design and LNA with QFN package and simulated results.

band. For frequencies from 3 GHz up to 7 GHz, the NF is lower than 3 dB. The overall performance summary of the designed LNA is given in Table 14.2.

14.3.2 PA Design

In early phased array radar, microwave tubes were key component for RF power amplification. Even today in some radar applications, microwave tubes, mainly miniature traveling-wave tubes (TWTs), are used as the RF PA for active phased arrays. However, it is not practical to apply TWT in active phased array antennas for each radiating element because of the large volume, weight, and cost of TWTs. Generally below X-band, silicon RFIC meets many phased array system requirements, but for efficient, linear power amplification, GaAs MMICs are much preferred. In most TRMs, GaAs MMIC amplifiers are used with typical output power levels in the range of 5W to 10W [7, 8]. Broader bandwidth, higher output power levels, increased PAE values, and higher operating voltages are some advantages of GaAs MMIC. For high-power applications, the use of amplifiers based on AlGaN/GaN is a very promising approach [9, 10].

The design of a broadband PA is considerably more complex than that of a linear amplifier. In a PA, an active device operates in a nonlinear regime (i.e., its properties depend not only on the terminations at the signal frequency but also on the signal power level and terminations at harmonics). The design discussed in this section is based on GaAs pHEMT. The starting point for the HEMT model is the drain current formulation. A common feature in the drain formulation [11, 12] is the drain voltage saturation parameter:

$$I_D \sim \tanh(\alpha V_D) \tag{14.5}$$

The drain current variations near pinch-off are given by [12]:

$$I_D \sim \beta(V_D - V_{DSO}) \tag{14.6}$$

The load-pull technique [13] is adapted to optimize the impedance for getting the maximum values of power efficiency and output power of the amplifier. The approximate value for the load impedance can be estimated as:

Table 14.2 Performance Summary of Designed LNA

Parameters	*Value*
Frequency	5 GHz
Voltage gain	6.7 dB
Return loss (S_{11})	–11 dB
NF	2.7
Input IP3 in-band	12 dBm
DC	4 mA
Supply voltage	3V

$$R_{opt} = \frac{V_{dc}}{\left(\frac{I_{max}}{2}\right)} = \frac{V_{dc}}{I_{dc}} \tag{14.7}$$

With the help of the load-pull technique, load and source pull analysis is carried out on the design. In this technique, PAE contours and output power contours are drawn in the Smith chart as shown in Figure 14.7. An optimum output impedance of the device is chosen using these contours. A similar procedure is used to analyze the effect of source-pull. The load impedance R_{opt} for optimum output power is determined based on the load-pull simualtion with a large-signal model. A matching network is then designed to match the impedance R_{opt}.

In the case of multistage PA, if the gate and drain-line inductors are matched, and the drain capacitance is made equal to the gate capacitance, then the input and output currents will be phase synchronized [14]. Assuming this condition and using image-impedance-matched terminations, the voltage gain can be derived as

$$\frac{V_{out}}{V_{in}} = \frac{-N \cdot g_m}{2 \cdot \sqrt{1 - \left(\omega / \omega_c\right)^2}} \sqrt{\frac{L}{C}} e^{-N\theta} \tag{14.8}$$

where N is the number of stages, g_m is stage transconductance, ω_c is cutoff frequency of the lines, and θ is the propagation constant of the lines. The performance of a multistage amplifier is limited by the weakest link in the cascade of stages from input to output. The amplifier can be optimized by recognizing the impact of gain, output power, and PAE from each stage on the overall performance. The overall PAE of a three-stage amplifier is given by [15]:

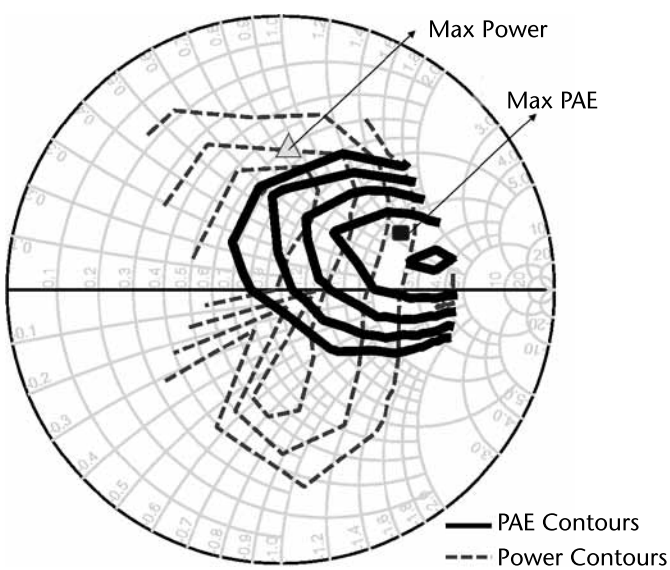

Figure 14.7 PAE contours and output power contours.

$$PAE \approx \frac{1}{1/PAE_3 + 1/(G_3 \cdot PAE_2) + 1/(G_2 \cdot G_3 \cdot PAE_1)} \tag{14.9}$$

where G_{1-3} and PAE_{1-3} are the respective gain and PAEs of each stage.

A two-stage MMIC balanced amplifier is designed to meet the requirements of a transmit phased array operating at 5 GHz with an output power in the range of 1W. The complete design consists of 2 two-stage amplifiers in parallel as shown in Figure 14.8. The input signal to the pair of amplifiers is split via a branch line coupler, which is implemented with microstrip lines. The outputs from the two amplifiers are combined via a branch line coupler identical to the one at the input. The design process includes evaluation of the HEMT device used in this amplifier, including determination of device transconductance g_m versus bias and load-pull analysis. This allows the designer to pick a bias point where the g_m is maximum, which also maximizes the gain. For a minimum NF, the optimal source impedance is calculated, as well as the corresponding load impedance for maximum gain, both as a function of bias voltage. Usually, the first-stage device is quite unstable by itself, and stabilization networks are added.

Input matching network is designed using shunt-C, series-L matching network to generate the desired source impedance for the input stage. An interstage matching network transforms the impedance seen looking into the second stage to the desired impedance to present to the first stage. Output matching is designed by using series-C, shunt-L or series-L, shunt-C networks for generating the desired load impedance for the second stage. Large signal and small signal FET performance is simulated using the circuit simulation models.

The PA matching networks are designed to provide a wide small signal and power bandwidth simultaneously. The PA is unconditionally stable and includes on-chip power supply bypassing capacitors. Lumped element capacitors and spiral inductors are used in design to reduce the size of the chip. Layout design, circuit simulation test bench, and PA results are shown in Figure 14.9. The maximum measured output power is 15W, when biased for class-AB operation with V_{DS} = 30V. The gain of the PA is 25 dB.

The overall performance summary of the designed LNA is given in Table 14.3.

14.3.3 MMIC SPDT Switch Design

SPDT switches are extensively used in phased array radars for T/R applications. SPDT switches are used to selectively couple signals between two RF ports, where

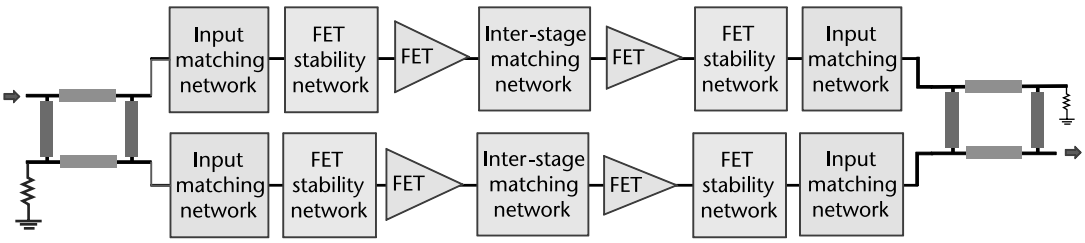

Figure 14.8 Design MMIC balanced PA topology.

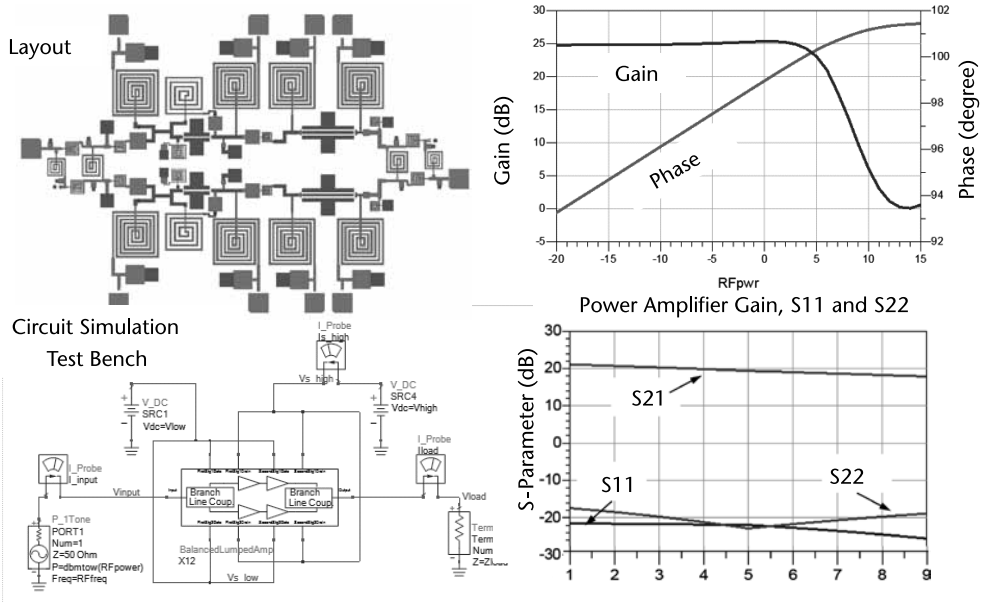

Figure 14.9 MMIC PA design, circuit simulation model, and results.

Table 14.3 Performance Summary of Designed PA

Parameters	*Value*
Frequency	5 GHz
Tx output power level	26.5 dBm
Vcc supply voltage	5V
PA gain	24 dB
PAE	11.80%
Package	QFN
1-dB compression point	25.7 dBm
NF (minimum)	2.8

it provides a simultaneous high isolation to the inactive path and low insertion loss for the active path. GaN HEMT is appropriate for high-power MMIC switch designs due to its high thermal conductivity, high breakdown voltage, and high electron mobility. High-power microwave SPDT switches are needed for high-power handling in phased array systems. Although a mechanical switch can handle high power, it is large, slow in switching time, heavy, and costly. Solid-state switches based on the pin diode can also handle high power, but it draws significant DC when the diodes conduct [16]. This is unacceptable for the low DC power systems. Another disadvantage of the PIN diode is that it is a current-controlled device; therefore, it requires more complex driver circuitry than voltage-controlled FETs. The GaAs FET switches draw very low DC compared to pin diode, but these have limited RF power-handling capability [17]. Design specifications of a typical SPDT switch are listed in Table 14.4.

Table 14.4 MMIC SPDT Switch Design Specifications

Parameters	*Value*
Frequency range	C-band, 5% bandwidth
On-state insertion loss	≤0.6 dB
Off-state isolation	≥30 dB
0.1-dB compression	≥4W (+36 dBm)
Switching time	≥25 ns
Return loss	≥10 dB

Rise time and fall time are fundamental to switch design. This is the time required for switching to take place between two states in the switch response. Rise time is defined as the period between the off state to the on state, typically from 10% of this condition to 90% of the square-law-detected RF power and can be expressed in terms of circuitry resistance ($R_{circuit}$) and load capacitance (C_{load}) as shown in (14.10) [18]:

$$T_r = 2.2R_{circuit}C_{load} \tag{14.10}$$

Conversely, fall time is the period between 90% on state to 10% off state and can be calculated using (14.11):

$$T_f = 2.2R_{circuit}C_{load} \tag{14.11}$$

FOM is used to rate the switching characteristics of different switching elements, which is based on capacitance realization when FET is in the off state (C_{off}) and R_{on} values. The FOM to rate SPDT switches can be represented by [19].

$$FOM = \frac{1}{2\pi C_{off}R_{on}} \tag{14.12}$$

In SPDT switch design, the three most common configurations are series diodes, shunt diodes, and a combination of series and shunt diodes. Many commercially available SPDT switches make use of both series and shunt devices in combination. The SPDT switch discussed in this section has been designed using standard series-shunt configuration. The MMIC design process kit contains metal semiconductor field effect transistors (MESFETs) with nonlinear models, which are used as basic switching elements. SPDT switch has one input and two output arms as shown in Figure 14.10.

RF power is directed into one of the arms by switching on the required arm and switching off the other arm. The active switch provides a low insertion loss and good return loss usually matched with 50Ω. The inactive switch should provide high isolation and high input impedance, ideally providing a perfect open circuit. With perfect isolation, ideally, no power should be detected in the off arm. However, due to the parasitic and coupling effects, some RF power leaks into the

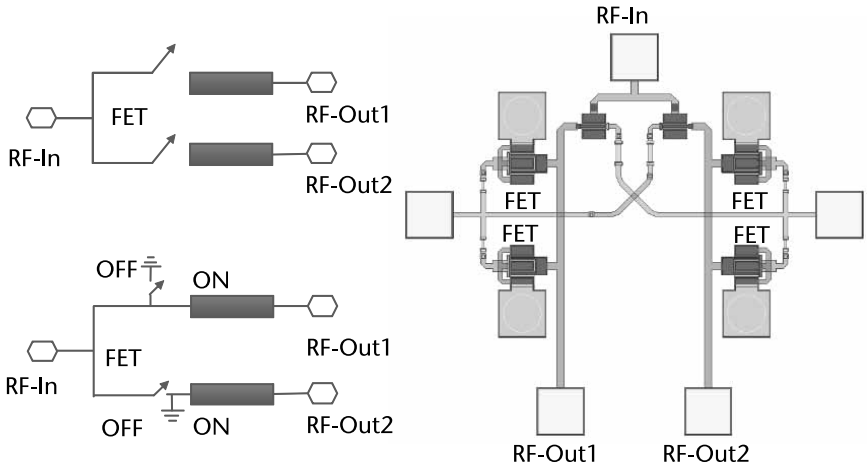

Figure 14.10 Basic topology of SPDT switch and layout design of SPDT switch.

off arm. The leaked power is grounded by placing a shunt MESFET in the on state as shown in Figure 14.10. This switch is designed based on GaAs MMIC for low insertion loss and high isolation from DC to 10 GHz. The use of FETs as switching elements is well recognized [20]. When the gate is biased at 0V (the on state), a small resistance is present between the source and drain. When the gate is biased beyond pinch-off (the off state), the source and drain are capacitively coupled.

The topology of the DC to 10 GHz SPDT switch is indicated in Figure 14.11. Switching FETs are used in a shunt configuration in conjunction with quarter-wave transformers. The circuit comprises two equal but independently biased arms; in a

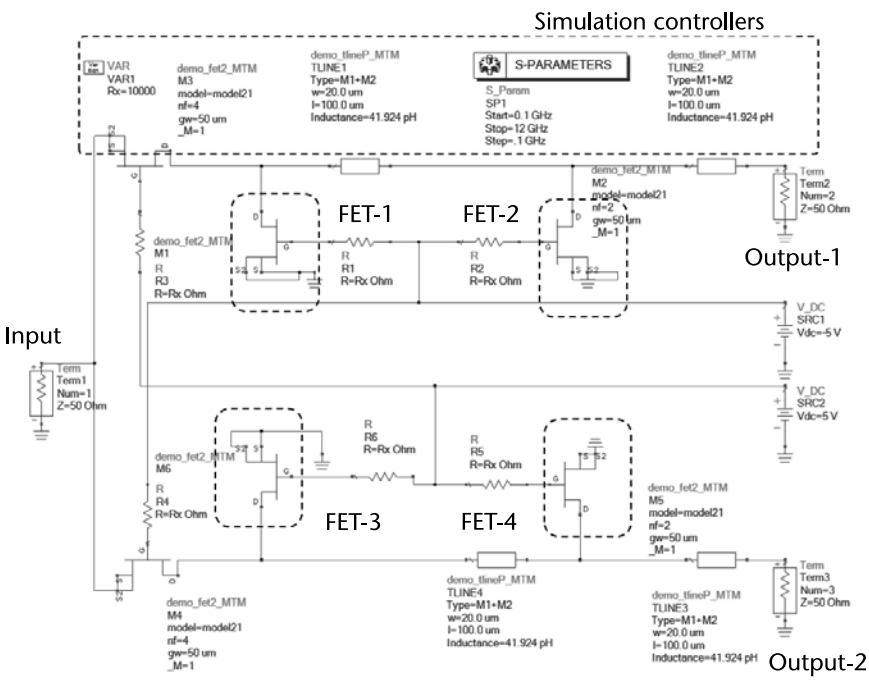

Figure 14.11 Circuit design of SPDT switch using MESFET.

normal operation, one arm passes the signal (the on arm) and the other arm isolates the signal (the off arm). The FETs are connected through series inductive lines. This improves the isolation by reducing the power detected in the off arm.

RF flows from source to drain when the gate is at 0V. Hence, series FETs have input and output at the source and drain, respectively. One single DC bias is used to connect all on devices and another single DC bias is used to connect all off devices. After verifying the basic switch action with idle components, these are replaced with MMIC design foundry components. The chip is packaged using QFN package. QFN chip size is 3.2 mm × 3 mm as shown in Figure 14.12. The small signal performance of the DC to 8-GHz switch is shown in Figure 14.12. Insertion loss is between 2 dB and 3 dB up to 10 GHz. Isolation is more than 30 dB in entire frequency band.

14.3.4 LTCC LPF

LTCC is a multilayer ceramic technology that has the ability to embed the passive elements, such as resistors, capacitors, and inductors, into a ceramic interconnect package. In this, the active elements are mounted in the top layer. As a multilayer

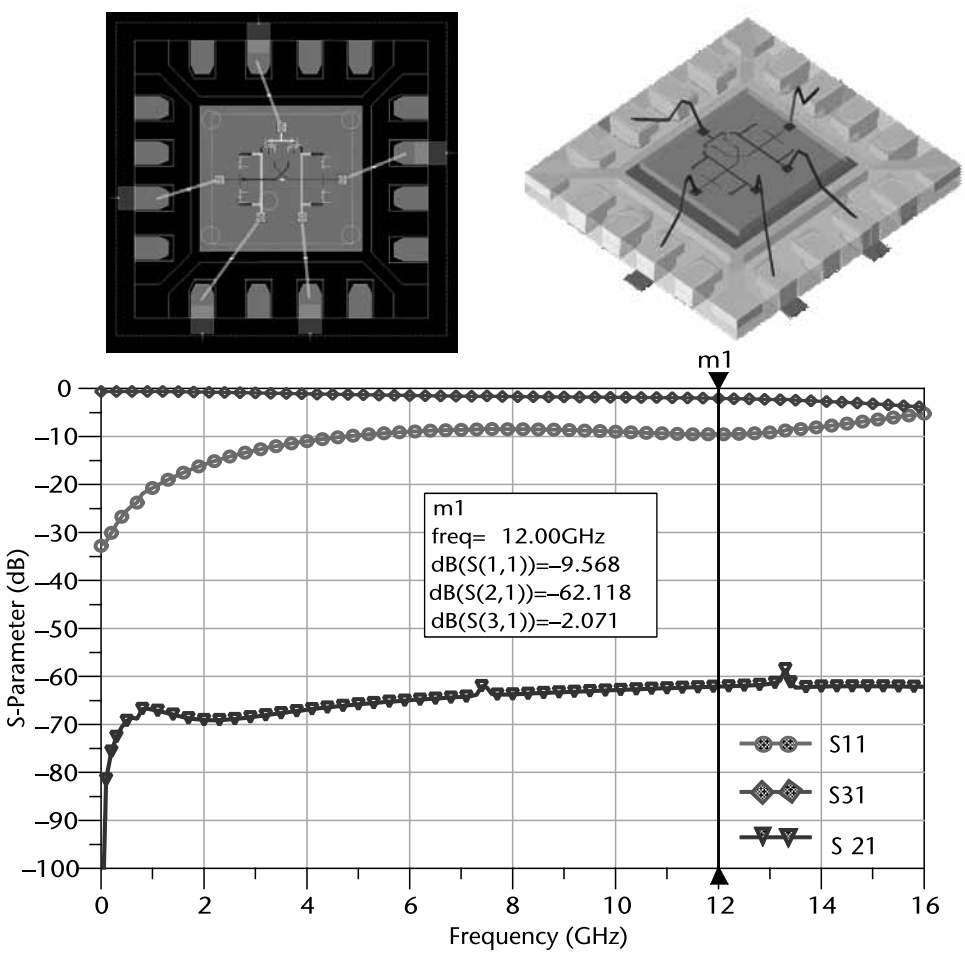

Figure 14.12 SPDT switch inside QFN package and S-parameter results.

ceramic technology, LTCC technology has an ability to print complicated circuits at each layer. Then all layers are punched and dried in parallel. These layers are then aligned, stacked, and co-fired into a highly compact structure at a temperature between 800°C and 900°C [21]. In LTCC, the substrate serves both as carrier for components and lines and as central part of the housing. The multilayer capability of LTCC is the enabler for a very compact design with nearly all control and supply lines buried in inner layers. One major drawback of LTCC is its poor thermal conductivity, which is usually in the order of 3–4 W/mK. Another disadvantage is the difficulty of managing the shrinkage control during the firing process.

The LPF is an important passive component in RF front-end sections. A good LPF has low passband insertion loss and high suppression at the rejection area. High suppression can be provided by generating finite transmission zeros at the rejection area. LTCC technology plays an important role in filter design. The size of the LTCC filter mostly depends upon the realized form of the inductance implemented in the LTCC structure. The inductances can be realized by the grounding transmission lines in LTCC structure, for the self-induction of the lines [22] or by the coupling effect between two transmission lines [23]. The filter, first optimized by the modern network synthesis method, is based on the lumped lowpass prototype filter. The LC circuit of common lowpass prototype filter is shown in Figure 14.13. LPF design has many different solutions, in which the most commonly used are the Butterworth filter and the Chebyshev filter. The Butterworth filter has flatter response characteristics, but the Chebyshev filter has steeper attenuation characteristics. A 3-pole LPF up to 6 GHz has been designed by using a spiral inductor and capacitor. The locations of the transmission zeros are estimated by the network analysis method. The filter is realized in the LTCC process and simulated by a full-wave FEM simulator.

The basic components' spiral inductor and capacitor have been designed with parameterized value. LPF results, as shown in Figure 14.14, have been optimizing at 5 GHz by varying parameters that change the value of the inductor (L) and

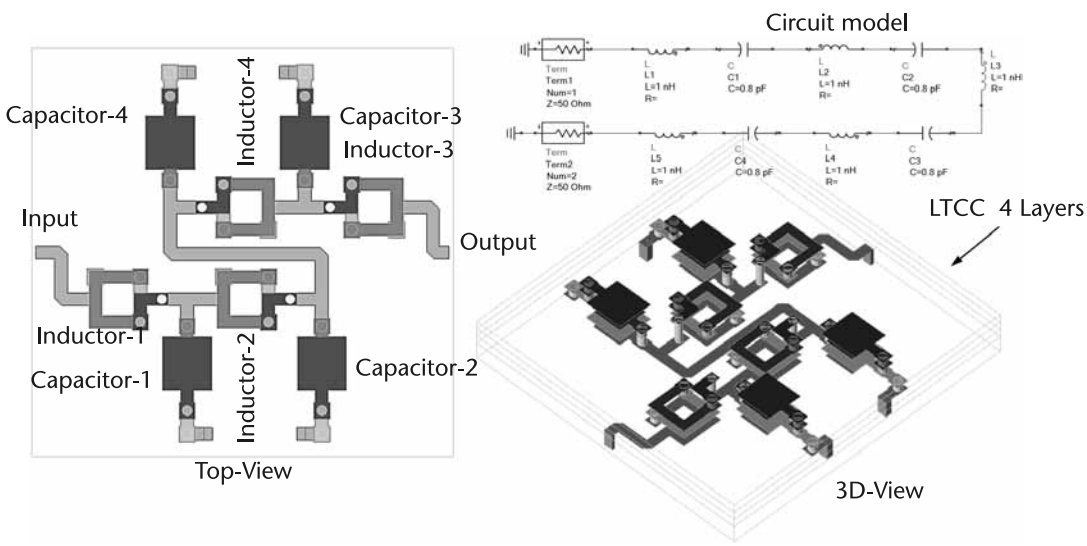

Figure 14.13 LTCC LPF circuit and layout design.

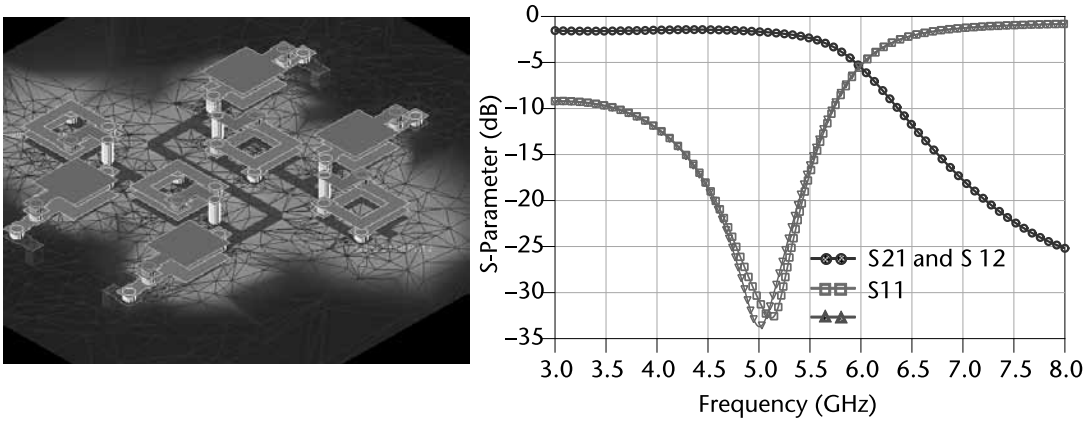

Figure 14.14 E-field on LPF design and simulation S-parameter data.

capacitor (C). The filter has a 3-dB passband from DC to 5.5 GHz. The insertion loss is less than 1.2 dB from DC to 5 GHz. The return loss is better than 10 dB from DC to 5.5 GHz. The volume of the filter is $2.5 \times 2.5 \times 0.5$ mm^3.

14.3.5 A 6-Bit MMIC Phase Shifter

Phase shifters are an essential component of the phased array system that provides the necessary insertion phase to each element in the antenna array. Phase shifters can be implemented as active or passive phase shifters. Active phase shifters also known as amplifier type phase shifters provide phase shift by continuously changing the device gain using gate control voltage [24]. They provide 0° to 360° phase shift with gain to compensate for losses from other components. However, active phase shifters suffer from large DC power consumption and have complex circuitry. In comparison, passive phase shifters have higher linearity with lower power consumption. They can further be classified as analog and digital phase shifters. Analog phase shifters provide continuous phase variation by changing the capacitance of the device using a control voltage, but require complex biasing networks and consume moderate DC power. Digital phase shifters provide a discrete set of phase shift states and consist of a cascade of several phase bits that increment the phase in binary steps. They are immune to noise on their voltage control lines and have negligible power consumption. Digital phase shifters find extensive applications in phased array antennas [25] and their resolution, along with the phase error, decides the precision of the BFN.

A 6-bit digital phase shifter provides 0°–360° phase shift in 64 discrete steps with 5.625° phase resolution. The phase shifter is designed using the pHEMT GaAs MMIC process. The process includes two metal interconnect layers, precision resistors, MIM capacitors, and inductors. The design of the phase shifter using this process enables on-chip integration with other active stages leading to a single-chip solution for the transmit module of the BFN. Each individual bit of the phase shifter needs to be designed using optimum topology to provide low insertion loss, flat phase shift response over the desired band of operation, and good tolerance to process variations. The line length L1 required for a phase shift of $\Delta\varnothing$ is calculated as:

$$\Delta\varnothing = \varnothing_{FET} - \beta L1 \tag{14.13}$$

$$L1 = \frac{(\varnothing_{FET} - \Delta\varnothing)\lambda_g}{2\pi} \tag{14.14}$$

where β, $\varnothing_{FET}$, and λ_g represent phase propagation constant, insertion phase of FET Q1, and guide wavelength of the signal in microstrip line, respectively.

Phase bit topology is shown in Figure 14.15. For 11.25° and 22.5° phase bits, the reference state is obtained when Q1, Q2 are turned on and Q3 is pinched off. The inductor L_p is used to resonate the off-state capacitance of Q3. In the phase shifting state, Q1 and Q2 are turned off and Q3 is turned on. For the 45° phase bit, the reference state is obtained when Q4 is turned on and Q5 is pinched off. In the phase-shifting state, Q4 is turned off and Q5 is switched on. The 90° and 180° phase shift designs are implemented using switched filter topology. The implementation of higher phase shift values using this topology provides a low amplitude imbalance compared to the embedded device type topology. The required phase shift is obtained by switching the signal between highpass filter and LPF networks matched for their insertion losses at the center frequency of operation. The filter

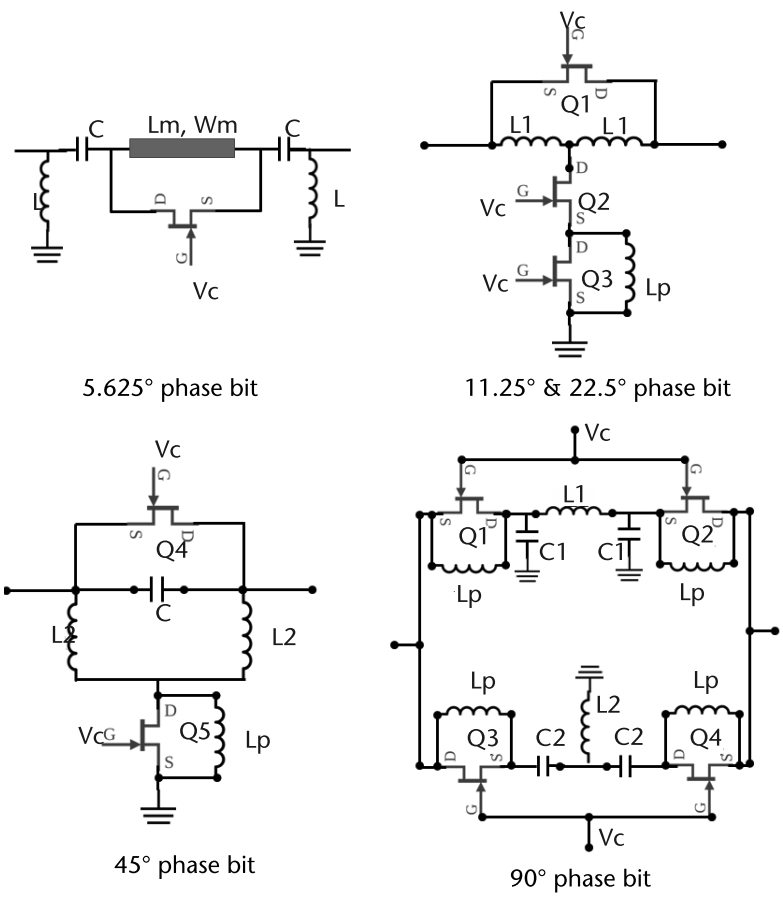

Figure 14.15 Circuit topologies of the phase shifter bits.

networks are connected between two SPDT switches as shown. When transistors Q1 and Q2 are switched on and Q3 and Q4 are off, the signal passes through the LPF network, providing a phase lag of (∅/2) to the signal. When the transistor biases are reversed, the signal passes through the highpass filter network, providing a phase lead of (∅/2) to the signal. Figure 14.16 shows the phase variation at the output of a 1:8 network using a 6-bit phase shifter.

All designed chips are placed in QFN package and then integrated onboard as shown in Figure 14.17. After the integration, TRM performance is validated by circuit design simulations. Component placing and trace routing connecting all the components on the board are other important aspects that are optimized.

14.3.6 Antenna with TRM

Any printed antenna element or array antenna discussed in this book can be integrated with T/R for phase array application. Phased arrays consist of arrays of radiating elements that combine energy in free space to form a single equivalent

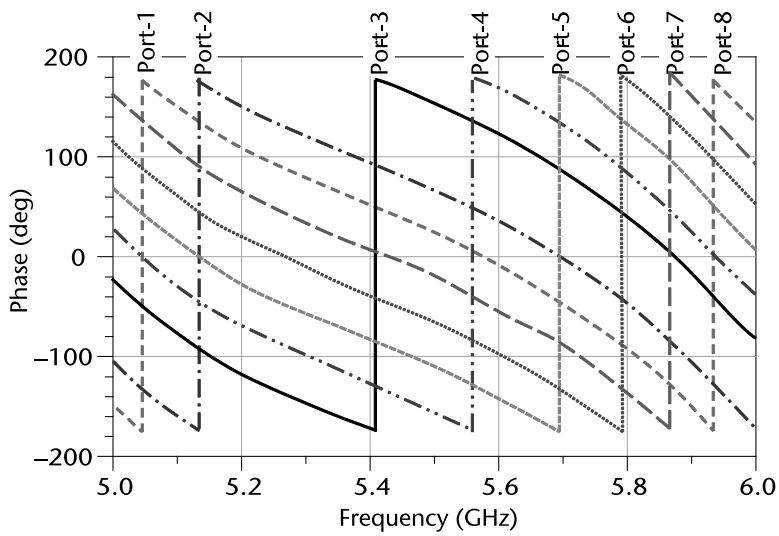

Figure 14.16 Phase variation at the output of a 1:8 network using a 6-bit phase shifter.

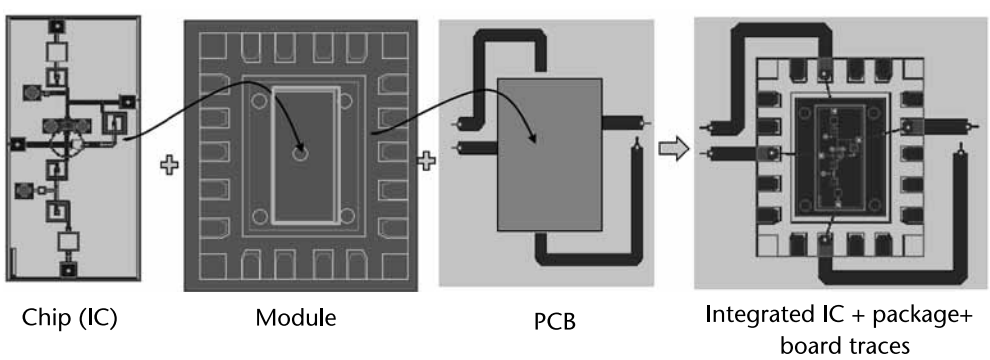

Figure 14.17 Integrated TRM components on PCB.

aperture. Sometime phased arrays are specifically designed to be uniform linear arrays, where the elements are equally spaced, so optimum phase adjustments result in constructive interference.

14.4 Design of Phased Array Radar Using the Transceiver Module

In the realization of a complete phase array system, TRM, along with an antenna system as shown in Figure 14.18, is designed and simulated. Simulation is undertaken to show the antenna pattern produced by an array of 8 linear arrays, each having 4 elements (12-dB gain) driven by the 8 channels of TRM. Phase shifters can be placed either after the TRM or before the TRM. Based on the phase shifter placement in which phase shifting is performed, phased arrays can be categorized into four district types: RF phase shifting, LO phase shifting, IF phase shifting, and digital phased arrays.

The hybrid beamforming technique is used in this design. Hybrid beamforming is a technique that can be used to screen beamforming between the digital and RF domains. RF system designers implement hybrid beamforming to balance flexibility and cost trade-offs while still maintaining a system that meets the required performance parameters. Hybrid beamforming designs are developed by combining multiple array elements into subarray modules, for example, in this design, four antenna elements are combined to form a subarray. A TRM is dedicated to a subarray in the array and therefore fewer TRMs are required in the system. The number of antenna elements in the subarray, and the positioning, can be selected to ensure that system-level performance is met across a range of steering angles.

Figure 14.19 shows a simulated return loss and antenna beam scanning of complete system. The return loss of each linear array is below –20 dB in the operating frequency band. The antenna beam scanning results are presented in Figure 14.19 in the form of rectangular plots showing the antenna responses versus

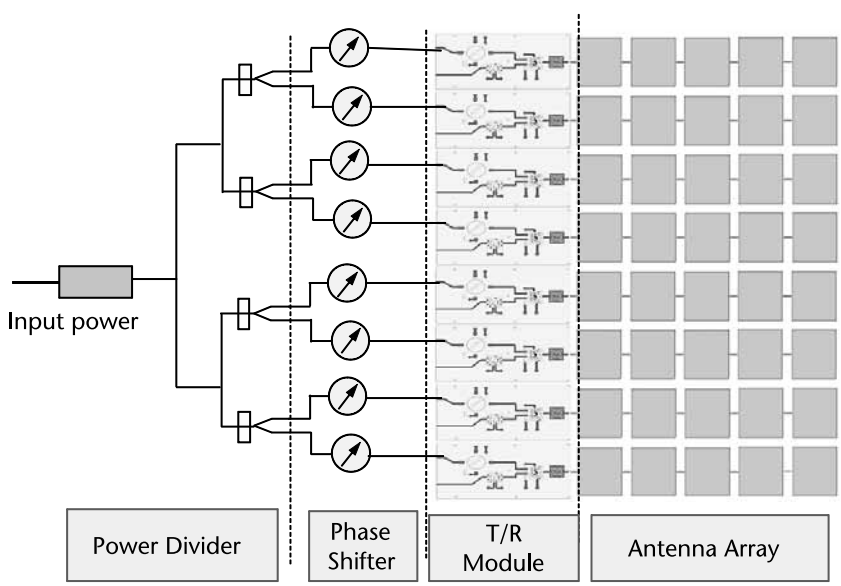

Figure 14.18 Phase array antenna along with designed TRM.

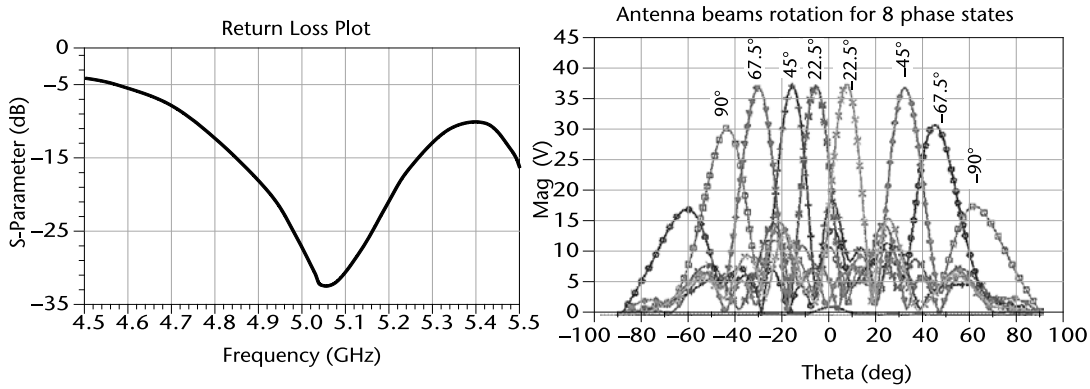

Figure 14.19 Return loss and squinting of antenna beam with variation of phase.

azimuth angle. The array beam is controlled by a single bias voltage applied at the input to the phased array.

A scan angle of 65° has been achieved. The 3-dB beamwidth is 17° at scan angle of 15° and 14° at the scan angle of 30° while the sidelobes are maintained at approximately below –12 dB. As shown in Figure 14.19, the antenna array beam is sequented with different phase values in the feeder network. Simulated return loss, insertion loss, and phase array patterns are given in Table 14.5.

14.5 Summary

The quest for increased bandwidth in the latest generation wireless communication systems, radar, phased arrays, and other high-performance RF applications imposes challenging demands on system integration, power consumption, and thermal management. In this chapter, C-band TRMs for phased array application was discussed.

Table 14.5 Results of a Complete Phased Array System

Design Name	*Parameters*	*Specification*
MMIC-SPDT Switch	Frequency range	DC to 8 GHz
	Insertion loss	<1 dB
	I/O return loss	<–15 dB
	Isolation	>30 dB
MMIC-LNA	Gain	6.7 dB
	NF	2.64 at 5.08 GHz
	Stability factor	1.43 at 5.08 GHz
MMIC-PA	Gain	18.2 dB
LTCC-LPF	Pass bandwidth	Up to 5.6 GHz
	Input/output return loss	<–15 dB
Microstrip antenna	Frequency range	5–5.3 GHz (±300 MHz)
	Polarization	Linear polarization
	Gain	7 dB
Transceiver system	Supply voltage	Single bias supply (3V)
	Overall, I/O return loss	<–20 dB

Various components of T/R models have been designed and simulated. The performance of a complete phased array system has been analyzed using the FEM and circuit simulation using active components. The transceiver system has been applied in an active phase array to demonstrate beam sequencing with variation of phase values. As an antenna designer only, antenna design is not sufficient; it is important to analyze antenna performance and behavior to check with all other components of TRM.

References

[1] Brookner, E., "Phase Arrays and Radars Past, Present and Future," *IEEE Microwave J.*, Vol. 49, No. 1, January 2006, pp. 24–46.

[2] Koriyama, S., et al., "Millimeterwave Ceramic Package for a Surface Mount," *IEEE MTT-S Int. Microw. Symp. Dig.*, Boston, MA, June 2000, pp. 61–64.

[3] Agrawal, A., and E. Holzman, "Beamformer Architectures for Active Phased-Array Radar Antennas," *IEEE Transactions on Antennas and Propagation*, Vol. 47, No. 3, March 1999, pp. 432–442.

[4] Del Alamo, J. A., "The High-Electron Mobility Transistor at 30: Impressive Accomplishments and Exciting Prospects," *2011 International Conference on Compound Semiconductor Manufacturing Technology*, Indian Wells, CA, May 16–19, 2011.

[5] Marsh, S., *Practical MMIC Design*, Norwood, MA: Artech House, 2006.

[6] Pozar, D. M., *Microwave Engineering*, 3rd ed., New York: John Wiley & Sons, 2005.

[7] Mancuso, Y., P. Gremillet, and P. Lacomme, "T/R-Modules Technological and Technical Trends for Phased Array Antennas," *IEEE Microwave Theory and Techniques Symposium Digest,* San Francisco, CA, June 2006, pp. 614–617.

[8] Hommel, H., and H. -P. Feldle, "Current Status of Airborne Active Phased Array (AESA) Radar Systems and Future Trends," *European Radar Conference Digest*, Amsterdam, 2004, pp. 121–124.

[9] Kinghorn, A. M., "Where Next for Airborne AESA Technology?" *IEEE Radar Conference Proceedings,* Rome, May 2008, pp. 287–290.

[10] Edwards, T., "Semiconductor Technology Trends for Phased Array Antenna Power Amplifiers," *European Radar Conference Proceedings*, Manchester, October 2006, pp. 269–272.

[11] Materka, A., and T. Kacprzak, "Computer Calculation of Large-Signal GaAs FET Amplifier Characteristics," *IEEE Transactions on Microwave Theory and Techniques*, Vol. MTT-33, No. 2, February 1985, pp. 129–135.

[12] Curtice, W., and M. Ettenberg, "A Nonlinear GaAs FET Model for Use in the Design of Output Circuits for Power Amplifiers," *IEEE Transactions on Microwave Theory and Techniques*, Vol. MTT-33, No. 12, December 1985, pp. 1383–1393.

[13] Cripps, S. C., *Advanced Techniques in RF Power Amplifier Design*, Norwood, MA: Artech House, 2006.

[14] Ballweber, B. M., R. Gupta, and D. J. Allstot, "A Fully Integrated 0.5-5.5 GHz CMOS Distributed Amplifier," *IEEE Journal of Solid-State Circuits*, Vol. 35, No. 2, February 2000, pp. 231–239.

[15] Cheung, T. S. D., and J. R. Long, "A 21-26-GHz SiGe Bipolar Power Amplifier MMIC," *IEEE Journal of Solid-State Circuits*, Vol. 40, No. 12, December 2005, pp. 2583–2597.

[16] Triquint Data Sheet, TGS4302, High Power Ka-Band SPDT Switch.

[17] Triquint Data Sheet, TGS2306, High Power DC-18GHz SPDT FET Switch.

[18] Viranjay, M. S., and G. Singh, *MOSFET Technologies for Double-Pole Four-Throw Radio-Frequency Switch,* New York: Springer, 2014.

[19] Tipirneni, N., "High Power III-Nitride Transistors for Energy Conversion," Ph.D. dissertation, Dept. Elec. Eng., Univ. of South Carolina: ProQuest, 2007.

[20] Ayasli, Y., "Microwave Switching with GaAs FETs," *Microwave Journal*, Vol. 25, No. 11, 1982, pp. 61–74.

[21] Scrantom, C. Q., and J. C. Lawson, "Where We Are and Where We're Going," *IEEE International Microwave Symposium Digest*, 1999, pp. 193–200.

[22] Tang, C. -W., "Harmonic-Suppression LTCC Filter with the Step-Impedance Quarter-Wavelength Open Stub," *IEEE Transactions on Microwave Theory and Techniques*, Vol. 52, No. 2, February 2004, pp. 617–624.

[23] Rambabu, K., and J. Bornemann, "Simplified Analysis Technique for the Initial Design of LTCC Filters with All-Capacitive Coupling," *IEEE Transactions on Microwave Theory and Techiques*, Vol. 53, No. 5, May 2005, pp. 1787–1791.

[24] Bahl, I. J., *Control Components Using Si, GaAs, and GaN Technologies*, Norwood, MA: Artech House, 2014.

[25] Xiaofeng, Y., and S. Jiangyi, "C-Band 6-Bit Phase Shifter for a Phase Array Antenna," *Journal of Semiconductors*, Vol. 34, No. 4, 2013, pp. 1–4.

Selected Bibliography

Andricos, C., I. J. Bahl, and E. L. Griffin, "C-Band 6-Bit GaAs Monolithic Phase Shifter," *IEEE Microwave Theory and Techniques*, Vol. MTT-33, December 1985.

Bessemoulin, A., et al., "A 1-Watt Ku-Band Power Amplifier MMIC Using Cost-Effective Organic SMD Package," *Proc. 34th Eur. Microw. Conf.*, October 2004, pp. 349–352.

Bettidi, A., et al., "X-Band Transmit/Receive Module MMIC Chipset on Emerging GaN and SiGe Technologies," *Proc. IEEE Phased Array Syst. Tech. Symp. Dig.* October 2010, pp. 250–255.

Cohen, E., et al., "A Bidirectional TX/RX Four-Element Phased Array at 60 GHz with RF-IF Conversion Block in 90-nm CMOS Process," *IEEE Transactions on Microwave Theory and Techniques,* Vol. 58, No. 5, May 2010, pp. 1438–1446.

Kang, D. W., et al., "Single and Four-Element Ka-Band Transmit/Receive Phased-Array Silicon RFICs with 5-Bit Amplitude and Phase Control," *IEEE Transactions on Microwave Theory and Techniques,* Vol. 57, No. 12, December 2009, pp. 3534–3543.

Ku, B. H., D. W. Kang, and S. C. Hong, "CMOS Integrated Circuits for X-Band Phased Array Systems," *Proc. 54th MWSCAS Symp.*, August 2011, pp. 1–5.

Mangraviti, G., et al., "A 4-Antenna-Path Beamforming Transceiver for 60 GHz Multi-Gb/s Communication in 28 nm CMOS," *IEEE Int. Solid-State Circuits Conf. (ISSCC) Dig. Tech. Papers*, February 2016, pp. 246–247.

Poon, A. S. Y., and M. Taghivand, "Supporting and Enabling Circuits for Antenna Arrays in Wireless Communications," *Proc. IEEE,* Vol. 100, No. 7, July 2012, pp. 2207–2218.

CHAPTER 15

Phased Array and BFN for 5G Communication Systems

15.1 Introduction

Phased array systems operating at millimeter wave are already a focused area of research by the emerging 5G communication market. Based on 5G applications requirement, there is an increasing interest in making broader use of the millimeter-wave frequency band for communications on small mobile platforms where narrow antenna beams from low-volume radiating apertures provide enhanced communication security. However, currently, millimeter-wave systems are not very user-friendly and are designed to be platform-specific, lacking interoperability, and are thus reserved for only the most complex platforms. To increase the use of millimeter-wave phased arrays and make them broadly applicable for 5G systems, many technical challenges must be addressed, including wideband frequency coverage, precision beam pointing, mesh networking, and antenna systems. Multibeam phased arrays have driven technology to use the millimeter-wave frequency spectrum for communication systems.

The 5G wireless communication is the next major phase of mobile communications standards beyond the current LTE-Advanced. To cater to 5G's faster speed (1 to 10 Gbps), the millimeter-wave frequency band has been recommended for 5G wireless communication. The unlicensed 60-GHz band has been targeted for a short-range high data rate communication system. This band is useful for many reasons, including a large amount of spectrum availability (7 GHz), suitability for frequency reuse, and high FCC effective isotropic radiated power (EIRP) limit (40 dBm) [1]. One major challenge in the implementation of 60-GHz wireless network is high path loss, implying a need for high-gain beamforming antennas.

Due to the 5G demand for high data rate communication, phased array systems are found to be significant in wireless communications. Phased arrays can adapt their radiation patterns and cancel out information in unwanted directions depending on the operating environment. This feature significantly contributes to the reception quality and data capacity in communication systems. Mobile communications networks use MIMO technology to achieve high data rates. With MIMO

beamforming, it is possible to reduce transmit power and still get better channel performance.

The BFN is the key component of multibeams antennas. BFNs are complex networks used to precisely control the phase and amplitude of the RF energy passing through them, which is conveyed to the radiating elements of an antenna [2–4]. In the 5G system, the devices will use a smart antenna array to beam-shape its own receiver sensitivity and transmit energy. The Butler matrix has been used widely over the years in the beamforming systems. The Butler matrix consists of many 90° hybrid couplers and fixed phase shifters. It has N input ports and N output ports to drive an array of N antenna elements [5–8]. It can produce N orthogonally space beams with the full gain of the array.

15.2 5G Communication System

In the past 10 to 15 years, the speed at which communication standards have developed has been very rapid. Cellular generation differs in four major aspects: radio access, bandwidth, data rates, and switching schemes. Initially, the cellular concept was introduced in the 1G technology, which made the large-scale mobile wireless communication possible. The 1G cellular system, mainly the analog system, had a bandwidth ranging from 10 to 30 kHz depending on system type and services. The 1G was only suitable for voice services. Digital communication has replaced the analog technology in the 2G, which significantly improved the wireless communication quality. The first release of the Third Generation Partnership Project (3GPP) LTE system was standardized in December 2008 timeframe, with commercial deployments in 2001. The first release of LTE-Advanced was in March 2011, which made LTE formally compliant with the International Telecommunication Union (ITU) definition of the 4G wireless technology, called IMT-Advanced. The 4G wireless networks can support data rates of up to 1 Gbps for low mobility, such as roaming/local wireless access, and up to 100 Mbps for high mobility such as mobile access. LTE and its extension, LTE-Advanced systems, are practical 4G systems. However, the industries and standards bodies are now organizing a timeframe to standardize 5G technology, which is expected to be around 2020.

The 5G use cases and their requirements have already been studied by many 5G research organizations, academic institutes, and telecommunications firms, as shown in Figure 15.1. The 5G can deliver up to 100 times the speeds that customers are currently getting with 4G LTE. It can also accommodate many more devices expected to attach to networks due to the expansion of the IoT.

These are some major advantages of the 5G technology:

- *Better education system:* A student sitting in any part of the world can attend the class.
- *Parallel multiple services:* A user can know the weather and location while talking with another person.
- *Easier and economical medical treatment:* A doctor can treat the patient located in another part of the world.

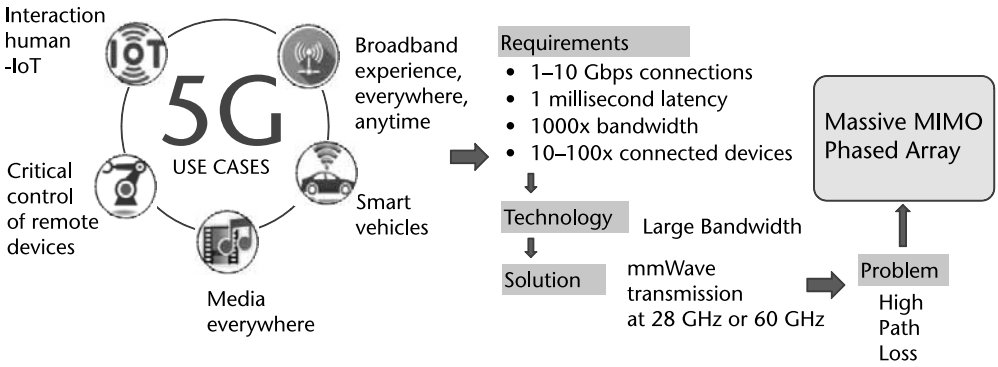

Figure 15.1 Applications of the 5G system and technology driven by the 5G requirements.

- *Easy monitoring and tracking:* A governmental organization and investigating agencies can monitor any part of the world.
- *Better disaster management:* Possible natural disasters including tsunamis and earthquakes can be detected faster.
- *Always connected and responsive mobile network:* Mobile data downloads will be much faster, and always on and responsive mobile Internet offers a power mobile experience. The 5G networks will enable secure access to cloud storage and access to enterprise applications.

15.2.1 Massive MIMO and Antenna Technologies

In 5G communication, a massive number of antenna elements in phased array enable beamforming technology, which combines radio waves and forms a single sharp beam. The beam compensates the propagation loss at higher frequencies and ensures a transmission area with radii of several hundred meters. This technology utilizes multiple propagation paths available in a radio communication channel between a mobile station and a base station. MIMO is a wireless network that allows the transmitting and receiving of more than one data signal simultaneously over the same radio channel, as discussed in Chapter 4. The usual MIMO networks tend to use two, four, or eight antennas as shown in Figure 15.2. However, massive MIMO is a system with a very high number of antennas (>100). The advantage of a MIMO network over a standard one is that it multiplies the capacity of a wireless connection without requiring more spectra. The more antennas with which the RF system is equipped, the greater number of possible signal paths and the better the performance in terms of data rate and link reliability.

The large number of antennas in a massive MIMO network will also make it far more resistant to interference and intentional jamming than current systems that only utilize a few antennas. In the 5G system, a large number of antennas increase the multiplexing capability for higher data rates with improved system capacity. As the 5G system will use millimeter waves or submillimeter waves, applying multi-antenna technologies in these higher frequency spectra have an advantage because of compact antenna sizes. Massive MIMO allows tens to thousands of arrays to be configured at the base station as shown in Figure 15.2. This enables more accurate

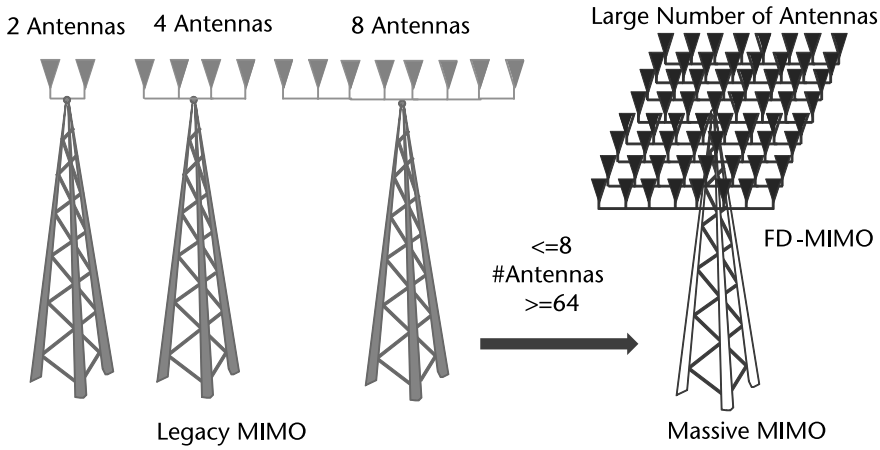

Figure 15.2 Massive MIMO and antenna array system.

beam control and higher spectral efficiency than legacy MIMO. Massive MIMO also includes the use of spatial multiplexing and interference mitigation to increase system capacity. These antennas provide substantial interference suppression for enhanced performance.

15.2.2 MIMO Antennas for Picocells

In the 5G communication system, the complete area will be dividing in picocell as shown in Figure 15.3. A picocell is a small cellular base terminal (CBT) typically covering a small area, such as offices, shopping malls, train stations, and stock exchanges. The size of a cell is from 10m to hundreds of meters. The same concept is used in 3G and 4G network also, but cell size is large in that, typically from hundreds of meters to some kilometers [9]. This infrastructure fulfills the capacity demand of a 5G system. In the 4G system, only a few antennas are needed that radiates the signal in all the direction, but in 5G this will be replaced with a massive phased array antenna system to cover both vertically and horizontally placed devices in a picocell.

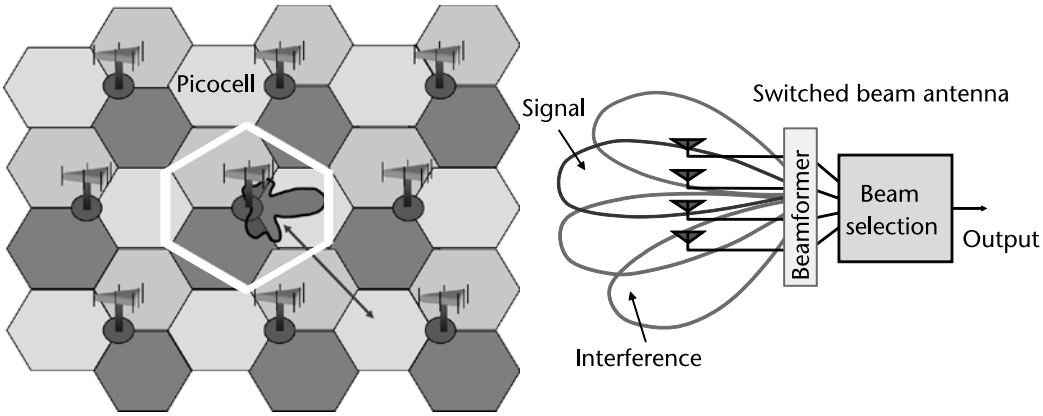

Figure 15.3 The cellular picocell concept and antenna BFN covering these cells.

15.2.3 Spectrum for 5G Communication

Currently, there has been a lot of discussion about the frequency spectrum that 5G technology will use. Cellular network operators all over the world are conducting trials with the objective to deploy the technology commercially. For 5G communication, different countries have proposed and are working on different frequency bands that range all the way from 2.4 to 71 GHz. Countries all over the world are using both low-frequency and high-frequency bands for the initial 5G trials. The 5G spectrums in some countries are shown in Table 15.1; around the world, these bands have been allocated or targeted.

15.2.4 Path Loss Model in a Cellular Cell

In a communication system, the path loss models describe the signal attenuation between the receive and transmit antennas as a function of the propagation distance and other parameters. Path loss is a key factor in the design of the 5G communications system. The channel path loss determines many elements of the communications system design such as the antenna gain, height, and transmitter power. Generally, path loss, which is scaled in decibels relative to a reference power or transmitted power, is assumed to have a linear dependence with logarithmic distance, expressed [9] as:

$$\overline{PL(d)}dB = \alpha + \overline{\beta}\ .10\log_{10}(d) \tag{15.1}$$

where $\overline{PL(d)}$ is a mean path loss over the distance, α is the floating intercept, $\overline{\beta}$ is a linear slope, and d is the distance between transmitter and receiver. Usually, the linear slope $\overline{\beta}$ is extracted by a best-fit linear regression to (15.1) using path loss values in the decibel scale versus the logarithm of measurement distances. The esti-

Table 15.1 5G Spectrum Consideration/Allocations in Various Countries

Country	*Low-Frequency Band*	*High-Frequency Band*
United States	2.5 GHz, 3.7–4.2 GHz, 3.55–3.7 GHz, 5.9–7.1 GHz	24.25–24.45 GHz, 24.75–25.25 GHz, 27.5–28.35 GHz, 38.6–40 GHz, 60–71 GHz
Finland	3.4–3.8 GHz	26.5–27.5 GHz
France	3.46–3.8 GHz	26 GHz
Germany	3.4–3.8 GHz	26–27.5 GHz
Ireland	3.4–3.8 GHz	26 GHz
Italy	3.6–3.8 GHz	26.5–27.5 GHz
Russia	3.4–3.8 GHz	26 GHz
Spain	3.4–3.8 GHz	26.5–27.5 GHz
United Kingdom	3.4–3.6 GHz, 3.6–3.8 GHz	26.5–27.5 GHz
China	3.3–3.6 GHz, 4.4–4.5 GHz, 4.8–5 GHz	24.25–27.5 GHz, 37–43.5 GHz
Japan	3.6–4.2 GHz, 4.4–4.9 GHz	27.5–28.28 GHz, 60–71 GHz
Korea	3.42–3.7 GHz	26.5–29.5 GHz
Australia	3.4–3.8 GHz	24–30 GHz
New Zealand	3.4–3.485 GHz, 3.51–3.587 GHz	24.25–28.35 GHz

mate approach employed is the least-square linear regression fit, in which the linear slope β can be derived by:

$$\bar{\beta} = \frac{\sum_i^n \left(d_i - \bar{d}\right) \mathrm{x} \left(PL_i - \overline{PL}\right)}{\sum_i^n \left(d_i - \bar{d}\right)^2} \tag{15.2}$$

where d_i is the distance of the ith measurement power delay profile (PDP) for a given antenna pointing angle and receiver location, d is the average distance in decibels of all d_i in decibels from the measurement snapshot, PL_i is the path loss value of the ith measurement snapshot in decibels, and $\overline{PL}$ is the average path loss of the entire data set in decibels, respectively. The constant α in decibels is the floating intercept of the linear regression fit in (15.1) that fits the data empirically, and can be thought of as a globally optimum reference attenuation set point that determines the tilt of the path loss model and is found as [9]:

$$\alpha(dB) = \overline{PL}(dB) - \beta.10\log_{10}(d) \tag{15.3}$$

15.2.5 The 60-GHz Spectrum for 5G Application

Currently, the portion of the EM spectrum that is used for mass wireless communications (Wi-Fi, cellular, Bluetooth, and so forth) falls under 0.5–6-GHz region, which is a fraction of the large spectrum, and is considerably crowded. This spectrum is also called the sub-6-GHz band. Engineers and researchers have been working for a long time studying other portions of the spectrum that can be used to develop wireless technologies. The unlicensed 60-GHz band is one of these options. Previously, the 60-GHz band was used only for point-to-point radio links like satellite-to-satellite communications, but now this band currently has several short-range, high-throughput wireless technologies. The rain attenuation is high in this frequency band and, because of that, the EM losses are significant. More importantly, at this frequency, there is a peak in oxygen absorption. Figure 15.4 shows the atmospheric attenuation at millimeter-wave frequencies. There is around 9 GHz of bandwidth in this unlicensed band, depending on the country. An antenna compatible with these applications needs to have a large bandwidth that covers the entire band.

The power ratio between the main lobe and sidelobes is about 13.2 dB in typical array antennas. By developing an antenna power-supply circuit that sends more power to antenna elements close to the center and diminishingly less power towards the periphery, it is possible to achieve low sidelobes with a power ratio of approximately 20 dB. This technique is also known as amplitude tapering feeding, which gives an improvement of 7 dB (or one-fifth, compared to the conventional amount). By applying this technology and arranging multiple antennas array so that each faces a slightly different direction, multiple users can simultaneously communicate without interfering with each other. Even if multiple users concentrate in one location and simultaneously communicate, the reduction of each user's transmission speeds can be minimized, which enables smooth, high-speed communications.

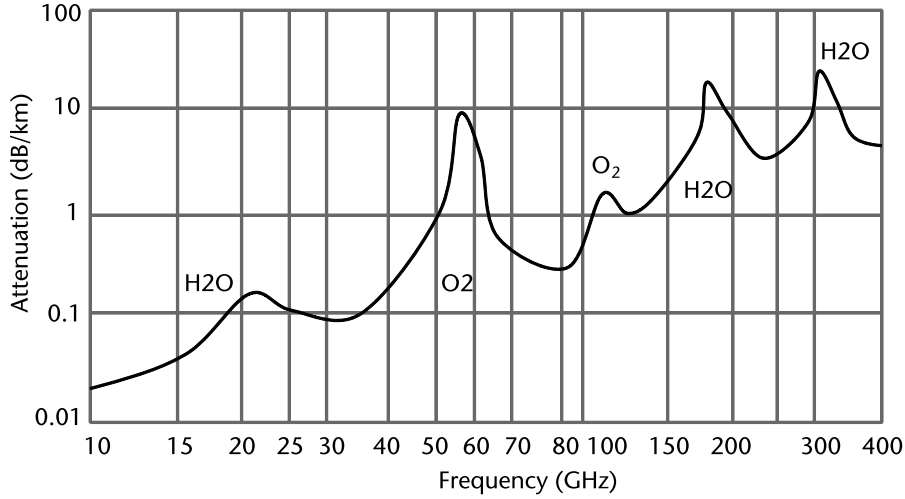

Figure 15.4 Atmospheric absorption of millimeter waves.

This allows the provision of a comfortable communications environment, even when watching high-resolution videos or uploading videos to the cloud.

15.3 Millimeter-Wave 5G BFN

Compared to the linear array, a planar array provides higher resolution of beam steering and more symmetrical patterns with lower sidelobes. Butler matrix-based BFN has been used extensively over the years. It is a cost-effective passive beamforming feed network for phased array antenna applications without needing active devices such as mixers, switches, phase shifters, and transceivers. However, the typical Butler matrix designs need to deploy many air bridges, vias, and bent cables that result in a complicated prototyping process. Planar and printented technology has enabled compact and cost-effective Buttler matrix-based BFNs. As shown in Figure 15.5, an 8-way Butler matrix is composed of twelve 3-dB quadrature couplers, 8

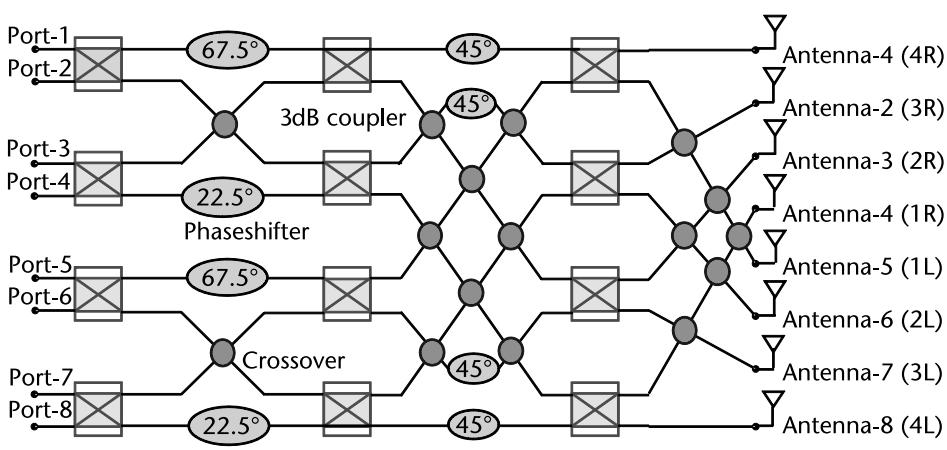

Figure 15.5 Block diagram of an 8 × 8 Butler matrix-based BFN and phased array system.

phase shifters, and 16 crossovers. The microstrip line-based 3-dB coupler and phase shifter are designed individually before integrating into a Butler matrix.

A planar Butler matrix is realized on a 4-mil-thick LCP substrate material and a dielectric constant of 3.2. The LCP substrate is used as a low-cost dielectric material for high-frequency antenna and passive networks design that provides a very reliable performance at high frequencies. It has very reliable electrical properties up to millimeter waves like the low dielectric constant of 3.2 and the low loss tangent of 0.002–0.004 at 60 GHz. Its permeability is comparable to that of glass and very close to that of ceramic. It has a low coefficient of thermal expansion (CTE) as low as 6.9×10^{-6}/K. These material properties make LCP a suitable candidate for multichip module (MCM) technology in millimeter-wave applications.

The design process block diagram of a complete 3-D full-dimension (FD)-MIMO phased array system is shown in Figure 15.6. In the first phase of the design, a single 8×8 Butler matrix beamformer is designed that can scan the antenna beam either horizontally or vertically at a time. To scan the antenna beam in all directions, an FD BFN is required. To make an FD beamformer, 8 such Butler matrix BFNs are stacked horizontally and 8 vertically to form a 3-D 64-port network for 64 elements of microstrip planar antenna array. There are three building blocks in this BFN: the microstrip-based 3-dB coupler, 0-dB crossover, and phase shifters. All these components are designed and optimized individually based on microstrip technology. The individual components, as well as the entire Butler matrix structure, are analyzed using the FEM EM solver. The hybrid coupler is used to generate signals 90° out of phase at its outputs. Crossover is used for crossing two RF transmission-line signals with a minimal coupling between them. By cascading two 90° hybrids, a crossover can be implemented. Three different 67.5°, 45°, and 22.5° phase shifters are designed and placed in a BFN.

The next phase in the design is to place all these designed components to form a Butler matrix BFN. It is designed by placing twelve 3-dB hybrid couplers, sixteen 0-dB crossovers, and eight phase shifters. A total of 36 components are used to design a single 8-port BFN. Using the principle of reciprocity, this structure can be

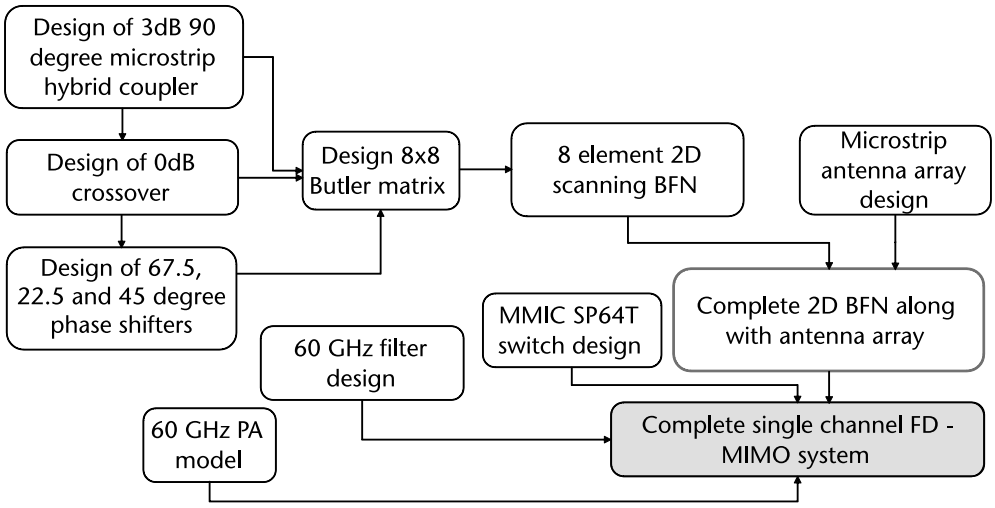

Figure 15.6 Design flow diagram of an 8×8 Butler matrix-based phased array system.

utilized in the same manner for receiving or transmitting antenna applications. At 60 GHz, the overall size of a beamformer is about 25 × 18 mm^2. The progressive phase delays at all antenna ports (from P1 to P8) for eight different input signals are given in Table 15.2. In this design, the MMIC SP64T is used to switch beams from one port to another in 64 antenna arrays.

15.3.1 A 3-dB Hybrid Coupler Design

The hybrid couplers are used to generate signals 90° out of phase at its outputs. The port closer to the input port is leading in phase by 90°. Port 4, located on the same side as input port 1, is isolated because there is no power reaching it. A quadrature hybrid or 90° hybrid is used to generate 90° out-of-phase signals at its outputs. The 3-dB hybrid coupler is designed using microstrip-based technology as shown in Figure 15.7. The size of a 3-dB coupler is 70 × 48 mils.

15.3.2 The 0-dB Crossover Design

The crossovers are an effective means of crossing two RF transmission-line signals with minimal coupling between them. It is also known as a 0-dB coupler. By cascading two 90° hybrids, a crossover can be implemented. The geometry used to

Table 15.2 Phase Distribution of 8 × 8 Butler Matrix

	Input Beam Port (in Degrees)							
Output	*4L (P2)*	*3L (P6)*	*2L (P4)*	*1L (P8)*	*1R (P1)*	*2R (P5)*	*3R (P3)*	*4R (P7)*
A1	157.5	157.5	135	90	–112.5	112.5	–135	–180
A2	–45	–90	–157.5	112.5	–135	–180	112.5	22.5
A3	112.5	22.5	–90	135	–157.5	112.5	0	–135
A4	–90	135	22.5	157.5	–180	45	–112.5	67.5
A5	67.5	–112.5	45	–180	157.5	–22.5	135	–90
A6	–135	0	112.5	–157.5	135	–90	22.5	112.5
A7	22.5	112.5	–180	–135	112.5	–157.5	–90	–45
A8	–180	–135	–112.5	–112.5	90	135	157.5	157.5
Δ Phase	157.5	112.5	67.5	22.5	–22.5	–67.5	–112.5	–157.5

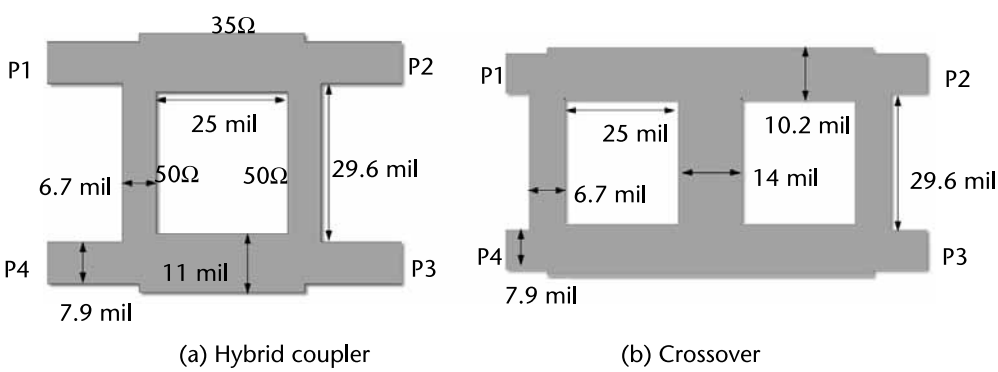

Figure 15.7 The 3-dB hybrid coupler and 0-dB crossover designs and dimensions.

implement the crossover is shown in Figure 15.7(b). The size of a 0-dB crossover is 90×48 mils.

15.3.3 The 22.5°, 45°, and 67.5° Phase Shifter Designs

The phase shifter is implemented using microstrip lines of different length. The length of the section corresponding to the $\varnothing$ radian phase shift is given by

$$\varnothing = (2\pi)/\lambda_L \tag{15.4}$$

where λ_L is the length of the line in fraction of wavelength, $\varnothing$ is the phase shift in radians, and λ is the wavelength.

15.3.4 The 8×8 BFN Design

The 8×8 BFN consists of eight RF inputs that independently feed eight RF outputs with varying phase delays as shown in Figure 15.8. The purpose of this network is to uniformly feed the eight antenna elements with progressive phase delays of 22.5°. This arrangement creates eight fixed radiating beams accessed by eight independent

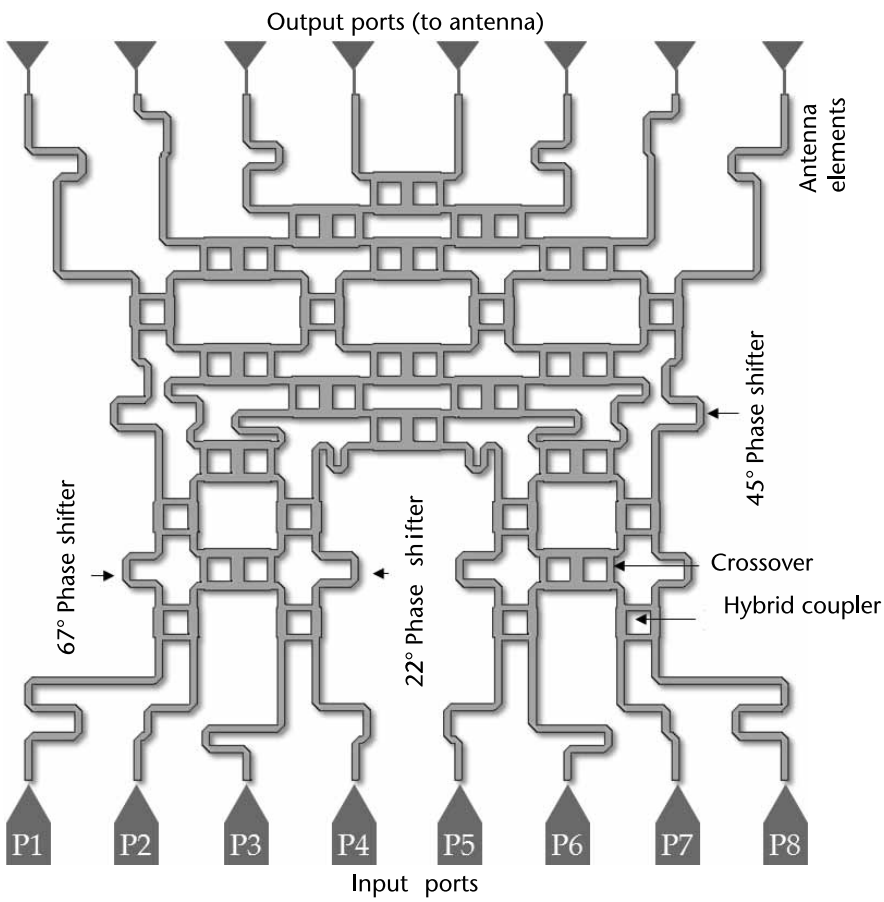

Figure 15.8 Layout design of an 8×8 Butler matrix.

inputs. The use of 90° hybrid couplers provides high isolation between each input port, which allows a switch network to toggle between these ports without affecting the antenna performance. The S-parameter of the Butler matrix is shown in Figure 15.9(a). These results correspond to the assigned ports shows the reflection coefficients when considering each port. Return loss is better than 10 dB across the frequency band of 58.3–61.5 GHz. Figure 15.9(b) shows the simulated phase shift at adjacent antenna elements for excitations.

15.4 A 60-GHz Microstrip Antenna Array Design

Millimeter-wave microstrip antenna, particularly around the center frequency of 60 GHz with the advantages of small volume, light weight, thin section, low cost, easy integration, and easy conformance, has attracted lots of interest in the antenna design for the 5G communication systems [10–16]. Considering the layout request of the 5G transceiver, normally the antenna should be in the same plane with the transceiver. The antenna array should be placed at one side of the transceiver in a limited space. At 60 GHz, the antenna design starts with the accurate determination of the single antenna element impedance characteristics allowing tuning the elementary antenna element over the desired frequency band. Table 15.3 provides an overview of the antenna array design specifications.

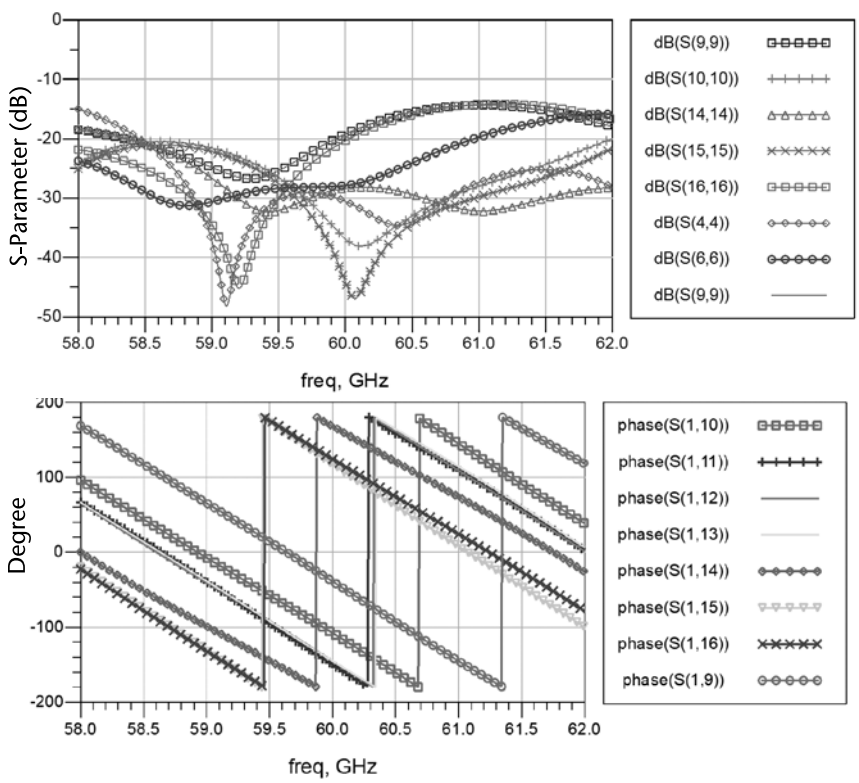

Figure 15.9 Simulation result of the Butler matrix: (a) reflection coefficient and (b) phase plot at output ports.

Table 15.3 Design Parameter of Antenna Array

Antenna Parameter	*Value*
Operating frequency	60 GHz
Substrate thickness	$h = 4$ mil
Substrate permittivity	$\varepsilon_r = 3.2$
Loss tangent	$\tan\delta = 0.004$
Bandwidth (–10-dB return loss)	1 GHz
Maximum gain (planar array)	22 dBi

A patch of 54 mils in size has been designed to operate at 60 GHz with a bandwidth of 1 GHz (10-dB return loss) and a peak gain of 6 dBi. The substrate has a thickness of 4 mils with a dielectric constant of 3.2. The design parameters of eight elements series-fed linear array are shown in Figure 15.10(a). Length and width of patch element are 54 mils and the spacing between array elements is $0.75\lambda_0$. A quarter-wavelength transformer of 3.7 mils is used to match patch impedance with feedline impedance. This transformer has a significant effect on the return losses due to changes in its characteristic impedance.

Eight linear antenna arrays are fed with eight outputs of BFN as shown in Figure 15.10(b). The excitation of each linear array is done by the center feeding along the microstrip feed line. The return loss is optimized by adjusting the patch dimensions and impedance transformer at the feeding point. As shown in Figure 15.11, a bandwidth of 1 GHz for –10-dB return losses has been achieved. The half-power

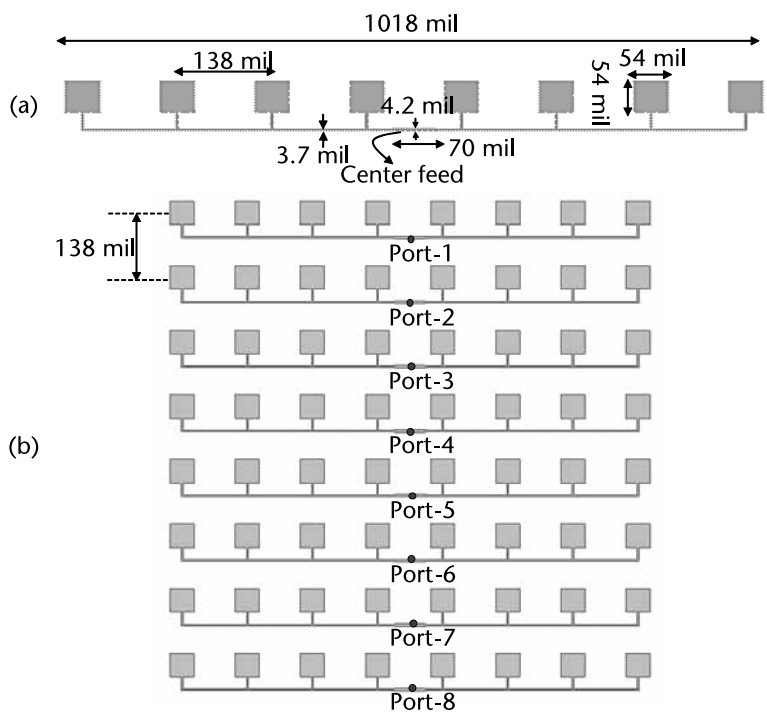

Figure 15.10 (a) Linear array of 8 elements and (b) planar array designs of 8 × 8 elements (all linear arrays are fed individually with the output of the Butler BFN).

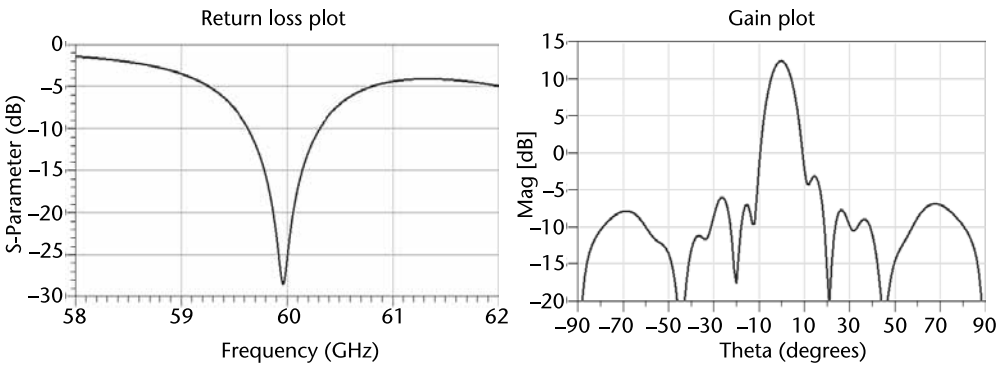

Figure 15.11 Linear array simulated antenna performance results: (a) return loss plot and (b) radiation pattern (phi = 0° cut) at 60 GHz.

beamwidth (HPBW) of the array is 8° and it undergoes negligible fluctuations over the frequency range from 59.5 to 60.5 GHz. In this frequency range, the maximum gain and sidelobe levels fluctuate ±0.7 dB and ±3.5 dB, respectively. Linear array antenna gain is 13 dBi as shown in Figure 15.11(b).

15.5 Phase Array System

The planar antenna array is integrated with an 8 × 8 Butler matrix in a single chip. As shown in Figure 15.12, the antenna is placed on a top layer of a chip stack-up, while the Butler matrix network is at the bottom layer of the chip.

Both antenna and BFN share a common ground plane. The output of BFN is connecting through via to linear microstrip array element. The complete system is

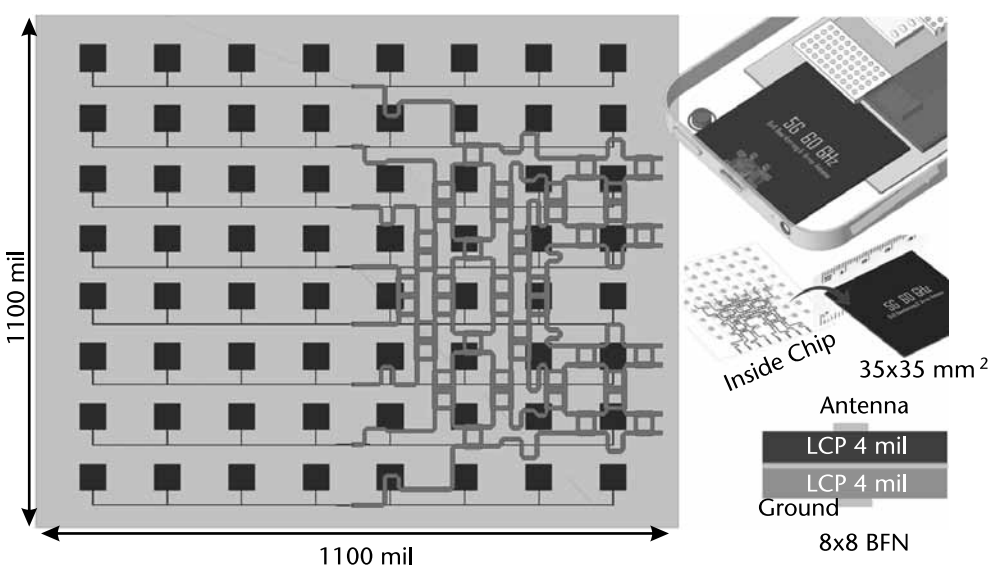

Figure 15.12 Integrations of BFN with planar antenna array.

simulated, and antenna beam scanning is plotted in Figure 15.13 with the RF signal to eight input ports of the Butler matrix.

The gain of 8 × 8 elements array antenna is 22 dBi. This antenna supports the 5G mobile communication to operate at the millimeter-wave frequency with beam scanning capability. The integrated array antenna and BFN are placed in a single 35 × 35 mm^2 chip. This chip can be easily integrated with other circuits, thereby making fabrication more cost-effective and suitable for 5G. For MIMO, the antenna array can be easily integrated with RF systems. Steerable beam ranging from –30° to +30° is achieved with this network.

15.6 FD-MIMO

In communications networks, MIMO technology is used to achieve high data rates. The MIMO approach implements a spatial diversity technique, using multiple transmit and receive antennas. The technique compensates for the signal fading effect, achieving increased channel capacity. FD-MIMO is one of the key technologies currently investigated for 5G. FD-MIMO utilizes many antennas (≥64) placed in a planar antenna array panel to realize high-order multi-user (MU)-MIMO transmissions. It provides link reliability and significant gains in wireless data rates by using large numbers of antennas at the base transceiver station (BTS). In an FD-MIMO system, a base station with a 2-D active array supports multi-user joint elevation and azimuth beamforming, which results in much higher cell capacity compared to conventional systems. As shown in Figure 15.14, the BTS antenna based on the FD-MIMO concept can scan in both the azimuth and elevation planes. With the acceptance of advanced digital signal processing schemes, an FD-MIMO antenna system can support higher-order MU-MIMO, which delivers a multifold improvement in system performance compared to conventional MIMO systems.

The base stations may contain hundreds of antennas using beamforming to focus their power on a tight beam toward the handset. Mobile handsets have room for six to ten antennas, but power and cost limitations on the handset may limit the number of antennas to one or two. As millimeter-wave spectrum has insufficient

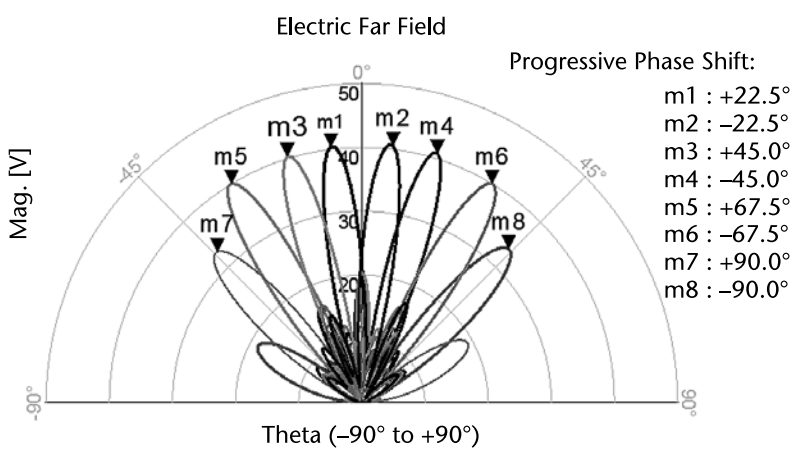

Figure 15.13 Phased array antenna beam scanning for eight RF inputs.

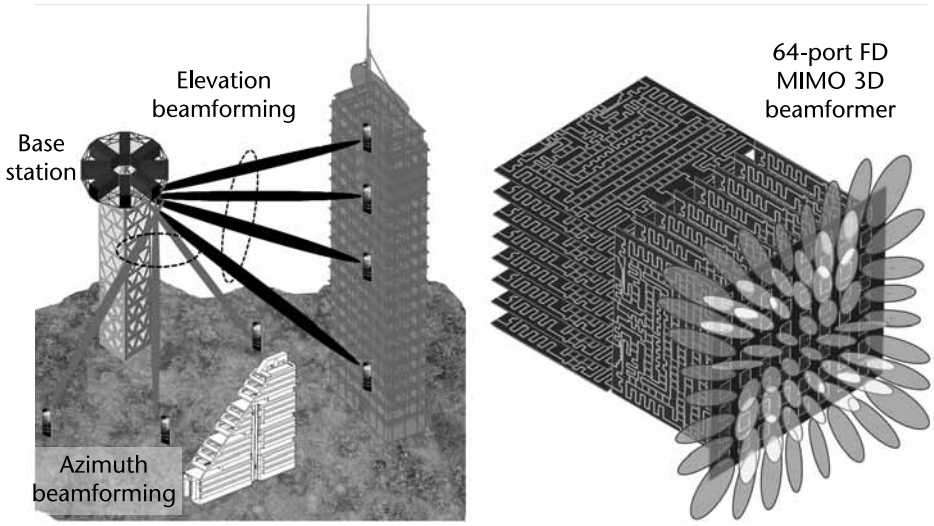

Figure 15.14 Beam scanning in a 5G FD-MIMO system and volumetric phased array BFN.

propagations characteristics, beamforming is thought to be an important element to control the direction of transmitted signals. As seen in Figure 15.14, there are multiple inputs that are communicating devices and multiple outputs that are antenna beams covering all the dimensions of space. That is why this technique is called the FD-MIMO.

15.7 FD-MIMO Phased Array System

A 3-D beamforming phase array is developed by stacking eight units of 8 × 8 BFN horizontally and eight units vertically and then these are combined as shown in Figure 15.15. There are a total of 64 input ports and 64 output ports fed to the antenna system.

To evaluate the performance of a 3-D phased array system, simulation is carried out using 64 switching circuits as shown in Figure 15.16 for 2-D scanning. The antenna scan angle is measured using this setup. In this setup, complete transmit chain including a PA, SP64T switch, and RF filter is used. The SP64T switch can be turned on for any specific port by turning biasing voltages (S1 port to S6 port) on and off as shown in Figure 15.16.

For each input port, there are a total of 64 antenna scan angles in both the vertical and horizontal directions as shown in Figure 15.17. This multibeam antenna has ±60° coverage utilizing eight individual narrow beam patterns each with a half-power beamwidth of 7°.

15.8 5G Communication System Design

The 5G wireless technology will enable gigabit data, ultralow latency, and massive connectivity for machine-to-machine (M2M), connected vehicles (V2X), and IoT applications. To accomplish these goals, 5G technology developers need to

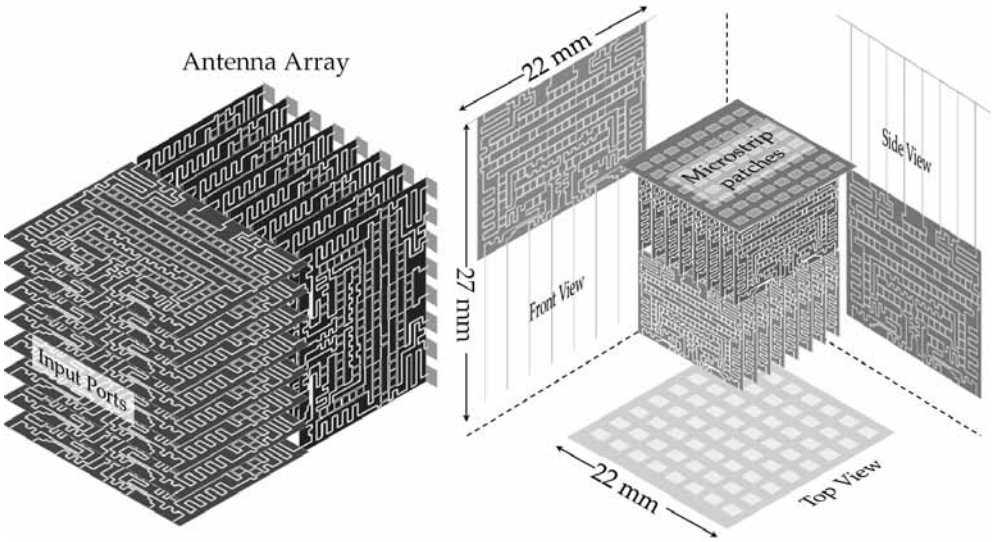

Figure 15.15 The 3-D BFN design and dimensions.

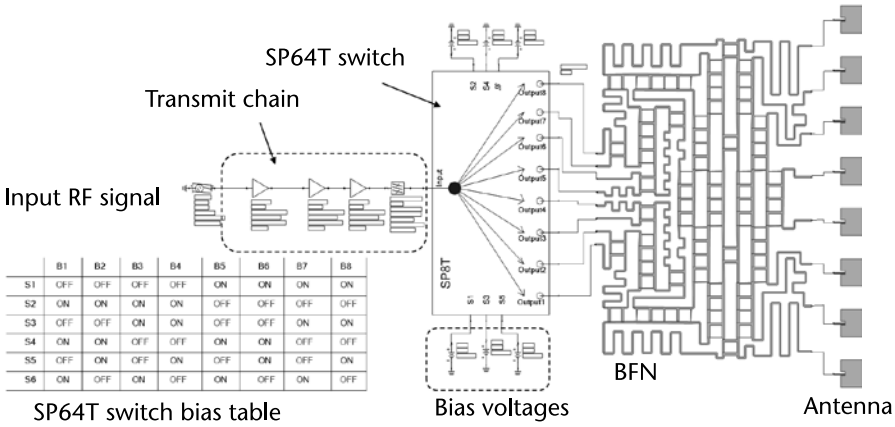

	B1	B2	B3	B4	B5	B6	B7	B8
S1	OFF	OFF	OFF	OFF	ON	ON	ON	ON
S2	ON	ON	ON	ON	OFF	OFF	OFF	OFF
S3	OFF	OFF	ON	ON	OFF	OFF	ON	ON
S4	ON	ON	OFF	OFF	ON	ON	OFF	OFF
S5	OFF	ON	OFF	ON	OFF	ON	OFF	ON
S6	ON	OFF	ON	OFF	ON	OFF	ON	OFF

Figure 15.16 BFN simulation setup along with the RF transmit chain.

perform many integrated and system-level simulation, such as beamforming antenna arrays along with RF system to achieve higher data rates by using millimeter-wave frequencies. To evaluate the performance, the BFN must be integrated into a system-level model and evaluated over a collection of the parameter, steering, and channel combinations [17, 18]. Because of the complexities of 5G antenna design, RF system engineers need to include the antenna characteristics in their simulations to correctly design the entire T/R system. All these activities are best done early in the design process.

As the industry moving toward highly integrated 5G phased-array systems, it is critical for in-house systems experts to work closely with hardware developers, with both fully exploring the capabilities and trade-offs among possible architectures and integration technologies [19–22]. An ideal phased array system design flow handles the start-to-finish front-end development, embedding RF/microwave

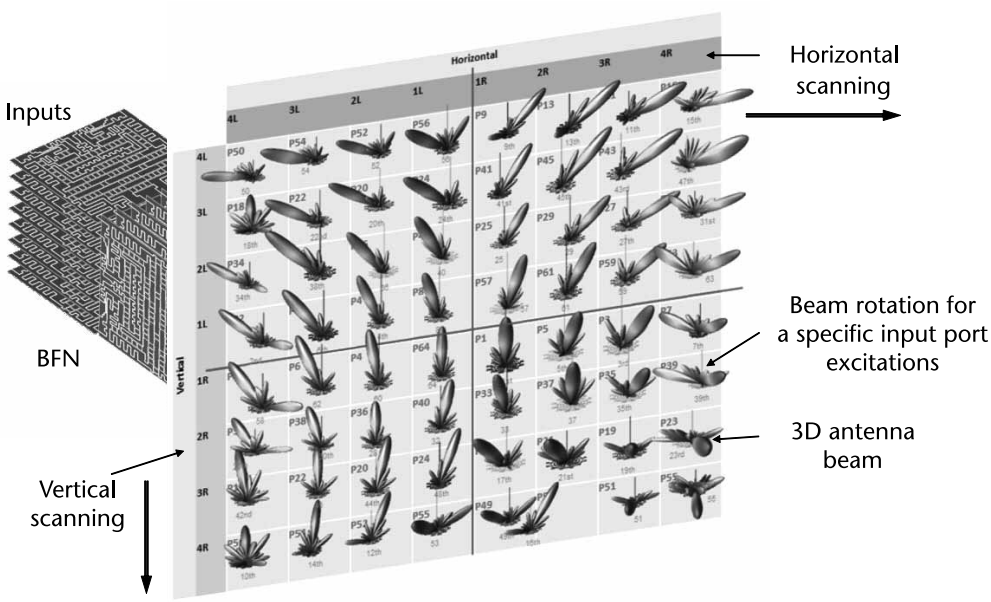

Figure 15.17 Volumetric beam rotation of phased array antenna for 64 RF inputs.

circuit simulation and/or measured data of components models within a phased-array system hierarchy. These analysis and simulations enable the system designer to select the optimum solution, ranging from hybrid modules through a fully integrated RFIC device, addressing the specific requirements of the targeted application. The inability of high-level system tools to accurately model the interactions between the RF components, which are typically specified and characterized individually, results in design failure, and high costs of development. Because the overall phased array performance is neither driven purely by the antenna nor by the microwave electronics in the feed network, combined analysis and simulation capture their interaction to accurately predict true system behavior. Circuit, system, and EM cosimulation together enable verification throughout the design process.

MIMO phased arrays and the corresponding RF and digital circuits are critical components of the 5G communication system. A balance must be made in these system designs to meet overall system performance goals and system-level cost objectives. The modeling of a complete system including RF, antenna, and signal processing components can help to verify design choices at the earliest phases of the project and reduce the associated challenges. In a phased array, system-level simulation can account for RF effects such as the S-parameters of off-the-shelf phase shifters and attenuators and X or S-parameters of nonlinear amplifiers and mixers. With this ability, users can characterize the radiation of spurious intermodulation signals from the array, which helps to avoid interference with nearby antennas.

In this section, system-level design and simulations method for incorporating 5G phased array antenna that is coupled to RF circuits is discussed. This method provides great accuracy with electrical modeling of a phased array antenna in the presence of the TRM and other subsystems of the 5G MIMO. Furthermore, the system simulator models the antenna and RF interaction to obtain a more realistic performance of the overall system. In a 5G system, more devices are being

integrated into packages that need different types of design and analysis tools. Innovative design flow and simulation methods are needed from the component level implementation all the way through to system-level performance verification.

The block diagram concept of 5G transceiver system is shown in Figure 15.18. It can be divided into three sections, the first section is the base-band system, the second part is the RF design block and the last section is the radiating element. In complete phased array design there are many design considerations for all these three sections:

- *Phased array system-level design considerations:* Drive system with modulated signals; simulation with various array geometries, tapers, imperfections, array mutual coupling, and element radiation patterns; and perform system-level digital signal processing simulation.
- *Phased array RF system design considerations:* RF circuit design for of individual elements (PA, LNA, mixer) of the RF link; and antenna arrays excited from the amplifier and feed network (EM excitation) antenna elements mismatch effects (main lobe gain, beamwidth, sidelobe suppression).
- *Phased array antenna design considerations:* Number of antenna elements, the shape of the phased array; and the spacing between the elements and the arrangement of the antenna elements.

A typical phased array antenna design includes parameters such as array geometry, element spacing, the lattice structure of the elements, and element tapering. Moreover, the effects of mutual coupling among antenna elements are important to characterize before the final design is implemented. After completing an initial configuration of the array design, architectural partitioning can be iteratively evaluated against the overall system performance goals. The 5G network will be very complex compared to other generation networks because of the requirements and technology as shown in Table 15.4, and that is a reason to evaluate system performance along with antenna design. Among these specifications, high data rate and data capacity are the driving force in 5G. To meet these requirements, the phased array system introduces the beam-steering function and enables the system to achieve a good link when incoming signals are coming from different angles, but the steering range will still be limited. The 5G network design starts

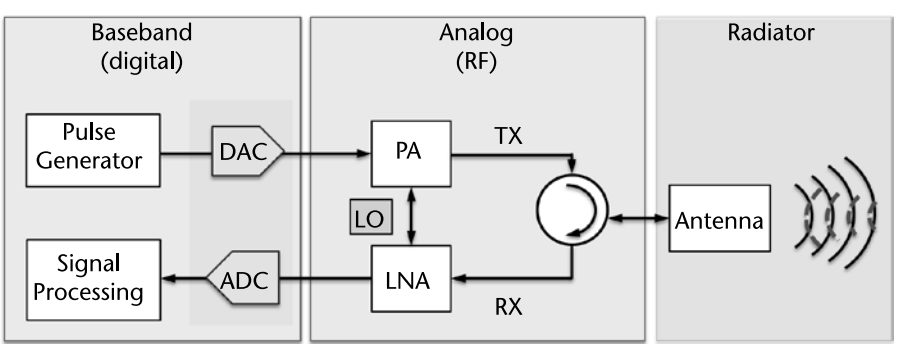

Figure 15.18 Block diagram of a typical communication system.

Table 15.4 All Generation Comparison

Parameters	*1G*	*2G*	*3G*	*4G*	*5G*
Development	1970–1980	1990–2001	2001–2010	2011–2015	2020
Data capacity	2 Kbps	Up to 64 Kbps	2 Mbps	Up to 1 Gbps	Up to 10 Gbps
Technology	Analog wireless	Digital wireless	FDD and TDD CDMA, WCDMA, UMTS	WLAN, OFDMA, MC-CDMA, network LMPS	Unified IP, broadband LAN/ WAN/PAN/ WLAN, OFDM modulation
Multiplexing	FDMA	TDMA	CDMA	CDMA	CDMA, BDMA
Switching type	Circuit	Circuit	Packet, Ckt	All packet	All packet
Handoff	H	H	H	H & V	H &V
Frequency	800–900 MHz	850–1,900 MHz	1.6–2.5 GHz	2–8 GHz	3 to 300 GHz
Core network	PSTN	PSTN	PSTN	Internet	Internet

with system-level simulation. In the first stage, the design blocks are replaced with behavior models to see the complete system performance and other parameters. In the real world, these behavior models of systems are replaced with actual designed components or hardware. The 5G communications will the user the perception of near infinite capacity. This requires a significant change in data rates that will be facilitated by a move to higher transmission frequencies where wider bandwidths are more readily available. System-level design and analysis of the 5G communication system along with phased array antenna array is discussed in the next section.

15.9 The 5G Phased Array System Design

Two critical technologies in the delivery of 5G services are the phased array antenna and hybrid BFN. Beamforming is at the heart of modern wireless communication systems such as 5G, LTE, and WLAN and is used in antenna arrays in radar, sonar, medical imaging, communication and audio systems [23, 24]. Beamforming controls the direction of the transmission or reception of signals at the antenna array and it is a key technique that is used to improve the SNR of received signals, eliminate undesirable interference sources, and focus transmitted signals on a specific location in 5G communication. To achieve a controlled and flexible beamforming in an active array design, it is desirable to have independent weighting control over each antenna array element. This requires separate TRMs for each antenna element.

15.9.1 System-Level Design and Simulation

Millimeter-wave front ends require substantial antenna and beamforming gain to overcome lossy propagation loss as compared to sub-6-GHz systems. The 27.5–29.5-GHz band is a strong candidate for the 5G system and much of the research undertaken to date has considered this band. Figure 15.19 shows a typical architecture of the millimeter-wave front-end communication system. The key parameters

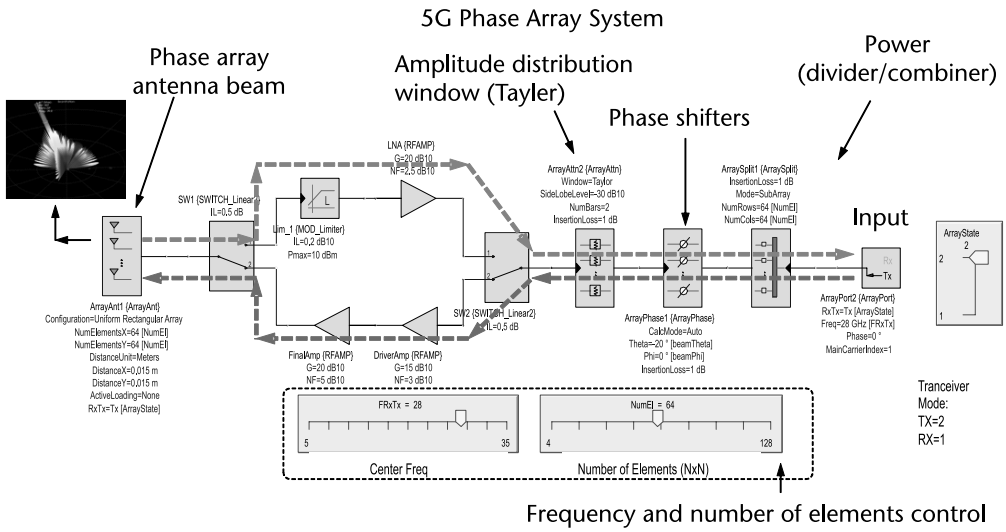

Figure 15.19 5G BFN system level simulation setup.

and specifications for the designed millimeter-wave MIMO transceiver system are listed in Table 15.5.

The system design supports all required phase shifting, path switching, and amplification to drive each antenna array element appropriately. The system engineer performs such simulations to generate design specifications and parameter values for each component used in this communication chain. These specifications are passed on to RF and antenna design engineers. RF engineers design millimeter-wave component circuits and characterize their models to capture the fluctuation of the individual device. Then the component level design is verified for the system-level performance evaluation.

Table 15.5 Key System Parameters of the 64-Channel 5G MIMO Transceiver System

Key System Specifications	*Values*
Receiver sensitivity	28.1 GHz
Signal bandwidth	1 GHz
Antenna array configuration	64 elements
Element gain	7.2 dBi
Array gain	22.8 dBi
Number of RF TRMs	64
Max. transmit power	27 dBm (10-dB backoff)
Max. EIRP for single stream	42 dBm (Tx power + element gain + array gain)
Transmit power dynamic range	27.7 dB
Receive power dynamic range	62 dB
Beam-steering range	Azimuth: ± 60°, Elevation: ± 60°
Duplexing scheme	Time division multiplexing (TDM)
OFDM subcarrier spacing	260 kHz

15.9.2 Antenna Design and Simulation

Printed antennas are very suitable antenna types for the 5G application. A 4 × 4 planar antenna as shown in Figure 15.20 is designed based on antenna specifications received from the system engineer. The antenna array is designed on RT Duroid 5880 substrate (ε_r of 2.2 and thickness of 0.79 mm). This antenna covers a 28-GHz 5G frequency band (25.5 GHz to 30 GHz) and the peak gain is 16 dBi. To achieve sufficient directivity, a beamwidth of 6° in the scanned direction is realized. Element spacing of 5.2 mm is chosen to prevent grating lobes, which are unintended beams (arising from spatial aliasing) that can degrade sensitivity. Because the wavelengths are small at millimeter-wave frequencies, this allows such arrays to be incorporated into a small chip form factor. Base stations are likely going to require hundreds of elements to meet the EIRP requirements for increased coverage, whereas end-user equipment may only require 16–32 elements.

The array EIRP must be chosen and the output power required per element at P1dB (P_{out}) is determined based on the number of array elements. Given an EIRP, P_{out} is calculated using:

$$P_{out} = EIRP - 10\log N - G_{ANT} + L_M \tag{15.5}$$

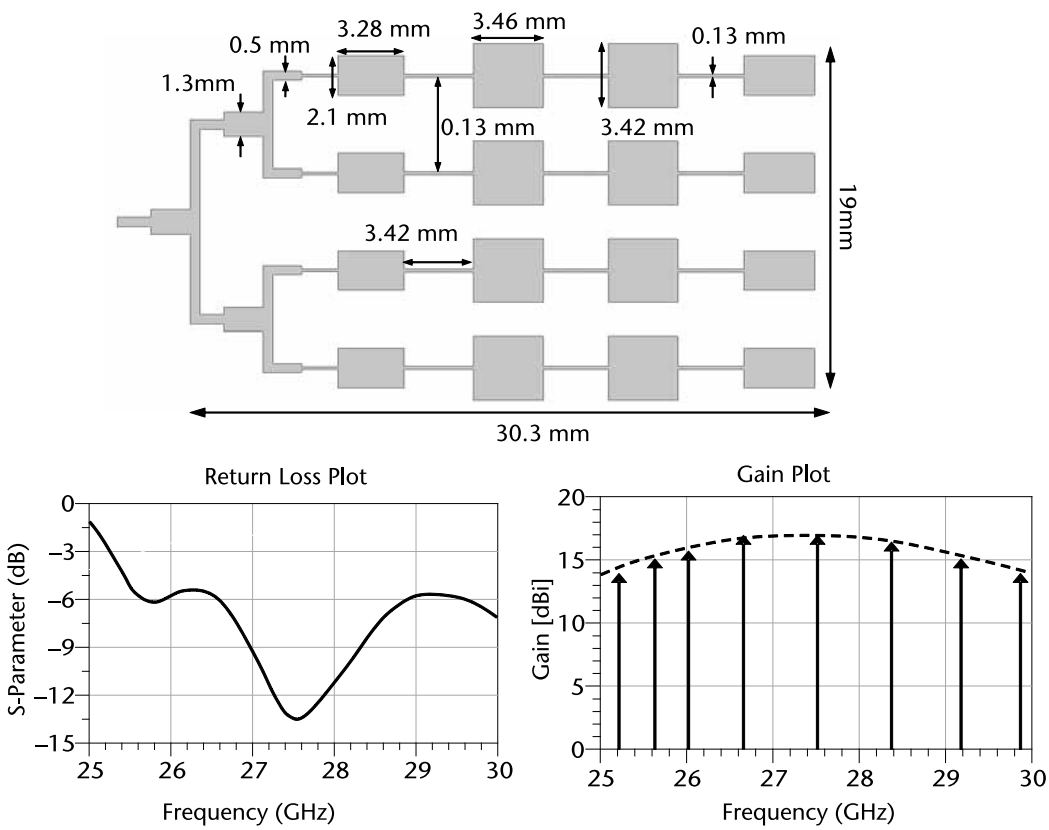

Figure 15.20 The 28-GHz 4 × 4 planar antenna array and simulated return loss and gain plot.

where N is the number of array elements, G_{ANT} is the N-element antenna gain assuming uniform distribution across the array and includes the antenna ohmic, mismatch loss, and feed line loss, and L_M is the power loss due to any amplitude and phase mismatch between the elements. Figure 15.21 presents the required P_{out} for different EIRP values and array sizes. In this design P_{out} is chosen around 10 dBm for low power consumption per chip and to mitigate the thermal issues. An EIRP of 43 dBm can be achieved with an array size of $N = 64$ (16×4 elements).

The array factor of a 2-D ($N_x \times M_y$) uniform planar array can be written as [25]

$$AF(\varnothing,\theta) = \sum_{n=0}^{N_x-1}\sum_{m=0}^{M_y-1} a_{nm} e^{-j2\pi \sin\varnothing\left(n\cos\theta d_x + m\sin\theta d_y\right)} / \lambda_0 \tag{15.6}$$

where $\varnothing$ is the azimuth angle, θ is the elevation angle, a_{nm} is the complex coefficient at each element, λ_0 is the wavelength in vacuum, and (d_x, d_y) represent the horizontal and vertical element spacings. For N_x-element uniform linear array at horizontal direction, the horizontal far-field radiation pattern is:

$$P(\varnothing) = E(\varnothing)\sum_{n=0}^{N_x-1} a_n e^{-j2\pi nd\sin\varnothing} / \lambda_0 \tag{15.7}$$

where $E(\varnothing)$ is the horizontal pattern of element, d is the element spacing, and a_n is the complex excitation at the nth element.

15.9.3 RF Circuit Design and Simulation

Normally, the design of an RF system is performed in a top-down approach, where the application requirements and constraints drive component design decisions. After getting the design specification of individual components from system engineers used in the transceiver chain, the RF engineer starts a realization of these components using circuit simulation. The circuit simulation setup in the ADS for a 4-channel transmit chain is shown in Figure 15.22. All major RF components

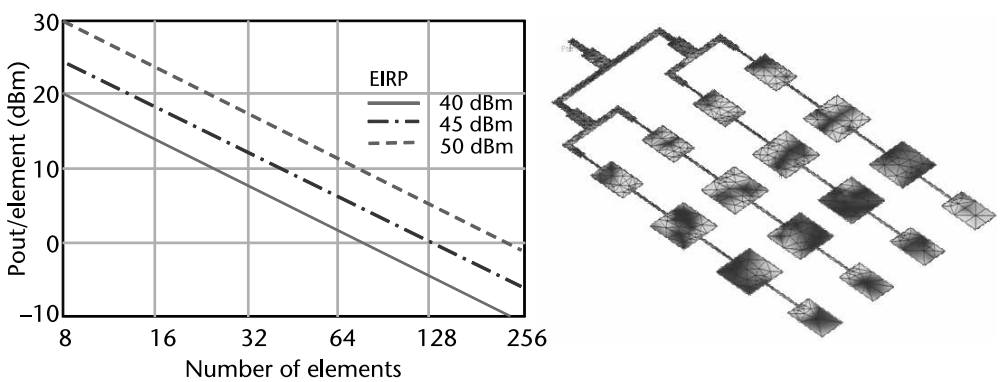

Figure 15.21 Required output power per element for different EIRP values versus number of array elements.

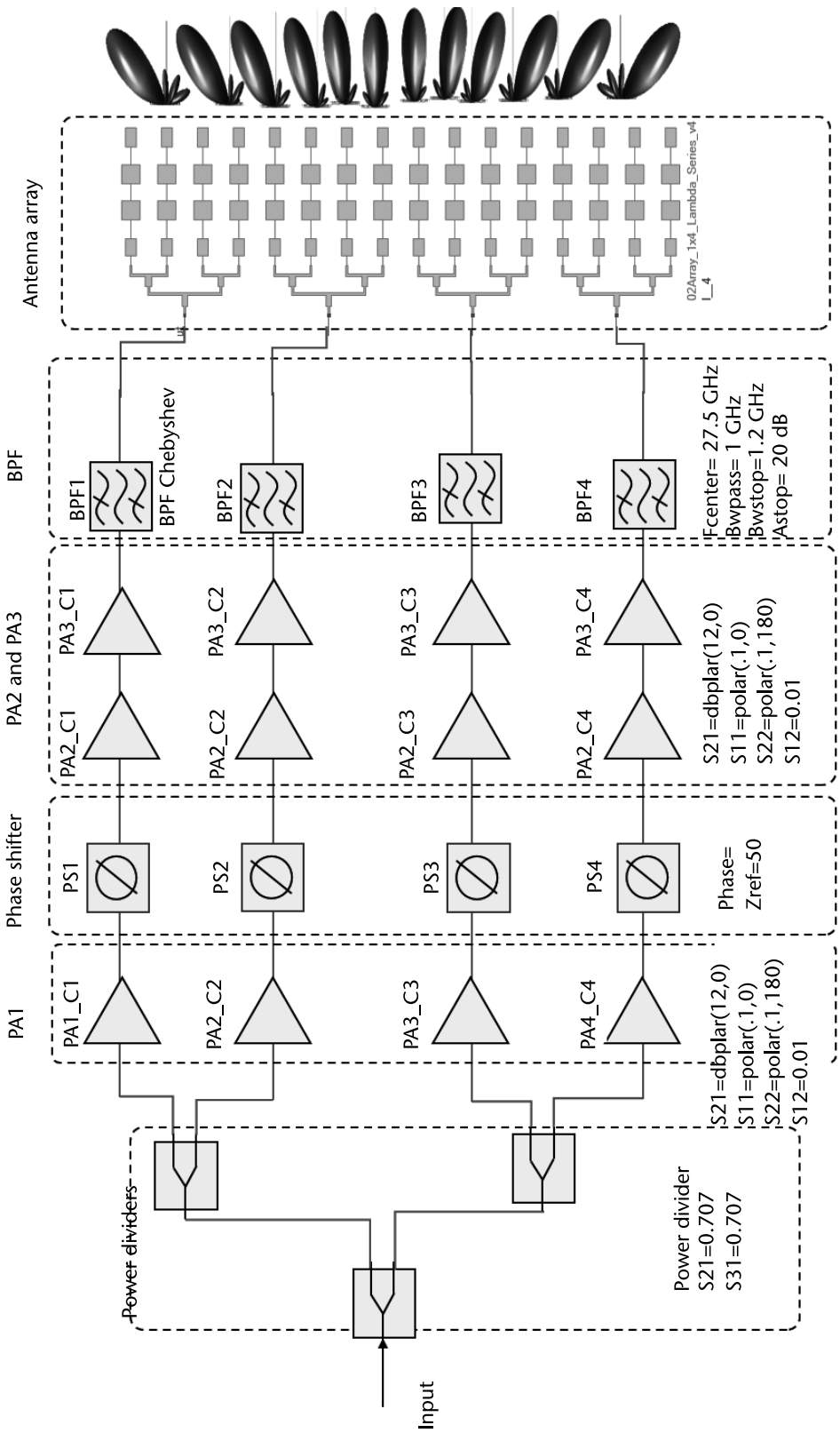

Figure 15.22 Four-channel 5G phased array transmit module schematic simulation setup and rotated antenna beams for different phase values.

(LNA, PA, filter, and phase shifter) of the transceiver chain are designed based on MMIC technology, as discussed in Chapter 14.

This communication system is built on a low-cost PCB that only consumed approximately 10W of DC power in either its transmit (Tx) or receive (Rx) modes. It interfaces to an array of a 4-antenna subarray, where each subarray is driven by one of four parallel PAs. Some degree of filtering is required immediately after each PA, for harmonic rejection and suppression of receive band noise and unwanted spurious outputs. The inputs to all communication channels are driven in-phase from a common RF input via a 4-way splitter as shown in Figure 15.22.

The performance of an RF PA dominate the overall transmitter (Tx) performance, as its PAE dictates the power and heat dissipation for the entire Tx. For enhanced user experience and massive MIMO antennas, the 5G system will require more PAs to be integrated into the RF front-end modules, making the design of a 5G PA more critical than that of a 4G PA design. The output power (P_{out}), linearity, reliability, cost, and form factors of a PA are all very important. SiGe BiCMOS processes are used for PA design. The 4-bit phase shifter is designed with pHEMT process as shown in Figure 15.23. This phase shifter allows the insertion phase of each channel to be set with a 22.5° resolution. The lower bits (22.5° and 45°) are implemented using switched-filter networks. Higher bits (90° and 180°) are implemented by switching between highpass filter and LPF networks.

15.10 System Validation and Test

Once the individual components have been designed and meet their individual performance requirements, it is needed to assess how they will perform when deployed in the actual operational environment for which they are intended. After completing design of individual circuit designs, the next step is the verification and test of the prototype hardware.

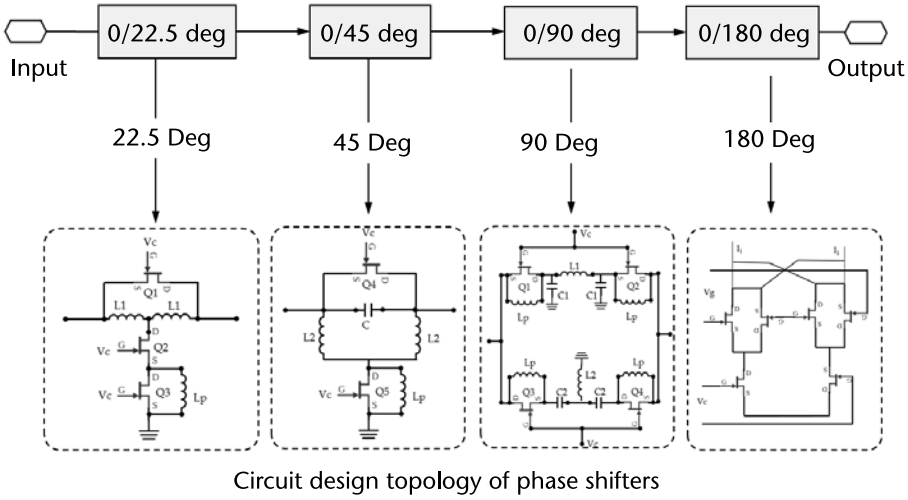

Figure 15.23 Four-bit phase shifter design.

As explained earlier, the millimeter-wave RF front-end components and phased array antenna are integrated into the package. Each component performance data is measured (like S-parameter, X-parameter, antenna patterns), and this data is used in system-level validation. In a system simulation, behavior models (like PA, LNA, antenna) are replaced with actual measured data. System-level simulation is carried out to see the actual performance of the complete system. There may be some degradation in the system performance with actual components. Based on system requirements, design components may need reoptimization of system-level changes. System-level validation is a kind of virtual test and it saves on the design cost and production cycle. Designed RF components of the communication system and antenna array are integrated in a 5G communication system as shown in Figure 15.24 along with digital baseband blocks. The local oscillator (LO) performance is critical in the millimeter-wave 5G communication system. One major contribution of the degradation of the modulation precision of the millimeter-wave transceiver system is the phase noise of LO. The influence of the phase noise on the error vector magnitude (EVM) can be expressed as [26]:

$$EVM_{PN} = \sqrt{\left(\int_{-\infty}^{\infty} S_{PN}(f)df\right)} = \sqrt{(PN_{INT})} \tag{15.8}$$

where $S_{PN}(f)$ is the phase noise spectrum density and PN_{INT} is the integral phase noise.

The simulated phase array 5G communication system antenna beams are shown in Figure 15.25. The main beam of array antenna always points in the direction of

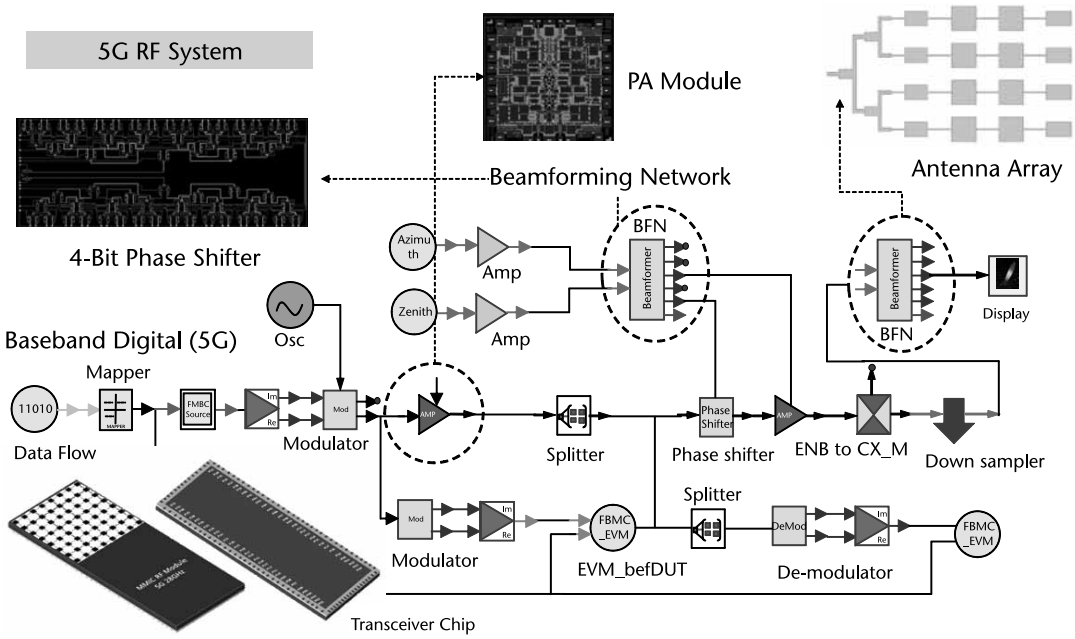

Figure 15.24 Complete 5G communication system validation along with designed components.

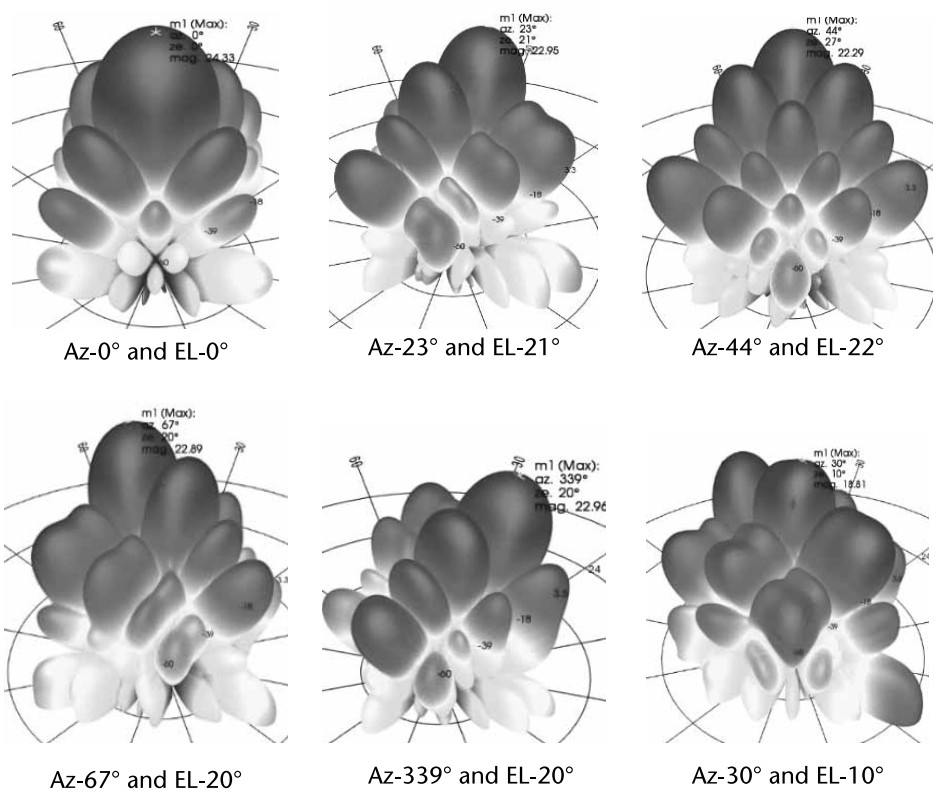

Figure 15.25 Antenna beam patterns for different phase shifts in the complete 5G system.

the increasing phase shift. The complete phased array network provides 64 beams with gains between 28 dBi and 29 dBi. It maintains a return loss less than –10 dB within the frequency band of 27.9–29.4 GHz. This multibeam antenna has ±60° beam coverage. The maximum value, which can be achieved for the field of view (FOV) of a phased array antenna, is 120° (60° left and 60° right). Grating lobes are generated beyond the FOV scan angle. Amplitude tapering can be applied to reduce sidelobe levels in the antenna array.

15.11 Massive MIMO Based on Digital Beamforming

In previous section, FD-MIMO phased array system is based on analog beamforming technique. The antenna array beam of massive MIMO system can be concentrated in a narrow range based on digital beamforming (DBF) technology also. The digital beamforming performs the phase shifting in the digital domain. The RF signal is first downconverted and then digitized using an analog-to-digital converter (ADC) whose digital output is passed to a digital baseband processing block where the beamforming operation is performed. The key technology of the massive is the active multibeam antenna system, which consists of multiple (≥ 64 antenna elements) and transceivers. Massive MIMO relies on spatial multiplexing and a simple method for spatial multiplexing is to deploy linear precoding like beamforming. In

practical systems, DBF technology has the advantages of flexibility, adaptive control, and accuracy. DBF technology is established with the development of advanced digital signal processing, by which transmitting and receiving the useful signal can be implemented with a high-gain narrow beam generated in the direction of the useful signal and null steering generated in the direction of interference. The conceptual diagram of DBF is shown in Figure 15.26.

The received signal vector of the antenna array with N elements is defined as X,

$$X = [x_1 x_2 x_3 \ldots x_N\ ]^T \tag{15.9}$$

where x_i refers to the complex signal received by the ith element.

$$x_i = I_i + jQ_i \tag{15.10}$$

The amplitude and phase of the ith received signal are expressed as [27–29]

$$|x_i| = \sqrt{\left(I_i^2 + Q_i^2\right)} \tag{15.11}$$

$$\varnothing_i = \arctan\left(Q_i / I_i\right) \tag{15.12}$$

To form the kth beam, the complex weighted coefficient W_{ik} is given by:

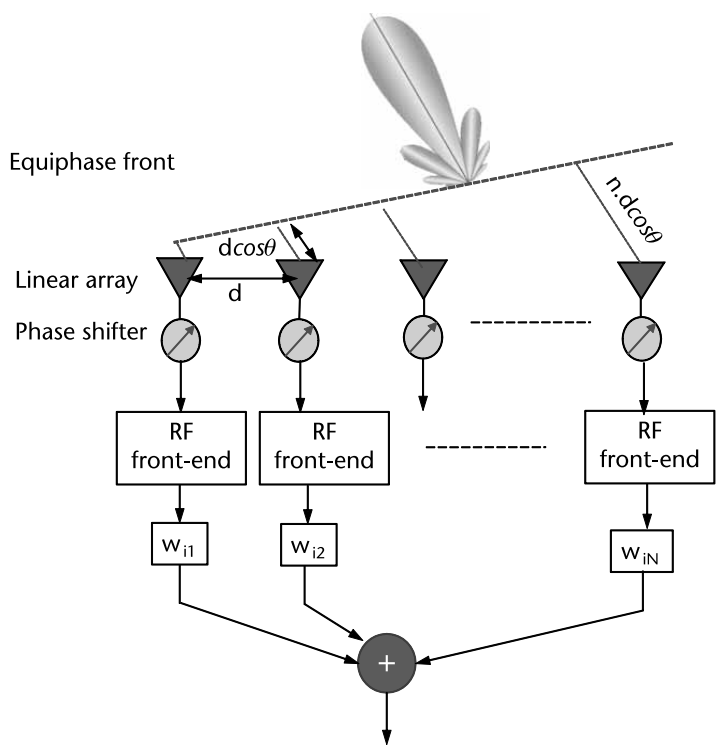

Figure 15.26 The conceptual diagram of a digital BFN.

$$W_{ik} = a_i \exp\left[-ji\Delta\varnothing_{Bk}\right] \tag{15.13}$$

Then the weight of W_k of the kth beam received signal vector is defined as:

$$W_k = \left[W_{1k}\, W_{2k} \ldots W_{Nk}\right] \tag{15.14}$$

The output $D_k(\theta)$ of the DBF system is described by:

$$D_k(\theta) = W^T X \tag{15.15}$$

where $|D_k(\theta)|$ is the radiation pattern of the kth beam.

In massive MIMO system based on digital beamforming, there are many challenges associated with implementation [26]. Each RF channel requires a high-speed, high-resolution ADC, which is challenging to implement and will increase the overall power consumption, especially in the case of large arrays.

15.12 Summary

Active millimeter-wave antennas and BFNs are planned to deploy in unprecedented volumes over the next few years, fueled by the rapidly emerging 5G wireless communications systems. The combination of high-performance silicon processes together with advanced analog and digital design techniques has accelerated the adoption of millimeter-wave ICs to the extent that advanced 5G and SATCOM networks are now anticipated several years earlier than the industry originally projected. The phased array antenna is one of the most important components in the 5G system. Emerging 5G radio access technologies will drastically change the landscape of not only the cellular communication ecosystem, but more specifically the way in which the 5G system and antennas are designed. As per 5G requirement for more data bandwidth, the 5G new radio (NR) will push into new frequency ranges traditionally reserved for satellite and defense applications. The associated adaptive antenna system technologies required to accomplish this and increase overall spectral efficiency, namely beamforming and massive MIMO. Where usually most of the radio functionality could be evaluated independent of the antenna system, the use of adaptive antenna system technologies makes it impossible to dissociate the radio performance from the antenna performance.

In this chapter, a beam-steerable phased array antenna at 60 GHz for a 5G FD-MIMO system was discussed, designed, and modeled and the results were presented. The designed phased array system has 3-D Butler matrix as its feed to achieve a steerable beam ranging from –60° to +60°. Both the feed and the array antenna are designed using waveguide technology resulting in low loss and high-power network. The design and simulation of a completed 5G communication system, BFN, and antenna design of a millimeter-wave 28-GHz transceiver with a beam-steered patch antenna array were also covered in this chapter. Design techniques are established to achieve the desired level of performance using the system, circuit, and EM simulation technologies.

References

[1] Doan, C., et al., "Design Considerations for 60 GHz CMOS Radios," *IEEE Communications Magazine*, Vol. 42, No. 12, December 2004, pp. 132–140.

[2] Lee, J., et al., "A Switched Array Antenna Module for Millimeter-Wave Wireless Communications," *Proc. Global Symp. Millim. Waves*, 2008, pp. 161–163.

[3] Thompson, J., et al., "5G Wireless Communication Systems: Prospects and Challenges," *IEEE Communications Magazine*, February 2014, pp. 62–65.

[4] Roh, W., et al, "Millimeter-wave Beamforming as an Enabling Technology for 5G Cellular Communications: Theoretical Feasibility and Prototype Results," *IEEE Communications Magazine*, Vol. 52, No. 2, 2014, pp. 106–113.

[5] Pattan, B., "The Versatile Butler Matrix," *Microwave Journal*, November 1, 2004.

[6] Gruszczynski, S., and K. Wincza, "Broadband 4x4 Butler Matrices as a Connection of Symmetrical Multisection Coupled-Line 3-dB Directional Couplers and Phase Correction Networks," *IEEE Transactions on Microwave Theory and Techniques*, Vol. 57, No. 1, 2009.

[7] Butler, J., and R. Howe, "Beamforming Matrix Simplify Design of Electronically Scanned Antennas," *Electron. Design*, No. 9, April 1966.

[8] Liang, J. W., and A. J. Paulraj, "On Optimizing Base Station Array Topology for Coverage Extension in Cellular Radio Networks," *45th IEEE Vehicular Technology Conference*, 1995, pp. 866–870.

[9] MacCartney, G. R., et al., "Path Loss Models for 5G Millimeter Wave Propagation Channels in Urban Microcells," *2013 IEEE Global Communications Conference (GLOBECOM)*, Atlanta, GA, 2013, pp. 3948–3953.

[10] Pandey, A. K., "Design of a Compact High Power Phased Array for 5G FD-MIMO System at 29 GHz," *2016 Asia-Pacific Microwave Conference (APMC)*, New Delhi, 2016, pp. 1–4.

[11] Hong, W., et al., "Design and Analysis of a Low-Profile 28 GHz Beam Steering Antenna Solution for Future 5G Cellular Applications," *IEEE MTT-S International Microwave Symposium (IMS2014)*, Tampa, FL, 2014, pp. 1–4.

[12] Khalily, M., et al., "Design of Phased Arrays of Series-Fed Patch Antennas with Reduced Number of the Controllers for 28-GHz mm-Wave Applications," *IEEE Antennas and Wireless Propagation Letters*, Vol. 15, 2016, pp. 1305–1308.

[13] Brookner, E., *Practical Phased-Array Antenna Systems*, Norwood, MA: Artech House, 1991.

[14] Cheon, Y., and Y. Kim, "Millimeter-Wave Phased Array Antenna with Wide Beam Coverage," *2016 10th European Conference on Antennas and Propagation (EuCAP)*, Davos, 2016, pp. 1–3.

[15] Helander, J., et al., "Performance Analysis of Phased Array Antennas in Cellular Handsets for 5G," *IEEE Antennas Wireless Propag. Lett.*, 2015.

[16] Zhang, J., et al., "5G Millimeter-Wave Antenna Array: Design and Challenges," *IEEE Wireless Communications*, Vol. 24, No. 2, April 2017, pp. 106–112.

[17] Rappaport, T. S., "Millimeter Wave Mobile Communications for 5G Cellular: It Will Work!" *IEEE Access,* May 30, 2013.

[18] Roh, W., et al., "Millimeter-Wave Beamforming as an Enabling Technology for 5G Cellular Communications: Theoretical Feasibility and Prototype Results," *IEEE Communications Magazine*, Vol. 52, No. 2, February 2014, pp. 106–113.

[19] Hong, W., "Design and Analysis of a Low-Profile 28GHz Beam Steering Antenna Solution for Future 5G Cellular Applications," *IEEE MTT-S International,* June 2014.

[20] Chang, S., W. Hong, and J. Oh, "Quantization Effects of Phase Shifters on 5G mmWave Antenna Arrays," *Proc. IEEE Int. Symp. Antennas Propag. USNC/URSI Nat. Radio Sci. Meet.*, Vancouver, BC, Canada, July 2015, pp. 2119–2120.

[21] Kibaroglu, K., M. Sayginer, and G. M. Rebeiz, "An Ultra-Low-Cost 32-Element 28 GHz Phased-Array Transceiver with 41 dBm EIRP and 1.0–1.6 Gbps 16-QAM Link at 300 Meters," *Proc. IEEE RFIC, Honolulu*, HI, June 2017, pp. 73–76.

[22] Valdes-Garcia, A., et al., "A Fully-Integrated Dual-Polarization 16-Element W-Band Phased-Array Transceiver in SiGe BiCMOS," *Proc. IEEE Radio Freq. Integr. Circuits Symp. (RFIC),* June 2013, pp. 375–378.

[23] Guo, C., et al., "Advances on Exploiting Polarization in Wireless Communications: Channels, Technologies, and Applications," *IEEE Commun. Surveys Tuts.*, Vol. 19, No. 1, First Quarter, 2017, pp. 125–166.

[24] Kildal, P. S., et al., "MIMO Characterization on System Level of 5G Microbase Stations Subject to Randomness in LOS," *IEEE Access*, Vol. 2, 2014, pp. 1062–1075.

[25] Bhattacharyya, A. K., *Phased Array Antennas: Floquet Analysis, Synthesis, BFNs and Active Array Systems*, New York: Wiley, 2006.

[26] Gu, Q., *RF System Design of Transceivers for Wireless Communications*, New York: Springer, 2005.

[27] Guangyi, Z., and Z. Yujie, *Phased Array Technology*, Beijing, China: Electronic Industry Press, 2006.

[28] Roh, W., et al, "Millimeter-Wave Beamforming as an Enabling Technology for 5G Cellular Communications: Theoretical Feasibility and Prototype Results," *IEEE Communications Magazine*, Vol. 52, February 2014, pp. 106–113.

[29] Yang, B., et al., "Digital Beamforming-Based Massive MIMO Transceiver for 5G Millimeter-Wave Communications," *IEEE Transactions on Microwave Theory and Techniques*, Vol. 66, No. 7, July 2018, pp. 3403–3418.

Selected Bibliography

Daftari, N., et al., "A Wideband 25-35 GHz 5-Bit Low Power 2x2 CMOS Beam Forming Network IC for Reconfigurable Phased Arrays," *IEEE CSICS*, New Orleans, LA, 2015, pp. 1–4.

Fettweis, G., and S. Alamouti, "5G: Personal Mobile Internet Beyond What Cellular Did to Telephony," *IEEE Communications Magazine*, Vol. 52, No. 2, February 2014, pp. 140–145.

Glazunov, A. A., et al., "Impact of the Spatial User Distribution on the Coverage Antenna Pattern of Maximum Ratio Combining in Random Line-of-Sight," *Proc. Eur. Conf. Antennas Propag.*, Lisbon, Portugal, 2015, pp. 1–5.

Golcuk, F., T. Kanar, and G. M. Rebeiz, "A 90–100-GHz 4×4 SiGe BiCMOS Polarimetric Transmit/Receive Phased Array with Simultaneous Receive-Beams Capabilities," *IEEE Transactions on Microwave Theory and Techniques*, Vol. 61, No. 8, August 2013, pp. 3099–3114.

Gu, X., et al., "W-Band Scalable Phased Arrays for Imaging and Communications," *IEEE Communications Magazine*, Vol. 53, No. 4, April 2015, pp. 196–204.

Jacomb-Hood, A., and E. Lier, "Multibeam Active Phased Arrays for Communications Satellites," *IEEE Microwave Magazine*, Vol. 1, No. 4, December 2000, pp. 40–47.

Kant, G. W., et al., "EMBRACE: A Multi Beam 20,000-Element Radio Astronomical Phased Array Antenna Demonstrator," *IEEE Transactions on Antennas and Propagation*, Vol. 59, No. 6, June 2011, pp. 1990–2003.

Kim, H. T., et al., "A 28 GHz CMOS Direct Conversion Transceiver with Packaged Antenna Arrays for 5G Cellular System," *Proc. IEEE Radio Freq. Integr. Circuits Symp. (RFIC),* June 2017, pp. 69–72.

Kim, S. Y., et al., "A Compact Antenna-in-Package 60-GHz SiGe BiCMOS Radio," *Proc. IEEE RFIC*, Tampa, FL, June 2014, pp. 287–288.

Liu, D., et al., *Advanced Millimeter Wave Technologies*, New York: John Wiley and Sons, 2009.
Liu, D., et al., "Antenna-in-Package Design Considerations for Ka-band 5G Communication Applications," *IEEE Transactions on Antennas and Propagation*, 2017.
Ojaroudiparchin, N., et al., "A Switchable 3D-Coverage Phased Array Antenna Package for 5G Mobile Terminals," *IEEE Antennas and Wireless Propagation Letters*, Vol. 15, 2016.
Ojaroudiparchin, N., M. Shen, and G. Pedersen, "Multi-Layer 5G Mobile Phone Antenna for Multi-User MIMO Communications," *Proc 23rd Telecommun. Forum Telfor*, November 2015, pp. 559–562.
Puglielli A., et al., "Design of Energy- and Cost-Efficient Massive MIMO Arrays," *Proc. IEEE,* Vol. 104, No. 3, March 2016, pp. 586–606.
Rajagopal, S., et al., "Antenna Array Design for Multi-Gbps mmWave Mobile Broadband Communication," *Proc. IEEE GLOBECOM'2011*, Houston, TX, 2011, pp. 1–6.
Sayginer, M. and G. M. Rebeiz, "An Eight-Element 2–16-GHz Programmable Phased Array Receiver with One, Two, or Four Simultaneous Beams in SiGe BiCMOS," *IEEE Transactions on Microwave Theory and Techniques*, Vol. 64, No. 12, December 2016, pp. 4585–4597.
Shahramian, S., M. J. Holyoak, and Y. Baeyens, "A 16-Element W-Band Phased Array Transceiver Chipset with Flip-Chip PCB Integrated Antennas for Multi-Gigabit Data Links," *Proc. IEEE RFIC*, Phoenix, AZ, May 2015, pp. 27–30.
Shakib, S., et al., "A Highly Efficient and Linear Power Amplifier for 28-GHz 5G Phased Array Radios in 28-nm CMOS," *IEEE J. Solid-State Circuits*, Vol. 51, No. 12, December 2016, pp. 3020–3036.
Tomkins, A., et al., "A 60 GHz, 802.11ad/WiGig-Compliant Transceiver for Infrastructure and Mobile Applications in 130 nm SiGe BiCMOS," *IEEE J. Solid-State Circuits*, Vol. 50, No. 10, October 2015, pp. 2239–2255.

APPENDIX A

Important Antenna and Electromagnetics Formulas

A.1 Maxwell's Equations

$$\nabla.E = \frac{\rho_v}{\epsilon} \text{ (Gauss's Law)} \tag{A.1}$$

$$\nabla.H = 0 \text{ (Gauss's Law for magnetism)} \tag{A.2}$$

$$\nabla \text{x} E = -\mu \frac{\partial H}{\partial t} \text{ (Faraday's Law)} \tag{A.3}$$

$$\nabla \text{x} H = J + \varepsilon \frac{\partial E}{\partial t} \text{ (Ampere's Law)} \tag{A.4}$$

A.2 Microstrip Antenna Radiation Pattern and Directivity

A measurement antenna radiation pattern is represented by a graphically surrounded sphere as shown in Figure A.1. Electric and magnetic fields (far-field radiation fields) at a distance equal to the radius of the sphere are measured in the E-plane and the H-plane.

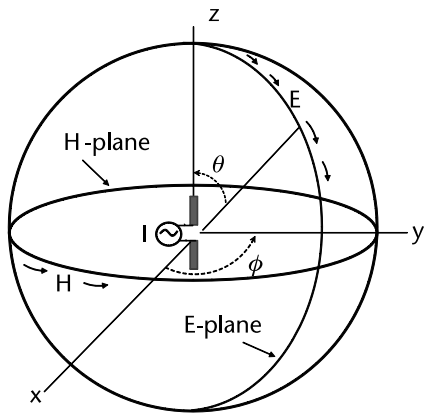

Figure A.1 Antenna-radiated fields evaluated on an imaginary sphere surrounding a dipole

For a rectangular microstrip patch antenna with length L and width W, the normalized radiation pattern (far-field intensity) is at a point $E(\theta, \varnothing)$ given by:

$$E_\theta = \frac{\sin\left(\frac{kW\sin\theta\sin\varnothing}{2}\right)}{\frac{kW\sin\theta\sin\varnothing}{2}}\cos\left(\frac{kL\sin\theta\cos\varnothing}{2}\right)\cos\varnothing \tag{A.5}$$

$$E_\varnothing = -\frac{\sin\left(\frac{kW\sin\theta\sin\varnothing}{2}\right)}{\frac{kW\sin\theta\sin\varnothing}{2}}\cos\left(\frac{kL\sin\theta\cos\varnothing}{2}\right)\sin\varnothing\cos\theta \tag{A.6}$$

where k is the wavenumber given by $k = 2\pi/\lambda$. The magnitude of the field is calculated by:

$$A(\theta,\varnothing) = \sqrt{E_\theta^{\,2} + E_\varnothing^{\,2}} \tag{A.7}$$

The directivity of antenna is calculated by

$$D(\theta,\varnothing) = \frac{4\pi R^2 P_{avg}(\theta,\varnothing)}{P_{rad}} \tag{A.8}$$

where $P_{avg} = \frac{1}{2}Re\left[\vec{E}\,x\,\vec{H}\right]$ is the radiation pointing vector (power per unit area) and P_{rad} is the total radiated power.

A.3 Antenna Bandwidth Calculation

The impedance bandwidth (BW) of the microstrip antenna is defined as the frequency range over which it is matched with that of the feed line within specified limits. The bandwidth is inversely proportional to its quality factor Q and is given as

$$BW = \frac{VSWR - 1}{Q\sqrt{VSWR}} \tag{A.9}$$

where VSWR is defined in terms of the input reflection coefficient τ

$$VSWR = \frac{1 + |\tau|}{1 - |\tau|} \tag{A.10}$$

The reflection coefficient τ is defined in terms of antenna input impedance Z_{in} and the characteristic impedance Z_0 of the feed line:

Table A.1 Important Parameters and Units

Parameter	*Symbol*	*Unit/Value*
Capacitance	C	F
Conductivity	σ	$1/\Omega \cdot$ m
Current	I	A
Current density	J	A/m^2
Dielectric constant	ε	F/m
Dielectric constant in space	ε_0	F/m
Electric field	E	V/m
Electric field displacement	D	V/m
Magnetic field	B	Tesla, Wb/m^2
Magnetic field strength	H	A/m
Magnetic flux	ψ	Wb
Magnetic potential	A	Wb/m
Mutual-inductance	M	H
Permeability	μ	H/m
Permeability in space	μ_0	H/m
Power	P	W
Relative dielectric constant	ϵ_r	
Resistance	R	Ω
Self-inductance	L	H
Skin depth	δ_s	M

$$\tau = \frac{Z_{in} - Z_0}{Z_{in} + Z_0} \tag{A.11}$$

Table A.1 shows a list of parameters and their units.

A.4 Constants

The following are constants:

- $\varepsilon_0 = 8.85419 \times 10^{-12}$ F/m
- $\mu_0 = 4\pi \times 10^{-7}$ H/m
- $\eta_0 \approx 377\Omega$

APPENDIX B

Designed Antenna Project List

No.	Project Name	Application	Chapter
1	Microstrip Patch Antenna	2.4-GHz ISM Band	2
2	Coaxial-Fed Patch Antenna	Coal Mine	2
3	Circular Polarized Millimeter-Wave Antenna	5G	2
4	Dual-Orthogonal Fed Square CP Antenna	GNSS and GPS	2
5	CPW-Fed Dual-Band WLAN Antenna	WLAN	3
6	Inverted-F Bluetooth Antenna	Bluetooth	3
7	Planar Inverted-F Antenna (PIFA)	LTE	3
8	MIMO Antenna Design	LTE	3
9	Mobile MIMO Antenna Design	Mobile Antenna	4
10	Reconfigurable Frequency and Polarization Antenna	Wireless Devices	5
11	Wilkinson Power Divider	High Port Isolation	6
12	Printed Antenna Array	Weather Radar	6
13	Circular Aperture Radar Microstrip Antenna Array	Radar	6
14	Multilayer Antenna Design	Broadband Applications	6
15	Millimeter Wave Antenna Array for Automotive Radar	Automotive Radar	6
16	Cylindrical Microstrip Antenna Analyses for Large Radii	Mobile Phone and Other Designs with Curvature	6
17	Cylindrical Microstrip Antenna Analyses for Small Radii	Mobile Phone and Other Designs with Curvature	6
18	Conformal Antenna on Missile Surface	Missile Application	6
19	Conformal Microstrip Antenna Array Fed with Waveguide	Airborne Remote Sensing	6
20	Dual-Polarized SAR Antennas Design	Microwave Imaging	7
21	Beamforming network using microstrip line	Microwave Imaging	8
22	Cosec square Shaped Pattern Array Antenna	Microwave Imaging	8
23	Square Coaxial Line Beamforming Network	High Power Feed	8
24	Dual-Frequency Shared Aperture Antenna Array	Microwave Imaging	9
25	Dual Polarized Feed Network	Microwave Imaging	10
26	Dual Polarized X-Band Array	Microwave Imaging	10
27	Microstrip Patch Antenna on Mushroom-Like EBG Structure	Broadband Applications	11
28	Uniplanar EBG Cells with Rectangular Microstrip Antenna	Broadband Applications	11

No.	Project Name	Application	Chapter
29	Bowtie Antenna with EBG Cells	Broadband Applications	11
30	Array Antenna Design Using EBG	Broadband Applications	11
31	Frequency Selective Surface (FSS)	FSS	11
32	Antennas on Photonic Bandgap (PBG)	High-Frequency Applications	11
33	Sierpinski Gasket Fractal Antenna	Compact Antennas	11
34	Square Shape Fractal Antenna	Compact Antennas	11
35	Koch Snowflake Fractal Antenna	Compact Antennas	11
36	Hilbert Antenna Array	Partial Discharge Detection	11
37	Hexagonal Monopole Antenna	Broadband Applications	11
38	Broadband Rectangular Patch	Broadband System	11
39	Slot Loaded Patch	Broadband System	11
40	Spiral Vivaldi Antenna	Broadband System	11
41	Wideband Antipodal Vivaldi Antenna	Broadband Applications	11
42	SIW Microstrip Patch Antenna	Healthcare	11
43	RFID Tag Antenna	RFID	12
44	Fat Tag or Dog Bone RFID Antenna	RFID	12
45	RFID Reader Antenna	RFID	12
46	GPS Spiral Antenna Design	GPS, GNSS	12
47	GPS Circular Spiral Antenna Design	GPS	12
48	Sine-Wave Meander Archimedean Spiral Antenna	GPS	12
49	Wireless Body Area Network (WBAN) Antenna	Healthcare	12
50	Dual-Band Wearable Antenna with EBG Structure	Healthcare	12
51	LPWAN IoT Antenna	IoT	12
52	Quasi-Yagi IoT Antenna Design	IoT	12
53	Automotive Glass Mounted FM/DAB Antennas	Automotive	13
54	Shark Fin Antenna	Automotive	13
55	LTE/GSM Antenna Design	Automotive	13
56	Grid Array Antenna for 24 GHz Automotive SRR	Automotive	13
57	Microstrip Comb-Line Antenna Arrays for LRR	Automotive	13
58	45° Amplitude Tapered Comb-Line Antenna Array	Automotive	13
59	ACC Radar Antenna Design	Automotive	13
60	Rotman Lens Design for Electronic Scanning of Antenna Beam	Automotive	13
61	Phased Array Antenna for ETC Application at 5.8 GHz	Automotive	13
62	MMIC Low-Noise Amplifier (LNA)	Phased Array	14
63	Power Amplifier Design	Phased Array	14
64	MMIC SPDT Switch	Phased Array	14
65	LTCC LPF Filter	Phased Array	14
66	Six-Bit MMIC Phase Shifter	Phased Array	14
67	Phased Array Radar Using Transceiver Module	Phased Array	14
68	Millimeter-Wave 5G 8 × 8 Butler Matrix-Based Beamforming Network	5G BFN	15
69	60-GHz Microstrip Antenna Array Design for 5G	5G Antenna Array	15
70	FD-MIMO Phased Array System	5G Phased Array	15
71	5G Phased Array	5G	15

Acronyms and Abbreviations

ACC	Adaptive cruise control
ADC	Analog-to-digital converter
ADS	Advanced Design System
AESA	Active electronic scanning array
AM	Amplitude modulation
AMC	Artificial magnetic conductor
APN	Airborne Doppler Navigator
AR	Axial ratio
ARNS	Aeronautical Radio Navigation Service
ASIC	Application specific integrated circuit
ASP	Aperture-stacked patch
AUT	Antenna Under Test
AVI	Automatic vehicle identification
AWACS	Airborne warning and control
AWS	Advanced Wireless Service
BFN	Beamforming network
BW	Bandwidth
CAD	Computer-aided design
CDMA	Code division multiple access
CEM	Computational electromagnetics
CISPR	Comité International Spécial des Perturbations Radioélectriques
CP	Circular polarization
CPW	Coplanar waveguide
CTA	Cross-traffic alert
CTR	Current taper ratio
CW/A	Collision warning/avoidance systems
DAB	Digital audio broadcasting
DBF	Digital beamforming
DBS	Direct broadcast satellite
DC	Direct current
DCS	Digital communications system
DCU	Digital control unit
DFW	Dielectric-filled waveguide
DMB	Digital multimedia broadcasting
DSRC	Dedicated short-range communications

EBG	Electromagnetic bandgap
ECU	Electronic control unit
EDA	Electronic design automation
EFIE	Electric field integral equation
EIRP	Effective isotropic radiative power
EM	Electromagnetic
EMC	Electromagnetic compatibility
EMI	Electromagnetic interference
ESA	Electronic scanning antenna
ETC	Electronic toll collection
EVM	Error vector magnitude
FAA	Frequency agile antenna
FDTD	Finite difference time domain
FEM	Finite element method
FET	Field effect transistor
FFT	Fast Fourier transform
FM	Frequency modulation
FMCW	Frequency-modulated continuous wave
FOV	Field of view
FRC	Fractal rectangular curve
FSS	Frequency selective surfaces
GAA	Grid array antenna
GHz	Gigahertz
GIS	Geographic Information Systems
GLONASS	Russian Global Navigation Satellite System
GNSS	Global Navigation Satellite System
GPS	Global Positioning System
GSM	Global System for Mobile Communications
HAC	Hearing aid compatibility
HFSS	High-frequency structure simulator
HIS	High impedance surface
HPBW	Half-power beamwidth
Hz	Hertz
IDFT	Inverse discrete Fourier transform
IFA	Inverted-F antenna
INS	Inertial Navigation System
IoT	Internet of Things
ISM	Industrial, Scientific, and Medical Band
ITS	Intelligent transport system
LCP	Liquid crystal polymer
LHCP	Left-hand circular polarization
LNA	Low-noise amplifier
LPWAN	Low-power wide area network
LTCC	Low temperature co-fired ceramic
LTE	Long Term Evolution
MCM	Multichip module
MEG	Mean effective gain
MFIE	Magnetic field integral equation

MHz	Megahertz
MICS	Medical Implant Communication Services
MIMO	Multiple-input multiple-output
MISO	Multiple-input single-output
MMIC	Microwave monolithic integrated circuits
MoM	Method of Moments
MSS	Mobile satellite service
MU-MIMO	Multi-user MIMO
NF	Noise figure
NRI	Negative Refractive Index
OBU	Onboard unit
PA	Power amplifier
PAA	Phased array antenna
PAE	Power-added efficiency
PAN	Personal area network
PBG	Photonic bandgap
PCB	Printed circuit board
PD	Partial discharge
PDF	Probability density function
PDP	Power display profile
PEC	Perfect electric conductor
PIFA	Planar inverted-F antenna
PMC	Perfect magnetic conductor
PNF	Planar near test facility
PTFE	Polytetrafluoroethylene
QFN	Quad-flat no-leads
RCS	Radar cross-section
RF	Radio frequency
RFID	Radio frequency identification
RHCP	Right-hand circular polarization
RL	Return loss
RKES	Remote keyless entry service
RNNS	Radio Navigation Satellite System
RSU	Roadside unit
SAM	Standard anthropomorphic model
SAR	Synthetic aperture radar
SCL	Square coaxial line
SDARS	Satellite Digital Audio Radio Service
SFCW	Stepped frequency continuous wave
SISO	Single-input single-output
SIW	Substrate-integrated waveguide
SLL	Sidelobe level
SMARSA	Sine-wave meander Archimedean spiral antenna
SNR	Signal-to-noise ratio
TCM	Transparent conducting material
TE	Transverse electric (mode/field)
TEM	Transverse electromagnetic (mode/field)
TM	Transverse magnetic (mode/field)

TPMS	Tire-pressuring monitoring system
T/R	Transmit/receive
TRM	Transmit-receive module
TTD	True time delay
UC-EBG	Uniplanar EBG
UHF	Ultrahigh frequency
UMTS	Universal Mobile Telecommunications System
UWB	Ultrawideband
VNA	Vector network analyzer
VSWR	Voltage standing wave ratio
WBAN	Wireless body area network
WCDMA	Wideband code division multiple access
WiGig	Wireless Gigabit Alliance
WiMax	Worldwide Interoperability for Microwave Access
XPD	Cross-polarization decoupling

About the Author

Anil Pandey received a B.E. in electronic and communication engineering from KEC in 2001, and master of technology (M. Tech) in RF microwave engineering from the Indian Institute of Technology (IIT) in Varanasi, India, in 2003. His M. Tech thesis was "Broadband Multilayer Printed Antennas." From 2003 to 2006, he was a scientist at the Indian Space Research Organization (ISRO) in Ahmedabad, India. Since 2007, he has been in the Design Engineering Software (DES) area of the research and development division at Keysight Technologies, India, where currently he is a principal engineer. He has conducted over 16 years of research in the area of printed antennas. He has worked on various projects involving a wide range of antenna technology, including printed antennas, broadband microstrip antennas, phased array systems, 5G, mobile phone antennas, automotive radar, SAR antennas, and multilayer microstrip arrays. He has successfully completed many research projects and also managed several projects in these fields.

Mr. Pandey's research interests include microwave and antenna engineering, automobile antennas, biomedical engineering, and communication and system engineering. During his work in ISRO, he gained experience in antenna designs, electronic design automation (EDA) tools, project management, and training. He developed microstrip phased array antennas and a high-power feed network for satellite remote-sensing applications. At Keysight Technologies, he managed and led groups and developed various active and passive microwave components by employing MMIC, LTCC, printed, and waveguide-based technologies. In addition, he developed wideband microstrip, MIMO antennas, mobile phone antennas, a 5G communication antenna system, radar antenna arrays, couplers, power dividers, and wideband monopulse comparators. Mr. Pandey has published more than 40 papers in journals and conference proceedings. He has two patents on RF microwave and antenna design. Additionally, he has served on the technical and organizational committees of several international conferences.

Index

0–9

0-db coupler, 373
3-db hybrid coupler, 373
3GPP, 366
5G, 1, 18–30, 43–54, 75–78, 217, 232, 277, 365
5G communication, 54, 365–375, 381–392
5G spectrums, 369
5G system, 22, 366–368, 381–392
60–GHz spectrum, 370
6-bit digital phase shifter, 357

A

ACC radar, 326–327
Active phased arrays, 129
Advanced Design System (ADS), 39, 59
Airborne SAR, 129, 141, 177, 197
Airborne Synthetic Aperture Radar (ASAR), 182
Air-surveillance radar, 178
AM/FM antennas, 311
Amplitude distribution, 171
Amplitude tapered antenna array, 322
Analog-to-digital converter (ADC), 390
Antenna, 1–22, 30–116, 121–300, 306–346, 357–407
Antenna array, 20–21, 122–129, 138, 159–210, 233, 274, 320, 339, 363, 393, 402
Antenna directivity, 46
Antenna diversity, 81, 83, 100
Antenna efficiency, 11
Antenna gain, 10, 42, 44, 65, 71, 218, 286, 327
Antenna mathematical modeling, 105
Antenna measurement, 45
Antenna pattern measurement, 46
Antenna pattern synthesis, 178
Antenna polarization, 110, 292
Antenna radiation pattern, 9–10, 47, 63–70, 121, 135, 150, 171–187, 283, 306, 397
Antenna switching, 106
Antipodal vivaldi antenna, 268–273, 402
Aperture coupling, 128, 168
Aperture-coupled feed, 35
Aperture-coupled microstrip antenna, 224
Archimedean spiral antenna, 291–293, 405
Array factor, 122–124, 180–181, 219–220, 386
Array feed network, 124
Array scan angle, 328
Artificial magnetic conductor (AMC), 236
Automotive antenna, 21, 305–316, 322, 324, 338
Automotive radar, 142–155, 232, 306–309, 325, 336, 337–338, 401
Axial ratio, 334, 403
Azimuth plane, 9, 121–150, 163–173, 186–188, 198, 204, 306–343, 361, 378, 386
Azimuthal radiation pattern, 17

B

Back lobes, 177, 267
Backscatter, 177, 202–203, 279–283
Backscattered signal, 161–164, 214, 278, 286
Balanced mode impedance, 112
Bandgap, 236–241, 251, 404–405
Bandwidth, 1–11, 17, 28–160, 172–399
Base transceiver station (BTS), 378
Beam squinting, 218
Beamforming network (BFN), 22, 129
Bidirectional radiation pattern, 2, 40
Biomedical antenna, 296
Biomedical engineering, 294
Bluetooth, 4, 18–21, 63–65, 71–80, 95, 96, 97, 295, 305–316, 370, 401
Bowtie antenna, 117, 244, 402

Breakdown phenomena, 191
Broadband antenna, 21, 51, 184, 235–254, 268–274
Broadband rectangular patch, 264, 402
Butler matrix, 334, 366–378, 392

C

Carpet fractal, 254
Cartesian (rectangular) coordinates, 9, 47
Car-to-car (C2C) communications, antenna, 314
Cavity model, 12–13, 28–29, 148
Chebyshev polynomials, 193
Circular aperture array antenna, 138
Circular polarization, 11, 42–43, 403
Circularly polarized microstrip patch antenna, 42
CISPR, 97–101, 403
Coal mine antenna, 40
Coaxial connector, 4, 34, 225
Coaxial feed, 35, 40–41, 139, 160, 191–197
Coefficient of thermal expansion (CTE), 372
Collision avoidance radar, 142, 214, 306
Collision warning/avoidance (CW/A), 326
Complex correlation, 84
Computational electromagnetics (CEM), 16
Conducted emissions, 95
Conducted susceptibility, 95
Conformal antenna, 20, 146–151
Connected vehicles (V2X), 379
Corporate feed network, 125, 132
Cosecant square shaped pattern, 179
CPW feed, 2, 60–62, 257
Crossover, 372–373
Cross-polarization, 8, 12–13, 36, 85, 129, 131, 166–197, 222–250, 270–290, 319
Cross-talk, 71
Customized printed antenna, 6
Cutoff frequency, 197, 246, 252, 292
Cylindrical microstrip antenna, 147

D

DAB antenna, 313
DAB band, 311
DC block capacitor, 110
Dedicated short-range communications (DSRC) antennas, 311
Dielectric material, 2, 32–38, 252–269
Dielectric substrate, 2, 27–31, 153, 239–264, 317–327
Differential-equation (DE) solvers, 16
Digital audio broadcasting (DAB), 21
Digital beamforming (DBF), 390
Digital control unit (DCU), 230
Directivity, 7, 10, 338, 397
Diversity technique, 79–85
Dog-bone RFID antenna, 282
Dolph-Chebyshev, 178, 322
Doppler effect detection, 331
Double negative (DNG) material, 236
DPDT, 107
Dual-band antenna, 55
Dual-polarization, 107–108, 128–129, 159, 201

E

EBG, 21, 235–246, 272–275, 296–297
Edge-coupled patch, 140
Edge-fed, 34, 205
Effective isotropic radiated power (EIRP), 217, 365
E-field, 62, 88–96, 116, 145–149, 251–298, 302–357
Electric field integral equation (EFIE), 14
Electrical field plot, 61
Electrically reconfigurable antenna, 105
Electromagnetic compatibility (EMC), 77
Electromagnetic field, 34
Electromagnetic Interference (EMI), 86
Electromagnetic wave, 1, 11, 32, 51
Electromagnetically coupled feed, 36
Electronic control unit (ECU), 311
Electronic design automation (EDA), 13
Electronic product code (EPC), 278
Electronic scanning antenna, 216, 232, 328, 403
EM spectrum, 161, 245, 370
EMC, 24, 77, 86, 93–101, 226, 404
EMI, 86–101, 248, 404
Envelope correlation, 84

E-plane, 11–12, 29, 169, 246, 328, 397
Error vector magnitude (EVM), 389
ETC System, 332

F

Fat-tag, 282
FD-MIMO, 129, 378–379, 390–393, 402
Federal Communications Commission (FCC), 77
FET, 105, 106, 351–362, 404
Field of view (FOV), 390
Figure of merit (FOM), 281, 347
Finite difference time domain (FDTD), 13
Finite element (FEM), 13
FMCW, 49, 142, 267, 306–307, 326–331, 404
Foam material, 142, 166
Foster canonical forms, 58
Fourier transform, 47, 178, 181, 404
FR4, 33, 41, 57, 67, 261, 264, 285, 291
Fractal antenna, 5, 23, 254, 260–262,274
Fractal rectangular curve (FRC), 254
Frequency diversity, 82
Frequency-independent antenna, 235, 292
Frequency-reconfigurable antennas, 105
Friis free-space formula, 281
Fringing field, 168
Front-to-back ratio, 165–169, 224, 285, 302
FSS, 18–21, 235–250, 272, 402, 404
Full-wave analysis, 13

G

Gaussian PDF, 83
Geometric optics (GO), 16
Glass-mounted FM/DAB antenna, 312
Global Positioning System (GPS), 1, 316
GLONASS, 23, 287–291, 404
GNSS, 18, 42–44, 287–294, 303, 401–402, 404
GPR antenna, 263, 264, 268
Grating lobes, 132, 141, 172, 201–202, 221, 249, 385
Green's function, 14, 17
Grid array antenna, 318–323, 337–338
GSM850, 52

H

HAC compliance, 86
Half-power beamwidth (HPBW), 8
Half-wave dipoles, 5
Hearing aid compatibility (HAC), 51
Hexagonal printed monopole, 263
High impedance surface (HIS), 239
High Speed Packet Access (HSPA), 51
Hilbert curve, 254, 261
Horizontal polarization, 11, 36, 113–114, 172, 230–231
HSPA+, 78
Hybrid phased array, 217

I

IEEE 802.11a, 55, 302
IEEE Bands, 17
IEEE802.11b, 55
Impedance matching, 28–64, 129, 168–285, 295
Impedance transform, 171
Implantable antennas, 295
Industrial, scientific, medical (ISM), 37
Inline series feed network, 126
Input impedance 46, 199
Integral-equation (IE) solvers, 16
Intermediate frequency (IF), 306
Internet of Things (IoT), 232, 278
Inverted-f antenna, 3, 22, 74, 118
IoT Antenna, 298
Isotropic antenna, 9, 10
ITU bands, 17

K

Koch snowflake, 254–260

L

LAN, 18, 80, 199, 383
L-band, 161, 165, 189, 202–204, 288–289
LHCP, 290, 334, 404
Linear array antenna, 122, 144, 207
Linear polarization, 11, 361
LNA, 216–217, 290, 341–351, 361, 382–389, 402, 404
Local oscillator (LO), 389

Logarithmic spiral antenna, 267
Log-periodic antenna, 5, 244, 254, 260
Long Term Evolution (LTE), 51
Low-frequency automobile antenna, 311
Lowpass filter (LPF), 341
Low-power wide area network (LPWAN), 299
LRR, 30–309, 318–321, 402
LTCC, 129, 274, 341–363, 402
LTE antenna, 66

M

Machine-to-machine (M2M), 298, 379
Magnetic field integral equation (MFIE), 14
Marchand balun, 285
Massive MIMO, 99–100, 367–368, 390–395
Mathematical modeling, 58, 110
Maximum available gain (MAG), 346
Maxwell's equations, 12, 14, 17, 92, 122, 239
Mean effective gain (MEG), 67
Mean time between failure (MTBF), 343
Meander antenna, 54, 280–281, 293, 343
Medical Implant Communication Services (MICS), 295
MEMS, 105, 117, 341
Metamaterials, 236, 274
Method of moments (MoM), 13
Microstrip antenna, 2, 20–50, 122–157, 174–211, 224, 243, 272–375, 397
Microstrip antenna arrays, 124–125, 154
Microstrip comb-line antenna, 320, 337, 402
Microstrip leaky waves, 7
Microstrip line feed, 34, 35
Microstrip patch, 2–13, 27–47, 123–164, 184–205, 223–225, 243–265, 301, 317, 334, 343
Microstrip-to-coplanar stripline (CPS), 285, 301
Microwave communication, 17
Microwave holography, 231
Microwave remote sensing, 20, 161, 179
Microwave sensing and imaging (MSI), 159
Millimeter-wave, 142–156, 325, 371–394
Millimeter-wave antenna array, 142–143, 393
MIMO system, 53, 80, 378–379, 390–392
Missile antennas, 151
MMIC, 129, 249, 334, 341–363, 373, 388, 402
Mobile communication, 6, 20, 30, 51–52,80, 277, 378
Mobile phone compliances, 86
Monopole antenna, 4, 23, 55–59, 74–76, 101, 118, 263
M-rating, 88
MRR, 308–309
Multiband antenna, 54–55, 103, 117,337
Multifrequency SAR, 202, 204
Multilayer feed network, 127
Multipaction, 190–191
Multipath propagation, 177, 334
Multiple-input and multiple-output (MIMO), 21
Multiple-input single-output (MISO), 81
Multistatic radar, 163
Mushroom-like EBG, 239, 401
Mutual coupling, 12–16, 52, 71–82, 106, 123–124, 148, 173, 221, 246–250, 292, 314–317, 382

N

NATO radio bands, 17
Negative Refractive Index (NRI), 236
Null perturbation technique, 129, 183–185, 197
Numerical techniques, 14

O

Ohmic resistance, 8
Operating frequency, 8
Over-the- air (OTA), 51

P

Parametric analysis, 60–61
Partial Discharge (PD), 260
Path loss model, 369
Pattern reconfigurable antenna, 106
Pattern synthesis, 20, 178–181, 197
PCB, 3, 37, 51–64, 70–93,125–126, 336–359, 388
PCS1900, 315
Perfect electric conductor (PEC), 237

Perfect magnetic conductor (PMC), 237
Perfectly matched layer (PML), 249
Personal area network (PAN), 277
Phantom model, 296
Phase shifter, 274, 357, 363, 374, 402
Phased array antenna, 21, 155, 213–234, 362, 393–394
Phased array radar, 213
Photonic bandgap (PBG), 236
Physical optics (PO), 16
Picocells, 368
PIFA, 3–7, 22–23, 52–54, 64–68, 74–76,109–110, 118
PIN diodes, 105–116
Planar array, 20, 121–189, 208, 209, 221–230, 371–386
Planar near-field measurement (PNF), 231
Polarimetric radar, 269
Polarization, 11, 20, 37–49, 82, 103–131, 155–174, 199, 210–234, 303, 361, 394
Power amplifier (PA), 96, 342
Power-added efficiency (PAE), 343
Precipitation Occurrence Sensor System (POSS), 129
Pressure monitoring system (TPMS), 21
Printed antenna, 1–33, 160–173, 235–277, 290–302
Printed antenna arrays, 20, 121–148, 152–156
Printed dipole antenna, 4, 118, 151, 164, 280
Printed inductor antenna, 4
Printed quasi-yagi antenna, 5
Printed wire board (PWB), 54
Probability density function (PDF), 83
Probe feed, 35, 261
Proximity EM coupled microstrip antenna, 224
Proximity-coupled feed, 36
Pseudomorphic HEMT (phemt), 346
Pulse repetition frequency (PRF), 183

Q

Q-factor, 235, 251
Quad polarization, 162
Quarter-wave transformer, 40, 132–134, 171
Quasi-Yagi antennas, 5, 300

R

Radio Frequency Identification (RFID), 4, 278, 285
Radar, 17–30, 121–183, 201–248, 263–269, 305–349, 361, 383
Radar cross-section (RCS), 248
Radiated emission, 93, 95
Radiated susceptibility, 95
Radiation pattern, 9, 47, 63, 74, 157, 309, 397
Radiation pattern reconfigurable antennas, 105
Radiation resistance, 8
Radio frequency (RF), 22
Radio navigation satellite system antennas (RNSS), 287
Rainfall radar, 129, 131, 135, 137
Reader antenna, 283, 284, 303, 402
Reconfigurable antenna, 104, 105, 117
Reflection coefficient, 9, 11, 59, 67, 108, 113, 193, 237, 240, 251, 299, 321, 325, 375, 399
Remote keyless entry service (RKES), 21
RF chokes, 110
RFID antenna, 278–285
RFID read range, 286
RFID tag, 277–283
RHCP, 290, 294, 405
RNSS frequency bands, 288
Rotman lens, 327, 329, 330
RT/duroid 5880, 33
Rumsey's principle, 253

S

SAR antenna, 21–22, 177–185, 190–198
SAR compliance, 87
Schelkunoff method, 178
SCL, 160, 183–197, 405
Sensitivity time control (STC), 177
Shared aperture antenna array, 204
Shark-fin antenna, 313, 315
Short-range radar (SRR), 142
Sidelobes, 11, 155
Sierpinski gasket, 254, 255, 258
Sierpinski gasket fractal antenna, 254, 402
Sierpinski triangles, 254
Signal fading, 80, 83, 99, 289, 378

Sine-wave meander archimedean spiral antenna, 293
Single-input multiple-output (SIMO), 81
Slot antenna, 2, 75, 118, 205, 273–274, 304, 339
Slot-loaded patch, 265
Smart antenna, 80, 366
Smartphone antenna, 20, 77–100
SNR, 82, 122, 178, 290–293, 344, 383, 405
Software-defined radio (SDR), 267
Solid-state power amplifiers (SSPA), 194
SP64T switch, 379
S-parameter, 46, 61
Spatial diversity, 82
Spatial multiplexing, 81, 368, 390
SPDT, 107, 341–362, 402
Specific absorption rate (SAR), 51, 65
Spiral antenna, 23, 235, 244, 260–269, 290–293
Spurious radiation, 28, 32–41, 138–142, 166, 224, 226
Square coaxial feeder network, 193
SRR, 142, 308–309, 318–323, 402
Stacked-patch, 141
Standard anthropomorphic model (SAM), 70
Stepped frequency continuous wave (SFCW), 263
Substrate integrated waveguide (SIW), 151, 269–274, 339
Surface current, 14, 62, 78, 116, 194
Surface current density, 14
Surface waves, 32, 33, 167, 226, 235–246, 270, 301
System validation, 388–389

T

T/R microwave module, 342
Tapered slot antennas, 2
Taylor amplitude taper, 322–325
Telemetry and Telecommand (TTC), 150
TEM, 189, 190, 287, 405
Time diversity, 82
TM_{10} mode, 13, 146
Total isotropic sensitivity (TIS), 53, 71
Total radiated power (TRP), 53
Transceiver, 21, 341–363, 384, 394, 395
Transmission line, 1–12, 28, 32, 55–57, 126–134, 143, 189, 264, 268, 284, 299, 319
Transmission line model, 12, 143
T-rating, 87, 88
Traveling-wave antenna, 235
TWTA, 194

U

UHF, 1, 17–18, 40, 260–286, 302–304, 333, 406
UHF band, 40, 280, 283
UHF Hilbert antenna array, 260
Ultrawideband (UWB), 142, 202, 244
Unidirectional radiation patterns, 2
Uniform EBG, 238
Unlicensed band, 262, 370
Unreinforced PTFE, Cuflon, 33
UWB antenna, 75, 117, 262–267
UWB fractal antenna, 256

V

Vector network analyzer (VNA), 46, 230
Via laser direct structuring (LDS), 6
Vivaldi antenna, 267
Voltage standing-wave ratio (VSWR), 8–11, 40, 46, 61, 75, 131, 178, 184, 187, 206, 218, 263–264, 293, 399, 406

W

Wearable antennas, 277, 296
Wi-Fi, 4, 51–55, 80, 97, 256, 279, 295, 313, 338, 370
Wilkinson power divider, 125, 156, 401
WiMAX, 4, 54, 66, 74, 75, 309, 338
Wireless Access in the Vehicular Environment (WAVE) protocol, 315
Wireless body area network (WBAN), 296, 402
Wireless communication, 1, 20–21, 42, 51–55, 80–81, 103–104, 117, 235, 272–277, 305, 311, 361–383
Wireless communications systems, 1, 5, 277

WLAN, 18–23, 37, 54–61, 73–80, 117–118, 156, 210, 233, 257, 303, 314–318, 383, 401
WLAN antennas, 20, 316
Woodward-Lawson pattern synthesis, 179

X

X-band, 159, 161, 189, 202–209, 222, 223, 300, 349

Y

Yagi-Uda antenna, 5

Recent Titles in the Artech House Antennas and Electromagnetics Analysis Library

Christos Christodoulou, Series Editor

Adaptive Array Measurements in Communications, M. A. Halim

Advanced Computational Electromagnetic Methods and Applications, Wenhua Yu, Wenxing Li, Atef Elsherbeni, Yahya Rahmat-Samii, editors

Advances in Computational Electrodynamics: The Finite-Difference Time-Domain Method, Allen Taflove, editor

Advances in FDTD Computational Electrodynamics: Photonics and Nanotechnology, Allen Taflove, editor; Ardavan Oskooi and Steven G. Johnson, coeditors

Analysis Methods for Electromagnetic Wave Problems, Volume 2, Eikichi Yamashita, editor

Antenna Design for Cognitive Radio, Youssef Tawk, Joseph Costantine, and Christos Christodoulou

Antenna Design with Fiber Optics, A. Kumar

Antenna Engineering Using Physical Optics: Practical CAD Techniques and Software, Leo Diaz and Thomas Milligan

Antennas and Propagation for Body-Centric Wireless Communications, Second Edition, Peter S. Hall and Yang Hao, editors

Antennas and Site Engineering for Mobile Radio Networks, Bruno Delorme

Antennas for Small Mobile Terminals, Kyohei Fujimoto and Koichi Ito, editors

Analysis of Radome-Enclosed Antennas, Second Edition, Dennis J. Kozakoff

Applications of Neural Networks in Electromagnetics, Christos Christodoulou and Michael Georgiopoulos

The Art and Science of Ultrawideband Antennas, Second Edition, Hans G. Schantz

AWAS for Windows Version 2.0: Analysis of Wire Antennas and Scatterers, Antonije R. Djordjević, et al.

Broadband Microstrip Antennas, Girsh Kumar and K. P. Ray

Broadband Patch Antennas, Jean-François Zürcher and Fred E. Gardiol

CAD of Microstrip Antennas for Wireless Applications, Robert A. Sainati

The CG-FFT Method: Application of Signal Processing Techniques to Electromagnetics, Manuel F. Cátedra, et al.

Computational Electrodynamics: The Finite-Difference Time-Domain Method, Third Edition, Allen Taflove and Susan C. Hagness

Design and Applications of Active Integrated Antennas, Mohammad S. Sharawi and Oualid Hammi

Electromagnetics and Antenna Technology, Alan J. Fenn

Electromagnetic Modeling of Composite Metallic and Dielectric Structures, Branko M. Kolundzija and Antonije R. Djordjević

Electromagnetic Waves in Chiral and Bi-Isotropic Media, I. V. Lindell, et al.

Electromagnetics, Microwave Circuit and Antenna Design for Communications Engineering, Peter Russer

Engineering Applications of the Modulated Scatterer Technique, Jean-Charles Bolomey and Fred E. Gardiol

Fast and Efficient Algorithms in Computational Electromagnetics, Weng Cho Chew, et al., editors

Frequency-Agile Antennas for Wireless Communications, Aldo Petosa

Fresnel Zones in Wireless Links, Zone Plate Lenses and Antennas, Hristo D. Hristov

Handbook of Antennas for EMC, Second Edition, Thereza Macnamara with John McAuley

Handbook of Reflector Antennas and Feed Systems, Volume I: Theory and Design of Reflectors, Satish Sharma, Sudhakar Rao, and Lotfollah Shafai, editors

Handbook of Reflector Antennas and Feed Systems, Volume II: Feed Systems, Lotfollah Shafai, Satish Sharma, and Sudhakar Rao, editors

Handbook of Reflector Antennas and Feed Systems, Volume III: Applications of Reflectors, Sudhakar Rao, Lotfollah Shafai, and Satish Sharma, editors

Introduction to Antenna Analysis Using EM Simulators, Hiroaki Kogure, Yoshie Kogure, and James C. Rautio

Iterative and Self-Adaptive Finite-Elements in Electromagnetic Modeling, Magdalena Salazar-Palma, et al.

LONRS: Low-Noise Receiving Systems Performance and Analysis Toolkit, Charles T. Stelzried, Macgregor S. Reid, and Arthur J. Freiley

Measurement of Mobile Antenna Systems, Second Edition, Hiroyuki Arai

Microstrip Antenna Design Handbook, Ramesh Garg, et al.

Microwave and Millimeter-Wave Remote Sensing for Security Applications, Jeffrey A. Nanzer

Mobile Antenna Systems Handbook, Third Edition, Kyohei Fujimoto, editor

Multiband Integrated Antennas for 4G Terminals, David A. Sánchez-Hernández, editor

New Foundations for Applied Electromagnetics: The Spatial Structure of Fields, Said Mikki and Yahia Antar

Noise Temperature Theory and Applications for Deep Space Communications Antenna Systems, Tom Y. Otoshi

Phased Array Antenna Handbook, Third Edition, Robert J. Mailloux

Phased Array Antennas with Optimized Element Patterns, Sergei P. Skobelev

Plasma Antennas, Theodore Anderson

Polarization in Electromagnetic Systems, Second Edition, Warren Stutzman

Practical Microstrip and Printed Antenna Design, Anil Pandey

Printed MIMO Antenna Engineering, Mohammad S. Sharawi

Quick Finite Elements for Electromagnetic Waves, Giuseppe Pelosi, Roberto Coccioli, and Stefano Selleri

Radiowave Propagation and Antennas for Personal Communications, Third Edition, Kazimierz Siwiak

Reflectarray Antennas: Analysis, Design, Fabrication and Measurement, Jafar Shaker, Mohammad Reza Chaharmir, and Jonathan Ethier

RF Coaxial Slot Radiators: Modeling, Measurements, and Applications, Kok Yeow You

Solid Dielectric Horn Antennas, Carlos Salema, Carlos Fernandes, and Rama Kant Jha

Switched Parasitic Antennas for Cellular Communications, David V. Thiel and Stephanie Smith

Ultrawideband Antennas for Microwave Imaging Systems, Tayeb A. Denidni and Gijo Augustin

Ultrawideband Short-Pulse Radio Systems, V. I. Koshelev, Yu. I. Buyanov, and V. P. Belichenko

Understanding Electromagnetic Scattering Using the Moment Method: A Practical Approach, Randy Bancroft

Wavelet Applications in Engineering Electromagnetics, Tapan Sarkar, Magdalena Salazar Palma, and Michael C. Wicks

For further information on these and other Artech House titles, including previously considered out-of-print books now available through our In-Print-Forever® (IPF®) program, contact:

Artech House
685 Canton Street
Norwood, MA 02062
Phone: 781-769-9750
Fax: 781-769-6334
e-mail: artech@artechhouse.com

Artech House
16 Sussex Street
London SW1V HRW UK
Phone: +44 (0)20 7596-8750
Fax: +44 (0)20 7630 0166
e-mail: artech-uk@artechhouse.com

Find us on the World Wide Web at: www.artechhouse.com